NANOSCIENCE EDITOR'S PICK 2021

EDITED BY: Fan Zhang and Zoe Pikramenou
PUBLISHED IN: Frontiers in Chemistry

frontiers Research Topics

ISSN 1664-8714
ISBN 978-2-88966-799-4
DOI 10.3389/978-2-88966-799-4

About Frontiers

Frontiers is more than just an open-access publisher of scholarly articles: it is a pioneering approach to the world of academia, radically improving the way scholarly research is managed. The grand vision of Frontiers is a world where all people have an equal opportunity to seek, share and generate knowledge. Frontiers provides immediate and permanent online open access to all its publications, but this alone is not enough to realize our grand goals.

Frontiers Journal Series

The Frontiers Journal Series is a multi-tier and interdisciplinary set of open-access, online journals, promising a paradigm shift from the current review, selection and dissemination processes in academic publishing. All Frontiers journals are driven by researchers for researchers; therefore, they constitute a service to the scholarly community. At the same time, the Frontiers Journal Series operates on a revolutionary invention, the tiered publishing system, initially addressing specific communities of scholars, and gradually climbing up to broader public understanding, thus serving the interests of the lay society, too.

Dedication to Quality

Each Frontiers article is a landmark of the highest quality, thanks to genuinely collaborative interactions between authors and review editors, who include some of the world's best academicians. Research must be certified by peers before entering a stream of knowledge that may eventually reach the public - and shape society; therefore, Frontiers only applies the most rigorous and unbiased reviews.
Frontiers revolutionizes research publishing by freely delivering the most outstanding research, evaluated with no bias from both the academic and social point of view. By applying the most advanced information technologies, Frontiers is catapulting scholarly publishing into a new generation.

What are Frontiers Research Topics?

Frontiers Research Topics are very popular trademarks of the Frontiers Journals Series: they are collections of at least ten articles, all centered on a particular subject. With their unique mix of varied contributions from Original Research to Review Articles, Frontiers Research Topics unify the most influential researchers, the latest key findings and historical advances in a hot research area! Find out more on how to host your own Frontiers Research Topic or contribute to one as an author by contacting the Frontiers Editorial Office: frontiersin.org/about/contact

NANOSCIENCE EDITOR'S PICK 2021

Topic Editors:
Fan Zhang, Fudan University, China
Zoe Pikramenou, University of Birmingham, United Kingdom

Citation: Zhang, F., Pikramenou, Z., eds. (2021). Nanoscience Editor's Pick 2021. Lausanne: Frontiers Media SA. doi: 10.3389/978-2-88966-799-4

Table of Contents

frontiers in Chemistry

ORIGINAL RESEARCH
published: 09 January 2019
doi: 10.3389/fchem.2018.00647

Development of Photo-Activated ROS-Responsive Nanoplatform as a Dual-Functional Drug Carrier in Combinational Chemo-Photodynamic Therapy

Yu-Cheng Chang[1], *Andrea C. del Valle*[1], *Huan-Pu Yeh*[1], *Yue He*[2]* *and Yu-Fen Huang*[1]*

[1] *Department of Biomedical Engineering and Environmental Sciences, National Tsing Hua University, Hsinchu, Taiwan,*
[2] *Laboratory of Quality & Safety Risk Assessment for Citrus Products, Ministry of Agriculture, Citrus Research Institute, Southwest University, Chongqing, China*

OPEN ACCESS

Edited by:
Huan-Tsung Chang,
National Taiwan University, Taiwan

Reviewed by:
Zhiqin Yuan,
Beijing University of Chemical Technology, China
Gareth Michael Ross,
Naresuan University, Thailand

***Correspondence:**
Yue He
yuehe@cric.cn
Yu-Fen Huang
yufen@mx.nthu.edu.tw

Specialty section:
This article was submitted to Nanoscience, a section of the journal Frontiers in Chemistry

Received: *19 October 2018*
Accepted: *12 December 2018*
Published: *09 January 2019*

Citation:
Chang Y-C, del Valle AC, Yeh H-P, He Y and Huang Y-F (2019) Development of Photo-Activated ROS-Responsive Nanoplatform as a Dual-Functional Drug Carrier in Combinational Chemo-Photodynamic Therapy. Front. Chem. 6:647. doi: 10.3389/fchem.2018.00647

Dual functional drug carrier has been a modern strategy in cancer therapy because it is a platform to elicit additive and synergistic effects through combination therapy. Photo-activated external stimuli such as reactive oxygen species (ROS) also ensure adequate drug delivery in a precise temporal and spatial manner. However, current ROS-responsive drug delivery systems usually require tedious synthetic procedures. A facile one-pot approach has been reported herein, to obtain self-assembled polymeric nanocarriers (NCs) for simultaneous paclitaxel (PTX)- and Rose Bengal (RB)-loading to achieve combined chemo-photodynamic therapy and controlled drug release in responsive to a light-induced ROS stimulus. To encapsulate these hydrophobic and hydrophilic drugs, chitosan (CTS), branched polyethylenimine (*b*PEI) and polyvinyl alcohol (PVA) were selected and fabricated into nanoblended matrices through an oil-in-water emulsion method. The amphiphilic properties of CTS permit simultaneous entrapment of PTX and RB, while the encapsulation efficiency of RB was further improved by increasing the amount of short-chain *b*PEI. During the one-step assembly process, bovine serum albumin (BSA) was also added to condense the cationic tripolymer mixtures into more stable nanocarriers (BNCs). Hyaluronic acid (HA) was subsequently grafted onto the surface of BNCs through electrostatic interaction, leading to the formation of HA-BSA/CTS/PVA/*b*PEI-blended nanocarriers (HBNCs) to achieve an efficient prostate-cancer-cell uptake. Importantly, in response to external light irradiation, HBNCs become destabilized owing to the RB-mediated photodynamic action. It allows an on-demand dual-payload release to evoke a simultaneous photodynamic and chemo treatment for cancer cell eradication. Thus, HBNCs present a new promising approach that exhibits a specific vulnerability to RB-induced photosensitization. The consequent dual-cargo release is also expected to successfully combat cancer through a synergistic anti-tumor effect.

Keywords: combined therapy, photodynamic thearpy, chemotherapy, ROS-responsive, nanocarrier

INTRODUCTION

As an extremely complex disease, cancer causes a serious threat to human health. It involves numerous tempo-spatial changes in cell physiology along with complex signaling pathways, enabling tumor cells to evade programmed cell death, thus making the treatment extremely challenging (Hanahan and Weinberg, 2000, 2011). Despite the fact that a multitude of promising therapeutic strategies has been developed, cancer remains a major cause of morbidity and mortality, as well as the top public health problem worldwide (Kanavos, 2006; Gellad and Provenzale, 2010; Siesling et al., 2015; Hopkins and Secrest, 2018). Chemotherapy, as an orthodox antitumor option in clinic (Chabner and Roberts, 2005; DeVita and Chu, 2008), is however, limited by its serious side effects, poor water-solubility of chemotherapeutic drugs, and intricate multidrug resistance, leading to undesired therapeutic outcomes in cancer treatment (Luqmani, 2005; Szakacs et al., 2006). To address this puzzle, combining chemotherapy with other different forms of treatments has become a promising strategy (Peng et al., 2008; Zhang et al., 2011, 2016; Wang et al., 2013).

Photodynamic therapy (PDT) (Dougherty et al., 1998; Nseyo et al., 1998), a popular, non-invasive cancer treatment, which relies on photosensitizing agents, O_2 and light activation to produce reactive oxygen species (ROS) for destructing cellular components and tumor vasculature, has attracted increasingly attention for combination therapy with chemotherapeutic drugs (Peng et al., 2008; Zhang et al., 2016). In recent years, nanomaterials such as polymer (Peng et al., 2008), liposomes (Ma et al., 2018), metal nanoparticles (Shiao et al., 2014) and hydrogels (Xu et al., 2017) have been considered as potential co-drug delivery vesicles for the simultaneous encapsulation of photosensitizer and chemo drug to realize combination therapy. This co-delivery system not only can lead to additive or synergistic drug interactions to confer a beneficial effect on treatment response, but also can deliver the therapeutic payloads in a spatiotemporally controlled manner in response to the specific endogenous or exogenous stimuli, while protecting premature drug leakage, degradation, or modification in the biological environment. Photoinduced ROS generation, for instance, has been considered as one potential trigger to achieve desired payload release profiles. Many polymer-based nanoparticles are composed of ROS-sensitive segments, which are readily oxidized and disintegrated in ROS-abundant conditions, making them ideal materials for oxidation-dependent drug release (Napoli et al., 2004; Gupta et al., 2012; Yue et al., 2016; Wei et al., 2018). Yue et al. developed a ROS-responsive polymer-based nanoparticle for applications in dual-functional drug delivery (Yue et al., 2016). A block copolymer comprised of triphenylphosphonium and polyethylene glycol (PEG) which was functionalized with thioketal linker-modified camptothecin, can encapsulate the photosensitizer Zinc phthalocyanine by blending the block copolymer with 1, 2-distearoyl-sn-glycero-3-phosphoethanolamine-N-[methoxy (polyethylene glycol)]. The thioketal linker is ROS-responsive and camptothecin can be released upon ROS cleavage, thus successfully realizing combinational chemo-photodynamic therapy. Wei et al. developed another ROS-responsive nanoplatform based on a protoporphyrin-conjugated and dual chemotherapeutics-loaded polymer micelle (Wei et al., 2018). This polymer comprised acetylated-chondroitin sulfate (AC-CS) as the hydrophilic block and protoporphyrin grafted on AC-CS via an ester bond as the hydrophobic block. Under a red light irradiation, ROS generation from protoporphyrin disassociated this polymer, allowing great improvement in therapeutic effect *via* the combination of chemotherapy and PDT.

Although promising, these polymer nanoparticles mentioned above usually require complicated synthetic routes to end up with desirable covalent linkers showing sufficient ROS-responsiveness. An ionically physical cross-linked network that is suitable for an efficient encapsulation of multiple drugs and subsequent cargo release activated by ROS is consequently highly demanded in cancer therapy. Based on the concept outlined in our recent work (Yeh et al., 2018), branched polyethylenimine (*b*PEI) can act as a photoinducible switch for effective cargo trapping and disposal in response to a photooxidation process sensitized by Rose Bengal (RB). A dual-functional stimuli-responsive nanocarrier was therefore designed herein, and obtained by ionically cross-linking of a self-assembled, amphiphilic polymeric network. We expect the entangled coacervate generated in this study, can potentiate the therapeutic efficacy via a concurrent treatment of PDT and chemotherapy. As depicted in **Figure 1**, a one-step oil-in-water emulsion-solvent evaporation method was utilized for nanoparticle fabrication. Paclitaxel (PTX), as a hydrophobic chemotherapeutic agent was dissolved in an oil phase (chloroform) and dispersed into an aqueous phase containing chitosan (CTS), polyvinyl alcohol (PVA), low molecular weight *b*PEI (1.8 kDa) as well as bovine serum albumin (BSA) and RB molecules, followed by emulsification. After the introduction of hyaluronic acid (HA), as a CD44-targeting agent (Peach et al., 1993), the gradual removal of the residual organic solvent by evaporation led to the formation of HA-BSA/CTS/PVA/bPEI-blended nanocarriers (HBNCs). The amphiphilic properties of the cationic tripolymer nanocarriers (NCs) permit effective entrapment of both PTX and negatively charged RB molecules. A more rigid polymeric matrix (BNCs) was also obtained with the inclusion of BSA during the single-pot non-covalent interaction. HA was electrostatically attached onto the BNCs surface, endowing the resultant HBNCs with prostate cancer-targeting capability. When irradiated with the external light, RB-induced ROS generation is expected to diminish the strength of ionic cross-links of HBNCs (Yeh et al., 2018), leading to the simultaneous release of the dual drugs. The dual-functional co-delivery platform can yield a synergistic therapeutic effect by the combination of PDT and chemo-cytotoxicity to improve the therapeutic efficacy in tumor cells.

EXPERIMENTAL SECTION

Chemicals

Poly(vinyl alcohol) (PVA) and branched polyethylenimine (*b*PEI) were purchased from Sigma-Aldrich (St. Louis, MO, USA) and Alfa Aesar (Ward Hill, MA, USA) with Mw of 9,000∼10,000

and 1,800 Da, respectively. The low molecular weight of chitosan was purchased from Polyscience, Inc (Warrington, PA, USA). Bovine serum albumin (BSA) was purchased from Sigma-Aldrich (St. Louis, MO, USA). Chloroform and acetonitrile were purchased from Merck Schuchardt (Hohenbrunn, Germany) and J.T. Baker (Center Valley, PA, USA), respectively. 2′,7′-Dichlorofluorescin diacetate (DCFH-DA), and 4,5,6,7-Tetrachloro-2′,4′,5′,7′-tetraiodofluorescein disodium salt (Rose Bengal) were purchased from Sigma-Aldrich (St. Louis, MO, USA). Paclitaxel was purchased from Seedchem (Vic Melbourne, Australia). Dried sodium hyaluronate (HA) (10–20 K Da) was purchased from Lifecore (Center Valley, PA, USA). Transferrin from human serum and 4',6-diamidino-2-phenylindole (DAPI) were purchased from Invitrogen (Carlsbad, CA, USA). DMEM, fetal bovine serum, and trypan blue were purchased from Grand Island, NY, USA. AlamarBlue was purchased from AbD Serotec (Oxford, OX5 1GE, UK). Sodium chloride, calcium chloride, magnesium chloride, potassium chloride, monopotassium phosphate, sodium phosphate dibasic, L-glucose were purchased from J.T.Baker (Center Valley, PA, USA). Dulbecco's phosphate-buffered saline (DPBS) was purchased from Biosource (Camarillo, CA, USA). Deionized water (18.2 M Ω cm) was used to prepare all of the aqueous solutions. For the cellular experiments, all of the reagents, buffers and culture medium were sterilized by steam autoclave (121°C, 40 min) or filtration (0.22 μm pore size, Millipore), and maintained under a sterile condition.

Cell Lines and Buffers

Tramp-C1 (transgenic adenocarcinoma of the mouse prostate), was obtained from American Type Culture Collection (ATCC, Manassas, VA, USA). Cells were cultured in suspension in DMEM medium supplemented with 10% FBS and 1% penicillin-streptomycin (Invitrogen, Carlsbad, CA, USA) at 37°C in a balanced air humidified incubator with an atmosphere of 5% CO_2. The cells were passaged every 2–3 days. Cell density for every experimental assay was determined using a hemocytometer; purity of cell density was determined by visual microscopic inspection of the nuclei stained by trypan blue.

Synthesis of CTS/PVA/*b*PEI-Blended Nanocarriers (NCs), HA-CTS/PVA/*b*PEI-Blended Nanocarriers (HNCs), BSA/CTS/PVA/*b*PEI-Blended Nanocarriers (BNCs) and HA-BSA/CTS/PVA/*b*PEI-Blended Nanocarriers (HBNCs)

CTS solutions of 5 mg/mL were prepared by dissolving chitosan in 0.5% aqueous acetic acid solution at room temperature with vortexing. PVA (10 k Da), *b*PEI (800 Da) and BSA were dissolved in water, respectively. NCs, HNCs, BNCs, and HBNCs were produced by emulsion/solvent evaporation method. The weight of CTS, PVA, *b*PEI, BSA and HA in different NCs were listed in **Table S1**. Chloroform (1 mL) with PTX was added into a various aqueous solution (4 mL) containing different polymeric mixtures. To form oil-in-water (O/W) emulsion, ultrasonication was then applied to the solution with an ice bath for 10 min using a tip-type Qsonica sonicator (pulse mode with on: 10 sec, off 10 sec, and output of 60). To prepare HNCs and HBNCs, HA solution was added into the responsive solution drop by drop accompany with vortexing (250 rpm/s) until $CHCl_3$ was completely evaporated. After solvent evaporation, the remaining polymer and solvent were removed by centrifugation (40,000 g, 20 min) and washed by phosphate buffer (PB, 10 mM) twice to obtain the purified polymeric NCs, HNCs, BNCs, and HBNCs.

Synthesis of HBNCs With Different Ratio of Polymer

HBNCs were produced by emulsion/solvent evaporation method. The weight ratios of CTS, PVA, *b*PEI and HA to BSA in different samples were listed in **Table 1**. The preparation and purification processes were the same with above.

Preparation of Paclitaxel (PTX) and Rose Bengal (RB)-Loaded Polymeric HBNCs

To fabricate PTX/RB incorporated nanoparticles, as shown in **Scheme S1**, RB (40 μM) was added to the aqueous polymer blend solution (4 mL), followed by the addition of 1 mL chloroform with 100 μM PTX. Then adopt the same synthetic strategy described above to form dual drugs-loaded polymeric HBNCs.

Characterization of the Physiochemical Properties of Polymeric NCs, HNCs, BNCs, and HBNCs

The hydrodynamic diameter and zeta potential values of the constructed polymeric NCs, HNCs, BNCs, and HBNCs were measured by a dynamic light scattering (DLS) instrument (Malvern Instruments, United Kingdom), respectively. The morphology and size were also confirmed by transmission electron microscopy (Hitachi, Tokyo, Japan).

Characterization of the Stability of NCs, HNCs, BNCs, and HBNCs in a Different Environment

NCs, HNCs, BNCs, and HBNCs were dissolved in DPBS and DMEM/FBS (10%), respectively. Make these nanoparticles to equilibrate with the environment for 1 h. The hydrodynamic diameter and zeta potential values of these constructed polymeric nanoparticles were measured by a DLS, respectively.

Characterization of Drugs Loading

The loading efficiency of RB into NCs, HNCs, BNCs, and HBNCs were determined by UV-Vis absorption spectrum measurement (Cary 100, Varian, Palo Alto, CA, USA), respectively. The absorption spectrum of the supernatant, substrate, and the original solution were measured to calculate the loading efficiency. The loading amount of PTX was quantified by high-performance liquid chromatography analysis (HPLC, Eclipse XDB-C18) using an eluent of H_2O/Acetonitrile (1:1) at 1.0 mL/min.

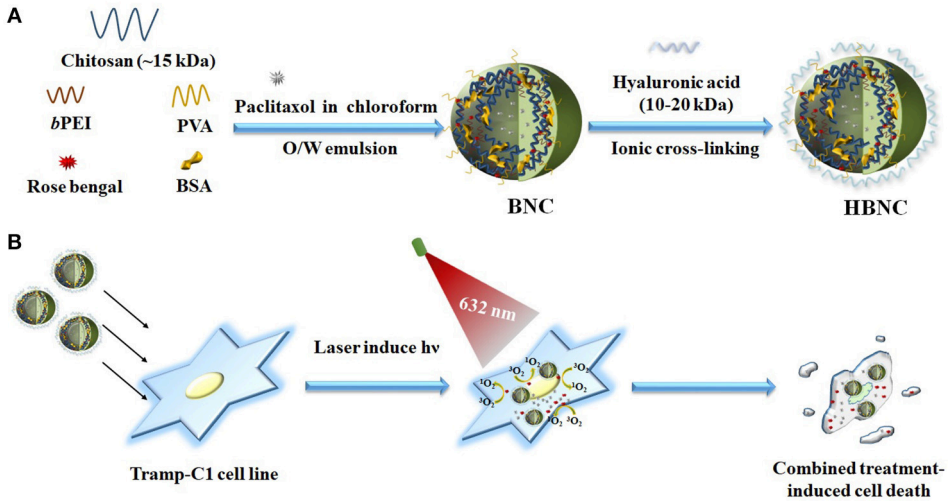

FIGURE 1 | Schematic illustration of fabrication of ROS-responsive polymeric nanocarriers for co-delivery of two different drugs (RB and PTX) through an oil-in-water emulsion method **(A)** and the possible mechanism in targeted PDT and chemotherapy to prostate cancer Tramp-C1 cells **(B)**.

TABLE 1 | Characterization of HBNCs with different constitutes in H_2O.

Sample	CTS (mg/mL)	PVA (mg/mL)	PEI (mg/mL)	BSA (mg/mL)	HA (mg/mL)	Size (d.nm)	Zeta (mv)	PDI	EE_{RB} (%)
(a)	1	0.4	0.4	0.1	0.2	220 ± 14	17.1 ± 2.5	0.18 ± 0.14	60.7 ± 2.7
(b)	0	0.4	1.0	0.1	0.2	246 ± 41	1.8 ± 1.3	0.57 ± 0.06	23.2 ± 4.2
(c)	1	0.04	0.4	0.1	0.2	870 ± 114	18.2 ± 0.6	0.43 ± 0.64	n.d.
(d)	1	0.4	0	0.1	0.2	238 ± 26	26.3 ± 1.4	0.38 ± 0.01	33.1 ± 0.3
(e)	1	0.4	0.4	0.1	0.4	516 ± 112	14.7 ± 0.4	0.31 ± 0.09	n.d.

EE, encapsulation efficiency; n.d., not determined.

Characterization of Stability of Dual Drugs-Loaded HBNCs in a Different Environment

RB/PTX-loaded HBNCs dispersed in DPBS containing 10% FBS was transferred to dialysis vials (3500 Da cutoff; Slide-A-Lyzer™ MINI Dialysis Devices) and dialyzed against DPBS at ambient temperature. The amount of drug remaining inside the dialysis tubing was quantified using a calibration curve at selected time intervals.

ROS Assay

ROS production of RB-loaded polymeric HBNCs and RB/PTX-loaded polymeric HBNCs were measured using the fluorescence probe DCFH-DA, respectively. 1 μL of DCFH-DA (1 mM) was added to RB-loaded HBNCs solution (200 μL) and RB/PTX-loaded HBNCs solution (200 μL) prior to light exposure (632 nm, 15 mW/cm^2) for 30, 60 and 120 min, respectively. The increase in fluorescence signal as a consequence of ROS generation was acquired using Fluorescence spectrophotometer at an excitation wavelength of 488 nm and an emission wavelength of 530 nm. Concurrently, ROS production by free RB (20 μM) was measured under the same condition as the control.

Intracellular ROS were further detected by flow cytometry using DCFH-DA. Briefly, Tramp-C1 cells were seeded at a density of 3 × 10^4 cells per 48-well plate for 12 h attachment. Cells were then incubated with RB, HBNCs, PTX-HBNCs, RB-HBNCs, and RB/PTX-HBNCs in complete culture medium for 6 h and washed twice in DPBS, respectively. Five milli meter DCFH-DA prepared in DPBS was added to the cells for 15 min at 37°C. Following 1 h red light exposure, cells were trypsinized and collected in the tube by centrifugation (1,000 g for 5 min) and resuspended in 200 μL washing buffer [4.5 g/L glucose and 5 mM $MgCl_2$ in DPBS] for flow cytometry analysis (excitation = 488 nm; emission = 530 nm). For each analysis, at least 10,000 events were counted.

Release of Drugs From Polymeric HBNCs Upon Light Irradiation

The release study was conducted as follows: RB/PTX-loaded HBNCs was dispersed in DPBS with 10% fetal bovine serum (pH 7.4) at 37°C. The complex solution (200 μL) was transferred to dialysis vials (3500 Da cutoff; Slide-A-Lyzer™ MINI Dialysis Devices) and dialyzed against DPBS at ambient temperature. After red light or green laser light (15 mW/cm^2) illumination for various periods, buffer solution outside the dialysis vials was then

taken for measurement at selected time intervals. The amount of RB release was quantified from the respective calibration curves. The release amount of PTX was quantified by HPLC.

Intracellular Uptake of RB/PTX-Loaded Polymeric HBNCs

To observe the cellular uptake of RB/PTX-loaded HBNCs, Tramp-C1 cells were seeded at a density of 2×10^4 cells on 10×10 mm sterile cover glasses inserted into 48-well plates for 12 h attachment. Cells were then incubated with RB/PTX-loaded HBNCs in complete culture medium for 6 h and washed twice in DPBS. For microscopic imaging, cells were fixed with 4% paraformaldehyde for 10 min and monitored by confocal laser scanning microscopy (C2 plus Confocal system, Nikon, Tokyo, Japan). Endosomes were stained with transferrin, Alexa Fluor 633 conjugate (200 nM) for 30 min. Nuclei were stained with 4',6-diamidino-2-phenylindole (DAPI, 1.0 μM) for 15 min.

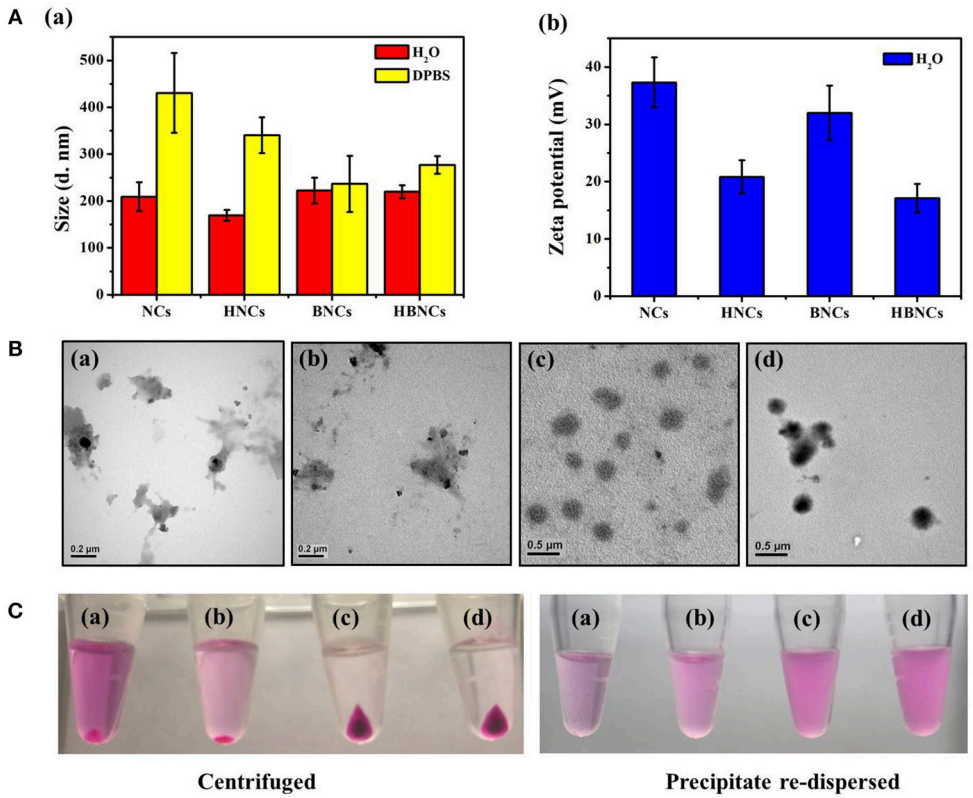

FIGURE 2 | (A) Hydrodynamic size distributions and zeta potentials, **(B)** TEM images and **(C)** digital images of (a) NCs, (b) HNCs, (c) BNCs, and (d) HBNCs, respectively. The RB and PTX concentration added to each sample was fixed at 32 μM and 20 μM, respectively.

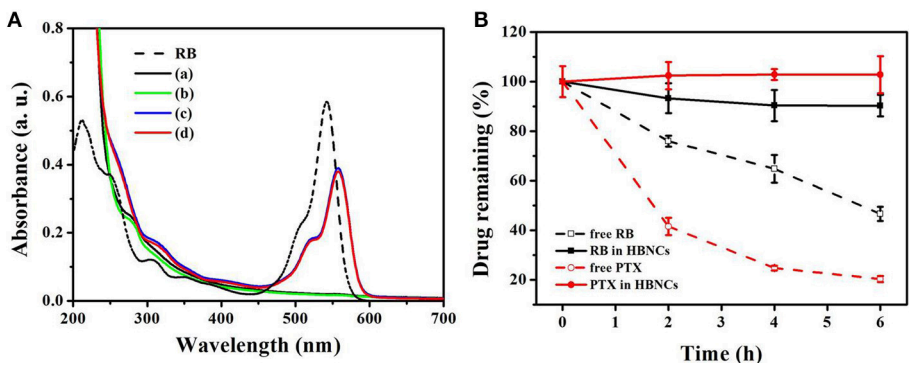

FIGURE 3 | (A) UV-Vis absorption spectra of free RB, (a) HBNCs, (b) PTX-HBNCs, (c) RB-HBNCs, and (d) RB/PTX-HBNCs. **(B)** The leakage of drug molecules from RB/PTX-loaded HBNCs in DPBS (10% FBS). Each sample was dialysis against DPBS for 0–6 h. The amount of drug remaining inside the dialysis tubing was quantified using a calibration curve.

Binding Affinity Analyses

Briefly, Tramp-C1 cells were seeded at a density of 3×10^4 cells per 48-well plate for 12 h attachment. Cells were then incubated with RB/PTX-BNCs and RB/PTX-HBNCs in complete culture medium for 6 h and washed twice in DPBS, respectively. Cells were trypsinized and collected in the tube by centrifugation (1,000 g for 5 min) and resuspended in 200 μL washing buffer for flow cytometry analysis (excitation = 488 nm; emission = 530 nm). For each analysis, at least 10,000 events were counted.

Cytotoxicity Assay

Tramp-C1 cells were seeded at a density of 5×10^3 cells per 96-well plate for 12 h. Cells were washed once and then incubated with HBNCs, RB-HBNCs, PTX-HBNCs, and RB/PTX-HBNCs in complete culture medium for 6 h and washed twice in DPBS, respectively. In PDT studies, treated cells were exposed to a red light (15 mW/cm^2) for 60 min. After irradiation, cells were kept in complete culture medium for an additional 48 h at 37°C in a 5% CO_2 atmosphere. For cytotoxicity measurement, 10 μL Cell Titer reagent (Promega, Madison, WI, USA) was added to each well and incubated for 2 h. The absorption was recorded at 570 nm and 600 nm using a plate reader, respectively. The percentage of cell viability was determined by comparing treated cells with the untreated control.

RESULTS AND DISCUSSION

Synthesis and Characterization of Co-drug (RB and PTX)-loaded Delivery Platform

The size distributions of the resulting NCs, HNCs, BNCs, and HBNCs were characterized by DLS analysis. As depicted in **Figure 2A**, the average hydrodynamic size was found to be approximately 200 nm in ddH_2O, while that of NCs showed the least uniform and polydispersed size distribution. The detection of a less positive value of the zeta potentials in HNCs and HBNCs than that of NCs and BNCs also suggests a successful surface grafting of HA via electrostatic interactions. Upon exposure to a buffer of high salinity (i.e., DPBS), a more pronounced increase of the aggregate size was observed for NCs (430.6 ± 84.9 nm) and HNCs (340.4 ± 38.2 nm) as compared to BNCs (236.7 ± 59.80 nm) and HBNCs (277.0 ± 18.7 nm), respectively. This finding suggests that the incorporation of BSA molecules into the cationic polymer nanoblends may strengthen the entangled network by the inclusion of numerous neighboring contacts (Dubois and Lavignac, 2014). TEM studies on particle morphology (**Figure 2B**) indeed show that NCs and HNCs exhibited a flaky and loosely packed structure, whereas BNCs and HBNCs possess a sphere-like compact structure. Next, the nanoparticles of different constitution were subjected to centrifugation and visualized by digital photographs in **Figure 2C**. Both of the BNCs and HBNCs presented the greatest quantity in the precipitate, indicating that nanoparticles made with BSA attain the highest production yield. The observation of an intense purple color (RB molecules) of the corresponding redispersion also suggests an improved formulation yield along with an enhanced cargo encapsulation efficiency. It is worthy to note that HNCs, as compared with NCs, was also identified to promote the mass production of colloidal nanoparticles. Therefore, the introduction of macroions of opposite charges (e.g., BSA or HA) has proved successful in condensation of flexible polyelectrolytes via multivalent counterion attractions. As expected, BNCs and HBNCs were found to be more stable in serum (10% FBS) containing culture medium than NCs and BNCs (**Figure S1**). No apparent sizes changes were observed for BNCs (214.2 ± 84.9 nm) and HBNCs (209.2 ± 34.3 nm) as compared to NCs (250.8 ± 103.6 nm) and HNCs (304.4 ± 93.5 nm), despite the fact that the surface adsorption of serum proteins may greatly improve the colloidal dispersibility in complex DMEM.

The optimal polymer constitute of the developed nanocarriers was systematically investigated based on the physicochemical properties and drug encapsulation efficiency (EE%). As shown in **Table 1**, sample (**a**) displayed a uniform size distribution of 220 ± 14 nm, a zeta potential of 17.1 ± 2.5 mV and RB loading efficiency of 60.7 ± 2.7%, indicating HBNCs are indeed an effective drug delivery nanoplatform. The nanocarriers without CTS (sample **b**) were also prepared with an elevated concentration of *b*PEI equal to that of CTS in sample **(a)** to ensure successful emulsification. Although sample **(b)** presents an acceptable hydrodynamic size, a remarkable decrease in RB loading (EE % = 23.2 ± 4.2%) was found. This is in accordance with the observation of a significant decline in zeta potential (1.8 ± 1.3 mV), revealing the essential structural function of CTS for skeletal network construction. PVA, a hydrophilic and water-soluble polymer, was chosen as a co-emulsifier to enhance the dispersion capability of the nanocarriers. As expected, nanocarriers prepared with a reduced amount of PVA (taken as 10 times lower) result in large hydrodynamic size (870 ± 114 nm in sample **(c)**). For nanocarriers lacking *b*PEI (sample **(d)**), a relatively low RB loading (33.1 ± 0.3%) was obtained. This result is consistent with the previous findings (Yeh et al., 2018), suggesting that *b*PEI with high charge densities (pK_a = 7.4–8.5) is effective for RB entrapment especially at physiological pH. Afterward, as described above, the positive value of zeta potential becomes less obvious after subjecting the nanocarrier to passivation with HA (**Figure 2A**). However, a twofold increase in the concentration of HA (sample **e**) leads no further change in zeta potential, but an increasing particle size (516 ± 112 nm); HA at a concentration of 0.2 mg/mL was chosen for further studies.

Dual Drugs Loading

Next, the encapsulation of RB and PTX into HBNCs was characterized by ultraviolet-visible (UV-Vis) spectra in **Figure 3A**. The maximum absorption of RB is located at

TABLE 2 | Drug encapsulation efficiency of different nanocarriers.

Sample	EE_{RB} (%)	EE_{PTX} (%)
NCs	40.8 ± 4.9	n.d.
HNCs	49.8 ± 1.4	44.7 ± 6.9
BNCs	60.4 ± 3.3	53.2 ± 7.9
HBNCs	60.7 ± 2.7	55.2 ± 8.9

n.d., not determined.

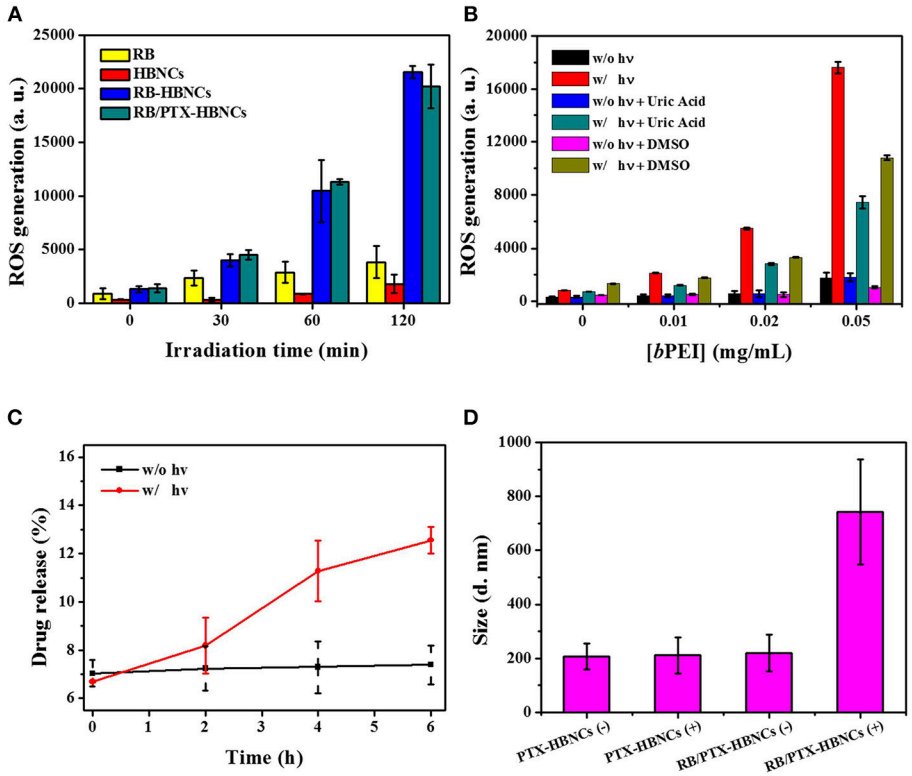

FIGURE 4 | (A) ROS generation analyses of drug-loaded HBNCs in DPBS. DCFH-DA (5 μM) was added to each drug suspension, followed by a red light irradiation (632 nm, 15 mW/cm^2) for 0–120 min. The concentration of RB was fixed at 40 μM. **(B)** ROS generation of RB in the presence of a serial concentration of *b*PEI triggered by 20-min light irradiation. **(C)** Light-induced RB release from co-drug loaded HBNCs in DPBS (10% FBS). An aliquot of sample was exposed to a red light for 0–6 h and the drug released at different time point was collected and measured by centrifugation at 40,000 g for 20 min at 4°C. **(D)** Hydrodynamic size changes of PTX-HBNCs and RB/PTX-HBNCs in DPBS (1% BSA) followed by light exposure (+) or darkness (–) of 6 h.

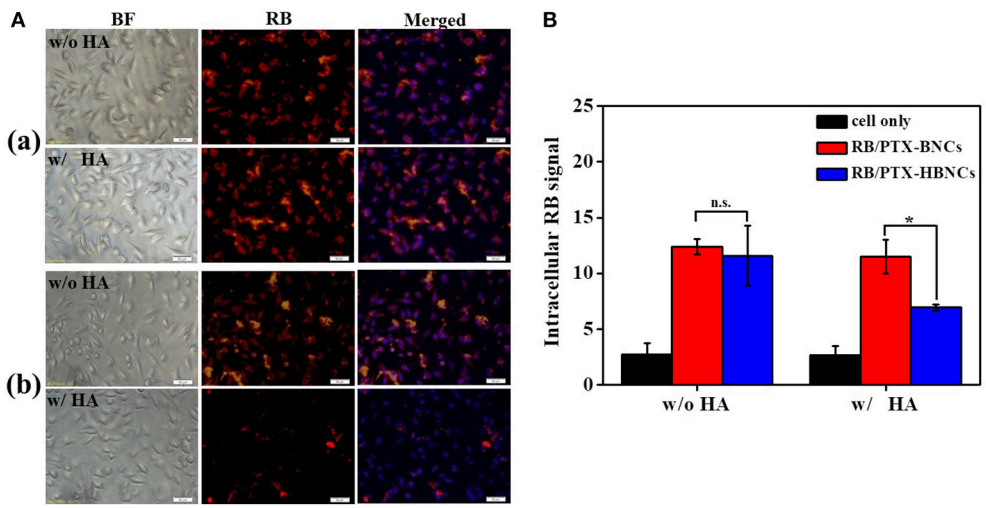

FIGURE 5 | For the competitive binding studies, free HA was employed as a competitor. Both of the (a) (RB/PTX-BNCs)- and (b) (RB/PTX-HBNCs)-treated cells were co-incubated with or without free HA (10 mg/mL) in culture medium for 4 h. Cellular uptake of RB/PTX-HBNCs was analyzed by using **(A)** microscopy and **(B)** flow cytometry. Scale bar: 50 μm. Statistical significance at a level of $^*p < 0.05$.

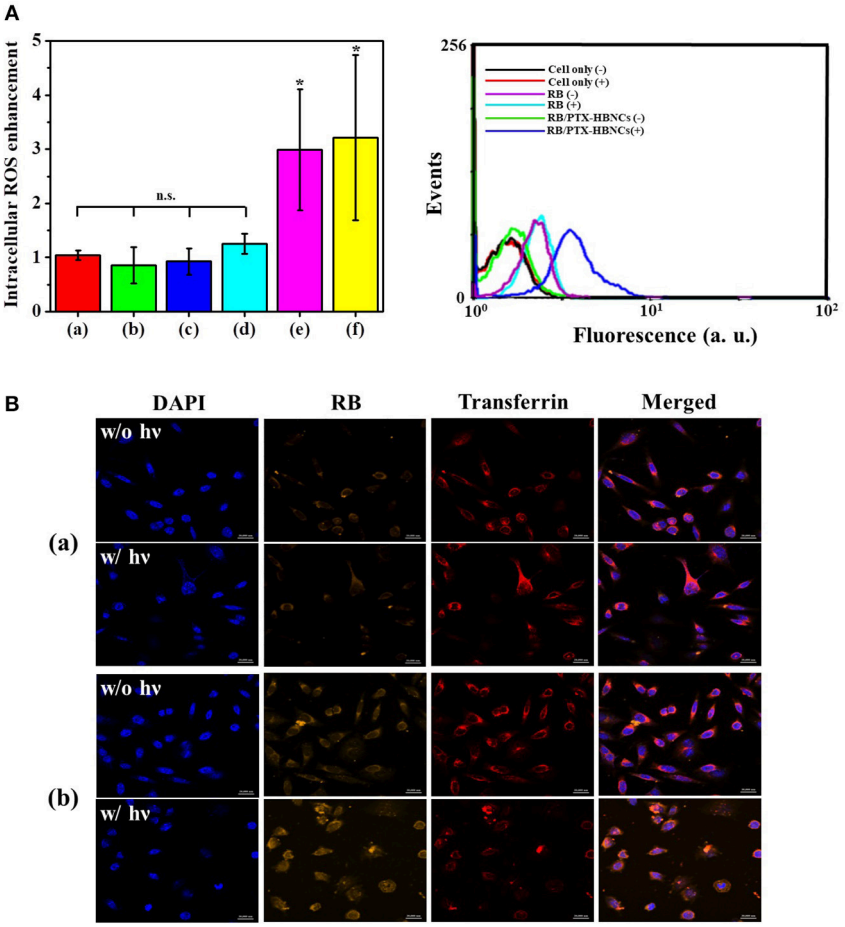

FIGURE 6 | (A) Flow-cytometric analyses of intracellular ROS generation within Tramp-C1 cells of different treatment. The levels of intracellular ROS were determined using DCFH-DA (5 μM). **(Left)** The elevated cytosolic ROS (F/F_0) of (a) non-treated cells, and cells incubated with (b) RB, (c) HBNCs, (d) PTX-HBNCs, (e) RB-HBNCs, (f) RB/PTX-HBNCs, respectively. The DCF signal of irradiated cells (F) was compared to that kept in darkness (F_0). **(Right)** Representative histograms of non-treated cells, RB-treated cells and (RB/PTX-HBNCs)-treated cells in response to a red light irradiation (632 nm, 15 mW/cm^2) for 1 h. **(B)** Confocal microscopic images of Tramp-C1 cells treated with **(a)** RB and **(b)** RB/PTX-HBNCs, respectively. RB concentration was fixed at 20 μM. After incubation in culture medium (10% FBS) for 6 h, cells were exposed to a red light for 1 h. Scale bar: 20 μm. n.s. > 0.05 and $^*p < 0.5$ vs. non-treated cells.

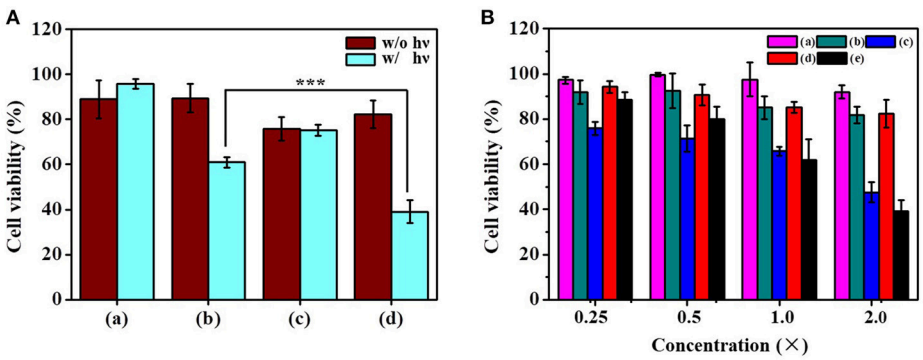

FIGURE 7 | Evaluation of the cytotoxicity of dual-functional drug carriers toward Tramp-C1. **(A)** Cells were incubated with (a) HBNCs, (b) RB-HBNCs, (c) PTX-HBNCs, and (d) RB/PTX-HBNCs in DMEM (10 % FBS) for 6 h, followed by a red light irradiation (1 h). The concentration of RB and PTX was fixed at 40 and 20 μM, respectively. **(B)** Viability of cells treated with serial concentrations of (a) RB (–), (b) RB (+), (c) PTX (–), (d) RB/PTX-HBNCs (–), and (e) RB/PTX-HBNCs (+), respectively. After drug treatment, the survival of cells followed by light exposure (+) was compared to that kept in darkness (–). 1 × of RB and PTX represents 20 μM and 10 μM, respectively. Statistical significance at a level of $^{***}p < 0.001$.

530 nm (dash line). The UV-Vis spectrum of payload-free HBNCs **(a)** shows no characteristic absorption bands in the visible region, while a gradual rise in absorption toward shorter wavelengths, indicating the existence of colloidal structures. The subsequent loading of PTX leads to negligible changes in the UV-Vis absorption of HBNCs **(b)**. Whereas, an obvious peak at 560 nm was observed for RB-loaded HBNCs **(c)**. The red shift related to RB molecules after entrapment, also confirms the contribution of electrostatic effects originating from the surrounding environment (Uppal et al., 2011). No apparent change was observed for co-drug loaded HBNCs **(d)** as compared to RB-loaded HBNCs **(c)**. As no characteristic absorption peak of PTX had been observed in the UV-Vis spectra, HPLC was used for further identification. The encapsulation efficiency (EE, %) of RB and PTX into NCs, HNCs, BNCs, and HBNCs was also compared, respectively. As displayed in **Table 2**, a more pronounced drug loading was revealed for BNCs and HBNCs ($EE_{RB}\%$ = c.a. 61%; $EE_{PTX}\%$ = c.a. 54%) as compared with its non-BSA counterpart ($EE_{RB}\% < 50\%$; $EE_{PTX}\% < 45\%$). The introduction of HA to NCs also displayed an enhanced drug loading. Based on the fact of the abovementioned results (**Figure 2C**), the extent of drug entrapment is well-correlated with the recovery efficacy of the as-prepared nanoparticles.

Premature drug leakage from co-drug loaded HBNCs was further confirmed by dialysis method. RB/PTX-loaded HBNCs dispersed in DPBS containing 10% FBS was dialyzed against DPBS at ambient temperature. Concurrently, free RB and PTX were also processed under the same condition as the control, respectively. As shown in **Figure 3B**, a negligible drug leakage (< 10%) was observed for RB/PTX-loaded HBNCs in 6 h under vigorous stirring, whereas the quantity of free drugs remaining inside the dialysis tubing continued to decline during the same period. This result implies that HBNCs was capable of reducing the non-specific drug action in complex biological conditions until triggered.

Photo-Activated ROS-Responsive Drug Release

In order to investigate the photoresponsive characteristics of the developed nanoplatform, RB/PTX-HBNCs in DPBS were subjected to light illumination with their energy transmitted through a red filter with a center wavelength of 632 nm. ROS generation was studied using an oxidation-sensitive fluorescent probe, 2′,7′-dichlorodihydrofluorescein diacetate (DCFH-DA). As shown in **Figure 4A**, the relative ROS level of free RB under light illumination retained low contents along with the increase in irradiation time. Whereas, RB-HBNCs and RB/PTX-HBNCs produced a significantly increased amount of ROS vs. their cargo-free counterpart upon light exposure. This result may be attributed to the coappearance of type I photosensitization reactions in the presence of tertiary amines (Pan et al., 2011), leading to an enhanced ROS generation. As expected, a considerable increase in ROS production was observed in subjects with elevated *b*PEI concentrations (**Figure 4B**). Upon the respective addition of DMSO (hydroxyl radical scavenger) and uric acid (peroxynitrite scavenger), DCF fluorescence declined significantly with samples consisting of *b*PEI than that of free RB, further suggesting the involvement of additional ROS species. On the other hand, the photosensitization processes of RB in different formulations have also been probed by electron paramagnetic resonance (EPR) spectroscopy. As shown in **Figure S2A**, EPR spectra revealed the formation of TEMP-$^1O_2$ adducts (type II photosensitization) in all three RB samples, followed by light irradiation. However, only the samples equipped with *b*PEI (**Figure S2B**) allowed for the detection of type I products: DMPO-OOH (a_N = 14.2 G, a_H^β = 11.4 G, and $a_H^{\gamma 1}$ = 1.2 G) and DMPO-OH adducts ($a_N = a_H^\beta$ = 14.9 G) (type I photosensitization) (Janzen et al., 1987; Zhao et al., 2001). These results further confirm that RB-HBNCs can act as dual type I/II photosensitizer for improved photodynamic action under light exposure.

Next, the on-demand drug release behavior was investigated for the co-drug loaded HBNCs in responsive to the light-induced photosensitization process. As exhibited in **Figure 4C**, the cumulative release of RB was gradually increased over an extended irradiation period, as the non-irradiated counterpart remained almost at the original level. This result is consistent with our previous finding (Yeh et al., 2018), showing a specific RB release of HBNCs is remotely controlled. The observation of a blue shift in the spectrum feature of RB also confirmed an appreciable decrease in the ionic strength within the network of RB/PTX-HBNCs upon light illumination (**Figure S3**). Moreover, the irradiated nanocarriers also allowed a concurrent release of additional guest cargos; an approximately 30% PTX release was detected from RB/PTX-HBNCs after 6 h of light exposure, whereas the drug leakage was negligible in the dark. It is worth noting that the colloidal stability of RB/PTX-HBNCs dramatically decreased and hence, *in situ* coagulation was found during the laser irradiation process., A remarkable increase in hydrodynamic size was detected for RB/PTX-HBNCs vs. PTX-HBNCs followed by light irradiation (**Figure 4D**), further suggesting the active role of RB in mediating the light activated ROS generation for structural destability and the subsequent payload release.

CD44-Targeted Cellular Uptake

After the detailed characterization of physiochemical properties of the dual drug-loaded HBNCs, their interaction with prostate cancer Tramp-C1 cells was investigated using fluorescence microscopy. As shown in **Figure S4**, an obvious RB signal was detected in cells treated with RB-HBNCs and RB/PTX-HBNCs as compared with those exposed to free RB and PTX-HBNCs, respectively. This finding suggests that HBNCs offered a superior cellular uptake efficiency than that of free drugs. Moreover, competitive binding assays of HBNCs targeting Tramp-C1 cells were also performed using excess HA (**Figure 5**). The fluorescence signal from cells treated with RB/PTX-HBNCs decreased dramatically when they were co-incubated with free HA ($p < 0.5$). Whereas, (RB/PTX-BNCs)-exposed cells exhibited a negligible change in fluorescence ($p > 0.5$). It is considered

that the cellular uptake of HBNCs by Tramp-C1 cells was accomplished by the specific recognition of HA with CD44 (Luo et al., 2000), showing great promise in targeted drug delivery. By contrast, BNCs without HA-surface grafting provided a strong positive charge (32.0 ± 4.8 mV in **Figure 2A-b**). It may eventually lead to undesirable side effects due to a high extent of non-specific cell interactions.

Intracellular ROS Generation and Drug Delivery

Next, the intracellular PDT action mediated by RB/PTX-HBNCs was studied using DCFH-DA. As shown in **Figure 6A**, after 1 h of irradiation, the relative ROS level in cells treated with RB-HBNCs (column **e**) and RB/PTX-HBNCs (column **f**) was significantly increased ($p < 0.5$). Conversely, no significant difference in ROS production was observed for cells exposed to their RB-free counterparts (column **c** and **d**, respectively). RB-treated cells (column **b**) also exhibited negligible fluorescence changes after light illumination. Collectively, it can be concluded that HBNCs displayed both enhanced cellular uptake and improved PDT performance. A detailed study on the intracellular payload release and drug distribution was further investigated using confocal microscopy (**Figure 6B**). After 6 h of incubation, a distinct RB fluorescence was observed within the endolysosomal compartment, colocalized with fluorescent transferrin (transferrin-Alexa633) in the (RB/PTX-HBNCs)-treated cells. When exposed to the red light, the fluorescence emitted from RB molecules was significantly increased and spread diffusely. By contrast, negligible RB fluorescence changes were observed for cells treated with free RB under the same irradiation condition. This result confirmed that HBNCs which served to deliver dual drugs to the targeted cancer cells are effective for controlled payload release in response to the photodynamic reaction.

In vitro Combination Therapy

To assess the anticancer activity of the dual functional drug carrier, Tramp-C1 cells were treated with RB/PTX-HBNCs and subjected to MTT assay for cell viability determination. As shown in **Figure 7A**, a minute toxic effect (< 18 ± 2%) was found in treated cells kept in the dark. However, a dramatic increase in cell death up to 61 ± 5% was observed when exposed to red light. This finding confirms the involvement of a phototoxic event that can be activated by an external trigger. In addition, the cytotoxic effects of RB-HBNCs and PTX-HBNCs were also assessed individually at equal drug concentration. PTX-HBNCs induced an approximately 24% decrease of cell viability while showing no response to photostimulation. In contrast, a viability reduction was detected, but to a lesser extent in (RB-HBNCs)-treated cells after light exposure. This finding indicates that the current approach is promising for on-demand dual-payload release, enabling simultaneous photodynamic and chemo actions for successful eradication of cancer cells. No cellular damage had been observed for cells treated with payload-free HBNCs, further suggesting a good biocompatibility of the developed nanocarrier. Moreover, the relative viability of cells incubated with free RB and light treatment was also examined. It was observed that <18 ± 6% of Tramp-C1 cells were killed at the maximum concentration tested (**Figure 7B**). This result correlates well with the previous finding (Yeh et al., 2018), showing that free RB is cell impermeant and thus of limited use *in vitro*. As for free PTX, an appreciable decrease in cell viability was detected in treated cells, owing to an adequate availability of small hydrophobic drugs toward cancer cells. However, PTX lacks sufficient tumor selectivity may potentiate the adverse side effects, leading to unwanted outcomes especially at high medication doses (Untch et al., 2016; Li et al., 2017). As compared to free drugs, RB/PTX-HBNCs showed a sufficient efficacy but a photo-triggerable anticancer activity is highly promising for targeted delivery of combined treatment in modern tumor therapy.

CONCLUSIONS

We successfully developed a new ROS responsive drug delivery platform based on tripolymer mixtures (CTS, *b*PEI, PVA) for co-delivering photodynamic drugs and chemotherapeutics, which effectively combines both PDT and chemotherapy to improve the therapeutic efficacy in tumor cells. BSA was used to condense cationic tripolymer mixtures into stable nanocarriers. This drug carrier can also be readily functionalized with targeting moieties (HA, CD44 receptor), not only for enhancing the specific internalization by tumor cells, but also lowering down carrier's zeta potential for suitable application in biological systems. Notably, the designed ROS-responsive nanocarrier appeared to on-demand dual drugs release and delivery. Therefore, an improved therapeutic efficacy has been successfully demonstrated *in vitro* through combination therapy. With the advantages of easy synthesis, good biocompatibility, high specific binding affinity, and controllable capability of drug release, this nanocarrier will facilitate the development of next-generation cancer therapy in the future.

AUTHOR CONTRIBUTIONS

Y-CC design and perform experiments. AdV complete the experiments. H-PY synthesis of nanocarriers. YH write the paper. Y-FH make important changes to the paper and approve the final paper to be published.

FUNDING

We appreciate financial support from the Ministry of Science and Technology (106-2113-M-007-008-, 106-2627-M-019-001-, 107-2113-M-007-022-, 107-2627-M-007-007-) of Taiwan, ROC and the National Natural Science Foundation of China (21405125).

SUPPLEMENTARY MATERIAL

The Supplementary Material for this article can be found online at: https://www.frontiersin.org/articles/10.3389/fchem.2018.00647/full#supplementary-material

REFERENCES

Chabner, B. A., and Roberts, T. G. (2005). Timeline - chemotherapy and the war on cancer. *Nat. Rev. Cancer* 5, 65–72. doi: 10.1038/nrc1529

DeVita, V. T., and Chu, E. (2008). A history of cancer chemotherapy. *Cancer Res.* 68, 8643–8653. doi: 10.1158/0008-5472.Can-07-6611

Dougherty, T. J., Gomer, C. J., Henderson, B. W., Jori, G., Kessel, D., Korbelik, M., et al. (1998). Photodynamic therapy. *J. Nat. Cancer Inst.* 90, 889–905. doi: 10.1093/jnci/90.12.889

Dubois, J. L. N., and Lavignac, N. (2014). Poly(amidoamine)s synthesis, characterisation and interaction with BSA. *Polymer Chem.* 5, 1586–1592. doi: 10.1039/c3py01121f

Gellad, Z. F., and Provenzale, D. (2010). Colorectal cancer: national and international perspective on the burden of disease and public health impact. *Gastroenterology* 138, 2177–2190. doi: 10.1053/j.gastro.2010.01.056

Gupta, M. K., Meyer, T. A., Nelson, C. E., and Duvall, C. L. (2012). Poly(PS-b-DMA) micelles for reactive oxygen species triggered drug release. *J. Control. Release* 162, 591–598. doi: 10.1016/j.jconrel.2012.07.042

Hanahan, D., and Weinberg, R. A. (2000). The hallmarks of cancer. *Cell* 100, 57–70. doi: 10.1016/S0092-8674(00)81683-9

Hanahan, D., and Weinberg, R. A. (2011). Hallmarks of cancer: the next generation. *Cell* 144, 646–674. doi: 10.1016/j.cell.2011.02.013

Hopkins, Z. H., and Secrest, A. M. (2018). Public health implications of google searches for sunscreen, sunburn, skin cancer, and melanoma in the United States. *Am. J. Health Promotion*. doi: 10.1177/089011711881175. [Epub ahead of print].

Janzen, E. G., Jandrisits, L. T., and Barber, D. L. (1987). Studies on the origin of the hydroxyl spin adduct of DMPO produced from the stimulation of neutrophils by phorbol-12-myristate-13-acetate. *Free Rad. Res. Commun.* 4, 115–123.

Kanavos, P. (2006). The rising burden of cancer in the developing world. *Ann. Oncol.* 17, 15–23. doi: 10.1093/annonc/mdl983

Li, F., Lu, J., Liu, J., Liang, C., Wang, M., Wang, L., et al. (2017). A water-soluble nucleolin aptamer-paclitaxel conjugate for tumor-specific targeting in ovarian cancer. *Nat. Commun.* 8:1390. doi: 10.1038/s41467-017-01565-6

Luo, Y., Ziebell, M. R., and Prestwich, G. D. (2000). A hyaluronic acid-taxol antitumor bioconjugate targeted to cancer cells. *Biomacromolecules* 1, 208–218. doi: 10.1021/bm000283n

Luqmani, Y. A. (2005). Mechanisms of drug resistance in cancer chemotherapy. *Med. Prin. Pract.* 14, 35–48. doi: 10.1159/000086183

Ma, J., Wu, H., Li, Y., Liu, Z., Liu, G., Guo, Y., et al. (2018). Novel core-interlayer-shell DOX/ZnPc Co-loaded MSNs@pH-Sensitive CaP@PEGylated liposome for enhanced synergetic chemo-photodynamic therapy. *Pharmaceutical Res.* 35:57. doi: 10.1007/s11095-017-2295-z

Napoli, A., Valentini, M., Tirelli, N., Muller, M., and Hubbell, J. A. (2004). Oxidation-responsive polymeric vesicles. *Nat. Mater.* 3, 183–189. doi: 10.1038/nmat1081

Nseyo, U. O., DeHaven, J., Dougherty, T. J., Potter, W. R., Merrill, D. L., Lundahl, S. L., et al. (1998). Photodynamic therapy (PDT) in the treatment of patients with resistant superficial bladder cancer: a long term experience. *J. Clin. Laser Med. Surg.* 16, 61–68.

Pan, Y., Kee, C. W., Chen, L., and Tan, C.-H. (2011). Dehydrogenative coupling reactions catalysed by Rose Bengal using visible light irradiation. *Green Chem.* 13, 2682–2685. doi: 10.1039/C1GC15489C

Peach, R. J., Hollenbaugh, D., Stamenkovic, I., and Aruffo, A. (1993). Identification of hyaluronic-acid binding-sites in the extracellular domain Of CD44. *J. Cell Biol.* 122, 257–264. doi: 10.1083/jcb.122.1.257

Peng, C.-L., Shieh, M.-J., Tsai, M.-H., Chang, C.-C., and Lai, P.-S. (2008). Self-assembled star-shaped chlorin-core poly(ε-caprolactone)–poly(ethylene glycol) diblock copolymer micelles for dual chemo-photodynamic therapies. *Biomaterials* 29, 3599–3608. doi: 10.1016/j.biomaterials.2008.05.018

Shiao, Y. S., Chiu, H. H., Wu, P. H., and Huang, Y. F. (2014). Aptamer-functionalized gold nanoparticles as photoresponsive nanoplatform for co-drug delivery. *ACS Appl. Mater. Interfaces* 6, 21832–21841. doi: 10.1021/am5026243

Siesling, S., Louwman, W. J., Kwast, A., van den Hurk, C., O'Callaghan, M., Rosso, S., et al. (2015). Uses of cancer registries for public health and clinical research in Europe: results of the European Network of Cancer Registries survey among 161 population-based cancer registries during 2010-2012. *Eur. J. Cancer* 51, 1039–1049. doi: 10.1016/j.ejca.2014.07.016

Szakacs, G., Paterson, J. K., Ludwig, J. A., Booth-Genthe, C., and Gottesman, M. M. (2006). Targeting multidrug resistance in cancer. *Nat. Rev. Drug Discov.* 5, 219–234. doi: 10.1038/nrd1984

Untch, M., Jackisch, C., Schneeweiss, A., Conrad, B., Aktas, B., Denkert, C., et al. (2016). Nab-paclitaxel versus solvent-based paclitaxel in neoadjuvant chemotherapy for early breast cancer (GeparSepto-GBG 69): a randomised, phase 3 trial. *Lancet Oncol.* 17, 345–356. doi: 10.1016/s1470-2045(15)00542-2

Uppal, A., Jain, B., Gupta, P. K., and Das, K. (2011). Photodynamic action of rose bengal silica nanoparticle complex on breast and oral cancer cell lines. *Photochem. Photobiol.* 87, 1146–1151. doi: 10.1111/j.1751-1097.2011.00967.x

Wang, Y., Wang, K., Zhao, J., Liu, X., Bu, J., Yan, X., et al. (2013). Multifunctional mesoporous silica-coated graphene nanosheet used for chemo-photothermal synergistic targeted therapy of glioma. *J. Am. Chem. Soc.* 135, 4799–4804. doi: 10.1021/ja312221g

Wei, X., Liu, L., Guo, X., Wang, Y., Zhao, J., and Zhou, S. (2018). Light-activated ros-responsive nanoplatform codelivering apatinib and doxorubicin for enhanced chemo-photodynamic therapy of multidrug-resistant tumors. *ACS Appl. Mater. Interfaces* 10, 17672–17684. doi: 10.1021/acsami.8b04163

Xu, L., Zhao, M., Yang, Y., Liang, Y., Sun, C., Gao, W., et al. (2017). A reactive oxygen species (ROS)-responsive low molecular weight gel co-loaded with doxorubicin and Zn(II) phthalocyanine tetrasulfonic acid for combined chemo-photodynamic therapy. *J. Mater. Chem. B* 5, 9157–9164. doi: 10.1039/c7tb02359f

Yeh, H. P., Del Valle, A. C., Syu, M. C., Qian, Y., Chang, Y. C., and Huang, Y. F. (2018). A new photosensitized oxidation-responsive nanoplatform for controlled drug release and photodynamic cancer therapy. *ACS Appl. Mater. Interfaces* 10, 21160–21172. doi: 10.1021/acsami.8b05205

Yue, C.X., Yang, Y.M., Zhang, C.L., Alfranca, G., Cheng, S.L., Ma, L.J., et al. (2016). ROS-responsive mitochondria-targeting blended nanoparticles: chemo-and photodynamic synergistic therapy for lung cancer with on-demand drug release upon irradiation with a single light source. *Theranostics* 6, 2352–2366. doi: 10.7150/thno.15433

Zhang, W., Guo, Z., Huang, D., Liu, Z., Guo, X., and Zhong, H. (2011). Synergistic effect of chemo-photothermal therapy using PEGylated graphene oxide. *Biomaterials* 32, 8555–8561. doi: 10.1016/j.biomaterials.2011.07.071

Zhang, W., Shen, J. L., Su, H., Mu, G., Sun, J. H., Tan, C. P., et al. (2016). Co-delivery of cisplatin prodrug and chlorin e6 by mesoporous silica nanoparticles for chemo-photodynamic combination therapy to combat drug resistance. *ACS Appl. Mater. Inter.* 8, 13332–13340. doi: 10.1021/acsami.6b03881

Zhao, H. T., Joseph, J., Zhang, H., Karoui, H., and Kalyanaraman, B. (2001). Synthesis and biochemical applications of a solid cyclic nitrone spin trap: a relatively superior trap for detecting superoxide anions and glutathiyl radicals. *Free Radical Biol. Med.* 31, 599–606. doi: 10.1016/s0891-5849(01)00619-0

Conflict of Interest Statement: The authors declare that the research was conducted in the absence of any commercial or financial relationships that could be construed as a potential conflict of interest.

frontiers in Chemistry

REVIEW
published: 19 March 2019
doi: 10.3389/fchem.2019.00131

Progress in Electrocatalytic Hydrogen Evolution Based on Monolayer Molybdenum Disulfide

Chuan Wang[1], Jinzhao Huang[1], Jiayue Chen[1], Zhongxin Xi[1] and Xiaolong Deng[2]**

[1] School of Physics and Technology, University of Jinan, Jinan, China, [2] School of Mathematics and Physics, Anhui University of Technology, Ma'anshan, China

Energy and environmental issues raise higher demands on the development of a sustainable energy system, and the electrocatalytic hydrogen evolution is one of the most important ways to realize this goal. Two-dimensional (2D) materials represented by molybdenum disulfide (MoS_2) have been widely investigated as an efficient electrocatalyst for the hydrogen evolution. However, there are still some shortcomings to restrict the efficiency of MoS_2 electrocatalyst, such as the limited numbers of active sites, lower intrinsic catalytic activity and poor interlayer conductivity. In this review, the application of monolayer MoS_2 and its composites with 0D, 1D, and 2D nanomaterials in the electrocatalytic hydrogen evolution were discussed. On the basis of optimizing the composition and structure, the numbers of active sites, intrinsic catalytic activity, and interlayer conductivity could be significantly enhanced. In the future, the study would focus on the structure, active site, and interface characteristics, as well as the structure-activity relationship and synergetic effect. Then, the enhanced electrocatalytic activity of monolayer MoS_2 can be achieved at the macro, nano and atomic levels, respectively. This review provides a new idea for the structural design of two-dimensional electrocatalytic materials. Meanwhile, it is of great significance to promote the study of the structure-activity relationship and mechanism in catalytic reactions.

Keywords: monolayer MoS_2, electrocatalytic hydrogen evolution, active sites, intrinsic catalysis, composite structure

OPEN ACCESS

Edited by:
Tianyou Zhai,
Huazhong University of Science and Technology, China

Reviewed by:
Xu Peng,
Hubei University, China
Shichun Mu,
Wuhan University of Technology, China

***Correspondence:**
Jinzhao Huang
ss_huangjinzhao@ujn.edu.cn
Xiaolong Deng
dengxl84@ahut.edu.cn

Specialty section:
This article was submitted to Nanoscience, a section of the journal Frontiers in Chemistry

Received: *16 January 2019*
Accepted: *20 February 2019*
Published: *19 March 2019*

Citation:
Wang C, Huang J, Chen J, Xi Z and Deng X (2019) Progress in Electrocatalytic Hydrogen Evolution Based on Monolayer Molybdenum Disulfide. Front. Chem. 7:131. doi: 10.3389/fchem.2019.00131

INTRODUCTION

The continuous growth of the population and the development of the industrialization process have accelerated the consumption of fossil energy, and brought serious environmental problems. Therefore, the development of sustainable energy system is one of the most important challenges today (Wang and Mi, 2017; Chi and Yu, 2018). At present, a promising method is to produce renewable energy through the electrochemically catalytic reaction, which converts the common materials, such as water, carbon dioxide, and nitrogen, into the high-energy carriers (hydrogen, oxygen, hydrocarbons, ammonia, etc.). After years of research and practice, many important advances have been made in electrochemical energy conversion (Gu et al., 2018; Mao et al., 2018; Xiong J. et al., 2018). Among them, hydrogen energy is considered as the most powerful candidate to alternate fossil energy due to its clean, renewable, and environmentally friendly properties and high energy density (Lin et al., 2017; Zhang S. et al., 2017). Among various methods of hydrogen energy production, electrocatalytic water splitting has attracted tremendous attention

because of its advantages of low cost, non-pollution and high efficiency (Wang et al., 2016). Moreover, the electrocatalytic cathode in this method is the key to determine the efficiency of water decomposition. So far, the Pt cathode possessing the near zero overpotential is considered to be the most effective catalytic cathode. However, it is difficult to be practically applied or industrialized due to its high cost and scarce resource (Eftekhari, 2017; Hou et al., 2017). Therefore, seeking for low-cost, abundant, high efficient, and environmentally friendly catalytic cathode materials has become a research hotspot. In the view of this point, many materials have been extensively explored, such as carbides, nitrides, sulfides, selenides, phosphides, and Mo-based non-noble metal electrocatalysts (Xie et al., 2014; Pu et al., 2016a,b,c, 2017, 2018; Voiry et al., 2016; Wei et al., 2016; Xie and Xie, 2016; Kou et al., 2017, 2018a,b; Jin et al., 2018). Among these materials, molybdenum disulfide (MoS_2) has attracted much more attention due to its low cost, high catalytic activity, high stability, large in-plane carrier mobility and good mechanical properties (Tan et al., 2017; Li et al., 2018; Wang et al., 2018a). Studies have shown that monolayer MoS_2 has higher electrocatalytic activity for hydrogen evolution. However, there are still some shortcomings, such as the limited numbers of active sites, lower intrinsic catalytic activity and poor interlayer conductivity. In order to further improve the electrocatalytic activity of monolayer MoS_2, researchers usually composite them with other materials. In this paper, the composite of monolayer MoS_2 with 0D, 1D, and 2D materials and its application in electrocatalytic hydrogen evolution are reviewed in order to provide guidance for related research. At present, there are two kinds of methods for preparing monolayer MoS_2. The first method is top-down approach, including mechanical stripping (Li et al., 2012), ion intercalation (Nurdiwijayanto et al., 2018) and liquid phase stripping (Zhao et al., 2016), and the second one is bottom-up approach, including chemical vapor deposition(CVD) (Liu et al., 2018) and wet chemical stripping (Zeng et al., 2017). The development strategy of sustainable energy pattern and catalyst based on the electrocatalysis are shown in **Figure 1**.

STRATEGIES FOR ELECTROCATALYTIC HYDROGEN EVOLUTION

As the electrocatalyst plays an important role in improving conversion efficiency in energy conversion process, the research of electrocatalyst is a crucial part in these conversion technologies. Up to now, the electrocatalysts suffer from the lack of types and low efficiency. What's more, the high expense leads them difficult to be practically used on a large scale. Many efforts have been made to solve these problems. For example, in order to improve the electrocatalytic activity, three strategies are usually proposed: one is to increase the number of active sites (from the view of the "quantity" aspect); the other is to increase the intrinsic activity of active sites (which belongs to the "quality" aspect); the third is to improve the conductivity of electrocatalysts by forming composites. These strategies are not mutually exclusive, but can be mutually complementary to improve the activity of catalysts simultaneously (Seh et al., 2017; Tang C. et al., 2018).

Two-dimensional materials such as MoS_2 have been extensively studied in the electrocatalytic hydrogen evolution due to their promising potential application prospect. However, there is still a big gap compared with Pt catalyst. Therefore, great efforts have been made to improve the electrocatalytic activity of MoS_2, including phase transformation (Tang and Jiang, 2016; Jiao et al., 2018; Wang J. et al., 2018), defect engineering (Xie et al., 2013a, 2017, 2019; Xie and Yi, 2015), nanocrystallization (Yun et al., 2017), doping (Xie et al., 2013b, 2016; Sun et al., 2014, 2018; Xiong Q. et al., 2018), modification (Benson et al., 2017; Wang Q. et al., 2018) and compounding (Jayabal et al., 2017; Zhai et al., 2018), etc.

The bulk phase MoS_2 is inert for the electrocatalytic hydrogen evolution, and the free energy of hydrogen adsorption on the base surface of MoS_2 is 1.92 eV. However, the theoretical results show that the ΔG_H of Mo (1010) is 0.08 eV at 50% hydrogen coverage, which is close to the optimum value ($\approx$0 eV) and exhibits the good electrocatalytic activity (Hinnemann et al., 2005). In addition, this propose is confirmed by the experimental results (Jaramillo et al., 2007). Theoretical and experimental studies have proved that the edge of MoS_2 is active. Therefore, exposing more edge sites of MoS_2 is an important method to enhance its electrocatalytic activity. Thus, the way to improve the electrocatalytic performance is classified to increase the "quantity" of active sites (Zhang J. et al., 2017). The electrocatalytic hydrogen evolution reaction is a two-electron transfer process, and the reaction rate depends largely on ΔG_H. If the bonding between H_2 and the surface is too weak, the adsorption (Volmer) step will limit the overall reaction rate; if the bonding is too strong, the desorption (Heyrovsky/Tafel) step will limit the reaction rate (Parsons, 1958; Wang et al., 2018b). Therefore, a highly active catalyst should have neither too strong nor too weak bonding intermediates. According to these points, by controlling the surface/interface properties of MoS_2, the surface electronic properties, surface adsorption behavior and hydrogen evolution reaction path can be optimized, which can promote the kinetic process of the electrocatalytic hydrogen evolution and enhance the intrinsic catalytic ability (Otyepková et al., 2017; Chen et al., 2018). The research in this field is to improve the electrocatalytic activity by optimizing the "quality" of the active site. It has been proved that the transport of electrons between MoS_2 layers needs to overcome certain barriers. The electron transport is dominated by the jump transport mode leading to the low transport efficiency, which limits the improvement of their electrocatalytic activities. So, the acceleration of the electron transport between layers is also an effective way to enhance the catalytic activity (Yu et al., 2013).

ELECTROCATALYTIC HYDROGEN EVOLUTION

Monolayer MoS_2

Monolayer MoS_2 exhibits relatively high electrocatalytic activity due to the exposure of more active sites, which can enhance

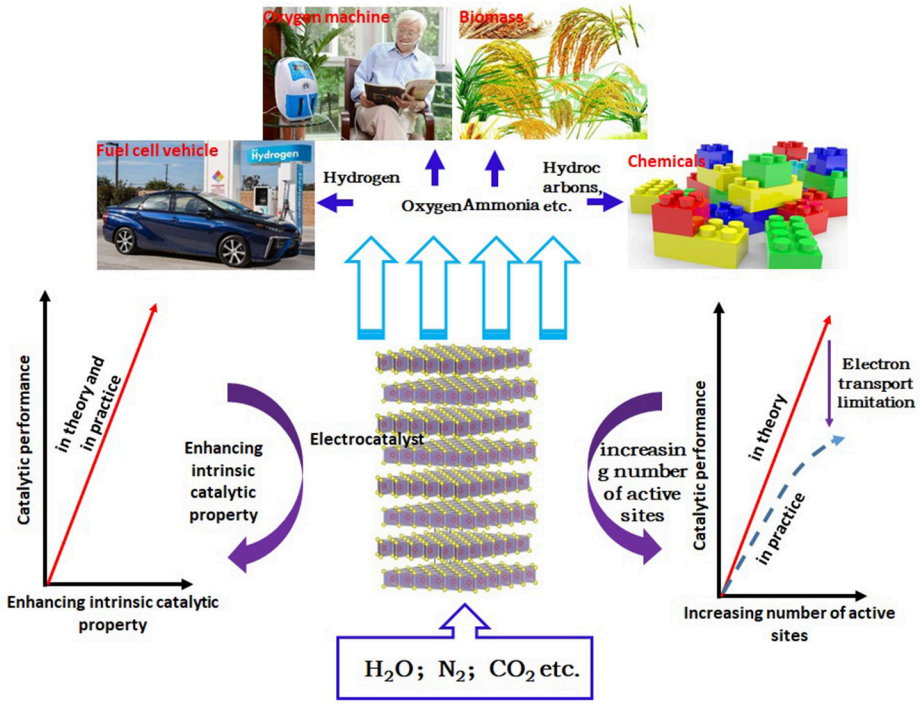

FIGURE 1 | Schematic diagram of sustainable energy pattern and catalyst development strategies based on the electrocatalysis.

the "quantity" of active sites. Zhang et al. prepared monolayer MoS_2 by low-voltage CVD method (Shi et al., 2014). By changing the growth temperature or the distance between source and substrate, the controllable boundary length of MoS_2 was successfully realized. The electrocatalytic hydrogen evolution results showed that the exchange current density increased linearly with the increase of boundary length. By changing the morphology of monolayer MoS_2, the boundary length could be further extended. The dendritic morphology enriched the boundary of monolayer MoS_2 to a great extent, which contributed greatly to the enhancement of the electrocatalytic activity (Zhang et al., 2014; Xu et al., 2018). Fractal monolayer MoS_2 can also promote the efficiency of the electrocatalytic hydrogen evolution reaction. The fractal monolayer MoS_2 synthesized on the surface of fused quartz can expose a large number of active sites at its edge. Besides, the existence of large internal stresses in the fractal monolayer MoS_2, causes more electrons to migrate to the edge active sites, further improving the electrocatalytic performance (Wan et al., 2018). This study also manifests that there is a linear relationship between the electrocatalytic hydrogen evolution activity and the number of marginal active sites of MoS_2. The inert surface of MoS_2 can be tuned into ordered porous structure by using template. The porous structure can increase the proportion of edge atoms (the number of active sites), resulting in the enhanced electrocatalytic performance (Su et al., 2018). MoS_2 nanosheets with rich 1T phase content can be prepared by the chemical peeling. These nanosheets possess many defects, which benefit to the good catalytic activity in the electrocatalytic hydrogen evolution (Voiry et al., 2013; Chang et al., 2016). Doping monolayer MoS_2 can activate the activity of the base surface and improve the catalytic activity. For example, the doping of transition metal element Co atoms can change the surface electronic structure of MoS_2 and the adsorption energy of hydrogen atoms, improving the catalytic performance (Hai et al., 2017; Lau et al., 2018). The post treatment on monolayer MoS_2 is also a strategy to enhance catalytic capacity. Processing with oxygen plasma can increase defects and interfaces in a large extent, which play a certain role in increasing active sites and enhancing intrinsic catalytic activity (Ye et al., 2016).

However, the electrocatalytic hydrogen evolution of monolayer MoS_2 is still limited. The number of active sites, intrinsic catalytic activity and interlayer conductance limit the further improvement of the electrocatalytic hydrogen evolution performance of monolayer MoS_2. The process for improving the electrocatalytic properties of monolayer MoS_2 is complicated or needs special equipments which may limit its practical application. In order to overcome the defects of monolayer MoS_2, it is necessary to composite monolayer MoS_2 with other low-dimensional materials.

Composition With 0D Materials

The electronic structure of the surface and the binding energy of the active intermediates can be modulated by compositing the single layer MoS_2 and 0D, 1D, and 2D materials, leading to the improvement of the electrocatalytic performance by means of the active sites on the "quality" aspect. At the same time, the interlayer conductance of MoS_2 can be enhanced by forming

the composite, which further improves the electrocatalytic activity from another aspect. Zhang et al. composited Pd, Pt, and Ag nanoparticles with monolayer MoS_2 by wet chemical method (Huang et al., 2013). The Pt nanoparticles with the size of 1-3 nm are successfully composited on the surface of monolayer MoS_2. The Pt-modified monolayer MoS_2 showed the excellent electrocatalytic performance with the neglected overpotential and the comparable Tafel slope of 40 mV/dec compared with pure MoS_2 and Pt, which could be ascribed to the effective collection and transport of electrons in the presence of Pt.

Polyoxometallates (POMs) possess excellent performance in catalysis, which is attributed to the abundant oxygen on the surfaces and rich negative charges (Huang J. et al., 2017; Huang et al., 2018b). Polyoxometallates have the abilities to accept multiple electrons and reversible redox properties, which means that they have the outstanding electronic transport properties (Ammam, 2013). The MoS_2 nanosheets were successfully exfoliated using the liquid phase exfoliation method assisted by formamide solvothermal treatment (Huang et al., 2018a). The monolayer MoS_2 and POM were stacked into a multilayer heterostructure by the layer-by-layer (LBL) method, and the

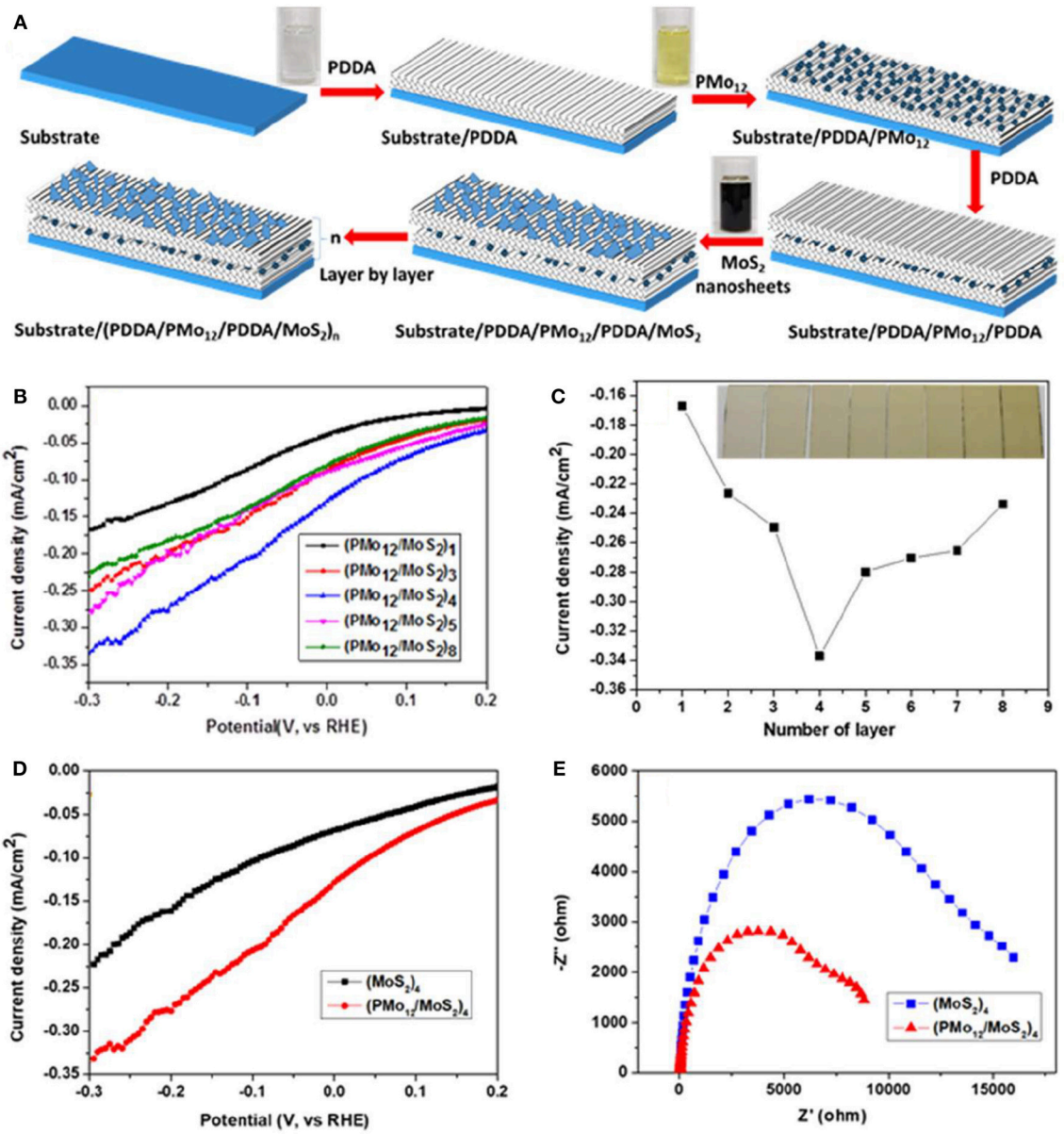

FIGURE 2 | (A) Process for building up the multilayer films $(PMo_{12}/MoS_2)_n$, **(B)** Polarization curves of multilayer $(PMo_{12}/MoS_2)_n$, **(C)** Current density as a function of layer number (inset of (c) Photograph of thin films of $(PMo_{12}/MoS_2)_n$ deposited on ITO with different number of layer), **(D)** Polarization curves of multilayer $(PMo_{12}/MoS_2)_4$ and $(MoS_2)_4$, **(E)** The EIS spectra of multilayer $(PMo_{12}/MoS_2)_4$ and $(MoS_2)_4$ (Huang et al., 2018a).

process for buildup of multilayer films is shown in **Figure 2A**. The electrocatalytic performance was improved due to the high electron transport performance of POMs and the electrochemical test results were plotted in **Figures 2B–E**.

Composition With 1D Materials

One-dimensional (1D) nanostructures offer the unique electronic transport channels. By compositing them with monolayer MoS_2, the carrier transport capacity can be improved and the carrier recombination can be reduced. At the same time, the composite structure can bring the modification of the interface and the change of electronic structure, then the electrocatalytic performance can be further improved. Kim group prepared monolayer MoS_2 by Li intercalation method (Ahn and Kim, 2017). 1D carbon nanotubes and MoS_2 nanosheets were composited by LBL method to form a multilayer structure. The fabrication process was shown in **Figure 3A**. The hydrogen evolution performance reached the optimum value with the Tafel slope of 62.7 mV/dec for the number of layers of 14. The enhanced catalytic performance was attributed to the high conductivity of carbon nanotubes, which increased the conductivity of interlayer of MoS_2, as shown in **Figures 3B,C**.

Xia et al. combined Au nanorods with MoS_2 to achieve surface plasmon resonance under auxiliary illumination, which increased the carrier concentration. Moreover, the improved carrier injection and carrier separation efficiency benefited from 1D structure can enhance the electrocatalytic efficiency (Shi et al., 2015).

Composition With 2D Materials

The calculation results pointed out that the combination of graphene oxide and MoS_2 could change the interface electronic structure, improve electron transport, and enhance electrocatalytic performance (Tang S. et al., 2018). The combination of graphene and monolayer MoS_2 could increase the number of active sites, accelerate the desorption rate of H_2 and enhance the efficiency of electron injection, and thus greatly boosted the electrocatalytic activity (Huang H. et al., 2017).

Sasaki team successfully exfoliated bulk MoS_2 to obtain monolayer by Li intercalation method, and the monolayer MoS_2 was verified to be 1T phase structure (Xiong P. et al., 2018). Then, it can be seen that the monolayer MoS_2 was successfully restacked with graphene to form composite structure by the flocculation method (**Figures 4A–E**). The electrochemical measurements (**Figures 4F–J**) showed that this structure exhibited excellent electrocatalytic hydrogen evolution performance with the overpotential of 88 mV and Tafel slope of 48.7 mV/dec. The long-term stability was also manifested at 10 mA/cm^2 for 10,00,00 s. The outstanding electrochemical properties could be originated from the enhanced electron transport and reduced Gibbs free energy of this unique structure.

According to the characteristics of 0D, 1D, 2D materials, it can play different roles in the composite structure, which can serve as an enhanced electron transport function, as well as to increase the active site, or to activate the in-plane properties. In the actual operation,

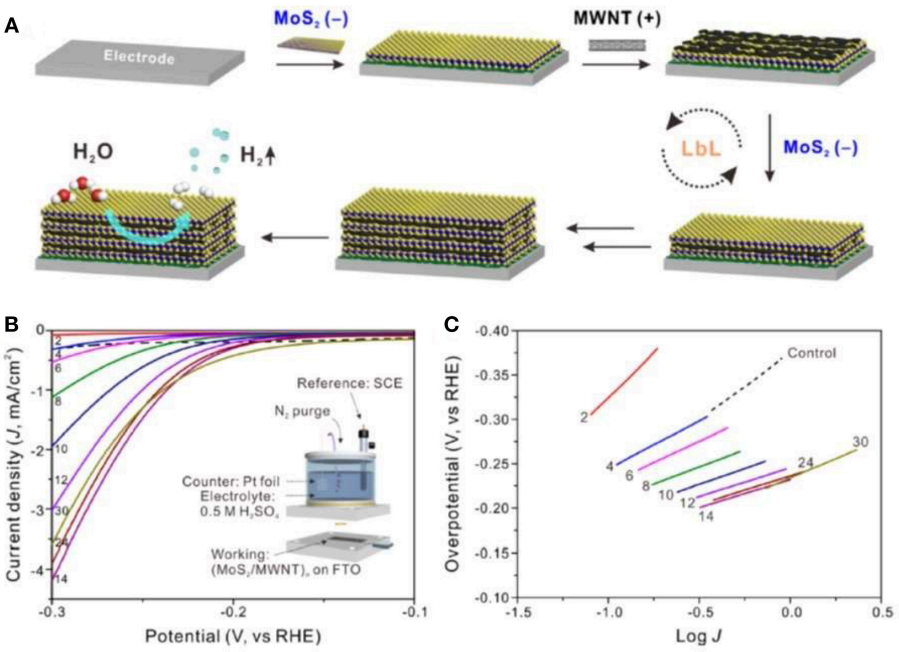

FIGURE 3 | (A) Schematic of the LbL assembly of $(MoS_2/MWNT)_n$ multilayer electrode, **(B)** Polarization curves of hybrid multilayer $(MoS_2/MWNT)_n$ electrodes (Inset of **B** is the experimental setup of the three-electrode system), **(C)** Corresponding Tafel plots (Ahn and Kim, 2017).

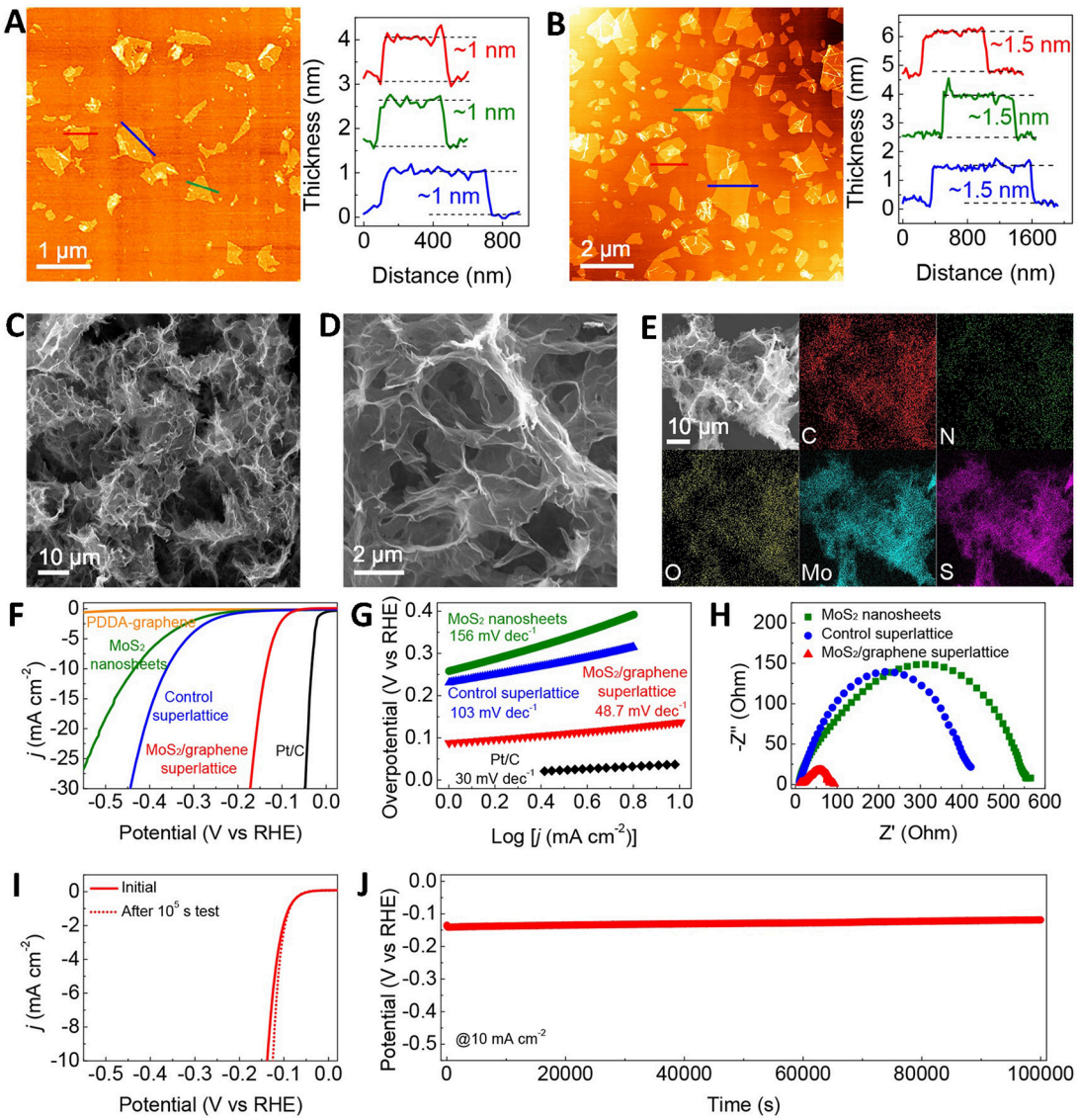

FIGURE 4 | (A) AFM images and height profiles for the exfoliated metallic MoS_2 nanosheets, **(B)** AFM images and height profiles for the PDDA-graphene nanosheets, **(C,D)** SEM images of the MoS_2/graphene superlattice with different magnifications, **(E)** SEM image and corresponding elemental mapping images of the MoS_2/graphene, **(F)** Polarization curves, **(G)** Tafel plots, **(H)** The EIS spectra, **(I)** The polarization curves of the MoS_2/graphene superlattice before and after the 10^5 s test, **(J)** Long-term stability measurement (Xiong P. et al., 2018).

the electrocatalytic performance can be improved with diverse composite structure in different aspects, such as intrinsic catalysis, increasing the number of active sites, and improving conductivity.

OUTLOOK

Monolayer MoS_2 has attracted extensive attention for the electrocatalytic hydrogen evolution. In order to overcome the limitations of active sites, low intrinsic catalytic activity and poor interlayer conductivity, surface modification and composite structure are carried out to improve the electrocatalytic performance. However, there are still some challenges to be worthy of further investigation. Firstly, the properties of composite structure, active site and interface of composite materials are not clear, and need to be studied by more detailed characterization methods; secondly, the comprehensive utilization of monolayer MoS_2 and its composite structures at the macro, nano and atomic levels will improve the efficiency of the electrocatalytic hydrogen evolution in principal, but involving the preparation, test and mechanism explanation of materials and devices. It belongs to the multi-disciplinary frontier field and can be studied through in-depth research. In-depth research on these issues can provide the clue for the improvement of the efficiency of the electrocatalytic hydrogen evolution and the deep insight of catalytic mechanism.

AUTHOR CONTRIBUTIONS

All authors listed have made a substantial, direct and intellectual contribution to the work, and approved it for publication.

FUNDING

This work was supported by the Natural Science Foundation of Shandong Province (Grant No. ZR2016FM30).

REFERENCES

Ahn, E., and Kim, B. S. (2017). Multidimensional thin film hybrid electrodes with MoS_2 multilayer for electrocatalytic hydrogen evolution reaction. *ACS Appl. Mater. Inter.* 9, 8688–8695. doi: 10.1021/acsami.6b15251

Ammam, M. (2013). Polyoxometalates: formation, structures, principal properties, main deposition methods and application in sensing. *J. Mater. Chem.* 1, 6291–6312. doi: 10.1039/C3TA01663C

Benson, E. E., Zhang, H., Schuman, S. A., Nanayakkara, S. U., Bronstein, N. D., Ferrere, S., et al. (2017). Balancing the hydrogen evolution reaction, surface energetics, and stability of metallic MoS_2 nanosheets via covalent functionalization. *J. Am. Chem. Soc.* 140, 441–450. doi: 10.1021/jacs.7b11242

Chang, K., Hai, X., Pang, H., Zhang, H., Shi, L., Liu, G., et al. (2016). Targeted synthesis of 2H- and 1T-phase MoS_2 monolayers for catalytic hydrogen evolution. *Adv. Mater.* 28, 10033–10041. doi: 10.1002/adma.201603765

Chen, S., Chen, X., Wang, G., Liu, L., He, Q., Li, X., et al. (2018). Reaction mechanism with thermodynamic structural screening for electrochemical hydrogen evolution on monolayer 1T' phase MoS_2. *Chem. Mater.* 30, 5404–5411. doi: 10.1021/acs.chemmater.8b02236

Chi, J., and Yu, H. (2018). Water electrolysis based on renewable energy for hydrogen production. *Chinese J. Catal.* 39, 390–394. doi: 10.1016/S1872-2067(17)62949-8

Eftekhari, A. (2017). Electrocatalysts for hydrogen evolution reaction. *Int. J. Hydrog. Energ.* 42, 11053–11077. doi: 10.1016/j.ijhydene.2017.02.125

Gu, M., Choi, J., Lee, T., Park, M., Shin, I., Hong, J., et al. (2018). Diffusion controlled multilayer electrocatalysts via graphene oxide nanosheets of varying sizes. *Nanoscale* 10, 16159–16168. doi: 10.1039/c8NR02883d

Hai, X., Zhou, W., Wang, S., Pang, H., Chang, K., Ichihara, F., et al. (2017). Rational design of freestanding MoS_2 monolayers for hydrogen evolution reaction. *Nano Energy* 39, 409–417. doi: 10.1016/j.nanoen.2017.07.021

Hinnemann, B., Moses, P. G., Bonde, J., Jørgensen, K. P., Nielsen, J. H., Horch, S., et al. (2005). Biomimetic hydrogen evolution: MoS_2 nanoparticles as catalyst for hydrogen evolution. *J. Am. Chem. Soc.* 36, 5308–5309. doi: 10.1002/chin.200525015

Hou, Y., Zhuang, X., and Feng, X., (2017). Recent advances in earth-abundant heterogeneous electrocatalysts for photoelectrochemical water splitting. *Small Methods* 1:1700090. doi: 10.1002/smtd.201700090

Huang, H., Huang, J., Liu, W., Fang, Y., and Liu, Y., (2017). Ultradispersed and single-layered MoS_2 nanoflakes strongly coupling with graphene: an optimized structure with high kinetics for the hydrogen evolution reaction. *ACS Appl. Mater. Inter.* 9, 39380–39390. doi: 10.1021/acsami.7b12038

Huang, J., Deng, X., Wan, H., Chen, F., Lin, Y., Xu, X., et al. (2018a). Liquid phase exfoliation of MoS_2 assisted by formamide solvothermal treatment and enhanced electrocatalytic activity based on $(H_3Mo_{12}O_{40}P/MoS_2)_n$ multilayer structure. *ACS Sustain. Chem. Eng.* 6, 5227–5237. doi: 10.1021/acssuschemeng.7b04873

Huang, J., Yao, N., Fu, K., and Deng, X., (2017). Low cost and high catalytic efficiency compo-site counter electrode NiS-$H_3Mo_{12}O_{40}P$ for dye-sensitized solar cells. *Mater. Lett.* 198, 65–68. doi: 10.1016/j.matlet.2017.03.176

Huang, J., Yao, N., Fu, K., Deng, X., Zhang, S., Hou, P., et al. (2018b). Enhanced dye-sensitized solar cell efficiency by insertion of a $H_3PW_{12}O_{40}$ layer between the transparent conductive oxide layer and the compact TiO_2 layer. *Sci. Adv. Mater.* 10, 867–871. doi: 10.1166/sam.2018.3241

Huang, X., Zeng, Z., Bao, S., Wang, M., Qi, X., Fan, Z., et al. (2013). Solution-phase epitaxial growth of noble metal nanostructures on dispersible single-layer molybdenum disulfide nanosheets. *Nat. Commun.* 4, 1444. doi: 10.1038/ncomms2472

Jaramillo, T. F., Jørgensen, K. P., Bonde, J., Nielsen, J. H., Horch, S., and Chorkendorff, I., (2007). Identification of active edge sites for electrochemical H_2 evolution from MoS_2 nanocatalysts. *Science* 317, 100–102. doi: 10.1126/science.1141483

Jayabal, S., Saranya, G., Wu, J., Liu, Y., Geng, D., and Meng, X., (2017). Understanding the high-electrocatalytic performance of two-dimensional MoS_2 nanosheets and their composite materials. *J. Mater. Chem. A* 5, 24540–24563. doi: 10.1039/C7TA08327K

Jiao, Y., Hafez, A. M., Cao, D., Mukhopadhyay, A., Ma, Y., and Zhu, H. (2018). Metallic MoS_2 for high performance energy storage and energy conversion. *Small* 14, 1800640. doi: 10.1002/smll.201800640

Jin, H., Guo, C., Liu, X., Liu, J., Vasileff, A., Jiao, Y., et al. (2018). Emerging two-dimensional nanomaterials for electrocatalysis. *Chem. Rev.* 118, 6337–6408. doi: 10.1021/acs.chemrev.7b00689

Kou, Z., Kai, X., Pu, Z., and Mu, S. (2017). Constructing carbon-cohered high-index (222) faceted tantalum carbide nanocrystals as a robust hydrogen evolution catalyst. *Nano Energy* 36, 374–380. doi: 10.1016/j.nanoen.2017.04.057

Kou, Z., Wang, T., Pu, Z., Wu, L., Xi, K., and Mu, S. (2018a). Realizing the extraction of carbon from WC for in situ formation of W/WC heterostructures with efficient photoelectrochemical hydrogen evolution. *Nanoscale Horiz.* 4, 196–201. doi: 10.1039/C8NH00275D

Kou, Z., Wang, T., Yi, C., Cao, G., Pu, Z., Zhu, C., et al. (2018b). Ultrafine molybdenum carbide nanocrystals confined in carbon foams via a colloid-confinement route for efficient hydrogen production. *Small Methods* 2:1700396. doi: 10.1002/smtd.201700396

Lau, T., Lu, X., Kulhavý, J., Wu, S., Lu, L., Wu, T. S., et al. (2018). Transition metal atom doping of the basal plane of MoS_2 monolayer nanosheets for electrochemical hydrogen evolution. *Chem. Sci.* 9, 4769–4776. doi: 10.1039/C8SC01114A

Li, H., Jia, X., Zhang, Q., and Wang, X. (2018). Metallic transition-metal dichalcogenide nanocatalysts for energy conversion. *Chem* 4, 1510–1537. doi: 10.1016/j.chempr.2018.03.012

Li, H., Yin, Z., He, Q., Li, H., Huang, X., Lu, G., et al. (2012). Fabrication of single- and multilayer MoS_2 film-based field-effect transistors for sensing NO at room temperature. *Small* 8, 63–67. doi: 10.1002/smll.201101016

Lin, L., Zhou, W., Gao, R., Yao, S., Zhang, X., Xu, W., et al. (2017). Low-temperature hydrogen production from water and methanol using Pt/α-MoC catalysts. *Nature* 544, 80–83. doi: 10.1038/nature21672

Liu, L., Wu, J., Wu, L., Ye, M., Liu, X., Wang, Q., et al. (2018). Phase-selective synthesis of 1T′ MoS_2 monolayers and heterophase bilayers. *Nat. Mater.* 17, 1108–1114. doi: 10.1038/s41563-018-0187-1

Mao, J., Wang, Y., Zheng, Z., and Deng, D. (2018). The rise of two-dimensional MoS_2 for catalysis. *Front. Phys.* 13, 138118. doi: 10.1007/s11467-018-0812-0

Nurdiwijayanto, L., Wu, J., Sakai, N., Ma, R., Ebina, Y., and Sasaki, T. (2018). Monolayer attachment of metallic MoS_2 on restacked titania nanosheets for efficient photocatalytic hydrogen generation. *ACS Appl. Energ. Mater.* 1, 6912–6918. doi: 10.1021/acsaem.8b01319

Otyepková, E., Lazar, P., and Luxa, J. (2017). Surface properties of MoS_2 probed by inverse gas chromatography and their impact on electrocatalytic properties. *Nanoscale* 9, 19236–19244. doi: 10.1039/c7nr07342a

Parsons, R. (1958). The rate of electrolytic hydrogen evolution and the heat of adsorption of hydrogen. *Faraday Soc.* 54, 1603–1611. doi: 10.1039/tf9585401053

Pu, Z., Amiinu, I. S., Gao, F., Xu, Z., Zhang, C., Li, W., et al. (2018). Efficient strategy for significantly decreasing overpotentials of hydrogen generation via oxidizing small molecules at flexible bifunctional CoSe electrodes. *J. Power Sources* 401, 238–244. doi: 10.1016/j.jpowsour.2018.08.085

Pu, Z., Amiinu, I. S., Kou, Z., Li, W., and Mu, S. (2017). RuP_2-based catalysts with platinum-like activity and higher durability for the hydrogen

evolution reaction at all pH values. *Angew. Chem. Int. Ed.* 56, 11559–11564. doi: 10.1002/anie.201704911

Pu, Z., Amiinu, I. S., Wang, M., Yang, Y., and Mu, S. (2016a). Semimetallic MoP_2: an active and stable hydrogen evolution electrocatalyst over the whole pH range. *Nanoscale* 8, 8500–8504. doi: 10.1039/c6nr00820h

Pu, Z., Wang, M., Kou, Z., Amiinu, I. S., and Mu, S. (2016b). Mo_2C quantum dot embedded chitosan-derived nitrogen-doped carbon for efficient hydrogen evolution in a broad pH range. *Chem. Commun.* 52, 12753–12756. doi: 10.1039/c6cc06267a

Pu, Z., Wei, S., Chen, Z., and Mu, S. (2016c). Flexible molybdenum phosphide nanosheet array electrodes for hydrogen evolution reaction in a wide pH range. *Appl. Catal. B-Environ.* 196, 193–198. doi: 10.1016/j.apcatb.2016.05.027

Seh, Z. W., Kibsgaard, J., Dickens, C. F., Chorkendorff, I., Nørskov, J. K., and Jaramillo, T. F. (2017). Combining theory and experiment in electrocatalysis: insights into materials design. *Science* 355:eaad4998. doi: 10.1126/science.aad4998

Shi, J., Ma, D., Han, G. F., Zhang, Y., Ji, Q., Gao, T., et al. (2014). Controllable growth and transfer of monolayer MoS_2 on Au foils and its potential application in hydrogen evolution reaction. *ACS Nano* 8, 10196–10204. doi: 10.1021/nn503211t

Shi, Y., Wang, J., Wang, C., Zhai, T. T., Bao, W. J., Xu, J. J., et al. (2015). Hot electron of Au nanorods activates the electrocatalysis of hydrogen evolution on MoS_2 nanosheets. *J. Am. Chem. Soc.* 137, 7365–7370. doi: 10.1021/jacs.5b01732

Su, S., Zhou, Q., Zeng, Z., Hu, D., Wang, X., Jin, M., et al. (2018). Ultra-thin alumina masks assisted nanopore patterning on monolayer MoS_2 for highly catalytic efficiency in hydrogen evolution reaction. *ACS Appl. Mater. Inter.* 10, 8026–8035. doi: 10.1021/acsami.7b19197

Sun, T., Wang, J., Chi, X., Lin, Y., Chen, Z., Ling, X., et al. (2018). Engineering the electronic structure of MoS_2 nanorods by N and Mn dopants for ultra-efficient hydrogen production. *ACS Catal.* 8, 7585–7592. doi: 10.1021/acscatal.8b00783

Sun, X., Dai, J., Guo, Y., Wu, C., Hu, F., Zhao, J., et al. (2014). Semimetallic molybdenum disulfide ultrathin nanosheets as an efficient electrocatalyst for hydrogen evolution. *Nanoscale* 6, 8359–8367. doi: 10.1039/c4nr01894j

Tan, C., Cao, X., Wu, X. J., He, Q., Yang, J., Zhang, X., et al. (2017). Recent advances in ultrathin two-dimensional nanomaterials. *Chem. Rev.* 117, 6225–6331. doi: 10.1021/acs.chemrev.6b00558

Tang, C., Wang, H. F., and Zhang, Q. (2018). Multiscale principles to boost reactivity in gas-involving energy electrocatalysis. *Acc. Chem. Res.* 51, 881–889. doi: 10.1021/acs.accounts.7b00616

Tang, Q., and Jiang, D. (2016). Mecha nism of hydrogen evolution reaction on 1T-MoS_2 from first principles. *ACS Catal.* 6, 4953–4961. doi: 10.1021/acscatal.6b01211

Tang, S., Wu, W., Zhang, S., Ye, D., Zhong, P., Li, X., et al. (2018). Tuning the activity of the inert MoS_2 surface via graphene oxide support doping towards chemical functionalization and hydrogen evolution: a density functional study. *Phys. Chem. Chem. Phys.* 20, 1861–1871. doi: 10.1039/C7CP06636H

Voiry, ,D., Salehi, M., Silva, ,R., Fujita, T., Chen, M., Asefa, T., et al. (2013). Conducting MoS_2 nanosheets as catalysts for hydrogen evolution reaction. *Nano Lett.* 13, 6222–6227. doi: 10.1021/nl403661s

Voiry, D., Yang, J., and Chhowalla, M., (2016). Recent strategies for improving the catalytic activity of 2D TMD nanosheets toward the hydrogen evolution reaction. *Adv. Mater.* 28, 6197–6206. doi: 10.1002/adma.201505597

Wan, Y., Zhang, Z., Xu, X., Zhang, Z., Li, P., Fang, X., et al. (2018). Engineering active edge sites of fractal-shaped single-layer MoS_2 catalysts for high-efficiency hydrogen evolution. *Nano Energy* 51, 786–792. doi: 10.1016/j.nanoen.2018.02.027

Wang, H., Li, C., Fang, P., Zhang, Z., and Zhang, J. Z., (2018a). Synthesis, properties, and optoelectronic applications of two-dimensional MoS_2 and MoS_2-based heterostructures. *Chem. Soc. Rev.* 47, 6101–6127. doi: 10.1039/C8CS00314A

Wang, H., Ouyang, L., Zou, G., Sun, C., Hu, J., Xiao, X., et al. (2018b). Optimizing MoS_2 edges by alloying isovalent W for robust hydrogen evolution activity. *ACS Catal.* 8, 9529–9536. doi: 10.1021/acscatal.8b02162

Wang, J., Cui, W., Liu, Q., Xing, Z., Asiri, A. M., and Sun, X., (2016). Recent progress in cobalt-based heterogeneous catalysts for electrochemical water splitting. *Adv. Mater.* 28, 215–230. doi: 10.1002/adma.201502696

Wang, J., Wang, N., Guo, Y., Yang, J., Wang, J., Wang, J., et al. (2018). Metallic-phase MoS_2 nanopetals with enhanced electrocatalytic activity for hydrogen evolution. *ACS Sustain. Chem. Eng.* 6, 13435–13442. doi: 10.1021/acssuschemeng.8b03324

Wang, Q., Zhao, Z., Dong, S., He, D., Lawrence, M. J., Han, S., et al. (2018). Design of active nickel single-atomdecorated MoS_2 as a pH-universal catalyst for hydrogen evolution reaction. *Nano Energy* 53, 458–467. doi: 10.1016/j.nanoen.2018.09.003

Wang, Z., and Mi, B. (2017). Environmental applications of 2D molybdenum disulfide (MoS_2) nanosheets. *Environ. Sci. Technol.* 51, 8229–8244. doi: 10.1021/acs.est.7b01466

Wei, G., Shi, Y., Zhang, Y., Zuo, L., Lu, H., Huang, Y., et al. (2016). Molybdenum carbide anchored on graphene nanoribbons as highly efficient all-pH hydrogen evolution reaction electrocatalyst. *Acs Sustain. Chem. Eng.* 4, 6313–6321. doi: 10.1021/acssuschemeng.6b00859

Xie, J., Gao, L., Jiang, H., Zhang, X., Lei, F., Hao, P., et al. (2019). Platinum nanocrystals decorated on defect-rich MoS_2 nanosheets for pH-universal hydrogen evolution reaction. *Cryst. Growth Des.* 19, 60–65. doi: 10.1021/acs.cgd.8b01594

Xie, J., Li, S., Zhang, X., Zhang, J., Wang, R., Zhang, H., et al. (2014). Atomically-thin molybdenum nitride nanosheets with exposed active surface sites for efficient hydrogen evolution. *Chem. Sci.* 5, 4615–4620. doi: 10.1039/C4SC02019G

Xie, J., Qu, H., Xin, J., Zhang, X., Cui, G., Zhang, X., et al. (2017). Defect-rich MoS_2 nanowall catalyst for efficient hydrogen evolution reaction. *Nano Res.* 10, 1178–1188. doi: 10.1007/s12274-017-1421-x

Xie, J., and Xie, Y. (2016). Transition metal nitrides for electrocatalytic energy conversion: opportunities and challenges. *Chem. Eur. J.* 22, 3588–3598. doi: 10.1002/chem.201501120

Xie, J., Xin, J., Cui, G., Zhang, X., Zhou, L., Wang, Y., et al. (2016). Vertically aligned oxygen-doped molybdenum disulfide nanosheets grown on carbon cloth realizing robust hydrogen evolution reaction. *Inorg. Chem. Front.* 3, 1160–1166. doi: 10.1039/C6QI00198J

Xie, J., and Yi, X. (2015). Structural engineering of electrocatalysts for the hydrogen evolution reaction: order or disorder? *Chemcatchem* 7, 2568–2580. doi: 10.1002/cctc.201500396

Xie, J., Zhang, H., Li, S., Wang, R., Sun, X., Zhou, M., et al. (2013a). Defect-rich MoS_2 ultrathin nanosheets with additional active edge sites for enhanced electrocatalytic hydrogen evolution. *Adv. Mater.* 25, 5807–5813. doi: 10.1002/adma.201301794

Xie, J., Zhang, J., Li, S., Grote, F., Zhang, X., Zhang, H., et al. (2013b). Controllable disorder engineering in oxygen-incorporated MoS_2 ultrathin nanosheets for efficient hydrogen evolution. *J. Am. Chem. Soc.* 136, 17881–17888. doi: 10.1021/ja4129636

Xiong, J., Di, J., and Li, H., (2018). Atomically thin 2D multinary nanosheets for energy-related photo. *Adv. Sci.* 5:180024. doi: 10.1002/advs.201800244

Xiong, P., Ma, R., Sakai, N., Nurdiwijayanto, L., and Sasaki, T., (2018). Unilamellar metallic MoS_2/graphene superlattice for efficient sodium storage and hydrogen evolution. *ACS Energy Lett.* 3, 997–1005. doi: 10.1021/acsenergylett.8b00110

Xiong, Q., Zhang, X., Wang, H., Liu, G., Wang, G., Zhang, H., et al. (2018). One-step synthesis of cobalt-doped MoS_2 nanosheets as bifunctional electrocatalysts for overall water splitting under both acidic and alkaline conditions. *Chem. Commun.* 54, 3859–3862. doi: 10.1039/C8CC00766G

Xu, W., Li, ,S., Zhou, S., Lee, J. K., Wang, S., Sarwat, S. G., et al. (2018). Large dendritic monolayer MoS_2 grown by atmospheric pressure chemical vapor deposition for electrocatalysis. *ACS Appl. Mater. Inter.* 10, 4630–4639. doi: 10.1021/acsami.7b14861

Ye, G., Gong, Y., Lin, J., Li, B., He, Y., Pantelides, S. T., et al. (2016). Defects engineered monolayer MoS_2 for improved hydrogen evolution reaction. *Nano Lett.* 16, 1097–1103. doi: 10.1021/acs.nanolett.5b04331

Yu, Y., Huang, S. Y., Li, Y., Steinmann, S. N., Yang, W., and Cao, L. (2013). Layer-dependent electrocatalysis of MoS_2 for hydrogen evolution. *Nano Lett.* 14, 553–558. doi: 10.1021/nl403620g

Yun, Q., Lu, Q., Zhang, X., Tan, C., and Zhang, H. (2017). Three-dimensional architectures constructed from transition metal dichalcogenide nanomaterials for electrochemical energy storage and conversion. *Angew. Chem*. 57, 626–646. doi: 10.1002/ange.201706426

Zeng, X., Hirwa, H., Wagner, V., Ortel, M., Nicolosi, V., and Nerl, H. C. (2017). Growth of large size two-dimensional MoS_2 flakes in aqueous solution. *Nanoscale* 9, 6575–6580. doi: 10.1039/C7NR00701A

Zhai, Z., Li, C., Zhang, L., Zhang, L., Wu, H. C., Zhang, L., et al. (2018). Dimensional construction and morphological tuning of heterogeneous MoS_2/NiS electrocatalysts for efficient overall water splitting. *J. Mater. Chem. A* 6, 9833–9838. doi: 10.1039/C8TA03304H

Zhang, J., Wu, J., Guo, H., Chen, W., Yuan, J., Martinez, U., et al. (2017). Unveiling active sites for the hydrogen evolution reaction on monolayer MoS_2. *Adv.Mater*. 29, 1701955. doi: 10.1002/adma.201701955

Zhang, S., Yang, H., Gao, H., Cao, R., Huang, J., and Xu, X. (2017). One-pot synthesis of CdS irregular nanospheres hybridized with oxygen-incorporated defect-rich MoS_2 ultrathin nanosheets for efficient photocatalytic hydrogen evolution. *ACS Appl. Mater. Inter*. 9, 23635–23646. doi: 10.1021/acsami.7b03673

Zhang, Y., Ji, Q., Han, G. F., Ju, J., Shi, J., Ma, D., et al. (2014). Dendritic, transferable, strictly monolayer MoS_2 flakes synthesized on $SrTiO_3$ single drystals for efficient electrocatalytic applications. *ACS Nano* 8, 8617–8624. doi: 10.1021/nn503412w

Zhao, G., Wu, Y., Shao, Y., and Hao, X. (2016). Large-quantity and continuous preparation of two-dimensional nanosheets. *Nanoscale* 8, 5407–5411. doi: 10.1039/c5nr07950k

Conflict of Interest Statement: The authors declare that the research was conducted in the absence of any commercial or financial relationships that could be construed as a potential conflict of interest.

frontiers in Chemistry

ORIGINAL RESEARCH
published: 16 May 2019
doi: 10.3389/fchem.2019.00280

Supramolecular Aptamers on Graphene Oxide for Efficient Inhibition of Thrombin Activity

Ting-Xuan Lin[1], *Pei-Xin Lai*[1], *Ju-Yi Mao*[1,2,3], *Han-Wei Chu*[1], *Binesh Unnikrishnan*[1], *Anisha Anand*[1] *and Chih-Ching Huang*[1,4,5*]

[1] *Department of Bioscience and Biotechnology, National Taiwan Ocean University, Keelung, Taiwan,* [2] *Doctoral Degree Program in Marine Biotechnology, National Taiwan Ocean University, Keelung, Taiwan,* [3] *Doctoral Degree Program in Marine Biotechnology, Academia Sinica, Taipei, Taiwan,* [4] *Center of Excellence for the Oceans, National Taiwan Ocean University, Keelung, Taiwan,* [5] *School of Pharmacy, College of Pharmacy, Kaohsiung Medical University, Kaohsiung, Taiwan*

Graphene oxide (GO), a two-dimensional material with a high aspect ratio and polar functional groups, can physically adsorb single-strand DNA through different types of interactions, such as hydrogen bonding and π-π stacking, making it an attractive nanocarrier for nucleic acids. In this work, we demonstrate a strategy to target exosites I and II of thrombin simultaneously by using programmed hybrid-aptamers for enhanced anticoagulation efficiency and stability. The targeting ligand is denoted as Supra-$TBA_{15/29}$ (supramolecular $TBA_{15/29}$), containing TBA_{15} (a 15-base nucleotide, targeting exosite I of thrombin) and TBA_{29} (a 29-base nucleotide, targeting exosite II of thrombin), and it is designed to allow consecutive hybridization of TBA_{15} and TBA_{29} to form a network of TBAs (i.e., supra-$TBA_{15/29}$). The programmed hybrid-aptamers (Supra-$TBA_{15/29}$) were self-assembled on GO to further boost anticoagulation activity by inhibiting thrombin activity, and thus suppress the thrombin-induced fibrin formation from fibrinogen. The Supra-$TBA_{15/29}$-GO composite was formed mainly through multivalent interaction between poly(adenine) from Supra-$TBA_{15/29}$ and GO. We controlled the assembly of Supra-$TBA_{15/29}$ on GO by regulating the preparation temperature and the concentration ratio of Supra-$TBA_{15/29}$ to GO to optimize the distance between TBA_{15} and TBA_{29} units, aptamer density, and aptamer orientation on the GO surfaces. The dose-dependent thrombin clotting time (TCT) delay caused by Supra-$TBA_{15/29}$-GO was >10 times longer than that of common anticoagulant drugs including heparin, argatroban, hirudin, and warfarin. Supra-$TBA_{15/29}$-GO exhibits high biocompatibility, which has been proved by *in vitro* cytotoxicity and hemolysis assays. In addition, the thromboelastography of whole-blood coagulation and rat-tail bleeding assays indicate the anticoagulation ability of Supra-$TBA_{15/29}$-GO is superior to the most widely used anticoagulant (heparin). Our highly biocompatible Supra-$TBA_{15/29}$-GO with strong multivalent interaction with thrombin [dissociation constant (K_d) = 1.9×10^{-11} M] shows great potential as an effective direct thrombin inhibitor for the treatment of hemostatic disorders.

Keywords: thrombin, aptamer, graphene oxide, self-assembly, anticoagulation

OPEN ACCESS

Edited by:
Xiaomin Li,
Fudan University, China

Reviewed by:
Wei Luo,
Donghua University, China
Peiyuan Wang,
Fujian Institute of Research on the Structure of Matter (CAS), China

***Correspondence:**
Chih-Ching Huang
huanging@ntou.edu.tw

Specialty section:
This article was submitted to Nanoscience, a section of the journal Frontiers in Chemistry

Received: *16 October 2018*
Accepted: *05 April 2019*
Published: *16 May 2019*

Citation:
Lin T-X, Lai P-X, Mao J-Y, Chu H-W, Unnikrishnan B, Anand A and Huang C-C (2019) Supramolecular Aptamers on Graphene Oxide for Efficient Inhibition of Thrombin Activity. Front. Chem. 7:280. doi: 10.3389/fchem.2019.00280

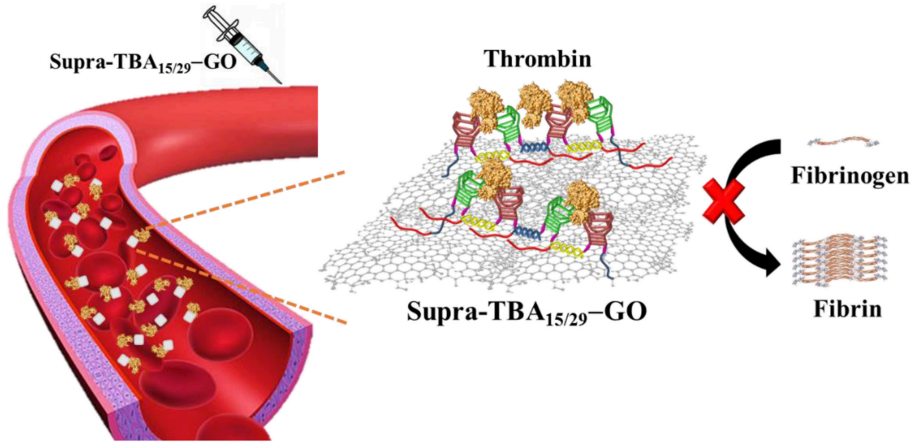

Graphical Abstract | A programmed thrombin binding aptamers immobilized on graphene oxide for strong inhibition of thrombin activity by targeting the exosites I and II of thrombin simultaneously.

INTRODUCTION

Stable and uninterrupted blood flow is important for maintaining a healthy life style. The human body has highly efficient bi-directional regulation of coagulation and hemolysis to prevent excessive blood flow out of injured wounds by forming clots and breaking down the clot when not needed (Doolittle, 2016; Rana and Neeves, 2016). In general, artificial triggering of blood coagulation processes is not needed, except in congenital hemophilia patients who lack factor VIII or factor IX, which can be treated by blood transfusion or injection of clotting factor (Morfini et al., 2013). On the contrary, many diseases are caused by the formation of thrombus (Previtali et al., 2011; Otsuka et al., 2016). Currently, predicting the exact place of thrombus formation in the body is difficult. So, when symptoms arise, serious issues tend to follow, which cause hemorrhage and ischemic necrosis of tissue/organs (Previtali et al., 2011; Suppiej et al., 2015). Therefore, preventing or controlling the clot formation in such cases is necessary. In a normal coagulation system, complex interactions of coagulation factors, platelets, cofactors, and regulators maintain homeostasis for the systematic regulation of bleeding and thrombus formation (Palta et al., 2014). The coagulation reaction has three pathways including the intrinsic pathway, the extrinsic pathway, and the common pathway (Gailani and Renné, 2007; Mackman et al., 2007). Among all the coagulation factors, thrombin (activated Factor II)—a glycosylated serine protease—is indispensable in the coagulation mechanism (Crawley et al., 2007; Smith et al., 2015). Its main function is to take charge of the most crucial and last step in the coagulation cascade reaction; the cleavage of fibrinogen and its activation into fibrin. Only then can fibrin bind to the glycoprotein IIb/IIIa receptor on platelets and connect with platelets and other coagulation factors to form a more solid clot in order to achieve hemostasis (Crawley et al., 2007). Therefore, targeting thrombin activity could be an effective strategy to control thrombosis. Heparin, argatroban, hirudin, and dabigatran are the commonly used anticoagulant drugs which inhibit thrombin activity (Lee and Ansell, 2011; Alquwaizani et al., 2013). Heparin is one of the common anticoagulants in clinical treatment of pulmonary embolism, venous thrombosis, and cerebral embolism (Jin et al., 1997; Zhang et al., 2018). However, heparin may cause an immune-mediated coagulation side effect of heparin-induced thrombocytopenia (HIT) (Pollak et al., 2011). HIT causes abnormal coagulation of platelets and triggers thrombosis symptoms, and the incidence is higher for high-molecular-weight heparin than that of low-molecular-weight heparin. Therefore, developing an anticoagulant with high stability and low side effects is an important and challenging issue.

Aptamers are short DNA or RNA strands selected *in vitro* or *in vivo* through systematic evolution of ligands by exponential enrichment (SELEX) for strong and specific recognition of their targets (Darmostuk et al., 2015; Huang et al., 2016a; Lyu et al., 2016; Pang et al., 2018). In the past two decades, many aptamers have been selected to target different anticoagulation factors for anticoagulation applications (Pagano et al., 2008; Nimjee et al., 2016; Zavyalova et al., 2016a; Chabata et al., 2018). However, many of them suffer from poor specificity, weak binding strength and can be easily degraded by nucleases present in the blood, which limit their successful applications *in vivo*. Even so, a 15-mer thrombin-binding aptamer (TBA_{15}) with specific G-quadruplex structures, which can resist digestion by nucleases, has been shown to extend anticoagulation activity in whole blood (Bock et al., 1992). TBA_{15} binds with thrombin (dissociation constant (K_d) of ~100 nM) at the fibrinogen-binding exosite I, resulting in the inhibition of thrombin activity (Padmanabhan et al., 1993). However, very high concentrations of TBA_{15} (in micromolar regime) are required to achieve an appropriate anticoagulant response due to its low binding affinity. Another 29-mer thrombin-binding aptamer (TBA_{29}) exhibits much stronger binding with exosite II of thrombin (K_d ~ 0.5 nM) (Tasset et al., 1997); however, it could not

inhibit thrombin activity toward the formation of fibrin from fibrinogen and thrombin-mediated platelet activation. Moreover, the short half-life of blood circulation of TBAs diminishes their anticoagulation potency *in vivo*.

Compared to free aptamers, aptamer-conjugated nanoparticles provide ultrahigh local aptamer densities on nanoparticle surfaces to increase their binding affinity to thrombin and resistance toward nuclease digestion (Liu et al., 2014; Jo and Ban, 2016; Urmann et al., 2016; Yang et al., 2018). In addition, each nanoparticle can be conjugated with different functional aptamers for multivalent binding of target proteins. A number of TBA-based nanocomposites have been developed by modification of TBAs on metallic, polymeric, and DNA origami nanoparticles for efficient binding of TBAs with thrombin to increase their anticoagulation potency (Rinker et al., 2008; Kim et al., 2010; Musumeci and Montesarchio, 2012; Riccardi et al., 2017; Kumar and Seminario, 2018; Lai et al., 2018). However, anchoring of TBAs on the nanoparticles requires extensive and tedious functionalization processes. In addition, the steric position, distance, and orientation of TBAs on the nanoparticles are difficult to manipulate. Thus, these nanocomposites are rarely employed for anticoagulation *in vivo* (Lai et al., 2018).

Graphene oxide (GO) has been reported to adsorb single-stranded nucleic acid chains by cooperative van der Waals' force, π-π stacking interaction, and hydrogen bonding interaction (Antony and Grimme, 2008; Varghese et al., 2009; Wu et al., 2011; Chen et al., 2014; Liu et al., 2016). Recently, some aptamer-adsorbed GO have been demonstrated for protein detection and cell labeling (Pu et al., 2011; Gao et al., 2015; Kim et al., 2015; Xiao et al., 2017). Most aptamers adopt specific conformational structures, which enable high specificity toward the targeting molecule (Rowsell et al., 1998; Tucker et al., 2012; Zavyalova et al., 2016b,c; Krauss et al., 2018). However, these unique conformational structures of aptamers are usually disrupted after adsorption onto GO. Moreover, the aptamer-adsorbed GO are not stable in human plasma due to the competitive adsorption between plasma components, such as high concentration proteins and aptamers on GO. As a result, the adsorbed aptamers tend to desorb from GO in human plasma (Wang et al., 2010; Mao et al., 2015; Zhu et al., 2015; Lu et al., 2016). In this study, we developed a simple strategy to target exosites I and II of thrombin simultaneously by using programmed hybrid-TBAs immobilized on partially reduced GO for enhanced stability of the TBAs and improved anticoagulation efficiency (**Scheme 1**). The targeting ligand is denoted as Supra-$TBA_{15/29}$ [$-(A_{20}h_{15}T_5TBA_{15/29}T_5h_{15})_n-$], containing a supramolecular structure of consecutive hybrid TBA_{15}/TBA_{29} units with multiple poly(adenine) (A_{20}) segments for immobilization on GO. GO has been shown to preferentially interact with single stranded (ss) DNA with poly(adenine) sequences (Ranganathan et al., 2016). The multi-segment A_{20} segments allow Supra-$TBA_{15/29}$ to anchor strongly on the GO surface, which results in the high stability of Supra-$TBA_{15/29}$-GO nanocomposites in human plasma. The Supra-$TBA_{15/29}$-GO nanocomposites possess superior anticoagulant activity to free both TBAs (TBA_{15} or TBA_{29}) and Supra-$TBA_{15/29}$. In addition, thromboelastography of whole-blood coagulation and rat-tail bleeding assays further demonstrate the strong anticoagulation ability of Supra-$TBA_{15/29}$-GO (**Graphical Abstract**).

RESULTS AND DISCUSSION

Formation of Supra-$TBA_{15/29}$

The oligonucleotide sequences of $A_{20}h_{15}T_5TBA_{15}T_5h_{15}$ ($sTBA_{15}$) and $h_{15}T_5TBA_{29}T_5h_{15}A_{20}$ ($sTBA_{29}$) are listed in **Table S1** (Supporting Information). The $sTBA_{15}$ and $sTBA_{29}$ comprised of three blocks, a 20-polyadenine (A_{20}) for anchoring on GO, two 15-base sequences (h_{15}) for consecutive hybridization, a 5-repeat thymidine (T_5) as a linker, and a TBA sequence providing functionality. TBA_{29} has a G-quadruplex structure with a loop and stem in the terminal, while TBA_{15} has only a G-quadruplex structure (Macaya et al., 1993; Padmanabhan et al., 1993). A previous study indicated that having two 7-mers inserted on each side of TBA_{15} unit introduces a loop and stem structure for stabilizing the G-quadruplex structures, thereby increasing their inhibitory potency (Hsu et al., 2012). By simply mixing $sTBA_{15}$ and $sTBA_{29}$ in phosphate-buffered saline (PBS; containing 25.0 mM tris-HCl, 150.0 mM NaCl, 5 mM KCl, 1.0 mM $MgCl_2$, and 1.0 M $CaCl_2$; adjusted to pH 7.4 using HCl) solution, the Supra-$TBA_{15/29}$ were formed through the consecutive hybridization of the h_{15} sequences (**Scheme S1A**, Supporting Information). In addition, we also prepared dimer TBA_{15}/TBA_{29} (di-$TBA_{15/29}$) by mixing $sTBA_{15}$ and $dTBA_{29}$ ($nh_{15}T_5TBA_{29}T_5h_{15}A_{20}$). The di-$TBA_{15/29}$ are formed by a single step hybridization between $sTBA_{15}$ and $dTBA_{29}$ (**Scheme S1B**). A control experiment with a mixture of $sTBA_{15}$ and $nTBA_{29}$ ($nh_{15}T_5TBA_{29}T_5nh_{15}A_{20}$) indicated that they could not hybridize with each other (**Scheme S1C**). For simplicity, we denote the mixture of $sTBA_{15}$ and $nTBA_{29}$ as nh-$TBA_{15/29}$. The hydrodynamic size of Supra-$TBA_{15/29}$ (∼207.8 nm) was larger than $sTBA_{15}$ (∼24.3 nm), $sTBA_{29}$ (∼25.6 nm), di-$TBA_{15/29}$ (∼53.7 nm), and the mixture of $sTBA_{15}$ and $nTBA_{29}$ (∼26.3 nm), determined by dynamic light scattering (DLS), which suggested the formation of a supramolecular TBA structure. The lower electrophoretic mobility of Supra-$TBA_{15/29}$ compared to that of $sTBA_{15}$, $sTBA_{29}$, and di-$TBA_{15/29}$ further confirmed the formation of Supra-$TBA_{15/29}$ through hybridization (**Figure S1**, Supporting Information) (Hellman and Fried, 2007). The gel electrophoresis result of Supra-$TBA_{15/29}$ shows a broad band, probably due to the formation of varying lengths of Supra-$TBA_{15/29}$. Based on the location and the width of the broad band, we propose that our Supra-$TBA_{15/29}$ consists of mainly 2–6 hybridized TBA units.

Thrombin Clotting Time of Supra-$TBA_{15/29}$

We evaluated the inhibitory ability of Supra-$TBA_{15/29}$ against thrombin in human plasma by thrombin clotting time (TCT) assays. The TCT test is a reliable diagnostic tool for bleeding and/or clotting disorder and screening of coagulation factors I (fibrinogen), IIa (thrombin), and XIII (fibrillation stabilizing factor) in the common coagulation pathways (Ignjatovic, 2013). We investigated the thrombin inhibitory activity of nh-$TBA_{15/29}$, di-$TBA_{15/29}$, and Supra-$TBA_{15/29}$, which were prepared by mixing $sTBA_{15}$ with $nTBA_{29}$, $dTBA_{29}$, and $sTBA_{29}$ (**Scheme S1**),

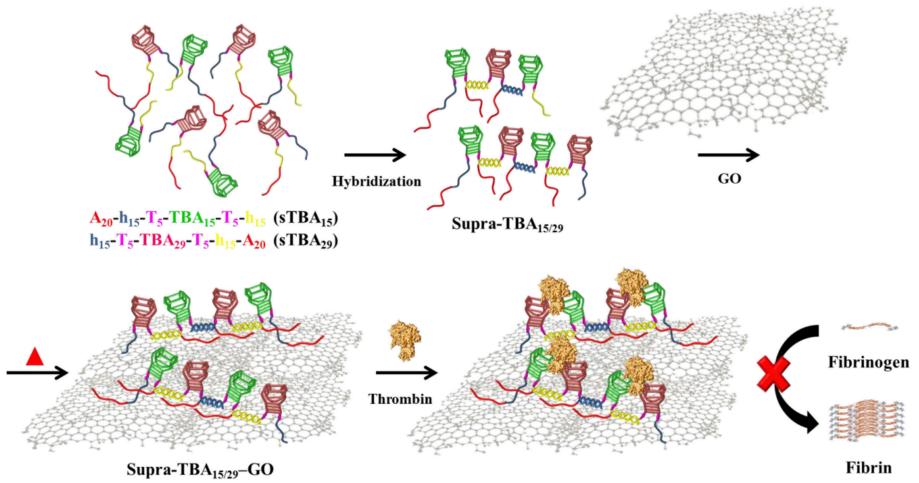

SCHEME 1 | Schematic representation of the synthesis of self-assembled programmed hybrid thrombin-binding aptamers on graphene oxide and their multivalent interaction with thrombin for enhanced anticoagulant activity.

respectively. We compared the inhibitory potencies of nh-$TBA_{15/29}$, di-$TBA_{15/29}$, and Supra-$TBA_{15/29}$ by real-time kinetics of coagulation, through recording the scattering light intensity as a function of time (**Figure 1A**). Fibrinogen (factor I) is a fibrous glycoprotein (∼45 nm) with a complex structure. It consists of three pairs of polypeptide chains (α-, β-, and γ-chains) linked together by 29 disulfide bonds (Mosesson, 2005). Soluble fibrinogen is converted into protofibrils by the cleavage of fibrinopeptides Aα and Bβ in the central region by thrombin via intermolecular interactions of knobs "A" and "B" in the central nodule and holes "a" and "b" at the ends of the molecules. The protofibrils further aggregate laterally to form fibers and then branch to form a three-dimensional network of the fibrin clots. The higher activity of thrombin results in the formation of a larger fibrin gel, which causes increased scattering of light. The concentration of the total of the TBAs was held constant (100 nM) in these experiments. Compared with the control (no inhibitor), which has a TCT value of 24 ± 1 s, Supra-$TBA_{15/29}$ prolonged the clotting time to 251 ± 21 s. The TCT values for nh-$TBA_{15/29}$ and di-$TBA_{15/29}$ were 54 ± 10 and 66 ± 15 s, respectively. The inhibitory activity of Supra-$TBA_{15/29}$ was superior to nh-$TBA_{15/29}$ and di-$TBA_{15/29}$ mainly due to synergistic effect. That is, simultaneous binding and blocking by the two aptamers of both of the exosites (exosite I and II) of thrombin and steric hindrance of relatively large Supra-$TBA_{15/29}$ to fibrinogen from accessing thrombin led to strong and synergistic inhibition of the thrombin-dependent coagulant activity (Hsu et al., 2011).

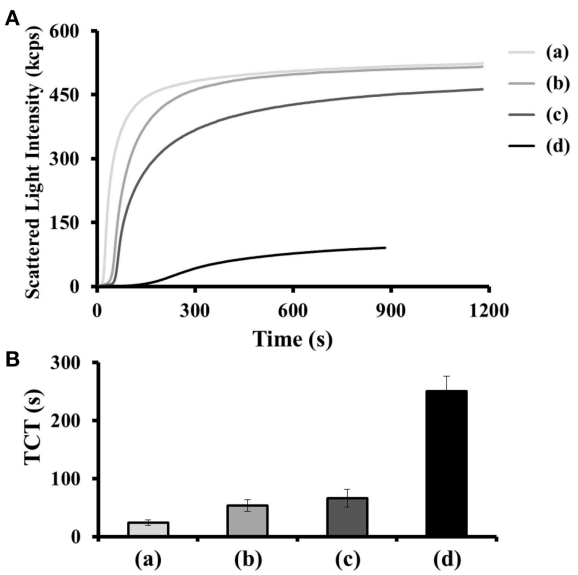

FIGURE 1 | (A) Scattering light intensity as a function of time for coagulating mixtures of thrombin (15 nM), human plasma (2-fold diluted), BSA (100 μM) in the **(a)** absence and **(b–d)** presence of **(b)** nh-$TBA_{15/29}$, **(c)** di-$TBA_{15/29}$, and **(d)** Supra-$TBA_{15/29}$ with a concentration of 100 nM (in terms of TBA). **(B)** TCT obtained from the light scattering intensities generated by the coagulation process. The TCT for each sample was noted as the time at which the differential scattering signal intensity reached the maximum. The longest time monitored in the clotting assays was set at 1,200 s. Error bars represent the standard deviations of experiments in triplicate.

Characterization of GO and Supra-$TBA_{15/29}$-GO

GO was synthesized by improved Hummers' method from graphite powder with a particle size of 7–11 μm (Hummers and Offeman, 1958; Marcano et al., 2010). The detailed procedure of synthesis of GO is given in the experimental section. The TEM image in **Figure S2A** (Supporting Information) shows that most of the as-synthesized GO with size ca. 200–300 nm are single layered. Atomic force microscopy (AFM) showed that the average size of a single-layer GO was ∼230 nm, and the monolayer thickness was about 1.1 nm (**Figure S2B**, Supporting Information). We prepared a series of Supra-$TBA_{15/29}$-GO nanocomposites and studied their inhibitory activities against thrombin. The Supra-$TBA_{15/29}$ ([TBA] = 2.5 μM) was mixed

with GO (20–80 μg mL^{-1}) in PBS containing 1.0 M NaCl at 25–90°C. After incubation for 2 h, the Supra-$TBA_{15/29}$-GO solutions were purified through three centrifugation and washing cycles. The Supra-$TBA_{15/29}$ on the GO was determined through the quantitation of unbound TBAs in the supernatant, and the results are listed in **Table S2**. The Supra-$TBA_{15/29}$ modified on GO formed Supra-$TBA_{15/29}$-GO mainly through van der Waals' force, π-π stacking, and hydrogen-bonding between poly(adenine) (A_{20}) from Supra-$TBA_{15/29}$ and GO (Antony and Grimme, 2008; Varghese et al., 2009; Chen et al., 2014). Previous studies revealed that purine bases (A and G) bind more strongly than the pyrimidines (T and C) (Park et al., 2014; Liu et al., 2016; Ranganathan et al., 2016). The DNA oligonucleotides possess much stronger [1–3 order(s) higher] association constants compared to the single nucleosides and longer DNA provides more binding sites for adsorption on GO. The AFM image of Supra-$TBA_{15/29}$-GO shows that Supra-$TBA_{15/29}$ was anchored on the surface of GO with a thickness of ∼16 nm (**Figure S2C**). The AFM result suggests a monolayer of Supra-$TBA_{15/29}$ was immobilized on either side of the GO, which is evident from the size of TBA (∼2.0 nm) and the length of $h_{15}T_5$ (∼6.8 nm; 0.34 nm bp^{-1}).

Temperature may affect the structure and flexibility of Supra-$TBA_{15/29}$ and is known to affect oxygen moieties on GO, which in turn could affect their interactions during Supra-$TBA_{15/29}$-GO synthesis (Lin et al., 2010; Geggier et al., 2011; Brunet et al., 2018). Heat treatment altered the density of Supra-$TBA_{15/29}$ on GO very significantly (**Table S2**) as a result of unfavorable entropy, partial denaturation of Supra-$TBA_{15/29}$, and mild reduction of GO at higher temperatures. The adsorption density of the Supra-$TBA_{15/29}$ on GO decreased with increasing concentration of GO used during the preparation of Supra-$TBA_{15/29}$-GO conjugates. In the series of Supra-$TBA_{15/29}$-GO prepared, the maximum adsorption density of Supra-$TBA_{15/29}$ on GO (using 20 μg mL^{-1} of GO and at 25°C for the preparation of Supra-$TBA_{15/29}$-GO) was calculated to be 47.1 nmol mg^{-1}, which revealed a high density of Supra-$TBA_{15/29}$ on the GO surface compared to the reported result for the saturated adsorption of poly-adenine (A_{15}) on GO (∼7.18 nmol mg^{-1}) (Lu et al., 2016). We conducted UV-vis absorption spectroscopy (**Figure S3**), Fourier-transform infrared spectroscopy (FT-IR; **Figure S4**), X-ray photoelectron spectroscopy (XPS; **Figure S5**), Raman spectroscopy (**Figure S6**), and elemental analysis (EA; **Table S2**) to characterize GO and understand the effect of temperature on the degree of reduction of GO. Our results indicate GO underwent only a slight reduction even after treatment at 90°C for 2 h. However, this slight reduction of GO played a crucial role in the anticoagulation potency and stability of Supra-$TBA_{15/29}$-GO in human plasma, which will be discussed in the following sections. The material is stored at 4°C when not in use and is stable up to 3 months.

Anticoagulant Activity of Supra-$TBA_{15/29}$-GO

In contrast to GO, which tends to aggregate in PBS of high ionic strength, the Supra-$TBA_{15/29}$-GO dispersion was very stable (no aggregation) when incubated in 1X PBS (**Figure S7**, Supporting Information). The hydrodynamic size of GO aggregates in PBS was ∼1,800 nm, whereas the size of Supra-$TBA_{15/29}$-GO (∼150 nm) did not change significantly with increasing the concentration of PBS. The high density of TBAs with high negative charge mainly contributed to the high stability of Supra-$TBA_{15/29}$-GO. On the other hand, the circular dichroism (CD) spectra of Supra-$TBA_{15/29}$-GO prepared at different temperatures (25–90°C) did not show significant difference with that of Supra-$TBA_{15/29}$ (**Figure S8**, Supporting Information), revealing that the G-quadruplex structure of TBAs were highly preserved after Supra-$TBA_{15/29}$ were adsorbed on GO. The TCT of Supra-$TBA_{15/29}$ and Supra-$TBA_{15/29}$-GO prepared with various concentrations of GO (20, 40 and 80 μg mL^{-1}) at 25, 45, 60, and 90°C is presented in **Figure 2**. TCT values for Supra-$TBA_{15/29}$-GO prepared with GO (40 μg mL^{-1}) at 25, 45, 60, and 90°C were ∼9, 26, 66, and three times longer, respectively, than that which was in the absence of inhibitor. The higher inhibitory activity of Supra-$TBA_{15/29}$-GO can be ascribed to the high specificity of the aptamers to block the exosite I and II binding sites and/or the active sites of thrombin for fibrinogen, and high ligand density on the GO surface. In addition, the 5′- and 3′-extended TBA molecules were anchored on GO through interactions between poly(adenine) and GO, which facilitated the exposure of major binding loops of TBA_{15} (T^3T^4 and $T^{12}T^{13}$ loops) and TBA_{29} ($T^{10}A^{11}$ and $T^{19}T^{20}$ loops) toward the bulk solution for access (binding) to thrombin. Previous reports revealed the binding of TBA_{15} and TBA_{29} to exosite I and exosite II of thrombin were through their $T^3T^4/T^{12}T^{13}$ loops and $T^{10}A^{11}/T^{19}T^{20}$ loops, respectively (Padmanabhan et al., 1993; Tasset et al., 1997).

The longest TCT time of 1,640 ± 20 s indicates that Supra-$TBA_{15/29}$-GO prepared with GO (40 μg mL^{-1}) at 60°C has the most significant impact on coagulation delay triggered by thrombin relative to the Supra-$TBA_{15/29}$ and other Supra-$TBA_{15/29}$-GO nanocomposites. Although Supra-$TBA_{15/29}$-GO prepared in the lower temperature (<60°C) possess higher TBA density on GO (**Table S2**), the Supra-$TBA_{15/29}$ tend to release from GO when incubated in human plasma due to the competitive interaction between high concentrated plasma components (e.g., serum albumin) and A_{20} of Supra-$TBA_{15/29}$ (**Figure S9**, Supporting Information) (Lu et al., 2016). We speculated that only a small portion of the A_{20} of the highly dense Supra-$TBA_{15/29}$ was adsorbed on GO and thus they were easily released from GO in complicated plasma. As a result, the anticoagulation ability was lower when the Supra-$TBA_{15/29}$ were prepared at 25 and 40°C. On the other hand, the Supra-$TBA_{15/29}$ probably disassembled when the Supra-$TBA_{15/29}$-GO was prepared at 90°C and resulted in much weaker anticoagulation activity than that of prepared at 60°C. The optimized Supra-$TBA_{15/29}$-GO prepared with GO (40 μg mL^{-1}) at 60°C exhibited the strongest inhibitory ability mainly due to an appropriate density, flexibility, and orientation of multivalent TBA on GO. All these factors are controllable by carefully controlling the concentration ratio of Supra-$TBA_{15/29}$ to GO and reaction temperature, and thereby the interaction between Supra-$TBA_{15/29}$ and GO. The appropriate orientation of the Supra-$TBA_{15/29}$ on the slightly reduced GO surface

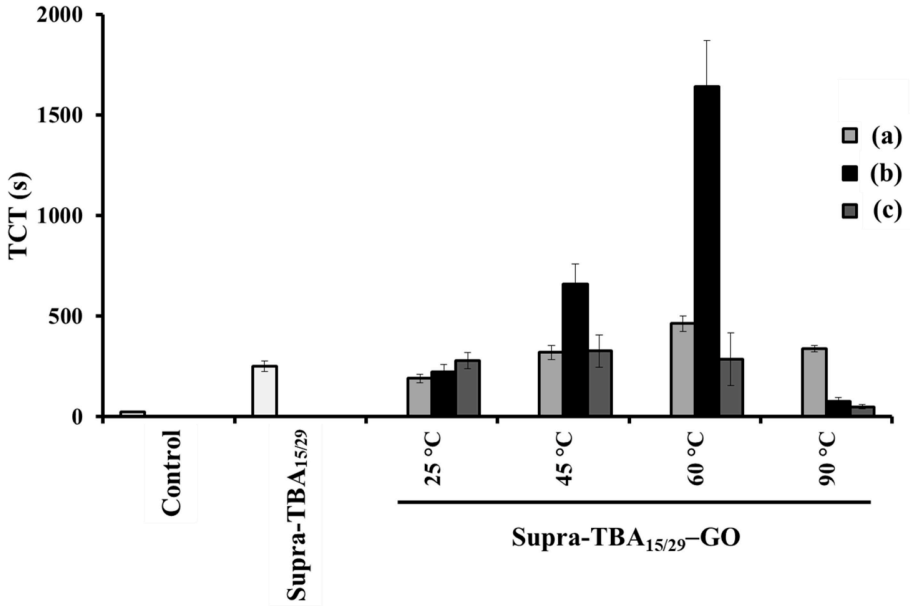

FIGURE 2 | Thrombin clotting time (TCT) of Supra-$TBA_{15/29}$ and Supra-$TBA_{15/29}$-GO prepared at different concentrations of GO **(a)** 20, **(b)** 40, and **(c)** 80 $\mu g\ mL^{-1}$ at different temperatures. The concentration of Supra-$TBA_{15/29}$ in all samples was 100 nM. The TCT assay in the absence of inhibitors serves as a control group. The error bars represent the standard deviations of experiments in triplicate. Other conditions were the same as those described in **Figure 1**.

and the desired distance between TBA_{15} and TBA_{29} resulted in a superior multivalent binding. Compared with free TBA_{15} ($K_d \sim 100$ nM) and TBA_{29} ($K_d \sim 0.5$ nM) (Padmanabhan et al., 1993; Tasset et al., 1997), Supra-$TBA_{15/29}$-GO prepared with GO (40 $\mu g\ mL^{-1}$) at 60°C exhibited much higher binding affinity toward thrombin ($K_d = 1.9 \times 10^{-11}$ M, **Figure S10**, Supporting Information). The Supra-$TBA_{15/29}$-GO prepared with GO (40 $\mu g\ mL^{-1}$) at 60°C also exhibited superior anticoagulation activity compared to our previously reported bivalent TBA_{15}/TBA_{29}-modified gold nanoparticles and GO (Huang et al., 2016b; Lai et al., 2018), probably because the particular flexible conformation and multivalency of Supra-$TBA_{15/29}$ structure on GO boosted their anticoagulation potency. A higher concentration of GO (80 $\mu g\ mL^{-1}$) for the preparation of Supra-$TBA_{15/29}$-GO prepared at 60°C leads to lower aptamer density and lower local concentration on its surface, and lower concentration of GO (20 $\mu g\ mL^{-1}$) might cause steric hindrance for thrombin binding due to undesired conformation of highly dense aptamers on its surface. On the other hand, the Supra-$TBA_{15/29}$-GO prepared at 90°C with 20 $\mu g\ mL^{-1}$ of GO exhibits a slightly better anticoagulant activity in comparison with that of 40 and 80 $\mu g\ mL^{-1}$ of GO. The slightly higher anticoagulant activity could be ascribed to the higher dense aptamers on the surface of GO with a concentration of 20 $\mu g\ mL^{-1}$ (**Table S2**, Supporting Information). The optimized Supra-$TBA_{15/29}$-GO prepared with GO (40 $\mu g\ mL^{-1}$) at 60°C was used throughout the experiment.

The dose-dependent TCT displayed in **Figure 3** clearly demonstrates that optimized Supra-$TBA_{15/29}$-GO has the highest inhibition of thrombin activity, in comparison with free Supra-$TBA_{15/29}$ and the four tested commercial anticoagulant drugs including heparin, argatroban, hirudin, and warfarin. The TCT delay caused by Supra-$TBA_{15/29}$-GO ([TBA] = 100 nM) was 5, 10, 14, 37, and 40 times longer than that caused by the Supra-$TBA_{15/29}$, heparin, argatroban, hirudin, and warfarin (0.1 μM), respectively. The TCT assays clearly indicated that the clotting time delay by Supra-$TBA_{15/29}$-GO was much longer than that of Supra-$TBA_{15/29}$ and the commercial anticoagulants. Our results reveal that Supra-$TBA_{15/29}$-GO is a stable and highly inhibitive nanocomposite for thrombin through elaborative construction of supramolecular TBA structures on the GO surface.

Thromboelastography

Platelets are tiny blood cell fragments that play an important role in blood clotting, including being activated to provide assembly sites for coagulation factor complex formation, combining with the fibrin clot and releasing agonists to amplify the platelet responses (De Candia, 2012). The evaluation of inhibition efficiency of Supra-$TBA_{15/29}$-GO by TCT assay has limitations, because they are conducted in plasma without platelets (thrombocytes). Therefore, we employed thrombin-activated thromboelastography (TEG) to study the kinetics of inhibition of clot formation in whole blood. Various parameters, such as the R time (time of latency from start of test to initial fibrin formation, amplitude of 2 mm), K time (time taken to achieve a certain level of clot strength, amplitude of 20 mm), α angle (measuring the speed at which fibrin build up and cross linking takes place), and MA (the ultimate strength of the fibrin clot) were measured using the TEG assay (Bolliger

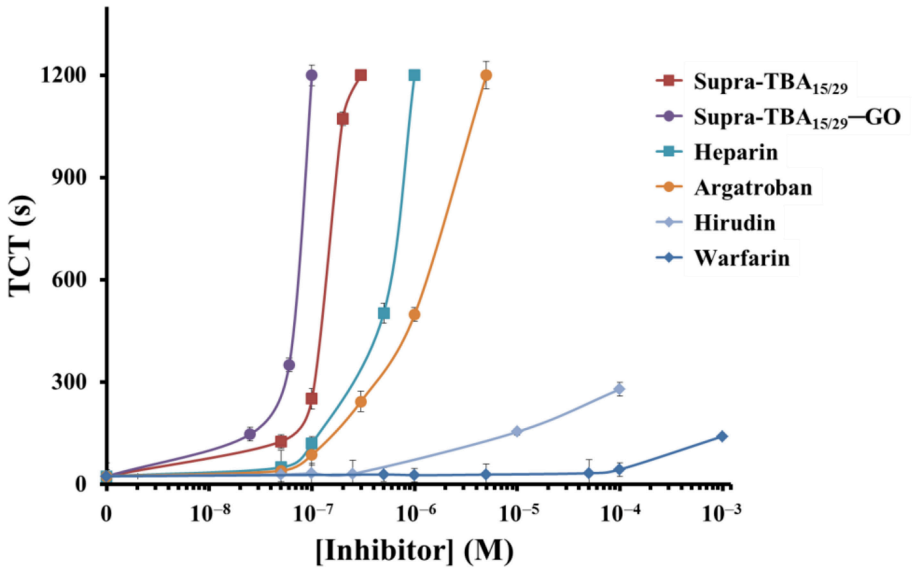

FIGURE 3 | Dose-dependence of the TCTs in human plasma in the presence of Supra-$TBA_{15/29}$, Supra-$TBA_{15/29}$-GO and commercial drugs heparin, argatroban, hirudin, and warfarin. The longest clotting assay time recorded was set at 1,200 s. Error bars represent the standard deviations of experiments in triplicate. Other conditions were the same as those described in **Figure 1**.

et al., 2012) to quantify the blood clot formation. As shown in **Figure 4**, Supra-$TBA_{15/29}$ ([TBA] = 100 nM) prolonged the R time (4.7 ± 0.4 min) as compared with the control (without inhibitor) (1.0 ± 0.1 min), whereas Supra-$TBA_{15/29}$-GO prolonged the R value to 9.8 ± 0.6 min revealing that Supra-$TBA_{15/29}$ exhibited a better inhibitory effect after it conjugated with GO. This result also indicates that Supra-$TBA_{15/29}$-GO in the whole blood sample can inhibit the coagulation pathway chain reaction more effectively than heparin (the most widely used anticoagulant) which prolonged the R value to 2.0 ± 0.2 min. Our results reveal that the anticoagulant activity of Supra-$TBA_{15/29}$-GO is about 5 times better than heparin in native human blood on the basis of R time values. Further, compared to the α angle, K time, and MA of Supra-$TBA_{15/29}$ and heparin, Supra-$TBA_{15/29}$-GO has the longest K time and smallest α angle and MA values, indicating that the clot (fibrinogen polymerization and platelet aggregation) formed has the lowest rate and strength.

Biocompatibility

Carbon nanomaterials are reported to possess good biocompatibility (Seabra et al., 2014; Bhattacharya et al., 2016; Ou et al., 2016). Although GO has been shown to cause the rupture of cell membrane, the magnitude of decrease in cell viability does not exceed 20% for 24 h or even longer time when the concentration of GO is <100 μg mL^{-1} (Liao et al., 2011; Fiorillo et al., 2015). Additionally, the cytotoxicity of GO is highly diminished after capping with biopolymers, such as proteins, oligonucleotide, and polysaccharide (Chong et al., 2015; Rezaei et al., 2016; Kenry, 2018; Liu et al., 2018; Ren et al., 2018). In this study, we used MTT assay to evaluate the cytotoxicity of Supra-$TBA_{15/29}$-GO toward different mammalian cells (**Figure S11A**, Supporting Information). Supra-$TBA_{15/29}$-GO did not show any cytotoxic effect toward human lung adenocarcinoma epithelial cell (A549), human liver cancer cell (Hep-G2), human umbilical cord vein endothelial cell (HUVEC), and human embryonic kidney cell (HEK293T). The cells showed cell viability of >95% even at 1.00 μM (in terms of TBA) $TBA_{15/29}$-GO concentration and 24 h of incubation. It is noteworthy to mention that the concentration of Supra-$TBA_{15/29}$-GO used for MTT assay was several times higher than the effective concentration of Supra-$TBA_{15/29}$-GO used for antithrombin activity in plasma (**Figures 2**, **3**) and whole blood (**Figure 4**). Live/dead cell viability staining (Calcein AM/EthD-1) was further employed for examining live and dead cells. Different concentrations of Supra-$TBA_{15/29}$-GO ([TBA] = 0.01–1.00 μM) were added into a 24-well plate containing HEK293T cells. The morphologies of the HEK293T cells after 24 h culture with different Supra-$TBA_{15/29}$-GO concentrations showed no obvious differences when compared to the control (**Figure S11B**, Supporting Information). Supra-$TBA_{15/29}$-GO-treated cells were similar to that of the control group (PBS-treated only) which displayed typical fibroblast-like morphology (Yan and Shao, 2006). Calcein AM is a non-fluorescent dye that can easily permeate into live mammalian cells with an intact cell membrane. The hydrolysis of calcein AM by intracellular esterases produces calcein, which can be well-retained in the cell cytoplasm. Calcein exhibits strong green fluorescence at 520 nm upon excitation at 480–500 nm. EthD-1 cannot permeate through intact plasma membranes of live cells, but can enter cells with damaged cell membranes, and exhibits a strong red fluorescence (∼40-fold) at ∼635 nm at excitation wavelengths

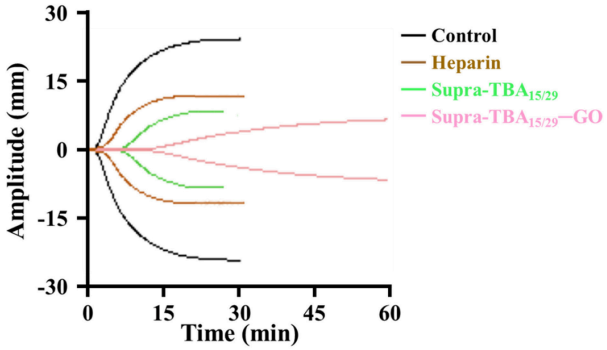

	R(min)	K(min)	α angle (deg)	MA(mm)
control	1.0±0.1	1.9±0.1	65.1±1.9	45.7±0.5
supra-$TBA_{15/29}$	4.7±0.4	N/A	32.5±2.8	15.6±0.3
supra-$TBA_{15/29}$-GO	9.8±0.6	N/A	9.6±1.5	11.4±0.1
Heparin	2.0±0.2	5.7±0.2	40.3±1.6	22.4±0.2

FIGURE 4 | Thromboelastography (TEG) of human whole blood treated with PBS control, heparin (100 nM), Supra-TBA15/29 (100 nM), and Supra-TBA15/29-GO (100 nM in term of TBA). N/A, not available.

of 480–500 nm when it binds to nucleic acids in dead cells. The live/dead cell viability after calcein AM/EthD-1 staining further proved the low cytotoxicity of Supra-$TBA_{15/29}$-GO, with concentrations as high as 1.00 μM and with green fluorescent cells predominating in the population (>98%). In addition, *in vitro* hemolysis experiments with defibrinated red blood cells (RBCs) did not show significant hemolysis for varying concentrations of Supra-$TBA_{15/29}$-GO (0–1.00 μM; **Figure S12**, Supporting Information). Overall, our results reveal that Supra-$TBA_{15/29}$-GO has good biocompatibility and low cytotoxicity toward mammalian cells.

In vivo Rat-Tail Bleeding Assay

Tail-bleeding assay in rat was performed to understand the anti-hemostatic effect of Supra-$TBA_{15/29}$-GO *in vivo*. The rats (∼200–250 g) were dosed (50 μL/100 g) by intravenous injection with heparin (2.0 μM), Supra-$TBA_{15/29}$ (2.0 μM), or Supra-$TBA_{15/29}$-GO (2.0 μM) and waited for 5 min. Then, the rat tails were fully transected 4 mm from the tip. The control group of rats dosed with PBS had an average blood clot weight of 918.6 ± 1.2 mg (n = 5), as shown in **Figure 5**. Compared with heparin, the Supra-$TBA_{15/29}$-GO-treated group showed superior anticoagulant effect. The blood clot weights of the Supra-$TBA_{15/29}$-GO-treated group (4,879 ± 900 mg; n = 5) were significantly heavier than that of the control group (P < 0.001) and the heparin-treated group (P < 0.05). The body weights of the Supra-$TBA_{15/29}$-GO treated rats were almost the same as those of the untreated group (P > 0.05, n = 5) 10 days post-dose (data not shown). In addition, all Supra-$TBA_{15/29}$-GO treated rats survived for the next 2 months and exhibited normal behavior. The *in vivo* rat-tail bleeding assay study indicated that highly biocompatible Supra-$TBA_{15/29}$-GO possesses great potential as a safe and efficient anticoagulant nanodrug for the treatment of thrombotic diseases, such as deep venous thrombosis, myocardial infarction, and thrombotic stroke.

CONCLUSIONS

In this study, highly stable and biocompatible supramolecular-aptamer functionalized GO nanosheets were prepared by a biomimetic approach. We successfully designed two different aptamers that can connectively hybridize and self-assemble on GO. AFM images showed that the Supra-$TBA_{15/29}$-GO was dispersed as 2D nanosheets. The Supra-$TBA_{15/29}$-GO was stable in high ionic strength solution as well as in human plasma. The structure of Supra-$TBA_{15/29}$ on GO is controllable by mediating the ratio of Supra-$TBA_{15/29}$ to GO and preparation temperature. The efficient inhibitory activity of Supra-$TBA_{15/29}$-GO against thrombin is due to precisely programmed TBA_{15} and TBA_{29}'s hybridized structure on GO leading to strong interactions with thrombin and steric hindrance from fibrinogen substrate. The dose-dependent TCT delay caused by Supra-$TBA_{15/29}$-GO was >10 times longer than that of the most widely used anticoagulant heparin. In addition, the TEG and rat-tail bleeding experiment further proved the superior anticoagulant activity of Supra-$TBA_{15/29}$-GO relative to heparin. In the future, GO with small sizes may be employed for preparing Supra-$TBA_{15/29}$-GO to more efficiently reduce the uptake from the reticuloendothelial system in animals. In addition, various aptamers which target with different coagulation factors can be co-programmed on GO for systematic inhibition of multiple coagulation factors. Moreover, bioaccumulation, biopsy, metabolism, and acute and chronic toxicity should be conducted in animal models to confirm the

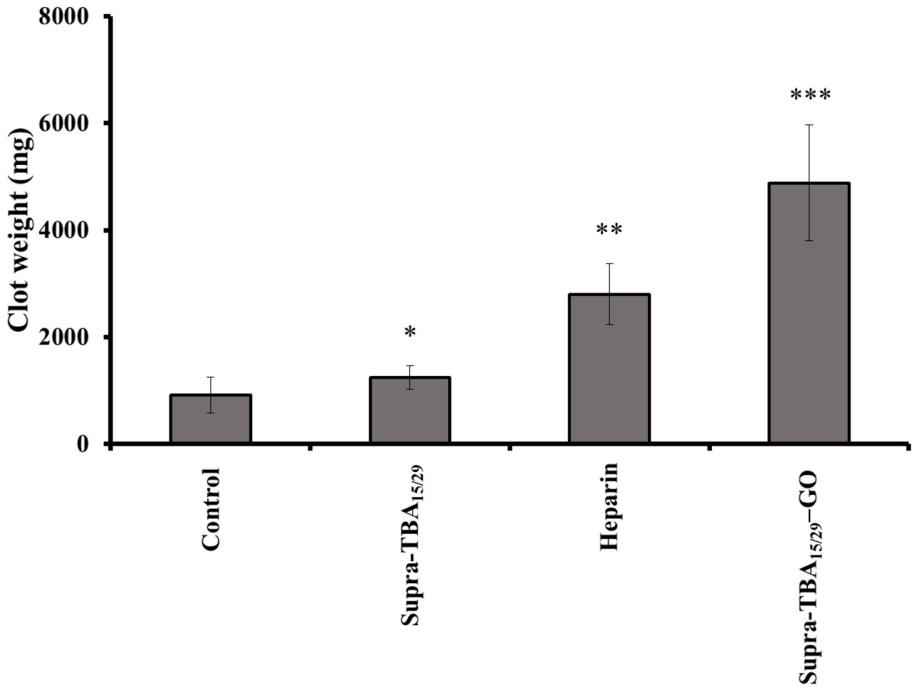

FIGURE 5 | The effect of Supra-$TBA_{15/29}$, heparin, and Supra-$TBA_{15/29}$-GO on rat-tail bleeding. Blood clots were collected after intravenous administration of the inhibitors (2.0 μM, 100 μL). Error bars represent the standard deviations of experiments in five rats. An asterisk indicates statistically significant differences (*$P < 0.05$, **$P < 0.01$, ***$P < 0.001$; $n = 5$) as compared with the control group.

potential of supramolecular aptamer-GO nanocomposites as a safe and viable drug.

EXPERIMENTAL METHODS

Synthesis and Characterization of GO

GO was prepared by a modified Hummer's method (Hummers and Offeman, 1958; Marcano et al., 2010). Briefly, concentrated sulfuric acid (90 mL) and concentrated phosphoric acid (10 mL) were mixed and added to graphite powder (0.75 g) in a round bottomed flask. Potassium permanganate (4.50 g) was slowly added to the mixture and maintained at 50°C for 12 h with continuous stirring. Then, the reaction mixture was allowed to cool and placed in an ice bath, followed by slowly adding deionized water (100 mL) and hydrogen peroxide (32%) to the mixture until the solution turned from dark purple to bright yellow. The supernatant was removed by centrifugation at 35,000 *g* for 30 min. The residue was washed repeatedly with 5 mM sodium phosphate buffer (pH 7.4) until the solution pH was close to 7. The as-obtained graphite oxide was exfoliated by sonication for 2 h (power 200 W). The unoxidized graphite and large particles were separated at a relative centrifugal force (RCF) of 15,000 *g* for 30 min, and its weight/volume concentration was calculated by lyophilisation. An atomic force microscope (Shimadzu SPM-9600 AFM, Shimadzu Co, Kyoto, Japan) was used to analyze the size of GO. The dynamic light scattering (DLS) and zeta potential experiments were performed using a Zetasizer 3000HS analyzer (Malvern Instruments, Malvern, UK). X-ray photoelectron spectroscopy (XPS) was performed using an ES-CALAB 250 spectrometer (VG Scientific, East Grinstead, UK) with Al Kα X-ray radiation as the X-ray excitation source. Binding energies were corrected using the C1s peak at 284.8 eV as the standard. We also analyzed GO at different degrees of oxidation by using a DXR Raman microscope (Thermo Fisher Scientific Inc., Waltham, MA, USA) equipped with a 50X objective, a Nd:YAG laser (532 nm) and a charge-coupled detector. FT-IR spectroscopy was performed by using a Cary 640 FT-IR spectrometer (Santa Clara, CA, USA).

Synthesis of Supra-$TBA_{15/29}$-GO

$A_{20}h_{15}T_5TBA_{15}T_5h_{15}$ ($sTBA_{15}$) and $h_{15}T_5TBA_{29}T_5h_{15}A_{20}$ ($sTBA_{29}$) (2.5 μM) were allowed to hybridize at 4°C for 1 h in PBS to form stable Supra-$TBA_{15/29}$. GO (40 μg mL^{-1}) was added to the Supra-$TBA_{15/29}$ and allowed to react. After 2 h of reaction, NaCl solution (1 M) was added and maintained at 4°C for 1 h. Finally, the solution was heated to 25, 45, 60, and 90°C and kept for 1 h. The resulting solution was centrifuged at an RCF of 35,000 *g* for 2 h and the residues were resuspended with PBS. After three centrifugation and washing cycles, the amount of Supra-$TBA_{15/29}$ adsorbed on GO was determined by quantitation of the un-adsorbed TBA in the supernatants by using Quant-iT™ OliGreen ssDNA Reagent. The material was stored at 4°C when not in use and found to be stable for up to 3 months.

Thrombin Clotting Time (TCT) Assay

TCT tests for the common coagulation pathway were performed with nh-$TBA_{15/29}$, di-$TBA_{15/29}$, Supra-$TBA_{15/29}$, Supra-$TBA_{15/29}$-GO, and four commercial anticoagulants (heparin, argatroban, hirudin, and warfarin). Analytical solution containing PBS (pH 7.4), bovine serum albumin (100 μM), inhibitor (100 nM), and human plasma (2-fold diluted) was allowed to react for 15 min, maintained at 37°C for 3 min, and then mixed with thrombin (15 nM). Scattered light intensity at 650 nm was recorded using an FP-6500 spectrophotometer (JASCO, Tokyo, Japan). The TCT was noted as the time at which the differential scattering signal intensity reached the maximum. The measurements were done in triplicates, and a single batch of plasma was used for each set of experiments.

Thromboelastography

The anticoagulation efficiency of Supra-$TBA_{15/29}$, Supra-$TBA_{15/29}$-GO and heparin in whole blood clots was evaluated by thromboelastography (Haemoscope corporation, Niles, IL, USA), which measures the progress of blood clot formation and platelet-fibrin bond strength and monitors the internal interactions in blood and the contributions of cellular content. The plasma samples from healthy volunteers with were drawn from the vein, transferred to tubes containing sodium citrate, and immediately centrifuged at a relative centrifugal force (RCF) of 3000 g (10 min, 4°C). The human plasma collection procedure was approved by the Chang Gung Memorial Hospital institutional review board (IRB-103-6474A3) and informed consent was obtained from the volunteers prior to the collection of the plasma. Prior to the experiment, plain disposable plastic TEG cups (Haemonetics) were maintained at 37°C. In total, 52 μL of anticoagulant (0.5 μM) in PBS and 288 μL of whole blood were mixed in a TEG cup and incubated at 37°C for 10 min. To initiate the whole blood coagulation at 37°C, 20 μL of thrombin solution (270 nM) was added to the above mixture. The clot formation was recorded until a stable clot was formed or 1 h had passed. The various parameters, such as the reaction kinetics, α angle, and maximum amplitude were calculated using the TEG® Analytical Software version (TAS) 4.2.3 (Haemonetics).

Rat-Tail Bleeding Time

We used rat tail bleeding time to compare the anticoagulant effect of inhibitors *in vivo* in male rats of the Sprague Dawley (SD) strain weighing between 200 and 250 g. The experiments were conducted after getting permission from the Institutional Animal Care and Use Committee of the National Laboratory Animal Center (Permit number License No. IACUC106049). The rats were anesthetized with Zoletil 50 with a dose of 100 μL/100 g body weight via subcutaneous injection. Supra-$TBA_{15/29}$ (2 μM), Supra-$TBA_{15/29}$-GO (2 μM; in terms of TBA) or heparin (2 μM) was administered by intravenous injection at a dose of 50 μL/100 g, followed by waiting for 5 min. Then, 4 mm of the rat tail-tip was cut off, and the tail was immersed in PBS at 37°C. The blood clot weight until cessation of bleeding was determined.

Statistical Analysis

Student's *t*-test was performed and *P*-values < 0.05 were considered significant. The probability of rat survival was determined by the Kaplan–Meier method.

See the Supporting Information for the details on the materials, determination of the binding constant of thrombin with Supra-$TBA_{15/29}$-GO, *in vitro* cytotoxicity assays, and hemolysis assays.

ETHICS STATEMENT

The animal experiments were conducted after getting permission from the Institutional Animal Care and Use Committee of the National Laboratory Animal Center (Permit number License No. IACUC106049).

AUTHOR CONTRIBUTIONS

C-CH conceived the original idea, supervised the project from start to finish, and supervised the manuscript preparation. T-XL and P-XL carried out the experiments. J-YM and H-WC provided feedback, interpretation of the results, and helped with the preparation of the manuscript. BU and AA helped with manuscript preparation. All authors discussed the results and contributed to the manuscript.

ACKNOWLEDGMENTS

This study was supported by the Ministry of Science and Technology of Taiwan under Contract Nos. 107-2622-M-019-001-CC2, 104-2628-M-019-001-MY3, 107-2811-M-019-507, and 106-3114-8-019-002.

SUPPLEMENTARY MATERIAL

The Supplementary Material for this article can be found online at: https://www.frontiersin.org/articles/10.3389/fchem.2019.00280/full#supplementary-material

REFERENCES

Alquwaizani, M., Buckley, L., Adams, C., and Fanikos, J. (2013). Anticoagulants: a review of the pharmacology, dosing, and complications. *Curr. Emerg. Hosp. Med. Rep.* 21, 83–97. doi: 10.1007/s40138-013-0014-6

Antony, J., and Grimme, S. (2008). Structures and interaction energies of stacked graphene–nucleobase complexes. *Phys Chem. Chem. Phys.* 10, 2722–2729. doi: 10.1039/b718788b

Bhattacharya, K., Mukherjee, S. P., Gallud, A., Burkert, S. C., Bistarelli, S., and Bellucci, S., et al. (2016). Biological interactions of carbon-based nanomaterials: from coronation to degradation. *Nanomed. Nanotechnol.* 12, 333–351. doi: 10.1016/j.nano.2015.11.011

Bock, L. C., Griffin, L. C., Latham, J. A., Vermaas, E. H., and Toole, J. J. (1992). Selection of single-stranded DNA molecules that bind and inhibit human thrombin. *Nature.* 355, 564–566. doi: 10.1038/355564a0

Bolliger, D., Seeberger, M. D., and Tanaka, K. A. (2012). Principles and practice of thromboelastography in clinical coagulation management and transfusion practice. *Transf. Med. Rev.* 26, 1–13. doi: 10.1016/j.tmrv.2011.07.005

Brunet, A., Salome, L., Rousseau, P., Destainville, N., Manghi, M., and Tardin, C. (2018). How does temperature impact the conformation of single DNA molecules below melting temperature? *Nucleic Acids Res.* 46, 2074–2081. doi: 10.1093/nar/gkx1285

Chabata, C. V., Frederiksen, J. W., Sullenger, B. A., and Gunaratne, R. (2018). Emerging applications of aptamers for anticoagulation and hemostasis. *Curr. Opin. Hematol.* 25, 382–388. doi: 10.1097/MOH.0000000000000452

Chen, J., Chen, L., Wang, Y., and Chen, S. (2014). Molecular dynamics simulations of the adsorption of DNA segments onto graphene oxide. *J. Phys. D Appl. Phys.* 47:505401. doi: 10.1088/0022-3727/47/50/505401

Chong, Y., Ge, C., Yang, Z., Garate, J. A., Gu, Z., and Weber, J. K., et al. (2015). Reduced cytotoxicity of graphene nanosheets mediated by blood-protein coating. *ACS Nano.* 9, 5713–5724. doi: 10.1021/nn5066606

Crawley, J. T. B., Zanardelli, S., Chion, C. K. N. K., and Lane, D. A. (2007). The central role of thrombin in hemostasis. *J. Thromb. Haemost.* 5, 95–101. doi: 10.1111/j.1538-7836.2007.02500.x

Darmostuk, M., Rimpelova, S., Gbelcova, H., and Ruml, T. (2015). Current approaches in SELEX: an update to aptamer selection technology. *Biotechnol. Adv.* 33, 1141–1161. doi: 10.1016/j.biotechadv.2015.02.008

De Candia, E. (2012). Mechanisms of platelet activation by thrombin: a short history. *Thromb. Res.* 129, 250–256. doi: 10.1016/j.thromres.2011.11.001

Doolittle, R. F. (2016). Some important milestones in the field of blood clotting. *J. Innate Immun.* 8, 23–29. doi: 10.1159/000442470

Fiorillo, M., Verre, A. F., Iliut, M., Peiris-Pagés, M., Ozsvari, B., and Gandara, R., et al. (2015). Graphene oxide selectively targets cancer stem cells, across multiple tumor types: implications for non-toxic cancer treatment, via "differentiation-based nano-therapy." *Oncotarget.* 6, 3553–3562. doi: 10.18632/oncotarget.3348

Gailani, D., and Renné, T. (2007). Intrinsic pathway of coagulation and arterial thrombosis. *Arterioscler. Thromb. Vasc. Biol.* 27, 2507–2513. doi: 10.1161/ATVBAHA.107.155952

Gao, L., Li, Q., Li, R., Yan, L., Zhou, Y., Chen, K., et al. (2015). Highly sensitive detection for proteins using graphene oxide-aptamer based sensors. *Nanoscale.* 7, 10903–10907. doi: 10.1039/c5nr01187f

Geggier, S., Kotlyar, A., and Vologodskii, A. (2011). Temperature dependence of DNA persistence length. *Nucleic Acids Res.* 39, 1419–1426. doi: 10.1093/nar/gkq932

Hellman, L. M., and Fried, M. G. (2007). Electrophoretic mobility shift assay (EMSA) for detecting protein–nucleic acid interactions. *Nat. Protoc.* 2, 1849–1861. doi: 10.1038/nprot.2007.249

Hsu, C.-L., Chang, H.-T., Chen, C.-T., Wei, S.-C., Shiang, Y.-C., and Huang, C.-C. (2011). Highly efficient control of thrombin activity by multivalent nanoparticles. *Chem. Eur. J.* 17, 10994–11000. doi: 10.1002/chem.201101081

Hsu, C.-L., Wei, S.-C., Jian, J.-W., Chang, H.-T., Chen, W.-H., and Huang, C.-C. (2012). Highly flexible and stable aptamer-caged nanoparticles for control of thrombin activity. *RSC Adv.* 2, 1577–1584. doi: 10.1039/c1ra00344e/

Huang, P.-J. J., Vazin, M., Lin, J. J., Pautler, R., and Liu, J. (2016a). Distinction of individual lanthanide ions with a DNAzyme beacon array. *ACS Sens.* 1, 732–738. doi: 10.1021/acssensors.6b00239

Huang, S.-S., Wei, S.-C., Chang, H.-T., Lin, H.-J., and Huang, C.-C. (2016b). Gold nanoparticles modified with self-assembled hybrid monolayer of triblock aptamers as a photoreversible anticoagulant. *J. Control. Release.* 221, 9–17. doi: 10.1016/j.jconrel.2015.11.028

Hummers, W. S. Jr., and Offeman, R. E. (1958). Preparation of graphitic oxide. *J. Am. Chem. Soc.* 80, 1339–1339. doi: 10.1021/ja01539a017

Ignjatovic, V. (2013). Thrombin clotting time. *Methods Mol. Biol.* 992, 131–138. doi: 10.1007/978-1-62703-339-8_10

Jin, L., Abrahams, J. P., Skinner, R., Petitou, M., Pike, R. N., and Carrell, R. W. (1997). The anticoagulant activation of antithrombin by heparin. *Proc. Natl. Acad. Sci. U.S.A.* 94, 14683–14688.

Jo, H., and Ban, C. (2016). Aptamer–nanoparticle complexes as powerful diagnostic and therapeutic tools. *Exp. Mol. Med.* 48:e230. doi: 10.1038/emm.2016.44

Kenry (2018). Understanding the hemotoxicity of graphene nanomaterials through their interactions with blood proteins and cells. *J. Mater. Res.* 33, 44–57. doi: 10.1557/jmr.2017.388

Kim, M.-G., Park, J. Y., Miao, W., Lee, J., and Oh, Y.-K. (2015). Polyaptamer DNA nanothread-anchored, reduced graphene oxide nanosheets for targeted delivery. *Biomaterials.* 48, 129–136. doi: 10.1016/j.biomaterials.2015.01.009

Kim, Y., Dennis, D. M., Morey, T., Yang, L., and Tan, W. (2010). Engineering dendritic aptamer assemblies as superior inhibitors of protein function. *Chem. Asian J.* 5, 56–59. doi: 10.1002/asia.200900421

Krauss, I. R., Napolitano, V., Petraccone, L., Troisi, R., Spiridonova, V., and Mattia, C. A., et al. (2018). Duplex/quadruplex oligonucleotides: role of the duplex domain in the stabilization of a new generation of highly effective anti-thrombin aptamers. *Int. J. Biol. Macromol.* 107, 1697–1705. doi: 10.1016/j.ijbiomac.2017.10.033

Kumar, N., and Seminario, J. M. (2018). Molecular dynamics study of thrombin capture by aptamers TBA26 and TBA29 coupled to a DNA origami. *Mol. Simul.* 44, 749–756. doi: 10.1080/08927022.2018.1448977

Lai, P.-X., Mao, J.-Y., Unnikrishnan, B., Chu, H.-W., Wu, C.-W., and Chang, H.-T., et al. (2018). Self-assembled, bivalent aptamers on graphene oxide as an efficient anticoagulant. *Biomater. Sci.* 6, 1882–1891. doi: 10.1039/c8bm00288f

Lee, C. J., and Ansell, J. E. (2011). Direct thrombin inhibitors. *Br. J. Clin. Pharmacol.* 72, 581–592. doi: 10.1111/j.1365-2125.2011.03916.x

Liao, K.-H., Lin, Y.-S., Macosko, C. W., and Haynes, C. L. (2011). Cytotoxicity of graphene oxide and graphene in human erythrocytes and skin fibroblasts. *ACS Appl. Mater. Interfaces.* 3, 2607–2615. doi: 10.1021/am200428v

Lin, Z. Y., Yao, Y. G., Li, Z., Liu, Y., Li, Z., and Wong, C.-P. (2010). Solvent-assisted thermal reduction of graphite oxide. *J. Phys. Chem. C.* 114, 14819–14825. doi: 10.1021/jp1049843

Liu, B., Salgado, S., Maheshwari, V., and Liu, J. (2016). DNA adsorbed on graphene and graphene oxide: fundamental interactions, desorption and applications. *Curr. Opin. Colloid Interface Sci.* 26, 41–49. doi: 10.1016/j.cocis.2016.09.001

Liu, Q., Jin, C., Wang, Y., Fang, X., Zhang, X., and Chen, Z., et al. (2014). Aptamer-conjugated nanomaterials for specific cancer cell recognition and targeted cancer therapy. *NPG Asia Mater.* 6:e95. doi: 10.1038/am.2014.12

Liu, X., Cheng, X., Wang, F., Feng, L., Wang, Y., and Zheng, Y., et al. (2018). Targeted delivery of SNX-2112 by polysaccharide-modified graphene oxide nanocomposites for treatment of lung cancer. *Carbohydr. Polym.* 185, 85–95. doi: 10.1016/j.carbpol.2018.01.014

Lu, C., Huang, P.-J. J., Liu, B., Ying, Y., and Liu, J. (2016). Comparison of graphene oxide and reduced graphene oxide for DNA adsorption and sensing. *Langmuir.* 32, 10776–10783. doi: 10.1021/acs.langmuir.6b03032

Lyu, Y., Chen, G., Shangguan, D., Zhang, L., Wan, S., and Wu, Y., et al. (2016). Generating cell targeting aptamers for nanotheranostics using cell-SELEX. *Theranostics.* 6, 1440–1452. doi: 10.7150/thno.15666

Macaya, R. F., Schultze, P., Smith, F. W., Roe, J. A., and Feigon, J. (1993). Thrombin-binding DNA aptamer forms a unimolecular quadruplex structure in solution. *Proc. Natl. Acad. Sci. U.S.A.* 90, 3745–3749.

Mackman, N., Tilley, R. E., and Key, N. S. (2007). Role of the extrinsic pathway of blood coagulation in hemostasis and thrombosis. *Arterioscler. Thromb. Vasc. Biol.* 27, 1687–1693. doi: 10.1161/ATVBAHA.107.141911

Mao, Y., Chen, Y., Li, S., Lin, S., and Jiang, Y. (2015). A graphene-based biosensing platform based on regulated release of an aptameric DNA biosensor. *Sensors.* 15, 28244–28256. doi: 10.3390/s151128244

Marcano, D. C., Kosynkin, D. V., Berlin, J. M., Sinitskii, A., Sun, Z., and Slesarev, A., et al. (2010). Improved synthesis of graphene oxide. *ACS Nano.* 4, 4806–4814. doi: 10.1021/nn1006368

Morfini, M., Coppola, A., Franchini, M., and Di Minno, G. (2013). Clinical use of factor VIII and factor IX concentrates. *Blood Transf.* 11, S55–S63. doi: 10.2450/2013.010s

Mosesson, M. W. (2005). Fibrinogen and fibrin structure and functions. *J. Thromb. Haemost.* 3, 1894–1904. doi: 10.1111/j.1538-7836.2005.01365.x

Musumeci, D., and Montesarchio, D. (2012). Polyvalent nucleic acid aptamers and modulation of their activity: a focus on the thrombin binding aptamer. *Pharmacol. Ther.* 136, 202–215. doi: 10.1016/j.pharmthera.2012.07.011

Nimjee, S. M., Povsic, T. J., Sullenger, B. A., and Becker, R. C. (2016). Translation and clinical development of antithrombotic aptamers. *Nucl. Acid Ther.* 26, 147–155. doi: 10.1089/nat.2015.0581

Otsuka, F., Yasuda, S., Noguchi, T., and Ishibashi-Ueda, H. (2016). Pathology of coronary atherosclerosis and thrombosis. *Cardiovasc. Diagn. Ther.* 6, 396–408. doi: 10.21037/cdt.2016.06.01

Ou, L., Song, B., Liang, H., Liu, J., Feng, X., and Deng, B., et al. (2016). Toxicity of graphene-family nanoparticles: a general review of the origins and mechanisms. *Part. Fibre Toxicol.* 13:57. doi: 10.1186/s12989-016-0168-y

Padmanabhan, K., Padmanabhan, K. P., Ferrara, J. D., Sadler, J. E., and Tulinsky, A. (1993). The structure of α-thrombin inhibited by a 15-mer single-stranded DNA aptamer. *J. Biol. Chem.* 268, 17651–17654.

Pagano, B., Martino, L., Randazzo, A., and Giancola, C. (2008). Stability and binding properties of a modified thrombin binding aptamer. *Biophys. J.* 94, 562–569. doi: 10.1529/biophysj.107.117382

Palta, S., Saroa, R., and Palta, A. (2014). Overview of the coagulation system. *Indian J. Anaesth.* 58, 515–523. doi: 10.4103/0019-5049.144643

Pang, X., Cui, C., Wan, S., Jiang, Y., Zhang, L., and Xia, L., et al. (2018). Bioapplications of cell-SELEX-generated aptamers in cancer diagnostics, therapeutics, theranostics and biomarker discovery: a comprehensive review. *Cancers.* 10:E47. doi: 10.3390/cancers10020047

Park, J. S., Goo, N.-I., and Kim, D. E. (2014). Mechanism of DNA adsorption and desorption on graphene oxide. *Langmuir.* 30, 12587–12595. doi: 10.1021/la503401d

Pollak, U., Yacobobich, J., Tamary, H., Dagan, O., and Manor-Shulman, O. (2011). Heparin-induced thrombocytopenia and extracorporeal membrane oxygenation: a case report and review of the literature. *J. Extra. Corpor. Technol.* 43, 5–12.

Previtali, E., Bucciarelli, P., Passamonti, S. M., and Martinelli, I. (2011). Risk factors for venous and arterial thrombosis. *Blood Transf.* 9, 120–138. doi: 10.2450/2010.0066-10

Pu, Y., Zhu, Z., Han, D., Liu, H., Liu, J., and Liao, J., et al. (2011). Insulin-binding aptamer-conjugated graphene oxide for insulin detection. *Analyst.* 136, 4138–4140. doi: 10.1039/c1an15407a

Rana, K., and Neeves, K. B. (2016). Blood flow and mass transfer regulation of coagulation. *Blood Rev.* 30, 357–368. doi: 10.1016/j.blre.2016.04.004

Ranganathan, S. V., Halvorsen, K., Myers, C. A., Robertson, N. M., Yigit, M. V., and Chen, A. A. (2016). Complex thermodynamic behavior of single-stranded nucleic acid adsorption to graphene surfaces. *Langmuir.* 32, 6028–6034. doi: 10.1021/acs.langmuir.6b00456

Ren, X., Li, J., Chen, C., Gao, Y., Chen, D., and Su, M., et al. (2018). Graphene analogues in aquatic environments and porous media: dispersion, aggregation, deposition and transformation. *Environ. Sci. Nano.* 5, 1298–1340. doi: 10.1039/c7en01258f

Rezaei, A., Akhavan, O., Hashemi, E., and Shamsara, M. (2016). Toward chemical perfection of graphene-based gene carrier via Ugi multicomponent assembly process. *Biomacromolecules.* 17, 2963–2971. doi: 10.1021/acs.biomac.6b00767

Riccardi, C., Krauss, I. R., Musumeci, D., Morvan, F., Meyer, A., and Vasseur, J.-J., et al. (2017). Fluorescent thrombin binding aptamer-tagged nanoparticles for an efficient and reversible control of thrombin activity. *ACS Appl. Mater. Interfaces.* 9, 35574–35587. doi: 10.1021/acsami.7b11195

Rinker, S., Ke, Y., Liu, Y., Chhabra, R., and Yan, H. (2008). Self-assembled DNA nanostructures for distance dependent multivalent ligand–protein binding. *Nat. Nanotechnol.* 3, 418–422. doi: 10.1038/nnano.2008.164

Rowsell, S., Stonehouse, N. J., Convery, M. A., Adams, C. J., Ellington, A. D., and Hirao, I., et al. (1998). Crystal structures of a series of RNA aptamers complexed to the same protein target. *Nat. Struct. Biol.* 5, 970–975. doi: 10.1038/2946

Seabra, A. B., Paula, A. J., de Lima, R., Alves, O. L., and Durán, N. (2014). Nanotoxicity of graphene and graphene oxide. *Chem. Res. Toxicol.* 27, 159–168. doi: 10.1021/tx400385x

Smith, S. A., Travers, R. J., and Morrissey, J. H. (2015). How it all starts: initiation of the clotting cascade. *Crit. Rev. Biochem. Mol. Biol.* 50, 326–336. doi: 10.3109/10409238.2015.1050550

Suppiej, A., Gentilomo, C., Saracco, P., Sartori, S., Agostini, M., and Bagna, R., et al. (2015). Paediatric arterial ischaemic stroke and cerebral sinovenous thrombosis. *Thromb. Haemost.* 113, 1270–1277. doi: 10.1160/TH14-05-0431

Tasset, D. M., Kubik, M. F., and Steiner, W. (1997). Oligonucleotide inhibitors of human thrombin that bind distinct epitopes. *J. Mol. Biol.* 272, 688–698. doi: 10.1006/jmbi.1997.1275

Tucker, W. O., Shum, K. T., and Tanner, J. A. (2012). G-quadruplex DNA aptamers and their ligands: structure, function and application. *Curr Pharm. Design.* 18, 2014–2026. doi: 10.2174/138161212799958477

Urmann, K., Modrejewski, J., Scheper, T., and Walter, J.-G. (2016). Aptamer-modified nanomaterials: principles and applications. *BioNanoMaterials.* 18, 1–2. doi: 10.1515/bnm-2016-0012

Varghese, N., Mogera, U., Govindaraj, A., Das, A., Maiti, P. K., and Sood, A. K., et al. (2009). Binding of DNA nucleobases and nucleosides with graphene. *ChemPhysChem.* 10, 206–210. doi: 10.1002/cphc.200800459

Wang, Y., Li, Z., Hu, D., Lin, C.-T., Li, J., and Lin, Y. (2010). Aptamer/graphene oxide nanocomplex for *in situ* molecular probing in living cells. *J. Am. Chem. Soc.* 132, 9274–9276. doi: 10.1021/ja103169v

Wu, M., Kempaiah, R., Huang, P.-J. J., Maheshwari, V., and Liu, J. (2011). Adsorption and desorption of DNA on graphene oxide studied by fluorescently labeled oligonucleotides. *Langmuir.* 27, 2731–2738. doi: 10.1021/la1037926

Xiao, K., Liu, J., Chen, H., Zhang, S., and Kong, J. (2017). A label-free and high-efficient GO-based aptasensor for cancer cells based on cyclic enzymatic signal amplification. *Biosens. Bioelectron.* 91, 76–81. doi: 10.1016/j.bios.2016.11.057

Yan, W., and Shao, R. (2006). Transduction of a mesenchyme-specific gene periostin into 293T cells induces cell invasive activity through epithelial-mesenchymal transformation. *J. Biol. Chem.* 281, 19700–19708. doi: 10.1074/jbc.M601856200

Yang, Y., Yang, X., Yang, Y., and Yuan, Q. (2018). Aptamer-functionalized carbon nanomaterials electrochemical sensors for detecting cancer relevant biomolecules. *Carbon.* 129, 380–395. doi: 10.1016/j.carbon.2017.12.013

Zavyalova, E., Golovin, A., Pavlova, G., and Kopylov, A. (2016a). Development of antithrombotic aptamers: from recognizing elements to drugs. *Curr. Pharm. Design.* 22, 5163–5176. doi: 10.2174/1381612822666161004163409

Zavyalova, E., Tagiltsev, G., Reshetnikov, R., Arutyunyan, A., and Kopylov, A. (2016b). Cation coordination alters the conformation of a thrombin-binding G-quadruplex DNA aptamer that affects inhibition of thrombin. *Nucl. Acid Ther.* 26, 299–308. doi: 10.1089/nat.2016.0606

Zavyalova, E., Ustinov, N., Golovin, A., Pavlova, G., and Kopylov, A. (2016c). G-quadruplex aptamers to human thrombin versus other direct thrombin inhibitors: the focus on mechanism of action and drug efficiency as anticoagulants. *Curr. Med. Chem.* 23, 2230–2244. doi: 10.2174/0929867323666160517120126

Zhang, Z., Li, Z., Li, J., and Liu, L. (2018). Effects of natural hirudin and low molecular weight heparin in preventing deep venous thrombosis in aged patients with intertrochanteric fracture. *Sci. Rep.* 8:8847. doi: 10.1038/s41598-018-27243-1

Zhu, Y., Cai, Y., Xu, L., Zheng, L., Wang, L., and Qi, B., et al. (2015). Building an aptamer/graphene oxide FRET biosensor for one-step detection of bisphenol A. *ACS Appl. Mater. Interfaces.* 7, 7492–7496. doi: 10.1021/acsami.5b00199

Conflict of Interest Statement: The authors declare that the research was conducted in the absence of any commercial or financial relationships that could be construed as a potential conflict of interest.

frontiers in Chemistry

ORIGINAL RESEARCH
published: 24 October 2019
doi: 10.3389/fchem.2019.00715

Gold Nanorods as Saturable Absorber for Harmonic Soliton Molecules Generation

Yiqing Shu[1], Penglai Guo[1], Xiaohui Li[1], Guian Li[1], Peng Wang[1], Ge Shen[1] and Jianqing Li[2]*

[1] School of Physics and Information Technology, Shaanxi Normal University, Xi'an, China, [2] School of Electronic Information Technology, Macau University of Science and Technology, Macau, China

Gold nanorods (GNRs) has been investigated in the field of chemistry, optoelectronics, and medicine for their tenability, compatibility, electromagnetics, and excellent photonics properties. Especially, GNRs, used to generate ultrashort pulse, have been studied recently. However, multiple pulses evolution based on GNRs needs to be further explored. In this article, GNRs are synthesized by seed-mediated growth method, characterized systematically and been chosen as saturable absorber (SA) to apply in ultrafast photonics. The GNRs SA presents a saturable intensity of 266 MW/cm^2, modulation depth of 0.6%, and non-saturable loss of 51%. Furthermore, a passively mode-locked erbium-doped fiber laser based on GNRs SA with femtosecond pulse is demonstrated. Thanks to the excellent properties of GNRs, by adjusting the cavity polarization direction with the proposed GNRs SA, soliton molecules operation with spectrum modulation period of 3.3 nm and pulse modulation interval of 2.238 ps is directly obtained. For the most important, 9th-order harmonic soliton molecules have been generated in the laser cavity for the first time. It is demonstrated that GNRs can be a novel type of non-linear optical (NLO) device and have potential applications in the field of ultrafast photonics.

Keywords: gold nanorods, non-linear optical properties, ultrafast photonics, mode-locked fiber laser, harmonic soliton molecules

OPEN ACCESS

Edited by:
Tianyou Zhai,
Huazhong University of Science and Technology, China

Reviewed by:
Ran Long,
University of Science and Technology of China, China
Xu Peng,
Hubei University, China
Tengfei Zhou,
University of Wollongong, Australia

****Correspondence:***
Xiaohui Li
lixiaohui0523@163.com

Specialty section:
This article was submitted to Nanoscience, a section of the journal Frontiers in Chemistry

Received: *13 May 2019*
Accepted: *10 October 2019*
Published: *24 October 2019*

Citation:
Shu Y, Guo P, Li X, Li G, Wang P, Shen G and Li J (2019) Gold Nanorods as Saturable Absorber for Harmonic Soliton Molecules Generation. Front. Chem. 7:715. doi: 10.3389/fchem.2019.00715

INTRODUCTION

Many researchers have been attracted by noble metal nano-materials, such as gold, silver, due to the strong non-linear optical (NLO) effects which caused by their surface plasmon resonances (SPR) (Oh et al., 2011; Tsutsui et al., 2011; Huang et al., 2014; Komarov et al., 2015; Fan and Zhang, 2016; Yang et al., 2018). These effects enable noble metal nano-materials get many potential applications in synthesize NLO devices, such as optical detectors, optical sensors, and optical absorbers (Jain et al., 2007; Zijlstra et al., 2009). Among these noble metal nano-materials, gold nanorods (GNRs) have two SPR peaks, one is transverse SPR (TSPR) and the other is longitudinal SPR (LSPR). The LSPR is particularly sensitive to the aspect ratio of the GNRs and could be flexibly tuned through a broad spectral ranging from the visible to the near-infrared regime (Gou and Murphy, 2005; Ming et al., 2009; Kang et al., 2013; Fang et al., 2014; Lopez-Lozano et al., 2014; Burrows et al., 2016; He et al., 2016). This indicates that GNRs could be used in diverse wavebands when they are needed.

In recent years, mode-locked and Q-switched fiber lasers using GNRs as SA have been demonstrated at different wavebands (1, 1.56, and 2 μm) (Kang et al., 2013, 2015; Wang X. et al., 2016; Chen et al., 2018).

Up to now, enormous experimental data and simulation results show that optical fiber lasers can produce many categories of pluses, such as conventional solitons (CSs), dissipative solitons, stretched pulse, self-similar pulse (Peng et al., 2013; Li et al., 2016; Wang Y. et al., 2016; Chai et al., 2018; Zhang et al., 2018; Wang et al., 2019). At the state of multi-soliton, harmonic mode locking (HML) would be formed when the solitons repel each other in a long range and uniformly fill in the whole laser cavity (Yang et al., 2007; Wang Z. et al., 2015; Fu et al., 2019). In addition, another kinds of multiple pulse called bound solitons (BSs) or soliton molecules would be formed as well, when the solitons repel each other in a short range and attract each other in a long range then transmit simultaneously (Komarov et al., 2008; Wang Y. et al., 2015).

Generally, fiber laser would work in one of the multi-soliton states. Nevertheless, coexistence between different kinds of multi-soliton states could also be generated in a passively mode-locked fiber lasers by precisely adjusting and optimizing the cavity parameters (Zhao et al., 2009; Luo et al., 2018; Zhang et al., 2019). Recently, researchers have reported that the two kinds of pulses, harmonic soliton molecules and rectangular noise-like pulses, can be coexisted in a fiber laser (Huang et al., 2016). In addition, different real saturable absorbers (SAs) can also be excellent composed for the generation of multiple pulses in the fiber laser cavity (Martinez et al., 2017; Lai et al., 2018). Other researchers reported that bound soliton and harmonic mode-locking soliton could be coexisted in an ultrafast fiber laser by MoS_2 SA for a photonic device (Liu et al., 2018). GNRs as a promising SA need to be further investigated in aspect of generating special kinds of multiple pulses in the fiber laser cavities (Lu et al., 2018).

Although some studies have reported silica-encased GNRs can also be used as SA to produce ultrashort pulses, the preparation process of SA is more complex and only traditional solitons are obtained in fiber laser cavity (Wang X. et al., 2016). In this article, GNRs are successfully synthesized by seed-mediated growth method and characterized by scanning electron microscope (SEM), transmission electron microscope (TEM), and absorption spectra in the visible and near-infrared regions (Johnson et al., 2002; Perezjuste et al., 2005; Chow, 2017). Then, harmonic mode-locking of soliton molecules in EDF laser based on GNRs SA is studied. Depositing the GNRs dispersion on a taper fiber, whose waist diameter and length of 15 μm and 1.5 mm, respectively, to fabricate SA. Using the GNRs SA to obtain ultrashort pulse in infrared region. The GNRs SA has been studied with a modulation depth of 0.6% and non-saturable loss of 51%. By adjusting the laser's polarization direction, 740.6 fs soliton molecules are directly obtained from the Er-doped fiber laser based on GNRs SA. Increasing the pump power, 9th-order harmonic soliton molecules are generated in the laser cavity for the first time. It's much faster than many works before (Kang et al., 2013). The SA exhibits excellent stability, after a month, a steady pulse can be obtained as before. This work further confirms that the GNRs are promising high-performance SA with many potential applications in many fields such as optical fiber communications, optical logic signal processing, and even materials processing, etc.

MATERIALS AND SYNTHESIS OF GNRs

Materials

Chloroauric acid ($HAuCl_4$), hexadecyltrimethyl ammonium bromide (CTAB), sodium borohydride ($NaBH_4$), silver nitrate ($AgNO_3$), hydrochloric acid (HCl), ascorbic acid (AA). All the glass wares are cleaned with deionized water by ultrasonic cleaning machines prior to the experiments.

Synthesis of GNRs

GNRs are synthesized by using the seed-mediated growth method reported previously. Briefly, $HAuCl_4$ (marked solution B) is added to 8 mL CTAB (marked solution A) and mixed in a magnetic stirrer at 35°C, $NaBH_4$ is added to the mixture with continuous stirring for 2 min. The color of the solution immediately changes from luminous yellow to dark brown. This change suggests that gold nanoparticles are successfully synthesized. The formed gold nanoparticles dispersion is sat in an incubator for 2 h to grow into seed solution and the seed solution are stable for a couple of weeks.

$AgNO_3$ (marked solution c) and $HAuCl_4$ (marked solution b) are added, respectively, to 20 mL CTAB (marked solution a), then added HCl to the solution (a) and mixed on a magnetic stirrer at 35°C (marked solution 1), AA is added to growth solution. Adding seed solution to growth solution and setting the mixture in an incubator for 12 h. Using deionized water to wash resulting solution repeatedly and centrifuging the resulting solution at 8,000 revolutions per min for 10 min once a time. Keeping the resulting solution in cold storage for further characterization. **Figure 1A** shows the preparation process of GNRs. **Figure 1B** shows the photograph of GNRs solution.

CHARACTERIZATION OF GOLD NANORODS (GNRs)

The SEM (the scale bar is 400 nm) and TEM (the scale bar is 40 nm) images of samples are shown in **Figures 2a–c** to characterize the obtained GNRs. Obviously, rod-shaped structure of samples are in the majority. By measuring we get the aspect ratio of GNRs about 2.5–8.5. It is interesting to note that seed particles also produce a significant amount of small rods and other secondary shapes, such as cone-shaped. In **Figure 2d** shows TEM image (HR-TEM) of GNRs. We can clearly observe a crystal lattice of GNRs in this image. The inset of **Figure 2d** shows the corresponding selective electron diffraction pattern. The GNRs prepared by seed growth method are single crystal structure, which is also indicated by the high resolution TEM of GNRs and the corresponding selective electron diffraction pattern.

Figure 3A shows the size distribution of the gold nanomaterials. The average diameters of these GNRs are 58.7 nm. The visible-near infrared (VIS-NIR) absorption is shown in **Figure 3B**. The samples have three higher absorption bands peaked at 0.5, 0.8, 1.5 μm, respectively. The absorption

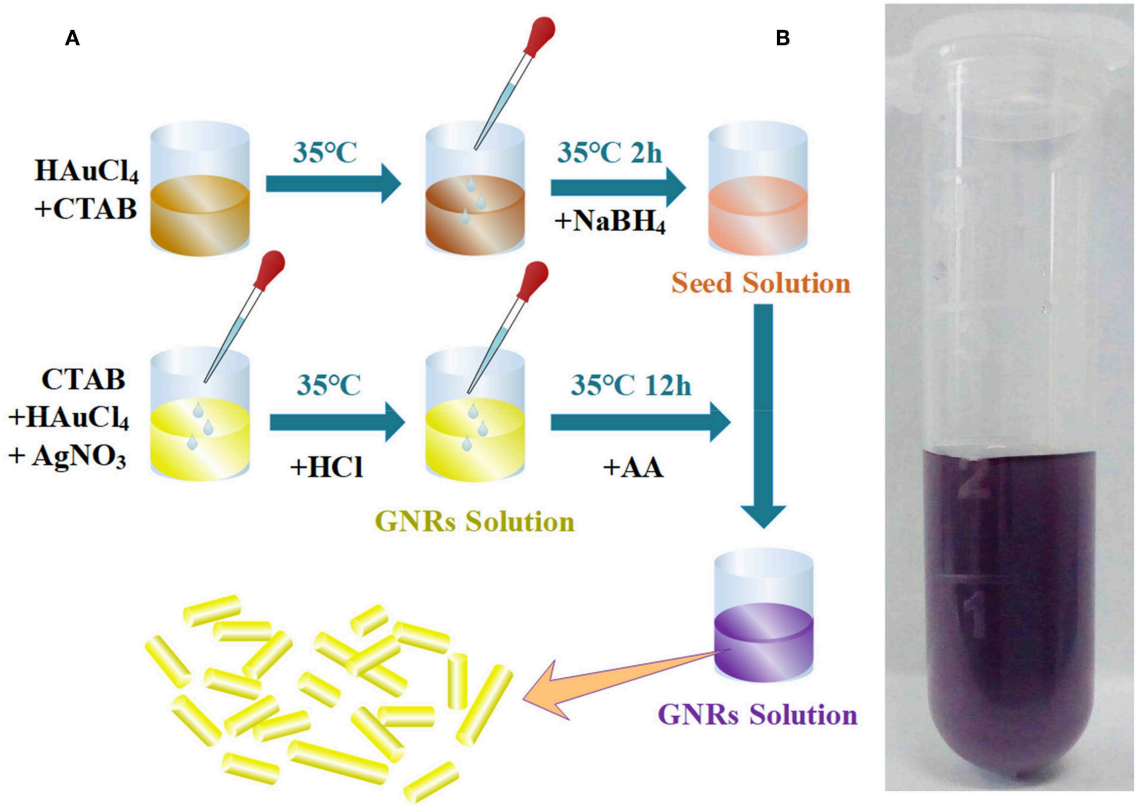

FIGURE 1 | (A) Preparation process of GNRs. **(B)** Photograph of GNRs water solution.

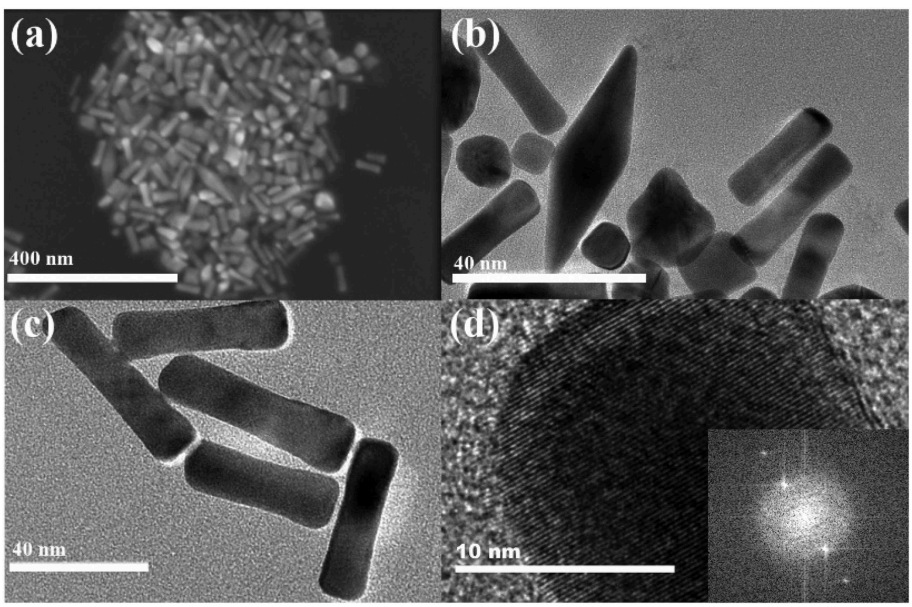

FIGURE 2 | (a) SEM image of gold nanomaterials. **(b,c)** TEM images of GNRs with 40 nm scale. **(d)** HR-TEM image of GNR with 10 nm scale, the inset shows the power spectrum of the image.

band peaked at 0.5 μm is caused by the TSPR with the diameter of GNRs is ∼14 nm. The second band peaked at 0.8 μm is caused by the small GNRs and other secondary shapes. The band we are interested in 1.5 μm caused by the LSPR of long GNRs, which provides a usability of our GNRs sample in ultrafast laser as a SA.

The fabrication processes of GNRs SA are described in **Figure 4**. After mechanical exfoliation, the bare fiber of single mode fiber (SMF) is burned and stretched, only in this way can we prepare a segment of taper fiber with waist diameter of 15 μm and length of 1.5 mm, this process is shown in **Figure 4a**. **Figure 4b** exhibits a model for preparing the GNRs SA by means of optical induced deposition. Injecting laser in the end of microfiber when dropping GNRs dispersion onto the surface of taper fiber. **Figure 4c** depicted a taper fiber reality image observed under a microscope and the black part attached to the surface of taper fiber is GNRs.

In order to further investigate the characteristics of GNRs, the non-linear absorption is measured by using balanced twin detector measurement technology. **Figure 5a** describes the measurement method of saturable absorption property about the GNRs. In this experiment, the pump source, a standard femtosecond pulse laser source whose center wavelength of 1563.3 nm, repetition rate of 21.4 MHz and pulse duration of 584 fs is divided into two parts by a 50/50 optical coupler after passing through attenuator which can be adjust the output power of standard laser source. One accesses power meter 1 directly, the other injects the GNRs SA before enters the power meter 2. The optical non-linear transmittance result is exhibited in **Figure 5b**. As shown here, the saturable intensity is 266 MW/cm^2, the modulation depth is ∼0.6%, and the non-saturable loss of 51%. Based on these experimental results, we apply GNRs as a SA in fiber laser for implementing mode-locking.

LASER PERFORMANCE AND DISCUSSIONS

To check the laser performance of GNRs SA, it is incorporated into a laser cavity to generate ultrashort pulse. The schematic of the passively mode-locked EDF ring laser is shown in **Figure 6**. A 0.5 m-long EDF offering a laser gain is pumped by 976 nm laser diode (LD) connecting a 980/1,550 nm wavelength division multiplexer (WDM). The polarization controller (PC) are utilized to control the light polarization state for achieving mode-locking and optimizing the laser operation. A polarization-independent isolator (PI-ISO) is used to guarantee the unidirectional operation. The GNRs SA

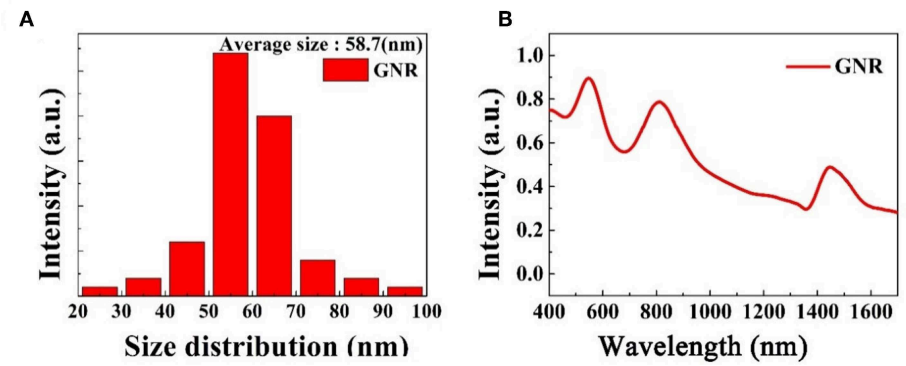

FIGURE 3 | (A) Size distribution of GNRs. **(B)** Absorption spectra of GNRs water solution.

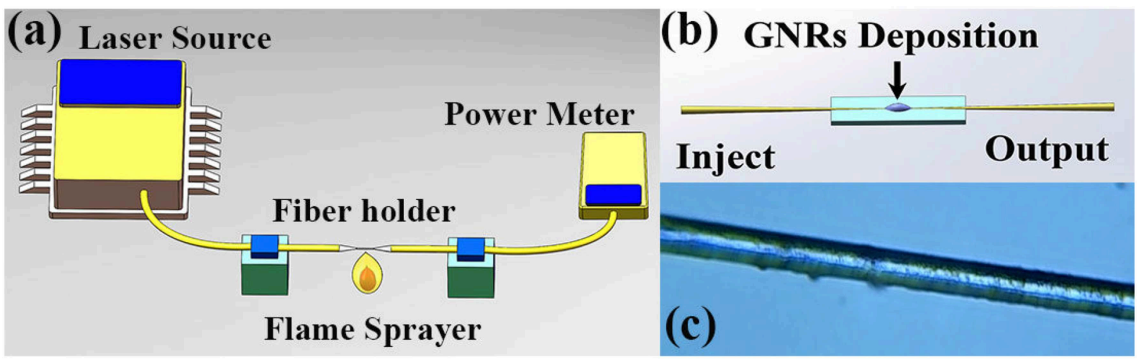

FIGURE 4 | (a) Experimental setup for fabricating a taper fiber. **(b)** Schematic diagram for deposition of GNRs material on taper fiber by injecting laser. **(c)** Image of the microscopical taper fiber-based GNRs SA.

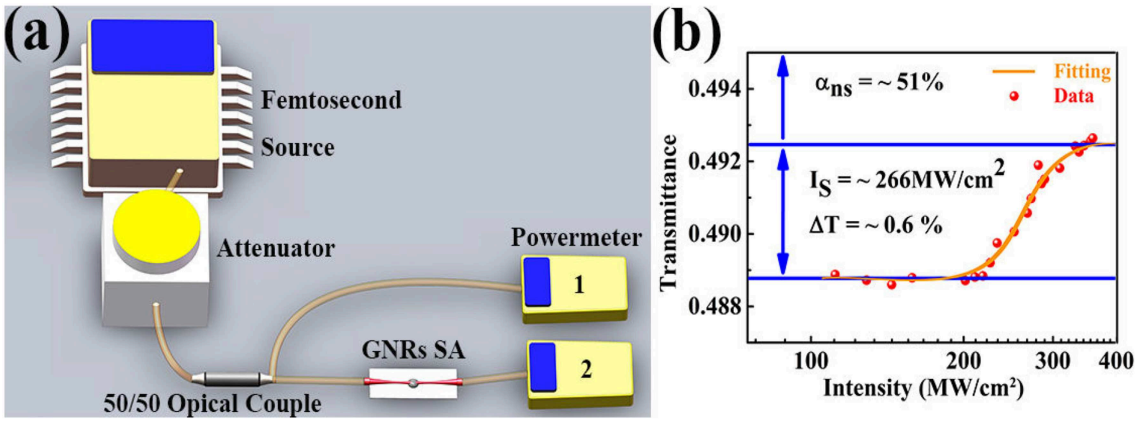

FIGURE 5 | (a) Measurement schematic of non-linear saturable absorption. **(b)** The saturable absorption curvey of gold nanomaterials SA.

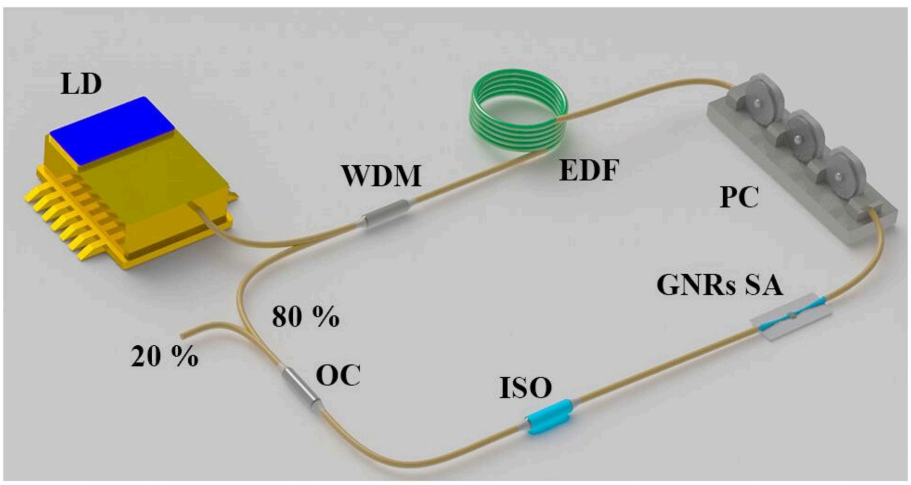

FIGURE 6 | Schematic diagram of the fiber laser cavity.

plays an essential role in this fiber laser cavity. A 20/80 fiber optical coupler (OC), the 20% is exported to detect intracavity laser performance and the other 80% turn back laser cavity to oscillate, is located in the end of cavity. The total cavity length is around ∼17 m corresponding to a fundamental repetition rate of 11.3 MHz. The spectrum and pulse train are monitored by an optical spectrum analyzer (Anritsu MS9710C), a real-time oscilloscope with resolution of 1 GHz (Rigon DS6104) and a photodetector with resolution of 2 GHz (Thorlabs DET01CFC). The radio frequency (RF) spectrum of the mode-locked operation is recorded by a radio frequency spectrum analyzer (Rohde & Schwarz FSC6). Moreover, the pulse duration and modulation interval are measured by an autocorrelator (Femtochrome FR-103XL).

Then simply increasing the pump power to 153 mW, the self-started soliton molecule mode-locking operation occurs. For further exploring the mode-locking operation, the pump power is increased to 314 mW. **Figure 7A** shows the typical soliton molecule spectrum obtains at the pump power of 203 mW. Here, spectrum modulation period of soliton molecule is 3.3 nm. **Figure 7B** presents the corresponding mode-locked pulse-train and we realize the pulse period is 88.4 ns. To verify the laser stability, we measure the radio frequency (RF) spectrum of the mode locking operation with a resolution bandwidth of 30 kHz and video bandwidth of 100 Hz. As presented in **Figure 7C**, the fundamental frequency peak locates at 11.3 MHz determined by the cavity length of ∼17 m, corresponding to the fundamental cavity repetition rate. The signal-to-noise ratio (SNR) is ∼47.2 dB, indicating the high stability of mode-locking operation. Moreover, the inset of **Figure 7C** shows RF spectrum measured under the 22.6 MHz span. Then, by using AC, the soliton modulation period and duration of the mode-locked pulse are identified. As described in **Figure 7D**, the soliton molecule delivers the pulse-train

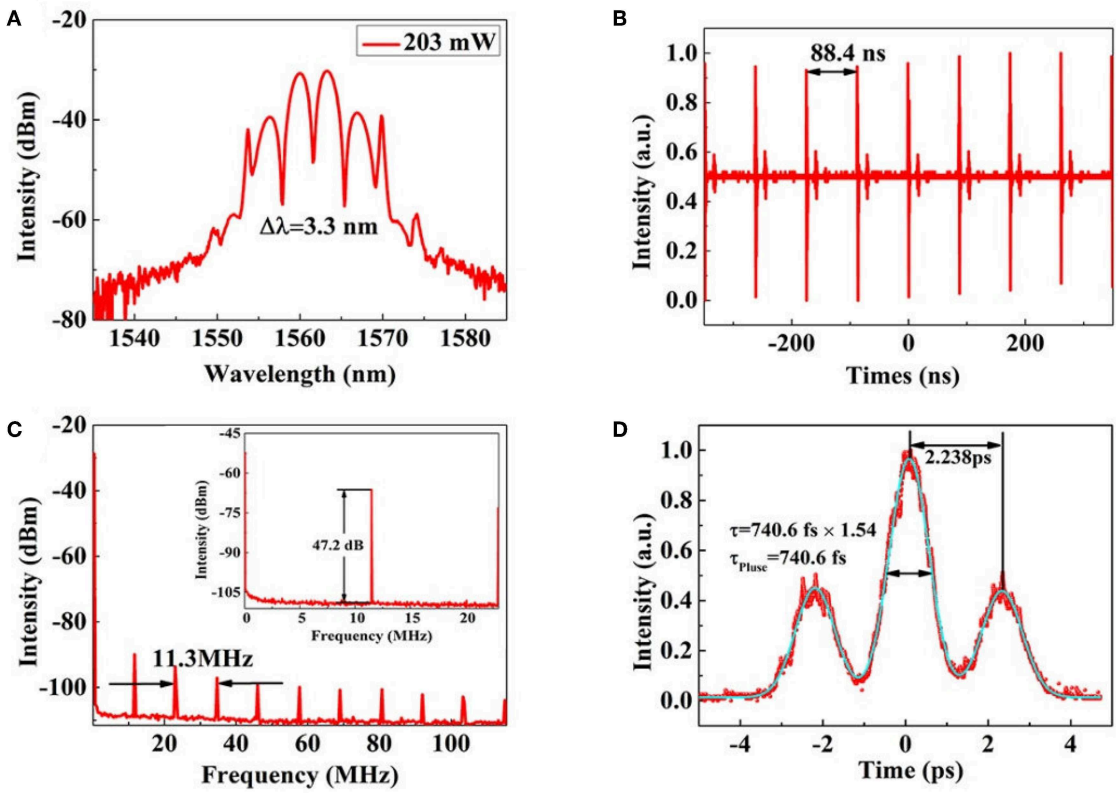

FIGURE 7 | (A) The typical soliton molecule spectrum obtained at the pump power of 203 mW. **(B)** The corresponding soliton molecule pulse-sequence. **(C)** RF spectrum around the fundamental repetition rate; **(D)** autocorrelation trace of partially coherent pulse generation.

with 740.6 fs duration and 2.238 ps soliton pulse modulation interval if the fit of the sech^2 pulse shape is assumed. There is a formula to describe the relationship between spectrum modulation period ($\Delta\lambda$) and pulse modulation interval (ΔT) of soliton molecule:

$$\Delta T = |\lambda_0|^2/(c\cdot\Delta\lambda) \quad (1)$$

Here, λ_0 and c mean center wavelength of mode-locked laser operation and speed of light. Their values are 1,560 nm and 3×10^8 m/s, respectively. Through theoretical calculation, our experimental results are consistent with the theoretical predictions.

After increasing the pump power gradually to the maximum of laser diode, fiber laser is still working in the mode-locked state. Moreover, the soliton molecule could maintain stable operation well at the maximum pump power of 350 mW, which means the optical damage threshold of GNRs SA is considerable high. **Figures 8A,B** show the spectrum and sequence evolution of soliton molecule with pump power from 153 to 314 mW. **Figure 8C** depicts the variation of the soliton molecule operation output power when we increasing the pump power. More importantly, the 9th-order harmonics soliton molecule is obtained during the process of increasing pump power. Optical spectrum, pulse sequence and autocorrelation trace of 9th order harmonics soliton molecule under 314 mW of pump power are exhibited in **Figures 8D–F**, respectively. We can discover that 9th soliton molecule has the 3.2 nm spectrum modulation period, 101.7 MHz fundamental frequency and 0.9 ps pulse duration with 2.7 ps soliton pulse modulation interval. In the experiment, we also check the significance of GNRs SA in fiber laser. GNRs SA is removed from the laser cavity. As a result, there is no soliton molecule operation even if the PC is rotated in a large range. The results demonstrate that the ultrafast properties of GNRs are accountable for the generation of the fiber laser.

As we know, not only the soliton molecules and harmonic mode-locking solution but many other kinds of pluses could also be generated in a fiber laser, such as soliton rain and noise-like pluses. Nevertheless, in our experiments, only two multi-soliton states are observed. Thanks to the high optical damage threshold of GNRs we would do more research on composite mode-locked operations based on GNRs SA and investigate the coexistence of multi-soliton dynamics.

CONCLUSION

In conclusion, GNRs are prepared by seed-mediated growth method and characterized by the technology of SEM, TEM, VIS-NIR absorption which noticed the micro-structure and the absorption of GNRs. By measuring the NLO response

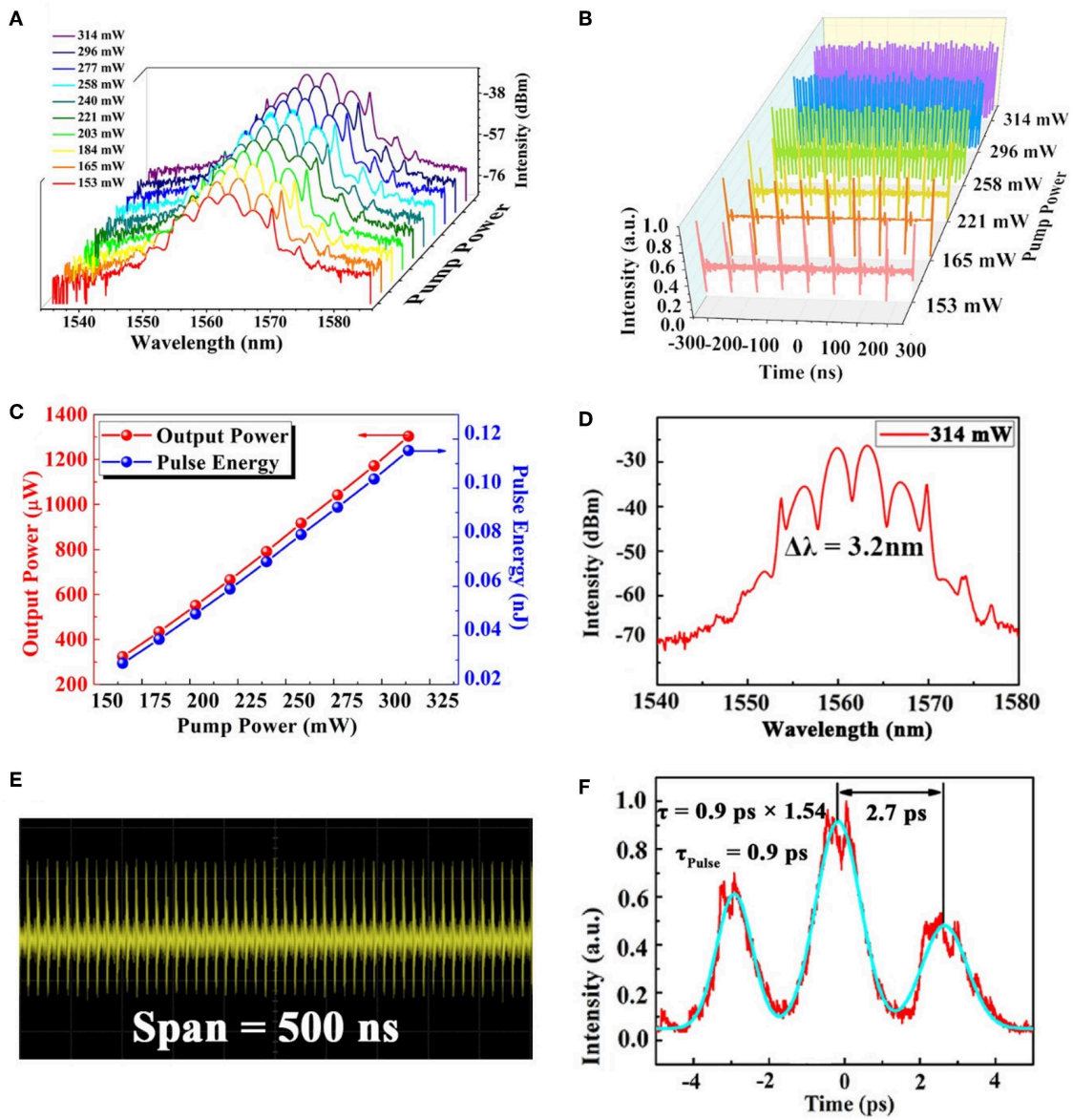

FIGURE 8 | (A) Evolution of optical spectrum with the pump power from 153 to 314 mW. **(B)** Pulse sequence evolution with pump power. **(C)** Output power of soliton molecule as a function of pump power. **(D)** Optical spectrum with 314 mW of pump power. **(E)** Pulse sequence of higher order harmonic soliton molecule under the pump power of 314 mW. **(F)** Autocorrelation trace of higher order harmonic soliton molecule under the pump power of 314 mW.

of GNRs, the obvious saturable absorption effect is identified which shows a modulation depth of 0.6%. And then, GNRs are used as a high-performance SA in a fiber laser for generating soliton molecule mode-locked pulse. By the GNRs SA, the 740.6 fs stable soliton molecule mode-locked pulse easily produced from the fiber laser. And 9th-order harmonics mode-locked soliton molecules obtained in the laser cavity for the first time. It turns out that the GNRs SA could be a really wonderful NLO material for preparation of saturable absorption device for ultrafast lasers. And has the great potential in many applications.

DATA AVAILABILITY STATEMENT

All datasets generated for this study are included in the article/supplementary files.

AUTHOR CONTRIBUTIONS

YS do experiment and write paper. XL providing guiding ideology and experimental equipment. PG process data and draw experimental images. GL provide materials needed for the

experiment. PW participate in the preparation of gold nanorods. GS purchase reagents for the experiment. JL modify the article.

FUNDING

This research was supported by the National Natural Science Foundation of China (61605106); funded projects for the Academic Leader and Academic Backbones, Shaanxi Normal University (18QNGG006); starting Grants of Shaanxi Normal University (Grant Nos. 1112010209, 1110010717); Fundamental Research Funds For the Central Universities (GK201802006); Open Research Fund of State Key Laboratory of Pulsed Power Laser Technology, Electronic Engineering Institute (No. SKL2017KF02); Open Fund of State Key Laboratory of Information Photonics and Optical Communications (Beijing University of Posts and Telecommunications), P. R. China (IPOC2017B012); Open Research Fund of State Key Laboratory of Transient Optics and Photonics, Chinese Academy of Sciences (Nos. SKLST201401, SKLST201809). Funded by the Science and Technology Development Fund, Macau SAR (File No. 002/2016/AFJ).

REFERENCES

Burrows, N. D., Lin, W., Hinman, J. G., Dennison, J. M., Vartanian, A. M., Abadeer, N. S., et al. (2016). Surface chemistry of gold nanorods. *Langmuir* 32, 9905–9921. doi: 10.1021/acs.langmuir.6b02706

Chai, T., Li, X. H., Feng, T. C., Guo, P. L., Song, Y., Chen, Y., et al. (2018). Few-layer bismuthene for ultrashort pulse generation in a dissipative system based on an evanescent field. *Nanoscale* 10, 17617–17622. doi: 10.1039/C8NR03068E

Chen, X., Li, P., Dun, Y., Song, T., and Ma, B. (2018). Nanosecond-pulsed Q-switched Nd: YAG laser at 1064 nm with a gold nanotriangle saturable absorber. *Appl. Phys. B* 124:92. doi: 10.1007/s00340-018-6952-7

Chow, K. K. (2017). Low pump threshold CVD graphene based passively harmonic mode-locked fibre laser. *Electron. Lett*. 53, 330–331. doi: 10.1049/el.2016.4325

Fan, Z. X., and Zhang, H. (2016). Crystal phase-controlled synthesis, properties and applications of noble metal nanomaterials. *Chem. Soc. Rev*. 45, 63–82. doi: 10.1039/C5CS00467E

Fang, C., Jia, H., Chang, S., Ruan, Q., Wang, P., Chen, T., et al. (2014). (Gold core)/ (titania shell) nanostructures for plasmon-enhanced photon harvesting and generation of reactive oxygen species. *Energy Environ. Sci*. 7, 3431–3438. doi: 10.1039/C4EE01787K

Fu, B., Li, J., Cao, Z., and Popa, D. (2019). Bound states of solitons in a harmonic graphene-mode-locked fiber laser. *Photon. Res.* 7, 116–120. doi: 10.1364/PRJ.7.000116

Gou, L., and Murphy, C. J. (2005). Fine-tuning the shape of gold nanorods. *Chem. Mater*. 17, 3668–3672. doi: 10.1021/cm050525w

He, J., Zheng, W., Ligmajer, F., Chan, C.-F., Bao, Z., Wong, K.-L., et al. (2016). Plasmonic enhancement and polarization dependence of nonlinear upconversion emissions from single gold nanorod@SiO2@CaF2:Yb3+,Er3+ hybrid core–shell–satellite nanostructures. *Light* 6:e16217. doi: 10.1038/lsa.2016.217

Huang, Y. F., Zhang, M., Zhao, L. B., Feng, J. M., Wu, D. Y., Ren, B., et al. (2014). Activation of oxygen on gold and silver nanoparticles assisted by surface plasmon resonances. *Angew. Chem*. 126, 2385–2389. doi: 10.1002/ange.201310097

Huang, Y. Q., Hu, Z. A., Cui, H., Luo, Z. C., Luo, A. P., and Xu, W. C. (2016). Coexistence of harmonic soliton molecules and rectangular noise-like pulses in a figure-eight fiber laser. *Opt. Lett*. 41, 4056–4059. doi: 10.1364/OL.41.004056

Jain, P. K., Huang, X., El-Sayed, I. H., and El-Sayed, M. A. (2007). Review of some interesting surface plasmon resonance-enhanced properties of noble metal nanoparticles and their applications to biosystems. *Plasmonics* 2, 107–118. doi: 10.1007/s11468-007-9031-1

Johnson, C. J., Dujardin, E., Davis, S. A., Murphy, C. J., and Mann, S. (2002). Growth and form of gold nanorods prepared by seed-mediated, surfactant-directed synthesis. *J. Mater. Chem*. 12, 1765–1770. doi: 10.1039/b200953f

Kang, Z., Gao, X., Zhang, L., Feng, Y., Qin, G., and Qin, W. (2015). Passively mode-locked fiber lasers at 1039 and 1560 nm based on a common gold nanorod saturable absorber. *Opt. Mater. Express* 5, 794–801. doi: 10.1364/OME.5.000794

Kang, Z., Xu, Y., Zhang, L., Jia, Z., Liu, L., Zhao, D., et al. (2013). Passively mode-locking induced by gold nanorods in erbium-doped fiber lasers. *Appl. Phys. Lett*. 103:041105. doi: 10.1063/1.4816516

Komarov, A., Haboucha, A., and Sanchez, F. (2008). Ultrahigh-repetition-rate bound-soliton harmonic passive mode-locked fiber lasers. *Opt. Lett*. 33, 2254–2256. doi: 10.1364/OL.33.002254

Komarov, A., Komarov, K., and Sanchez, F. (2015). Harmonic passive mode locking of bound-soliton structures in fiber lasers. *Opt. Commun*. 354, 158–162. doi: 10.1016/j.optcom.2015.05.070

Lai, X., Li, J., Luo, H., Zhu, C., Hai, Y., Shi, Y., et al. (2018). High power passively Q-switched Er3+-doped ZBLAN fiber laser at 2.8 μm based on a semiconductor saturable absorber mirror. *Laser Phys. Lett*. 15:085109. doi: 10.1088/1612-202X/aac549

Li, X., Wu, K., Sun, Z., Meng, B., Wang, Y., Yu, X., et al. (2016). Single-wall carbon nanotubes and graphene oxide-based saturable absorbers for low phase noise mode-locked fiber lasers. *Sci. Rep*. 6:25266. doi: 10.1038/srep25266

Liu, M., Luo, A. P., Xu, W. C., and Luo, Z. C. (2018). Coexistence of bound soliton and harmonic mode-locking soliton in an ultrafast fiber laser based on MoS2-deposited microfiber photonic device. *Chin. Opt. Lett*. 16:020008. doi: 10.3788/COL201816.020008

Lopez-Lozano, X., Barron, H., Mottet, C., and Weissker, H. C. (2014). Aspect-ratio- and size-dependent emergence of the surface-plasmon resonance in gold nanorods–an ab initio TDDFT study. *Phys. Chem. Chem. Phys*. 16, 1820–1823. doi: 10.1039/C3CP53702A

Lu, S., Du, L., Kang, Z., Li, J., Huang, B., Jiang, G., et al. (2018). Stable dissipative soliton generation from Yb-doped fiber laser modulated via evanescent field interaction with gold nanorods. *IEEE Photon. J*. 10, 1–8. doi: 10.1109/JPHOT.2018.2872405

Luo, Y., Xiang, Y., Liu, B., Qin, Y., Sun, Q., Tang, X., et al. (2018). Dispersionmanaged soliton molecules in a near zero-dispersion fiber laser. *IEEE Photon. J*. 10, 1–11. doi: 10.1109/JPHOT.2018.2874949

Martinez, A., Al Araimi, M., Dmitriev, A., Lutsyk, P., Li, S., Mou, C., et al. (2017). Low-loss saturable absorbers based on tapered fibers embedded in carbon nanotube/polymer composites. *APL Photon*. 2:126103. doi: 10.1063/1.4996918

Ming, T., Zhao, L., Yang, Z., Chen, H., Sun, L., Wang, J., et al. (2009). Strong polarization dependence of plasmon-enhanced fluorescence on single gold nanorods. *Nano Lett*. 9, 3896–3903. doi: 10.1021/nl902095q

Oh, M. K., Baik, H. J., Kim, S. K., and Park, S. (2011). Multiple surface plasmon resonances in silver and copper nanorods. *J. Mater. Chem*. 21, 19069–19073. doi: 10.1039/c1jm13613e

Peng, J., Zhan, L., Luo, S., and Shen, Q. S. (2013). Generation of soliton molecules in a normal-dispersion fiber laser. *IEEE Photon. Technol. Lett*. 25, 948–951. doi: 10.1109/LPT.2013.2257720

Perezjuste, J., Pastorizasantos, I., Lizmarzan, L., and Mulvaney, P. (2005). Gold nanorods: synthesis, characterization and applications. *Coord. Chem. Rev*. 249, 1870–1901. doi: 10.1016/j.ccr.2005.01.030

Tsutsui, Y., Hayakawa, T., Kawamura, G., and Nogami, M. (2011). Tuned longitudinal surface plasmon resonance and third-order nonlinear optical properties of gold nanorods. *Nanotechnology* 22:275203. doi: 10.1088/0957-4484/22/27/275203

Wang, C., Wang, L., Li, X. H., Luo, W., Feng, T. C., Zhang, Y., et al. (2019). Few-layer bismuthene for femtosecond soliton molecules generation in Er-doped fiber laser. *Nanotechnology* 30:025204. doi: 10.1088/1361-6528/aae8c1

Wang, X., Luo, Z., Liu, M., Tang, R., Luo, A., and Xu, W. (2016). Wavelength-switchable femtosecond pulse fiber laser mode-locked by silica-encased gold nanorods. *Laser Phys. Lett.* 13:045101. doi: 10.1088/1612-2011/13/4/045101

Wang, Y., Alam, S. U., Obraztsova, E. D., Pozharov, A. S., Set, S. Y., and Yamashita, S. (2016). Generation of stretched pulses and dissipative solitons at 2 mum from an all-fiber mode-locked laser using carbon nanotube saturable absorbers. *Opt. Lett*. 41, 3864–3867. doi: 10.1364/OL.41.003864

Wang, Y., Mao, D., Gan, X., Han, L., Ma, C., and Xi, T. (2015). Harmonic mode locking of bound-state solitons fiber laser based on MoS (2) saturable absorber. *Opt. Express* 23, 205–210. doi: 10.1364/OE.23.000205

Wang, Z., Zhan, L., Majeed, A., and Zou, Z. (2015). Harmonic mode locking of bound solitons. *Opt. Lett*. 40, 1065–1068. doi: 10.1364/OL.40.001065

Yang, L. Z., Wang, Y. C., Cheng, G. F., Wang, Y. S., and Zhao, W. (2007). Harmonic mode-locked ytterbium-doped fibre ring laser. *Chin. Phys. Lett*. 24, 944–946. doi: 10.1088/0256-307X/24/4/026

Yang, X., Sun, Z., Low, T., Hu, H., Guo, X., Garcia De Abajo, F. J., et al. (2018). Nanomaterial-based plasmon-enhanced infrared spectroscopy. *Adv. Mater*. 30:e1704896. doi: 10.1002/adma.201704896

Zhang, M., Wu, Q., Zhang, F., Chen, L., Jin, X., Hu, Y., et al. (2019). 2D black phosphorus saturable absorbers for ultrafast photonics. *Adv. Opt. Mater*. 7:1800224. doi: 10.1002/adom.201800224

Zhang, Y., Li, X. H., Qyyum, A., Chai, T., Guo, P. L., Feng, J. J., et al. (2018). PbS nanoparticles for ultrashort pulse generation in optical communication region. *Part. Part. Syst. Charact.* 35:1800341. doi: 10.1002/ppsc.201800341

Zhao, L. M., Tang, D. Y., Cheng, T. H., Lu, C., Tam, H. Y., Fu, X. Q., et al. (2009). Passive harmonic mode locking of soliton bunches in a fiber ring laser. *Opt. Quant. Electron*. 40, 1053–1064. doi: 10.1007/s11082-009-9301-6

Zijlstra, P., Chon, J. W., and Gu, M. (2009). Five-dimensional optical recording mediated by surface plasmons in gold nanorods. *Nature* 459, 410–413. doi: 10.1038/nature08053

Conflict of Interest: The authors declare that the research was conducted in the absence of any commercial or financial relationships that could be construed as a potential conflict of interest.

frontiers in Chemistry

ORIGINAL RESEARCH
published: 15 November 2019
doi: 10.3389/fchem.2019.00783

Improved Alignment of PEDOT:PSS Induced by *in-situ* Crystallization of "Green" Dimethylsulfone Molecules to Enhance the Polymer Thermoelectric Performance

Qiang Zhu[1], *Erol Yildirim*[2], *Xizu Wang*[1], *Xiang Yun Debbie Soo*[1], *Yun Zheng*[1], *Teck Leong Tan*[2], *Gang Wu*[2], *Shuo-Wang Yang*[2]* and *Jianwei Xu*[1,3]*

[1] *Institute of Materials Research and Engineering, A*STAR (Agency for Science, Technology and Research), Singapore, Singapore,* [2] *Institute of High Performance Computing, A*STAR (Agency for Science, Technology and Research), Singapore, Singapore,* [3] *Department of Chemistry, National University of Singapore, Singapore, Singapore*

Dimethylsulfone ($DMSO_2$), a small organic molecule, was observed to induce the alignment of poly(3,4-ethylenedioxythiophene): poly(4-styrenesulfonate) (PEDOT:PSS) via *in-situ* crystallization in PEDOT:PSS mixture, which was verified by field emission scanning electron microscopy (FESEM), X-ray diffraction (XRD) and atomic force microscopy (AFM). A chemically stable dopant, $DMSO_2$, remarkably raised the electrical conductivity of the PEDOT:PSS film, which was fabricated from pre-mixed solution of PEDOT:PSS and $DMSO_2$, up to 1080 S/cm, and more importantly, such a PEDOT:PSS film showed a long-term humidity stability and it retained near 90% electric conductivity after 60 days, suggesting $DMSO_2$ is promising for an eco-friendly alternative to replace dimethyl sulfoxide (DMSO), ethylene glycol (EG) and various acids dopants that have been widely employed to dope and post-treat PEDOT:PSS. Pairwise interaction energies and free energy of solvation between PEDOT:PSS and $DMSO_2$ were calculated by first-principles and molecular mechanics, respectively, revealing the mechanism of $DMSO_2$ in enhancing the electrical conductivity.

Keywords: dimethylsulfone, PEDOT:PSS, thermoelectric, polymer alignment, crystallization

OPEN ACCESS

Edited by:
Sumeet Walia,
RMIT University, Australia

Reviewed by:
Ayaskanta Sahu,
New York University, United States
Syed Mubeen Jawahar Hussaini,
The University of Iowa, United States

***Correspondence:**
Shuo-Wang Yang
yangsw@ihpc.a-star.edu.sg
Jianwei Xu
jw-xu@imre.a-star.edu.sg

Specialty section:
This article was submitted to Nanoscience, a section of the journal Frontiers in Chemistry

Received: *14 July 2019*
Accepted: *30 October 2019*
Published: *15 November 2019*

Citation:
Zhu Q, Yildirim E, Wang X, Soo XYD, Zheng Y, Tan TL, Wu G, Yang S-W and Xu J (2019) Improved Alignment of PEDOT:PSS Induced by in-situ Crystallization of "Green" Dimethylsulfone Molecules to Enhance the Polymer Thermoelectric Performance. Front. Chem. 7:783. doi: 10.3389/fchem.2019.00783

INTRODUCTION

In the past few decades, we have witnessed great progress on thermoelectric devices due to its capability to directly convert waste heat into electricity. The efficiency of the thermoelectric materials is evaluated via the dimensionless figure-of-merit: $ZT = S^2\sigma T/\kappa$, where S, σ, *T, and* κ are Seebeck coefficient, electrical conductivity, thermal conductivity and absolute temperature, respectively. Previously, inorganic materials such as Bi_2Te_3, BiSb, SiGe, and other metal alloys (Han et al., 2014; Zhao and Tan, 2014) were extensively studied, achieving a commendable *ZT* of about 2 (Culebras et al., 2014b). These materials were fabricated into various devices, which were used in niche applications including refrigeration and power generation. Nevertheless, these inorganic materials are intrinsically disadvantaged because of their scarcity on earth, non-flexibility and toxicity, thus limiting their wide application in thermoelectric modules (Hu et al., 2015a). To overcome such drawbacks, conducting polymers (CPs) are currently studied as alternative

TE materials, given their advantages, such as tunable electric conductivity and low thermal conductivity (Choy, 1977; Kim et al., 2013; Park et al., 2013).

The typical CPs that have been widely studied to date include polyacetylene (Kaneko et al., 1993), polypyrrole (PPy) (Kemp et al., 1999), polyaniline (PANI) (Yoon et al., 1995; Mateeva et al., 1998), polythiophene (PTH) (Hu et al., 2013) and poly(3,4-ethylenedioxythiophene):poly(styrenesulfonate) (PEDOT:PSS) (Zhang et al., 2010). The TE performance of CPs are still much lower than their inorganic counterparts due to their intrinsically low electrical conductivity and relatively low Seebeck coefficient (Culebras et al., 2014b; McGrail et al., 2015). Though the electrical conductivity can be enhanced, the Seebeck coefficient usually decreases correspondingly due to the trade-off relationship between them, resulting in a low power factor, termed as $P = S^2\sigma$ (Yao et al., 2010). Several approaches have been widely investigated to improve TE performance of the CPs, including (1): nanostructuring CPs, (2): hybridization with other nanostructures, including metallic and carbon-based materials and (3): surface modifications or post-treatment. In the first approach, various CP nanostructures, such as PEDOT nanostructures including nanorods, nanofibers, nanotubes (Hu et al., 2015b), and PPy nanotubes (Wu et al., 2014) have been systematically studied. A significant improvement in TE performance has been observed for these CPs-nanostructure composites as compared to the corresponding bulky CPs. However, the synthesis and fabrication of such nanostructures sometimes involve complicated synthesis and disproportionate scale-up, which limits their applications. The second approach has been widely investigated, which takes advantages of each respective component of the hybrid, high electric conductivity or high Seebeck coefficient, to "balance" the composite materials' properties (Zhang et al., 2010; Moriarty et al., 2013; Xu et al., 2013; Park et al., 2014a). Thus, an optimum power factor can be obtained via higher energy-filtering efficiency through the joint adjunct between nanoparticles and CPs (Choi et al., 2016). The highest ZT obtained so far is about <0.5 and mechanism for the hybrid materials is unfortunately not fully understood due to many challenging factors involved in the complicated system (Zhang et al., 2010; Kumar et al., 2018). The third approach is to tune the surface morphology through various doping approaches or post-treatments. In this approach, PEDOT:PSS has been the dominant CP to be extensively studied with various post-treatments (McGrail et al., 2015; Wei et al., 2015). The main aim for process or treatment is to remove the insulating polymer PSS from PEDOT:PSS. Various organic solvents (DMSO, EG and other chemicals) and inorganic salts have also been widely used to increase its electrical conductivity in a few magnitudes so that the power factor can be significantly increased (Zhang et al., 2010; Culebras et al., 2014a). Post-treatment by immersing the PEDOT:PSS films into EG or acid solution was also studied (Culebras et al., 2014a; Park et al., 2014b). The mechanism is well-studied and the phase separation of PEDOT is observed in several studies (Timpanaro et al., 2004; Crispin et al., 2006). Our previous modeling study also demonstrated that PSS-DMSO interaction was stronger than these in the PEDOT-PSS, PEDOT-DMSO and PSS-PSS interactions. Thus, dissolution of insulating PSS shells to release PEDOT conducting cores for self-aggregation is the main mechanism for the enhancement of electrical conductivity (Yildirim et al., 2018).

Aligning conducting polymers is a good method to tune carrier transport properties, and thus improve the thermoelectric properties. In order to align polymers, both common template synthesis and post-treatment methods have been investigated. Feng et al. reported the use of electrospinning and oxidative chemical polymerization to feasibly synthesize PEDOT fibers and tubes (Feng et al., 2013). Aligned PEDOT structures can be obtained through the template synthesis, but the whole process of the template synthesis is quite complicated and the template polymer has to be employed and removed in the fabrication. Another example is vapor-phase polymerization, in which an oxidant is used as a template and EDOT monomers stack via a bottom-up approach for well-ordered PEDOT crystals (Kim et al., 2007; Laforgue and Robitaille, 2010). Lee also proposed to post-treat a pre-fabricated PEDOT:PSS film with sulfuric acid. High-angle annular dark-field scanning transmission electron microscopy (HAADF-STEM) and X-ray powder diffraction (XRD) studies revealed that the PEDOT fibril structure was observed, resulting in a remarkably high electrical conductivity (4,380 S/cm). (Kim et al., 2014) Toward this goal, there seems no report using small molecules to induce the PEDOT:PSS polymer alignment. The major challenge of this is that the most commonly used molecules, such as DMSO, EG, acids and hydrazine are liquid which is unable to shape the polymer in a well-oriented way.

In this paper, we first identified a small molecule, dimethylsulfone ($DMSO_2$), which is water-soluble and miscible with PEDOT:PSS well. $DMSO_2$ is able to crystallize from the PEDOT:PSS system and indirectly align PEDOT:PSS through the hydrogen bonding interactions. Such alignment significantly increases electrical conductivity of PEDOT to 1080 S/cm, comparable to DMSO and EG, suggesting that $DMSO_2$ is a green alternative to replace widely used DMSO and EG for solvent treatment of PEDOT:PSS. Furthermore, $DMSO_2$ has several advantageous properties in term of non-toxicity, solid and high solubility in water. These properties make $DMSO_2$ appropriate for wearable electronics devices that are required to direct contact with human skins.

EXPERIMENT SECTION

Materials

Microscopic glass slides (25 mm by 75 mm), dimethylsulfone (purity ≥98%) were purchased from Sigma Aldrich. PEDOT:PSS aqueous solution (PH1000, Heraeus Clevios) was purchased from Heraeus, Germany. All other solvents, such as EG, ethanol and distilled water were used as received without further purification.

Sample Preparation

Glass slides were first pre-treated by immersing in *aqua regia* for 2 days at ambient temperature to enhance its hydrophilic property. The glass slides were the further washed consecutively with distilled water, isopropanol, and acetone prior to being dried under air flow. Preparation of 1% $DMSO_2$ in PEDOT:PSS is used

as an example. Dimethylsulfone (4.0 mg) was added into a 2-mL sample vial containing 400.0 mg of PEDOT:PSS aqueous solution at ambient temperature. The pre-mixed solution was stirred under vortex for 5 min to ensure that $DMSO_2$ is fully dissolved in PEDOT:PSS prior to ultrasonication for 20 min. The as-prepared solution was loaded onto the 2.5 × 2.5 cm^2 pre-treated glass slide and left to stand for 5 min at ambient temperature. It was then further cured at 80°C for 40 min to obtain a thin film. In some cases, shrinkage was observed during the curing stage at 80°C; a glass pipette can be used to spread the solution so that a uniform film can be prepared.

Post-treatment

The as-prepared doped PEDOT:PSS film annealed on the glass substrate was immersed in solvents, such as water, methanol and ethanol respectively for 1 h at ambient temperature. The glass substrate together with the film was then carefully taken out and dried over the hotplate at 80°C for 30 min. The corresponding films obtained are then for the electrical conductivity measurements.

Characterization

The morphologies of the PEDOT:PSS films were studied using field emission scanning electron microscope (FESEM) on JSM6700F and atomic force microscopy (AFM) on Nanoscope IIIa instrument, Digital Instrument. XRD Measurement was performed on PANalytical X'Pert PRO High Resolution XRD. The electrical conductivity of PEDOT:PSS films were measured by Loresta-GP MCP-T600 (Mitsubishi Low Resistivity Meter) at room temperature. The thicknesses of the films were determined with a KLA Tencor P-16+ Surface Profiler. The Seebeck coefficient was measured by the custom-made measurement system equipped with an SA Peltier cooler (298 K - ΔT) and a Peltier heater (298 K + ΔT). Two microthermocouples (TCs) of 0.20 mm diameter were placed on the sample abreast of two electrodes connected to a Keithley 2400 source meter. The Seebeck coefficient was estimated by a linear fit to the measured ΔV vs. ΔT at different electrode spaces.

Calculation of Interaction Energies

Pairwise interaction energies between PEDOT:PSS components and solvents are critical for elaborating molecular mechanism of solvent treatment in PEDOT:PSS. Pairwise interactions are calculated between solvents and components of PEDOT:PSS. The solvents include $DMSO_2$, DMSO, EG and *N*-methyl pyrrolidone (NMP), while the components of PEDOT:PSS are neutral PEDOT trimer, polystyrene sulfonic acid trimer (PSSH), negatively charged PSS^- trimer with one deprotonated PSS monomer, and positively charged radical $PEDOT^+$ trimer in the polaron state. Trimer structures were used for the PSS and the PEDOT, since it was experimentally determined that three PEDOT monomers possess one positive charge (Volkov et al., 2017). Initial structure pairs for density functional theory (DFT) calculations were determined by generating a large number of molecular configurations with excluded-volume constraints to determine energetically favorable configurations by employing statistical mechanics techniques (Fan et al., 1992). At least 12 lowest energy structures were determined for each of binary interactions between PEDOT and $DMSO_2$. DFT calculations were performed by using M06-2X (Zhao and Truhlar, 2008) functional with 6-31+g(d) basis set in Gaussian16.A.03 software (Frisch et al., 2019). Both vacuum and implicit solvent methods for water are considered during the calculations. IEF-PCM implicit water continuum model is used to represent water solution (Tomasi et al., 2005).

Free Energy of Solvation (ΔG_{sol}) Calculations

Free energies of solvation (ΔG_{sol}) were calculated for $DMSO_2$, $EDOT_9^{-3}$ and SS_{18}^{-3} solutes in DMSO, EG, tetrahydrofuran (THF), acetone, N,N-dimethyl formamide (DMF), NMP, CH_2Cl_2, hexane, MeOH and water solvents under periodic boundary conditions based on the coupling parameter method and thermodynamic integration algorithm (**Figure S3**) (Steinbrecher et al., 2011) The free energy of solvation was determined in three steps. Firstly, we computed the ideal free of energy of solvation (ΔG_{id}) by determining the free energy change associated with the discharge of the solute ($DMSO_2$, $EDOT_9^{-3}$, and SS_{18}^{-3}) in vacuum. Then the neutral solute molecule was brought into contact with the solvent molecules; the free energy change for this step is called vdW free energy of solvation (ΔG_{vdw}). Lastly, the solvated and discharged solute molecules are charged again in solvent to determine the electrostatic free energy of solvation (ΔG_{el}) (Biovia, 2017). Total free energy of solvation (ΔG_{sol}) was calculated as the sum of the free energy contributions from ideal, vdW and electrostatic free energies of solvation (Equation 1), noting that experimental densities were used for the solvents in free energy calculations.

$$\Delta G_{sol} = \Delta G_{id} + \Delta G_{vdw} + \Delta G_{el} \quad (1)$$

COMPASS (Condensed-Phase Optimized Molecular Potentials for Atomistic Simulation Studies) force field was used to validate solubility and phase properties of polymers in solution (Sun, 1998; Yildirim et al., 2015).

RESULTS AND DISCUSSIONS

Figure 1 shows some common additives including DMSO, EG, NMP, and $DMSO_2$ used in the PEDOT:PSS for electrical conductivity enhancement. DMSO, EG, and NMP are in liquid forms at room temperature with high boiling point. During the process of film curing, high temperature has to be employed to vaporize these additives into ambient environment. To overcome this disadvantage, $DMSO_2$ is screened as a potential dopant. Unlike DMSO, EG and NMP, $DMSO_2$ is a solid and the sulfur atom in the molecule is at its highest oxidation state, making it more chemically stable. The fabrication process for PEDOT:PSS with $DMSO_2$ *via* drop-cast is shown in **Figure 2**, which is very similar to that of the commonly used DMSO, EG (Zhang et al., 2010) and other inorganic additives (Culebras et al., 2014a). It includes mixing PEDOT:PSS with additives, drop-cast of the solution onto the glass substrate and curing at a given temperature. When DMSO and inorganic acids are used

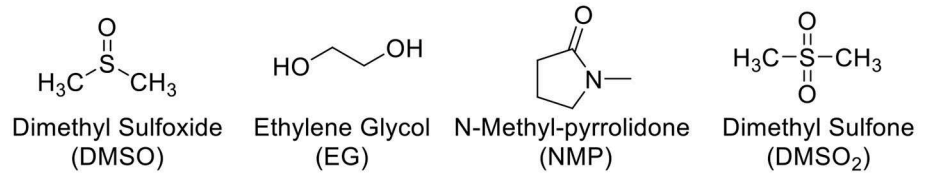

FIGURE 1 | Chemical structures of different additives to PEDOT:PSS.

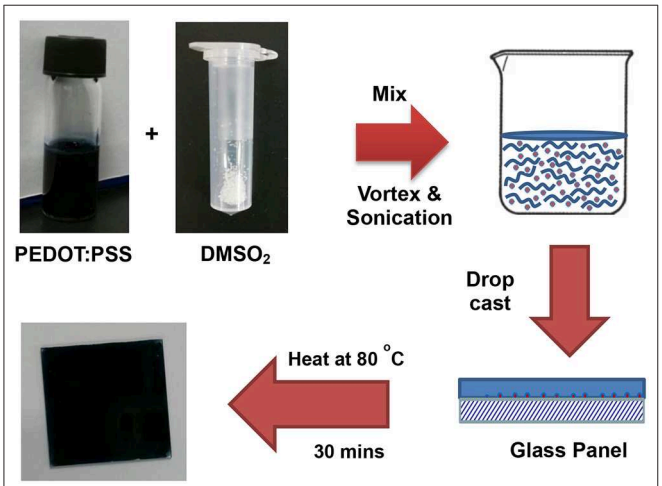

FIGURE 2 | Fabrication process for sulfone $DMSO_2$ as additive to PEDOT:PSS.

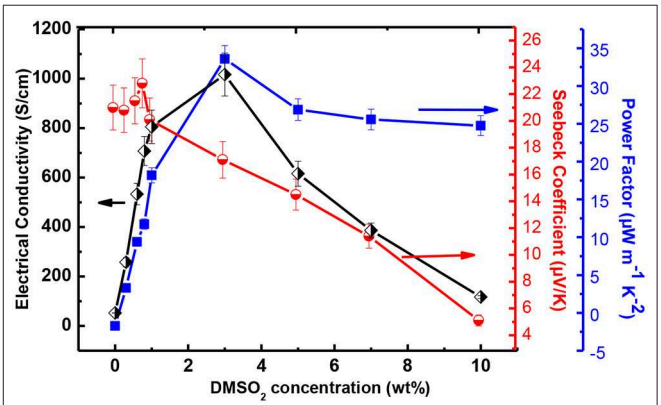

FIGURE 3 | The electrical conductivity, Seebeck coefficient and power factor at ambient temperature for $DMSO_2$ doped PEDOT:PSS at different loading.

to dope PEDOT:PSS, a closed encasement or a fume-hood is required for the film preparation and curing process due to toxic and hazardous vapor caused by these volatile solvents. However, the processing and fabrication of solid $DMSO_2$ doped PEDOT films do not require a confined environment as no hazardous solvent vapor is produced. This opens up a new means to fabricate PEDOT:PSS films, which reduces the potential damage to human health and also lowers the fabrication cost. Similarly, electronic devices employing PEDOT:PSS and $DMSO_2$ as an additive would be much safer to consumers, particularly in the event that demands the stringent safety regulations such as wearable devices.

The thermoelectric performance in terms of electrical conductivity with respect to $DMSO_2$ concentration was measured and results are shown in **Figure 3**. The pristine PEDOT:PSS gave an electrical conductivity of 0.2 S/cm. With the increase in $DMSO_2$ loading, the electrical conductivity gradually increased and reached close to 1,100 S/cm. When over 3% additive loading was added, the decrease in electrical conductivity was observed, possibly due to the un-evenness of as-prepared film at high additive loading. Another plausible reason is that $DMSO_2$ play a somewhat insulation role if more loading of it applies, leading to the reduction in the electrical conductivity. This trend of electrical conductivity with respect to the amount of $DMSO_2$ added is very similar to known DMSO, EG, NMP and others dopants. Interestingly, the electrical conductivity of PEDOT:PSS remained almost constant despite curing temperatures between 60-120°C, showing more advantages than processes using NMP or EG, which require a higher temperature and a much longer curing time to vaporize out the high boiling-point additives. The Seebeck coefficient was also measured and data are summarized in **Figure 3**. The Seebeck coefficient shows an overall decreasing trend with the increase of loading of $DMSO_2$, and a highest Seebeck coefficient of 23 μV/K was achieved at 1% loading of $DMSO_2$. The carrier concentration usually leads to a proportional increment of electrical conductivity. However, the Seebeck coefficient varies inversely due to the trade-off relationship between these two parameters. (Yao et al., 2010) The power factor increased sharply at a $DMSO_2$ loading of <3%. At a higher $DMSO_2$ loading, the power factor dropped. A highest power factor of 32 $\mu W/mK^2$ was obtained at 3% loading of $DMSO_2$. The figure of merit (ZT) was approximately estimated to be 0.02 assuming that the thermal conductivity of PEDOT is 0.54 $Wm^{-1}K^{-1}$ (Kyaw et al., 2017). The current ZT value is smaller than those reported (**Table S1**), but it is believed that it could be greatly improved if the further post-treatment that is able to reduce the doping level is performed to increase its Seebeck coefficient.

AFM and FESEM were used to understand the interaction between sulfone and PEDOT:PSS. AFM images were taken to observe the roughness for pristine and $DMSO_2$-doped PEDOT:PSS films (**Figure 4**). Similar to the observation by Alshareef (Kumar et al., 2016), the rms roughness for pristine PEDOT:PSS is 1.8 nm (**Figure 4A**), showing very smooth and

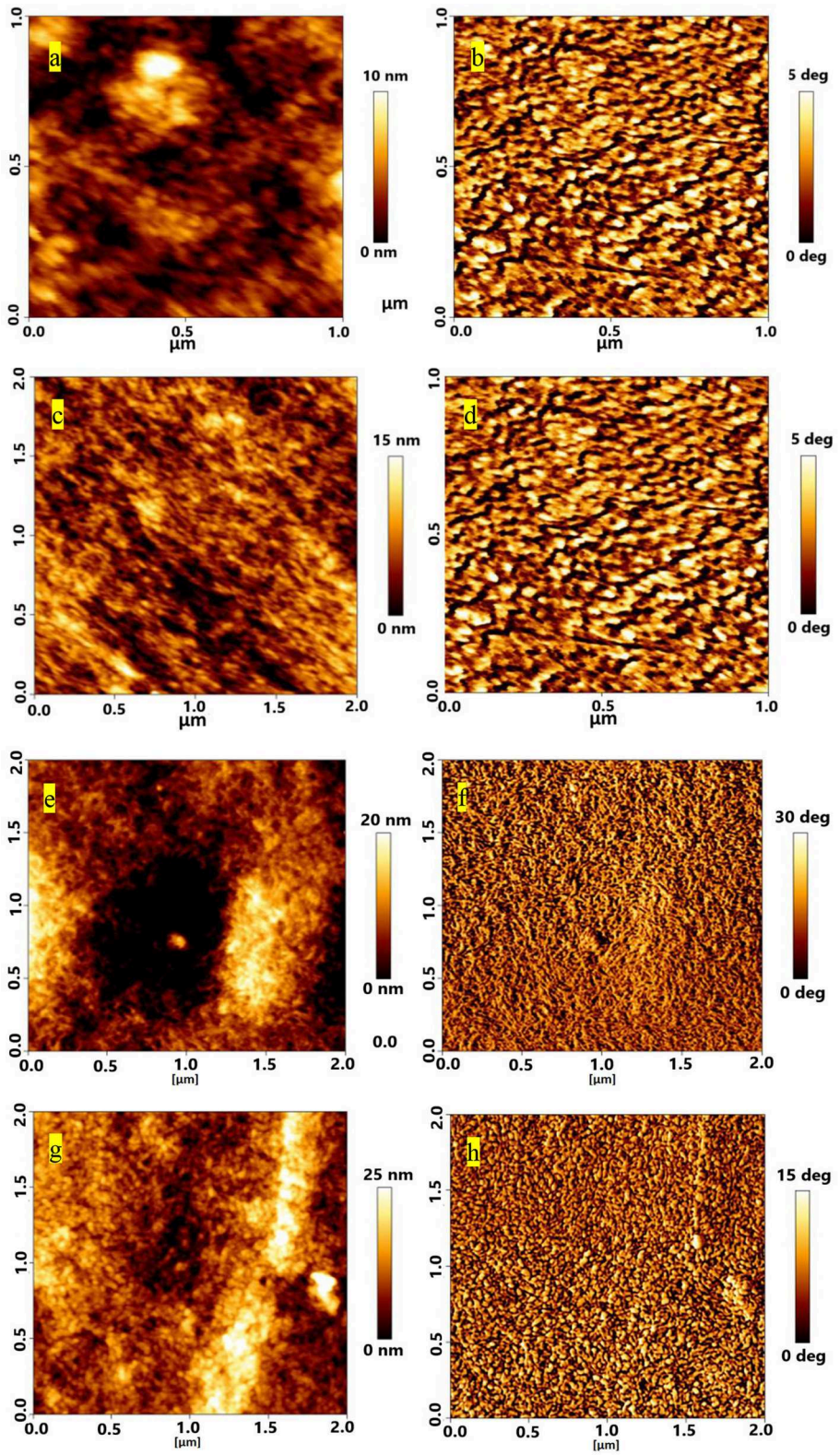

FIGURE 4 | AFM topography images of different loading of $DMSO_2$ in PEDOT:PSS films for **(a)** pristine **(c)** 1% **(e)** 3% and **(g)** 5%; corresponding phase images are shown on right panels **(b,d,f,h)**.

uniform film as prepared. Upon adding $DMSO_2$ into PEDOT:PSS at 1, 3, and 5% loading (**Figures 4C,E,G**), film roughness is ascending with the similar trend. At 1% loading (**Figure 4C**), the roughness was 4 nm with tiny fibrous structures observed by topography and phase images. Accordingly, 5.0 and 5.3 nm and 8.1 nm roughness were observed by careful examination on AFM images, showing that tiny crystal-like bright rods with regular shape was observed in their phase images (**Figures 4B,D,F,H**). The bright rods could be the uniform crystals which were formed by $DMSO_2$ during the curing process. Unlike conventional additives, such as liquid DMSO, EG, and NMP, $DMSO_2$ is in a solid form, and more chemically stable as the sulfur atom in $DMSO_2$ is fully oxidized.

FESEM images were used to examine the surface morphology for all the films doped with sulfone (**Figure 5**). Interestingly, a clear long fibrous structure embedded in the surface was found in the film prepared by 3% $DMSO_2$ in PEDOT:PSS. Such a long crystal structure helped well-orientation of the PEDOT:PSS backbone so that carriers can move in a more efficient way, resulting in higher electrical conductivity. In literature, three approaches have been used to enhance electrical conductivity of PEDOT:PSS. The first was the de-doping process through tuning the charge carrier concentration along the polymer chains. Bubnova et al. reported the use of tetrakis(dimethylamino)ethylene to tune the electron distribution along PEDOT:*p*-toluenesulfonate (PEDOT:Tos) to enhance electrical conductivity significantly (Bubnova et al., 2011; Tomlinson et al., 2015). The second approach is the secondary doping with organic solvents or counter-ions so as to tune the polymer chain conformation. For example, when DMSO or EG is employed in PEDOT:PSS solution, the strong Van der Waals interactions between the polar group of DMSO/EG and PEDOT:PSS chains can lead to a structural change from a benzoid to a quinoid structure in the polymer chains, resulting in a few magnitude of electrical conductivity enhancement (Jiang et al., 2008; Yue et al., 2012). The third approach is to remove the excess of insulation polymer, PSS, in the PEDOT:PSS system through post-treatment with DMSO, EG or acids (Kim et al., 2013). In contrast, in our $DMSO_2$ doped PEDOT:PSS system, the electrical conductivity enhancement is similarly due to the polymer alignment but induced by *in-situ* crystallization of solid $DMSO_2$ dopant as observed by microscopy images.

To further verify the polymer alignment of PEDOT:PSS induced by $DMSO_2$ crystallization, the X-ray diffraction (XRD) is used to check the diffraction of the pristine, $DMSO_2$-doped PEDOT:PSS and pure $DMSO_2$ crystals (**Figure 6**). Four characteristic peaks: $2\theta = 3.7°$, $6.6°$, $17.7°$, and $26.0°$ were observed on pristine sample which is consistent with the recent work published by Lee et al. (Kim et al., 2014) The low diffraction at 3.7°, 6.6° and high diffraction at 17.7°, and 26.0° was attributed to the lamella stacking between two distinct alternate ordering PEDOT/PSS and inter-chain ring stacking between PEDOT:PSS, respectively. Due to the random orientation of polymer chains in the pristine PEDOT:PSS, it can be observed that much stronger diffraction at 6.6° than at 3.7° is observed, and the intensity ratio between the diffractions of 6.6 and 3.7° is 1.50. XRD shows that the diffraction at 6.6° is significantly reduced when $DMSO_2$ was loaded into PEDOT:PSS, while the diffraction at 3.7, 17.7, and 26.0° remained relatively unchanged. More importantly, the intensity ratio between the diffraction of 6.6 and 3.7° become 0.49. This observation demonstrates that the polymers orient in a more ordered way toward one particular lamella stacking between the two distinct alternate ordering of PEDOT:PSS.

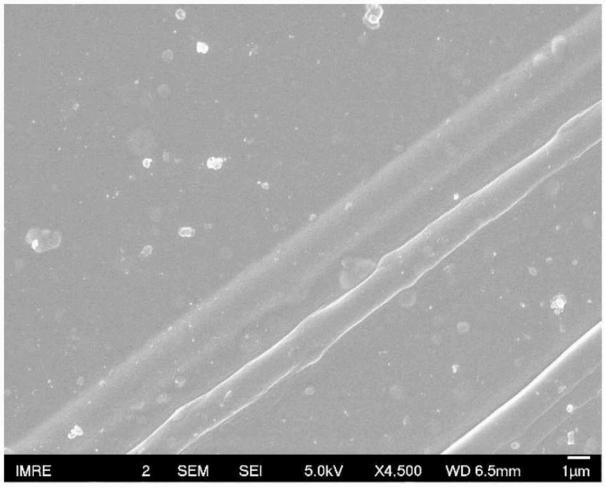

FIGURE 5 | FESEM micrograph of 3% $DMSO_2$ in PEDOT:PSS.

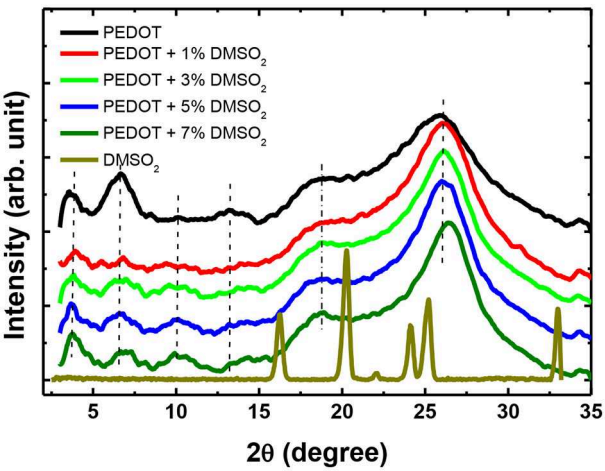

FIGURE 6 | XRD patterns of pristine, $DMSO_2$-doped PEDOT:PSS and $DMSO_2$ crystals.

Meantime, the XRD diffraction patterns for pure $DMSO_2$ crystal are also measured for comparison. Characteristic diffraction peaks at 17.2°, 20.5°, 24.0, 26.1 and 32.5° were observed. However, when doped with PEDOT:PSS, no diffraction signals are observed indicating that the $DMSO_2$ crystal is wrapped by polymer chains, which is consistent with AFM studies (**Figure 4**). In other words, PEDOT:PSS is aligned in a more ordered manner, which is indirectly induced by $DMSO_2$ crystals wrapped by PEDOT:PSS.

Pairwise interaction energies were analyzed to explain observed enhancement in thermoelectric properties. Optimized

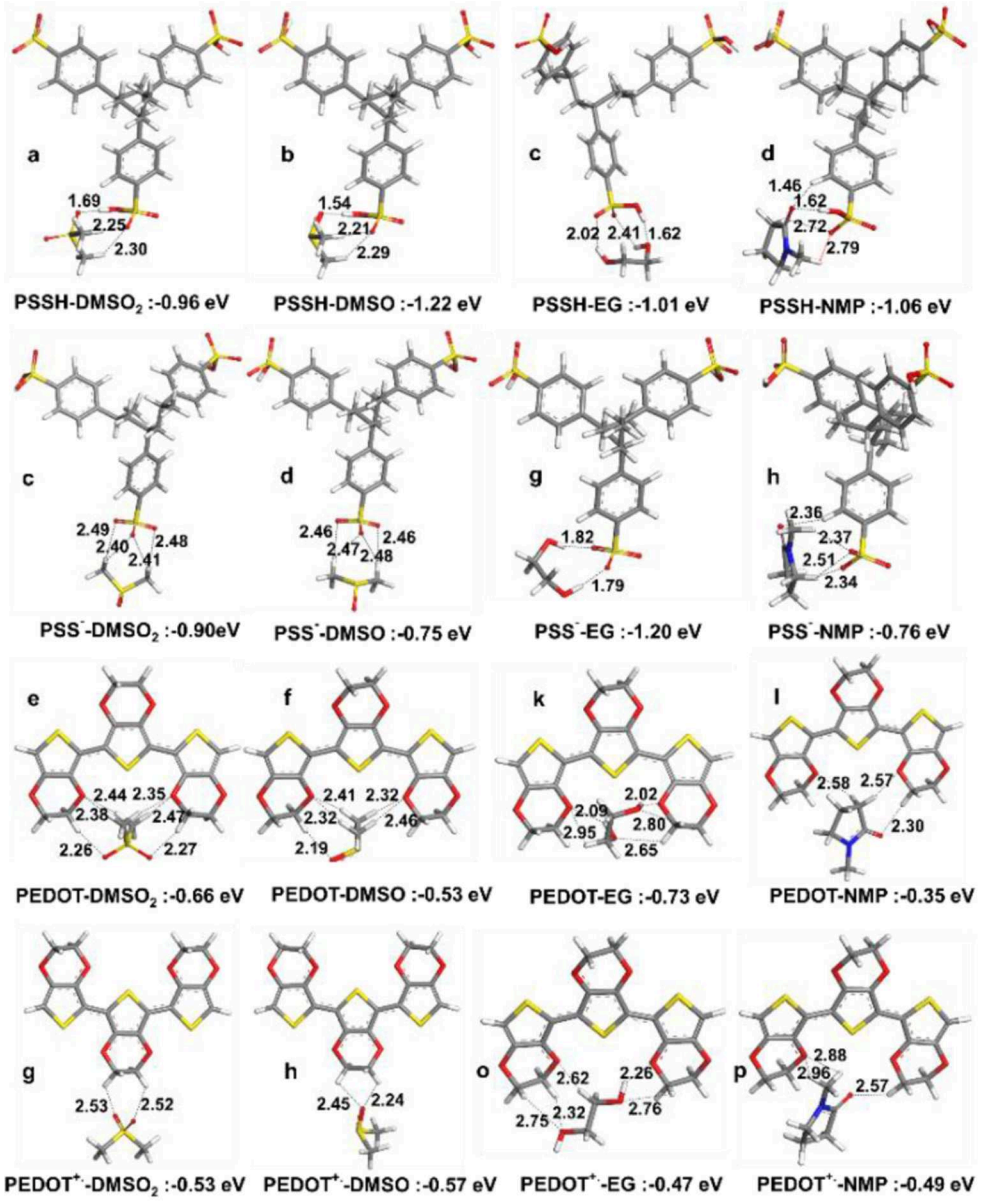

FIGURE 7 | Optimized lowest energy structures and interaction energies in vacuum for **(a–d)** PSSH trimer with $DMSO_2$, DMSO, EG, and NMP, **(e–h)** PSS^- trimer with $DMSO_2$, DMSO, EG and NMP, **(i–l)** PEDOT trimer with $DMSO_2$, DMSO, EG, and NMP, **(m–p)** $PEDOT^{+\cdot}$ trimer with DMSO, $DMSO_2$, EG, and NMP.

structures for the PSSH with $DMSO_2$, DMSO, EG and NMP are given in **Figures 7A–D**, where interactions with the PSSH are found to follow the order of DMSO > $DMSO_2$ > NMP > EG. Hydrogen bonding is the main interactions, e.g., oxygen atoms in both DMSO and $DMSO_2$ would form hydrogen bonds with the –S-O-H in sulfonic acid group of the PSSH. In addition to strong hydrogen bonding, methyl hydrogens in DMSO and $DMSO_2$ interact and surround the two other sulfonate oxygen atoms in the PSSH, leading to the $–SO_3H$ groups in the PSSH to diminish interactions with other PSS and PEDOT chains. Therefore, separation of the excess insulating PSSH shell from the PSS^- doped $PEDOT^{+\cdot}$ chains is believed to be a main mechanism. On the other hand, stronger hydrogen bonding interaction is not possible between the deprotonated PSS^- anion and DMSO and $DMSO_2$, which consist mainly of relatively weaker $–CH\cdots O^-$ interaction. Hence, we found that the PSSH had much stronger interaction with all solvents compared to the PSS^- except for EG; EG solvent can form two strong hydrogen bonds with the deprotonated PSS^-. The difference in the solvation mechanism between EG and DMSO explains why big electrical conductivity enhancement was observed by co-solvent treatment in previous studies (Shi et al., 2015).

Neither PEDOT nor $PEDOT^{+\cdot}$ in the polaron state can form any hydrogen bonds with solvent molecules, and therefore their interactions with solvents are generally much weaker, where solvent molecules prefer to interact with oxygen atoms in the

dioxyethylene group (-OCH_2CH_2O-) and solvent oxygen atoms weakly interact with the –CH moieties of PEDOT. This implies that solvents are mainly interacting with the PSS shell, leaving the conductive PEDOT core to remain intact. The most important consequence here is that the lowest energy structures suggest similar enhancement mechanism and comparable performance for DMSO and $DMSO_2$. The interactions are weaker than under water solvation effect, showing the advantage of post treatment compared to solution treatment.

For solvent interactions with single PSSH, PSSH-DMSO has stronger interaction compared to $DMSO_2$. However, $DMSO_2$ with two oxygen atoms is bifunctional and thus is able to coordinate with two PSSH monomers (see **Figure 8** for solvent interactions). DMSO and $DMSO_2$ have higher interaction energies with the PSSH compared to EG and NMP. The difference among solvents is lowered under implicit water solvation effect for ternary interaction. According to the calculated interaction energies, the PSSH-solvent interaction can have two effects on the system, i.e., (i) chain expansion and phase separation of the PSSH shell as a result of decreasing PSS-PSS interactions, and (ii) charge screening and phase separation of PSS-PEDOT. Partial reduction of the excess PSSH shell that covers the conducting PEDOT components enhances the connectivity between PEDOT phases, directly resulting in the enhancement of electrical conductivity.

Based on AFM, FESEM, and XRD and theoretical studies, we propose a mechanism for electrical conductivity enhancement by $DMSO_2$ in **Figure 9**, illustrating a schematic for the role of $DMSO_2$ in doping PEDOT:PSS and polymer orientation arising from the crystallization. When water molecules slowly evaporate upon heating, the $DMSO_2$ concentration increases and thus its self-interaction leads to the formation of fibrous crystals. Such a fibrous structure triggers the alignment of long PSS chains resulting in well-orientation of PEDOT and better connection between PEDOT units absorbed to PSS chain to improve the electrical conductivity. In literature, it has well-reported that the PSS insulating polymer can be separated through DMSO, EG, or acid treatment (Culebras et al., 2014a; Park et al., 2014b).

Free energy of solvation calculations were performed in periodic cells for the PSS, PEDOT, and $DMSO_2$ solvation by organic solvents to understand the observed variation in structural and electrical conductivity properties (**Figure 10**). Since all the calculated solvation free energies are negative, mixing is expected in all cases. The highest $|\Delta G_{sol}|$ is observed for the solvation of the PSS chain (across almost all solvents), proving that the mechanism of conductivity enhancement via the PSS phase separation. Hexane, which has the lowest $|\Delta G_{sol}|$ around the PSS chain and $DMSO_2$ molecules, does not have any effect on the electrical conductivity and film thickness. THF and CH_2Cl_2 solvents, which have high $|\Delta G_{sol}|$ for PEDOT chains and good miscibility with the PSS chains, have low electrical conductivity and big thickness due to polymer expansion. The solvents that enhance electrical conductivity of PEDOT:PSS films treated with $DMSO_2$ should thus have high values of $|\Delta G_{sol}|$ for either PSS solvation or $DMSO_2$ solvation. Besides, ideal solvent should have lower solvation free energy for PEDOT as a solute. As an example, DMSO can wash away insulating $DMSO_2$ crystals in PEDOT:PSS, decrease thickness of films and enhance electrical conductivity. DMSO has similar electrical conductivity enhancement mechanism with $DMSO_2$. That is the reason

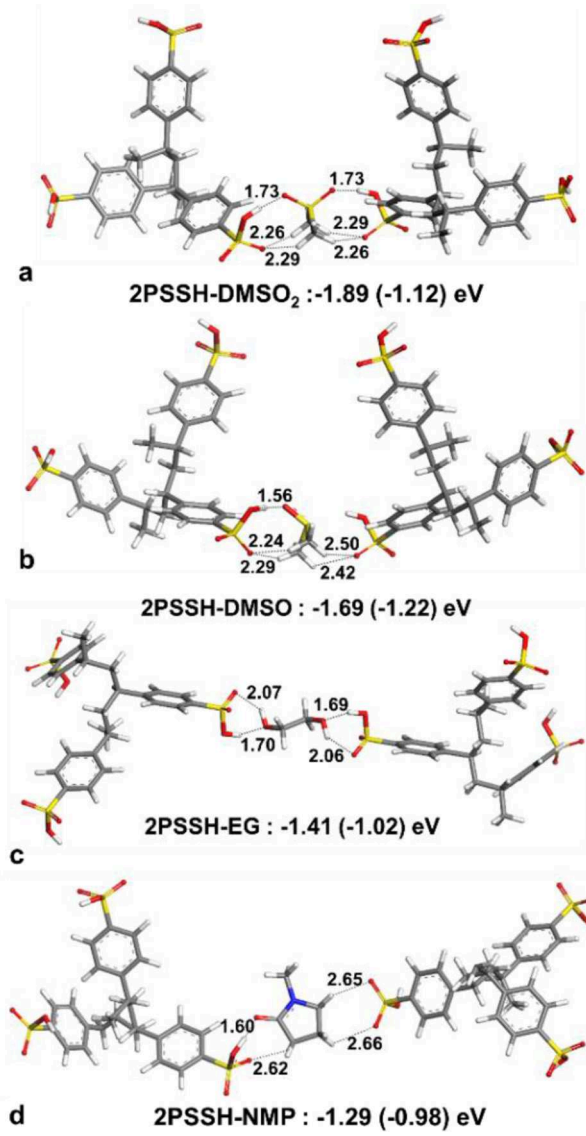

FIGURE 8 | Optimized lowest energy structures and interaction energies of two PSSH trimers with **(a)** $DMSO_2$, **(b)** DMSO, **(c)** EG, and **(d)** NMP. Interaction energies calculated with water solvation effect are given in parenthesis.

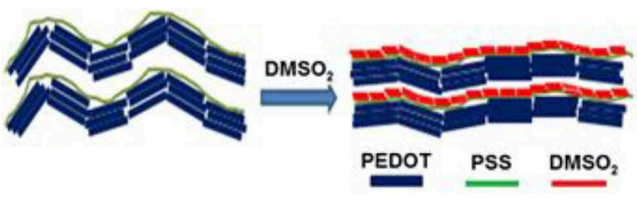

FIGURE 9 | The cartoon process for the interaction between $DMSO_2$ and PEDOT:PSS.

why further electrical conductivity enhancement is limited. Acetone also have similar effect with strong solvation of $DMSO_2$, decreasing thickness and slightly enhances the conductivity. Solvents that have strong solvation of both $DMSO_2$ and the PSS chains, such as EG and DMF should simultaneously decrease film thickness and enhance electrical conductivity. The mechanism of solvent interaction with the PSS chains is important so that secondary solvent with different interaction mechanism with the PSS chains compared to $DMSO_2$ can separate the remaining PSS chains to enhance conductivity further.

In order to obtain the electric properties of PEDOT:PSS films with different concentration of $DMSO_2$, the Van der Pauw–Hall measurements were performed. **Table 1** lists the carrier mobility (μ), concentration (n) and conductivity of PEDOT:PSS with $DMSO_2$. The carrier mobility improved significantly with the increase of the concentration of additive in PEDOT:PSS film. It is reasonable to conclude that the enhancement in electric conductivity of PEDOT:PSS is due to the incorporation of $DMSO_2$. The carrier concentration increases with the increase of additive concentrations but slightly decrease when the concentration of $DMSO_2$ is over 3%. As $DMSO_2$ does not behave like a reducing agent to cause the change in the oxidation level of PEDOT. The increase in carrier concentration is probably due to the release of trapped carriers by polymer chains. $DMSO_2$ treatment induces the polymer alignment along a particular direction and thus pushes out the carriers from the polymer chains entangled with the PSSH. On the other hand, $DMSO_2$ with two oxygen atoms is bifunctional and thus is able to coordinate with two PSSH monomers. Based on the modeling (vide supra) partial reduction of the excess PSSH shell that covers the conducting PEDOT components enhances the connectivity between PEDOT phases, as a result, perhaps freeing more carriers and increasing the electric conductivity.

In addition, the long-term stability for our pre-mixed PEDOT:PSS and $DMSO_2$ solution is also investigated. Chemical de-doping with tetrakis(dimethylamino)ethylene, secondary doping with polar organic solvents like DMSO, EG and NMP have been used to obtain high electrical conductivity. However, it is known that most mixtures of PEDOT:PSS and solvent dopants cannot be stored for a long duration. **Figure 11** shows that pre-mixed solution of $DMSO_2$ and PEDOT:PSS can be stored at 2–6°C for up to 2 months without significant change of the electrical conductivity, benefiting many applications.

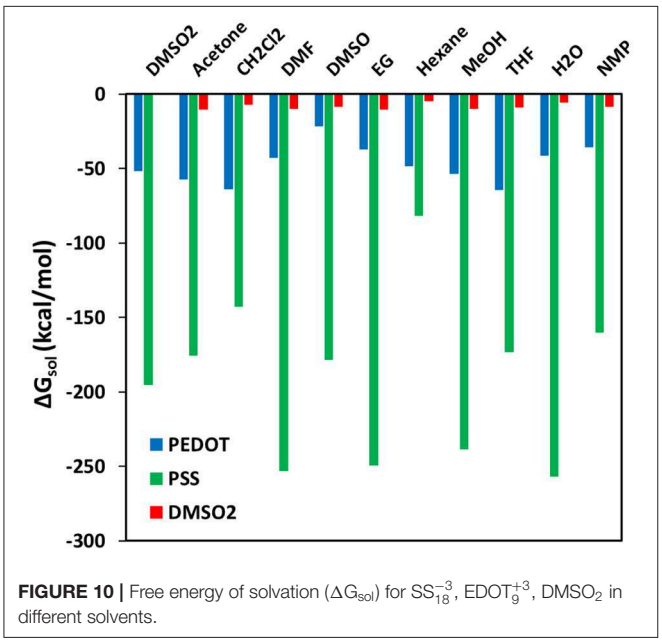

FIGURE 10 | Free energy of solvation (ΔG_{sol}) for SS_{18}^{-3}, $EDOT_9^{+3}$, $DMSO_2$ in different solvents.

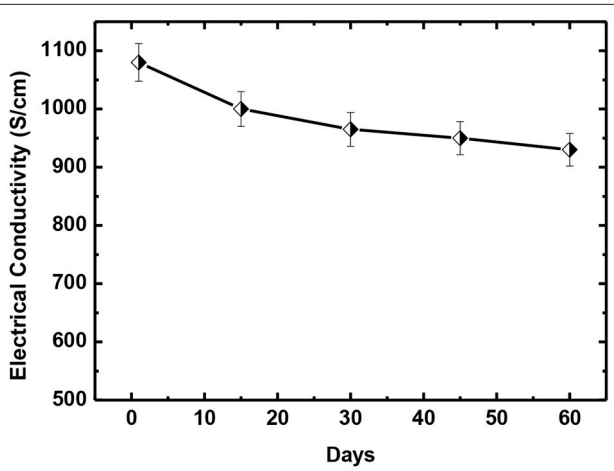

FIGURE 11 | The long term stability of pre-mix solution of $DMSO_2$ and PEDOT:PSS.

TABLE 1 | Comparison of electric properties of PEDOT:PSS film with $DMSO_2$.

Additive loading(%)	μ (cm^2/V-s)	n (cm^{-3})	δ(S/cm)	Seebeck (S/cm)	PF (μW/mK^2)
0	0.228 ± 0.06	4.73 ± 0.12 × 10^{18}	0.2 ± 0.1	21 ± 0.17	0.006 ± 0.001
0.3	1.14 ± 0.1	4.83 ± 0.22 × 10^{20}	154 ± 7	20.8 ± 0.17	6.7 ± 0.6
0.6	3.18 ± 0.2	3.90 ± 0.2 × 10^{20}	340 ± 217	21.5 ± 0.17	15.7 ± 1.4
0.8	7.88 ± 0.3	2.45 ± 0.22 × 10^{20}	412 ± 20	22.8 ± 0.18	21.4 ± 1.9
1	9.01 ± 0.4	2.51 ± 0.22 × 10^{20}	609 ± 30	20.1 ± 0.16	24.6 ± 2.2
3	10.391 ± 0.5	2.82 ± 0.22 × 10^{20}	1080 ± 50	17.1 ± 0.13	31.5 ± 2.8
5	10.221 ± 0.5	2.49 ± 0.22 × 10^{20}	875 ± 43	14.5 ± 0.12	18.4 ± 1.7
7	10.7 ± 0.5	2.47 ± 0.25 × 10^{20}	835 ± 42	11.4 ± 0.1	10.9 ± 0.9

CONCLUSION

As an alternative to conventional additives, $DMSO_2$ was identified as a dopant for the PEDOT: PSS to raise the electrical conductivity from 0.2 to 1080 S/cm with 3% loading. The enhancement in electrical conductivity is due to polymer alignment induced by crystallization of $DMSO_2$ in the PEDOT:PSS system. The modeling study revealed that the interactions at the molecular level demonstrated that $DMSO_2$ had comparable interaction energies with conventional solvents, which is responsible for conductivity enhancement. This new additive has an edge over other traditional dopants/additives as it is environmentally friendly, non-toxic, and has an easy doping process without additional treatment. Furthermore, PEDOT:PSS doped with $DMSO_2$ is stable and "green," making it highly desired for industrial applications. $DMSO_2$ is unable to contribute to improvement in the Seebeck coefficient due to the inability of $DMSO_2$ to change the oxidation level of PEDOT. Our next step would be to introduce an additional post-treatment that enables to enhance the Seebeck coefficient, and thus leads to the high power factor of PEDOT.

DATA AVAILABILITY STATEMENT

All datasets generated for this study are included in the article/**Supplementary Material**.

AUTHOR CONTRIBUTIONS

QZ, and JX conceived and designed the experiments. QZ, YZ, XW, and XS performed the experiments and contributed to the film fabrication, measurement, and data analysis. EY, TT, GW, and S-WY contributed to modeling and analysis. QZ, EY, and JX wrote and revised the paper.

FUNDING

This work was financially supported by the Agency for Science, Technology and Research (A*STAR), Industry Alignment Fund, Pharos Hybrid thermoelectric materials for ambient applications Program (Grant Nos.: 1527200019, 1527200021, and 1527200024).

ACKNOWLEDGMENTS

The authors would like to acknowledge the support from the Institute of Materials Research and Engineering (IMRE), Agency for Science, Technology and Research (A*STAR).

SUPPLEMENTARY MATERIAL

The Supplementary Material for this article can be found online at: https://www.frontiersin.org/articles/10.3389/fchem.2019.00783/full#supplementary-material

REFERENCES

Biovia, D. S. (2017). *BIOVIA Discovery Studio 2017 R2: A Comprehensive Predictive Science Application for the Life Sciences*. San Diego, CA. Available online at: http://accelrys.com/products/collaborative-science/biovia-discovery-studio

Bubnova, O., Khan, Z. U., Malti, A., Braun, S., Fahlman, M., Berggren, M., et al. (2011). Optimization of the thermoelectric figure of merit in the conducting polymer poly (3, 4-ethylenedioxythiophene). *Nat. Mater.* 10, 429–433. doi: 10.1038/nmat3012

Choi, J., Lee, J. Y., Lee, S. S., Park, C. R., and Kim, H. (2016). High-performance thermoelectric paper based on double carrier-filtering processes at nanowire heterojunctions. *Adv. Energy Mater.* 6:1502181. doi: 10.1002/aenm.201502181

Choy, C. L. (1977). Thermal conductivity of polymers. *Polymer* 18, 984–1004. doi: 10.1016/0032-3861, 90002-7

Crispin, X., Jakobsson, F., Crispin, A., Grim, P., Andersson, P., Volodin, A., et al. (2006). The origin of the high conductivity of poly (3, 4-ethylenedioxythiophene)-poly (styrenesulfonate)(PEDOT-PSS) plastic electrodes. *Chem. Mater.* 18, 4354–4360. doi: 10.1021/cm061032+

Culebras, M., Gomez, C., and Cantarero, A. (2014a). Enhanced thermoelectric performance of PEDOT with different counter-ions optimized by chemical reduction. *J. Mater. Chem. A* 2, 10109–10115. doi: 10.1039/C4TA01012D

Culebras, M., Gómez, C. M., and Cantarero, A. (2014b). Review on polymers for thermoelectric applications. *Materials* 7, 6701–6732. doi: 10.3390/ma7096701

Fan, C. F., Olafson, B. D., Blanco, M., and Hsu, S. L. (1992). Application of molecular simulation to derive phase diagrams of binary mixtures. *Macromolecules* 25, 3667–3676. doi: 10.1021/ma00040a010

Feng, Z.-Q., Wu, J., Cho, W., Leach, M. K., Franz, E. W., Naim, Y. I., et al. (2013). Highly aligned poly (3, 4-ethylene dioxythiophene)(PEDOT) nano-and microscale fibers and tubes. *Polymer* 54, 702–708. doi: 10.1016/j.polymer.2012.10.057

Frisch, M., Trucks, G., Schlegel, H., Scuseria, G., Robb, M., Cheeseman, J., et al. (2019). *Gaussian 16, Revision A*. Wallingford, CT: Gaussian, Inc.

Han, S., Zhai, W., Chen, G., and Wang, X. (2014). Morphology and thermoelectric properties of graphene nanosheets enwrapped with polypyrrole. *RSC Adv.* 4, 29281–29285. doi: 10.1039/C4RA04003A

Hu, F., Cai, Q., Liao, F., Shao, M., and Lee, S.-T. (2015a). Recent advancements in nanogenerators for energy harvesting. *Small* 11, 5611–5628. doi: 10.1002/smll.201501011

Hu, X., Chen, G., Wang, X., and Wang, H. (2015b). Tuning thermoelectric performance by nanostructure evolution of a conducting polymer. *J. Mater. Chem. A* 3, 20896–20902. doi: 10.1039/C5TA07381B

Hu, Y., Shi, H., Song, H., Liu, C., Xu, J., Zhang, L., et al. (2013). Effects of a proton scavenger on the thermoelectric performance of free-standing polythiophene and its derivative films. *Synth. Met.* 181, 23–26. doi: 10.1016/j.synthmet.2013.08.006

Jiang, F.-X., Xu, J.-K., Lu, B.-Y., Xie, Y., Huang, R.-J., and Li, L.-F. (2008). Condensed matter: electronic structure, electrical, magnetic, and optical properties: thermoelectric performance of poly (3, 4-ethylenedioxythiophene): poly (styrenesulfonate). *Chin. Phys. Lett.* 25, 2202–2205. doi: 10.1088/0256-307X/25/6/076

Kaneko, H., Ishiguro, T., Takahashi, A., and Tsukamoto, J. (1993). Magnetoresistance and thermoelectric power studies of metal-nonmetal transition in iodine-doped polyacetylene. *Synth. Met.* 57, 4900–4905. doi: 10.1016/0379-6779(93)90836-L

Kemp, N., Kaiser, A., Liu, C. J., Chapman, B., Mercier, O., Carr, A., et al. (1999). Thermoelectric power and conductivity of different types of polypyrrole. *J. Polym. Sci. Part B: Polym. Phys.* 37, 953-960.

Kim, G. H., Shao, L., Zhang, K., and Pipe, K. P. (2013). Engineered doping of organic semiconductors for enhanced thermoelectric efficiency. *Nat. Mater.* 12, 719–723. doi: 10.1038/nmat3635

Kim, J. Y., Kwon, M. H., Min, Y. K., Kwon, S., and Ihm, D. W. (2007). Self-Assembly And Crystalline Growth Of Poly (3, 4-Ethylenedioxythiophene) Nanofilms. *Adv. Mater. Weinheim.* 19, 3501–3506. doi: 10.1002/adma.200602163

Kim, N., Kee, S., Lee, S. H., Lee, B. H., Kahng, Y. H., Jo, Y. R., et al. (2014). Highly Conductive PEDOT: PSS Nanofibrils Induced by Solution-Processed Crystallization. *Adv. Mater. Weinheim.* 26, 2268–2272. doi: 10.1002/adma.201304611

Kumar, P., Zaia, E. W., Yildirim, E., Repaka, D. V. M., Yang, S.-W., Urban, J. J., et al. (2018). Polymer morphology and interfacial charge transfer dominate over energy-dependent scattering in organic-inorganic thermoelectrics. *Nat. Commun.* 9:5347. doi: 10.1038/s41467-018-07435-z

Kumar, S. R. S., Kurra, N., and Alshareef, H. N. (2016). Enhanced high temperature thermoelectric response of sulphuric acid treated conducting polymer thin films. *J. Mater. Chem. C* 4, 215–221. doi: 10.1039/C5TC03145A

Kyaw, A. K. K., Yemata, T. A., Wang, X., Lim, S. L., Chin, W. S., Hippalgaonkar, K., et al. (2017). Enhanced thermoelectric performance of PEDOT:PSS films by sequential post-treatment with formamide. *Macromol. Mater. Eng.* 303:1700429. doi: 10.1002/mame.201700429

Laforgue, A., and Robitaille, L. (2010). Production of conductive PEDOT nanofibers by the combination of electrospinning and vapor-phase polymerization. *Macromolecules* 43, 4194–4200. doi: 10.1021/ma9027678

Mateeva, N., Niculescu, H., Schlenoff, J., and Testardi, L. (1998). Correlation of Seebeck coefficient and electric conductivity in polyaniline and polypyrrole. *J. Appl. Phys.* 83, 3111–3117. doi: 10.1063/1.367119

McGrail, B. T., Sehirlioglu, A., and Pentzer, E. (2015). Polymer composites for thermoelectric applications. *Angew. Chem. Int. Ed.* 54, 1710–1723. doi: 10.1002/anie.201408431

Moriarty, G. P., Briggs, K., Stevens, B., Yu, C., and Grunlan, J. C. (2013). Fully organic nanocomposites with high thermoelectric power factors by using a dual-stabilizer preparation. *Energy Technol.* 1, 265–272. doi: 10.1002/ente.201300018

Park, G. O., Roh, J. W., Kim, J., Lee, K. Y., Jang, B., Lee, K. H., et al. (2014a). Enhanced thermoelectric properties of germanium powder/poly (3, 4-ethylenedioxythiophene): poly (4-styrenesulfonate) composites. *Thin Solid Films* 566, 14–18. doi: 10.1016/j.tsf.2014.07.011

Park, H., Lee, S. H., Kim, F. S., Choi, H. H., Cheong, I. W., and Kim, J. H. (2014b). Enhanced thermoelectric properties of PEDOT: PSS nanofilms by a chemical dedoping process. *J. Mater. Chem. A* 2, 6532–6539. doi: 10.1039/C3TA14960A

Park, T., Park, C., Kim, B., Shin, H., and Kim, E. (2013). Flexible PEDOT electrodes with large thermoelectric power factors to generate electricity by the touch of fingertips. *Energy Environ. Sci.* 6, 788–792. doi: 10.1039/c3ee23729j

Shi, H., Liu, C., Jiang, Q., and Xu, J. (2015). Effective approaches to improve the electrical conductivity of PEDOT: PSS: a review. *Adv. Electron. Mater.* 1:1500017. doi: 10.1002/aelm.201500017

Steinbrecher, T., Joung, I., and Case, D. A. (2011). Soft-core potentials in thermodynamic integration: comparing one-and two-step transformations. *J. Comput. Chem.* 32, 3253–3263. doi: 10.1002/jcc.21909

Sun, H. (1998). COMPASS: An ab initio force-field optimized for condensed-phase applications overview with details on alkane and benzene compounds. *J. Phys. Chem. B* 102, 7338–7364. doi: 10.1021/jp980939v

Timpanaro, S., Kemerink, M., Touwslager, F., De Kok, M., and Schrader, S. (2004). Morphology and conductivity of PEDOT/PSS films studied by scanning–tunneling microscopy. *Chem. Phys. Lett.* 394, 339–343. doi: 10.1016/j.cplett.2004.07.035

Tomasi, J., Mennucci, B., and Cammi, R. (2005). Quantum mechanical continuum solvation models. *Chem. Rev.* 105, 2999–3094. doi: 10.1021/cr9904009

Tomlinson, E. P., Willmore, M. J., Zhu, X., Hilsmier, S. W., and Boudouris, B. W. (2015). Tuning the thermoelectric properties of a conducting polymer through blending with open-shell molecular dopants. *ACS Appl. Mater. Interfaces* 7, 18195–18200. doi: 10.1021/acsami.5b05860

Volkov, A. V., Wijeratne, K., Mitraka, E., Ail, U., Zhao, D., Tybrandt, K., et al. (2017). Understanding the capacitance of PEDOT:PSS. *Adv. Funct. Mater.* 27:1700329. doi: 10.1002/adfm.201700329

Wei, Q., Mukaida, M., Kirihara, K., Naitoh, Y., and Ishida, T. (2015). Recent progress on PEDOT-based thermoelectric materials. *Materials* 8, 732–750. doi: 10.3390/ma8020732

Wu, J., Sun, Y., Pei, W.-B., Huang, L., Xu, W., and Zhang, Q. (2014). Polypyrrole nanotube film for flexible thermoelectric application. *Synth. Met.* 196, 173–177. doi: 10.1016/j.synthmet.2014.08.001

Xu, K., Chen, G., and Qiu, D. (2013). Convenient construction of poly (3, 4-ethylenedioxythiophene)–graphene pie-like structure with enhanced thermoelectric performance. *J. Mater. Chem. A* 1, 12395–12399. doi: 10.1039/c3ta12691a

Yao, Q., Chen, L., Zhang, W., Liufu, S., and Chen, X. (2010). Enhanced thermoelectric performance of single-walled carbon nanotubes/polyaniline hybrid nanocomposites. *ACS Nano* 4, 2445–2451. doi: 10.1021/nn1002562

Yildirim, E., Wu, G., Yong, X., Tan, T. L., Zhu, Q., Xu, J., et al. (2018). A theoretical mechanistic study on electrical conductivity enhancement of DMSO treated PEDOT:PSS. *J. Mater. Chem. C* 6, 5122–5131. doi: 10.1039/C8TC00917A

Yildirim, E., Zhang, Y., Lutkenhaus, J. L., and Sammalkorpi, M. (2015). Thermal transitions in polyelectrolyte assemblies occur via a dehydration mechanism. *ACS Macro Lett.* 4, 1017–1021. doi: 10.1021/acsmacrolett.5b00351

Yoon, C., Reghu, M., Moses, D., Cao, Y., and Heeger, A. (1995). Transports in blends of conducting polymers. *Synth. Met.* 69, 255–258. doi: 10.1016/0379-6779(94)02439-6

Yue, R., Chen, S., Liu, C., Lu, B., Xu, J., Wang, J., et al. (2012). Synthesis, characterization, and thermoelectric properties of a conducting copolymer of 1, 12-bis (carbazolyl) dodecane and thieno [3, 2-b] thiophene. *J. Solid State Electrochem.* 16, 117–126. doi: 10.1007/s10008-011-1292-0

Zhang, B., Sun, J., Katz, H., Fang, F., and Opila, R. (2010). Promising thermoelectric properties of commercial PEDOT: PSS materials and their Bi2Te3 powder composites. *ACS Appl. Mater. Interfaces* 2, 3170–3178. doi: 10.1021/am100654p

Zhao, D., and Tan, G. (2014). A review of thermoelectric cooling: materials, modeling and applications. *Appl. Therm. Eng.* 66, 15–24. doi: 10.1016/j.applthermaleng.2014.01.074

Zhao, Y., and Truhlar, D. G. (2008). The M06 suite of density functionals for main group thermochemistry, thermochemical kinetics, noncovalent interactions, excited states, and transition elements: two new functionals and systematic testing of four M06-class functionals and 12 other functionals. *Theor. Chem. Acc.* 120, 215–241. doi: 10.1007/s00214-007-0310-x

Conflict of Interest: The authors declare that the research was conducted in the absence of any commercial or financial relationships that could be construed as a potential conflict of interest.

frontiers in Chemistry

ORIGINAL RESEARCH
published: 08 January 2020
doi: 10.3389/fchem.2019.00870

Improved Thermoelectric Properties and Environmental Stability of Conducting PEDOT:PSS Films Post-treated With Imidazolium Ionic Liquids

Temesgen Atnafu Yemata[1,2], *Yun Zheng*[1], *Aung Ko Ko Kyaw*[1,3], *Xizu Wang*[1], *Jing Song*[1], *Wee Shong Chin*[2*] and *Jianwei Xu*[1,2*]

[1] Institute of Materials Research and Engineering, Agency for Science, Technology, and Research (A*STAR), Singapore, Singapore, [2] Department of Chemistry, National University of Singapore, Singapore, Singapore, [3] Department of Electrical and Electronic Engineering, Southern University of Science and Technology, Shenzhen, China

OPEN ACCESS

Edited by:
Mahendra Dashrath Shirsat,
Dr. Babasaheb Ambedkar Marathwada University, India

Reviewed by:
Xiaoji Xie,
Nanjing Tech University, China
Arshad Saleem Bhatti,
COMSATS Institute of Information Technology, Pakistan

***Correspondence:**
Wee Shong Chin
chmcws@nus.edu.sg
Jianwei Xu
jw-xu@imre.a-star.edu.sg

Specialty section:
This article was submitted to Nanoscience, a section of the journal Frontiers in Chemistry

Received: 15 July 2019
Accepted: 03 December 2019
Published: 08 January 2020

Citation:
Yemata TA, Zheng Y, Kyaw AKK, Wang X, Song J, Chin WS and Xu J (2020) Improved Thermoelectric Properties and Environmental Stability of Conducting PEDOT:PSS Films Post-treated With Imidazolium Ionic Liquids. Front. Chem. 7:870. doi: 10.3389/fchem.2019.00870

Poly(3,4-ethylenedioxythiophene):poly(styrenesulfonate) (PEDOT:PSS) is one of the most popular conducting polymers and widely used as polymer thermoelectric materials, and its thermoelectric performance could be improved by a variety of post-treatment processes. This paper reported two series of post-treatment methods to enhance the thermoelectric performance. The first series method included pre-treatment of PEDOT:PSS film with formamide, followed by imidazolium-based ionic liquids. The second series method included pre-treatment of PEDOT:PSS film with formamide, followed by sodium formaldehyde sulfoxylate, and finally imidazolium-based ionic liquids. Two series of post-treatment methods significantly improved the power factor of PEDOT:PSS when compared to that of PEDOT:PSS treated with formamide only. For example, using the first series post-treatment method with 40 vol.% ionic liquid 1-butyl-3-methylimidazolium bis(trifluoromethanesulfonyl) amide, the Seebeck coefficient of the PEDOT:PSS film increased from 14.9 to 28.5 μV/K although the electrical conductivity reduced from 2,873 to 1,701 S/cm, resulting in a substantial improvement in the overall power factor from 63.6 to 137.8 μW/K^{2}m. The electrical conductivity enhancement in the formamide-treatment process was in part ascribed to the removal of the insulating PSS component. Further treatment of PEDOT:PSS film with ionic liquid caused dedoping of PEDOT and hence increased in Seebeck coefficient. In contrast, second series post-treatment method led to the reduction in electrical conductivity from 2,873 to 641 S/cm but a big improvement in the Seebeck coefficient from 14.9 to 61.1 μV/K and thus the overall power factor reached up to ~239.2 μW/K^{2}m. Apart from the improvement in electrical conductivity, the increase in Seebeck coefficient is on account of the substantial dedoping of PEDOT polymer to its neutral form and thus leads to the big improvement of its Seebeck coefficient. The environmental stability of ionic liquid-treated PEDOT:PSS films were examined. It was found that the ionic liquid treated PEDOT:PSS retained

more than 70% Seebeck coefficient and electrical conductivity at 75% RH humidity and 70°C for 480 h. The improved long-term TE stability is attributed to the strong ionic interaction between sulfonate anions and bulky imidazolium cations that effectively block the penetration of water and lessen the tendency to take up water from the air.

Keywords: conducting polymer, PEDOT:PSS, thermoelectric, ionic liquids, environmental stability

INTRODUCTION

Thermoelectric (TE) materials are able to directly convert heat into electricity and *vice versa* (Bell, 2008; Snyder and Toberer, 2011). TE devices have been thought as promising "green" power generators and they play an essential role in harvesting low-grade heat like waste heat or exhausted heat that is usually dissipated to the environment. The performance of TE materials largely depends on the dimensionless figure-of-merit (ZT), $ZT = \sigma S^2 T/\kappa$ where σ is electrical conductivity, S is Seebeck coefficient, T is absolute temperature, and κ is thermal conductivity (Snyder and Toberer, 2011). More recently, traditional inorganic materials such as SnSe (Chang et al., 2018; Lee et al., 2019), PbTe (Tan et al., 2016; Chen et al., 2017), GeTe (Li et al., 2018), and $Cu_2Se_{0.5}S_{0.5}$ (Ren, 2017) with ZT values of over 2 have been reported. Despite their impressive TE performance, the drawbacks such as high cost, scarcity, toxicity, and low processability limit their commercial applications. Moreover, most of these promising inorganic TE materials have good performance when operating temperatures exceed 300–400°C. They may not function well for ambient temperature heat recovery as a large amount of waste heat in our surroundings is below 200°C (Yoo et al., 2015). Therefore, organic TE materials with high performance at ambient temperature have gained increasing interest in recovering a huge amount of low temperature waste heat (Yoo et al., 2015).

Conductive polymers (CPs) have immerged as promising TE materials due to the tunable σ, low κ, and relatively low production cost. The commonly studied CPs include polyaniline (PANi) (Yoon et al., 1995; Mateeva et al., 1998; MacDiarmid, 2001), poly(3,4-ethylenedioxythiophene):poly(styrenesulfonate) (PEDOT:PSS) (Zhang et al., 2010), polypyrrole (PPy) (Kemp et al., 1999), polyacetylene (PAc) (Kaneko et al., 1993), and polythiophene (PTH) (MacDiarmid, 2001; Hu et al., 2013). Other CPs, like uniaxially aligned iodine (I_2)-doped PAc, has a power factor ($PF = S^2\sigma$) of $\sim$ 1,350 $\mu W/K^2m$, but it has no practical application due to its poor stability and processability (Cowen et al., 2017). On the contrary, PPy and PANi have good stability but poor *PFs* of less than 10 $\mu W/K^2m$ (Li et al., 2010; Liang et al., 2017). Currently, the TE performance of CPs cannot rival that of state-of-the-art inorganic counterparts. However, the TE performance of CPs has been improved significantly over the years, showing very promising ZT values for applications.

Recently, among the CPs, PEDOT:PSS has attracted great attention due to the high σ, intrinsically low κ, water-processability, and commercial availability (Khan et al., 2015; Wei et al., 2015). Several approaches have been widely investigated to enhance the TE performance of PEDOT:PSS, such as post treatment (Fan et al., 2017), electrochemical oxidation (Park et al., 2013), and hybrid approach (Zhang et al., 2010), etc. PEDOT:PSS can form hybrids with different carbon sources, metallic nanomaterials or inorganic TE materials. This allows hybrid materials to tap on the advantages of each component, such as a large S or σ to balance individual TE characteristics to give an optimum TE performance (Zhang et al., 2010; Moriarty et al., 2013; Xu et al., 2013; Park et al., 2014a). The other challenge is the incompatibility of the two components (i.e., PEDOT:PSS and additives) as observed in many cases, where phase separation of a single component leads to non-uniform films. Surface modification through post-treatment (Mcgrail et al., 2015; Wei et al., 2015) has also proven effective in improving the TE performance of PEDOT:PSS films by removing the insulating PSS segment from PEDOT:PSS. The typical process is to immerse PEDOT:PSS film in dimethyl sulfoxide (DMSO), ethylene glycol (EG) (Culebras et al., 2014; Park et al., 2014b) or inorganic acid solution. Inorganic salts and organic solvents with high dielectric constants have demonstrated the ability in increasing the σ of PEDOT by a few orders of magnitude, giving rise to a significant enhancement in PF (Zhang et al., 2010; Culebras et al., 2014). The highest PF can reach up to 469 $\mu W/K^2m$, leading to a large ZT value of 0.42 at 300 K (Kim et al., 2013). These post-treatments can increase the concentration of charge carriers and bipolarons. However, the high doping level in general results in a small S because of the extra charge carriers (Park et al., 2014b). Therefore, appropriate methods that improve S are desired as the ZT involves the square of S. Previous studies already demonstrated that the PF could be improved by regulating the redox level through an electrochemical or chemical method (Tsai et al., 2011; Bubnova et al., 2012), thus achieving the optimum TE properties through the control of charge carrier concentration. For instance, Park et al. reported PEDOT:PSS film with an optimized PF of 112 $\mu W/K^2m$ by treating with a mixture of DMSO and hydrazine (Park et al., 2014b). Also, Lee et al. employed a multistep process of ultrafiltration and dedoping by hydrazine to treat PEDOT:PSS and achieved a PF of 115.5 $\mu W/K^2m$ (Lee et al., 2014a). Moreover, Park et al. reported an improved PF of 1,270 $\mu W/K^2m$ by controlling the electrochemical oxidation of PEDOT films (Park et al., 2013). Recently, Fan et al. treated PEDOT:PSS films with sulfuric acid and different concentrations of sodium hydroxide. They reported an improved σ of 2,170 S/cm, an S of 39.2 $\mu V/K$, and hence a PF of 334 $\mu W/K^2m$ at room temperature (Fan et al., 2017). More recently, Fan et al. have demonstrated that 1-ethyl-3-methylimidazolium dicyanamide (EMIM-DCA) treated PEDOT:PSS films had an ultrahigh PF of 754 $\mu W/K^2m$ and a ZT of 0.75 at room temperature (Fan et al., 2018). Moreover, Saxena

et al. treated PEDOT:PSS film with EMIM-DCA in THF solution. They observed the simultaneous improvement of σ and S, and a maximum PF of 170 $\mu W/K^2m$ had been obtained because of the binary nature of both ionic liquids and PEDOT:PSS (Saxena et al., 2019). Therefore, approaches that can only slightly lower the high σ of formamide-treated PEDOT:PSS films while significantly improve the S could be effective for improving the TE properties of PEDOT:PSS films.

In this work, we reported the enhancement of the S and ZT of PEDOT:PSS films with ionic liquids (ILs) treatment. The effect of anions associated with ILs on the TE properties of treated PEDOT:PSS films were also investigated, revealing that the type of anions played a somewhat role in affecting the TE properties. PEDOT:PSS films treated with 40 vol.% IL, 1-butyl-3-methylimidazolium bis(trifluoromethanesulfonyl) amide (BMIM-TFSI), achieved a highest PF of 239.2 $\mu W/K^2m$, and it also demonstrated a very good environmental stability, indicating that our approach is potential for practical TE application in the future.

EXPERIMENTAL SECTION

Materials

PEDOT:PSS solution (Clevios PH 1000, PEDOT:PSS weight ratio = 1:2.5 and concentration by mass = 1.3%) was purchased from Heraeus. Formamide, sodium formaldehyde sulfoxylate (SFS), 1-butyl-3-methylimidazolium tetrafluoroborate (BMIM-BF4), 1-butyl-3-methylimidazolium trifluoromethanesulfonate (BMIM-OTf) or 1-butyl-3-methylimidazolium bis(trifluoromethanesulfonyl) amide (BMIM-TFSI) were purchased from Sigma-Aldrich. All chemicals were used as received without further purification. The chemical structures of ionic liquids are shown in **Scheme 1**.

Sample Preparation

PEDOT:PSS solution was filtered using a 0.45 μm poly (vinylene difluoride) PVDF syringe filter. The glass substrates were cleaned with deionized (DI) water, detergent, acetone, and isopropanol in an ultrasonic bath consecutively and dried with nitrogen gas. The glass substrate was subjected to ultraviolet (UV)-ozone surface treatment for 15 min before use.

Pristine PEDOT:PSS Films

PEDOT:PSS films were prepared by drop-casting a 300 μL of PEDOT:PSS solution on the pre-cleaned glass substrate using a micropipette. The deposited sample was firstly dried in air at 50°C for 30 min to mainly drive off the H_2O solvent and then kept at 80°C for another 10 min to further remove the residual solvent. Finally, the PEDOT:PSS films were annealed at 130°C for 10 min to ensure complete evaporation of the solvent. The final thickness of each dried PEDOT:PSS film was in the range of 8–10 μm.

Formamide Post-treatment

For the post-treatment process, 140 μL formamide was first dropped onto the PEDOT:PSS films on a hot plate at 180°C and then the films were dried for about 10 min to remove the residual formamide. Afterward, the formamide treated PEDOT:PSS films were cooled to room temperature in air, and these films were rinsed with DI water and then dried again on a hot plate at 140°C for 5 min. The detailed procedures for treatment can be found in our previous work (Kyaw et al., 2018).

Sodium Formaldehyde Sulfoxylate (SFS) Post-treatment

Next, treatment with a salt solution was performed by dropping 150 μL aqueous SFS solution onto a formamide pretreated PEDOT:PSS film on a hot plate at 140°C. The film became dry after ∼5 min. The SFS treated PEDOT:PSS film was cooled to room temperature in air, rinsed with DI water for three times to wash away the salt, and then dried at 140°C again.

IL Post-treatment

The post-treatment with ILs was conducted at room temperature. Initially, three ILs (ILs) (BMIM-TFSI, BMIM-BF_4, and BMIM-OTf) with concentrations of i.e., 0, 20, 40, 60, 80, and 100 vol.% ILs in methanol were prepared. Then pre-treated PEDOT:PSS films with formamide and SFS were further treated with ILs in methanol according to the following steps: 150 μl IL in methanol was dropped onto PEDOT:PSS film at room temperature and left for 30 min. Next, the samples were dried by the aid of blowing N_2 gas at a pressure of 0.15 MPa for another 30 min to remove the residual solvent of IL. Then the films were rinsed by dipping the films in DI water for three times and then finally annealed at an elevated temperature of 140°C under air to remove the residual solvent. These treated samples were cooled down to room temperature before TE property measurements. All treatments were conducted at their optimized treatment temperatures and conditions. **Scheme 2** illustrates detailed PEDOT:PSS film preparation and post-treatment with formamide, SFS, and various ILs.

Characterization

The thicknesses of PEDOT:PSS films was measured before and after treatment using KLA-Tencor P-10 surface profiler with a detection limit of 100 Å (10 nm). The sheet resistance (Rs) of the films was determined by the four-point probe method (Laresta-GP MCP-T610 from Mitsubishi Chemical) at the room temperature. The Loresta-GP MCP-T610 meter includes standard accessories PSP probe (MCP-TP06P [4-pins, inter-pin distance 1.5 mm, pin points 0.26R, spring pressure 70 g/pin is intelligent)] and probe checker [RMH112 (MCP-TP06P)]. The edges of the film were located at 10 mm from the measurement point. The σ is the inverse of the resistivity ρ_H, which is calculated in terms of the equation: $\rho_H = R_S t$ where Rs and t are resistance and thickness of the film, respectively (Krupka, 2013).

The S was obtained with a homemade setup in a humidity-controlled room with a relative humidity (RH) of 55% (**Figure S1**). It consists of two stages (about 5 mm apart), one of which is integrated with a heater to generate a temperature gradient in the test sample. First, two Au electrodes with 20 mm long, 1 mm wide, and 2 mm apart were thermally evaporated on the film. To minimize the experimental error, PEDOT: PSS film

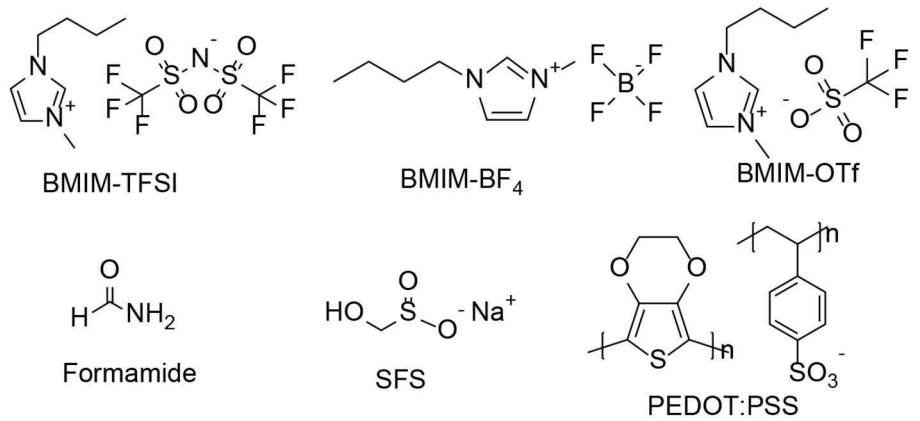

SCHEME 1 | Chemical structures of BMIM-TFSI, BMIM-BF_4, BMIM-OTF, SFS, formamide, and PEDOT:PSS.

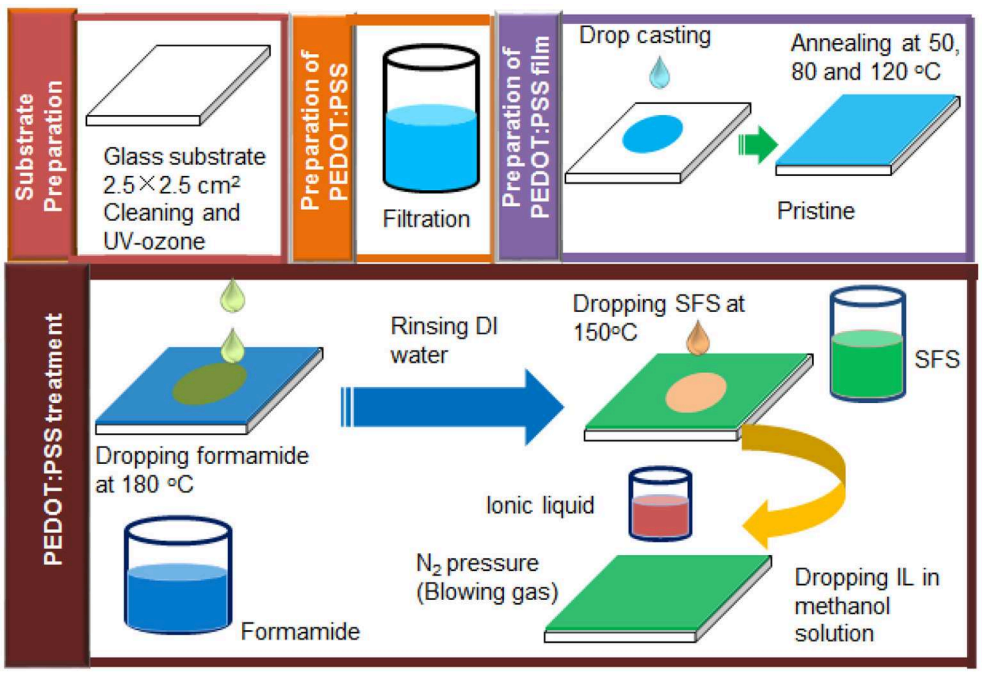

SCHEME 2 | Schematic of sample preparation for pristine and various IL-treated PEDOT:PSS films.

outside the area of electrodes was removed. The Au electrodes were connected to a Keithley 2,400 source meter through the probes to obtain the voltage difference (ΔV). Simultaneously, K-type thermocouples were connected to a data logger (Omron ZR-RX45) to collect the actual temperatures of the PEDOT:PSS film. The voltage probes and thermocouples were placed at the same temperature zone on each side so that the measured voltage corresponded to the actual thermal gradient between the two voltage probes. The measured thermovoltage was corrected by the thermovoltage of Au wire to obtain the absolute S of the films. S was estimated based on the slope of the linear relationship between thermoelectric voltage and the temperature difference of the two probes (i.e., $S = -\Delta V/\Delta T$). The Hall coefficient R_H was measured using a Hall-effect measurement system (Ecopia HMS-5000) with the van der Pauw method. First, the Ag electrodes were deposited onto the film through a shadow mask. The carrier concentration n and mobility μ were calculated using the following equations: $n = 1/(|R_H| \times e)$ *and* $\mu = |R_H|/\rho_H$, where e is electron charge. The κ was calculated using the equation $\kappa = b^2/Cp\rho_m$, where ρ_m, b, Cp are density, thermal effusivity, and specific heat capacity, respectively. The b was measured with a Pulsed Light Heating Nano TR (NETZSCH) system with an ultrafast pulsed laser flash method using the front heating-front detection mode, which is

designed for the thermal analysis of 30 nm −20 μm thin films. The *Cp* was measured independently by differential scanning calorimeter (DSC) (Mettlier Toledo DSC1). The ρ_m at room temperature was calculated from the mass and volume of the film. For all measurements, at least 10 samples for each measurement were prepared at the same conditions, and measurements were carried out at least five times for each sample to obtain the statistical results. X-ray diffraction (XRD) patterns of the films were obtained by a D8 Advance System (Bruker Corporation) equipped with a Cu K_α X-ray source, $\lambda = 0.15406$ nm. The Raman spectroscopy measurements were conducted on a Raman microscope (Renishaw) with a laser wavelength of 785.5 nm, a laser beam spot size of 200 μm and an accumulation time of 30 s. The absorption spectra measurement was performed on a UV-Vis-NIR spectrophotometer (Shimadzu, UV-3600). The films were spin-coated on quartz substrates. X-ray photoelectron spectroscopy (XPS) of the films were obtained by the Theta Probe Angle-Resolved X-ray Photoelectron Spectrometer (ARXPS) System (Thermo Scientific) using monochromated, micro-focused Al K_α X-ray photons ($h\upsilon$ =1486.6 eV) at a base pressure of 1×10^{-9} Torr and a step size of 0.1 eV. The curve fitting was carried out using the Avantage software. Atomic force microscopy (AFM) images were taken on a Bruker Dimension Icon AFM using the tapping mode. Ultraviolet photoelectron spectroscopy (UPS) measurement of the films was obtained by using the He I photon (21.22 eV) radiation line from a discharge lamp, with an experimental resolution of 0.15 eV. All UPS measurements of the onset of photoemission for determining the Φ were performed using standard procedures with a −4.5 V bias applied to the sample. The films were prepared by drop-casting a PEDOT:PSS solution onto a pre-cleaned silicon substrate.

Stability Study of PEDOT:PSS Films

PEDOT:PSS films were placed in a humidity controlled chamber and their TE performance was measured at varied temperature and humidity conditions in order to study the effect of humidity on TE properties of PEDOT:PSS films (Kim et al., 2016). In this study, the stability study was conducted using a constant climate chamber (Memmert HPP 110) in the temperature range from +0°C to +70°C, as well as the active humidification and dehumidification from 10 to 90% RH.

RESULTS AND DISCUSSION

Film Post-treatment and TE Properties

Three different ILs, 1-butyl-3-methylimidazolium bis(trifluoromethanesulfonyl) amide (BMIM-TFSI), 1-butyl-3-methylimidazolium tetrafluoroborate (BMIM-BF_4) or 1-butyl-3-methylimidazolium trifluoromethanesulfonate (BMIM-OTf) in methanol were used for this study. ILs are composed of positively and negatively charged species (i.e., binary nature). In these three ILs, the cation is always BMIM, and only the anion is different. All post-treatment methods are summarized in **Table 1**.

TABLE 1 | Post-treatments methods of PEDOT:PSS films.

Post-treatment Series	Post-treatment methods	Reagents used	Procedures
1	F-PEDOT:PSS	Formamide	Drop 140 μL formamide onto the PEDOT:PSS films at 180°C and dry for about 10 min. Then rinse with DI water and dry again on a hot plate at 140° C for 5 min.
	ILs-F-PEDOT:PSS	Formamide + Ionic liquid	The three ILs (BMIM-TFSI, BMIM-BF4, and BMIM-OTf) with 0, 20, 40, 60, 80, and 100 vol.% ILs in methanol were prepared and was dropped onto F-PEDOT:PSS film at room temperature and left for 30 min and finally dry blowing N_2 gas. Then rinse with DI water and dry again on a hot plate at 140° C for 5 min.
2	F-PEDOT:PSS	Formamide	Drop 140 μL formamide onto the PEDOT:PSS films at 180°C and dry for about 10 min. Then rinse with DI water and dry again on a hot plate at 140° C for 5 min.
	SFS-F-PEDOT:PSS	Formamide + Sodium formaldehyde sulfoxylate	Drop 150 μL aqueous SFS solution onto F-PEDOT:PSS film at 140° C and dry for about 5 min. Then rinse with DI water and dry again on a hot plate at 140° C for 5 min.
	ILs-SFS-F-PEDOT:PSS	Formamide + Sodium formaldehyde sulfoxylate + Ionic liquid	The three ILs (BMIM-TFSI, BMIM-BF4, and BMIM-OTf) with 0, 20, 40, 60, 80, and 100 vol.% ILs in methanol were prepared and was dropped onto SFS-F-PEDOT:PSS film at room temperature and left for 30 min and finally dry blowing N_2 gas. Then rinse with DI water and dry again on a hot plate at 140° C for 5 min.

Figures 1A,C,E show the *S*, σ, and *PF* of the PEDOT:PSS films treated by sequential formamide and ILs with various concentrations. The PEDOT:PSS films were pre-treated with formamide, and then ILs in methanol were dispersed onto the PEDOT:PSS films (first series post-treatment: IL-F-PEDOT:PSS). Introduction of IL treatment reduced the σ, while noticeably improved the *S* of IL-F-PEDOT:PSS films. It is worth noting that the σ and *S* of IL-F-PEDOT:PSS films almost remain unchanged when the concentration of ILs increases from 20 to 80%, suggesting that they are less affected by the concentration of the ILs. Treatment with 20–100 vol.% BMIM-TFSI (i.e., BMIM-TFSI-F-PEDOT:PSS) led to an enhancement of the *S* from ∼14.9 to ∼28.1 μV/K and a significant reduction in the σ from ∼2,873 to ∼1,678 S/cm. Overall, in comparison to the *PF* of around 65 $\mu W/K^2m$ without IL treatment, the optimal *PF* reaches 137.8 $\mu W/K^2m$ when 40 vol.% BMIM-TFSI solution is used. Interestingly, the type of anions plays a certain role in improving *S*. TFSI is the most efficient to enhance the magnitude of the *S*, followed by OTf and BF_4. The possible rationale is because of the binary nature of both PEDOT:PSS and ILs, which consist of

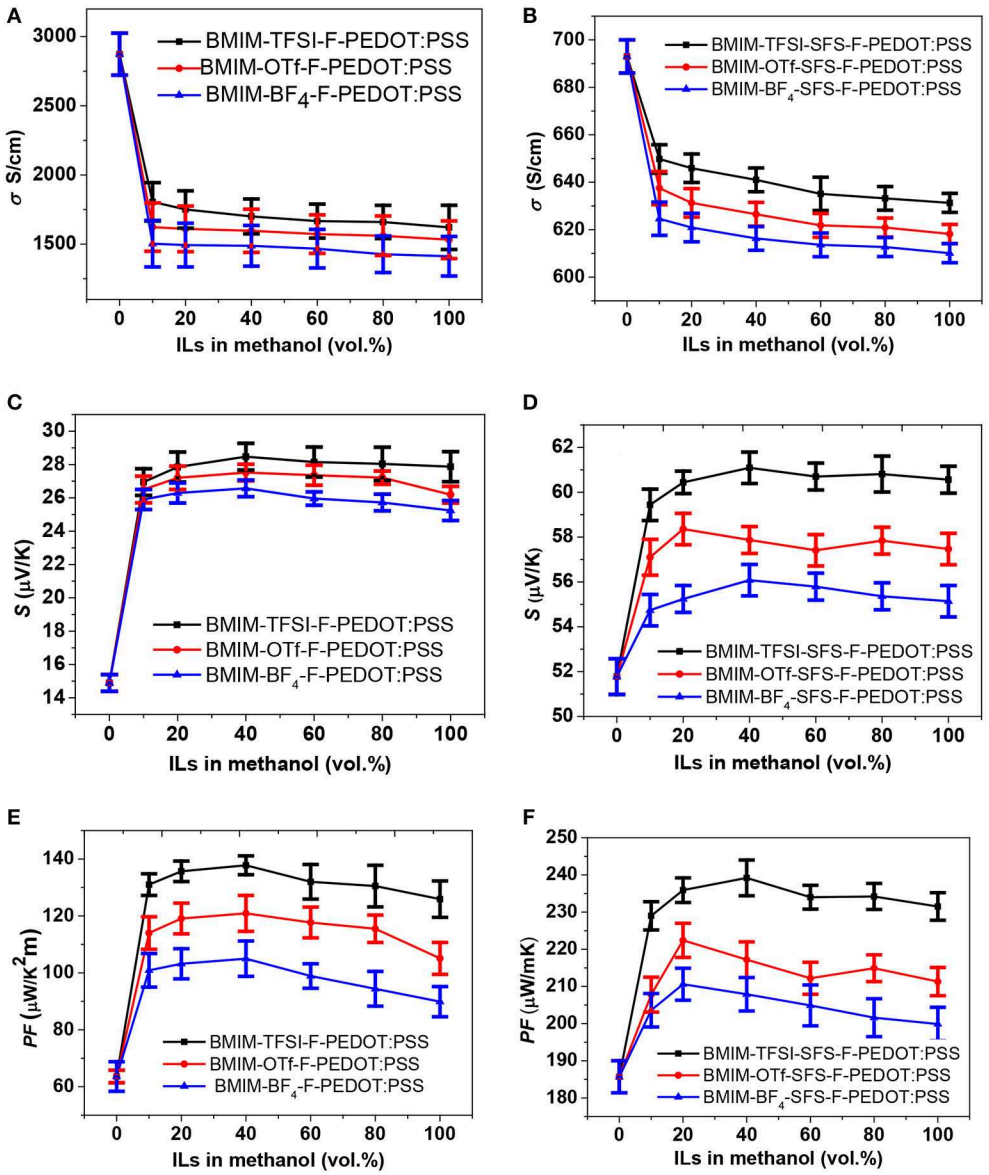

FIGURE 1 | TE properties of PEDOT:PSS films vs. vol.% ILs. ILs-F-PEDOT:PSS films: **(A)** σ, **(C)** *S*, and **(E)** *PF*; ILs-SFS-F-PEDOT:PSS films: **(B)** σ, **(D)** *S*, and **(F)** *PF*.

positively and negatively charged species. These charged species in ILs, for example, negatively charged TFSI and positively charged BMIM, will interact with correspondingly positively charged polymer PEDOT and negatively charged PSS chains via electrostatic interactions.

In the second series post-treatment, SFS was introduced to treat PEDOT:PSS before applying ILs treatment. Based on our previous findings (Yemata et al., unpublished), subsequent treatment of F-PEDOT:PSS with SFS can reduce the doping level, and as a result, improve the *PF* of PEDOT:PSS films. The σ, *S*, and *PF* of the ILs-SFS-F-PEDOT:PSS films with different concentrations of ILs are summarized in **Figures 1B,D,F**. The σ of ILs-SFS-F-PEDOT:PSS film was only slightly lower than that of the SFS-F-PEDOT:PSS films (631–649 vs. 693 S/cm), while the S became higher. BMIM-TFSI-SFS-F-PEDOT:PSS films exhibited an improved *S* of ∼60.8 μV/K compared to SFS-F-PEDOT:PSS (51.8 μV/K), while the σ (∼631 S/cm) decreased slightly. Consequently, the *PF* of BMIM-TFSI-SFS-F-PEDOT:PSS reached 239 $\mu W/K^2m$, about ∼29% enhancement over that of F-SFS-PEDOT:PSS. Similar to the first series post-treatment, the *PF* was nearly independent on the IL concentration, resulting in an average *PF* of 235 $\mu W/K^2m$ for BMIM-TFSI-SFS-F-PEDOT:PSS films. These values are among the highest *PFs* reported in the literature (**Table S2**) (Bubnova et al., 2011; Lee et al., 2014a; Park et al., 2014b; Wang et al., 2015; Yi et al., 2015; Fan et al., 2017). This enhancement in the *PF*

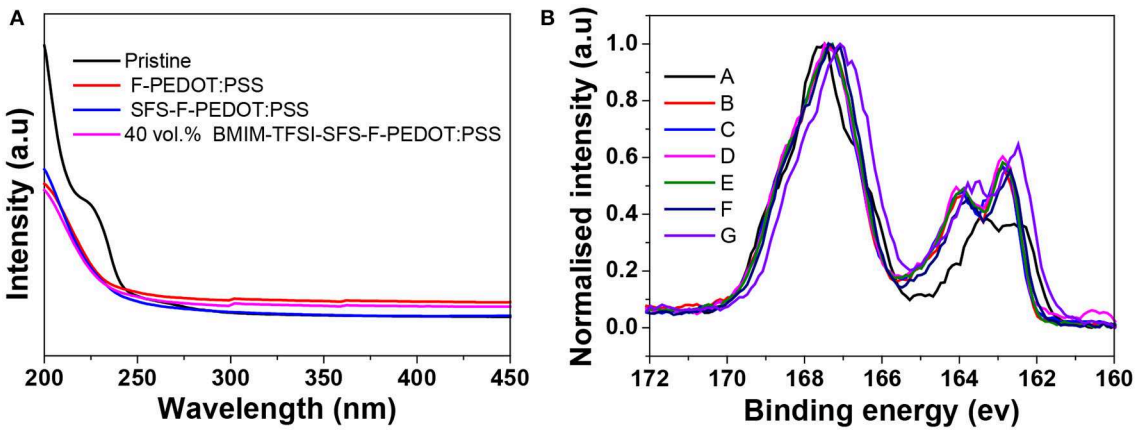

FIGURE 2 | (A) UV-vis absorption spectra of the pristine, F-PEDOT:PSS, SFS-F-PEDOT:PSS and BMIM-TFSI-SFS-F-PEDOT:PSS films. **(B)** S 2p core-level spectra of the pristine, F-PEDOT:PSS, and BMIM-TFSI-SFS-F-PEDOT:PSS films treated with various vol.% BMIM-TFSI in methanol. Pristine (A), F-PEDOT:PSS (B), SFS-F-PEDOT:PSS (C), 40 vol.% BMIM-TFSI-SFS-F-PEDOT:PSS (D), 60 vol.% BMIM-TFSI-SFS-F-PEDOT:PSS (E), 80 vol.% BMIM-TFSI-SFS-F-PEDOT:PSS (F), and 100 vol.% BMIM-TFSI-SFS-F-PEDOT:PSS (G).

is mainly due to the interaction of PSS^- groups with $BMIM^+$, which tunes n in the PEDOT domains and thus significantly enlarges the S but does not compromise the σ too much. Besides, control samples were also prepared by treating the F-PEDOT:PSS and SFS-F-PEDOT:PSS films with pure methanol (i.e., MeOH-F-PEDOT:PSS and MeOH-SFS-F-PEDOT:PSS) to verify that the observed changes are not related to interactions of the solvent with the PEDOT:PSS film. MeOH-F-PEDOT:PSS and MeOH-SFS-F-PEDOT:PSS control films showed *PF*s of 92.5 and 189 $\mu W/K^2m$, respectively. These values are smaller than those of the IL-F-PEDOT:PSS and IL-SFS-F-PEDOT:PSS films. Therefore, ILs in methanol has a more significant influence on the S and σ of PEDOT:PSS films than pure methanol.

Mechanism of TE Properties Enhancement of ILs Treated Films

Figure 2A shows the UV absorption spectra of the pristine, F-PEDOT:PSS and SFS-F- PEDOT:PSS and BMIM-TFSI-SFS-F-PEDOT:PSS films. The absorption band located at 225 nm was assigned to the PSS. Generally, the decreased intensity of the absorption band at 225 nm of PEDOT:PSS films shows the loss of PSSH from the PEDOT:PSS films. Compared with the spectrum of F-PEDOT:PSS that showed remarkable reduction in intensity at 225 nm, both spectra of SFS-F-PEDOT:PSS and BMIM-TFSI-SFS-F-PEDOT:PSS were almost the same, indicating that, similar to other treatments (Xia et al., 2012), formamide-treatment effectively removed PSSH, resulting in an increase in the σ compared to the pristine film.

The S_2p X-ray photoemission spectroscopy (XPS) was employed to study the influence of IL treatment (**Figure 2B**). The doublet XPS bands with binding energies between 166 and 172 eV were assigned to the S_2p band of the sulfur atoms in PSS, whereas XPS peaks with binding energies between 162 and 166 eV were assigned to the S_2p band of the sulfur atoms of PEDOT (Crispin et al., 2003; Kim et al., 2011). It can be seen from **Figure 2B** that the S_2p intensity of PEDOT relative to PSS increases due to the removal of PSS after BMIM-TFSI treatment (Xia and Ouyang, 2009). The ratios of the PSS peak to PEDOT peak dropped from 2.5 for the pristine film to 1.02 for the SFS-F-PEDOT:PSS film, indicating that a substantial amount of PSS was removed in the treated films. The removal of PSS was also verified by the reduction in the film thickness. The thickness of the pristine film was 6 μm. In contrast, the thickness of IL-SFS-F-PEDOT:PSS, F-PEDOT:PSS and SFS-F-PEDOT:PSS film was reduced significantly to 2.3, 2.5, and 2.1 μm, respectively. Also, the S2p bands in the PEDOT increased and shifted to a higher binding energy (163.5 ev vs. 164.2 ev) after IL treatment, indicating the decrease in the doping level after treatment, and the lower doping level in CPs invariably led to a reduced σ. The dedoping with IL slightly affected the σ while significantly improve the S. The *PF* of PEDOT:PSS film attained its optimum value at a specific oxidation state as the S increased and the σ tends to decrease at lower oxidation levels, which is consistent with the previous report (Khan et al., 2000).

The oxidation level of PEDOT:PSS thin films treated with the chemical dedoping agent was determined with UV-Vis-NIR absorption spectroscopy (**Figure 3A**). PEDOT exists in a form of neutral, polaron (a radical cation charge carrier) and bipolaron (a di-cation charge carrier) state (**Figure 3B**). The pristine and F-PEDOT:PSS films show a broad absorption band covering the beginning of the infrared region domain, and this band is attributed to bipolaron ($PEDOT^{2+}$). After binary dedoping (IL-F-PEDOT:PSS & IL-SFS-F-PEDOT:PSS), the oxidation level changes and the main peaks shifted to 900 nm for polaron ($PEDOT^+$) and to 600 nm for neutral (PEDOT) redox states (Chung et al., 1984; Garreau et al., 2001; Im and Gleason, 2007; Bubnova et al., 2011). Nevertheless, this further binary dedoping with ILs steps leads to the formation of neutral states of PEDOT chains at a high intensity (i.e., the absorption intensity is higher for IL-SFS-F-PEDOT:PSS films than that for SFS-F-PEDOT:PSS

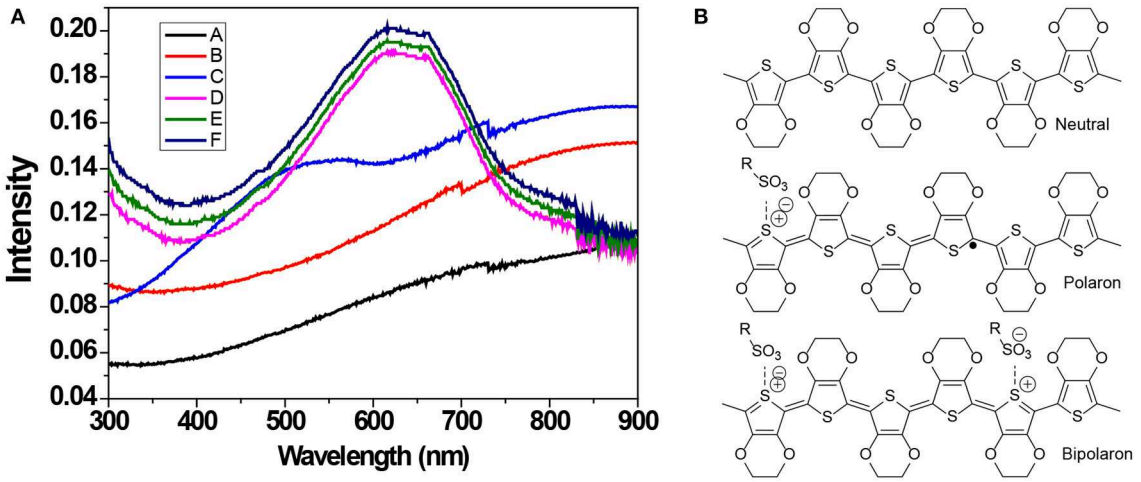

FIGURE 3 | (A) UV-Vis-NIR absorption spectra of pristine, F-PEDOT:PSS, and BMIM-TFSI-SFS-F-PEDOT:PSS films treated with various vol.% of BMIM-TFSI in methanol. Pristine (A), F-PEDOT:PSS (B), SFS-F-PEDOT:PSS (C), 40 vol.% BMIM-TFSI-SFS-F-PEDOT:PSS (D), 60 vol.% BMIM-TFSI-SFS-F-PEDOT:PSS (E), and 80 vol.% BMIM-TFSI-SFS-F-PEDOT:PSS (F). **(B)** A schematic Illustration of the transition of PEDOT chains from bipolaron (a di-cation charge carrier) to polaron (a radical cation charge carrier) and neutral chain during dedoping with IL.

films). This indicates that the PEDOT chains in the neutral state can remain in the neutral states upon binary dedoping but with a higher intensity, resulting in further enhancement in the *S* due to a lower *n*.

Raman spectroscopy was used to further investigate the conformational changes in polymers and to study the change in the doping level of PEDOT:PSS films. **Figure 4A** displays the Raman spectra of the untreated and BMIM-TFSI-SFS-F-PEDOT:PSS treated films. The peaks at 987, 1,130, and 1,257 cm^{-1} came from the deformation of oxyethylene ring, the PSS component, and the vibrational mode of Cα-Cα' symmetric interring stretching, respectively (Garreau et al., 1999, 2001; Han et al., 2011; Farah et al., 2012). Also, the peak around 1,509 cm^{-1} was originated from the asymmetrical vibration of $C_\alpha = C_\beta$ in PEDOT and the peak around 1,369 cm^{-1} was assigned to the symmetric Cβ-Cβ stretching (Garreau et al., 1999). The structure of the pristine PEDOT is made up of the benzoid and quinoid forms in which the conjugated benzoid structure owns a localized π-electron largely unaffected by external stimuli, while the quinoid form of PEDOT holds a delocalized state of π-electrons which can be affected by solvent treatment (Ouyang et al., 2005). In the electrically active and oxidized state, there are positive charges on the PEDOT polymer backbone which are balanced with an anion, either a small molecular anion or a macromolecular anion such as the PSS^- (Ouyang et al., 2005). The vibrational bands at 1424 cm^{-1} can be ascribed to the stretching vibration on the Cα = Cβ of the five-member ring of the pristine PEDOT films. These vibrational bands were shifted to around 1,417 cm^{-1} for IL-SFS-F-PEDOT:PSS films (**Figure 4B**), suggesting a change from a predominately coil conformation (benzoid structure) to a mixed linear-coil conformation (quinoid structure) in the PEDOT chain (Garreau et al., 1999; Łapkowski and Pron, 2000), resulting in a quinoid dominant structure. The PSS chains are connected to the PEDOT chains through Coulombic interactions and have a coiled structure (core-shell) because of the repulsion among the long PSS chains (Lang et al., 2009a). This IL treatment could weaken the ionic interaction between the PEDOT and the PSS, resulting in phase separation between the PSS and the PEDOT and a linear conformation of the PEDOT chains. The same observations were reported on Raman analysis of EG treated PEDOT:PSS films (Ouyang et al., 2004). The partial removal of PSS is manifested by the reduction in the intensity of the Raman fingerprints of treated films compared to pristine films. Moreover, the peak at 1,424 cm^{-1} for the pristine shifted to 1,417 cm^{-1} upon IL treatment (**Figure 4B**), indicating that the doping level changed from bipolaron in the pristine to a neutral state in the IL-treated films as evident by UV-vis-NIR spectra and XPS. This Raman spectra along with UV-vis-NIR spectra and XPS indicate that the oxidation level changes from bipolaron to neutral upon dedoping lead to the slight decrease in the σ and the significant increase in the *S* due to the decrease in the *n* (Luo et al., 2013).

The surface of treated films is highly non-uniform and with enhanced particle size, which leads to a more readily charge transport and thus an improved σ compared to the pristine film. While the untreated film does not show any apparent grains (**Figures S2a,d**), implying that the PSS chains are well-intermixed with the PEDOT chains and the PSS-rich domains mostly cover the film. The strong phase separation between the PSS-rich shell and the PEDOT-rich core besides the depletion of PSS chain were found in the treated films resulting in the interconnected large grains of PEDOT (**Figure S2** and **Figure 5**) (Na et al., 2009; Luo et al., 2013, 2014). After dedoping with ILs the interconnection of the PEDOT-rich grains was enhanced, resulting in an enhanced σ compared to the pristine film. This could partially address why ILs treatment improves *PF* with a slight degradation of the σ.

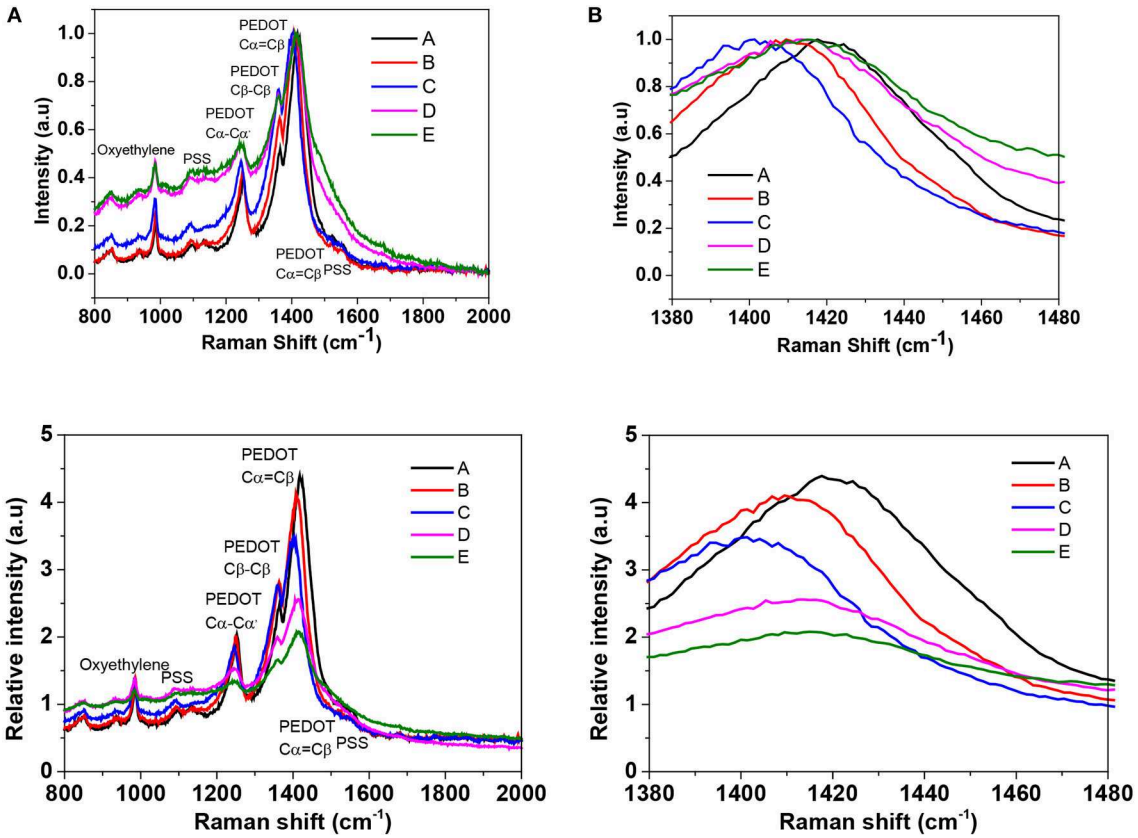

FIGURE 4 | (A) Raman spectra of pristine PEDOT:PSS film and BMIM-TFSI-SFS-F-PEDOT:PSS films treated with different vol.% of BMIM-TFSI in methanol. Pristine (A), SFS-F-PEDOT:PSS (B), 40 Vol.% BMIM-TFSI-SFS-F-PEDOT:PSS (C), 60 Vol.% BMIM-TFSI-SFS-F-PEDOT:PSS (D), and 80 Vol.% BMIM-TFSI-SFS-F-PEDOT:PSS (E). **(B)** Zoom in spectra in the wavelength range of 1,380 to 1,480 cm^{-1}.

Hall measurements were carried out to measure the n and the μ in order to further confirm the conformational change of the PEDOT chain and the phase segregation of the PSSH due to the binary dedoping with the IL. The results showed that all the prepared films were hole-type carrier dominated. In the p-type semiconductors, the σ is given by the relationship: $\sigma = en\mu$, where n, e, and μ is the charge carrier concentration, electron charge, and charge carrier mobility, respectively (Hiroshige et al., 2007). The σ of the pristine and treated PEDOT:PSS films (as shown in **Table 2**) is in the same order of magnitude with the measured value (**Table S1**), demonstrating the reliability of the current measurements. The slightly decreased σ of the ILs dedoped PEDOT:PSS film was mainly caused by the one-order-of-magnitude reduction in the n as the μ varied slightly. This may be ascribed to the interaction between ILs molecules and the PSS monomers, and thus inhibit the carrier supply from the PSS. Generally, the S effectively varies with the slight doping or dedoping concentration as manifested in the current work that the dedoping effect of ILs contributes to the significant enhancement in the S.

In addition to TE performance of the films, the ILs treatment on the PEDOT:PSS films may also affect other properties of PEDOT:PSS films relevant to the device operation, such as the work function (Φ). Ultraviolet photoelectron spectroscopy (UPS) is a key technique to determine the Φ of surfaces by measuring the secondary-electron cut-off (Ec). The influence of the Φ and the valence band on the pristine and treated PEDOT:PSS films was determined using UPS measurements (**Figure 6**). The Φ could be obtained from the equation, $\Phi = h\nu - Ec$, based on the UPS measurements where the spectral width secondary-electron cut-off (Ec) is obtained from the energy gap between the inelastic secondary electron emission cutoff and the Fermi edge and $h\nu$ is the photon energy of the UPS light source (Janardhanam et al., 2015; Kim et al., 2018). We found that IL treatment caused a reduction in the Φ from 4.7 to 4.4 eV (**Figure 6**). For PEDOT:PSS thin films, a range of the Φ from 4.7 to 5.4 eV has been reported (Scott et al., 1999; Greczynski et al., 2001; Mäkinen et al., 2001; Havare et al., 2012) which is similar to the result shown in **Figure 6**. The spread in the Φ values is assumed to be related to differences in the top layer, which may contain an excess of the PSS (Jönsson et al., 2003; Huang et al., 2005; Snaith et al., 2005; Crispin et al., 2006). The PSS-rich top layer may be modified by the addition of high-boiling solvents (Huang et al., 2005; Snaith et al., 2005; Hwang et al., 2006) and other processing conditions (Koch et al., 2007).

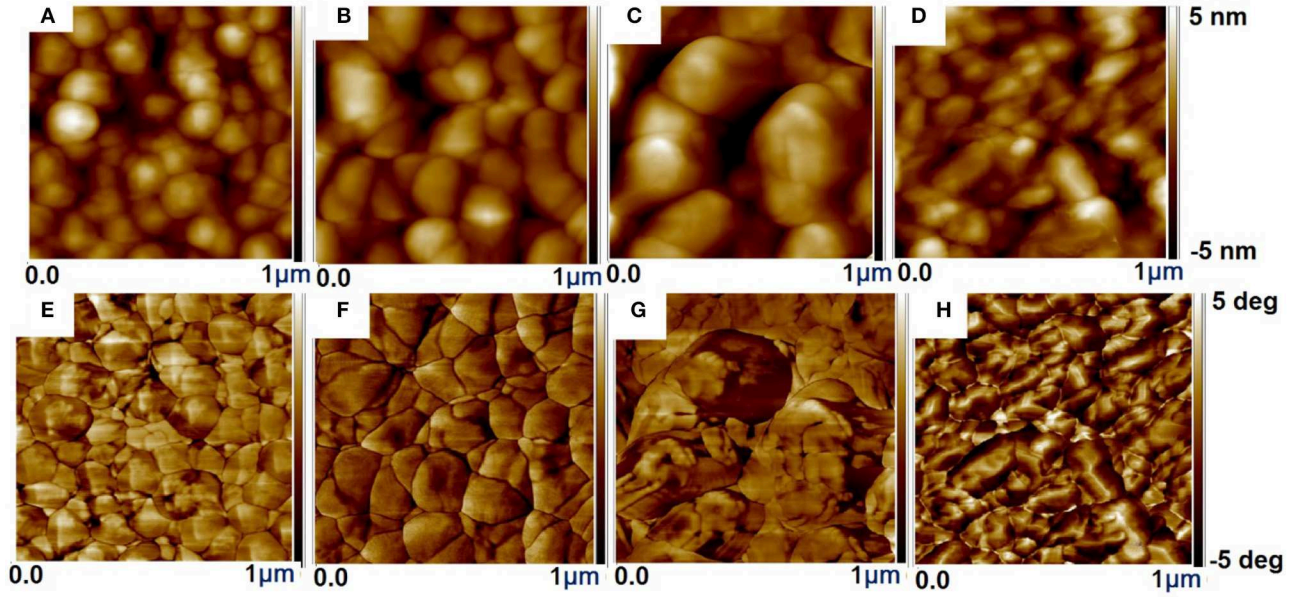

FIGURE 5 | The AFM surface morphology IL-SFS-F-PEDOT:PSS films treated with various vol.% ILs in methanol. Height images: IL-SFS-F-PEDOT:PSS films treated with **(A)** 40 vol.% BMIM-TFSI, **(B)** 60 vol.% BMIM-TFSI, **(C)** 40 vol.% BMIM-OTf, and **(D)** 60 vol.% BMIM-BF_4 in methanol. Phase images: IL-SFS-F-PEDOT:PSS films treated with **(E)** 40 vol.% BMIM-TFSI, **(F)** 60 vol.% BMIM-TFSI, **(G)** 40 vol.% BMIM-OTf, and **(H)** 60 vol.% BMIM-BF_4 in methanol. The scanned area is 1 × 1 μm^2 for each image.

TABLE 2 | Calculated σ and experimentally determined n and μ of the sequential formamide (three times) and 100 mM SFS pre-treated PEDOT:PSS films at various vol.% BMIM-TFSI in methanol by the aid of blowing N_2 gas.

Treatment methods (vol.% BMIM-TFSI in methanol)	μ (cm^2/Vs)	n (cm^{-3})	σ (S/cm)
Untreated	0.42 ± 0.03	4.1 ± 0.3×1018	0.28 ± 0.1
F-PEDOT:PSS	1.08 ± 0.1	1.56 ± 0.1×1022	2693.7 ± 201.8
0	0.58 ± 0.04	5.32 ± 0.5×1021	493.72 ± 41
20	0.51 ± 0.05	5.11 ± 0.3×1021	416.97 ± 37
40	0.48 ± 0.04	5.01 ± 0.7×1021	384.77 ± 31
60	0.43 ± 0.04	4.87 ± 0.63×1021	335.05 ± 29
80	0.41 ± 0.05	4.65 ± 0.45×1021	305.04 ± 21
100	0.38 ± 0.05	4.61 ± 0.39×1021	280.2 ± 16

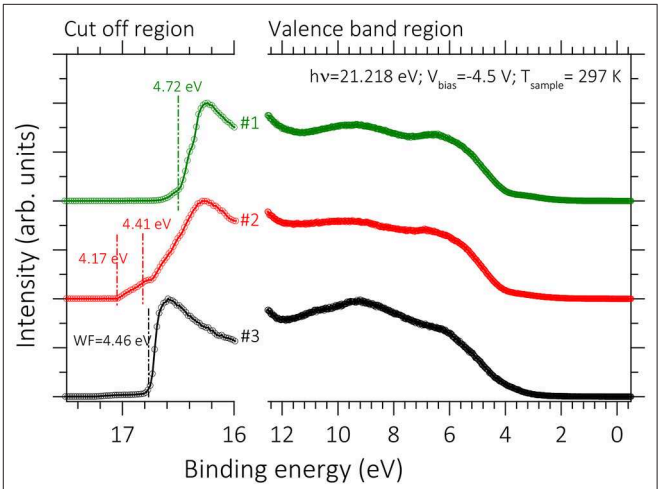

FIGURE 6 | UPS spectra of pristine and BMIM-TFSI-SFS-F-PEDOT:PSS films treated with various vol.% BMIM-TFSI in methanol using He I photon (21.22 eV). Pristine (#1), BMIM-TFSI-SFS-F-PEDOT:PSS treated with 0 vol.% (#2), and 40 vol.% BMIM-TFSI in methanol. Φ values calculated from the cut off position (estimated by linear extrapolation).

The S gives the energetic difference between the transport level ($E\mu$) and the Fermi level (E_F) by its value and the transport type (p or n by its sign). The theoretical result indicates, the S generally depends on the Fermi level as expressed (Fritzsche, 1971; Nollau et al., 2000):

$$S(T) = \frac{1}{eT} \frac{\int [E_F(T) - E]\delta\sigma(E)dE}{\int \delta\sigma(E)dE} \quad (1)$$

where $\delta\sigma(E)$ is the differential conductivity at energy E, E_F is the Fermi level, and e is the electronic charge. The integrations extend over the entire energy range. This derivation holds for both delocalized and localized states, i.e., band and hopping transport, only the assumption of a Fermi system is necessary. With a further assumption of unipolar charge carrier transport at one narrow transport level ($E\mu$) Equation (1) provides:

$$S(T) = \frac{E_F(T) - E_\mu}{eT} \quad (2)$$

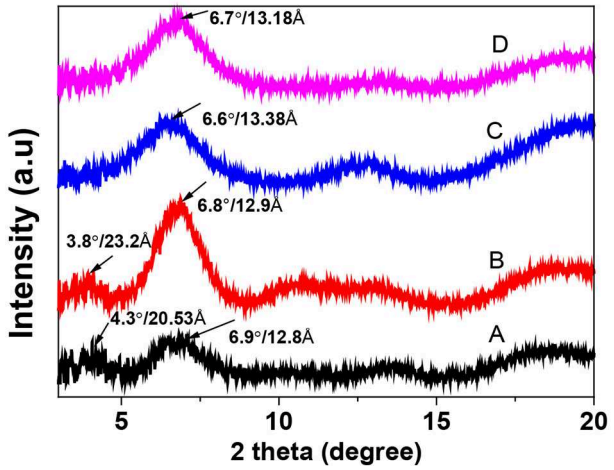

FIGURE 7 | X-ray diffraction (XRD) patterns of pristine and BMIM-TFSI-SFS-F-PEDOT:PSS films treated at various vol.% BMIM-TFSI in methanol. A refers to Pristine, B refers to F-PEDOT:PSS, C refers to SFS-F-PEDOT:PSS, and D refers to 40 vol.% BMIM-TFSI-SFS-F-PEDOT:PSS.

In the transport state, the energy difference $E_F(T) - E_\mu$ is interrelated to the carrier concentration $n(T)$ (Nollau et al., 2000; Sze and Ng, 2006). The variation of about one order decrease of the carrier concentration will increase the $E_F(T) - E_\mu$, and thus enhance the S according to Equation (2). A similar tendency was observed in doped organic semiconductors between the n and TE properties including the σ and S (Nollau et al., 2000). Moreover, as the S relies on the local band structure of the material, the removal of the PSS could transform the local band structure of PEDOT:PSS. Thus, the enhancement in the S may be due to a probable change in the band structure.

The crystallinity of PEDOT:PSS films was studied with the XRD (**Figure 7**). The pristine film displayed two characteristic peaks at 2θ values of 4.3° and 6.9° corresponding to the lattice d spacing of 20.5 Å and 12.8 Å, which were calculated in terms of Bragg's law ($2dsin\ \theta = \lambda$). They can be assigned to the lamella stacking distance d (100) of the two distinct alternate ordering of PEDOT and the PSS chain. BMIM-TFSI-SFS-F-PEDOT:PSS films showed a slight change from 12.8 to 13.8 Å in the lamella stacking distance of the alternate ordering of PEDOT and the PSS chain (**Figure 7**). It also displayed relatively sharper diffraction peaks with the higher intensity in the low angle reflections at 2θ of 6.7° in comparison with the XRD patterns of the pristine PEDOT:PSS. This corresponded separately to the lamella stacking distance d (100) of two distinct alternate orderings of the PEDOT and the PSS chains, suggesting a higher crystallization degree of the PEDOT:PSS film. Besides, for BMIM-TFSI-SFS-F-PEDOT:PSS film, the 2θ is further shifted to 6.7° corresponding to a lattice d spacing of 13.8 Å, and a fair improvement in diffraction peak intensity was observed. These results demonstrate that the IL treatment makes PEDOT:PSS films to prefer a specific lamella stacking between the PEDOT chains, resulting in the improved crystallinity of the PEDOT:PSS films. The (100) diffraction peak intensity was significantly improved, attributable to the improvement of the number of ordered aggregates associated with interchain π-π stacking between the PEDOT chain and the enhancement of the crystallinity of the PEDOT:PSS film. Therefore, the XRD results displayed that compared to the pristine films, IL dedoped PEDOT:PSS films showed an enhanced interchain coupling of PEDOT:PSS with a more densely packed PEDOT and lamella stacking between two assemblies, resulting in an improved S of the films through interface scattering (Kim et al., 2014; Wang et al., 2018).

TABLE 3 | The thermal properties (ρ, Cp, b, and κ) of the pristine and 40 vol.% BMIM-TFSI-SFS-F-PEDOT:PSS films. The obtained κ values were at room temperature.

Code	b (J/S$^{0.5}$m^2)	Cp (J/gK)	ρm (g/cm^3)	κ (W/m)
Untreated	1175	1.5	1.6	0.57
40 vol.% BMIM-TFSI-SFS-F-PEDOT:PSS	785.2	1.56	1.62	0.27

Moreover, the thermal properties of PEDOT:PSS films were investigated and the ρ, b, Cp, and κ of the pristine and BMIM-TFSI-SFS-F-PEDOT:PSS films are measured (**Table 3**). The κ of the pristine PEDOT:PSS film was in accordance with those reported by independent groups (Lee et al., 2014a; Wang et al., 2015, 2018). The pulsed light heating thermoreflectance method was used to determine b at room temperature (Baba et al., 2011; Kyaw et al., 2018). The thermalreflectacne signals of the pristine and 40 vol.% BMIM-TFSI-SFS-F-PEDOT:PSS film after the nanosecond-pulse heating was detected by the probe beam (**Figure S3**). The effusivity values derived from the curve fitting are given in **Table 3**. The Cp was obtained using DSC and the ρ_m was calculated from the mass and the volume of the film at room temperature. As illustrated in **Table 3** the κ of BMIM-TFSI-SFS-F-PEDOT:PSS films was reduced compared to that of the pristine PEDOT:PSS film. The reduced κ could be because of the removal of excess PSS. Therefore, the dimensionless ZT at 300K was calculated based on the obtained cross plane κ of 0.27 W/mK and the corresponding highest PF of 239.2 μW/K^{2}m. The ZT value of the BMIM-TFSI-SFS-F-PEDOT:PSS film was ∼ 0.26 whereas the pristine PEDOT:PSS was ∼5.6 $\times 10^{-6}$ at 300K. This dramatic enhancement in ZT in the 40 vol.% BMIM-TFSI-SFS-F-PEDOT:PSS films indicate that our treatment technique is effective for the enhancement of the TE properties of PEDOT:PSS film.

PEDOT:PSS Film Stability Study

The PEDOT:PSS film stability by measuring the σ, κ, and S of their films at a given humidity and temperature was investigated. The pristine and treated films were put in a humidity chamber at 75% RH and 70°C for up to 480 h to investigate the PEDOT:PSS film stability. In this test, 20 batches of samples were prepared and the σ, κ, and S were periodically monitored throughout the stability test. The results of the pristine PEDOT:PSS film were in agreement with the previous reports by the majority of groups on atmospheric exposure of PEDOT:PSS films (Nardes

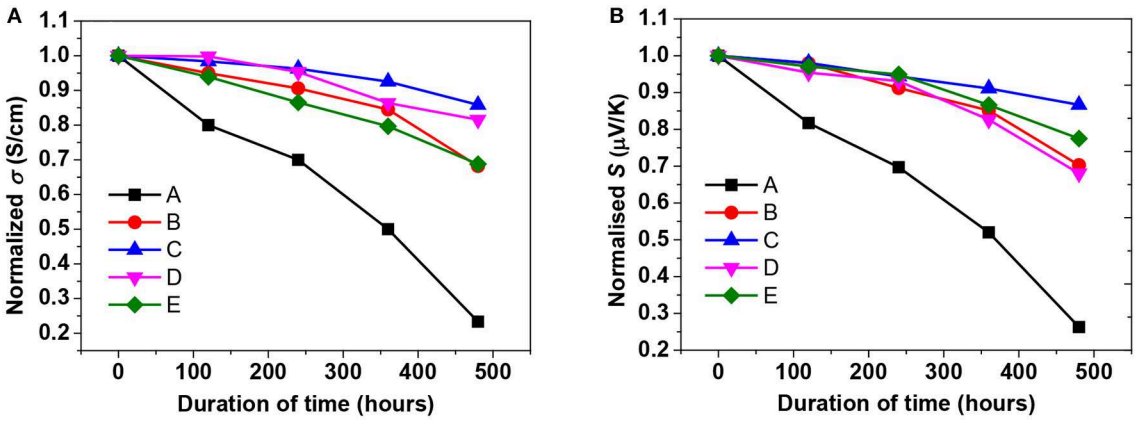

FIGURE 8 | The reduced TE properties of the pristine, formamide treated, and BMIM-TFSI-SFS-F-PEDOT:PSS films treated with various vol.% BMIM-TFSI in methanol. **(A)** σ and **(B)** S of the pristine and treated PEDOT:PSS films. Pristine (A), F-PEDOT:PSS (B), SFS-F-PEDOT:PSS (C), 40 vol.% BMIM-TFSI-SFS-F-PEDOT:PSS (D), and 60 Vol.% BMIM-TFSI-SFS-F-PEDOT:PSS (E). Vertical: *Si/S0* and $\sigma i/\sigma 0$ where ($\sigma 0$ and *S0*) and (*Si* and σi) are S and σ at t = 0 h and the time at which the S and σ were recorded respectively, kept over 480 h under high humidity (75% RH) and high temperature (70°C) conditions.

et al., 2008; Kim et al., 2011; Alemu et al., 2012; McCarthy et al., 2014; Cho et al., 2016). As shown in **Figure 8**, the σ and S of all samples gradually decreased with the increasing exposure time. The relative decrements in the σ in the harsh conditions after 480 h for the pristine PEDOT:PSS film was 77%, while ILs treated PEDOT:PSS films reduced by ∼22%, indicating the long-term stability was enhanced through the ILs treatment. It was well noted that the significant reduction in the σ of pristine PEDOT:PSS film was owing to the hygroscopic and acidic PSS that picks up water easily (De Jong et al., 2000; Fehse et al., 2008). Since the σ deterioration occurred due to absorption of water in the PSS phase (Van Reenen and Kemerink, 2014), the reduction of the PSS in treated PEDOT:PSS film resulted in less water absorption, and subsequently the film was more stable even in a harsh environment. Furthermore, the highly compact-structure brought by the depletion of PSS and the polymer rearrangement may improve the σ as well as stability (Nardes et al., 2008). In addition, the stability enhancement may relate to a strong ionic interaction between sulfonate anions and bulky imidazolium cations that blocking the penetration of water into the PEDOT:PSS film and reducing the water uptake. Blending imidazolium derivatives with acidic PEDOT:PSS solutions leads to neutralization of the solution, remarkably enhancing the stability with minimal loss of the σ; in well agreement with the previous report (Cho et al., 2016).

Furthermore, the cross plane κ was observed to be slightly increased for 40 vol.% BMIM-TFSI-SFS-F-PEDOT:PSS films while the cross-plane κ was noticed to be decreased for the pristine PEDOT:PSS film with harsh conditions. The result is in good accordance with a previously observed decline in the elastic modulus of PEDOT:PSS at high humidity conditions (Lang et al., 2009b), i.e., $\kappa = (\text{elastic constant})^{1/2}$ (Hsieh et al., 2011). Hence, the slight increase of κ in BMIM-TFSI-SFS-F-PEDOT:PSS films could be due to the film having less PSS and hence less softening conditions and less hygroscopic.

Based on our various observations, we suggest a model for the mechanism of TE properties enhancement for ILs-SFS-F-PEDOT:PSS films (**Figure 9**). **Figure 10** also illustrates conformational changes of PEDOT chains for untreated and treated films. Formamide, a polar solvent, with a high dielectric constant induces a strong screening effect between the counter ions and the charge carriers, reducing the interactions between the negatively charged PSS and the positively charged PEDOT. This results in an enlargement of PEDOT chains and the easier removal of PSS due to the change in their conformation from coils to elongated structures (Kim et al., 2002). When SFS ($HOCH_2SO_2Na$) was further introduced into the PEDOT:PSS films, $HOCH_2SO_2^-$ and Na^+ ions penetrated into the PEDOT:PSS film, the $HOCH_2SO_2^-$ ions could replace the PSS counter ion and bind to the PEDOT segment as the new counter ion, and the Na^+ ions bound to the PSS anions during the treatment. The decreased steric hindrance and dramatically reduced binding effect exerted by PSS led to the conductive PEDOT chain further to elongate and achieve an extended conformation. This extended conformation led to stronger interchain interactions, resulting in a significantly enhanced σ of PEDOT:PSS that facilitates charge transport among the polymer chains (Xia and Ouyang, 2011; Culebras et al., 2014). Further addition of ILs e.g. BMIM-TFSI effectively segregated the PEDOT from the PSS, resulting in conformational changes and in turn an increase in mobility. Also, BMIM-TFSI treatment led to electrostatic interactions of the negatively charged PSS with the positively charged BMIM cation and dissociation of the ionic bond between BMIM and TFSI. This led to further elongation of the conductive PEDOT chain to achieve an extended conformation. **Figure 10** illustrates conformational changes of the PEDOT chains and a sequential formamide and binary dedoping. This linear-like conformation could change chemical states of PEDOT chains that affect the carrier density in the PEDOT:PSS films (Park et al., 2014b).

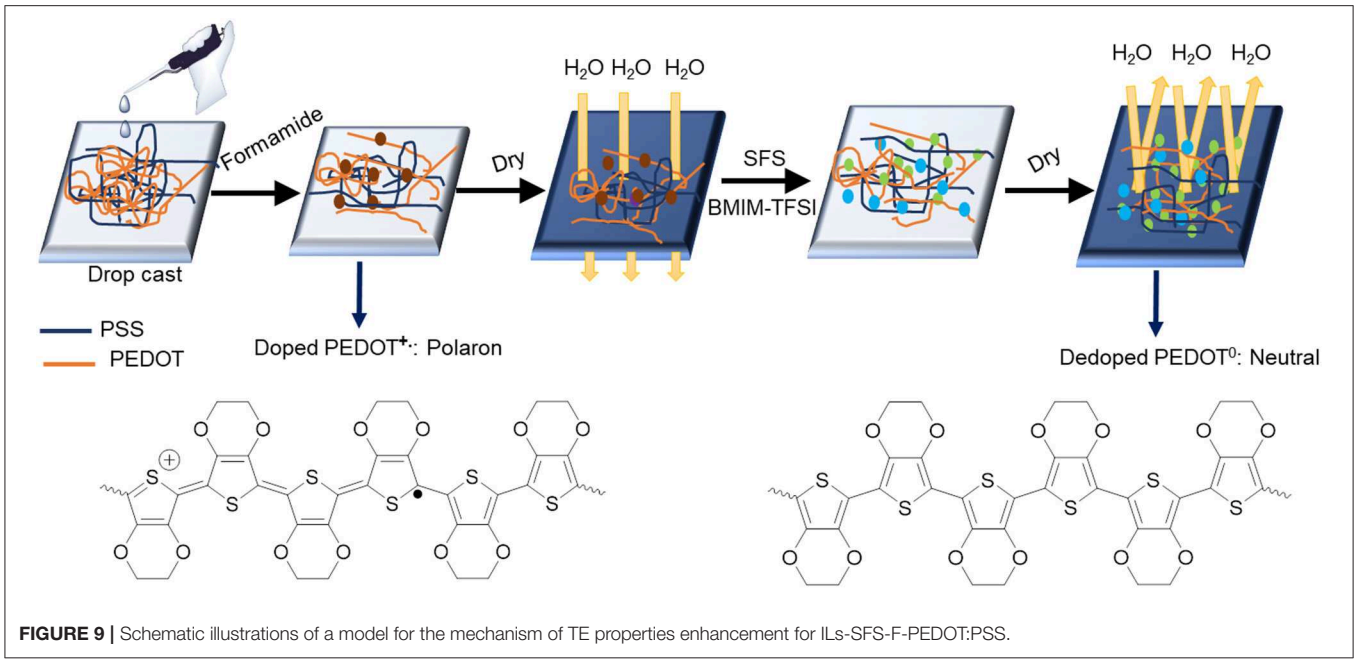

FIGURE 9 | Schematic illustrations of a model for the mechanism of TE properties enhancement for ILs-SFS-F-PEDOT:PSS.

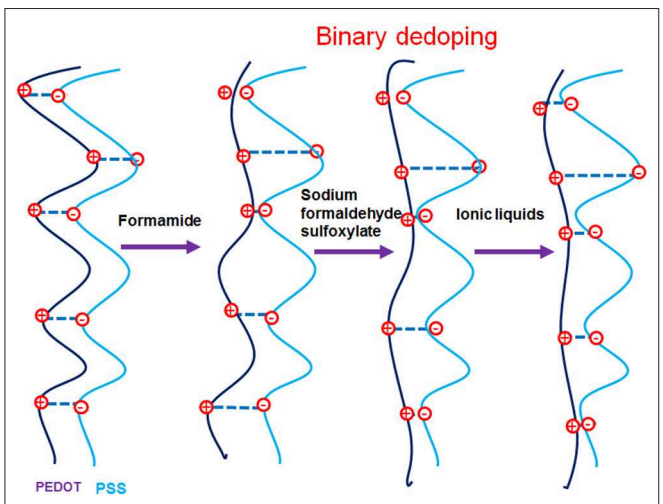

FIGURE 10 | Illustrations of conformational changes of PEDOT chains with binary dedoping with SFS and ILs.

CONCLUSION

In this study, two series post-treatments using ILs as one of the key steps were reported. Both series post-treatments considerably enhanced TE properties of PEDOT:PSS films. The first series post-treatment resulted in a big jump in the power factor from 63.6 to 137.8 $\mu W/K^2m$, corresponding to post-treatment with formamide only, and post-treatment with both formamide and IL, respectively. An additional post-treatment step with SFS was introduced before applying to IL treatment, and the power factor could be further improved to more than 230 $\mu W/K^2m$. A large tendency to enhance the power factor likely mainly originated from the improvement in the Seebeck coefficient S, which was increased from 14.9 to 28.5 and then 61 $\mu V/K$ although the electrical conductivity σ reduced from a few thousand to in the range of 630–650 S/cm. Compared to the F-PEDOT:PSS film, the improvement in the S is because of the decrease in the carrier concentration n by roughly 70% in the case of BMIM-TFSI treated PEDOT:PSS. The enhancement in the S could also be explained by the dedoping process as evidenced by the absorption spectra in which a characteristic absorption peak at 600 nm appeared. The types of anions associated with ILs also played a role in affecting the magnitude of the power factor in an order of TFSI > OTf > BF_4. On the other hand, the cross-plane κ reduced from 0.57 W/mK for the pristine film to 0.27 W/mK for BMIM-TFSI-SFS-F-PEDOT:PSS film is largely due to the removal of the PSS. Hence, under the optimum treatment condition, the estimated ZT of ~0.26 was achieved at 300 K, revealing the potential in the application for harvesting low-grade heat or waste thermal energy.

DATA AVAILABILITY STATEMENT

All datasets generated for this study are included in the article/**Supplementary Material**.

AUTHOR CONTRIBUTIONS

TY, WC, and JX conceived and designed the experiments. TY and YZ performed the experiments and contributed to the film fabrication, measurement, and data analysis. AK, XW, and

JS contributed to analysis tools, helped with the analysis, and discussed the data. TY wrote the paper. WC and JX helped revise the paper.

FUNDING

This work was financed by the Agency for Science, Technology and Research (A*STAR), Industry Alignment Fund, Pharos Hybrid thermoelectric materials for ambient applications Program (Grant Nos. 1527200019 and 1527200021).

ACKNOWLEDGMENTS

TY would like to thank the SINGA scholarship from the A*STAR Graduate Academy especially. AK would like to thank the start-up fund from SUSTech.

SUPPLEMENTARY MATERIAL

The Supplementary Material for this article can be found online at: https://www.frontiersin.org/articles/10.3389/fchem.2019.00870/full#supplementary-material

REFERENCES

Alemu, D., Wei, H.-Y., Ho, K.-C., and Chu, C.-W. (2012). Highly conductive PEDOT: PSS electrode by simple film treatment with methanol for ITO-free polymer solar cells. *Energy Environ. Sci.* 5, 9662–9671. doi: 10.1039/c2ee22595f

Baba, T., Taketoshi, N., and Yagi, T. (2011). Development of ultrafast laser flash methods for measuring thermophysical properties of thin films and boundary thermal resistances. *Jpn. J. Appl. Phys.* 50:11RA01. doi: 10.1143/JJAP.50.11RA01

Bell, L. E. (2008). Cooling, heating, generating power, and recovering waste heat with thermoelectric systems. *Science* 321, 1457–1461. doi: 10.1126/science.1158899

Bubnova, O., Berggren, M., and Crispin, X. (2012). Tuning the thermoelectric properties of conducting polymers in an electrochemical transistor. *J. Am. Chem. Soc.* 134, 16456–16459. doi: 10.1021/ja305188r

Bubnova, O., Khan, Z. U., Malti, A., Braun, S., Fahlman, M., Berggren, M., et al. (2011). Optimization of the thermoelectric figure of merit in the conducting polymer poly (3, 4-ethylenedioxythiophene). *Nat. Mater.* 10:429. doi: 10.1038/nmat3012

Chang, C., Wu, M., He, D., Pei, Y., Wu, C.-F., Wu, X., et al. (2018). 3D charge and 2D phonon transports leading to high out-of-plane ZT in n-type SnSe crystals. *Science* 360, 778–783. doi: 10.1126/science.aaq1479

Chen, Z., Jian, Z., Li, W., Chang, Y., Ge, B., Hanus, R., et al. (2017). Lattice dislocations enhancing thermoelectric PbTe in addition to band convergence. *Adv. Mater.* 29:1606768. doi: 10.1002/adma.201606768

Cho, A., Kim, S., Kim, S., Cho, W., Park, C., Kim, F. S., et al. (2016). Influence of imidazole-based acidity control of PEDOT: PSS on its electrical properties and environmental stability. *J. Polym. Sci. B Polym. Phys.* 54, 1530–1536. doi: 10.1002/polb.24048

Chung, T.-C., Kaufman, J., Heeger, A., and Wudl, F. (1984). Charge storage in doped poly (thiophene): optical and electrochemical studies. *Phys. Rev. B* 30:702. doi: 10.1103/PhysRevB.30.702

Cowen, L. M., Atoyo, J., Carnie, M. J., Baran, D., and Schroeder, B. C. (2017). Organic materials for thermoelectric energy generation. *ECS J. Solid State Sci. Technol.* 6, N3080–N3088. doi: 10.1149/2.0121703jss

Crispin, X., Jakobsson, F., Crispin, A., Grim, P., Andersson, P., Volodin, A., et al. (2006). The origin of the high conductivity of poly (3, 4-ethylenedioxythiophene)– poly (styrenesulfonate)(PEDOT– PSS) plastic electrodes. *Chem. Mater.* 18, 4354–4360. doi: 10.1021/cm061032+

Crispin, X., Marciniak, S., Osikowicz, W., Zotti, G., Van Der Gon, A., Louwet, F., et al. (2003). Conductivity, morphology, interfacial chemistry, and stability of poly (3, 4-ethylene dioxythiophene)–poly (styrene sulfonate): a photoelectron spectroscopy study. *J. polym. sci. B Polym. Phys.* 41, 2561–2583. doi: 10.1002/polb.10659

Culebras, M., Gómez, C., and Cantarero, A. (2014). Enhanced thermoelectric performance of PEDOT with different counter-ions optimized by chemical reduction. *J. Mater. Chem. A* 2, 10109–10115. doi: 10.1039/C4TA01012D

De Jong, M., Van Ijzendoorn, L., and De Voigt, M. (2000). Stability of the interface between indium-tin-oxide and poly (3, 4-ethylenedioxythiophene)/poly (styrenesulfonate) in polymer light-emitting diodes. *Appl. Phys. Lett.* 77, 2255–2257. doi: 10.1063/1.1315344

Fan, Z., Du, D., Guan, X., and Ouyang, J. (2018). Polymer films with ultrahigh thermoelectric properties arising from significant seebeck coefficient enhancement by ion accumulation on surface. *Nano Energy* 51, 481–488. doi: 10.1016/j.nanoen.2018.07.002

Fan, Z., Li, P., Du, D., and Ouyang, J. (2017). Significantly enhanced thermoelectric properties of PEDOT: PSS films through sequential post-treatments with common acids and bases. *Adv. Energy Mater.* 7:1602116. doi: 10.1002/aenm.201602116

Farah, A. A., Rutledge, S. A., Schaarschmidt, A., Lai, R., Freedman, J. P., and Helmy, A. S. (2012). Conductivity enhancement of poly(3,4-ethylenedioxythiophene)-poly(styrenesulfonate) films post-spincasting. *J. Appl. Phys.* 112:113709. doi: 10.1063/1.4768265

Fehse, K., Meerheim, R., Walzer, K., Leo, K., Lövenich, W., and Elschner, A. (2008). Lifetime of organic light emitting diodes on polymer anodes. *Appl. Phys. Lett.* 93:312. doi: 10.1063/1.2975369

Fritzsche, H. (1971). A general expression for the thermoelectric power. *Solid State Commun.* 9, 1813–1815. doi: 10.1016/0038-1098(71)90096-2

Garreau, S., Duvail, J., and Louarn, G. (2001). Spectroelectrochemical studies of poly (3, 4-ethylenedioxythiophene) in aqueous medium. *Synth. Met.* 125, 325–329. doi: 10.1016/S0379-6779(01)00397-6

Garreau, S., Louarn, G., Buisson, J., Froyer, G., and Lefrant, S. (1999). In situ spectroelectrochemical Raman studies of poly (3, 4-ethylenedioxythiophene)(PEDT). *Macromolecules* 32, 6807–6812. doi: 10.1021/ma9905674

Greczynski, G., Kugler, T., Keil, M., Osikowicz, W., Fahlman, M., and Salaneck, W. R. (2001). Photoelectron spectroscopy of thin films of PEDOT–PSS conjugated polymer blend: a mini-review and some new results. *J. Electron Spectros. Relat. Phenomena* 121, 1–17. doi: 10.1016/S0368-2048(01)00323-1

Han, Y. K., Chang, M. Y., Huang, W. Y., Pan, H. Y., Ho, K. S., Hsieh, T. H., et al. (2011). Improved performance of polymer solar cells featuring one-dimensional pedot nanorods in a modified buffer layer. *J. Electrochem. Soc.* 158, K88–K93. doi: 10.1149/1.3534201

Havare, A. K., Can, M., Demic, S., Kus, M., and Icli, S. (2012). The performance of OLEDs based on sorbitol doped PEDOT: PSS. *Synth. Met.* 161, 2734–2738. doi: 10.1016/j.synthmet.2011.10.011

Hiroshige, Y., Ookawa, M., and Toshima, N. (2007). Thermoelectric figure-of-merit of iodine-doped copolymer of phenylenevinylene with dialkoxyphenylenevinylene. *Synth. Met.* 157, 467–474. doi: 10.1016/j.synthmet.2007.05.003

Hsieh, W.-P., Losego, M. D., Braun, P. V., Shenogin, S., Keblinski, P., and Cahill, D. G. (2011). Testing the minimum thermal conductivity model for amorphous polymers using high pressure. *Phys. Rev. B* 83:174205. doi: 10.1103/PhysRevB.83.174205

Hu, Y., Shi, H., Song, H., Liu, C., Xu, J., Zhang, L., et al. (2013). Effects of a proton scavenger on the thermoelectric performance of free-standing polythiophene and its derivative films. *Synth. Met.* 181, 23–26. doi: 10.1016/j.synthmet.2013.08.006

Huang, J., Miller, P. F., Wilson, J. S., De Mello, A. J., De Mello, J. C., and Bradley, D. D. (2005). Investigation of the effects of doping and post-deposition treatments on the conductivity, morphology, and work function of poly (3, 4-ethylenedioxythiophene)/poly (styrene sulfonate) films. *Adv. Funct. Mater.* 15, 290–296. doi: 10.1002/adfm.200400073

Hwang, J., Amy, F., and Kahn, A. (2006). Spectroscopic study on sputtered PEDOT· PSS: role of surface PSS layer. *Org. Electron.* 7, 387–396. doi: 10.1016/j.orgel.2006.04.005

Im, S. G., and Gleason, K. K. (2007). Systematic control of the electrical conductivity of poly (3, 4-ethylenedioxythiophene) via oxidative chemical vapor deposition. *Macromolecules* 40, 6552–6556. doi: 10.1021/ma0628477

Janardhanam, V., Yun, H.-J., Jyothi, I., Lee, J., Hong, H., Reddy, V. R., et al. (2015). Energy-level alignment and electrical properties of Al/p-type Si Schottky diodes with sorbitol-doped PEDOT: PSS as an organic interlayer. *J. Alloys Compd.* 637, 84–89. doi: 10.1016/j.jallcom.2015.02.210

Jönsson, S., Birgerson, J., Crispin, X., Greczynski, G., Osikowicz, W., Van Der Gon, A. D., et al. (2003). The effects of solvents on the morphology and sheet resistance in poly (3, 4-ethylenedioxythiophene)–polystyrenesulfonic acid (PEDOT–PSS) films. *Synth. Met.* 139, 1–10. doi: 10.1016/S0379-6779(02)01259-6

Kaneko, H., Ishiguro, T., Takahashi, A., and Tsukamoto, J. (1993). Magnetoresistance and thermoelectric power studies of metal-nonmetal transition in iodine-doped polyacetylene. *Synth. Met.* 57, 4900–4905. doi: 10.1016/0379-6779(93)90836-L

Kemp, N., Kaiser, A., Liu, C., Chapman, B., Mercier, O., Carr, A., et al. (1999). Thermoelectric power and conductivity of different types of polypyrrole. *J. Polym. Sci. A Polym. Chem.* 37, 953–960.

Khan, M., Armes, S., Perruchot, C., Ouamara, H., Chehimi, M., Greaves, S., et al. (2000). Surface characterization of poly (3, 4-ethylenedioxythiophene)-coated latexes by X-ray photoelectron spectroscopy. *Langmuir* 16, 4171–4179. doi: 10.1021/la991390+

Khan, Z. U., Bubnova, O., Jafari, M. J., Brooke, R., Liu, X., Gabrielsson, R., et al. (2015). Acido-basic control of the thermoelectric properties of poly (3, 4-ethylenedioxythiophene) tosylate (PEDOT-Tos) thin films. *J. Mater. Chem. C* 3, 10616–10623. doi: 10.1039/C5TC01952D

Kim, G., Shao, L., Zhang, K., and Pipe, K. P. (2013). Engineered doping of organic semiconductors for enhanced thermoelectric efficiency. *Nat. Mater.* 12, 719–723. doi: 10.1038/nmat3635

Kim, G.-H., Kim, J., and Pipe, K. P. (2016). Humidity-dependent thermoelectric properties of poly (3, 4-ethylenedioxythiophene): poly (styrene sulfonate). *Appl. Phys. Lett.* 108:093301. doi: 10.1063/1.4942598

Kim, J., Jung, J., Lee, D., and Joo, J. (2002). Enhancement of electrical conductivity of poly (3, 4-ethylenedioxythiophene)/poly (4-styrenesulfonate) by a change of solvents. *Synth. Met.* 126, 311–316. doi: 10.1016/S0379-6779(01)00576-8

Kim, K. M., Ahn, S., Jang, W., Park, S., Park, O. O., and Wang, D. H. (2018). Work function optimization of vacuum free top-electrode by PEDOT: PSS/PEI interaction for efficient semi-transparent perovskite solar cells. *Solar Energy Mater. Solar Cells* 176, 435–440. doi: 10.1016/j.solmat.2017.11.002

Kim, N., Kee, S., Lee, S. H., Lee, B. H., Kahng, Y. H., Jo, Y. R., et al. (2014). Highly conductive PEDOT: PSS nanofibrils induced by solution-processed crystallization. *Adv. Mater.* 26, 2268–2272. doi: 10.1002/adma.201304611

Kim, Y. H., Sachse, C., Machala, M. L., May, C., Müller-Meskamp, L., and Leo, K. (2011). Highly conductive PEDOT: PSS electrode with optimized solvent and thermal post-treatment for ITO-free organic solar cells. *Adv. Funct. Mater.* 21, 1076–1081. doi: 10.1002/adfm.201002290

Koch, N., Vollmer, A., and Elschner, A. (2007). Influence of water on the work function of conducting poly (3, 4-ethylenedioxythiophene)/poly (styrenesulfonate). *Appl. Phys. Lett.* 90:043512. doi: 10.1063/1.2435350

Krupka, J. (2013). Contactless methods of conductivity and sheet resistance measurement for semiconductors, conductors and superconductors. *Meas. Sci. Technol.* 24:062001. doi: 10.1088/0957-0233/24/6/062001

Kyaw, A. K. K., Yemata, T. A., Wang, X., Lim, S. L., Chin, W. S., Hippalgaonkar, K., et al. (2018). Enhanced thermoelectric performance of PEDOT: PSS films by sequential post-treatment with formamide. *Macromol. Mater. Eng.* 303:1700429. doi: 10.1002/mame.201700429

Lang, U., Müller, E., Naujoks, N., and Dual, J. (2009a). Microscopical investigations of PEDOT: PSS thin films. *Adv. Funct. Mater.* 19, 1215–1220. doi: 10.1002/adfm.200801258

Lang, U., Naujoks, N., and Dual, J. (2009b). Mechanical characterization of PEDOT: PSS thin films. *Synth. Met.* 159, 473–479. doi: 10.1016/j.synthmet.2008.11.005

Łapkowski, M., and Pron, A. (2000). Electrochemical oxidation of poly (3, 4-ethylenedioxythiophene)—"in situ" conductivity and spectroscopic investigations. *Synth. Met.* 110, 79–83. doi: 10.1016/S0379-6779(99)00271-4

Lee, S. H., Park, H., Kim, S., Son, W., Cheong, I. W., and Kim, J. H. (2014a). Transparent and flexible organic semiconductor nanofilms with enhanced thermoelectric efficiency. *J. Mater. Chem. A* 2, 7288–7294. doi: 10.1039/C4TA00700J

Lee, S. H., Park, H., Son, W., Choi, H. H., and Kim, J. H. (2014b). Novel solution-processable, dedoped semiconductors for application in thermoelectric devices. *J. Mater. Chem. A* 2, 13380–13387. doi: 10.1039/C4TA01839G

Lee, Y. K., Luo, Z., Cho, S. P., Kanatzidis, M. G., and Chung, I. (2019). Surface oxide removal for polycrystalline SnSe reveals near-single-crystal thermoelectric performance. *Joule* 3, 719–731. doi: 10.1016/j.joule.2019.01.001

Li, J., Tang, X., Li, H., Yan, Y., and Zhang, Q. (2010). Synthesis and thermoelectric properties of hydrochloric acid-doped polyaniline. *Synth. Met.* 160, 1153–1158. doi: 10.1016/j.synthmet.2010.03.001

Li, J., Zhang, X., Chen, Z., Lin, S., Li, W., Shen, J., et al. (2018). Low-symmetry rhombohedral GeTe thermoelectrics. *Joule* 2, 976–987. doi: 10.1016/j.joule.2018.02.016

Liang, L., Chen, G., and Guo, C.-Y. (2017). Polypyrrole nanostructures and their thermoelectric performance. *Mater. Chem. Front.* 1, 380–386. doi: 10.1039/C6QM00061D

Luo, J., Billep, D., Blaudeck, T., Sheremet, E., Rodriguez, R. D., Zahn, D. R., et al. (2014). Chemical post-treatment and thermoelectric properties of poly (3, 4-ethylenedioxylthiophene): poly (styrenesulfonate) thin films. *J. Appl. Phys.* 115:054908. doi: 10.1063/1.4864749

Luo, J., Billep, D., Waechtler, T., Otto, T., Toader, M., Gordan, O., et al. (2013). Enhancement of the thermoelectric properties of PEDOT: PSS thin films by post-treatment. *J. Mater. Chem. A* 1, 7576–7583. doi: 10.1039/c3ta11209h

MacDiarmid, A. G. (2001). Synthetic metals: a novel role for organic polymers. *Synth. Met.* 125, 11–22. doi: 10.1016/S0379-6779(01)00508-2

Mäkinen, A., Hill, I., Shashidhar, R., Nikolov, N., and Kafafi, Z. (2001). Hole injection barriers at polymer anode/small molecule interfaces. *Appl. Phys. Lett.* 79, 557–559. doi: 10.1063/1.1386400

Mateeva, N., Niculescu, H., Schlenoff, J., and Testardi, L. (1998). Correlation of Seebeck coefficient and electric conductivity in polyaniline and polypyrrole. *J. Appl. Phys.* 83, 3111–3117. doi: 10.1063/1.367119

McCarthy, J. E., Hanley, C. A., Brennan, L. J., Lambertini, V. G., and Gun'ko, Y. K. (2014). Fabrication of highly transparent and conducting PEDOT: PSS films using a formic acid treatment. *J. Mater. Chem. C* 2, 764–770. doi: 10.1039/C3TC31951B

Mcgrail, B. T., Sehirlioglu, A., and Pentzer, E. (2015). Polymer composites for thermoelectric applications. *Angew. Chem. Int. Ed.* 54, 1710–1723. doi: 10.1002/anie.201408431

Moriarty, G. P., Briggs, K., Stevens, B., Yu, C., and Grunlan, J. C. (2013). Fully organic nanocomposites with high thermoelectric power factors by using a dual-stabilizer preparation. *Energy Technol.* 1, 265–272. doi: 10.1002/ente.201300018

Na, S.-I., Wang, G., Kim, S.-S., Kim, T.-W., Oh, S.-H., Yu, B.-K., et al. (2009). Evolution of nanomorphology and anisotropic conductivity in solvent-modified PEDOT: PSS films for polymeric anodes of polymer solar cells. *J. Mater. Chem.* 19, 9045–9053. doi: 10.1039/b915756e

Nardes, A. M., Kemerink, M., De Kok, M., Vinken, E., Maturova, K., and Janssen, R. (2008). Conductivity, work function, and environmental stability of PEDOT: PSS thin films treated with sorbitol. *Org. Electron.* 9, 727–734. doi: 10.1016/j.orgel.2008.05.006

Nollau, A., Pfeiffer, M., Fritz, T., and Leo, K. (2000). Controlled n-type doping of a molecular organic semiconductor: Naphthalenetetracarboxylic dianhydride (NTCDA) doped with bis (ethylenedithio)-tetrathiafulvalene (BEDT-TTF). *J. Appl. Phys.* 87, 4340–4343. doi: 10.1063/1.373413

Ouyang, J., Chu, C. W., Chen, F. C., Xu, Q., and Yang, Y. (2005). High-conductivity poly (3, 4-ethylenedioxythiophene): poly (styrene sulfonate) film and its application in polymer optoelectronic devices. *Adv. Funct. Mater.* 15, 203–208. doi: 10.1002/adfm.200400016

Ouyang, J., Xu, Q., Chu, C.-W., Yang, Y., Li, G., and Shinar, J. (2004). On the mechanism of conductivity enhancement in poly (3, 4-ethylenedioxythiophene): poly (styrene sulfonate) film through solvent treatment. *Polymer* 45, 8443–8450. doi: 10.1016/j.polymer.2004.10.001

Park, G. O., Roh, J. W., Kim, J., Lee, K. Y., Jang, B., Lee, K. H., et al. (2014a). Enhanced thermoelectric properties of germanium powder/poly (3,

4-ethylenedioxythiophene): poly (4-styrenesulfonate) composites. *Thin Solid Films* 566, 14–18. doi: 10.1016/j.tsf.2014.07.011

Park, H., Lee, S. H., Kim, F. S., Choi, H. H., Cheong, I. W., and Kim, J. H. (2014b). Enhanced thermoelectric properties of PEDOT: PSS nanofilms by a chemical dedoping process. *J. Mater. Chem. A* 2, 6532–6539. doi: 10.1039/C3TA14960A

Park, T., Park, C., Kim, B., Shin, H., and Kim, E. (2013). Flexible PEDOT electrodes with large thermoelectric power factors to generate electricity by the touch of fingertips. *Energy Environ. Sci.* 6, 788–792. doi: 10.1039/c3ee23729j

Ren, Z. (2017). Thermoelectrics and materials today physics. *Elsevier* 1, 2–6. doi: 10.1016/j.mtphys.2017.05.001

Saxena, N., Pretzl, B., Lamprecht, X., Bießmann, L., Yang, D., Li, N., et al. (2019). Ionic liquids as Post-treatment agents for simultaneous improvement of seebeck coefficient and electrical conductivity in PEDOT: PSS Films. *ACS Appl. Mater. Interfaces* 11, 8060–8071. doi: 10.1021/acsami.8b21709

Scott, J., Malliaras, G., Chen, W., Breach, J.-C., Salem, J., Brock, P., et al. (1999). Hole limited recombination in polymer light-emitting diodes. *Appl. Phys. Lett.* 74, 1510–1512. doi: 10.1063/1.123599

Snaith, H. J., Kenrick, H., Chiesa, M., and Friend, R. H. (2005). Morphological and electronic consequences of modifications to the polymer anode 'PEDOT: PSS'. *Polymer* 46, 2573–2578. doi: 10.1016/j.polymer.2005.01.077

Snyder, G. J., and Toberer, E. S. (2011). "Complex thermoelectric materials," in *Materials For Sustainable Energy: A Collection of Peer-Reviewed Research and Review Articles from Nature Publishing Group*, eds V. Dusastr, J.-M. Tarascon, and M. Gratzel (Pasadena, CA: World Scientific), 101–110. doi: 10.1142/9789814317665_0016

Sze, S. M., and Ng, K. K. (2006). *Physics of Semiconductor Devices*. Hsinchu; San Jose, CA: John Wiley & Sons. doi: 10.1002/0470068329

Tan, G., Shi, F., Hao, S., Zhao, L.-D., Chi, H., Zhang, X., et al. (2016). Non-equilibrium processing leads to record high thermoelectric figure of merit in PbTe–SrTe. *Nat. Commun.* 7:12167. doi: 10.1038/ncomms12167

Tsai, T.-C., Chang, H.-C., Chen, C.-H., and Whang, W.-T. (2011). Widely variable Seebeck coefficient and enhanced thermoelectric power of PEDOT: PSS films by blending thermal decomposable ammonium formate. *Org. Electron.* 12, 2159–2164. doi: 10.1016/j.orgel.2011.09.004

Van Reenen, S., and Kemerink, M. (2014). Correcting for contact geometry in Seebeck coefficient measurements of thin film devices. *Org. Electron.* 15, 2250–2255. doi: 10.1016/j.orgel.2014.06.018

Wang, J., Cai, K., and Shen, S. (2015). A facile chemical reduction approach for effectively tuning thermoelectric properties of PEDOT films. *Org. Electron.* 17, 151–158. doi: 10.1016/j.orgel.2014.12.007

Wang, X., Kyaw, A. K. K., Yin, C., Wang, F., Zhu, Q., Tang, T., et al. (2018). Enhancement of thermoelectric performance of PEDOT: PSS films by post-treatment with a superacid. *RSC Adv.* 8, 18334–18340. doi: 10.1039/C8RA02058B

Wei, Q., Mukaida, M., Kirihara, K., Naitoh, Y., and Ishida, T. (2015). Recent progress on PEDOT-based thermoelectric materials. *Materials* 8, 732–750. doi: 10.3390/ma8020732

Xia, Y., and Ouyang, J. (2011). PEDOT: PSS films with significantly enhanced conductivities induced by preferential solvation with cosolvents and their application in polymer photovoltaic cells. *J. Mater. Chem.* 21, 4927–4936. doi: 10.1039/c0jm04177g

Xia, Y., Sun, K., and Ouyang, J. (2012). Highly conductive poly (3, 4-ethylenedioxythiophene): poly (styrene sulfonate) films treated with an amphiphilic fluoro compound as the transparent electrode of polymer solar cells. *Energy Environ. Sci.* 5, 5325–5332. doi: 10.1039/C1EE02475B

Xia, Y. J., and Ouyang, J. Y. (2009). Salt-induced charge screening and significant conductivity enhancement of conducting poly(3,4-ethylenedioxythiophene):Poly(styrenesulfonate). *Macromolecules* 42, 4141–4147. doi: 10.1021/ma900327d

Xu, K., Chen, G., and Qiu, D. (2013). Convenient construction of poly (3, 4-ethylenedioxythiophene)–graphene pie-like structure with enhanced thermoelectric performance. *J. Mater. Chem. A* 1, 12395–12399. doi: 10.1039/c3ta12691a

Yi, C., Wilhite, A., Zhang, L., Hu, R., Chuang, S. S., Zheng, J., et al. (2015). Enhanced thermoelectric properties of poly (3, 4-ethylenedioxythiophene): poly (styrenesulfonate) by binary secondary dopants. *ACS Appl. Mater. Interfaces* 7, 8984–8989. doi: 10.1021/acsami.5b01960

Yoo, D., Kim, J., Lee, S. H., Cho, W., Choi, H. H., Kim, F. S., et al. (2015). Effects of one-and two-dimensional carbon hybridization of PEDOT: PSS on the power factor of polymer thermoelectric energy conversion devices. *J. Mater. Chem. A* 3, 6526–6533. doi: 10.1039/C4TA06710J

Yoon, C., Reghu, M., Moses, D., Cao, Y., and Heeger, A. (1995). Transports in blends of conducting polymers. *Synth. Met.* 69, 255–258. doi: 10.1016/0379-6779(94)02439-6

Zhang, B., Sun, J., Katz, H., Fang, F., and Opila, R. (2010). Promising thermoelectric properties of commercial PEDOT: PSS materials and their Bi2Te3 powder composites. *ACS Appl. Mater. Interfaces* 2, 3170–3178. doi: 10.1021/am100654p

Conflict of Interest: The authors declare that the research was conducted in the absence of any commercial or financial relationships that could be construed as a potential conflict of interest.

frontiers in Chemistry

ORIGINAL RESEARCH
published: 15 January 2020
doi: 10.3389/fchem.2019.00919

Constructing Hierarchical Porous Carbons With Interconnected Micro-mesopores for Enhanced CO_2 Adsorption

*Hainan Zhang[1], Zeming Wang[2], Xudong Luo[1], Jinlin Lu[1], Shengnan Peng[1], Yongfei Wang[1] and Lu Han[1]**

[1] School of Materials and Metallurgy, University of Science and Technology Liaoning, Anshan, China, [2] School of Chemical and Processing Engineering, University of Leeds, Leeds, United Kingdom

A high cost-performance carbon dioxide sorbent based on hierarchical porous carbons (HPCs) was easily prepared by carbonization of raw sugar using commercially available nano-$CaCO_3$ as a double-acting template. The effects of the initial composition and carbonization temperature on the micro-mesoporous structure and adsorption performance were examined. Also, the importance of post-activation behavior in the development of micropores and synthesis route for the formation of the interconnected micro-mesoporous structure were investigated. The results revealed excellent carbon dioxide uptake reaching up 2.84 mmol/g (25°C, 1 bar), with micropore surface area of 786 m^2/g, micropore volume of 0.320 cm^3/g and mesopore volume of 0.233 cm^3/g. We found that high carbon dioxide uptake was ascribed to the developed micropores and interconnected micro-mesoporous structure. As an expectation, the optimized HPCs offers a promising new support for the high selective capture of carbon dioxide in the future.

Keywords: hierarchical porous carbons, template method, micro-mesoporous structure, activation, carbon dioxide adsorption

OPEN ACCESS

Edited by:
Kezhen Qi,
Shenyang Normal University, China

Reviewed by:
Qingrui Zhang,
Yanshan University, China
Jiyang Li,
State Key Laboratory of Inorganic Synthesis and Preparative Chemistry, Jilin University, China

***Correspondence:**
Lu Han
hanlu@ustl.edu.cn

Specialty section:
This article was submitted to Nanoscience, a section of the journal Frontiers in Chemistry

Received: *10 November 2019*
Accepted: *18 December 2019*
Published: *15 January 2020*

Citation:
Zhang H, Wang Z, Luo X, Lu J, Peng S, Wang Y and Han L (2020) Constructing Hierarchical Porous Carbons With Interconnected Micro-mesopores for Enhanced CO_2 Adsorption. Front. Chem. 7:919. doi: 10.3389/fchem.2019.00919

INTRODUCTION

Carbon dioxide has gradually increased in the atmosphere over the past century, resulting in increasing concerns about the global warming and climate change (Kanki et al., 2016; Qi et al., 2017; Li et al., 2019). In order to reduce the carbon dioxide content in the air, people began to develop new energy, such as hydrogen energy (Qi et al., 2019), degradation of pollutants and sewage (Sun et al., 2018; Chen et al., 2019), among others, but fundamentally solve the problem of carbon dioxide pollution. However, although carbon dioxide is considered as the main greenhouse gas, it is a transformable carbon resource (Garbarino et al., 2014; Son et al., 2014; Pullar et al., 2019). In the presence of a suitable catalyst, the captured carbon dioxide molecules can be converted into synthetic natural gas, such as methane (Lavoie, 2014; Wang et al., 2016; Xia et al., 2019). Therefore, promoting the development of carbon dioxide capture and storage (CCS) has important social significance and great economic value (Han et al., 2012; Hayat et al., 2019).

Tremendous research has been devoted to the development of new technologies for CCS, especially those based on high-performance sorbents for carbon dioxide capture (Liang et al., 2004; Santis et al., 2016; Patel et al., 2017; Zhu et al., 2019). Novel solid sorbents capable of

reversibly capturing carbon dioxide through dry adsorption process have many distinct advantages over wet absorption and adsorption-coupled membrane separation. These include low investment, the moderate energy cost for regeneration, and large capacity at room temperature (Yaumi et al., 2017). In the past decade, various types of solid sorbents have been attempted for CCS. Examples include zeolites (Megías-Sayago et al., 2019), modified porous silicas (Dassanayake et al., 2017), metal organic frameworks (MOFs) (Shi et al., 2019), calcium looping sorbents (Zhu et al., 2017), polymer membranes (Ahmad et al., 2016; Zhang et al., 2019), and nanoporous carbons (NCs) (Lee et al., 2014). In particular, MOFs and NCs have received much attention due to their excellent capture performance. However, MOFs are still not feasible economically and sensitive to water, resulting in failure due to structural damage.

On the other hand, NCs offer many promising applications as catalyst supports (Kim et al., 2005; Song et al., 2019), advanced electrodes (Liu et al., 2010; Xu et al., 2019), and energy-storage materials (Wu et al., 2009), among others. Various types of NCs showed promise as alternatives to carbon dioxide capture, such as modified activated carbons (Lu et al., 2008), nitrogen-doped carbon molecular sieves (Patiño et al., 2014), and hierarchical porous carbons (HPCs) (Xia et al., 2014). These NCs presented several particular features like hydrophobic surface properties, superior thermal stability, and excellent chemical resistance, as well as some potential advantages in terms of extensive sources, tunable nano-pore structure, and controllable synthesis.

In view of the physical behavior during the adsorption process, the microporous structure was found more favorable for adsorption (Fan et al., 2013). Moreover, incorporation of basic groups into carbon framework, especially nitrogen-containing species doping was found highly praised in improving carbon dioxide selective adsorption performance (Wei et al., 2013). However, the realization of both micropore-enriched structures and nitrogen-doped modification depends heavily on the raw materials and synthesis route. For instance, Lu et al. reported the direct pyrolysis of copolymers based on resorcinol, formaldehyde, and lysine using the mannich reaction to fabricated nitrogen-doped porous carbon monolith (Hao et al., 2010). They measured high adsorption capacity reaching up 3.13 mmol/g at room temperature and 1 atm. Sun et al. reported a one-pot melting-assisted strategy using resorcinol and p-phthalaldehyde as carbon precursors, melamine as a nitrogen source, and Pluronic F127 as a surfactant under self-pressurized solvent-free conditions (Zhang et al., 2015). The resulting carbon material had a hierarchical porous structure with high surface area of 748 m^2/g, and exhibited excellent capacity of 2.73 mmol/g at 298 K and 1 bar.

From the standpoint of structural design, Qiu et al. synthesized a novel carbon sorbent with a special bimodal microporous structure (Li Y. et al., 2013). The carbonized porous aromatic framework (PAF-1) derivatives were formed by high-temperature KOH activation showed unexpectedly superior carbon dioxide capture capacity reaching up to 7.2 mmol/g at 273 K and 1 bar. However, the starting materials are seldom used and the synthesis route was complicated and cumbersome. To overcome these problems, Jaroniec et al. designed two different tailored routes to develop microporous and mesoporous carbon spheres to demonstrate that the site-occupying silica in carbon spheres works as hard templates for the large mesopores (Marszewska and Jaroniec, 2017). The resulting mesoporosity enabled faster transfer of carbon dioxide from the bulk to the micropores and effectively improved the diffusion process. The best sorbent showed carbon dioxide uptakes as high as 4.0 mmol/g (23°C, 1 bar) and 7.8 mmol/g (0°C, 1 bar). Despite the improvement in NCs, the main drawbacks related to cost and technology transfer to industrial applications remain to be solved when used for CCS. At present, the research mainly focuses on employing low-cost resources to develop efficient and economical synthesis routes for sorbents with ideal performances.

In this study, HPCs with abundant micropores were prepared using a simple and cost effective route. To optimize microporosity and mesoporosity of HPCs, several influencing factors based on the ratio of raw materials and carbonization temperature were investigated, and related synthesis mechanisms were examined. The resulting materials showed promising features toward CCS on a commercial scale.

EXPERIMENTAL

Synthesis of HPCs

The commercial nano-$CaCO_3$ (ca. 40∼60 nm in size from Chengdu Aike Reagent) served as a hard template and micropore producer. Raw sugar was used as the carbon precursor. HPCs were prepared by dispersing nano-$CaCO_3$ in the raw sugar aqueous solution at the mass ratios of raw sugar to $CaCO_3$ varying from 2:8 to 5:5. The resulting homogeneous solution was then left to evaporated and dried in a water bath at 85°C. The collected semi-dry powders were dried thoroughly and then kept at 700 or 900°C for 2 h under flowing nitrogen (99.999%). The carbonized mixture was treated with 2 M HCl solution and then washed several times with distilled water, resulting in a solid product after drying overnight at 100°C. For comparison, a tentative sample was also obtained via post-activation method for HPCs at 700°C for 1 h under flowing carbon dioxide (50 cm^3/min). The as-made carbon materials were labeled as HPCs*-*x*-*y*, where the superscript * represents the activated sample, and lowercase *x* and *y* are the share of raw sugar in dried raw materials and carbonization temperature, respectively.

Characterization and Evaluation of HPCs

Thermogravimetric (TG) analysis was carried out using a thermal analysis system (STA 449/F3, Netzsch) with heating rate of 10°C /min under nitrogen flow. The carbon yield of HPCs samples was calculated from the weight of resultant carbons divided by the weight of dried raw materials. X-ray powder diffraction (XRD) pattern was measured on a diffractometer (Bruker D8 ADVANCE) with a scanning rate of 2°/min, using Cu Kα radiation. The microstructure of samples were observed by field emission scanning electron microscopy (FESEM, Carl Zeiss, Supra 40). The structures and morphologies of the activated sample were characterized by transmission electron microscopy (TEM) (JEM-2100F JEOL, 200 kV). The

microporosity and mesoporosity properties of samples were analyzed by the nitrogen adsorption-desorption isotherms at −196°C (Micrometrics, ASAP 3020). Specific surface areas of samples were determined using the Brunauer-Emmett-Teller (BET) equation. The total pore volume was calculated from the nitrogen adsorption amount at the relative pressure of 0.995. The mesoporous volumes of samples were determined using the Barrett-Joyner-Halanda (BJH) method. The micropore area and volume were estimated by the t-plot method (Brunauer et al., 1938). The pore size distributions were derived from the adsorption branch of nitrogen isotherms using the BJH method (Sing, 1985). The carbon dioxide adsorption performance of the sample was measured at 25 and 0°C using a carbon dioxide adsorption instrument (JWGB, JW-BK112). Prior to adsorption measurement, all samples were degassed at 200°C for 12 h.

RESULTS AND DISCUSSION

TG Analysis

The carbonization process of raw sugar-$CaCO_3$ mixtures was studied by TG analysis in the temperature range from 25 to 1,000°C under nitrogen flow, and the results are shown in **Figure 1**. The decomposition temperature of nano-$CaCO_3$ was estimated to about 660°C, and carbonization of pure raw sugar occurred at around 200°C with a carbon yield of ca. 19% at 900°C. Compared to pure raw sugar, the decomposition of the mixture was delayed from 300 to 660°C. This was attributed to incorporated nano-$CaCO_3$ in the matrix. Above 660°C, the weight loss dropped rapidly, indicating that carbon consumption process occurred above 660°C. Since the decomposition of $CaCO_3$ into CaO and carbon dioxide above this temperature, it can be concluded that carbon dioxide gas reacted with carbon walls, leading to its oxidation into CO and removal. This etching process was known as "inner-activation" effect, which was first detected in the carbonization process of PF (phenol formaldehyde) resin and $CaCO_3$ composite (Zhao et al., 2010). To investigate the porous texture of the prepared carbons, two series were prepared by changing the carbonization temperature: HPCs-*x*-700 series (x = 2, 3, 4, and 5) carbonized at 700°C as the initial stage of etching reaction and HPCs-*x*-900 series (x = 2, 3, 4, and 5) carbonized at 900°C as the mature stage of etching reaction.

The carbon yield of both HPCs-*x*-700 and HPCs-*x*-900 series (x = 2, 3, 4, and 5) as a function of the mass ratio of raw sugar:$CaCO_3$ is shown in **Figure 2**. Now that carbon dioxide occurred above 700°C, adequate carbon dioxide might consume more carbon according to the reaction: $CO_2+C \rightarrow 2CO$ (Zhao et al., 2010). **Figure 2** confirmed this assumption, showing that both series with a total of eight samples consumed carbon according to the above reaction. At the same initial composition, more carbon dioxide were produced as carbonization temperature rose. Thus, the carbon consumption of HPCs-*x*-900 series was higher than that of HPCs-*x*-700 series. At the same carbonization temperature, the carbon consumption gradually decreased as $CaCO_3$ ratio in the mixture reduced. Thus, an increase in carbon yield was linked to the decrease of carbon dioxide emissions. The effect of carbon dioxide post-activation on porous texture of various carbons had been studied thoroughly (Liou, 2010; Li Y. et al., 2013; Wickramaratne and Jaroniec, 2013a), and the effect of inner-activation on microstructure of HPCs materials needs further investigation as well.

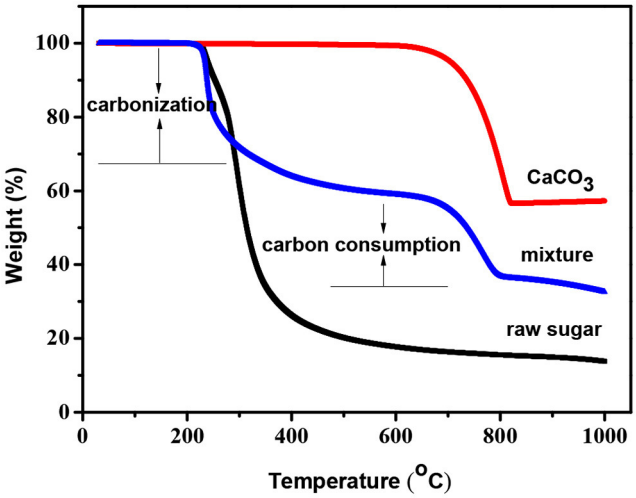

FIGURE 1 | TG curves of raw sugar, nano-$CaCO_3$, and raw sugar-$CaCO_3$ mixture (ratio of raw sugar:$CaCO_3$ = 5:5) under nitrogen flow.

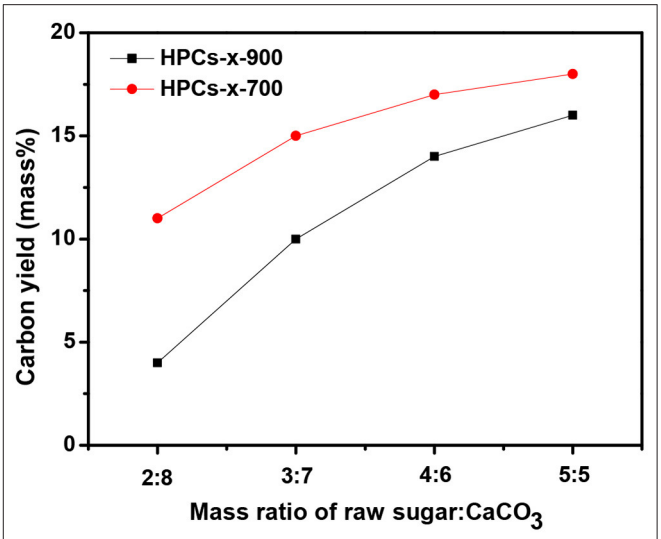

FIGURE 2 | Carbon yield of HPCs-*x*-900 and HPCs-*x*-700 samples as a function of the mass ratio of raw sugar:$CaCO_3$.

XRD Patterns

Typical XRD pattern was exhibited in **Figure 3** to verify the graphitic characteristics of carbon. A sharp diffraction peak located at $2\theta \approx 23°$ and a broad diffraction peak located at $2\theta \approx 44°$ were clearly identified, indexed to the (002) reflection of pure graphitic lattice and the (100) reflection of the graphitic carbon, respectively (Xu et al., 2011). This structure might be beneficial to enhance catalytic effect for carbon dioxide conversion when the carbon combines with active materials (Wang et al., 2016).

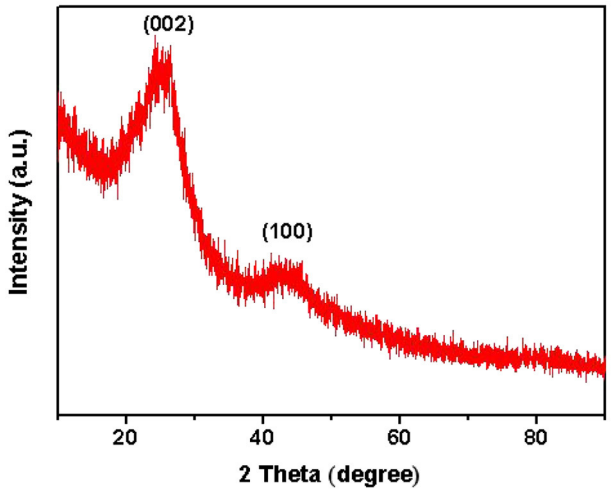

FIGURE 3 | XRD pattern of HPCs-5-900.

FESEM Images

The morphological evolution from raw sugar-$CaCO_3$ physical mixture into HPCs was depicted in **Figure 4**, using a series of FESEM images (a∼f). In **Figures 4a,b**, the pristine raw sugar displayed a dense structure filled with apparent inclusions, corresponding to the nano-$CaCO_3$ particles with their aggregates shown in the inset of **Figure 4a**. After high temperature carbonization above 700°C, the raw sugar was converted into graphitic carbon as demonstrated by TG and XRD, and the nano-$CaCO_3$ decomposed into nano-CaO and carbon dioxide as confirmed by TG. As shown in **Figures 4c,d**, the as-received product depicted highly porous structure rich with fine pores, retaining no memory of pristine raw sugar-$CaCO_3$ structure. After removal of CaO fillers, largely interconnected mesopores of 20∼100 nm in diameter were formed in the carbon matrix, which were different from the morphology of matrix embedded with nano-CaO particles.

TEM Images

To further investigate the microstructure of micropore-enriched HPCs after activation with carbon dioxide gas, a typical HPCs*-5-900 sample was characterized by TEM. As shown in **Figures 5a,b**, the edges at high magnification displayed well-developed three-dimensional system of the interconnected pores built by random carbon walls <10 nm in thickness to produce loose nanostructures. In **Figures 5c,d**, the magnified TEM image of the circular region by white circles in **Figure 5a**. The pore region was detected by the reaction of dilute hydrochloric acid solution with site-occupying template. The inwall of carbon was rough and curly, implying the structural disintegration of carbon and existence of fine micropores. The external carbon structure illustrated a dendritic arrangement with abundant micropores, suggesting the successful activation resulting from extrinsic carbon dioxide against carbon.

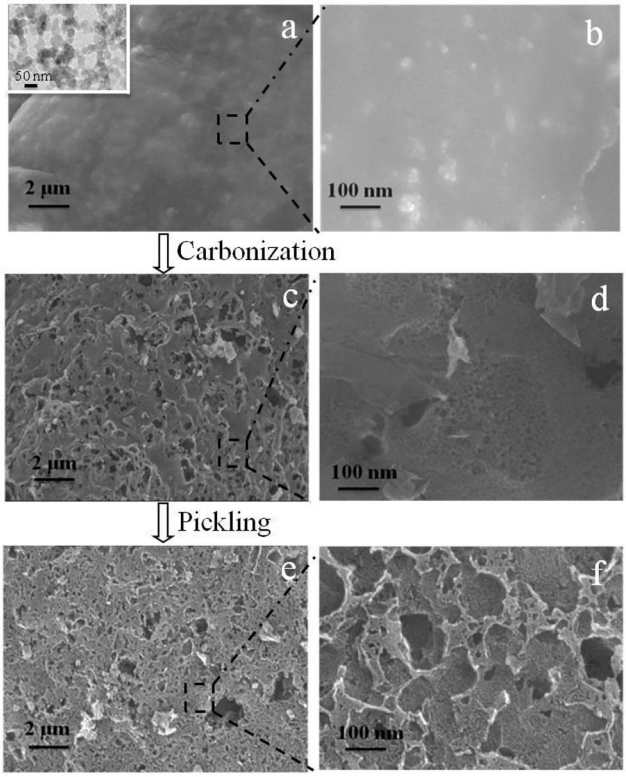

FIGURE 4 | FESEM images of **(a)** and **(b)** raw sugar-$CaCO_3$ mixture matrix (inset of **(a)** is the TEM image of nano-$CaCO_3$ particles), **(c,d)** carbonized matrix embedded with templates, and **(e,f)** HPCs.

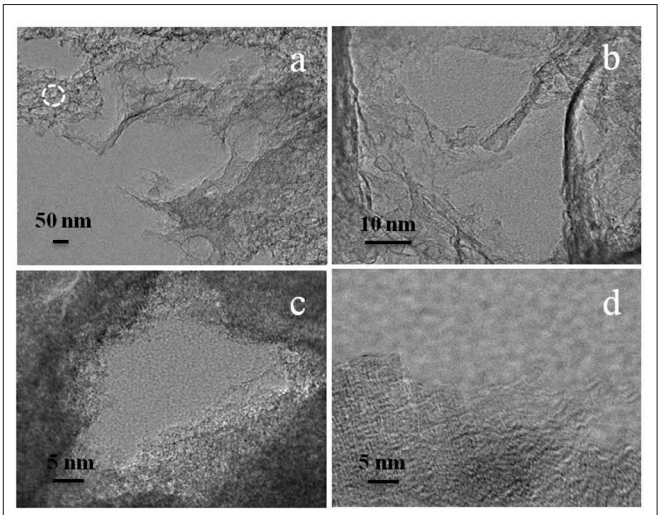

FIGURE 5 | TEM images of HPCs*-5-900 showing: **(a)** edges of carbon, **(b)** randomly carbon walls, **(c)** site-occupying region, and **(d)** micropore-enriched edges after carbon dioxide gas activation.

Nitrogen Adsorption/Desorption Isotherms

In **Figures 6A,B**, the nitrogen adsorption/desorption isotherms of HPCs-*x*-700 and HPCs-*x*-900 series (x = 2, 3, 4, and 5), respectively. The nitrogen adsorption/desorption isotherms

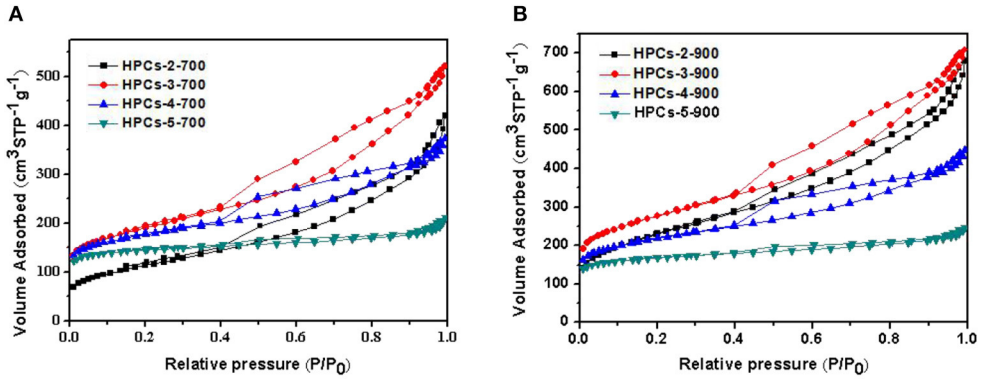

FIGURE 6 | Nitrogen adsorption/desorption isotherms of HPCs samples carbonized under nitrogen at **(A)** 700°C and **(B)** 900°C for 2 h.

of two series were typical Langmuir IV curves with distinct hysteresis loops, indicating the presence of mesopores created by the removal of site-occupying $CaCO_3$ or CaO. The significant increase of adsorption volume at low-pressure range ($P/P_0 < 0.1$) indicated the existence of abundant micropores. Three imaginable and reasonable sources caused the micropores to form: the voids derived from high-temperature pyrolysis of raw sugar, carbon dioxide escape routes during $CaCO_3$ decomposition, and fine etching pores in carbon wall. Although there is no adsorption hysteresis in the macropore range (> 300 nm), the existence of micron level voids in the carbon matrix was clearly confirmed in the preceding FESEM images. Thus, it could be suggested that the formation of voids was mainly attributed to leaching of the aggregates of template particles (Li T. et al., 2013).

Table 1 lists the calculated adsorption parameters for both series carbonized at 700 and 900°C, respectively. All HPCs samples showed high surface areas ranging from 408 to 986 m^2/g and large total pore volumes varying from 0.327 to 1.095 cm^3/g. For HPCs-*x*-700 or HPCs-*x*-900 series ($x = 2$, 3, 4, and 5), as x increased, V_{meso} decreased gradually but V_{micro}, V_{micro}/V_{total}, $S_{BET-micro}$, and $S_{BET-micro}/S_{BET}$ rose gradually. This indicated a regular transition from mesoporosity to microporosity when mass ratio of raw sugar/$CaCO_3$ increased. The former was attributed to the decrease in the amount of site-occupying $CaCO_3$. For each HPCs series, both micropore volume and surface area increased as raw sugar ratio rose. As suggested by **Figure 2**, carbon yield rose as raw sugar ratio increased, in accordance with the changed trend of micropore volume and surface area. The inner-activation effect of carbon dioxide on the carbon matrix had also been confirmed by the previous discussion. The etching effect was greatly determined by respective content and dependency state of carbon dioxide and carbon, according to the reaction: $CO_2+C \rightarrow 2CO$. Thus, it can be concluded that the development of micropores did not only depend on carbon dioxide discharge derived from inner-activation but also closely associated with the essential amount of carbon matrix. Note that data presented here were slightly different from those reported in previous research (Zhao et al., 2010),

TABLE 1 | Textural properties of all related HPCs samples.

Sample	S_{BET} (S^a_{BET-mi}) (m^2/g)	S_{BET-mi}/S_{BET}	V_t (V^b_{mi}) (cm^3/g)	V^c_{me}	V_{mi}/V_t
HPCs-2-700	408 (59)	0.145	0.650 (0.024)	0.626	0.037
HPCs-3-700	684 (252)	0.368	0.714 (0.107)	0.607	0.149
HPCs-4-700	646 (375)	0.580	0.578 (0.156)	0.422	0.270
HPCs-5-700	562 (491)	0.874	0.327 (0.195)	0.132	0.596
HPCs-2-900	822 (231)	0.281	1.052 (0.100)	0.952	0.095
HPCs-3-900	986 (383)	0.388	1.095 (0.165)	0.930	0.151
HPCs-4-900	793 (457)	0.576	0.693 (0.193)	0.500	0.278
HPCs-5-900	638 (532)	0.834	0.382 (0.215)	0.167	0.563
HPCs*-5-900	936 (786)	0.840	0.553 (0.320)	0.233	0.579

[a]The micropore surface area was estimated using the t-plot method. [b]The micropore volume was estimated using the t-plot method. [c]The mesopore volume was estimated by BJH method.

and could be attributed to differences in the carbon source. In fact, the carbon source used in previous studies was phenolic resin. The effect of other carbon sources, such as resorcinol-formaldehyde mixture, sucrose, phenolic resin and polyacrylonitrile on porous texture will be reported in future publications.

Moreover, the HPCs-*x*-900 series exhibited higher S_{BET}, $S_{BET-micro}$, and V_{micro} than those samples with the same raw materials ratio carbonized at 700°C, but the carbon yield of HPCs-*x*-700 series was higher than that of the carbonized samples at 900°C. This demonstrated that carbonization at 900°C could ensure the complete decomposition of $CaCO_3$, and samples were thoroughly activated. In addition, the gap in amount of micropores between every two samples with the same raw materials ratio but carbonized at 900 and 700°C, respectively, became narrow due to the weakening of carbon dioxide inner-activation effect with decrease in amount of $CaCO_3$. Specifically, the difference in micropore volume between HPCs-2-900 and HPCs-2-700 was estimated to 0.076 cm^3/g. However, these values decreased to 0.058, 0.037 and 0.020 cm^3/g, respectively, as the value of x rose from 3 to 5. Also, S_{BET-mi}/S_{BET} and V_{mi}/V_t increased to 0.834 and 0.563, respectively, as the value of x rose

to 5. The microporosity structure was more prominent, especially for HPCs-5-700 and HPCs-5-900 samples.

To develop large volumes of small micropores for high carbon dioxide uptakes, the carbon dioxide activation was performed on HPCs-5-900 at 700°C for 1 h under flowing carbon dioxide. **Figure 7A** shows the nitrogen adsorption/desorption isotherms of HPCs-5-900 and HPCs*-5-900 samples. HPCs*-5-900 illustrated Langmuir IV type curves with distinct hysteresis loop, indicating the presence of constricted mesopores, similar to that of HPCs-5-900 sample. As expected, the nitrogen adsorption amount of HPCs*-5-900 in the low-pressure range (<0.1) was significantly higher than that of HPCs-5-900 because the former was activated by carbon dioxide and its micropore volume is enlarged by almost 50%. The pore size

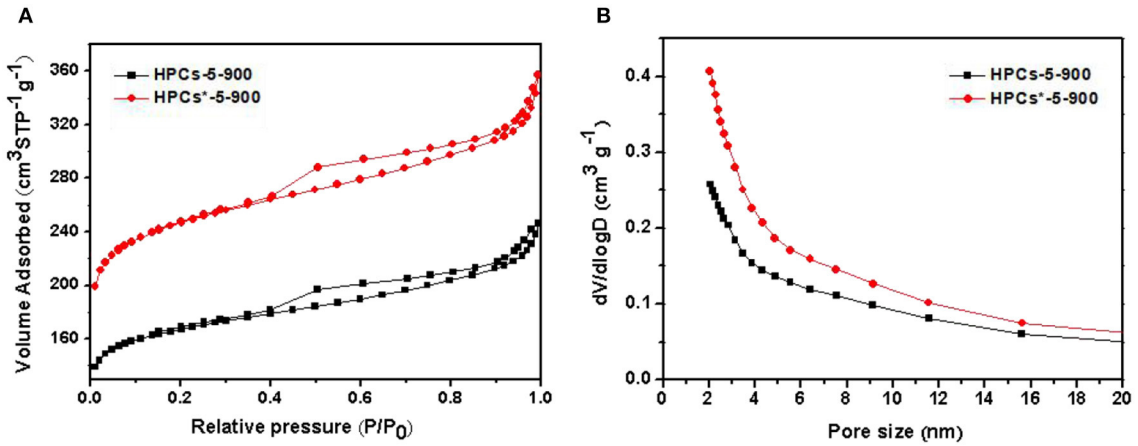

FIGURE 7 | (A) Nitrogen adsorption/desorption isotherms of HPCs-5-900 and HPCs*-5-900. **(B)** The corresponding pore size distributions curves calculated by BJH method.

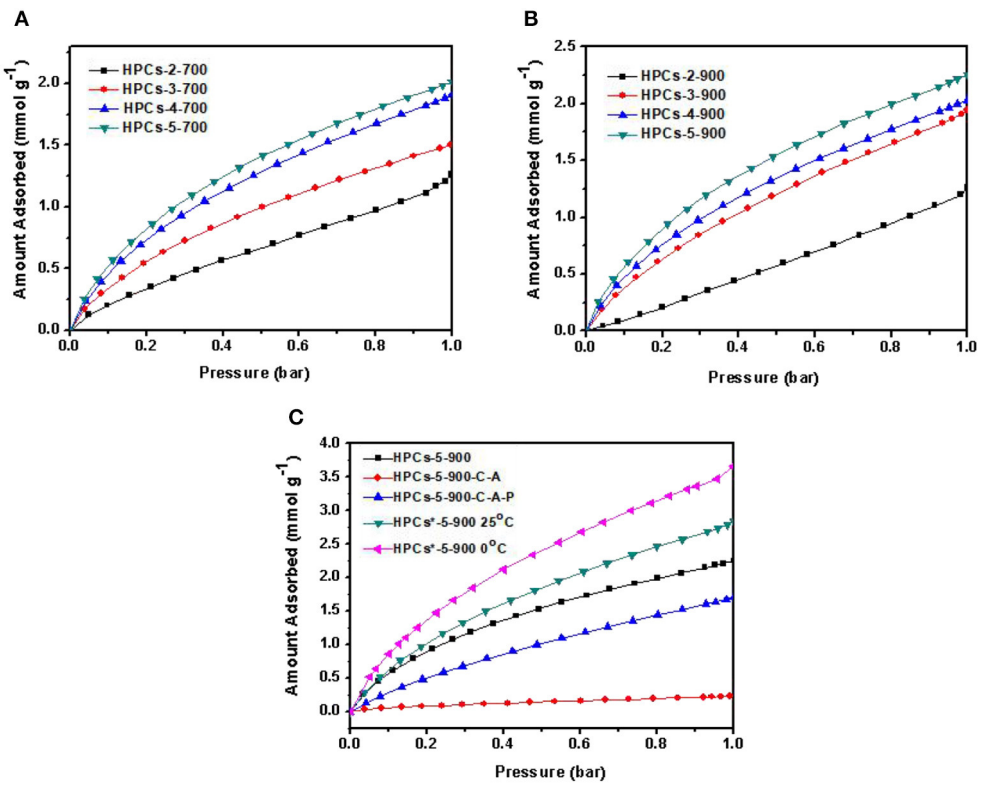

FIGURE 8 | Carbon dioxide adsorption isotherms measured at 25°C for HPCs series carbonized at **(A)** 700°C and **(B)** 900°C. **(C)** Carbon dioxide adsorption isotherms measured for a series of HPCs-5-900 samples obtained by different routes.

distributions of HPCs-5-900 and HPCs*-5-900 samples obtained by BJH method are inserted in **Figure 7B**. It clearly suggested that the amount of micropores in the activated sample was superior to that of the unactivated sample, demonstrating the benefits of carbon dioxide post-activation. On the other hand, a slight increase in the mesopore volume was carefully observed from the hysteresis loop and the data listed in **Table 1**. The development of mesopores was also caused by carbon dioxide activation that widened all pores existed in HPCs samples or produced new pores in the carbon matrix. In other words, a part of micropores connected to become mesopores or newborn mesopores directly germinated in the carbon matrix when carbon dioxide etching reaction occurred (Li T. et al., 2013; Marszewska and Jaroniec, 2017).

Carbon Dioxide Adsorption Isotherms

The carbon dioxide adsorption isotherms of HPCs-*x*-700 and HPCs-*x*-900 series at 25°C are shown in **Figures 8A,B**, respectively. HPCs-5-900 showed the best performance toward carbon dioxide adsorption and the maximum value of adsorption capacity was estimated to 2.25 mmol/g at 25°C and 1 bar. Although HPCs-3-900 depicted the highest total pore volume of 1.095 cm^3/g and mesopore volume of 0.930 cm^3/g (**Table 1**), HPCs-5-900 possessed a superior micropore volume of 0.215 cm^3/g, occupying ∼56% of total pore volume. Hence, it can be concluded that the highest carbon dioxide adsorption performance of HPCs-5-900 necessarily originated from its huge amount of micropore volume. Despite using fillers, such as SiO_2 (Feng et al., 2014; Marszewska and Jaroniec, 2017), MgO (Meng and Park, 2012) and porous concrete (Günther et al., 2012) in the preparation of porous carbon materials, nano-$CaCO_3$ particles showed preferable advantages over other oxide fillers for hierarchical porous structure because they served simultaneously as mesopore templates and micropore producers (Zhao et al., 2010; Liu et al., 2013). The decomposition products of nano-$CaCO_3$ particles results in nano-sized CaO particles and carbon dioxide gas, responsible for the formation of mesopores and micropores in carbon matrix, respectively. Thus, a series of HPCs with varying degrees of microporosity and mesoporosity can easily be obtained by adjusting the ratio of raw sugar/$CaCO_3$ and carbonization temperature. From an economic standpoint, the mass ratio of raw sugar/$CaCO_3$ as 1:1 is favorable. Besides, development of microporosity for carbon dioxide adsorption by setting the carbonization temperature at 900°C is desirable.

The chemical adsorption of carbon dioxide on HPCs materials is almost impossible due to the absence of basic groups like nitrogen-containing species in carbon. Since HPCs*-5-900 possessed a typical hierarchical porous structure with ultra-high micropores and moderate mesopores, and also exhibited a superior carbon dioxide uptake, it clearly demonstrated that the physical uptake was closely related to this micro-mesoporous structure. The importance of mesopores in carbon dioxide capture was recently reported (Wickramaratne and Jaroniec, 2013a,b; Marszewska and Jaroniec, 2017). In the case of HPCs materials, the synthetic route was adjusted in this study to deduce the necessity of mesopores in micropore-enriched carbon. As shown in **Figure 8C**, compared to HPCs-5-900, the sample obtained by preliminary carbonization, subsequent activation and final pickling (labeled as HPCs-5-900-C-A-P) exhibited a smaller carbon dioxide uptake of 1.69 mmol/g (25 °C, 1 bar). Specifically, the carbon dioxide uptake of HPCs-5-900-C-A (carbonized and activated without the pickling process) just reached to 0.17 mmol/g at 25 °C and 1 bar. The CO_2 adsorption properties of the prepared all related HPCs samples are shown in **Table 2**.

The essential difference from HPCs-5-900, which was just the process order, would definitively affect the carbon dioxide adsorption performance. The presence of site-occupying CaO particles in carbon matrix caused two negative effects on carbon dioxide diffusion. One was related to the post-activation effect and the other was linked to the development of interconnected micro-mesoporous structure. The presence of template particles blocked activation gas diffusion from the bulk phase to the interior, resulting in delayed pore-creating reaction. For HPCs-5-900-C-A, the almost negligible carbon dioxide uptake resulted from both effects. In the case of HPCs-5-900-C-A-P, the removal of these particles during the last step resulted in interconnected micro-mesoporous structure and improved carbon dioxide diffusion from the bulk phase to micropores. Therefore, the carbon dioxide uptake increased dramatically compared to HPCs-5-900-C-A, but still lower than HPCs-5-900. Thus, the removal of site-occupying templates before carbon dioxide activation was beneficial for activation gas transfer in unobstructed path and played a significant role in improving the microporous textures. The obtained hierarchical porous structure was very important in improving the carbon dioxide uptake. In addition, as shown in **Table 3**, we compared the texture properties of samples in this work with the carbon samples of different structures reported in the previous literature.

CONCLUSIONS

In this study, a series of high-quality and cost-effective carbon dioxide sorbents based on HPCs are successfully synthesized by carbonizing raw sugar-$CaCO_3$ composite precursors. Both

TABLE 2 | CO_2 adsorption properties of all related HPCs samples.

Sample	HPCs-2-700	HPCs-3-700	HPCs-4-700	HPCs-5-700	HPCs-2-900	HPCs-3-900	HPCs-4-900	HPCs-5-900	HPCs*-5- 900
$N^a_{co_2}$ (mmol/g)	1.26	1.5	1.91	2.02	1.26	1.94	2.03	2.25	2.84[b]/3.66[c]

[a] *The carbon dioxide uptake at 25°C and 1 bar.* [b,c] *The carbon dioxide adsorption performance was measured at 25 and 0°C, respectively.*

TABLE 3 | The comparison of textural properties of samples in this work with the literature values.

Carbon structure	T (°C)	S_{BET} (m^2/g)	V_t (cm^3/g)	V_{mi} (cm^3/g)	N_{co_2} (mmol/g) (Condition)	References
Hierarchical porous carbons	900°C	936	0.553	0.32	2.84 (25°C 1 bar)	This work
Hierarchical macroporous nitrogen-doped carbons	600°C	682.8	–	–	2.69 (25°C 1 bar)	Li et al., 2016
Hierarchical porous graphene-based carbons	850°C	459	1.17	0.11	1.76 (0°C 1 bar)	Xia et al., 2014
Ordered mesoporous carbon	850°C	1400	1.02	0.42	2.64 (25°C 1 bar)	Mahurin et al., 2014
Nitrogen-doped microporous carbons	800°C	2567	1.49	1.25	2.78 (25°C 1 bar)	Fan et al., 2013
Nitrogen-doped mesoporous carbons	600°C	537	0.47	0.17	2.8 (25°C 1 bar)	Wei et al., 2013
Mesoporous carbon	900°C	3325	2.25	0.98	2.4 (25°C 1 bar)	Huang et al., 2016
Mesoporous carbon	800°C	974	1.93	0.1	2.41 (25°C 1 bar)	Lee et al., 2014
Mesoporous carbon	800°C	748	0.49	0.23	2.73 (25°C 1 bar)	Zhang et al., 2015

starting materials are mass-produced and low-cost and the whole fabrication process only involved three steps. The carbonization and inner-activation reaction occurred synchronously, and their combination effectively induced regional micropores. The removal of site-occupying templates ensured the formation of the interconnected micro-mesoporous structure built by ultrathin carbon walls. The well-developed micropore-enriched structure was further improved through the final post-activation process. The combination of nano-$CaCO_3$ incorporation and carbon dioxide post-activation were found to have significant beneficial effects on the structural controllability, especially the microporosity and mesoporosity. The best structural property with t-plot micropore surface area of 786 m^2/g and micropore volume of 0.320 cm^3/g were translated into excellent carbon dioxide uptake of 2.84 mmol/g at 25°C and 3.66 mmol/g at 0°C. Overall, the proposed synthesis methodology of HPCs looks promising for future applications in the field of carbon dioxide catalytic conversion.

DATA AVAILABILITY STATEMENT

All datasets generated for this study are included in the manuscript.

AUTHOR CONTRIBUTIONS

LH was the most important contributor of manuscript, and other authors have made a lot of contributions in experiments and writing of manuscript.

FUNDING

This work was supported by the National Natural Science Foundation of China (51504133), the Project of Liaoning Science and Technology Agency (20170540465) and the 2019 Project of Liaoning Education Department (2019LNJC20).

REFERENCES

Ahmad, N. A., Leo, C. P., Ahmad, A. L., and Mohammad, A. W. (2016). Separation of CO_2 from hydrogen using membrane gas absorption with PVDF/PBI membrane. *Int. J. Hydrogen Energy* 41, 4855–4861. doi: 10.1016/j.ijhydene.2015.11.054

Brunauer, S., Emmett, P. H., and Teller, E. (1938). Adsorption of gases in multimolecular layers. *J. Am. Chem. Soc.* 60, 309–319. doi: 10.1021/ja01269a023

Chen, H., Zhang, S., Zhao, Z., Liu, M., and Zhang, Q. (2019). Application of dopamine functional materials in water pollution control. *Prog. Chem.* 31, 571–579. doi: 10.7536/PC180823

Dassanayake, R. S., Gunathilake, C., Dassanayake, A. C., Abidi, N., and Jaroniec, M. (2017). Amidoxime-functionalized nanocrystalline cellulose-mesoporous silica composites for carbon dioxide sorption at ambient and elevated temperatures. *J. Mater. Chem. A* 5, 7462–7473. doi: 10.1039/C7TA01038A

Fan, X., Zhang, L., Zhang, G., Shu, Z., and Shi, J. (2013). Chitosan derived nitrogen-doped microporous carbons for high performance CO_2 capture. *Carbon* 61, 423–430. doi: 10.1016/j.carbon.2013.05.026

Feng, S., Li, W., Shi, Q., Li, Y., Chen, J., Ling, Y., et al. (2014). Synthesis of nitrogen-doped hollow carbon nanospheres for CO_2 capture. *Chem. Commun.* 50, 329–331. doi: 10.1039/C3CC46492J

Garbarino, G., Riani, P., Magistri, L., and Busca, G. (2014). A study of the methanation of carbon dioxide on Ni/Al_2O_3 catalysts at atmospheric pressure. *Int. J. Hydrogen Energy* 39, 11557–11565. doi: 10.1016/j.ijhydene.2014.05.111

Günther, D., Beckmann, J., Schöneich, M., Schmidt, P., and Klepel, O. (2012). Porous concrete as a template for the synthesis of porous carbon materials. *Carbon* 50, 3096–3098. doi: 10.1016/j.carbon.2012.02.039

Han, J. H., Ryu, J. H., and Lee, I. B. (2012). A preliminary infrastructure design to use fossil fuels with carbon capture and storage and renewable energy systems. *Int. J. Hydrogen Energy* 37, 17321–17335. doi: 10.1016/j.ijhydene.2012.08.117

Hao, G. P., Li, W. C., Qian, D., and Lu, A. H. (2010). Rapid synthesis of nitrogen-doped porous carbon monolith for CO_2 capture. *Adv. Mater.* 22, 853–857. doi: 10.1002/adma.200903765

Hayat, A., Rahman, M. U., Khan, I., Khan, J., Sohail, M., Yasmeen, H., et al. (2019). Conjugated electron donor-acceptor hybrid polymeric carbon nitride as a photocatalyst for CO_2 reduction. *Molecules* 24:1779. doi: 10.3390/molecules24091779

Huang, K., Chai, S. H., Mayes, R. T., Tan, S., Jones, C. W., and Dai, S. (2016). Significantly increasing porosity of mesoporous carbon by $NaNH_2$ activation for enhanced CO_2 adsorption. *Micropor. Mesopor. Mat.* 230, 100–108. doi: 10.1016/j.micromeso.2016.04.041

Kanki, K., Maki, H., and Mizuhata, M. (2016). Carbon dioxide absorption behavior of surface-modified lithium orthosilicate/potassium carbonate prepared by ballmilling. *Int. J. Hydrogen Energy* 41, 18893–18899. doi: 10.1016/j.ijhydene.2016.06.158

Kim, P., Kim, H., Joo, J. B., Kim, W., Song, I. K., and Yi, J. (2005). Preparation and application of nanoporous carbon templated by silica particle for use as a catalyst support for direct methanol fuel cell. *J. Power Sources* 145, 139–146. doi: 10.1016/j.jpowsour.2005.01.070

Lavoie, J. M. (2014). Review on dry reforming of methane, a potentially more environmentally-friendly approach to the increasing natural gas exploitation. *Front. Chem.* 2:81. doi: 10.3389/fchem.2014.00081

Lee, S. Y., Jang, D. I., Bae, S. T., and Park, S. J. (2014). Facile synthesis of nitrogen-enriched mesoporous carbon for carbon dioxide capture. *Int. J. Hydrogen Energy* 39, 12347–12352. doi: 10.1016/j.ijhydene.2014.03.086

Li, D., Chen, Y., Zheng, M., Zhao, H., Zhao, Y., and Sun, Z. (2016). Hierarchically structured porous nitrogen-doped carbon for highly selective CO_2 capture. *ACS Sustainable Chem. Eng.* 4, 298–304. doi: 10.1021/acssuschemeng.5b01230

Li, T., Yang, G., Wang, J., Zhou, Y., and Han, H. (2013). Excellent electrochemical performance of nitrogen-enriched hierarchical porous carbon electrodes prepared using nano-$CaCO_3$ as template. *J. Solid State Electr.* 17, 2651–2660. doi: 10.1007/s10008-013-2167-3

Li, X., Yu, J., Jaroniec, M., and Chen, X. (2019). Cocatalysts for selective photoreduction of CO_2 into solar fuels. *Chem. Rev.* 119, 3962–4179. doi: 10.1021/acs.chemrev.8b00400

Li, Y., Ben, T., Zhang, B., Fu, Y., and Qiu, S. (2013). Ultrahigh gas storage both at low and high pressures in KOH-activated carbonized porous aromatic frameworks. *Sci. Rep.* 3:2420. doi: 10.1038/srep02420

Liang, Y., Harrison, D. P., Gupta, R. P., Green, D. A., and McMichael, W. J. (2004). Carbon dioxide capture using dry sodium-based sorbents. *Energy Fuels* 18, 569–575. doi: 10.1021/ef030158f

Liou, T. H. (2010). Development of mesoporous structure and high adsorption capacity of biomass-based activated carbon by phosphoric acid and zinc chloride activation. *Chem. Eng. J.* 158, 129–142. doi: 10.1016/j.cej.2009.12.016

Liu, B., Shioyama, H., Jiang, H., Zhang, X., and Xu, Q. (2010). Metal-organic framework (MOF) as a template for syntheses of nanoporous carbons as electrode materials for supercapacitor. *Carbon* 48, 456–463. doi: 10.1016/j.carbon.2009.09.061

Liu, H., Cao, C. Y., Wei, F. F., Jiang, Y., Sun, Y. B., Huang, P. P., et al. (2013). Fabrication of macroporous/mesoporous carbon nanofiber using $CaCO_3$ nanoparticles as dual purpose template and its application as catalyst support. *J. Phys. Chem. C* 117, 21426–21432. doi: 10.1021/jp4078807

Lu, C., Bai, H., Wu, B., Su, F., and Hwang, J. F. (2008). Comparative study of CO_2 capture by carbon nanotubes, activated carbons, and zeolites. *Energy Fuels* 22, 3050–3056. doi: 10.1021/ef8000086

Mahurin, S. M., Górka, J., Nelson, K. M., Mayes, R. T., and Dai, S. (2014). Enhanced CO_2/N_2 selectivity in amidoxime-modified porous carbon. *Carbon* 67, 457–464. doi: 10.1016/j.carbon.2013.10.018

Marszewska, J., and Jaroniec, M. (2017). Tailoring porosity in carbon spheres for fast carbon dioxide adsorption. *J. Colloid Interf. Sci.* 487, 162–174. doi: 10.1016/j.jcis.2016.10.033

Megías-Sayago, C., Bingre, R., Huang, L., Lutzweiler, G., Wang, Q., and Louis, B. (2019). CO_2 adsorption capacities in zeolites and layered double hydroxide materials. *Front. Chem.* 7:551. doi: 10.3389/fchem.2019.00551

Meng, L. Y., and Park, S. J. (2012). Influence of MgO template on carbon dioxide adsorption of cation exchange resin-based nanoporous carbon. *J. Colloid Interf. Sci.* 366, 125–129. doi: 10.1016/j.jcis.2011.09.019

Patel, H. A., Byun, J., and Yavuz, C. T. (2017). Carbon dioxide capture adsorbents: chemistry and methods. *ChemSusChem* 10, 1303–1317. doi: 10.1002/cssc.201601545

Patiño, J., Gutiérrez, M. C., Carriazo, D., Ania, C. O., Fierro, J. L. G., Ferrer, M. L., et al. (2014). DES assisted synthesis of hierarchical nitrogen-doped carbon molecular sieves for selective CO_2 versus N_2 adsorption. *J. Mater. Chem. A* 2, 8719–8729. doi: 10.1039/C4TA00562G

Pullar, R. C., Novais, R. M., Caetano, A. P. F., Barreiros, M. A., Abanades, S., and Oliveira, F. A. C. (2019). A review of solar thermochemical CO_2 splitting using ceria-based ceramics with designed morphologies and microstructures. *Front. Chem.* 7:601. doi: 10.3389/fchem.2019.00601

Qi, K., Cheng, B., Yu, J., and Ho, W. (2017). A review on TiO_2-based Z-scheme photocatalysts. *Chin. J. Catal.* 38, 1936–1955. doi: 10.1016/S1872-2067(17)62962-0

Qi, K., Xie, Y., Wang, R., Liu, S., and Zhao, Z. (2019). Electroless plating Ni-P cocatalyst decorated g-C_3N_4 with enhanced photocatalytic water splitting for H_2 generation. *Appl. Surf. Sci.* 466, 847–853. doi: 10.1016/j.apsusc.2018.10.037

Santis, A. D., Ingham, D. B., Ma, L., and Pourkashanian, M. (2016). CFD analysis of exhaust gas recirculation in a micro gas turbine combustor for CO_2 capture. *Fuel* 173, 146–154. doi: 10.1016/j.fuel.2016.01.063

Shi, W., Xu, X., Ye, C., Sha, D., Yin, R., Shen, X., et al. (2019). Bimetallic metal-organic framework-derived carbon nanotube-based frameworks for enhanced capacitive deionization and Zn-air battery. *Front. Chem.* 7:449. doi: 10.3389/fchem.2019.00449

Sing, K. S. W. (1985). Reporting physisorption data for gas/solid systems with special reference to the determination of surface area and porosity (Recommendations 1984). *Pure Appl. Chem.* 57, 603–619. doi: 10.1351/pac198557040603

Son, I. H., Lee, S. J., and Roh, H. S. (2014). Hydrogen production from carbon dioxide reforming of methane over highly active and stable MgO promoted Co-Ni/γ-Al_2O_3 catalyst. *Int. J. Hydrogen Energy* 39, 3762–3770. doi: 10.1016/j.ijhydene.2013.12.141

Song, H., Liu, Z., Gai, H., Wang, Y., Qiao, L., Zhong, C., et al. (2019). Nitrogen-dopped ordered mesoporous carbon anchored Pd nanoparticles for solvent free selective oxidation of benzyl alcohol to benzaldehyde by using O_2. *Front. Chem.* 7:458. doi: 10.3389/fchem.2019.00458

Sun, Q., Yang, Y., Zhao, Z., Zhang, Q., Zhao, X., Nie, G., et al. (2018). Elaborate design of polymeric nanocomposites with Mg(ii)-buffering nanochannels for highly efficient and selective removal of heavy metals from water: case study for Cu(ii). *Environ. Sci. Nano* 5, 2440–2451. doi: 10.1039/C8EN00611C

Wang, W., Chu, W., Wang, N., Yang, W., and Jiang, C. (2016). Mesoporous nickel catalyst supported on multi-walled carbon nanotubes for carbon dioxide methanation. *Int. J. Hydrogen Energy* 41, 967–975. doi: 10.1016/j.ijhydene.2015.11.133

Wei, J., Zhou, D., Sun, Z., Deng, Y., Xia, Y., and Zhao, D. (2013). A controllable synthesis of rich nitrogen-doped ordered mesoporous carbon for CO_2 capture and supercapacitors. *Adv. Funct. Mater.* 23, 2322–2328. doi: 10.1002/adfm.201202764

Wickramaratne, N. P., and Jaroniec, M. (2013a). Activated carbon spheres for CO_2 adsorption. *ACS Appl. Mater. Interfaces* 5, 1849–1855. doi: 10.1021/am400112m

Wickramaratne, N. P., and Jaroniec, M. (2013b). Importance of small micropores in CO_2 capture by phenolic resin-based activated carbon spheres. *J. Mater. Chem. A* 1, 112–116. doi: 10.1039/C2TA00388K

Wu, X. L., Jiang, L. Y., Cao, F. F., Guo, Y. G., and Wan, L. J. (2009). $LiFePO_4$ nanoparticles embedded in a nanoporous carbon matrix: superior cathode material for electrochemical energy-storage devices. *Adv. Mater.* 21, 2710–2714. doi: 10.1002/adma.200802998

Xia, K., Tian, X., Fei, S., and You, K. (2014). Hierarchical porous graphene-based carbons prepared by carbon dioxide activation and their gas adsorption properties. *Int. J. Hydrogen Energy* 39, 11047–11054. doi: 10.1016/j.ijhydene.2014.05.059

Xia, Y., Tian, Z., Heil, T., Meng, A., Cheng, B., Cao, S., et al. (2019). Highly selective CO_2 capture and its direct photochemical conversion on ordered 2D/1D heterojunctions. *Joule* 3, 2792–2805. doi: 10.1016/j.joule.2019.08.011

Xu, B., Shi, L., Guo, X., Peng, L., Wang, Z., Chen, S., et al. (2011). Nano-$CaCO_3$ templated mesoporous carbon as anode material for Li-ion batteries. *Electrochim. Acta* 56, 6464–6468. doi: 10.1016/j.electacta.2011.04.130

Xu, K., Pan, Q., Zheng, F., Zhong, G., Wang, C., Wu, S., et al. (2019). Hierarchical nitrogen-doped porous carbon microspheres as anode for high performance sodium ion batteries. *Front. Chem.* 7:733. doi: 10.3389/fchem.2019.00733

Yaumi, A. L., Abu Bakar, M. Z., and Hameed, B. H. (2017). Recent advances in functionalized composite solid materials for carbon dioxide capture. *Energy* 124, 461–480. doi: 10.1016/j.energy.2017.02.053

Zhang, Q., Bolisetty, S., Cao, Y., Handschin, S., Adamcik, J., Peng, Q., et al. (2019). Selective and efficient removal of fluoride from water: *in situ* engineered amyloid fibril/ZrO_2 hybrid membranes. *Angew. Chem. Int. Ed.* 58, 6012–6016. doi: 10.1002/anie.201901596

Zhang, Z., Wang, B., Zhu, C., Gao, P., Tang, Z., Sun, N., et al. (2015). Facile one-pot synthesis of mesoporous carbon and N-doped carbon for CO_2 capture by a novel melting-assisted solvent-free method. *J. Mater. Chem. A* 3, 23990–23999. doi: 10.1039/C5TA06465A

Zhao, C., Wang, W., Yu, Z., Zhang, H., Wang, A., and Yang, Y. (2010). Nano-$CaCO_3$ as template for preparation of disordered large mesoporous carbon with hierarchical porosities. *J. Mater. Chem.* 20, 976–980. doi: 10.1039/B911913B

Zhu, B., Wageh, S., Al-Ghamdi, A. A., Yang, S., Tian, Z., and Yu, J. (2019). Adsorption of CO_2, O_2, NO and CO on s-triazine-based g-C_3N_4 surface. *Catalysis Tdy.* 335, 117–127. doi: 10.1016/j.cattod.2018.09.038

Zhu, Q., Zeng, S., and Yu, Y. (2017). A model to stabilize CO_2 uptake capacity during carbonation-calcination cycles and its case of CaO-MgO. *Environ. Sci. Technol.* 51, 552–559. doi: 10.1021/acs.est.6b04100

Conflict of Interest: The authors declare that the research was conducted in the absence of any commercial or financial relationships that could be construed as a potential conflict of interest.

frontiers in Chemistry

ORIGINAL RESEARCH
published: 20 February 2020
doi: 10.3389/fchem.2020.00089

Fatsia Japonica-Derived Hierarchical Porous Carbon for Supercapacitors With High Energy Density and Long Cycle Life

Huiling Li[1], *Lihua Cao*[1], *Feng Wang*[1], *Gaigai Duan*[1], *Wenhui Xu*[2], *Changtong Mei*[1]*, *Guoying Zhang*[3,4], *Kunming Liu*[5], *Meng Yang*[6] *and Shaohua Jiang*[1,3,4]*

[1] *Co-Innovation Center of Efficient Processing and Utilization of Forest Resources, College of Materials Science and Engineering, Nanjing Forestry University, Nanjing, China,* [2] *School of Pharmacy, Jiangxi University of Traditional Chinese Medicine, Nanchang, China,* [3] *Shangdong Key Laboratory of Biochemical Analysis, Qingdao, China,* [4] *College of Chemistry and Molecular Engineering, Qingdao University of Science and Technology, Qingdao, China,* [5] *School of Metallurgical and Chemical Engineering, Jiangxi University of Science and Technology, Ganzhou, China,* [6] *Xiangyang Environmental Protection Monitoring Station, Xiangyang, China*

OPEN ACCESS

Edited by:
Zhengping Zhou,
North Dakota State University,
United States

Reviewed by:
Assad Ullah Khan,
Micron Technology, Inc., United States
Lisha Yang,
University of Nevada, Reno,
United States

***Correspondence:**
Changtong Mei
mei@njfu.edu.cn
Shaohua Jiang
shaohua.jiang@njfu.edu.cn

Specialty section:
This article was submitted to Nanoscience, a section of the journal Frontiers in Chemistry

Received: *15 December 2019*
Accepted: *27 January 2020*
Published: *20 February 2020*

Citation:
Li H, Cao L, Wang F, Duan G, Xu W, Mei C, Zhang G, Liu K, Yang M and Jiang S (2020) Fatsia Japonica-Derived Hierarchical Porous Carbon for Supercapacitors With High Energy Density and Long Cycle Life. Front. Chem. 8:89. doi: 10.3389/fchem.2020.00089

Fatsia Japonica seed, which is mainly composed of glucose, has potential as a porous carbon matrix precursor for supercapacitors that can achieve high-value utilization. Cost-effective hierarchical porous carbon materials (HPC) were prepared from Fatsia Japonica by annealing at high temperature. The pore size and distribution of the HPC can be precisely controlled and adjusted by altering the activation temperature. The HPC obtained at 600°C showed favorable features for electrochemical energy storage, with a surface area of 870.3 m^2/g. The HPC for supercapacitors (a three-electrode system) exhibited good specific capacitance of 140 F/g at a current density of 1 A/g and a long cycling life stability (87.5% remained after 10,000 cycles). In addition, the HPC electrode showed an excellent energy density of 23 Wh/Kg. Such hierarchical porous biomass-derived carbon would be a good candidate for application in the electrodes of supercapacitors due to its simple preparation process and the outstanding electrochemical performance.

Keywords: supercapacitors, hierarchical porous carbon, biomass materials, energy density, long cycle life

INTRODUCTION

With the development of modern social science and technology and the increasing energy demand for power, a new generation of energy devices with advanced, low cost, and sustainable sources have attracted great attention from industry, including supercapacitors (SCs), Li-ion batteries (LIBs), and fuel cells (Shao et al., 2018; Ma et al., 2019; Lei et al., accepted). SCs have been considered as one of the most promising energy storage devices in the last decade for applications in portable electronic devices, vehicles, etc. (Han et al., 2019d; Wang et al., 2019). Due to their high energy density, long cycle life, and fast discharge/charge characteristics, SCs bridge the gap between conventional electrolytic capacitors and LIBs. Based on their energy storage mechanism, supercapacitors can be divided into two categories: electric double-layer capacitors (EDLC) and pseudo-capacitors (Choi et al., 2019; Zhao et al., 2019b). However, the key to the electrochemical performance of SCs lies in the choice and design of electrode materials. Recently, porous carbonaceous materials have been

widely commercialized as active materials for SCs on the basis of their controllable porosity, high specific surface area, and electrochemical stability, but the dramatic drawback of commercial EDLC is a relatively low energy density in the range of 5–10 Wh/Kg (Borenstein et al., 2017; Zhao et al., 2019a; Wang et al., 2020).

Over the years, much effort has been applied toward improving the energy density of carbonaceous materials, such as facilitating a controllable hierarchical porous structure and designing the nanostructure to improve specific surface area and ion transport (Li and Wei, 2013; Benzigar et al., 2018) and doping heteroatoms (N, S, P, etc.) to introduce active reaction sites (Chen et al., 2019; Yan et al., 2019). The most fascinating work is the heteroatom-doping through template method, which can form structural defects on the surface of carbon material to increase conductivity and improve wettability (Huijuan et al., 2017; Li et al., 2017). Na et al. (2017) fabricated nitrogen and fluorine-doped mesoporous carbon nanofibers (NFMCNFs) by the hydrothermal method and a subsequent vacuum plasma process. The NFMCNF electrode exhibited a high specific capacitance of 252.6 F/g at a current density of 0.5 A/g. Lv et al. (2018) prepared N and P co-doped carbon hollow spheres (NPCHSs) through a carbonization and subsequent chemical activation route. The NPCHSs present a high specific surface area of 1,155 m^2/g due to their 3D connected porous structure and a high specific capacitance of 232 F/g at a current density of 1 A/g. Mao et al. (2017) reported N_2-doped graphite (NG) as the negative electrode and a kind of mesoporous $NiCo_2O_4$ nanorod/graphene oxide ($NiCo_2O_4$/GO) composite as the positive electrode. The symmetric supercapacitor displayed high energy density of 34.3 Wh/Kg at a power density of 800 W/Kg. Thus, the prepared porous carbon materials with heteroatom- doping can obviously improve electrochemical performance. However, most active carbons (ACs) on improving electrochemical performance introduce heteroatoms by chemical and physical routes, which can result in high cost, environmentally destructive, and complicated manufacturing. Biomass and its derivatives, not only benefiting from renewable, low-cost, and environmentally friendly properties and but also from being rich in other elements such as nitrogen and oxygen, have been considered as prospective carbon precursors (Abioye and Ani, 2015; Lu et al., 2018; Hou et al., 2019). Many porous carbonaceous materials based on natural sources have been prepared, such as willow catkins (Wang et al., 2015), tea leaves (Song et al., 2019), corncob (Karnan et al., 2017), peanut shell (He et al., 2013), banana peels (Zhang et al., 2016), bamboo (Zequine et al., 2016), seaweed (Ye et al., 2018), biomass-based composites (Sun et al., 2017; Han et al., 2019a) etc., which show good electrochemical performance for EDCL.

Fatsia Japonica, a subtropical species, is native to southern Japan as well as southern China. The plants are commonly used as a graceful ornamental tree and have potential medicinal value (Luo et al., 2012; Shi et al., 2017). The seeds, appearing from October to May of the next year, have a long maintenance period and are plentiful in the tree, so they can be picked at any time. Little research on the composition of Fatsia Japonica has been reported (Ye et al., 2014). Aokia et al. (1981) have analyzed the chemical constituents of the essential oils in the stems, leaves, and fruits of the Fatsia Japonica. A total of 97 compounds were identified in the essential oils extracted from the roots, leaves, and fruits of the Fatsia Japonica, mainly including monoterpenoids and their oxides and semiquinones and their oxides. Thus, the seeds, with have potential as medicines, are rich in other elements (oxygen etc.) besides carbon, which could result in a decrease in cyclic stability due to the provision of a reacting active site. However, biomass material with more oxygen atoms has a self-doping effect that improves the electrochemical performance and wettability of carbon materials. Moreover, the seeds have strong solution absorption capacity due to their macropore structure, which provides an excellent platform for further optimizing their structure and properties (Kil et al., 2008). In order to realize transformation into higher-value products, we induced the seeds to become carbonized under low temperature in our preliminary work. We can observe from scanning electron microscopy (SEM) that the carbon materials obtained possess many macropores, which can be easily controlled to form a hierarchical porous structure. Herein, the aim of our research work is to exploit a novel biomass material with a controllable pore distribution and enrich the choice of precursors for electrode materials of EDLC.

In this work, a facile method involving pre-carbonization at low temperature and subsequent pyrolysis and activation with KOH at high temperatures was developed to fabricate hierarchical porous carbon materials (HPCs) derived from Fatsia Japonica. The HPCs obtained showed remarkable features of good conductivity, high energy density, and promising electrochemical properties. The relationships between the structural characteristics, activation temperatures, and electrochemical performance were investigated intensively.

MATERIALS

The seeds of Fatsia Japonica were obtained from the trees around our laboratory (Nanjing China). All other chemicals were of reagent grade without further purification. Deionized water was used throughout the experiments.

Preparation of Hierarchical Porous Carbon (HPC)

Prior to the synthesis of HPCs, the fresh seeds were first pretreated by soaking in aqueous HCl solution (1 M) for about 2 h, followed by washing with deionized water and oven drying at 60°C for 12 h. Subsequently, the dried seeds were pre-carbonized in a muffle furnace at 300°C to remove other organic substances thoroughly. The sample of pre-carbonized seeds obtained was named PCS. The mixture was then transferred to a crucible, followed by annealing and activating at the desired temperature for 12 h under an N_2 atmosphere (Zhang and Chen, 2015; Hou et al., 2019). The temperature was raised to 300°C at a rate of 3°C/min, then at a rate of 5°C/min. To prepare various HPCs, different carbonization and activation temperatures (e.g., 500, 600, 700, and 800°C) were investigated, and the corresponding samples were designated as HPC-500, HPC-600, HPC-700, and HPC-800, respectively.

Characterization of HPC Samples

Field emission scanning electron microscopy (FESEM) measurements were performed on a JEOL JSM-7001F microscope at an accelerating voltage of 10 kV to observe the morphologies and structures of the samples. The pore structure of the obtained samples was examined through nitrogen adsorption/desorption experiments at 77 K using a micromeritics apparatus (ASAP 2020 V3.02 H). The specific surface area was measured based on the Brunauer-Emmett-Teller (BET) method, and the BJH method was used to calculate the pore size distribution and pore volumes. Raman spectra were collected from a Raman spectrometer (Jobin Yvon, HR800). X-ray photoelectron spectroscopy (XPS) was performed on a KRATOS Axis Ultra photoelectron spectrometer using Al Kα radiation at a power of 225 W.

Electrochemical Measurement

The electrochemical performance of the prepared HPCs was measured by using a three-electrode system in 6 M KOH aqueous electrolyte at room temperature. An Hg/HgO electrode (saturated in 1 M KOH solution) and platinum sheets were used as reference electrode and counter electrodes, respectively. The working electrode was prepared by pressing a slurry mixture of the obtained HPC (80 wt%), acetylene black (10 wt%), and polyvinylidene fluoride (PVDF, 10 wt%) onto a piece of Nickel foam and then dried at 60°C for 12 h. The surface area of the working electrode is about 1 cm^2, and the mass loading of the active materials is about 2 mg/cm^2. Cyclic voltammetry (CV), galvanostatic charge-discharge (GCD), and electrochemical impedance spectroscopy (EIS) tests were carried out on a CHI 600 electrochemical workstation (Shanghai Chenhua, China). The working voltages window was commonly between −1 and 0.1 V.

The specific capacitance in the three-electrode system was calculated from the GCD curves according to the following Equation (1). The energy density and power density were calculated using Equation (2) and Equation (3), respectively.

$$C = \frac{I^* \Delta t}{m^* \Delta V} \tag{1}$$

$$E = \frac{1}{2} C^* \Delta V^2 \tag{2}$$

$$P = \frac{E}{\Delta} t \tag{3}$$

where C is the specific capacitance (F/g), I is the discharge current (A), Δt is the discharge time (s), m represents the mass of active material in the electrode (g), ΔV is the potential change in discharge (V), E is the energy density (Wh/Kg), and P is the power density (W/Kg).

The symmetric supercapacitors using two equal-power electrodes were assembled into a button battery system, and 6 M KOH was used as the electrolyte. The specific capacitance of symmetric supercapacitors was calculated by Equation (4).

$$C = \frac{4I\Delta t}{m\Delta V} \tag{4}$$

where m (g) is the total mass of the active material.

RESULTS AND DISCUSSION

The formation process of HPCs from the seeds of Fatsia Japonica is simply illustrated in **Scheme 1**. Briefly, the fresh seeds were pre-treated with hydrochloric acid (HCl) to remove the inorganic substances preliminarily and then pre-carbonized at a low temperature (300°C) to remove other organic substances. To further optimize the pore structure, pre-carbonized seeds were mixed with KOH and then carbonized at 500, 600, 700, and 800°C, respectively.

The morphologies of HPCs fabricated at different activation temperatures and the PCS without activation are shown in **Figure 1**. Compared to the PCS sample (**Figure 1F**), the samples prepared by the activation process present a sheet-like structure rather than a bulk structure, which shows that the activation process contributes to the fabrication of a porous structure through the activation agent (KOH) etching the wall of the PCS sample with a macropore structure. Based on **Figure 1**, the activation temperature has a major effect on the morphologies and structures of the resultant samples. The samples with different activation temperatures present different degrees of etching by KOH activation. The sample activated at 500°C (**Figure 1A**) exhibits a continuous sheet-like structure. As the temperature rises, the flaky morphology of the samples varies from thinner to fragmented. Especially, the sample HPC-800 (**Figure 1F**) presents a fragmented structure, which is attributed to the strong etching of KOH in the walls of the macropores or the inside of the sample and causes the pores to be larger, breaking up the sheet structure (**Figure 1E**). However, HPC-600 presents a complete layered lamellar structure (**Figures 1B,C**). Compared to HPC-500 and HPC-700, the sample of HPC-600 exhibits a uniform 3D network structure, which is promising for electrolyte ion diffusion (Benzigar et al., 2018). Thus, the sample pyrolyzed at 600°C shows a uniformly connected lamellar structure, which can provide fast channels for ion diffusion during the charge and discharge process.

Raman spectra of the samples are shown in **Figure 2**. Two obvious peaks located at 1,350 and 1,590 cm^{-1} for all the samples correspond to the D and G band, respectively. The G band is related to the degree of graphitization, while the D band is associated with local defects and disordered properties of HPCs (Zheng et al., 2017; He et al., 2019). The intensity ratio I_D/I_G represents the degree of structural graphitization. A higher value means a lower degree of graphitization. The I_D/I_G values of the samples were 0.930, 0.903, 0.933, 0.964, and 0.980, corresponding to HPC-500, HPC-600, HPC-700, HPC-800, and PCS, respectively. As the activation temperature increases from 500 to 600°C, the I_D/I_G value increases, and it tends to decrease from 600 to 800°C. It is observed that the defect degree of the obtained HPC decreases and the degree of graphitization increases at 600°C. Thus, HPC-600 displays a higher degree of graphitization and lower defect degree, so it may possess good conductivity.

Heteroatom doping is one of the common strategies for preparing high-performance supercapacitor carbon materials (Hou et al., 2018; Lee et al., 2018; Kim et al., 2019; Wu et al., 2019). Seeds are rich in a variety of active ingredients, so it is inferred

SCHEME 1 | Schematic illustration of the fabrication process of HPCs.

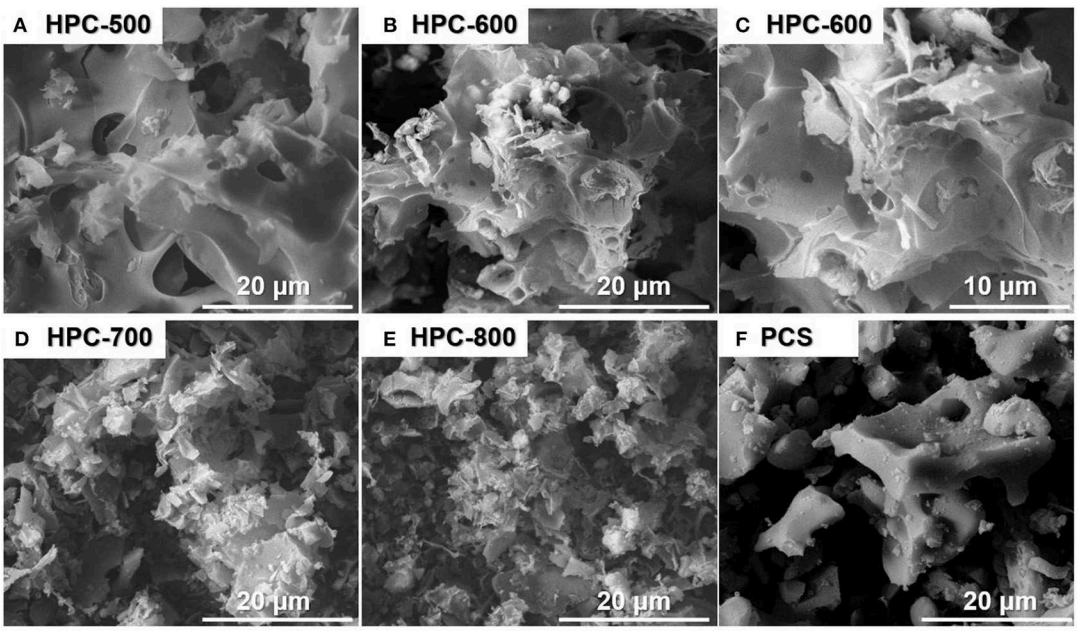

FIGURE 1 | FESEM images of the HPCs prepared at different activation temperatures **(A–E)** and the PCS **(F)**.

that the biomass-derived carbon materials should have self-doped heteroatoms present within them. Thus, XPS (**Figure 3**) was carried out to study the surface chemical composition of the resulting sample. The full XPS spectra of HPC-600 derived from the seeds is shown in **Figure 3A**, from which C 1s, N 1s, and O 1s can be observed. The atomic percentages of C,

N, and O were 82.4, 1.01, and 12.59%, respectively. The high-resolution spectrum of C 1s could be divided into four regions, which is credited to C-N (284.5 eV), C-C/C=C (284.9 eV), C-O (285.8 eV), and C=O (287.5 eV), respectively (**Figure 3B**). The N 1s (**Figure 3C**) spectrum reveals the presence of four nitrogen-based components, including pyridine nitrogen-oxide (N-X, 401.5 eV), graphitic nitrogen (N-Q, 400.8 eV), pyrrolic N (N-5, 399.8 eV), and pyridinic N (N-6, 398.7 eV). The O 1s spectrum was fitted to two individual peaks located at 531.7 and 533.2 eV, corresponding to C = O and C-O, respectively (**Figure 3D**). It can be speculated that the wettability of the prepared HPC could be improved due to heteroatoms (N, O) and high O atomic content (12.59%), which could contribute to the electrochemical performance of electrode materials.

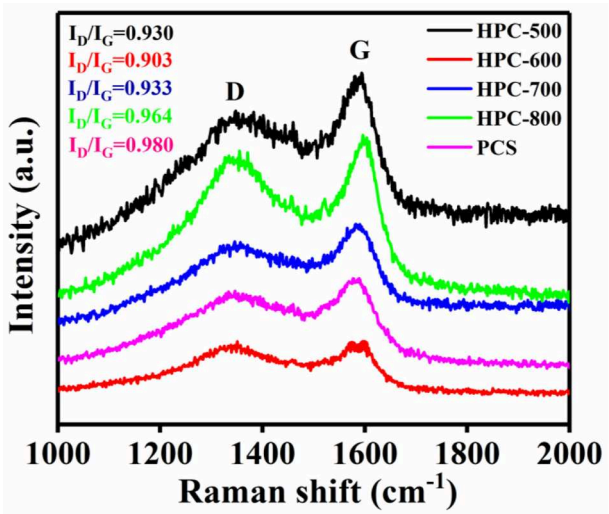

FIGURE 2 | Raman spectra of the HPCs prepared at different temperatures.

To further determine the relationship between morphology and porous structure and examine the formation of hierarchical pores, measurements by BET N_2 adsorption/desorption technology were carried out; the results are depicted in **Figure 4**. According to the nitrogen adsorption and desorption isotherms (**Figure 4A**), the major sorption for the sample of HPC-600 occurs at a low relative pressure from 0.05 to 0.3 and exhibits hysteresis between adsorption and desorption, which is attributed to an obvious capillary phenomenon with the increase in relative pressure. Thus, the sample of HPC-600 shows the IV type nitrogen sorption isotherm, suggesting the existence of mesopores and macropores (Qu et al., 2015). However, the sample of PCS exhibits the II type nitrogen sorption isotherm and hysteresis at relative pressures from 0.01 to 0.8, which only demonstrate the emergence of weak gas-solid interaction. These findings are further supported by the pore size distribution (**Figures 4C,D**). The main pore widths for the sample of HPC-600 are about 2.2 nm and between 60 and 120 nm, which demonstrate the existence of smaller mesopores and macropores, respectively. For the sample of PCS, the pore size is distributed over macropore widths (> 50 nm), which is consistent with

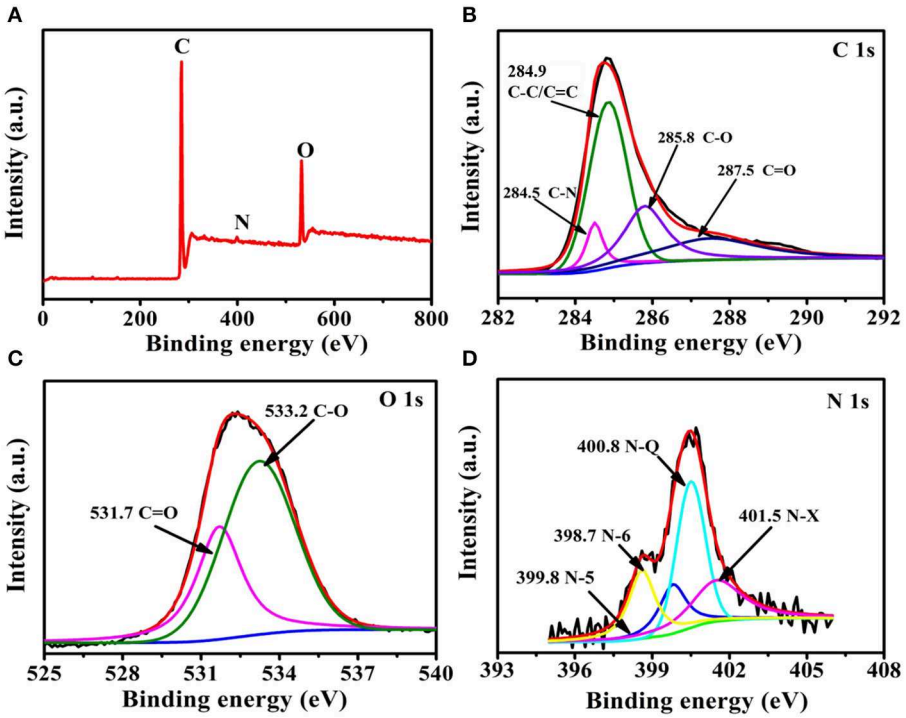

FIGURE 3 | XPS spectra of HPC-600: **(A)** full energy spectrum, **(B)** C 1s, **(C)** O 1s, and **(D)** N 1 s.

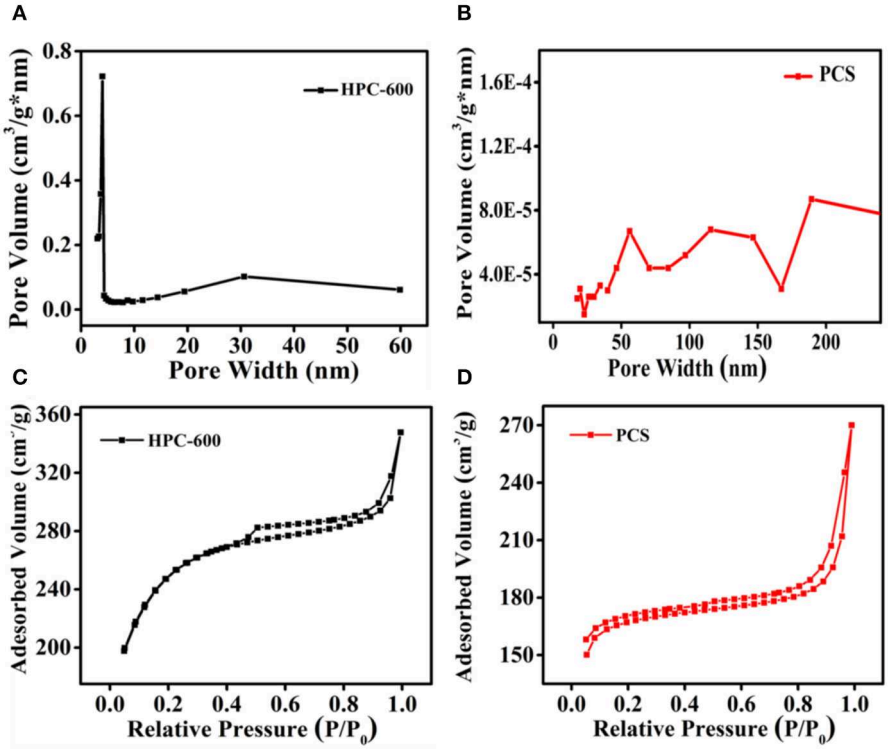

FIGURE 4 | (A,B) Pore size distribution curves of HPC-600 and PCS, and **(C,D)** nitrogen adsorption/desorption isotherms of HPC-600 and PCS.

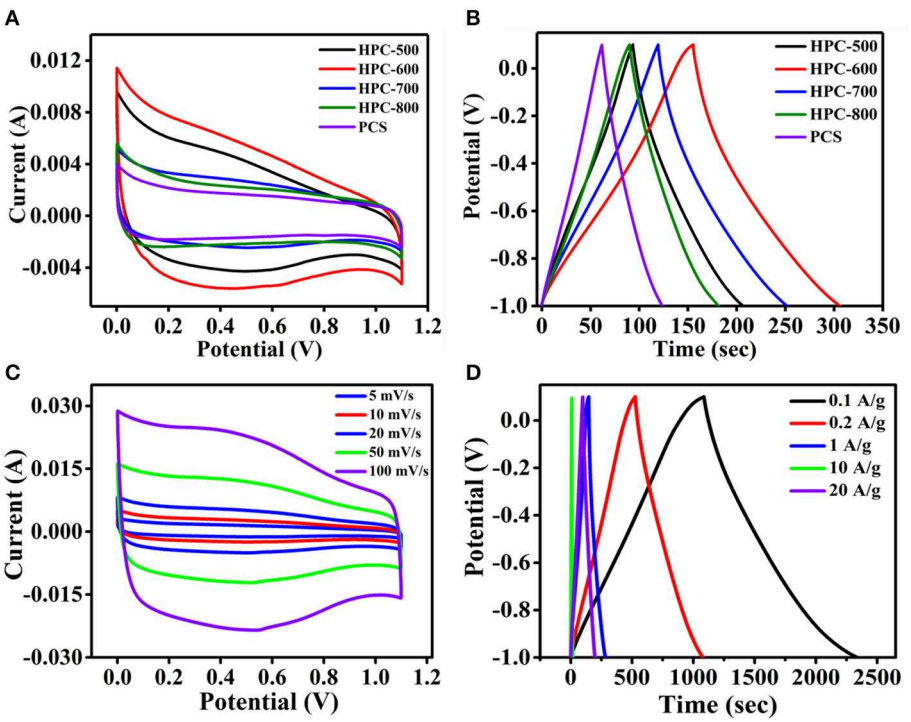

FIGURE 5 | (A) CV curves of the samples HPC-500, HPC-600, HPC-700, HPC-800, and PCS at a scan rate of 10 mV/s; **(B)** GCD curves of HPCs at a current density of 1 A/g; **(C)** CV curves of HPC-600 at different scan rates; **(D)** GCD curves of the sample of HPC-600 at different current densities.

the observed nitrogen sorption isotherms. The specific surface area of HPC-600 (870.3 m^2/g) was significantly higher than that of the PCS (510.6 m^2/g), as were the pore volumes, which offers more contact area for electrolyte penetration. Ordering hierarchical pores can not only provide excellent accessibility to active sites and enhanced mass transport and diffusion during charge and discharge but also improve the specific surface area and electronic and ionic conductivity (Benzigar et al., 2018; Han et al., 2019c). Therefore, combined with the results of FESEM (**Figure 1B**), it can be concluded that HPC-600, with a 3D lamella-like structure, successfully possesses a hierarchical porous structure, which could accelerate the transport of electrons and diffusion of ions in electrolyte, improving the electrochemical performance.

The relationship between a hierarchical porous structure and electrochemical performance can be explained by the activation reaction. At high temperature, the KOH primarily penetrates inside the pore wall of the pre-carbide sample and reacts on the surface of carbon materials to form nanopores or mesopores. Products such as K_2CO_3 are then obtained and continually corrode inside the pre-carbide sample to form a more porous and three-dimensional connected porous structure (Lu et al., 2010; Zhang and Chen, 2015; Eftekhari, 2018). Herein, as the activation temperature raised, the more violent the reaction between KOH and carbon, and the larger the pore volume formed.

To evaluate the electrochemical performance of the hierarchical porous carbon, cyclic voltammetry (CV) and galvanostatic charge/discharge tests were carried out with a three-electrode configuration in an aqueous solution of 6 M KOH; the results are depicted in **Figure 5**. The CV curves of all samples are displayed from **Figure 5A**. One can see that all samples displayed a nearly rectangular shape at 10 mV/s, indicating the formation of an electric double layer and ideal capacitive behaviors. The results can be demonstrated from the GCD curves of all samples at the same current density (**Figure 5B**). **Figure 5B** shows that all samples present an equicrural quasi-triangle shape. However, based on the specific capacitance calculation in equation (3), the discharge time of sample HPC-600 was longer than those of the others, and the specific capacitance was about 140 F/g. This value of specific capacitance is larger than or at a similar level to other carbon materials, as summarized in **Table 1**. It is demonstrated that the sample of HPC-600 possesses better electrochemical performance, due to the evenly distributed mesopore structure and complete 3D lamella-like structure, which provide fast channels for easy ion diffusion in electrolyte.

The capacitive performance of the hierarchical porous materials of HPC-600 was further measured with CV measurement at the same voltage window and GCD measurement at different current densities. **Figure 5C** depicts the CV curves of HPC-600. The HPC does not have faradic current effects during charge and discharge, and the sample presented a quasi-rectangular shape at different scan rates. In addition, as the scan rate increased, HPC-600 was still closer to a rectangular shape. It can be demonstrated that the HPC-600 exhibits excellent rate capability and good electrochemical behavior. This is further shown by the GCD measurement results in **Figure 5D**. The GCD curves are almost linearly symmetrical and display a slight IR drop, even at a high current density of 10 A/g, which implies good reversibility and conductivity. The specific capacitance of the HPC calculated by equation (3) was about 140 F/g at a current density of 1 A/g. This is attributable to the smaller mesopores and connected flaky structure.

The Nyquist plots of HPCs and PCS in a frequency range from 100 kHz to 10 mHz at an open circuit potential in 6 M KOH electrolyte are shown in **Figures 6A**,**B.** All samples display a semicircuit-like shape at the high-frequency region, which is ascribed to interface resistance of electrodes and contact resistance between electrodes and collectors. Although the resistance value of HPC-500 was measured to be about 1.5 Ω, the inherent impendence of HPC-600, HPC-700, HPC-800, and PCS was close to 0.21 Ω, 0.22, 0.08, and 0.06 Ω, respectively, which reveals good electronic transport over the regime and good conductivity of prepared samples. At low frequency, other sample curves are nearly vertically linear (∼90°), apart from the HPC-800 electrode (∼45°), due to over-activation at high temperatures to form destroyed. The slope at low frequency region signifies the degree of ionic penetration from the electrolyte to the surface of the electrode. The larger the slope of the curve, the easier it is for ionic diffusion to occur during the charge/discharge process. The HPC-600 electrode presents the lowest impedance due to having developed a hierarchical pore structure, which implies that HPC-600 could possess better conductivity and excellent ionic diffusion capability (Ding et al., 2018; Han et al., 2019b).

The specific capacitances of HPC-600 at different current densities are shown in **Figure 7A.** The specific capacitance at

TABLE 1 | Comparison of electrochemical performance of carbon-based supercapacitors.

Carbon type	Activating agent	Electrolyte type	Current density	Specific capacitance	References
Banana fiber-derived carbon	$ZnCl_2$	1 M Na_2SO_4	0.5 A/g	74 F/g	Sun and Sun, 2002
Oil palm kernel shell-based carbon	Steam activation	1 M KOH	0.5 A/g	123 F/g	Misnon et al., 2015
Corn stalk core	KOH	3 M KOH	1 A/g	140 F/g	Yu et al., 2018
Rice husk-derived carbon	H_3PO_4	1 M Na_2SO_4	1 A/g	112 F/g	Ganesan et al., 2014
MWCN/activated CNFs	NH_3 steam	6 M KOH	0.5 A/g	160 F/g	Deng et al., 2013
PAN- and PVP-based CNF	None	0.5 H_2SO_4	0.2 A/g	104.5 F/g	Liu et al., 2015
PAN/PMMA-CFs	None	6 M KOH	1 A/g	140 F/g	Zhou et al., 2019
HPC	KOH	6 M KOH	1 A/g	140 F/g	This work

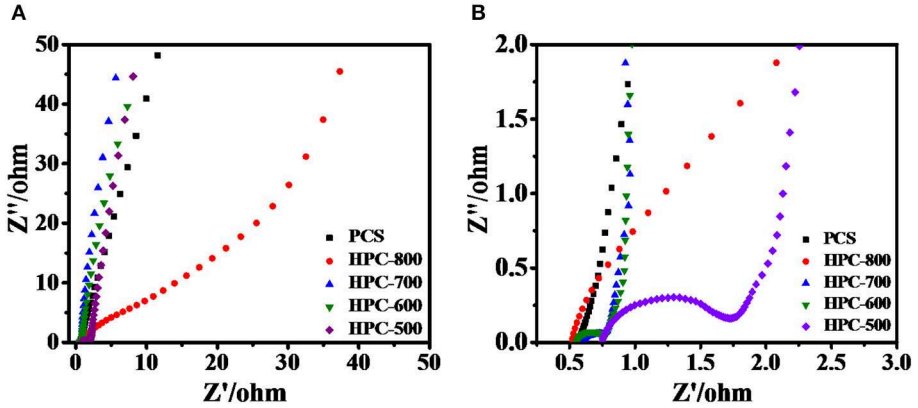

FIGURE 6 | (A) Nyquist plots of HPCs and PCS electrodes, and **(B)** enlarged plots of the high frequency region.

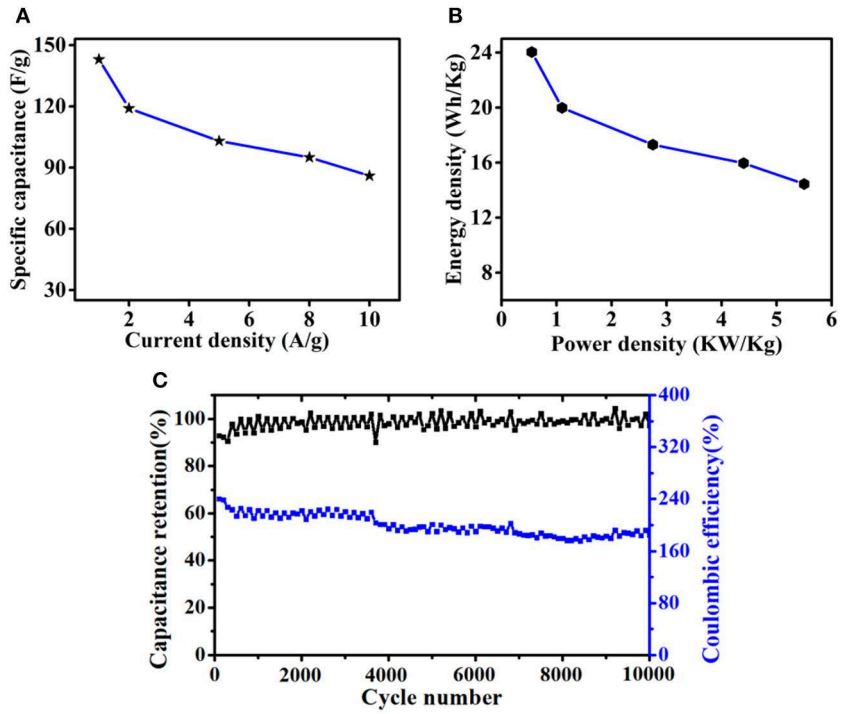

FIGURE 7 | (A) The specific capacitance values of an HPC-600 electrode at different scan rates; **(B)** Ragone plot of an HPC-600 electrode; **(C)** cycling performance of an HPC-600 electrode in a symmetric supercapacitor at a current density of 0.5 A/g.

different current densities increased with increasing activation time. While the current density was 10 A/g, the specific capacitance could still retain 86 F/g. Energy density and power density are two practical parameters for evaluating the overall energy and power properties of SCs. As shown in **Figure 7B**, in an aqueous electrolyte system, the HPC-600-based supercapacitor displays a high energy density of 23 Wh/Kg at a power density of 550 W/Kg and remained at 15 Wh/Kg at 5,500 W/Kg. The results can be attributed to the excellent rate capability of HPC-600 and certify that the power density could vary in a wide range without obviously compromising the energy density. Furthermore, cycle stability is an important factor determining whether the material can be used in practical applications. As shown in **Figure 7C**, HPC-600 as the electrode materials was assembled into a symmetric supercapacitor. The cycle stability of HPC-600 was examined by continuous cycling at 0.5 A/g over 10,000 cycles, and the capacitance retention was 87.5% at 0.5 A/g, demonstrating excellent electrochemical cycling stability

for the HPC-600 electrode. In addition, the coulombic efficiency remained 99.9% after 10,000 cycles.

CONCLUSIONS

In summary, a high-performance hierarchical porous carbon for use as supercapacitor electrode materials was successfully achieved by a simple pyrolysis and KOH-activation process. The prepared HPCs derived from Fatsia Japonica show an unusual interconnected hierarchical porous structure composed of meso- and micro- pores despite having a specific surface area of 870.3 m^2/g. Under optimized conditions, the HPC-600 obtained exhibits a high specific capacitance (140 F/g at a current density of 1 A/g) and also shows excellent cycling stability (87.5% retention after 10,000 cycles). Moreover, the HPC-600-based supercapacitor possesses a power density of about 550 W/Kg and a high energy density of about 23 Wh/Kg, which is about 20% higher than commercial activated carbons. Therefore, it is greatly promising that the sustainable and environmental HPC at activation temperature of 600°C can be used as commercial supercapacitors electrode materials employing Fatsia Japonica, considering the simple large-scale production method and high electrochemical performance.

DATA AVAILABILITY STATEMENT

All datasets generated for this study are included in the article/supplementary material.

AUTHOR CONTRIBUTIONS

SJ provided the idea of the article and corrected the article. HL conducted the experiment and writing. LC assisted in experiments and solved problems on the experiment. FW solved problems on the experiment. GD solved problems on the experiment and corrected data graph. WX provided advice and correction on the revised manuscript. CM provided financial support and instructed the experiment. GZ revised the manuscript and provided final proof. KL and MY provided testing condition.

FUNDING

This work was financially supported by the National Science Foundation of China (51803093 and 51903123), Natural Science Foundation of Jiangsu Province (BK20180770 and BK2019), and open project of the Chemistry Department of Qingdao University of Science and Technology (QUSTHX201921).

REFERENCES

Abioye, A. M., and Ani, F. N. (2015). Recent development in the production of activated carbon electrodes from agricultural waste biomass for supercapacitors: a review. *Renew. Sustain. Energy Rev.* 52, 1282–1293. doi: 10.1016/j.rser.2015.07.129

Aokia, T., Shido, K., Takahashi, Y., and Suga, T. (1981). Structures of 3,28-O-bisglycosidic triterpenoid saponins of fatsia japonica. *Phytochemistry* 20, 1681–1686. doi: 10.1016/S0031-9422(00)98554-6

Benzigar, M. R., Talapaneni, S. N., Joseph, S., Ramadass, K., Singh, G., Scaranto, J., et al. (2018). Recent advances in functionalized micro and mesoporous carbon materials: synthesis and applications. *Chem. Soc. Rev.* 47, 2680–2721. doi: 10.1039/C7CS00787F

Borenstein, A., Hanna, O., Attias, R., Luski, S., Brousse, T., and Aurbach, D. (2017). Carbon-based composite materials for supercapacitor electrodes: a review. *J. Mater. Chem. A* 5, 12653–12672. doi: 10.1039/C7TA00863E

Chen, D., Yang, L., Li, J., and Wu, Q. (2019). Effect of self-doped heteroatoms in biomass-derived activated carbon for supercapacitor applications. *Chem. Select* 4, 1586–1595. doi: 10.1002/slct.201803413

Choi, C., Ashby, D. S., Butts, D. M., DeBlock, R. H., Wei, Q., Lau, J., et al. (2019). Achieving high energy density and high power density with pseudocapacitive materials. *Nat. Rev. Mater.* 5, 5–19. doi: 10.1038/s41578-019-0142-z

Deng, L., Young, R. J., Kinloch, I. A., Abdelkader, A. M., Holmes, S. M., De Haro-Del Rio D. A., et al. (2013). Supercapacitance from cellulose and carbon nanotube nanocomposite fibers. *ACS Appl. Mater. Interf.* 5, 9983–9990. doi: 10.1021/am403622v

Ding, Q., Xu, X., Yue, Y., Mei, C., Huang, C., Jiang, S., et al. (2018). Nanocellulose-mediated electroconductive self-healing hydrogels with high strength, plasticity, viscoelasticity, stretchability, and biocompatibility toward multifunctional applications. *ACS Appl. Mater. Interf.* 10, 27987–28002. doi: 10.1021/acsami.8b09656

Eftekhari, A. (2018). On the mechanism of microporous carbon supercapacitors. *Mater. Today Chem.* 7, 1–4. doi: 10.1016/j.mtchem.2017.11.004

Ganesan, A., Mukherjee, R., Raj, J., and Shaijumon, M. M. (2014). Nanoporous rice husk derived carbon for gas storage and high performance electrochemical energy storage. *J. Porous Mater.* 21, 839–847. doi: 10.1007/s10934-014-9833-4

Han, J., Ding, Q., Mei, C., Wu, Q., Yue, Y., and Xu, X. (2019a). An intrinsically self-healing and biocompatible electroconductive hydrogel based on nanostructured nanocellulose-polyaniline complexes embedded in a viscoelastic polymer network towards flexible conductors and electrodes. *Electrochim. Acta* 318, 660–672. doi: 10.1016/j.electacta.2019.06.132

Han, J., Lu, K., Yue, Y., Mei, C., Huang, C., Wu, Q., et al. (2019b). Nanocellulose-templated assembly of polyaniline in natural rubber-based hybrid elastomers toward flexible electronic conductors. *Indus. Crops Prod.* 128, 94–107. doi: 10.1016/j.indcrop.2018.11.004

Han, J., Wang, H., Yue, Y., Mei, C., Chen, J., Huang, C., et al. (2019c). A self-healable and highly flexible supercapacitor integrated by dynamically cross-linked electro-conductive hydrogels based on nanocellulose-templated carbon nanotubes embedded in a viscoelastic polymer network. *Carbon* 149, 1–18. doi: 10.1016/j.carbon.2019.04.029

Han, J., Wang, S., Zhu, S., Huang, C., Yue, Y., Mei, C., et al. (2019d). Electrospun core-shell nanofibrous membranes with nanocellulose-stabilized carbon nanotubes for use as high-performance flexible supercapacitor electrodes with enhanced water resistance, thermal stability, and mechanical toughness. *ACS Appl. Mater. Interf.* 11, 44624–44635. doi: 10.1021/acsami.9b16458

He, H., Huang, D., Tang, Y., Wang, Q., Ji, X., Wang, H., et al. (2019). Tuning nitrogen species in three-dimensional porous carbon via phosphorus doping for ultra-fast potassium storage. *Nano Energy* 57, 728–736. doi: 10.1016/j.nanoen.2019.01.009

He, X., Ling, P., Qiu, J., Yu, M., Zhang, X., Yu, C., et al. (2013). Efficient preparation of biomass-based mesoporous carbons for supercapacitors with both high energy density and high power density. *J. Power Sour.* 240, 109–113. doi: 10.1016/j.jpowsour.2013.03.174

Hou, H., Xu, W., and Ding, Y. (2018). The recent progress on high-performance polymer nanofibers by electrospinning. *J. Jiangxi Norm, Univer.* 42, 551–564. doi: 10.16357/j.cnki.issn1000-5862.2018.06.01

Hou, L., Hu, Z., Wang, X., Qiang, L., Zhou, Y., Lv, L., et al. (2019). Hierarchically porous and heteroatom self-doped graphitic biomass carbon for supercapacitors. *J. Colloid Interf. Sci.* 540, 88–96. doi: 10.1016/j.jcis.2018.12.029

Huijuan, C., Yibo, G., Limin, G., Liang, W., Zhen, Z., and Zhangquan, P. (2017). Heteroatom-doped carbon materials and their composites as electrocatalysts for CO_2 reduction. *J. Mater. Chem. A* 6, 18782–18793. doi: 10.1039/C8TA07430E

Karnan, M., Subramani, K., Srividhya, P. K., and Sathish, M. (2017). Electrochemical studies on corncob derived activated porous carbon

for supercapacitors application in aqueous and non-aqueous electrolytes. *Electrochim. Acta* 228, 586–596. doi: 10.1016/j.electacta.2017.01.095

Kil, M. J., Kim, K. J., Cho, J. K., and Park, C. H. (2008). Formaldehyde gas removal effects and physiological responses of fatsia japonica and epipremnum aureum according to various light. *Intensity* 26, 189–196. doi: 10.1007/s10658-007-9256-z

Kim, C., Zhu, C., Aoki, Y., and Habazaki, H. (2019). Heteroatom-doped porous carbon with tunable pore structure and high specific surface area for high performance supercapacitors. *Electrochim. Acta* 314, 173–187. doi: 10.1016/j.electacta.2019.05.074

Lee, J.-S. M., Briggs, M. E., Hu, C.-C., and Cooper, A. I. (2018). Controlling electric double-layer capacitance and pseudocapacitance in heteroatom-doped carbons derived from hypercrosslinked microporous polymers. *Nano Energy* 46, 277–289. doi: 10.1016/j.nanoen.2018.01.042

Lei, Y., Wang, Q., Peng, S., Ramakrishna, S., Zhang, D., and Zhou, K. (accepted). Electrospun inorganic nanofibers for oxygen electrocatalysis: design, fabrication and progress. *Adv. Energy Mater*. doi: 10.1002/aenm.201902115

Li, X., and Wei, B. (2013). Supercapacitors based on nanostructured carbon. *Nano Energy* 2, 159–173. doi: 10.1016/j.nanoen.2012.09.008

Li, Y., Miao, P., Zhou, W., Gong, X., and Zhao, X. (2017). N-doped carbon-dots for luminescent solar concentrators. *J. Mater. Chem. A* 5, 21452–21459. doi: 10.1039/C7TA05220K

Liu, Y., Zhou, J., Chen, L., Zhang, P., Fu, W., Zhao, H., et al. (2015). Highly flexible freestanding porous carbon nanofibers for electrodes materials of high-performance all-carbon supercapacitors. *ACS Appl. Mater. Interf.* 7, 23515–23520. doi: 10.1021/acsami.5b06107

Lu, C., Xu, S., and Liu, C. (2010). The role of K2CO3 during the chemical activation of petroleum coke with KOH. *J. Analyt. Appl. Pyrol.* 87, 282–287. doi: 10.1016/j.jaap.2010.02.001

Lu, S.-Y., Jin, M., Zhang, Y., Niu, Y., Jiechang, G., and Li, C. (2018). Chemically exfoliating biomass into a graphene-like porous active carbon with rational pore structure, good conductivity, and large surface area for high-performance supercapacitors. *Adv. Energy Mater.* 8:1702545. doi: 10.1002/aenm.201702545

Luo, R., Liu, B., Xie, Y., Li, Z., Huang, W., Yuan, J., et al. (2012). SOAPdenovo2: an empirically improved memory-efficient short-read de novo assembler. *Gigascience* 1:18. doi: 10.1186/2047-217X-1-18

Lv, B., Li, P., Liu, Y., Lin, S., Gao, B., and Lin, B. (2018). Nitrogen and phosphorus co-doped carbon hollow spheres derived from polypyrrole for high-performance supercapacitor electrodes. *Appl. Surf. Sci.* 437, 169–175. doi: 10.1016/j.apsusc.2017.12.171

Ma, W., Li, W., Liu, R., Cao, M., Zhao, X., and Gong, X. (2019). Carbon dots and AIE molecules for highly efficient tandem luminescent solar concentrators. *Chem. Commun.* 55, 7486–7489. doi: 10.1039/C9CC02676B

Mao, J. W., He, C. H., Qi, J. Q., Zhang, A. B., Sui, Y. W., He, Y. Z., et al. (2017). An asymmetric supercapacitor with mesoporous $NiCo_2O_4$ nanorod/graphene composite and N-doped graphene electrodes. *J. Electron. Mater.* 47, 512–520. doi: 10.1007/s11664-017-5809-x

Misnon, I. I. N., Zain, K. M., Aziz, R. A., Vidyadharan, B., and Jose, R. (2015). Electrochemical properties of carbon from oil palm kernel shell for high performance supercapacitors. *Electrochim. Acta* 174, 78–86. doi: 10.1016/j.electacta.2015.05.163

Na, W., Jun, J., Park, J. W., Lee, G., and Jang, J. (2017). Highly porous carbon nanofibers co-doped with fluorine and nitrogen for outstanding supercapacitor performance. *J. Mater. Chem. A* 5, 17379–17387. doi: 10.1039/C7TA04406B

Qu, W. H., Xu, Y. Y., Lu, A. H., Zhang, X. Q., and Li, W. C. (2015). Converting biowaste corncob residue into high value added porous carbon for supercapacitor electrodes. *Bioresour. Technol.* 189, 285–291. doi: 10.1016/j.biortech.2015.04.005

Shao, Y., El-Kady, M. F., Sun, J., Li, Y., Zhang, Q., Zhu, M., et al. (2018). Design and mechanisms of asymmetric supercapacitors. *Chem. Rev.* 118, 9233–9280. doi: 10.1021/acs.chemrev.8b00252

Shi, N. N., Du, Y. X., Chen, F. R., Ruan, H. C., and Yang, X. J. (2017). First report of leaf spot caused by colletotrichum fructicola on Japanese fatsia (Fatsia japonica) in Fujian Province in China. *Plant Dis.* 101, 1552–1552. doi: 10.1094/PDIS-12-16-1720-PDN

Song, X., Ma, X., Li, Y., Ding, L., and Jiang, R. (2019). Tea waste derived microporous active carbon with enhanced double-layer supercapacitor behaviors. *Appl. Surf. Sci.* 487, 189–197. doi: 10.1016/j.apsusc.2019.04.277

Sun, Y., and Sun, G. (2002). Synthesis, characterization, and antibacterial activities of novel N-halamine polymer beads prepared by suspension copolymerization. *Macromolecules* 35, 8909–8912. doi: 10.1021/ma020691e

Sun, Z., Song, W., Zhao, G., and Wang, H. (2017). Chitosan-based polymer gel paper actuators coated with multi-wall carbon nanotubes and MnO2 composite electrode. *Cellulose* 24, 4383–4392. doi: 10.1007/s10570-017-1416-5

Wang, H., Biswas, S. K., Zhu, S., Lu, Y., Yue, Y., Han, J., et al., (2020). Self-healable electro-conductive hydrogels based on core-shell structured nanocellulose/carbon nanotubes hybrids for use as flexible supercapacitors. *Nanomaterials* 10:E112. doi: 10.3390/nano10010112

Wang, K., Zhao, N., Lei, S., Yan, R., Tian, X., Wang, J., et al. (2015). Promising biomass-based activated carbons derived from willow catkins for high performance supercapacitors. *Electrochim. Acta* 166, 1–11. doi: 10.1016/j.electacta.2015.03.048

Wang, Y., Qu, Q., Gao, S., Tang, G., Liu, K., He, S., et al. (2019). Biomass derived carbon as binder-free electrode materials for supercapacitors. *Carbon* 155, 706–726. doi: 10.1016/j.carbon.2019.09.018

Wu, H., Yuan, W., Zhao, Y., Han, D., Yuan, X., and Cheng, L. (2019). B, N-dual doped sisal-based multiscale porous carbon for high-rate supercapacitors. *RSC Adv.* 9, 1476–1486. doi: 10.1039/C8RA09663E

Yan, J., Zhu, D., Lv, Y., Xiong, W., Liu, M., and Gan, L. (2019). Water-in-salt electrolyte ion-matched N/O codoped porous carbons for high-performance supercapacitors. *Chin. Chem. Lett.* 31, 579–582. doi: 10.1016/j.cclet.2019.05.035

Ye, T., Li, D., Liu, H., She, X., Xia, Y., Zhang, S., et al. (2018). Seaweed biomass-derived flame-retardant gel electrolyte membrane for safe solid-state supercapacitors. *Macromolecules* 51, 9360–9367. doi: 10.1021/acs.macromol.8b01955

Ye, X., Yu, S., Lian, X. Y., and Zhang, Z. (2014). Quantitative determination of triterpenoid glycosides in Fatsia japonica Decne. & Planch. using high performance liquid chromatography. *J. Pharmaceuti. Biomed. Analy.* 88, 472–476. doi: 10.1016/j.jpba.2013.09.017

Yu, K., Zhu, H., Qi, H., and Liang, C. (2018). High surface area carbon materials derived from corn stalk core as electrode for supercapacitor. *Diamond Relat. Mater.* 88, 18–22. doi: 10.1016/j.diamond.2018.06.018

Zequine, C., Ranaweera, C. K., Wang, Z., Singh, S., Tripathi, P., Srivastava, O. N., et al. (2016). High per formance and flexible supercapacitors based on carbonized bamboo fibers for wide temperature applications. *Sci. Rep.* 6:31704. doi: 10.1038/srep31704

Zhang, X., and Chen, W. (2015). Mechanisms of pore formation on multi-wall carbon nanotubes by KOH activation. *Micropor. Mesopor. Mater.* 206, 194–201. doi: 10.1016/j.micromeso.2014.12.002

Zhang, Y., Gao, Z., Song, N., and Li, X. (2016). High-performance supercapacitors and batteries derived from activated banana-peel with porous structures. *Electrochim. Acta* 222, 1257–1266. doi: 10.1016/j.electacta.2016.11.099

Zhao, Z., Wang, X., Yao, M., Liu, L., Niu, Z., and Chen, J. (2019a). Activated carbon felts with exfoliated graphene nanosheets for flexible all-solid-state supercapacitors. *Chin. Chem. Lett.* 30, 915–918. doi: 10.1016/j.cclet.2019.03.003

Zhao, Z., Zeng, L., Cheng, G., Yu, L., and Zeng, H. (2019b). Ni/Co-based metal-organic frameworks as electrode material for high performance supercapacitors. *Chin. Chem. Lett.* 30, 605–609. doi: 10.1016/j.cclet.2018.10.018

Zheng, M., Zhang, S., Chen, S., Lin, Z., Pang, H., and Yu, Y. (2017). Activated graphene with tailored pore structure parameters for long cycle-life lithium–sulfur batteries. *Nano Res.* 10, 4305–4317. doi: 10.1007/s12274-017-1659-3

Zhou, Z., Liu, T., Khan, A. U., and Liu, G. (2019). Block copolymer–based porous carbon fibers. *Sci. Adv.* 5:eaau6852. doi: 10.1126/sciadv.aau6852

Conflict of Interest: The authors declare that the research was conducted in the absence of any commercial or financial relationships that could be construed as a potential conflict of interest.

frontiers in Chemistry

ORIGINAL RESEARCH
published: 28 February 2020
doi: 10.3389/fchem.2020.00150

Comparative Study on the Regeneration of Fe_3O_4@Graphene Oxide Composites

Zhongliang Hu, Xiaojing Zhang, Jingying Li and Yirong Zhu**

Department of Inorganic Nonmetallic Material, College of Metallurgy and Material Engineering, Hunan University of Technology, Zhuzhou, China

In this study, two kinds of composites with the structure of graphene oxide (GO) sheets wrapped magnetic nanoparticles were investigated on their regeneration. The composites have a similar core-shell structure, but the interactions between the core and shell are quite different, which are electrostatic and covalent. They were characterized by scanning/transmission electron microscopy, power X-ray diffraction, and vibrating sample magnetometer analysis. Their morphologies and structures of the samples had been revealed using methylene blue and Pb(II) as adsorbates during regeneration. The results showed that the composites with covalent bonding interaction could maintain a stable core-shell structure and present a good regeneration performance for adsorption-desorption of methylene blue and Pb(II). The composites with electrostatic interaction could approximately preserve its core-shell structure and could be recyclable for adsorption-desorption of methylene blue, however, they would disintegrate its core-shell structure during adsorption/desorption of Pb(II), thus greatly decreasing their regeneration performance. The regeneration mechanisms of the composites were analyzed, which could provide a useful theoretical guide to design the GO sheets wrapped magnetic nanoparticles composites.

Keywords: graphene oxide, regeneration, Fe_3O_4, core-shell structure, magnetic graphene based composites

OPEN ACCESS

Edited by:
Angang Dong,
Fudan University, China

Reviewed by:
Huaibin Shen,
Henan University, China
Yanbin Cui,
Institute of Process Engineering (CAS), China

****Correspondence:***
Zhongliang Hu
david10103@sina.com
Yirong Zhu
zhuyirong2004@163.com

Specialty section:
This article was submitted to Nanoscience, a section of the journal Frontiers in Chemistry

Received: *12 December 2019*
Accepted: *17 February 2020*
Published: *28 February 2020*

Citation:
Hu Z, Zhang X, Li J and Zhu Y (2020) Comparative Study on the Regeneration of Fe_3O_4@Graphene Oxide Composites. Front. Chem. 8:150. doi: 10.3389/fchem.2020.00150

INTRODUCTION

Due to the unique structure and excellent characteristics, graphene and its derivatives have attracted more and more interests in the scientific community (Geim and Novoselov, 2007; Smith and Rodrigues, 2015; Nandhanapalli et al., 2019). Recently, graphene-based composites have been largely investigated as adsorption materials, which displayed excellent performances for adsorption of heavy metal ions, organic and dyes (Mi et al., 2012; Sitko et al., 2013; Yoon et al., 2016; Liu et al., 2018; Li et al., 2019). Notably, magnetic graphene oxide (GO) composites have been regarded as promising adsorbents for water purification because they could be easily separated from solution under an external magnetic field, thus overcoming the limitation of GO's difficult separation in solution (Chandra et al., 2010; He et al., 2010; Ma et al., 2018). However, GO sheets tend to restack, thus inevitably reducing their surface area and adsorption capacity (Bourlinos et al., 2003).

To further improve the performance, some researchers have attempted to wrap Fe_3O_4 nanoparticles (NPs) with GO sheets and the obtained GO@Fe_3O_4 displayed excellent adsorption performance toward pollutants (Wei et al., 2012; Pan et al., 2016). Compared with the magnetic GO composites where Fe_3O_4 is deposited on GO sheets, the GO@Fe_3O_4 composites have two obvious advantages. Firstly, they have much more stable structure because the connection area between

GO and Fe_3O_4 is much more extensive; secondly, the restacking of GO sheets could be completely avoided, thereby enhancing their performances.

We have synthesize magnetic GO composites as environmental materials recently (Hu et al., 2009, 2010, 2012). Fe_3O_4 NPs have been successfully encapsulated with GO sheets though electrostatic interaction and covalent bonding, and both of the GO-based composites exhibited excellent adsorption toward contaminants in solution (Hu et al., 2017, 2020). Further researches revealed that the two kinds of composites displayed quite different regeneration toward heavy metal ions and organics. It is known that good regeneration is the prerequisite for the commercial application of the GO-based adsorbents due to their relatively high cost. Therefore, the investigations on the regeneration of GO-based adsorbents are very meaningful for related researches. Unfortunately, there exist rarely systematic studies on the regeneration of GO-based composites. Previous surveys only involved their adsorption capacity after several cycles, but the associated regeneration mechanisms including the morphology and structure evolution during regeneration had been scarcely investigated.

In this paper, our investigations are focused on the regeneration processes and the mechanisms of two kinds of Fe_3O_4@GO composites, which had been successfully synthesized in our previous study. Although both of the Fe_3O_4@GO samples have similar a core-shell structure, in which GO sheets are tightly connected with magnetic NPs, the interactions linking the core and shell are quite different, which are electrostatic and covalent, respectively. Methylene blue and Pb(II) were used as typical adsorbates to elucidate the evolution of the morphologies and structures of both samples during regeneration in detail. To the best of our knowledge, it is firstly reported to systematically investigate the regeneration mechanisms of the Fe_3O_4@GO composites, and the study could provide a theoretical guide for improving the regeneration of GO-based composites, thus accelerating their practical application.

EXPERIMENTAL

Materials

Graphite (100 mesh, XFnano), ferric chloride hexahydrate ($FeCl_3{\cdot}6H_2O$, Sinopharm), ethylene glycol (Sinopharm), polyethylene glycol (PEG 4000, Sinopharm), sodium acetate trihydrate ($NaAc{\cdot}3H_2O$, Sinopharm), tetraethyl orthosilicate (Sinopharm), poly(diallyldimethylammonium chloride) (PDDA, Sinopharm), 3-aminopropyl triethoxysilane (APTES, Sinopharm), 1-ethyl-3-(3-dimethylaminopropyl) carbodiimide hydrochloride (EDC, Sinopharm), n-hydroxysuccinimide (NHS, Sinopharm), ammonia water (28 wt.%, Sinopharm), hydrochloric acid (Sinopharm), lead nitrate [$Pb(NO_3)_2$, Sinopharm], methylene blue (MB, Sinopharm).

Materials Synthesis

Synthesis of GO Wrapped Fe_3O_4 Composites by Electrostatic Interaction

The synthesis procedures of GO wrapped Fe_3O_4 composites by electrostatic interaction (Fe_3O_4@GO-e) were described elsewhere in detail (Hu et al., 2020). The preparation steps included synthesis of Fe_3O_4, SiO_2 coating on Fe_3O_4, introduction of PDDA on Fe_3O_4 and encapsulation of GO's sheets on magnetic particles. SiO_2 coating endowed Fe_3O_4 with rich hydorphilic groups such as –OH, which can attract PDDA molecules with positive charges, and the positive charges on Fe_3O_4 could induced the coating of GO's sheets with negative charges, forming a core-shell structure. In brief, solvothermal synthesized Fe_3O_4 NPs were coated with a layer of SiO_2 by a modified Stoker method (Gao et al., 2013), then the surface modified Fe_3O_4 NPs were mixed with PDDA solution. At the same time, the graphite oxide prepared by Hummers' method (Hummers and Offeman, 1958) was dispersed in distilled water. The dispersed GO solution was mixed with the above solution, and reacted for 8h. After washing, separation and drying, Fe_3O_4@GO-e was obtained.

Synthesis of GO Sheets Wrapped Fe_3O_4 Composites by Covalent Bonding

The detailed synthesis processes of GO sheets wrapped Fe_3O_4 composites by covalent bonding (Fe_3O_4@GO-c) could be found elsewhere (Hu et al., 2017), and they were composed of the following steps: synthesis of Fe_3O_4, SiO_2 coating on Fe_3O_4, amination surface on Fe_3O_4 and final coupling reaction between GO and Fe_3O_4. The former procedures of solvothermal synthesis of Fe_3O_4 NPs and subsequent SiO_2 coating were same as those of GO@Fe_3O_4-e except for some parameter modifications. After SiO_2 coating, the amination on the surface of the magnetic NPs was carried out using APTES precursor, thus endowing the magnetic particles with rich amino groups on their surface. Meanwhile, the graphite oxide prepared by Hummers' method was dispersed in distilled water and its pH value was adjusted with a buffer solution. Subsequently, EDC and NHS were added into the GO solution, and finally the mixed solution reacted with aminated Fe_3O_4 NPs, resulting in the formation of Fe_3O_4@GO-c.

Materials Characterization

Scanning electron microscopy (SEM) images were obtained using a JEOL JSM-6360LV or Hitachi S4800. Transmission electron microscope (TEM, Tecnai G2 F20, FEI, USA) was utilized to investigate the morphology and microstructure of the sample. The powder X-ray diffraction (XRD) patterns of the samples were collected from a Bruker D8 advanced diffractometer using Cu-Kαradiation ($\lambda = 0.1514$ nm) in the 2θ range of 10–80°. The magnetic experiments were performed on a Lakeshore 7407 vibrating sample magnetometer at room temperature.

Adsorption Experiments

MB, a common dye pollutant, and Pb(II), a typical heavy metal ion, were used as adsorbates for the study. The adsorption experiments were carried out on a shaker with a shaking speed of 200 rpm at 30°C.

For MB adsorption tests, 50 mg of the sample and 50 mL of MB solution (150 mg/L, pH = 8) were mixed in a 100 mL air-tight glass conical flask. The adsorption equilibrium was reached after 2 h of agitation. Subsequently, the adsorbent was separated using a hand-held permanent magnet. The supernatant was collected for concentration measurements

by UV-vis spectrophotometry. The adsorption capacity was calculated based on the following formula:

$$q_e = \frac{(C_0 - C_e)V}{M} \quad (1)$$

where q_e refers to the adsorption equilibrium capacity, C_0 and C_e denote the initial and equilibrium concentrations, respectively, V is the solution volume, and M represents the adsorbent's mass.

For Pb(II) adsorption, the experimental procedures were same as the above ones except for modifications of the following parameters. The initial concentration of Pb(II) solution was 300 mg/L, and its pH value was adjusted to 6 before adsorption tests. The adsorption equilibrium time was set as 12 h. The Pb(II) concentration in the supernatant was measured by atomic absorption spectrophotometry and the adsorption capacity toward Pb(II) was obtained according to Equation (1).

Desorption and Regeneration Experiments

The MB-loaded and Pb(II)-loaded samples were utilized to evaluate the regeneration performance. For MB desorption, the regeneration of the sample was carried out by immersing it in ethanol solution under mechanical stirring for 30 min. For Pb(II) desorption, the regeneration of the sample was performed by soaking it in the presence of 0.01 M of HCl under ultrasonication for 30 min.

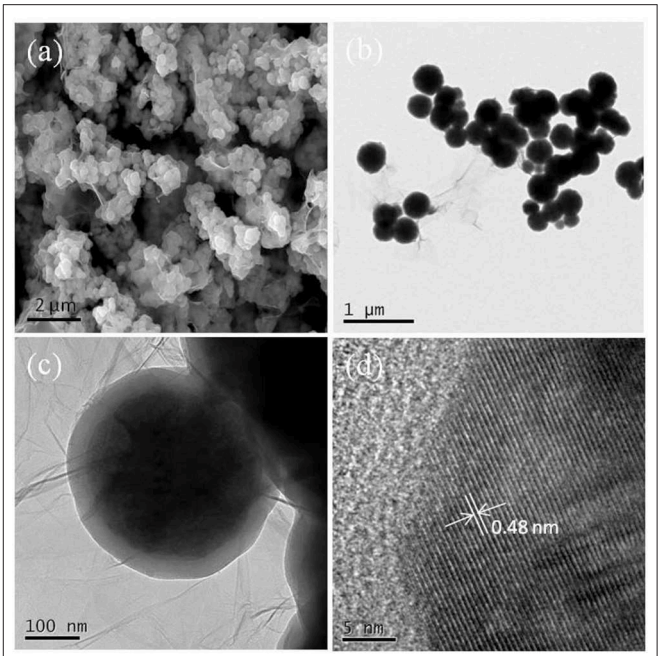

FIGURE 1 | (a) SEM image of Fe_3O_4@GO-e, **(b)** TEM image of Fe_3O_4@GO-e, **(c)** magnified TEM image of **(b)**, and **(d)** high-resolution TEM image of Fe_3O_4@GO-e.

RESULTS AND DISCUSSIONS

SEM/TEM Analyses of the Fe_3O_4@GO Samples

SEM/TEM could intuitively reveal the morphologies and textures of the samples. The SEM/TEM images of the Fe_3O_4@GO-e sample are shown in **Figure 1**. From the SEM image (**Figure 1a**), it could be clearly observed that the Fe_3O_4 NPs or Fe_3O_4 NP aggregations are tightly wrapped by the silk-like GO sheets. The TEM images of the sample (**Figures 1b,c**) further demonstrate that the corrugated GO sheets are compactly connected with the magnetic NPs. The high-resolution TEM of the sample is displayed in **Figure 1d**, in which the atomic lattice fringes could be distinctly observed. The interplanar spacing (∼0.48 nm) could be attributed to the (111) lattice plane of the Fe_3O_4 crystal. In this study, the good structure of the Fe_3O_4@GO-e sample could be ascribed to the utilization of Fe_3O_4 NPs with large surface area, rich -OH groups on the surface introduced by SiO_2 coating, and PDDA with positive charges which could strongly attract the negative GO sheets.

Figure 2 shows the SEM/TEM images of the Fe_3O_4@GO-c sample. Compared with the Fe_3O_4@GO-e sample, Fe_3O_4@GO-c also presents a core-shell structure, where the magnetic NPs are roundly encapsulated by the wrinkled silk-like GO sheets. Its SEM image is similar to Fe_3O_4@GO-e's, indicating that the encapsulation effect of the sample is good as Fe_3O_4@GO-e's. However, the TEM images exhibit that the crinkly GO sheets are more densely and firmly grafted to the magnetic NPs surface, inferring that the sample has a more stable structure than Fe_3O_4@GO-e. The structure difference between two samples could be reasonably deduced that the covalent bonding in Fe_3O_4@GO-c is much stronger than the electrostatic interaction in Fe_3O_4@GO-e. This difference could have a significant influence on their regeneration.

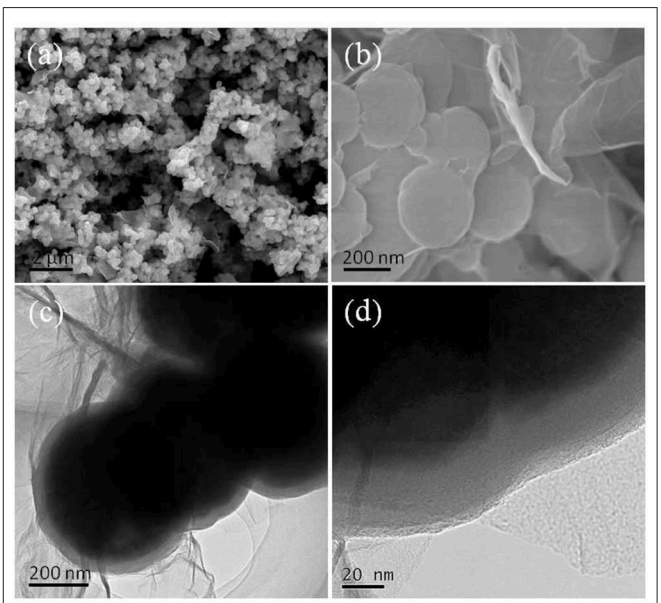

FIGURE 2 | (a) SEM image of Fe_3O_4@GO-c, **(b)** magnified SEM image of **(a)**, **(c)** TEM image of Fe_3O_4@GO-c, and **(d)** magnified image of **(c)**.

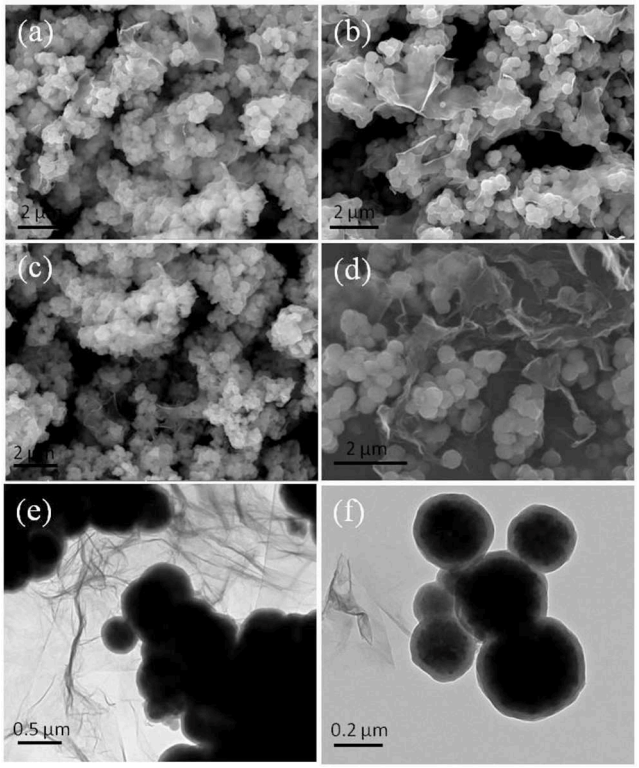

FIGURE 3 | SEM images of the samples after five cycles **(a)** Fe_3O_4@GO-c toward MB, **(b)** Fe_3O_4@GO-e toward MB, **(c)** Fe_3O_4@GO-c toward Pb(II), and **(d)** Fe_3O_4@GO-e toward Pb(II); TEM images of the samples after five cycles **(e)** Fe_3O_4@GO-c toward Pb(II) and **(f)** Fe_3O_4@GO-e toward Pb(II).

Morphology and Structure Analyses of the Fe_3O_4@GO Samples After Regeneration

The regenerability of the sample has much to do with its evolution of morphology and structure during adsorption-desorption recycling. **Figure 3** displays the SEM/TEM images of the samples after five cycles of adsorption-desorption toward MB and Pb(II). Compared with the morphology before adsorption test, the morphology of Fe_3O_4@GO-c changed little (**Figures 3a,c,e**), indicating that it could maintain its structure during regeneration toward MB and Pb(II). As a result, it could be recyclable. The next tests of adsorption-desorption further demonstrate that the stable structure is beneficial to enhancing its regenerability.

Nevertheless, the Fe_3O_4@GO-e sample had quite different morphologies and structures after adsorption-desorption recycling toward MB and Pb(II). From **Figure 3b**, it can be seen that the morphology and core-shell structure of Fe_3O_4@GO-e are approximately preserved, manifesting that the Fe_3O_4@GO-e sample could keep stable during regeneration toward MB. However, after adsorption-desorption toward Pb(II), its morphology and structure had completely changed. **Figure 3d** clearly shows that the magnetic NPs are not wrapped by GO sheets and instead they lie on GO sheets via weak connection. The TEM image (**Figure 3f**) further shows that the GO sheets have been almost separated from the magnetic NPs. Obviously, the Fe_3O_4@GO-e sample had disintegrated and its core-shell structure had been destroyed.

XRD and Magnetic Property Analyses

XRD technique is a powerful tool for structure characterization, and the structure variation of the Fe_3O_4@GO samples mainly lies in whether the GO sheets could still wrap the magnetic NPs or disintegrate from the NPs. The XRD patterns of Fe_3O_4@GO samples before and after recycling are shown in **Figure 4**. It is evident that all samples have the typical XRD pattern of magnetite (JCPDS No. 19-0629), indicating that the Fe_3O_4 NPs retain their original crystalline structure. It should be paid attention to the peaks variation at the 2θ range of 20–30° for the magnetic GO composites. The composites tend to appear with a broad XRD peak at 20–30° when metal NPs are deposited on the graphene sheets, which is due to the loose stacking of graphene sheets (Ai et al., 2011; Guo et al., 2015; Wu et al., 2016). However, in our case, there existed almost no peak at 20–30° for the Fe_3O_4@GO samples (**Figure 4A**). It could be explained that the peak at 20–30° is attributed to the stacking of the tiled GO sheets, which would disappear for the wrapped GO sheets. As for the regenerated samples, their XRD patterns are very different from the aboves. From **Figure 4B**, it could be seen that the regenerated Fe_3O_4@GO-c sample has a negligible peak whereas the regenerated Fe_3O_4@GO-e has a tiny peak at 20–30°. It could be deduced that the core-shell structure of Fe_3O_4@GO-c could be well maintained and Fe_3O_4@GO-e could generally preserve the core-shell structure during regeneration toward MB. However, after desorbing Pb(II), the Fe_3O_4@GO-e sample displays an intensive and broad peak at 20–30° (**Figure 4C**), manifesting that most GO sheets are separated from the magnetic NPs. On the contrary, the XRD peak of Fe_3O_4@GO-c are almost same as that in **Figure 4A**, verifying that it could well maintain core-shell structure during adsorption-desorption of Pb(II). The XRD results inherently reveal the structure evolution of Fe_3O_4@GO during adsorption-desorption process, which are highly consistent with the SEM/TEM characterizations. The results further clarify the structure evolution of the Fe_3O_4@GO samples during adsorption-desorption process.

The magnetism of novel carbon materials plays a pivotal role for their application as adsorbents (Ren et al., 2019; Zhang et al., 2019). The maximum saturation magnetizations of the GO-based samples are listed in **Table 1**, from which it could be seen that they change slightly after five cycles of adsorption-desorption toward MB or Pb(II). The negligible variation in magnetization can be deduced that the magnetism of the samples comes from Fe_3O_4 NPs and they are well-preserved in the samples after recycling. The good magnetization is very helpful to facilitate the post-processing of the GO composites. However, after desorption-desorption of Pb(II), the Fe_3O_4@GO-e sample has completely disintegrated its core-shell structure. As a result, a mixture of magnetic NPs and GO sheets was formed, therefore, it had to be separated from solution by membrane filtration instead of external magnet.

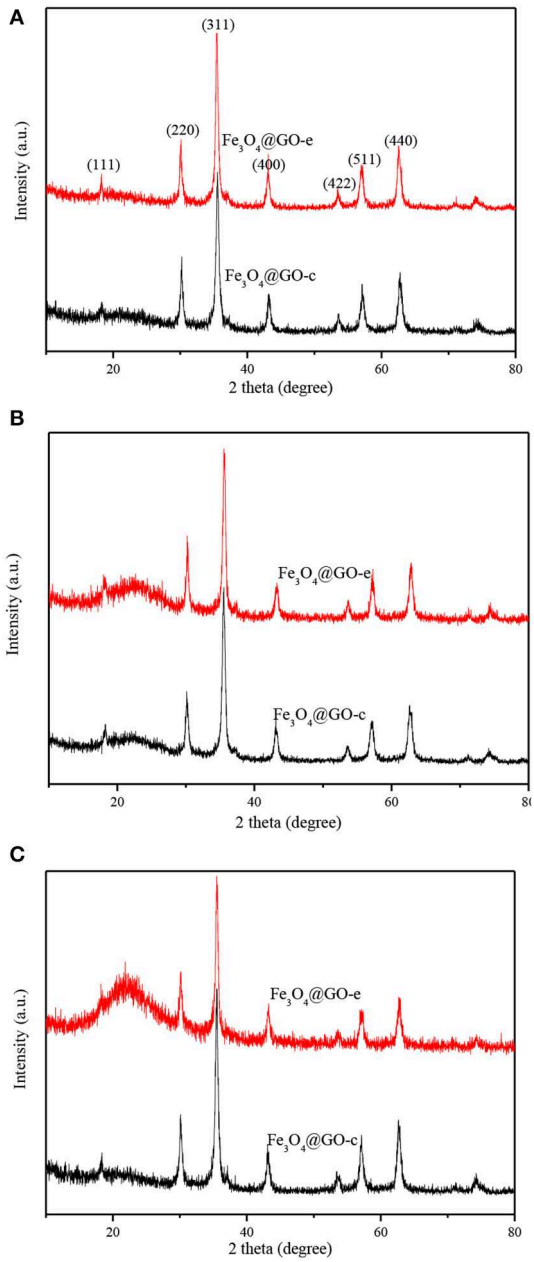

FIGURE 4 | XRD patterns of Fe_3O_4@GO-e and Fe_3O_4@GO-c **(A)**, and Fe_3O_4@GO-e and Fe_3O_4@GO-c after five adsorption-desorption cycles toward MB **(B)** and Pb(II) **(C)**.

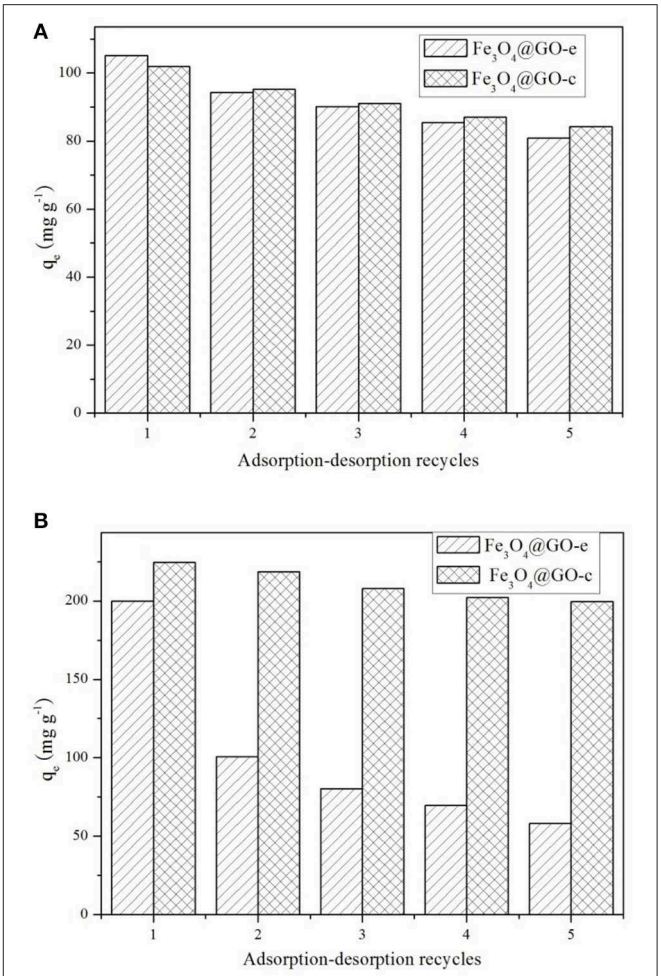

FIGURE 5 | Adsorption-desorption recycling tests toward **(A)** MB and **(B)** Pb(II).

Regeneration Study

The adsorption-desorption tests for the samples were repeated five times using MB and Pb(II) as the adsorbates, and the results are displayed in **Figure 5**. Before recycling, Fe_3O_4@GO-e exhibits an adsorption capacity of 105.5 mg/g toward MB, which is a little higher than Fe_3O_4@GO-c (102.4 mg/g). However, Fe_3O_4@GO-c displays a greater initial adsorption amount (224.5 mg/g) than Fe_3O_4@GO-e (199.8 mg/g). It could be attributed to the fact that Fe_3O_4@GO-c is rich of $-NH_2$ groups, which can help to chelate Pb(II). From **Figure 5A**, it could be observed that both of the Fe_3O_4@GO samples could maintain good regeneration even after five cycles toward MB, and the Fe_3O_4@GO-e and Fe_3O_4@GO-c samples could hold 77% and 83% adsorption capacities, respectively. Nevertheless, the samples present very different regeneration performances toward Pb(II). From **Figure 5B**, it could be seen that Fe_3O_4@GO-c could maintain ∼89% adsorption capacity after five cycles whereas Fe_3O_4@GO-e only possesses ∼29% adsorption capacity. Moreover, for the initial cycle, the adsorption capacity of Fe_3O_4@GO-e has been drastically decreased, inferring that its structure has greatly changed.

It is well-known that the performance of a composite is highly related to its structure. Therefore, it could be reasonably deduce that the significant variation of the Fe_3O_4@GO-e sample in adsorption capacity toward Pb(II) is attributed to the disintegration of its core-shell structure. Indeed, during desorption of Fe_3O_4@GO-e toward Pb(II), there existed black

TABLE 1 | The maximum saturation magnetisms of the Fe_3O_4@GO samples before and after five cycles of adsorption-desorption toward MB and Pb(II).

Samples / emu g^{-1}	No recycling	After five cycles toward MB	After five cycles toward Pb(II)
Fe_3O_4@GO-e	61.0	59.5	59.1
Fe_3O_4@GO-c	57.1	55.8	55.3

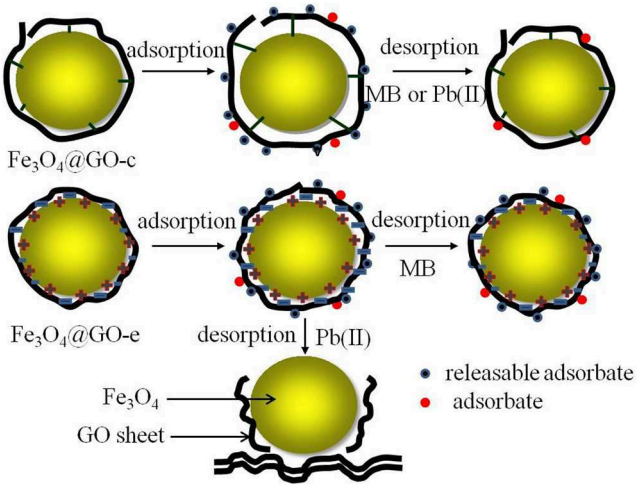

FIGURE 6 | Sketch illustrating the structure evolution of Fe_3O_4@GO-c and Fe_3O_4@GO-e.

GO sheets in solution, which could not be separated by an external magnet, fully demonstrating that the GO sheets had been separated from the composites and dispersed in solution. The slight decrement in adsorption capacities in other cases could be explained that the pre-adsorbed amounts could not be totally released from adsorption sites (Zhang et al., 2013), hence verifying that their core-shell structures had been well-preserved. In this study, only Pb(II) was used for the investigation, but, as a typical heavy metal ion, the related results may be applied to other heavy metal ions because they had a similar adsorption mechanism by Fe_3O_4@GO-e and other GO-based adsorbents (Hu et al., 2017).

Structure Evolutions of the Fe_3O_4@GO Samples During Regeneration Process

The structure evolution of the adsorbents during regeneration is closely related to their regeneration performance. Therefore, it is very beneficial to improving the structural stability by adoption of pertinent measures.

In this study, both Fe_3O_4@GO samples have a similar core-shell structure, in which the magnetic NPs are tightly wrapped by GO sheets. However, the interactions between the core and shell are completely different, which are electrostatic and covalent. The Fe_3O_4@GO-c sample has a stable structure due to the firm covalent bonding that could resist the acid and ethanol environment during regeneration, resulting in good regeneration performance toward MB and Pb(II). For the Fe_3O_4@GO-e sample, its structure is not very stable owing to the weak electrostatic connection, but it could still maintain its core-shell structure in ethanol solution, thus resulting in a reasonable regeneration performance toward MB.

Unfortunately, when desorbing Pb(II) in acid solution, the Fe_3O_4@GO-e sample would disassemble due to the following reasons: (1) H^+ ions could attract GO sheets with negative charges; (2) A great number of H^+ ions in solution could endow GO sheets with positive charges, and it would repel the magnetic NPs with the same charges. The sketch illustrating the structure evolution during regeneration is presented in **Figure 6**.

CONCLUSION

Two kinds of composites with the structure of GO sheets wrapped magnetic nanoparticles composites had been successfully synthesized, and their regeneration had been investigated using MB and Pb(II) as adsorbates. Both samples have a similar core-shell structure, and the linking forces between core and shell are electrostatic and covalent, respectively. During regeneration, the GO@Fe_3O_4-c sample could resist the erosion from ethanol and acid solution, and could well maintain its core-shell structure. After five cycles, it still holds the adsorption capacity ∼83% toward MB and ∼89% toward Pb(II), respectively. The GO@Fe_3O_4-e sample could preserve ∼77% adsorption capacity toward MB, and could roughly keep the core-shell structure after five cycles. However, it would completely disassemble its core-shell structure, resulting in only ∼29% adsorption capacity toward Pb(II) after five cycles. The related regeneration mechanism and the structure evolution during regeneration had been proposed, which could provide a theoretical guide for designing and improving the GO-based composites.

DATA AVAILABILITY STATEMENT

The datasets generated for this study are available on request to the corresponding author.

AUTHOR CONTRIBUTIONS

ZH and XZ conducted the most experiments. JL and YZ performed the characterization and data analysis. All authors involved the analysis of experimental data and manuscript preparation.

ACKNOWLEDGMENTS

The authors would like to acknowledge the financial support from the National Natural Science Foundation of China (Nos. 21576075, 21376069).

REFERENCES

Ai, L., Zhang, C., and Chen, Z. (2011). Removal of methylene blue from aqueous solution by a solvothermal-synthesized graphene/magnetite composite. *J. Hazard. Mater.* 192, 1515–1524. doi: 10.1016/j.jhazmat.2011.06.068

Bourlinos, A. B., Gournis, D., Petridis, D., Szabo, T., Szeri, A., and Dekany, I. (2003). Graphite oxide: chemical reduction to graphite and surface modification with primary aliphatic amines and amino acids. *Langmuir* 19, 6050–6055. doi: 10.1021/la026525h

Chandra, V., Park, J., Chun, Y., Lee, J. W., Hwang, I. C., and Kim, S. (2010). Water-dispersible magnetite-reduced graphene oxide composites for arsenic removal. *ACS Nano* 4, 3979–3986. doi: 10.1021/nn1008897

Gao, J., Ran, X., Shi, C., Cheng, H., Cheng, T., and Su, Y. (2013). One-step solvothermal synthesis of highly water-soluble, negatively charged superparamagnetic Fe_3O_4 colloidal nanocrystal clusters. *Nanoscale* 5, 7026–7033. doi: 10.1039/c3nr00931a

Geim, A. K., and Novoselov, K. S. (2007). The rise of graphene. *Nat. Mater.* 6, 183–191. doi: 10.1038/nmat1849

Guo, L., Ye, P., Wang, J., Fu, F., and Wu, Z. (2015). Three-dimensional Fe_3O_4-graphene macroscopic composites for arsenic and arsenate removal. *J. Hazard. Mater.* 298, 28–35. doi: 10.1016/j.jhazmat.2015.05.011

He, F., Fan, J., Ma, D., Zhang, L., Leung, C., and Chan, H. (2010). The attachment of Fe_3O_4 nanoparticles to graphene oxide by covalent bonding. *Carbon* 48, 3039–3144. doi: 10.1016/j.carbon.2010.04.052

Hu, Z., Aizawa, M., Wang, Z., and Hatori, H. (2009). Palladium precursor for highly-efficient preparation of carbon nanasheet-palladium nanoparticles composites. *Carbon* 47, 3365–3380. doi: 10.1016/j.carbon.2009.08.008

Hu, Z., Aizawa, M., Wang, Z., Yoshizawa, N., and Hatori, H. (2010). Synthesis and characteristics of graphene oxide-derived carbon nanosheet-Pd nanosized particle composites. *Langmuir* 26, 6681–6688. doi: 10.1021/la9040166

Hu, Z., Chen, Y., Hou, Q., Yin, R., Liu, F., and Chen, H. (2012). Characterization of graphite oxide after heat treatment. *New J. Chem.* 36, 1373–1377. doi: 10.1039/c2nj20833d

Hu, Z., Qin, S., Huang, Z., Zhu, Y., Xi, L., and Li, Z. (2017). Recyclable graphene oxide-covalently encapsulated magnetic composite for highly efficient Pb(II) removal. *J. Environ. Chem. Eng.* 5, 4630–4638. doi: 10.1016/j.jece.2017.09.003

Hu, Z., Zhang, X., Cui, H., and Li, Z. (2020). Novel magnetic nanocluster@graphene oxide composites for potential application in environmental adsorption. *J. Nanosci. Nanotechno.* 20, 1814–1821. doi: 10.1166/jnn.2020.17357

Hummers, W. S., and Offeman, R. E. (1958). Preparation of graphite oxide. *J. Am. Chem. Soc.* 80, 1339–1339. doi: 10.1021/ja01539a017

Li, M., Liu, Y., Zeng, G., Liu, N., and Liu, S. (2019). Graphene and graphene-based nanocomposites used for antibiotics removal in water treatment: a review. *Chemosphere* 226, 360–380. doi: 10.1016/j.chemosphere.2019.03.117

Liu, X., Xu, X., Sun, J., Alsaedi, A., Hayat, T., Li, J., et al. (2018). Insight into the impact of interaction between attapulgite and graphene oxide on the adsorption of U(VI). *Chem. Eng. J.* 343, 217–224. doi: 10.1016/j.cej.2018.02.113

Ma, Y., Shao, W., Sun, W., Kou, Y., Li, X., and Yang, H. (2018). One-step fabrication of β-cyclodextrin modified magnetic graphene oxidenanohybrids for adsorption of Pb(II), Cu(II) and methylene blue in aqueous solutions. *Appl. Surf. Sci.* 459, 544–553. doi: 10.1016/j.apsusc.2018.08.025

Mi, X., Huang, G., Xie, W., Wang, W., Liu, Y., and Gao, J. (2012). Preparation of graphene oxide aerogel and its adsorption for Cu^{2+} ions. *Carbon* 50, 4856–4864. doi: 10.1016/j.carbon.2012.06.013

Nandhanapalli, K. R., Mudusu, D., and Lee, S. (2019). Functionalization of graphene layers and advancements in device applications. *Carbon* 152, 954–985. doi: 10.1016/j.carbon.2019.06.081

Pan, S., Chen, X., Shen, H., Li, X., Cai, M., Zhao, Y., et al. (2016). Rapid and effective sample cleanup based on graphene oxide-encapsulated coreeshell magnetic microspheres for determination of fifteen trace environmental phenols in seafood by liquid chromatographyetandem mass spectrometry. *Anal. Chim. Acta* 919, 34–46. doi: 10.1016/j.aca.2016.02.035

Ren, L., Lin, H., Meng, F., and Zhang, F. (2019). One-step solvothermal synthesis of Fe_3O_4@carbon composites and their application in removing of Cr (VI) and congo red. *Ceram. Int.* 45, 9646–9652. doi: 10.1016/j.ceramint.2018.11.132

Sitko, R., Turek, E., Zawisza, B., Malicka, E., Talik, E., Helmann, J., et al. (2013). Adsorption of divalent metal ions from aqueous solutions using graphene oxide. *Dalton Trans.* 42, 5682–5689. doi: 10.1039/c3dt33097d

Smith, S. C., and Rodrigues, D. F. (2015). Carbon-based nanomaterials for removal of chemical and biological contaminants from water: a review of mechanisms and applications. *Carbon* 91, 122–143. doi: 10.1016/j.carbon.2015.04.043

Wei, H., Yang, W., Xi, Q., and Chen, X. (2012). Preparation of Fe_3O_4@graphene oxide core-shell magnetic particles for use in protein adsorption. *Mater. Lett.* 82, 224–226. doi: 10.1016/j.matlet.2012.05.086

Wu, X., Shi, Y., Zhong, S., Lin, H., and Chen, J. (2016). Facile synthesis of Fe_3O_4-graphene@mesoporous SiO_2 nanocomposites for efficient removal of methylene blue. *Appl. Surf. Sci.* 378, 80–86. doi: 10.1016/j.apsusc.2016.03.226

Yoon, Y., Park, W. K., Hwang, T. M., Yoon, D. H., Yang, W. S., and Kang, J. W. (2016). Comparative evaluation of magnetite-graphene oxide and magnetite-reduced graphene oxide composite for As(III) and As(V) removal. *J. Hazard Mater.* 304, 196–204. doi: 10.1016/j.jhazmat.2015.10.053

Zhang, J., Zhai, S., Li, S., Xiao, Z., Song, Y., An, Q., et al. (2013). Pb(II) removal of Fe_3O_4@SiO_2-NH_2 core-shell nanomaterials prepared via a controllable sol-gel process. *Chem. Eng. J.* 215–216, 461–471. doi: 10.1016/j.cej.2012.11.043

Zhang, M., Ma, X., Li, J., Huang, R., Guo, L., Zhang, X., et al. (2019). Enhanced removal of As(III) and As(V) from aqueous solution using ionic liquid-modified magnetic graphene oxide. *Chemosphere* 234, 196–203. doi: 10.1016/j.chemosphere.2019.06.057

Conflict of Interest: The authors declare that the research was conducted in the absence of any commercial or financial relationships that could be construed as a potential conflict of interest.

frontiers in Chemistry

ORIGINAL RESEARCH
published: 28 February 2020
doi: 10.3389/fchem.2020.00146

CO_2 Capture With Absorbents of Tertiary Amine Functionalized Nano–SiO_2

Nanjun Lai[1,2,3,4]*, *Qingru Zhu*[1,4], *Dongyu Qiao*[5], *Ke Chen*[6], *Lei Tang*[1,4], *Dongdong Wang*[1,4], *Wei He*[1], *Yuemei Chen*[1] and *Tong Yu*[1]

[1] School of Chemistry and Chemical Engineering, Southwest Petroleum University, Chengdu, China, [2] State Key Laboratory of Oil and Gas Geology and Exploitation, Chengdu University of Technology, Chengdu, China, [3] State Key Laboratory of Polymer Molecular Engineering, Fudan University, Shanghai, China, [4] Key Laboratory of Oilfield Chemistry (KLOC), CNPC, Beijing, China, [5] Engineer Technology Research Institute, CNPC Xibu Drilling Engineering Company Limited, Ürümqi, China, [6] China National Offshore Oil Corporation (CNOOC) Energy Development Company Limited, Tianjin, China

To improve CO_2 adsorption performance of nanoparticle absorbents, a novel tertiary amine functionalized nano–SiO_2 (NS–NR_2) was synthesized based on the 3–aminopropyltrimethoxysilane (KH540) modified nano–SiO_2 (NS–NH_2) via methylation. The chemical structure and performances of the NS–NR_2 were characterized through a series of experiments, which revealed that NS–NR_2 can react with CO_2 in water and nanofluid with low viscosity revealed better CO_2 capture. The CO_2 capture mechanism of NS–NR_2 was studied by kinetic models. From the correlation coefficient, the pseudo second order model was found to fit well with the experiment data. The influencing factors were investigated, including temperature, dispersants, and cycling numbers. Results has shown the additional surfactant to greatly promote the CO_2 adsorption performance of NS–NR_2 because of the better dispersity of nanoparticles. This work proved that NS–NR_2 yields low viscosity, high capacity for CO_2 capture, and good regenerability in water. NS–NR_2 with high CO_2 capture will play a role in storing CO_2 to enhanced oil recovery in CO_2 flooding.

Keywords: nano–SiO_2, tertiary amine, CO_2 capture, low viscosity, regenerability

OPEN ACCESS

Edited by:
Qing You,
China University of Geosciences, China

Reviewed by:
Helei Liu,
University of British Columbia, Canada
Guillermo Javier Copello,
National Council for Scientific and Technical Research (CONICET), Argentina

***Correspondence:**
Nanjun Lai
lainanjun@126.com

Specialty section:
This article was submitted to Nanoscience, a section of the journal Frontiers in Chemistry

Received: *11 November 2019*
Accepted: *17 February 2020*
Published: *28 February 2020*

Citation:
Lai N, Zhu Q, Qiao D, Chen K, Tang L, Wang D, He W, Chen Y and Yu T (2020) CO_2 Capture With Absorbents of Tertiary Amine Functionalized Nano–SiO_2. Front. Chem. 8:146. doi: 10.3389/fchem.2020.00146

INTRODUCTION

In recent years, humans have been endangered by greenhouse effect leading to global warming. Carbon dioxide (CO_2) emission source from the burn of fossil fuels catches much attention because of it is a major factor to the greenhouse effect (Sarkodie and Strezov, 2019). One method to assuage the greenhouse effect is to capture CO_2 from emission sources and then save it in stratum or apply it for enhanced oil recovery in low permeability reservoirs. Therefore, a feasible approach called carbon capture and storage (CCS) technologies have developed, including membranes, cryogenic distillation, gas adsorption with liquids or solids, and others (Benson and Orr, 2011; Bui et al., 2018). However, membrane–based separation is not a suitable way for CO_2 capture because perfection wants to be made in the areas of CO_2 selectivity, permeability, cost, and performance depletion over time (all caused by a variety of factors). Moreover, because of the high energy costs involved, cryogenic distillation is not optimally suitable. Solvents and solid sorbents have been reported for CO_2 capture, such as basic solvents, supported amine, and ammonium materials, as the primary

classes of chemical sorbents (Heydari-Gorji et al., 2011; Darunte et al., 2016; Hahn et al., 2016; Sanz-Perez et al., 2016; Kong et al., 2019). The adsorption of CO_2 by solvents is a commercially available method, but the regeneration process of the solvents is highly energy intensive and expensive (Rochelle, 2009). The adsorption of CO_2 by solid sorbents has recently attracted much attention in the study of CO_2 capture (Lee and Park, 2015).

Nano silica (SiO_2) solid sorbents have been investigated for CO_2 capture given their high pore volume, large surface, and ease of functionality (Liu et al., 2016; Lai et al., 2017, 2019; Wang et al., 2019). Jiao et al. (2015) prepared mesoporous silica (MSU–J) with a wormhole framework texture, the surface of MSU–J was modified with triethylenetetramine (TETA) for CO_2 capture. Hahn et al. (2016) reported the primary amine, secondary amine, and bibasic amine species functionalized porous SiO_2 and discussed the mechanism of CO_2 adsorption on the SiO_2. Bae (2017) showed that the 3–(2–aminoethylamino) propyldimethoxymetylsilane modified silica can be used as an adsorbent to improve CO_2 capture performance and obtained capture CO_2 capacity of 2.24 mmol/g. The surface of SiO_2 usually has been functionalized with primary and secondary amines for CO_2 capture. Amine modified SiO_2 reacted with CO_2 to form carbamate or bicarbonate species based on the acid–based chemical interaction for improved CO_2 adsorption (Huang et al., 2003). Without the presence of water, the amine groups reacted with CO_2 molecules to create the carbamates group. As another specific, the presence of water impairs this amino group adsorption (Ma et al., 2017). Therefore, the functionalized nano–SiO_2 with water impede is needed to further investigated in future development.

It is difficult to destroy the steady carbon–nitrogen bond of carbamate that is formed in primary amine and secondary amines reaction with CO_2. Also, fascinating tertiary amines as absorbents generate bicarbonates to replace carbamates when tertiary amines reacting with CO_2 (Crooks and Donnellan, 1990; Vaidya and Kenig, 2007) thereby leading to low energy for regeneration of absorbents. Therefore, tertiary amine as an energy saving absorbent is appropriate comparing with primary amines and secondary amines (Gao et al., 2017). Particularly, the rate of primary amines and secondary amines with CO_2 is faster than tertiary amines (Liu et al., 2019a). However, the solubility of CO_2 is higher in tertiary amines solution than one in primary amines and secondary amines solution due to different reaction mechanisms. For example, the reaction molar ratio of tertiary amine and CO_2 is 1:1 to formed bicarbonate structure, while the reaction molar ratio of primary amine or secondary amine and CO_2 is 0.5:1 to formed carbamate structure (Sartorl and Savage, 1983). Tertiary amine can be able to generate a bicarbonate due to no hydrogen on nitrogen when reacted with CO_2 and H_2O, resulting in a better CO_2 adsorption and lower energy depletion for regeneration (Xiao et al., 2016, 2019). Moreover, kinetics is important since it can explain the dynamic adsorption of the sorbent, a lot of kinetic models are applied to the CO_2 adsorption property of tertiary amine (Liu et al., 2019b).

Therefore, this study aimed to develop a sorbent to avert the limits of aqueous amine solutions and take advantage of tertiary amines for CO_2 capture. The tertiary amine loaded nano–SiO_2 was synthesized, and the CO_2 capture performance was studied in the presence of water. The CO_2 adsorption mechanism was investigated by kinetics, and the viscosity of the absorbent dispersion was measured before and after CO_2 adsorption. Finally, tertiary amine functionalized nano–SiO_2 (NS–NR_2) was investigated further in terms of temperature, dispersants, and cycling numbers.

EXPERIMENTAL SECTION

Materials

Methylbenzene(C_7H_8), 3–(trimethoxysilyl)−1–propanamine (KH−540), ethanol (C_2H_5OH), formic acid (HCOOH), formaldehyde (HCHO), hydrochloric acid (HCl), N, N–dimethylformamide (DMF), and sodium hydroxide (NaOH) were purchased from Chengdu Kelong Chemical Reagent Factory (Sichuan, China). Nano–SiO_2 (10–20 nm) was obtained from Aladdin Chemistry Co. (Shanghai, China). All chemical reagents were analytical–grade. CO_2 (g) and N_2 (g) were purchased from Jingli Gas Company (Chengdu, China). Water was double deionized with a Millipore Milli Q system to produce the 18 MM deionized water.

Synthesis and Characterization of Tertiary Amine Functionalized Nano–SiO_2

The nano–SiO_2 loaded with primary amines (NS–NH_2) was prepared first using 3–Aminopropyltrimethoxysilane (KH540) as modifiers, and then it was used as the matrix material to synthesize branched nanomaterials with a tertiary amine group on its surface (NS–NR_2) via methylation of primary amines based on formic acid and formaldehyde. The mechanism is shown in **Figure 1**.

The specific reaction conditions of NS–NH_2, NS–NR_2, and the preparation methods of the nanofluid are shown in **Supplementary Materials**. It is worth noting that add anhydride to promote unreacted primary amine groups undergo acetylation. The optimum reaction conditions of NS–NR_2 are displayed in **Table 1**.

Fourier transform–Infrared (FT–IR) spectra were acquired by the KBr pellet method using a WQF520 spectrometer. Thermogravimetric analysis (TGA) was conducted on a synchronous comprehensive thermal analyzer (Netzsch Scientific Instruments). The microtopography of NS–NR_2 was characterized using an electron microscope (ZEISS Libra 200 FE). The carbon and nitrogen contents were detected by elemental analysis using a Var10EL III instrument. The hydrodynamic diameter and proportion of the nanoparticles were received by a BI 200SM wide-angle dynamic light scattering (DLS) instrument. The rheological property of NS–NR_2 dispersion was measured with a HAAKE MARS III rheometer at 25°C to assess the viscosity.

CO_2 Adsorption and Desorption

NS–NR_2 dispersion was introduced into a gas adsorption bottle. The gas adsorption bottle was put in a constant temperature water bath. The gas flow of CO_2 was controlled at 1 L/min by a gas

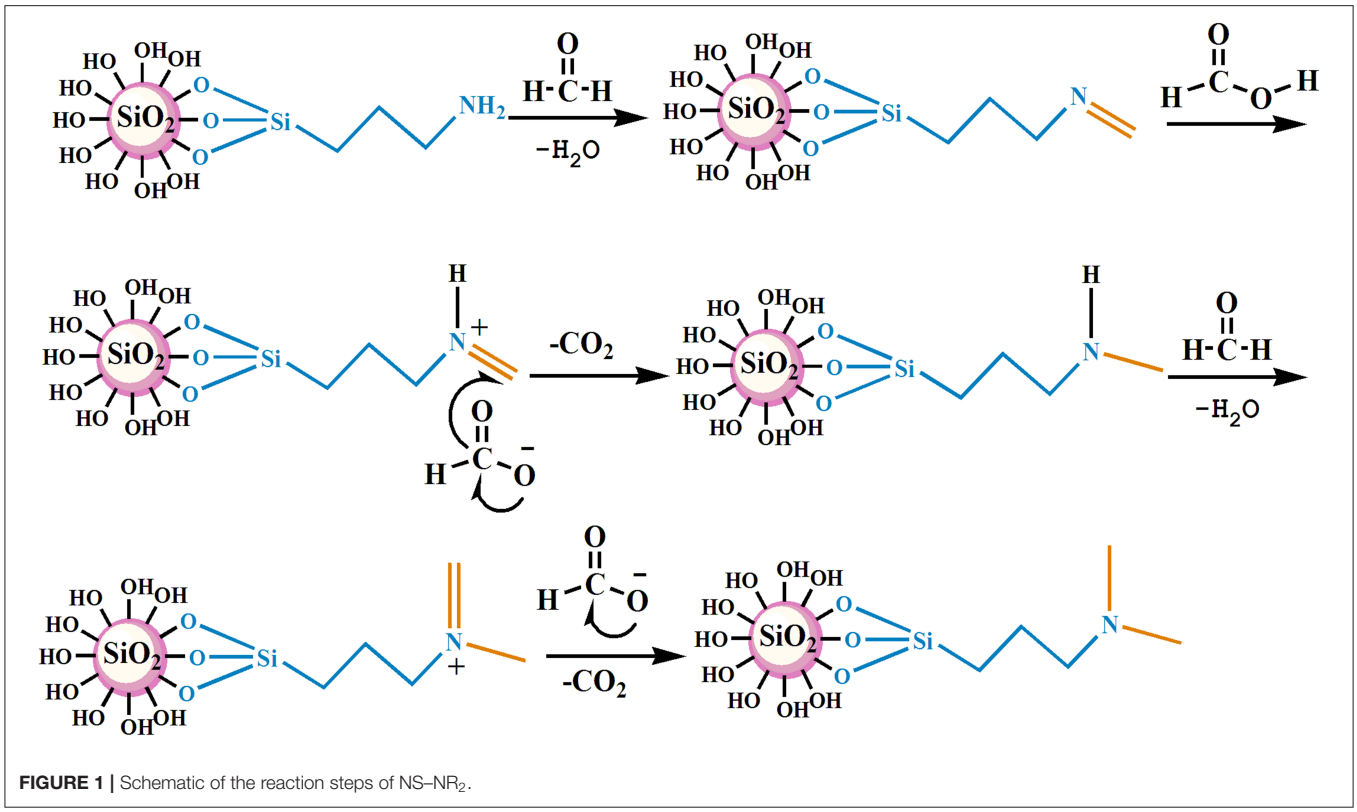

FIGURE 1 | Schematic of the reaction steps of NS–NR_2.

TABLE 1 | Conditions of NS–NR_2.

Time (h)	Temperature (°C)	NS-NH_2: HCOOH: HCHO (g:mol:mol)	Solvent (mL)
12	90	1:6:6	60

flow controller, and CO_2 was bubbling into the high concentrated sulfuric acid to adsorb microscale water in CO_2 gas in a hermetic wild-mouth bottle. After that, the dry CO_2 was flowed through the gas adsorption bottle to reacted with absorbent in the water. The mass change of dispersion was confirmed by an accurate analytical balance (±0.1 mg) until the weight has no change. The amount of adsorption CO_2 on nanoparticles could be calculated under a control test (no nanoparticles). As shown in **Figure S1**, most of the tests were implemented to assure repeatability of the method. The CO_2 adsorption capacity of NS–NR_2 was measured using a gas adsorption system, as shown in **Figure S2**. The CO_2 desorption experiment was simply carried out by bubbling N_2 around 1 L/min instead of injecting CO_2 and keeping the system temperature at 25°C to avoid the huge energy depletion.

The mechanism studies of CO_2 adsorption into NS–NR_2 are often executed using kinetic models including pseudo first order, pseudo second order, and intraparticle diffusion model. The parameter R^2 and relative error (ε) were applied to evaluate the reliability of kinetic models in predicting adsorption capacity, as defined in Equation (1). Based on Equation (1), $q_{e,cal}$ is the predicted date acquired from the model analysis, and $q_{e,exp}$ is the experiment date.

$$\varepsilon(\%) = \frac{q_{ecal} - q_{eexp}}{q_{eexp}} \times 100\% \tag{1}$$

The pseudo first order model that introduced by Langergren in 1898 year (Langergren, 1898) is shown in Equation (2):

$$\log(q_e - q_t) = \log(q_e) - (\frac{k_1}{2.303})t \tag{2}$$

where q_t is the adsorption capacity at a special time, q_e is the adsorption capacity at equilibrium, k_1 is the constant of pseudo first order with a unit of 1/min. The pseudo second order model (Ho and McKay, 1999) is represented by Equations (3) and (4):

$$\frac{t}{q_t} = \frac{1}{k_2 q_e^2} + \frac{t}{q_e} \tag{3}$$

$$h = k_2 \cdot q_e^2 \tag{4}$$

where q_t is the adsorption capacity at a special time, q_e is the adsorption capacity at equilibrium, k_2 is the constant of pseudo second order with a unit of g/mmol min. The intraparticle diffusion model offers the diffusion mechanism of matter in adsorption process as defined in Equation (5):

$$q_t = kt^{1/2} + C \tag{5}$$

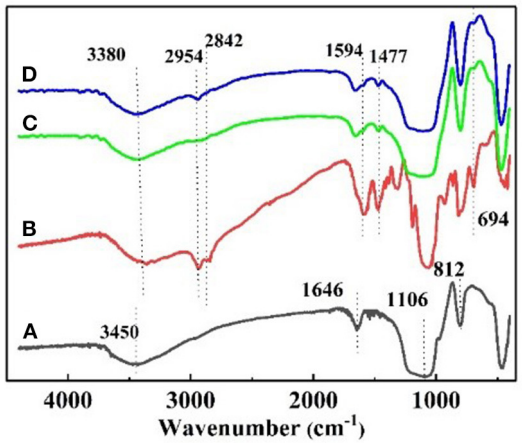

FIGURE 2 | (A) FT-IR spectra of raw SiO_2, **(B)** KH540, **(C)** NS–NH_2, and **(D)** NS–NR_2.

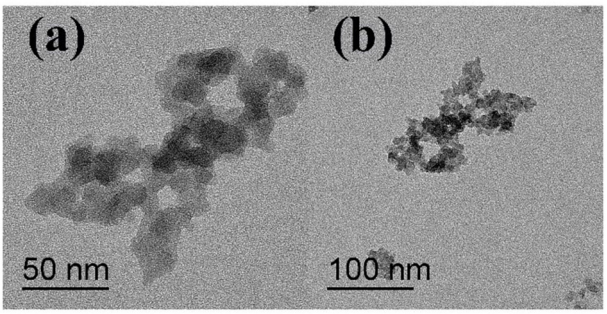

FIGURE 3 | TEM image of NS–NR_2 (the scale bars in **a** is 50 nm and **b** is 100 nm).

Where q_t is the adsorption capacity at a special time (mmol/g), k is the rate constant of intraparticle diffusion (mmol/g $min^{1/2}$) and C (mmol/g) is as the thickness of the boundary layer; the intercept is positively correlated with the boundary layer. (Hameed et al., 2008; Yousef et al., 2011). Mass transfer of adsorbate to the adsorbent surface (bulk diffusion) and film diffusion into the internal sites (intraparticle diffusion) and other steps occur in the process of adsorption.

RESULTS AND DISCUSSION

Characterization

The FT–IR spectrum of the nanoparticles is shown in **Figure 2**. **Figure 2A** shows the strong adsorption peaks at around 3,450 and 1,646 cm^{-1}, suggest the stretching vibration of the –O–H bonds on the surface of silica. The adsorption peaks near 1,106 and 812 cm^{-1} are the adsorption peaks of the Si–O–Si group, which are characteristic adsorption peaks of SiO_2. In the FT–IR spectra of KH540, the adsorption peaks around 3,380 and 1,594 cm^{-1} are the –N–H stretching and NH_2 deformation of hydrogen bonded amino groups (Jiao et al., 2015). The adsorption peak at 1,477 cm^{-1} is C–N, and the peaks at 2,954 and 2,842 cm^{-1} are feature adsorption peak of $–CH_3$ and $–CH_2$-, respectively. The peak at 694 cm^{-1} is the adsorption peak of Si–C (Titinchi et al., 2014). In the FT–IR spectra of NS–NH_2, the 2,954 cm^{-1} peak of $–CH_3$ disappeared, elucidating that the primary amine was grafted on the surface of SiO_2. In **Figure 2D**, the adsorption peak of $–CH_3$ is shown to appear, indicating that $–(CH_2)_3NH_2$ reacted to $–(CH_2)_3N(CH_3)_2$ on the surface of nano–SiO_2.

The microscopic structure of the nanoparticles is shown in **Figure 3** as observed from the TEM morphology. The diameter of NS–NR_2 was shown to be approximately 15 nm. The nanoparticles aggregated slightly because of the particle size being in the nanometer scale (Zhao et al., 2014). The evidence from DLS analysis (**Figures 4A,B**) shown the hydrodynamic diameter of NS–NR_2 to be approximately 123.6 nm with uniform size distribution. Moreover, it was found that the diameter distribution of nude particles was wider and the agglomeration was more serious than that of the modified nanoparticles.

The element contents of raw SiO_2, NS–NH_2, and NS–NR_2 are shown in **Table 2**. Carbon and nitrogen contents are present in raw SiO_2 because many SiO_2 materials are often synthesized in an aqueous organic solvent, resulting in remaining carbon and nitrogen in such materials. The contents of carbon and nitrogen for NS–NH_2 were shown to be 5.22 and 1.65 mmol/g, respectively, and for NS–NR_2 were shown to be 7.14 and 1.39 mmol/g, respectively. The contents of these elements were much higher than raw SiO_2. The nitrogen amount in NS–NR_2 was lower than that of NS–NH_2 because when the molar amount of carbon increases, the molar amount of nitrogen decreases in fixed mass products. The molar ratio of carbon to nitrogen is 3.16, 5.13 in NS–NH_2 (SiO_2-C_3H_8N) and NS–NR_2 (SiO_2-$C_5H_{10}N$), respectively. Here, the molar ratio of carbon to nitrogen was adopted to further confirm the grafting of tertiary amines on nano–SiO_2.

The successful synthesis of NS–NR_2 could also be proved by thermos gravimetric analysis (TGA). Based on the TGA curves in **Figure 5**, the weight retention of raw nano-SiO_2, NS–NH_2 and NS–NR_2 at 900°C under the air atmosphere were 96.86, 89.38, and 87.06%, respectively. For raw nano-SiO_2, the mass depletion is attributed to the surface dihydroxylation. In terms of the structure of NS–NH_2 and NS–NR_2, when the temperature up to 900°C, the primary amine and tertiary amine chains were grafted on the nano-SiO_2 has decomposed, respectively. Therefore, compared with the TGA curve of raw nano-SiO_2, the surface of nano-SiO_2 was modified to primary amine. The different weight loss between in the NS–NH_2 and NS–NR_2 indicated that tertiary amine was synthesized from primary amine successfully.

CO_2 Adsorption and Kinetic Studies

Any amine with a pKa value >5 can react with CO_2 in the presence of water (Field and Grolimund, 1988). According to **Figure S3A**, the pH value of NS–NR_2 dispersion decreased gradually with the addition of diluted hydrochloric acid (0.01 mol/L). The second derivative of the V_{HCl}-pH curve was obtained (**Figure S3B**), with the zero point of the second

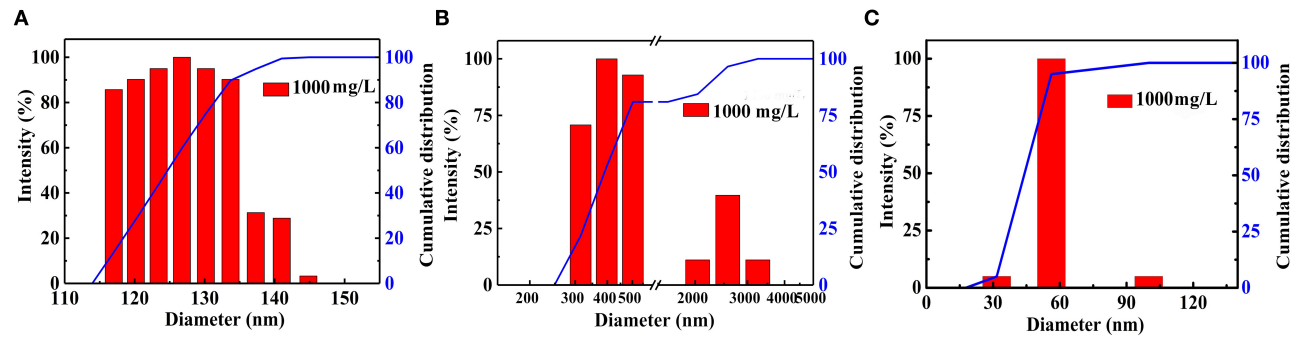

FIGURE 4 | Diameter distribution of **(A)** NS–NR_2 and **(B)** nude nanoparticles in water; **(C)** Diameter distribution of NS–NR_2 in PEG−400 solution (1,000 mg/L).

TABLE 2 | Element contents on nanoparticles.

Sample	C (mmol/g)	N (mmol/g)	Molar ratio of C/N
Raw SiO_2	0.15	0.18	0.85
NS-NH_2	5.22	1.65	3.16
NS-NR_2	7.14	1.39	5.13

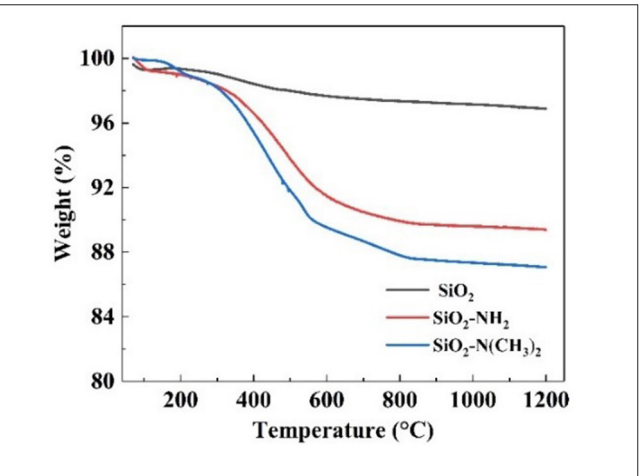

FIGURE 5 | TGA thermograms of raw nano–SiO_2, NS–NH_2, and NS–NR_2.

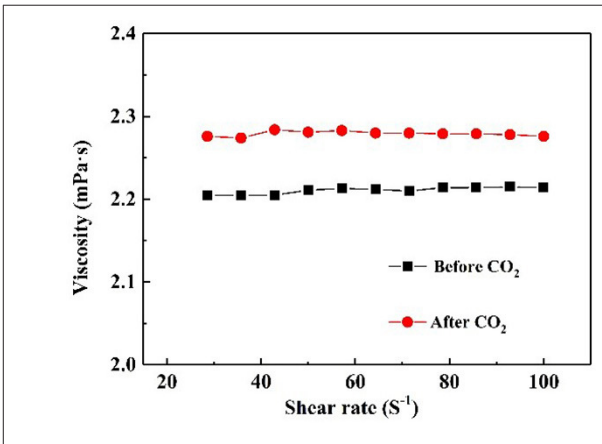

FIGURE 6 | Viscosity of NS–NR_2 dispersion before and after adsorption of CO_2 as a function of shear rate.

derivative corresponding to the extreme point of the curve in **Figure S3A**. As a result, the pKa value was 7.08. The pKa value of 7.08 indicates that NS–NR_2 dispersion can complete adsorption of CO_2. Along with the aeration of CO_2 at 1 L/min, the pH value of NS–NR_2 dispersion dropped rapidly in the first 5 min, after which there were no changes in pH value for 20 min, as shown in **Figure S3C**, which means that NS–NR_2 dispersion (0.1 wt.%) completely saturated CO_2 at 1 L/min CO_2 gas velocity in 20 min.

It is well-known that CO_2 capture is significant influenced by the viscosity of absorbent (Xiao et al., 2019). **Figure 6** demonstrates the rheological property of NS–NR_2 dispersion before and after adsorption CO_2. A rheological plateau in the shear rate region was found for NS–NR_2 dispersion. Before CO_2 adsorption, the nanofluid viscosity was 2.23 mPa·s. After saturation with CO_2, there was a nanofluid viscosity increase to 2.96 mPa·s. This viscosity change is consistent with the ionic liquids in Xiao et al.'s work (Xiao et al., 2019). A possible conclusion is the increase of electrostatic interaction of chains on the NS–NR_2 surface due to CO_2 adsorption (**Figure 7**), resulting in the higher viscosity. However, unlike the high viscosity of ionic liquids, the nanofluid viscosity was very low. The CO_2 capture was not influenced by the increased viscosity.

The CO_2 adsorption capacity of NS–NR_2 was 25 mmol CO_2/g NS–NR_2 in water (0.1 wt.%) at 25°C, as shown in **Table 3**. Compared with other materials (with CO_2 adsorption capacity of 0.1–21.45 mmol/g) (Yu et al., 2012), NS–NR_2 in water has a better CO_2 adsorption capacity.

Kinetic models, such as pseudo first order, pseudo second order, and intraparticle diffusion model, were applied to model the test data. The pseudo first order model is mostly appropriated to describe purely physisorption process without considering the any chemical reaction between CO_2 molecules and sorbent. The pseudo second order model is mostly appropriated to describe purely chemisorption processes with stable chemical bonds between CO_2 molecules and the sorbent. The comparison between the test curves and simulative curves are shown

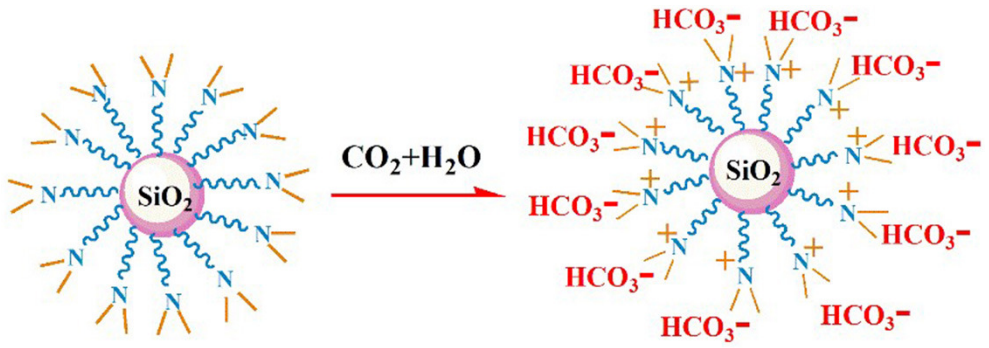

FIGURE 7 | The process for NS–NR_2 reacting with CO_2.

TABLE 3 | CO_2 adsorption of samples at 25°C.

Samples	Volume	CO_2 adsorption
Nanofluid (NS-NR_2 of 0.06g)	60mL	5.55mmol
Water	60mL	4.05mmol

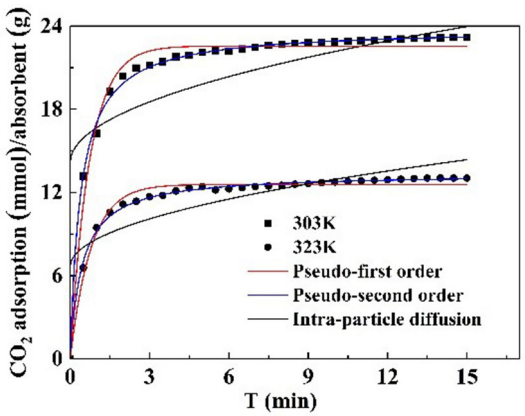

FIGURE 8 | Kinetic plot of CO_2 adsorption models at various temperatures.

TABLE 4 | Kinetic parameters of CO_2 adsorption on NS-NR_2.

Kinetic model	Parameter	Temperature (°C)	
		30	50
	$q_{e,exp}$ (mmol/g)	23.16	13.03
Pseudo first order	$q_{e,cal}$ (mmol/g)	22.49	12.58
	K_1 (1/min)	3.16	2.84
	R^2	0.9795	0.9777
	Relative error, ε (%)	2.89	3.45
Pseudo second order	$q_{e,cal}$ (mmol/g)	23.82	13.37
	K_2 (g/mmol min)	0.10	0.17
	h (mmol/g min)	56.74	30.39
	R^2	0.9977	0.9963
	Relative error, ε (%)	2.84	2.61
Intra-particles diffusion	K (mmol/g $min^{1/2}$)	2.54	1.99
	C(mmol/g)	14.13	6.64
	R^2	0.5044	0.6011

in **Figure 8**. The model parameters of kinetic at different temperatures and their corresponding coefficients are shown in **Table 4**. The R^2 parameters of pseudo second order and pseudo first order models with experimental data were 0.99 and 0.97, respectively. The relative error for the pseudo second order model, ε, was lower than pseudo first order model. Compared with the R^2, ε parameters, the pseudo second order model was found to fit well with the experiment data. Therefore, chemisorption of CO_2 on nanoparticles plays a dominant role in CO_2 capture.

The pseudo first order model and pseudo second order model provide interaction insight into the actual mechanism of CO_2 adsorption. The surface of the particles is grafted with functional groups to adsorb CO_2. This surface adsorption was further verified by the intraparticle diffusion. The model parameters of intraparticle diffusion are revealed in **Table 4**. It is notable that no linear curve can pass through the origin point that is thought to be caused by intraparticle diffusion, suggesting that intraparticle diffusion is not the only factor controlling CO_2 adsorption rate at all tested temperatures (Rashidi et al., 2013). Therefore, the adsorption process is not completely controlled by intraparticle diffusion, surface diffusion also plays a role in the whole CO_2 adsorption process.

Effect of Some Factors on CO_2 Adsorption With NS–NR_2

Effect of Temperature

A CO_2 capture test was implemented using 0.1 wt.% nanofluid at contrast temperatures of 25, 30, 40, 50, and 60°C, respectively. The CO_2 adsorption- temperature curve is revealed in **Figure 9A**. It is obvious that the maximum CO_2 loading on the nanoparticles decreased at higher temperatures. Higher temperatures go against CO_2 adsorption that is an exothermic reaction. The CO_2 adsorption of NS–NR_2 compared with that of MSU–J modified with TETA (Jiao et al., 2015) at higher temperatures

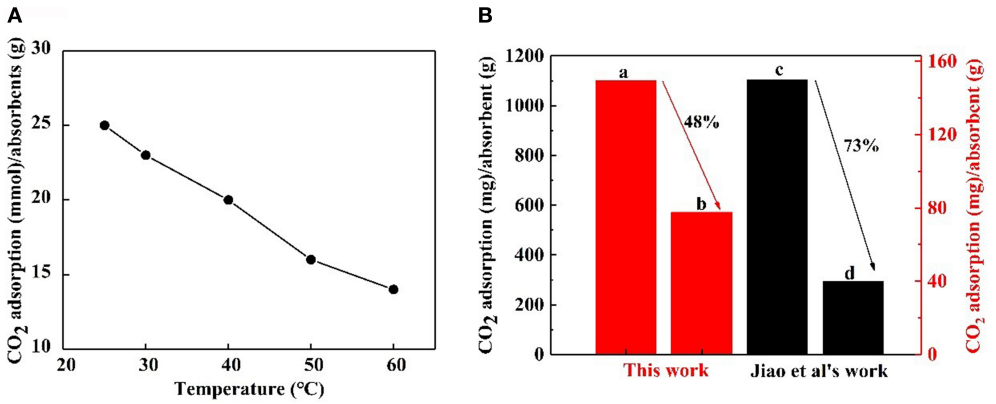

FIGURE 9 | (A) CO_2 adsorption of NS-NR_2 in water at different temperatures. **(B)** CO_2 adsorption of NS–NR_2 at **(A)** 25°C and **(B)** 60°C; CO_2 adsorption of MSU–J at **(C)** 25°C and **(D)**55°C.

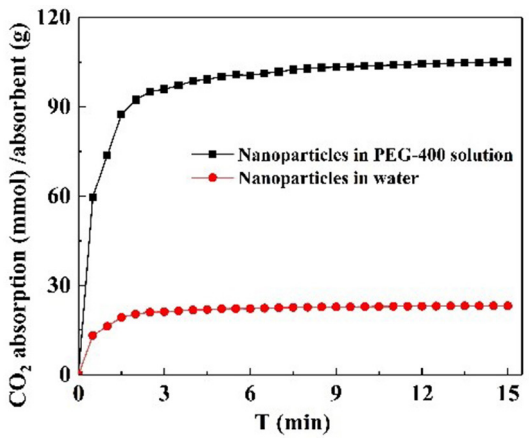

FIGURE 10 | CO_2 adsorption of NS-NR_2 in different dispersants.

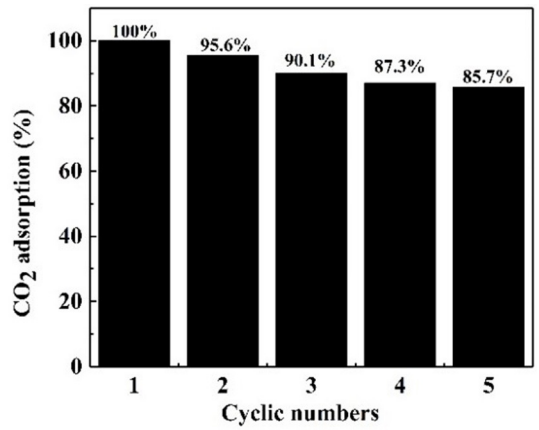

FIGURE 11 | Cyclicity of NS–NR_2 adsorbent in water.

is displayed in **Figure 9B**. The relative comparison presents a view of the advantages of the proposed nanoparticles although a slight difference in the experimental conditions. For the NS–NR_2 absorbent in this work, the CO_2 loading at 60°C decreased to 48% of the CO_2 loading at 25°C, while the CO_2 loading of MSU–J at 55°C decreased to 73% of the CO_2 loading at 25°C. This result can be ascribed to the different mechanisms of CO_2 adsorption. For modified MSU–J absorbent, huge energy was used to generate carbamate group with CO_2. But adsorption of CO_2 loaded nanoparticles enabled bicarbonate formation much easier because of the physical adsorption and chemical adsorption. This result indicates that the NS–NR_2 in this work can capture more CO_2 at higher temperatures.

Effect of Dispersants

CO_2 adsorption capacity in different dispersant agents were investigated. According to the previous test is shown in **Figure S3C**, it was not necessary to perform the experiment for longer than 20 min. Hence, CO_2 adsorption with NS–NR_2 was performed at a temperature of 30°C in different dispersants during this period of 15 min. CO_2 adsorption curves are drawn in **Figure 10**. The maximum CO_2 loading of NS–NR_2 was changed in water or PEG−400 dispersants. The maximum CO_2 loadings of NS–NR_2 in water and PEG−400 solution was 23.16 and 105.34 mmol/g, respectively. This result can be explained by the diameter distribution of nanoparticles, where the diameter distribution in water was 123.6 nm and in PEG−400 solution was 56.7 nm (**Figure 4C**). The tertiary amine groups as specific sites for CO_2 adsorption grafted on the surface of nano–SiO_2 to endow the adsorbents with CO_2 adsorption. Therefore, the more specific sites were exposed on the surface of nanoparticles because of better dispersibility. The dispersibility of nanoparticles is certified by the Derjaguin Landau Verwey Overbeek (DLVO) theory on interparticle interaction potential (Ilyas et al., 2014). The interaction among nanoparticles is caused by electrostatic repulsion and steric resistance in the PEG−400 solution. In addition, using PEG−400 as the dispersant is inexpensive and has lower surfactivity. Surfactants with similar properties can also be

used to disperse the nanoparticles for CO_2 capture. Therefore, adding the surfactant improved CO_2 adsorption by enhancing the dispersibility of nanoparticles.

Effect of Cycling Numbers

It is crucial that an absorbent is reusable and retains an efficient CO_2 adsorption capacity (Ma et al., 2017). Therefore, the regeneration tests of the NS–NR_2 absorbent was carried out at 25°C. After CO_2 adsorption in the nanofluid for 20 min, the nanofluid was shifted to CO_2 desorption for regeneration. The CO_2 desorption test was executed for another 20 min by bubbling N_2 around 1 L/min before the absorbent was used for the next round of adsorption. As illustrated in **Figure 11**, five cycles of adsorption were implemented and the initial CO_2 adsorption of absorbent was set as the 100 % baseline. After five cycles, NS–NR_2 adsorbent shown favorable regeneration capacity with a slight decrease of 14.3% in water for NS–NR_2 compared to the initial capacity. The results shown regeneration and efficient CO_2 adsorption capacity of nanoparticles adsorbent. Considering cycling capacity, NS–NR_2 material shows intriguing regeneration ability for CO_2 adsorption.

CONCLUSION

This work synthesized tertiary amino functionalized nano–SiO_2 successfully. The measurements of pKa value and nanofluid viscosity change proved that NS-NR_2 can react with CO_2 in water and nanofluid has a low viscosity. NS–NR_2 shown better CO_2 adsorption capacity, and adsorption kinetics revealed the pseudo second order model was found to fit well with the experiment data. The influence of factors such as temperature, dispersants, and cycling numbers on CO_2 adsorption was investigated. Results indicated higher temperature to work against CO_2 adsorption of NS–NR_2. The CO_2 adsorption performance of NS–NR_2 was greatly promoted because of a better dispersity of nanoparticles with added surfactant. After recycling of absorbent, the NS–NR_2 maintained an efficient CO_2 capture and shown favorable regeneration capacity. The measurements of NS–NR_2 properties on the bases of viscosity, kinetic models, CO_2 capture, and regeneration manifests that NS–NR_2 exhibits satisfying performance to capture CO_2. NS–NR_2 with high CO_2 capture will play a role in storing CO_2 to enhanced oil recovery in CO_2 flooding.

DATA AVAILABILITY STATEMENT

All datasets generated for this study are included in the article/**Supplementary Material**.

AUTHOR CONTRIBUTIONS

NL, QZ, and LT conceived the idea. QZ, WH, TY, and YC implemented the preparation, characterization, and measurement of NS–NR_2. QZ wrote the manuscript. DQ and KC came up with ideas for the manuscript. QZ, LT, and DW discussed and analyzed the experiment data. LT and DW revised the manuscript. NL supervised the whole research work.

FUNDING

This work was supported by the National Natural Science Foundation of China (No. 51674208); Nanchong Science and Technology Project (NC17SY4017); State Key Laboratory of Molecular Engineering of Polymers (Fudan University) (No. K2017-25); PetroChina Innovation Foundation (No. 2018D−5007–0207); Open Foundation of State Key Laboratory of Oil and Gas Geology and Exploitation (Cheng Du University of Technology) (No. PLC20180103); Basic Research Programs of Sichuan Province (No. 2018JY0515); and the Undergraduate Extracurricular Open Experiment of Southwest Petroleum University (KSZ18440, KSZ18441, KSZ18442).

SUPPLEMENTARY MATERIAL

The Supplementary Material for this article can be found online at: https://www.frontiersin.org/articles/10.3389/fchem.2020.00146/full#supplementary-material

REFERENCES

Bae, J. Y. (2017). CO_2 capture by amine-functionalized mesoporous hollow silica. *J. Nanosci. Nanotechno.* 17, 7418–7422. doi: 10.1166/jnn.2017.14778

Benson, S. M., and Orr, F. M. (2011). Carbon dioxide capture and storage. *MRS Bull.* 33, 303–305. doi: 10.1557/mrs2008.63

Bui, M., Adjiman, C. S., Bardow, A., Anthony, E. J., Boston, A., Brown, S., et al. (2018). Carbon capture and storage (CCS): the way forward. *Energy Environ. Sci.* 11, 1062–1176. doi: 10.1039/C7EE02342A

Crooks, J. E., and Donnellan, J. P. (1990). Kinetics of the reaction between carbon dioxide and tertiary amines. *J. Org. Chem.* 55, 1372–1374. doi: 10.1021/jo00291a056

Darunte, L. A., Walton, K. S., Sholl, D. S., and Jones, C. W. (2016). CO_2 capture via adsorption in amine-functionalized sorbents. *Curr. Opin. Chem. Eng.* 12, 82–90. doi: 10.1016/j.coche.2016.03.002

Field, S. M., and Grolimund, K. (1988). Basicity limits for solutes in supercritical fluid chromatography with a carbon dioxide mobile phase. *J. High Res. Chrom.* 11, 727–729. doi: 10.1002/jhrc.1240111010

Gao, H., Xu, B., Han, L., Luo, X., and Liang, Z. (2017). Mass transfer performance and correlations for CO_2 absorption into aqueous blended of DEEA/MEA in a random packed column. *AIChE J.* 63, 3048–3057. doi: 10.1002/aic.15673

Hahn, M. W., Jelic, J., Berger, E., Reuter, K., Jentys, A., and Lercher, J. A. (2016). Role of amine functionality for CO_2 chemisorption on silica. *J. Phys. Chem. B* 120, 1988–1995. doi: 10.1021/acs.jpcb.5b10012

Hameed, B. H., Tan, I. A. W., and Ahmad, A. L. (2008). Adsorption isotherm, kinetic modeling and mechanism of 2,4,6-trichlorophenol on coconut husk-based activated carbon. *Chem. Eng. J.* 144, 235–244. doi: 10.1016/j.cej.2008.01.028

Heydari-Gorji, A., Belmabkhout, Y., and Sayari, A. (2011). Polyethylenimine-impregnated mesoporous silica: effect of amine loading and surface alkyl chains on CO_2 adsorption. *Langmuir* 27, 12411–12416. doi: 10.1021/la202972t

Ho, Y. S., and McKay, G. (1999). Pseudo-second order model for sorption processes. *Process Biochem.* 34, 451–465. doi: 10.1016/S0032-9592(98)00112-5

Huang, H. Y., Yang, R. T., Chinn, D., and Munson, C. L. (2003). Amine-grafted MCM-48 and silica xerogel as superior sorbents for acidic gas removal from natural gas. *Ind. Eng. Chem. Res.* 42, 2427–2433. doi: 10.1021/ie020440u

Ilyas, S. U., Pendyala, R., and Marneni, N. (2014). Preparation, sedimentation, and agglomeration of nanofluids. *Chem. Eng. Technol.* 37, 2011–2021. doi: 10.1002/ceat.201400268

Jiao, J., Cao, J., and Lv, P. P. (2015). Amine-immobilized three-dimensional wormhole mesostructured MSU-J silica for CO_2 adsorption: effect of amine loading and temperature on the adsorption capacity. *Chem. Lett.* 44, 928–930. doi: 10.1246/cl.141151

Kong, X., Li, S., Stromme, M., and Xu, C. (2019). Synthesis of porous organic polymers with tunable amine loadings for CO_2 capture: balanced physisorption and chemisorption. *Nanomaterials* 9:E1020. doi: 10.3390/nano9071020

Lai, N., Li, S., Liu, L., Li, Y., Li, J., and Zhao, M. (2017). Synthesis and rheological property of various modified nano-SiO_2/AM/AA hyperbranched polymers for oil displacement. *Russ. J. Appl. Chem.* 90, 480–491. doi: 10.1134/S1070427217030235

Lai, N., Tang, L., Jia, N., Qiao, D., Chen, J., Wang, Y., et al. (2019). Feasibility study of applying modified nano-SiO_2 hyperbranched copolymers for enhanced oil recovery in low-mid permeability reservoirs. *Polymers.* 11:E1483. doi: 10.3390/polym11091483

Langergren, S. (1898). Zur theorie der sogenannten adsorption gelster stoffe. Kungliga Svenska Vetenskapsakademiens. *Handlingar* 24, 1–39.

Lee, Y., and Park, J. (2015). A review on solid adsorbents for carbon dioxide capture. *J. Ind. Eng. Chem.* 23, 1–11. doi: 10.1016/j.jiec.2014.09.001

Liu, H., Chan, C., Tontiwachwuthikul, P., and Idem, R. (2019a). Analysis of CO_2 equilibrium solubility of seven tertiary amine solvents using thermodynamic and ANN models. *Fuel* 249, 61–72. doi: 10.1016/j.fuel.2019.02.088

Liu, H., Idem, R., and Tontiwachwuthikul, P. (2019b). Novel models for correlation of solubility constant and diffusivity of N_2O in aqueous 1-dimethylamino-2-propanol. *Chem. Eng. Sci*. 203, 86–103. doi: 10.1016/j.ces.2019.03.073

Liu, Y., Huang, N., Yu, Y., Zheng, C., Deng, N., and Liu, J. (2016). Bioactive SiO_2@Ru nanoparticles for osteogenic differentiation of mesenchymal stem cells via activation of Akt signaling pathways. *J. Mater. Chem. B* 4, 4389–4401. doi: 10.1039/C5TB01898F

Ma, Y., Wang, Z., Xu, X., and Wang, J. (2017). Review on porous nanomaterials for adsorption and photocatalytic conversion of CO_2. *Chinese J. Catal.* 38, 1956–1969. doi: 10.1016/S1872-2067(17)62955-3

Rashidi, N. A., Yusup, S., and Hameed, B. H. (2013). Kinetic studies on carbon dioxide capture using lignocellulosic based activated carbon. *Energy* 61, 440–446. doi: 10.1016/j.energy.2013.08.050

Rochelle, G. T. (2009). Amine scrubbing for CO_2 capture. *Science* 325, 1652–1654. doi: 10.1126/science.1176731

Sanz-Perez, E. S., Murdock, C. R., Didas, S. A., and Jones, C. W. (2016). Direct capture of CO_2 from ambient air. *Chem. Rev.* 116, 11840–11876. doi: 10.1021/acs.chemrev.6b00173

Sarkodie, S. A., and Strezov, V. (2019). Effect of foreign direct investments, economic development and energy consumption on greenhouse gas emissions in developing countries. *Sci. Total Environ.* 646, 862–871. doi: 10.1016/j.scitotenv.2018.07.365

Sartorl, G., and Savage, D. W. (1983). Sterically hindered amines for CO_2 removal from gases. *Ind. Eng. Chem. Fundam.* 22, 239–249. doi: 10.1021/i100010a016

Titinchi, S. J. J., Piet, M., Abbo, H. S., Bolland, O., and Schwieger, W. (2014). Chemically modified solid adsorbents for CO_2 capture. *Energy Proc.* 63, 8153–8160. doi: 10.1016/j.egypro.2015.12.337

Vaidya, P. D., and Kenig, E. Y. (2007). CO_2-alkanolamine reaction kinetics: a review of recent studies. *Chem. Eng. Technol.* 30, 1467–1474. doi: 10.1002/ceat.200700268

Wang, F., Gao, S., Pan, J., Li, X., and Liu, J. (2019). Short-chain modified SiO_2 with high absorption of organic PCM for thermal protection. *Nanomaterials* 9:E657. doi: 10.3390/nano9040657

Xiao, M., Liu, H., Gao, H., Olson, W., and Liang, Z. (2019). CO_2 capture with hybrid absorbents of low viscosity imidazolium-based ionic liquids and amine. *Appl. Energy* 235, 311–319. doi: 10.1016/j.apenergy.2018.10.103

Xiao, M., Liu, H., Idem, R., Tontiwachwuthikul, P., and Liang, Z. (2016). A study of structure–activity relationships of commercial tertiary amines for post-combustion CO_2 capture. *Appl. Energy* 184, 219–229. doi: 10.1016/j.apenergy.2016.10.006

Yousef, I., ElEswed, B., and AlMuhtaseb, A. A. H. (2011). Adsorption characteristics of natural zeolites as solid adsorbents for phenol removal from aqueous solutions: kinetics, mechanism, and thermodynamics studies. *Chem. Eng. J.* 171, 1143–1149. doi: 10.1016/j.cej.2011.05.012

Yu, C. H., Huang, C. H., and Tan, C. S. (2012). A review of CO_2 capture by absorption and adsorption. *Aerosol Air Qual. Res.* 12, 745–769. doi: 10.4209/aaqr.2012.05.0132

Zhao, Y., Pan, Y., Nitin, N., and Tikekar, R. V. (2014). Enhanced stability of curcumin in colloidosomes stabilized by silica aggregates. *LWT Food Sci. Technol.* 58, 667–671. doi: 10.1016/j.lwt.2014.03.017

Conflict of Interest: DQ was employed by the Engineer Technology Research Institute, CNPC Xibu Drilling Engineering Company Limited company.

The remaining authors declare that the research was conducted in the absence of any commercial or financial relationships that could be construed as a potential conflict of interest.

frontiers in Chemistry

ORIGINAL RESEARCH
published: 23 March 2020
doi: 10.3389/fchem.2020.00184

Functionalized Graphene Oxide Thin Films for Anti-tumor Drug Delivery to Melanoma Cells

Livia E. Sima[1], Gabriela Chiritoiu[1], Irina Negut[2], Valentina Grumezescu[2], Stefana Orobeti[1,2], Cristian V. A. Munteanu[3], Felix Sima[2] and Emanuel Axente[2]**

[1] *Department of Molecular Cell Biology, Institute of Biochemistry, Romanian Academy, Bucharest, Romania,* [2] *Photonic Investigations Laboratory, Center for Advanced Laser Technologies, National Institute for Lasers, Plasma and Radiation Physics, Magurele, Romania,* [3] *Department of Bioinformatics and Structural Biochemistry, Institute of Biochemistry, Romanian Academy, Bucharest, Romania*

OPEN ACCESS

Edited by:
Xiaomin Li,
Fudan University, China

Reviewed by:
Peiyuan Wang,
Fujian Institute of Research on the Structure of Matter (CAS), China
Liang Chen,
Fudan University, China

***Correspondence:**
Livia E. Sima
lsima@biochim.ro
Emanuel Axente
emanuel.axente@inflpr.ro

Specialty section:
This article was submitted to Nanoscience, a section of the journal Frontiers in Chemistry

Received: *01 November 2019*
Accepted: *28 February 2020*
Published: *23 March 2020*

Citation:
Sima LE, Chiritoiu G, Negut I, Grumezescu V, Orobeti S, Munteanu CVA, Sima F and Axente E (2020) Functionalized Graphene Oxide Thin Films for Anti-tumor Drug Delivery to Melanoma Cells. Front. Chem. 8:184. doi: 10.3389/fchem.2020.00184

Since Graphene discovery, their associated derivate nanomaterials, Graphene Oxide (GO) and reduced-GO were in the forefront of continuous developments in bio-nano-technology due to unique physical-chemical properties. Although GO nano-colloids (GON) were proposed as drug release matrix for targeting cancer cells, there is still a concern regarding its cytotoxicity issues. In this study, we report on the fabrication of functional GON bio-coatings by Matrix-Assisted Pulsed Laser Evaporation (MAPLE) to be used as drug carriers for targeting melanoma cells. We first performed a thorough *in vitro* cytotoxicity assay for comparison between GON and protein functionalized GON coatings. As functionalization protein, Bovine Serum Albumin (BSA) was non-covalently conjugated to GO surface. Safe concentration windows were identified in cytotoxicity tests by live/dead staining and MTS assays for five different human melanoma cell lines as well as for non-transformed melanocytes and human dermal fibroblasts. Hybrid GON-BSA nano-scaled thin coatings incorporating Dabrafenib (DAB) and Trichostatin A (TSA) inhibitors for cells bearing $BRAF^{V600E}$ pathway activating mutation were assembled on solid substrates by MAPLE technique. We further demonstrated the successful immobilization for each drug-containing GON-BSA assembling systems by evaluating cellular BRAF activity inhibition and histone deacetylases activity blocking, respectively. DAB activity was proven by the decreased ERK phosphorylation in primary melanoma cells (SKmel28 $BRAF^{V600E}$ cell line), while TSA effect was evidenced by acetylated histones accumulation in cell's nuclei (SKmel23 BRAF WT cell line). In addition, melanoma cells exposed to GON-BSA coatings with compositional gradient of inhibitors evidenced a dose-dependent effect on target activity. Such functional bio-platforms could present high potential for cell-biomaterial interface engineering to be applied in personalized cancer therapy studies.

Keywords: nanomaterials, graphene oxide, thin films, MAPLE, cytotoxicity, drug delivery, melanoma

INTRODUCTION

Carbon-based nanomaterials are extensively used in various fields of nanoscience and nanotechnology due to their exclusive physicochemical properties. Several applications are actively explored in microelectronics, energy-related materials, sensors, and biomedical field (Kuzum et al., 2014; Hong et al., 2015; Li et al., 2017). Among other low-dimensional carbon allotropes, Graphene, a two-dimensional nano-scaled carbon layer, and its derivatives, e.g., Graphene Oxide (GO) and reduced-GO exhibit distinctive advantages, such as large surface area and unique optical properties, as reviewed in Dreyer et al. (2010) and Ferrari et al. (2015). Recent advances are intensively explored in nanomedicine for the synthesis of cell-instructive microenvironments, the targeted applications being related to drug/gene delivery for cancer therapy, bacteria-killing, tissue engineering platforms, engineering stem cell responses, biosensing, and cellular imaging (Negut et al., 2018).

However, studies have shown that nanomaterials may have side-effects on health and human exposure risks were associated with both engineered and environmental nanoparticles (Chang et al., 2011; Dusinska et al., 2015; Guadagnini et al., 2015). The issue is complex since no standard reference to assess nanomaterials cytocompatibility is available. From materials point of view, there are several variables to be considered, such as nanomaterial size, shape, surface chemistry and charge, crystal structure and bandgap, dissolution, and composition-property relationship. Nevertheless, several biochemical indicators of cell proliferation, apoptosis, necrosis, oxidative stress, DNA damage could be investigated to have an integrated analysis of the biocompatibility in case of a specific foreign substance interaction with cells in culture. Predictive toxicology and high-throughput screening using compositional and combinatorial nanomaterial libraries were generally proposed to evaluate hazard scenarios (Nel et al., 2013).

It has been suggested that GO could have distinctive advantages of reduced toxicity over carbon nanotubes (CNTs), owing to its excellent aqueous solubility (without the need to use surfactant to de-bundle and disperse in water), as well as due to lack of metal catalyst impurities considered the cause of oxidative stress related to CNTs (Loh et al., 2010). It was also evidenced that the as-oxidized bare GO does not significantly interfere with A549 cell viability up to a concentration of 50 mg/L (Chang et al., 2011).

It was shown that the cytotoxicity of graphene-based nanomaterials is highly dependent on their functionalization (Oliveira et al., 2015), which gives opportunities to use this type of materials in bio-nano-technology and personalized medicine applications. Some studies evidenced that in case of 2D carbon-based nanomaterials, several parameters influences cytotoxicity (as e.g., particle size, morphology, oxygen content, surface charge, and moreover their concentration) when tested on human erythrocytes, skin fibroblasts (Liao et al., 2011) and neural phaeochromocytoma-derived PC12 cells (Zhang et al., 2010) and revealed the benefits of GO surface coating with Chitosan (Liao et al., 2011). Moreover, it has been reported that functionalized graphene, including GO and GO modified with various macromolecules such as proteins (Bovine Serum Albumine-BSA Mu et al., 2012 and Fetal Bovine Serum-FBS Hu et al., 2011), Chitosan (Liao et al., 2011), Dextran (Zhang et al., 2011), peptides (Bhunia and Jana, 2011), have significantly reduce cytotoxicity.

It became then generally accepted that the surface functionalization of graphene-based nanomaterials is critical to improve solubility, biocompatibility and availability, enhance drug-loading and release efficiency for biomedical applications. There are two main technical approaches for GO surface modification: (i) covalent functionalization, typically carried out by organic reactions, and (ii) non-covalent conjugation with molecules such as polymers (PEG), DNA, proteins, as comprehensively addressed elsewhere (Negut et al., 2018). Among several routes of surface modification, functionalization of carbon nanomaterials with proteins was found the most adequate for biomedical applications (Oliveira et al., 2015).

Matrix Assisted Pulsed Laser Evaporation (MAPLE) is an additive physical vapor deposition technique developed for functionalization of solid substrates with protein and composite coatings. When compared to other classical deposition methods (e.g., drop-cast, spin-coating, dip-coating, Langmuir-Blodgett), this method provides high experimental versatility and relatively facile control of coating thickness even for ultrathin films, the possibility to preserve materials properties even for very delicate compounds, providing adherent and uniform coatings on centimeter sized substrates, micro-fabrication of multilayers from multi-target system, and possibility to generate gradient coatings in a single-step process (Sima et al., 2016; Axente et al., 2018; Axente and Sima, 2020). However, current drawbacks are related to difficulties to fabricate large-area coatings (tens of centimeters) with high uniformity. This method allows the preparation of various drug concentrations to be immobilized as thin layers with controlled thickness covering the substrate material.

Laser-assisted synthesis of thin organic coatings of high-molecular mass such as biopolymers, proteins, and enzymes present various technical challenges. In our previous studies (Sima et al., 2016; Axente et al., 2018; Axente and Sima, 2020) we reported synthesis of highly-functional organic, inorganic and hybrid coatings, for biomedical applications. MAPLE technique proved adequate for the delicate laser transfer of biopolymers, as e.g., levan, a high molecular weight, water-soluble bacterial exopolysaccharide (β2,6-linked fructan). Levan exhibits distinct biomedical applications, having anticancer activity, anti-inflammatory, anticytotoxic, and antitumoral properties as reviewed elsewhere (Oner et al., 2016). Sima et al. (2011c) reported for the first time on pure and oxidized Levan nanostructured thin films assembling by MAPLE. The authors evidenced a high potential of cell proliferation for both coatings (with certain predominance for oxidized Levan) by *in vitro* colorimetric assays. Extracellular matrix proteins, such as fibronectin (FN) and vitronectin were also assembled as thin layers on solid substrates by MAPLE, while preserving their biological functions (Sima et al., 2011a,b). Later, our group (Sima et al., 2015), reported on the possibility to fabricate hybrid inorganic–organic thin implant coatings by laser-based

techniques. Pulsed Laser Deposition was first used for the deposition of hydroxyapatite (HA) coatings, followed by MAPLE technique for assembling FN layers on top for creating a biomimetic interface for implant applications. The authors shown that <7 μg FN per cm^2 onto HA surface is appropriate for improving adhesion, spreading, and differentiation of osteoprogenitor cells.

In this study, non-covalent surface functionalization of GO nano-colloids (GON) with Bovine Serum Albumin (BSA) protein was carried out following the protocol described elsewhere (Mu et al., 2012). We have first evaluated the cytotoxicity of GON and GON-BSA conjugates with respect to several human melanoma cell lines, as compared to normal melanocytes and human dermal fibroblasts, used as non-transformed controls. The goal is to propose a workflow for screening relevant compounds with potential anti-tumor therapeutic effect by using an innovative nano-scaled thin coating platform that contains immobilized active inhibitors for targeting key pathways and processes in cancer cells.

A laser-based approach, MAPLE, is employed herein for assembling such thin coatings on a solid substrate and fabrication of the testing platform aimed at delivery of drugs for skin cancer therapeutic response assessment. As proof-of-concept, we have incorporated BRAF and histone deacetylase (HDAC) inhibitors into GON-BSA systems and validated the functionality of these devised assemblies as molecular weapons against human melanoma cells.

EXPERIMENTAL SECTION

Materials

Graphene oxide nano-colloids (GON) dispersed in H_2O (2 mg/mL), paraformaldehyde (PFA), methanol and all the reagents used for solutions were purchased from Sigma Aldrich. Bovine Serum Albumin (BSA) and goat serum were purchased from Santa Cruz Biotechnology. The signaling pathway inhibitors Dabrafenib/GSK2118436 (DAB) and Trichostatin A (TSA) were purchased from Selleckchem (www.Selleckchem.com).

Preparation of GON-BSA Suspensions

The procedure for non-covalent surface functionalization of GON nanomaterials was performed following the protocols described in Mu et al. (2012). Briefly, GON and BSA solutions (2 mg/mL in MilliQ H_2O) were mixed 1:1 with gentle pipetting and named GONB thereafter. After overnight (O/N) incubation at 37°C, the suspensions were centrifuged at 16 000 g for 30 min at 4°C. The pellet was then washed 3 times with PBS and centrifuged at 16 000 g, 10 min each time. Finally, GONB particles were resuspended in sterile water for further experiments. Further, six serial dilutions (3×) were performed, up to a concentration of ∼1.37 μg/mL. All the solutions were UV sterilized before cell cultures experiments. Alternatively, 50 μL of each GON and GONB solutions, having fixed concentrations of 16 and 48 μg/mL, respectively were drop-casted on glass substrates of 10 × 10 mm^2, to be tested in duplicate for each cell line.

MAPLE Experiments

Detailed protocols for thin coating assembling by MAPLE were addressed elsewhere (Sima et al., 2016; Axente et al., 2018; Axente and Sima, 2020) and briefly described in the following. The procedure consists of laser irradiation of a cryogenic target by a pulsed UV laser beam (**Figure 1**). The target usually contains the solute molecules dissolved in an appropriate laser beam absorbing solvent. During laser irradiation, solute molecules are transferred onto a solid substrate placed parallel to the target by evaporation of the frozen solvent. Specifically, the laser-induced material ejection is generated backward from the solid cryogenic target surface. The evaporated biomolecules flux is then collected on solid substrates, growing, pulse by pulse, a thin coating of thickness from few to several hundreds of nanometers. The target was prepared by immersing aqueous solution of either GON, GONB or GONB-inhibitor in liquid nitrogen. After solidification, the target is placed inside a stainless-steel reaction chamber and evaporated using an UV excimer KrF* laser source (Lambda Physics Coherent, COMPexPro 205 model) delivering pulses at $\lambda = 248$ nm, with pulse duration $\tau_{FWHM} = 25$ ns, operated at $\upsilon = 10$ Hz. Batches of thin coatings were grown on glass and silicon substrates placed parallel to the target surface at a separation distance of 40 mm. Before depositions, the substrates were cleaned in successive ultrasonic baths of acetone, ethanol, and deionized water. The substrates were kept at room temperature, the depositions being performed in a dynamic pressure of $\sim 2 \times 10^{-2}$ mbar. After optimization trials, 25.000 subsequent pulses of <1 J cm^{-2} incident laser fluence were applied for the synthesis of each structure. Two irradiation protocols were employed: GONB-inhibitor thin coatings with the same composition were obtained by rotating the substrates ($\upsilon_{rot} = 10$ rot/min, **Figure 1A**), while coatings with compositional gradient were obtained by keeping the substrates fixed (**Figure 1B**). Here, the main evaporation flux was directed to sample C1, and a concentration gradient to C3 is naturally achieved due to material spreading along the radial-orthogonal direction of the substrates (x direction in **Figure 1B**). The goal of adopting this irradiation geometry was designed to generate compositional gradient coatings, in a single-step process, and to investigate a dose-dependent effect, with respect to inhibitor spatial distribution.

Physical-Chemical Characterization of GON and GONB Nanocomposites

Morphological investigations of the nanomaterials were performed by scanning electron microscopy (SEM) (FEI-Inspect S50, Japan) and atomic force microscopy (AFM) (TT AFM Workshop, USA) in vibrating mode. All AFM images were recorded on 15 × 15 μm^2 areas. Optical absorption spectra of the solutions were also recorded with a double beam spectrophotometer (Thermo Scientific, model Evolution 220) in the 200–900 nm wavelength range. Fourier transform infrared (FTIR) spectrometry studies were performed in absorption mode with a Shimadzu 8400S instrument. Forty scans were carried out on each sample while the investigated range was set to 500–4,000 cm^{-1} with a resolution of 4 cm^{-1} wavenumber.

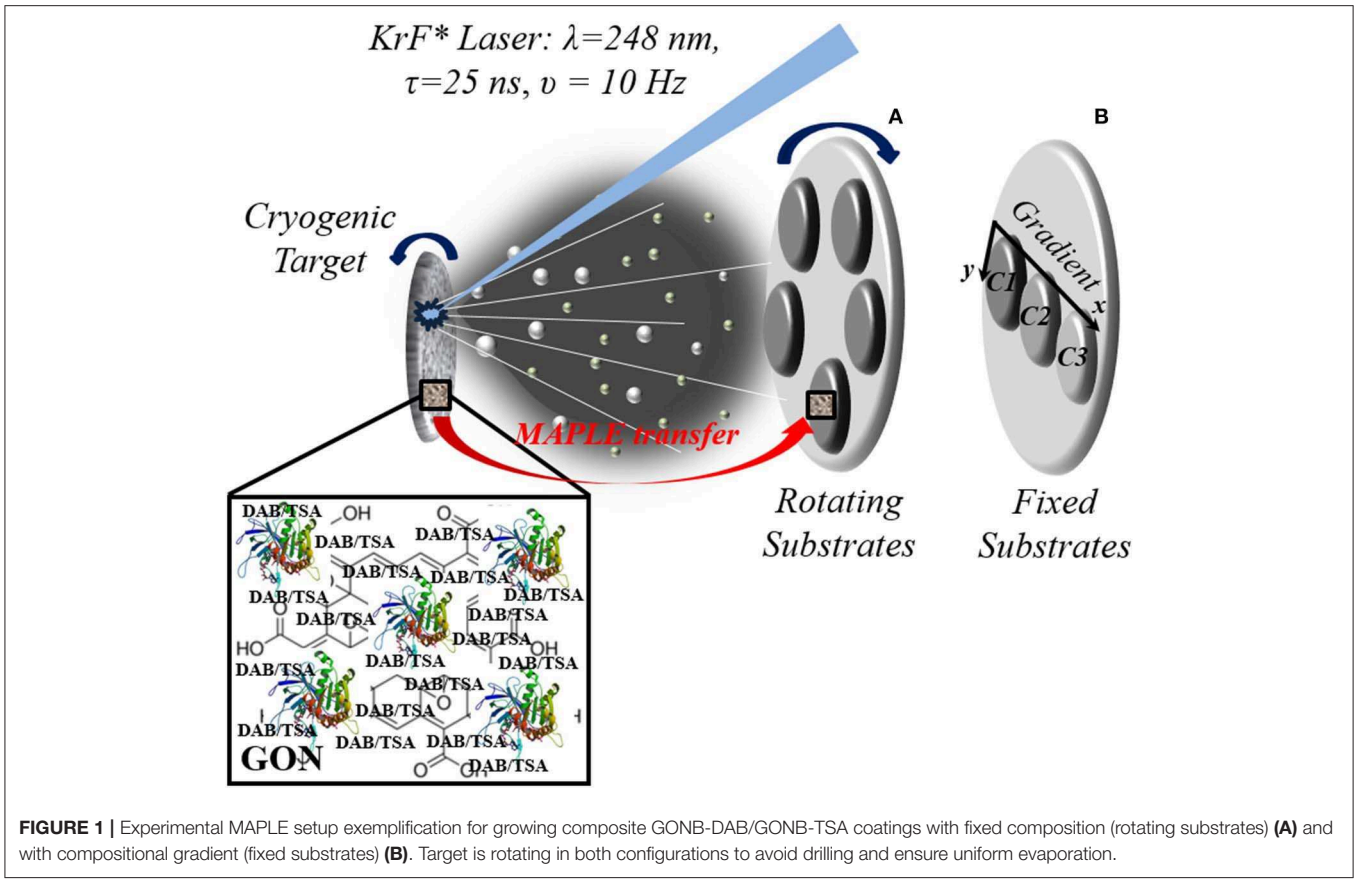

FIGURE 1 | Experimental MAPLE setup exemplification for growing composite GONB-DAB/GONB-TSA coatings with fixed composition (rotating substrates) **(A)** and with compositional gradient (fixed substrates) **(B)**. Target is rotating in both configurations to avoid drilling and ensure uniform evaporation.

Cell Cultures

Seven model human cell lines were used in this study (see **Table 1** for phenotype details). A375 and human dermal fibroblasts (HDF) were grown in DMEM high-glucose medium (Gibco, #31966), supplemented with 10% inactivated fetal bovine serum (FBS) and 1% Penicillin/Streptomycin (Pen/Strep). SKmel28, SKmel23, MelJuSo were grown in RPMI (Gibco, #61870) supplemented with 10% inactivated FBS, 1% Sodium Pyruvate, 1% HEPES, 1% Non-Essential Amino Acids (NEAA), 1% Pen/Strep. MNT-1 were grown in DMEM high-glucose medium, supplemented with 20% inactivated FBS, 10% AIM-V and 1% Pen/Strep. All supplements were from Gibco. Normal human epidermal melanocytes (NHEM) were grown in MBMTM-4 Basal Medium (#CC-3250) supplemented with MGMTM-4 SingleQuotsTM Supplements (#CC-4435) (LONZA). For experiments, the cells were counted and plated at different densities, as follows: MNT-1: 33,333/cm2, MelJuSo, Skmel28, SKmel23: 16,700/cm2, A375: 13,500/cm2, NHEM: 10,667/cm2, and HDF: 4,000/cm2 followed by culture in standard conditions or in the presence of GON/GONB colloidal suspensions or films.

TABLE 1 | Cell lines characteristics.

Cells	Malignancy phenotype	Mutation status	Pigmentation
MNT-1	Primary melanoma	BRAF V600E	Highly pigmented
SKmel28	Primary melanoma	BRAF V600E	Amelanotic
MelJuSo	Primary melanoma	BRAF wt; N-Ras Q61K	Amelanotic
A375	Metastatic melanoma	BRAF V600E	Amelanotic
SKmel23	Metastatic melanoma	BRAF wt	Pigmented
NHEM	Normal primary melanocytes		Pigmented
HDF	Normal dermal fibroblasts		–

In vitro Assays of Cytotoxicity and Graphene Constructs Functionality

Cell Viability Assessment by MTS Assay

The influence of graphene nanomaterials on melanoma cells viability and proliferation after culture in the presence of different serial dilutions of GON and GONB, respectively was assessed using CellTiter 96® Aqueous One Solution Cell Proliferation Assay kit (Promega). Cells were seeded in 96-well plates in the densities stated above and left to attach. The following day, freshly obtained GONB were added in parallel with GON as 3-fold dilution series to the cell monolayers, after 30 min UV sterilization. Cells were grown in the presence of graphene for 72 h. The optical density at 450 nm was determined 1 h after MTS reagent was added and incubated at 37°C. All the nano-colloidal solutions were tested in triplicate, against untreated cells used as controls, the results being expressed as mean values after background substraction. The absorbance values are directly proportional with the number of the

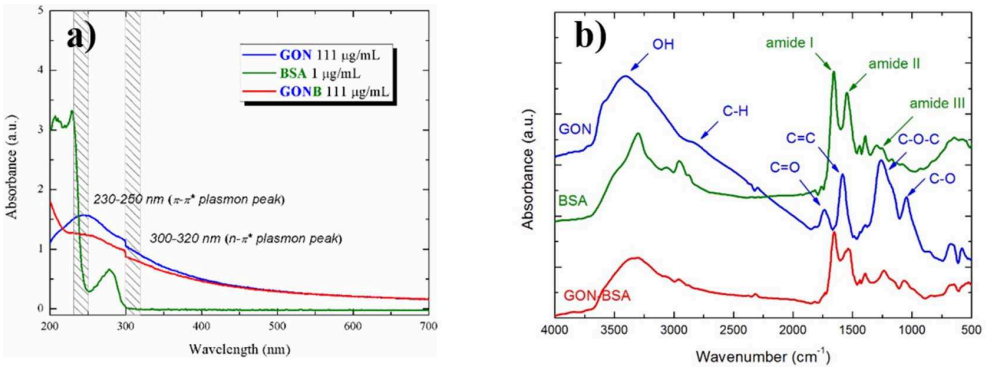

FIGURE 2 | UV-Vis absorbance **(a)** and FT-IR spectra **(b)** of GON, BSA, and GONB nanomaterials.

metabolically active cells grown in the presence of the tested nanomaterials. For testing graphene interference with the assay, several readings were performed for comparison: (1) the 96-well plate containing the graphene dilutions and added MTS; (2) the plate containing 72 h grown A375 cells only; (1+2) the plate containing cells to which we added the graphene media dilutions plus MTS read at time t0 and after 1 h incubation at 37°C.

Cell Viability Assessment by Live/Dead Staining

The evaluation of cells viability and cytotoxicity of the serial dilutions of nano-colloids as well as GON and GONB thin films synthesized by MAPLE was performed using a LIVE/DEAD Viability/Cytotoxicity Assay Kit (Life Technologies) that allowed the simultaneous identification of live vs. dead cells by fluorescence assessment. The method is based on the evaluation of two characteristic parameters of cellular viability, namely the esterase intracellular activity and plasma membrane integrity. To this purpose, cells are incubated with two dyes: Calcein and Ethidium homodimer (EthD-1). The former is a non-fluorescent molecule, having the ability to penetrate by diffusion the cell membrane, which in the presence of intracellular esterase is modified to become fluorescent and is retained in viable cells. The later can penetrate the cells only if the membrane is damaged and its fluorescence is amplified up to 40 times, upon linking to nucleic acids.

We used 1 μM Calcein and 2 μM EthD-1 in PBS to stain live and dead cells, respectively, at 72 h upon seeding in the presence of graphene. The staining was performed 30 min at room temperature, followed by washing with PBS and fixing with 4% PFA to allow timely analysis of all tested samples. Finally, the samples were subjected to Hoechst nucleus staining (1:3,000) and mounting with ProLong Gold Antifade Reagent (Life Technologies). The samples were scanned with the TissueFAXSiPlus (TissueGnostics, Vienna, Austria) automated image cytometry system that allows whole specimen reconstitution for analysis and archiving.

For evaluating the cytotoxicity of the GONB/GONB-inhibitors films, cells were seeded onto the films coated glass surface and were in direct contact with the films during the course of the experiment.

Graphene-Inhibitors Functionality Assessment by Immunofluorescence Microscopy

All samples were investigated by fluorescence microscopy after staining with Alexa Fluor 488 Phalloidin (Life Technologies) in combination with either anti-phospho-ERK (1:1,000, Cell Signaling, #4695) or anti-acetyl histone H3 (1:1,000, Abcam, #ab47915) antibodies. After 72 h of cell culture onto GONB-DAB or GONB-TSA thin films, cells were gently washed with PBS to remove non-attached cells and serum proteins. The adherent cells were fixed with 4% PFA solution for 15 min at room temperature (RT) or with ice cold 100% methanol for 5 min at −20C°. After fixation, for phospho-ERK labeling, cells were permeabilized with 0.3% Triton-X-100 (TX) in PBS for 3 min, and then blocked for 30 min at RT in 5% goat serum diluted in permeabilization buffer. For acetyl histone H3, the cells were directly blocked in 1% BSA, 10% normal goat serum, 0.3 M glycine diluted in 0.1 % PBS-Tween for 1 h. The cells were stained with primary antibodies O/N at 4°C. After removing the excess of unbound antibodies, the cells were incubated in a buffer solution (1% BSA in 0.3% PBS-TX) containing the secondary antibody conjugated to Alexa Fluor 594 (1:400) (Life Technologies) and the Phalloidin conjugated to Alexa Fluor 488 (1:100) that binds specifically the actin filaments. After 30 min, cells were washed, stained for 1 min with Hoechst (Sigma) and then mounted on slides using the Prolong Gold Antifade Reagent solution (Life Technologies). Cells were finally analyzed using the ZEISS Axio Imager Z1 microscope and the AxioVision software. The gradient coatings were examined using the TissueFAXSiPlus system (TissueGnostics, Vienna, Austria).

RESULTS

Physico-Chemical Characterization of the Nanomaterials

UV-Vis absorption spectra of the starting GON, BSA and GONB solutions are presented in **Figure 2a**. BSA spectrum (green curve) exhibits two absorption peaks at about 220 and 280 nm. The strong one at around 220 nm reflected the absorption of the backbone of BSA, while the weak absorption peak at around 280 nm is specific to the aromatic amino acids (Trp, Tyr, and Phe) (Xu et al., 2013). In case of GON (blue curve), two plasmonic

peaks in the 230–250 nm (π-π^*) and 300–320 nm (n-π^*) regions are attributed to C=C and C=O transitions, respectively (Konios et al., 2014). GONB spectrum (red curve) contains both GON and BSA peaks. This represents the evidence of the GON-BSA mixture and the first confirmation of the successful GON functionalization with BSA protein.

The UV-Vis results were supported by the IR absorption spectra, with respect to successful non-covalent GO conjugation with BSA. In **Figure 2b** there are shown the spectra of GON (blue curve), BSA (green curve), and GONB (red curve) in the 4,000–500 cm^{-1} range. GON spectra is characterized by the absorption bands of –OH (~3,400 cm^{-1}), C=O (~1,700 cm^{-1}), C=C (~1,600 cm^{-1}), C-O-C (~1,200 cm^{-1}) and C-O (~1,050 cm^{-1}) vibrations (Konios et al., 2014). Protein spectra is dominated by the vibration bands characteristic to amides (I, II, and III) at around 1,650, 1,540, and 1,250 cm^{-1}, respectively (Pauthe et al., 2002). GON functionalization with BSA is evidenced in the mixed GONB spectra that contains all the peaks belonging to the initial materials.

Next, we used the functionalized GONB nanomaterials to include two different signaling pathway inhibitors with potential use as anti-melanoma drugs: dabrafenib (DAB) and Trichostatin A (TSA). In order to validate the functionality of our proposed assemblies we performed experiments to estimate the drug loading content and the released fractions of TSA from GONB nanoparticles in different pH conditions. In order to eliminate possible sample handling artifacts, we opted for the analysis of the unbound and released TSA fractions by direct infusion using

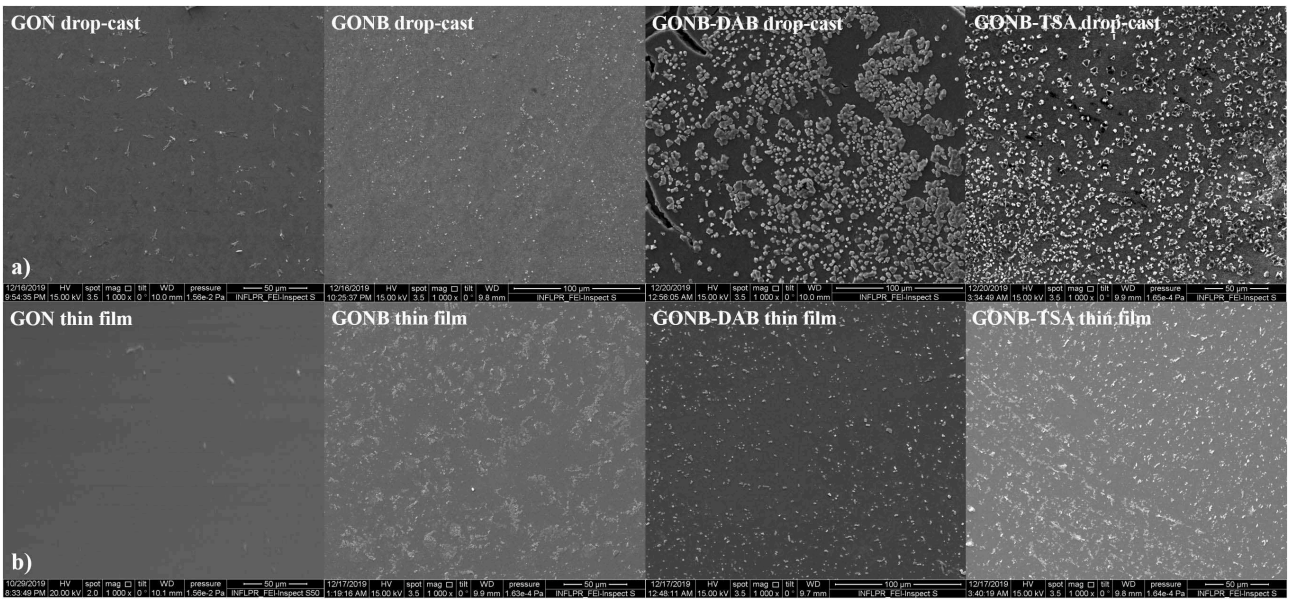

FIGURE 3 | SEM images of drop-casted **(a)** and thin coatings **(b)** for GON, GONB, GONB-DAB, and GONB-TSA deposited on Silicon substrates.

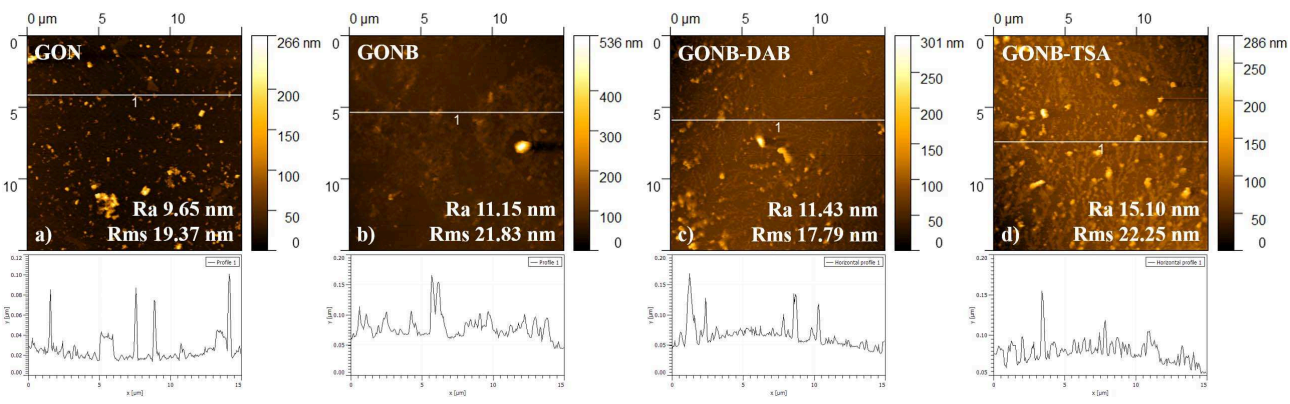

FIGURE 4 | AFM images and height profiles of GON **(a)**, GONB **(b)**, GONB-DAB **(c)**, and GONB-TSA **(d)** thin films grown on Si, after scanning of 15 × 15 μm^2.

nanoESI (ElectroSpray Ionization) and High-Resolution Mass Spectrometry (HRMS). Previous works have shown that direct injection MS analysis of small molecules can be used to estimate their concentration level in a sample (Zhang et al., 2004; Alfazema et al., 2005). We first tested the linearity of the signal by infusing solutions with different concentrations of standard TSA (**Supplementary Figure 1I**). We observed a linear signal for concentrations up to low μM, confirming previous results (Zhang et al., 2004; Alfazema et al., 2005). We next interrogated unbound and released samples, for TSA identification and quantification. Analysis of the precursor ions confirmed the presence of the TSA protonated precursor molecular ion at m/z 303.17 in both categories of samples (**Supplementary Figures 1C–E**). The m/z was similar to the one obtained by simulation of the TSA spectrum (**Supplementary Figure 1A**) and with the ion identified in the standard sample (**Supplementary Figure 1B**). Further comparison of the MS/MS fragmentation spectra with the standard (**Supplementary Figure 1F**) confirmed the identification of TSA in both unbound and released samples (**Supplementary Figures 1G,H**). We defined quality criteria for the confirmation of TSA in each analyzed sample as described under *Supplementary Materials and Methods* section. Once confirmed (**Supplementary Table 1**), we next estimated by regression analysis the level of TSA based on the precursor ion intensity measured in each sample (**Supplementary Figure 1J**). We assessed the TSA concentration in the unbound fraction in the lower nanomolar, corresponding to <5% of TSA remained compared with the starting concentration of 125 μM (**Supplementary Figure 1I**, red dot corresponds to the estimated TSA). Furthermore, our results revealed a decreasing pattern, with time, of the TSA concentration level in the released samples, regardless of the pH used for sample collection (**Supplementary Figure 1J**).

Morphological Investigations of the Thin Nanomaterial Films

Figure 3 shows SEM images of GON, GONB, GONB-DAB, and GONB-TSA drop-casted (**Figure 3a**) and thin coating grown on Silicon substrates by MAPLE (**Figure 3b**). The thin coatings look uniform, compact and do not present any sign of cracks and peeling, evidencing a high adherence to the substrates. Smoother coating surfaces could be evidenced in case of GON thin films while the presence of the protein was found to change drastically the morphology, which results in higher roughness. Micrometers-sized regular structures could be related to the crystallized salts from the buffer solutions transferred along with the protein on solid substrates (Sima et al., 2011b). Nanoscale features of the coatings were evaluated by AFM topographical analyses on the surfaces. **Figure 4** presents 2D images of GON, GONB, GONB-DAB, and GONB-TSA thin coatings along with their surface roughness parameters and height profiles. In **Figure 4a**, the spatial distribution of a single graphene sheet of 1 μm lateral dimension and 20 nm height can be noticed from GON sample. In comparison, GONB revealed a significant morphological modification with surface height profiles changing accordingly (**Figure 4b**). In addition, the roughness parameters of the GONB surfaces (Ra and Rms) were found higher compared to those obtained on simple GON (**Figure 4b**). GONB-DAB thin coatings exhibited similar topographical characteristics with GONB samples (**Figure 4c**), whereas GONB-TSA indicated the highest roughness values (**Figure 4d**). More insights in the surface topographical aspects

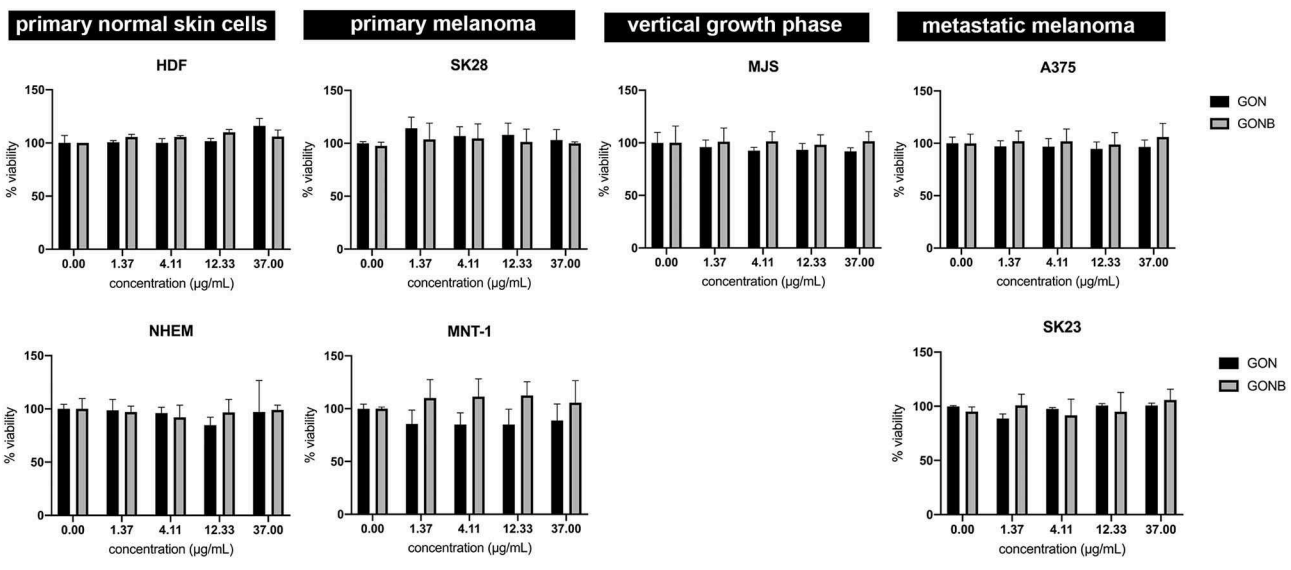

FIGURE 5 | MTS assay results showing no cytotoxicity for both GON (black columns) and GONB (gray columns) on controls and malignant skin cells up to concentrations of 37 μg/mL.

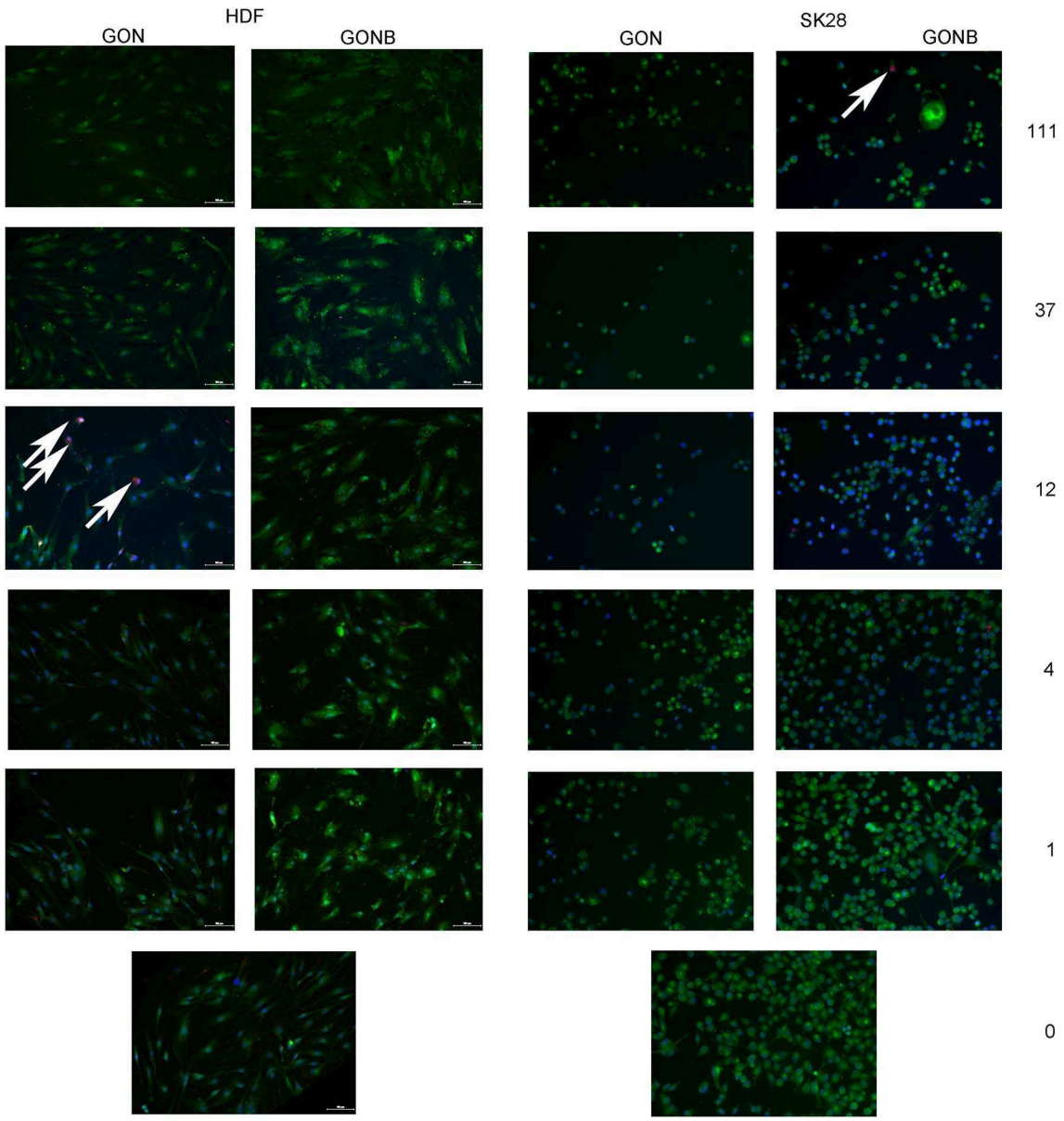

FIGURE 6 | Representative fields of view obtained by TissueFAXS scanning of GON and GONB solutions treated HDF or SK28 cells, evidencing superior biocompatibility of BSA functionalized GON (GONB) when compared to simple GON. The white arrows indicate the EthD-1 stained dead cells nuclei. Viable cells stained with calcein are visible in green. Scale bar = 100 μm.

can be found in **Supplementary Figure 2** where the 3D surface profiles are depicted.

Cytotoxicity Assays of Nanocomposite Solutions and Thin Films

Quantitative Assessment of Cytotoxic Potential of Graphene Colloidal Solutions

In order to assess the cytocompatibility degree of both GON/GONB solutions and thin films, we have performed cell biology experiments on representative cell lines, on both normal phenotype cells e.g., dermal fibroblasts and melanocytes (used as normality controls) and cell lines exhibiting various stages of tumorigenicity encountered in malignant melanoma (A375, MJS, MNT-1, SKmel23, SKmel28).

The goal of the first set of experiments was to identify the maximum graphene nanoparticles concentrations that can be safely applied without inducing cytotoxic effects, to be further assembled in form of thin coatings by MAPLE. In addition, we compared the simple and functionalized nanomaterials in

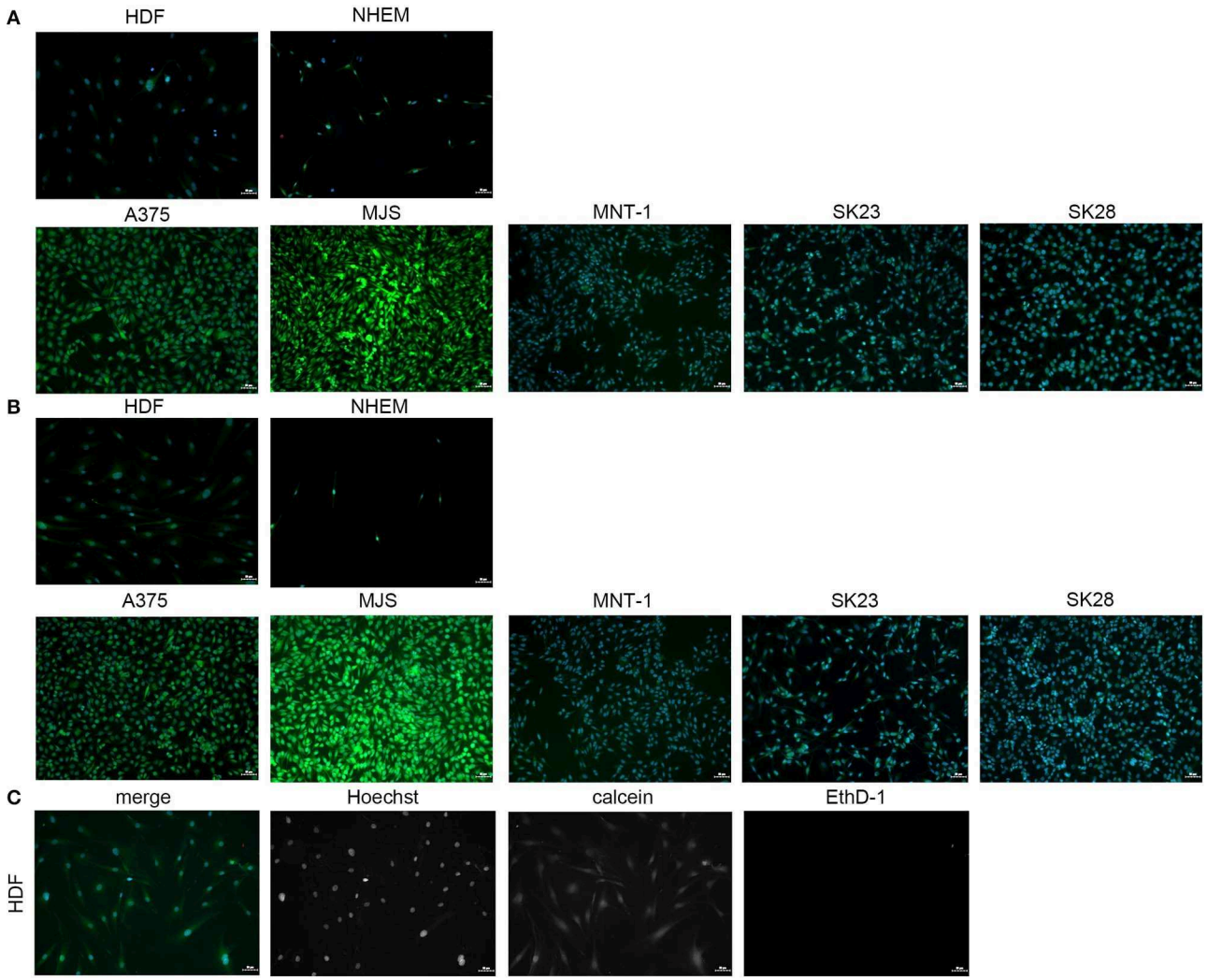

FIGURE 7 | Immunofluorescence microscopy images obtained by scanning GON **(A)** and GONB **(B)** thin films obtained by MAPLE upon culture with normal skin cells and melanoma cells. The images revealed high biocompatibility for both GON and GONB thin films on control and human melanoma skin cells grown after 72 h. Viable cells are shown in green due to calcein staining. Dead cells were not detected. Merged images were obtained by overlapping the TissueFAXS captured fields of view on each fluorescence channel for detection of Hoechst, calcein, and EthD-1 **(C)**. Images correspond to HDFs grown on standard cover slip borosilicate glass. Scale bar = 50 μm.

order to identify the best host matrix for melanoma inhibitor embedding and release. An ideal delivery platform should not affect the normal skin cells, while the tumor cells should undergo apoptosis following exposure to targeted drugs with inhibitory activity against specific signaling pathways that mediate tumors growth and resistance to chemotherapeutics.

We have first investigated the influence of GON and GONB 3-fold serial dilutions (in the range of 0–1,000 μg/mL) on both primary control cells and melanoma cell lines by quantifying metabolically active cells using the MTS assay at 72 h upon treatment. During the optimization process we observed that graphene preparations interfere with absorbance measurements at 450 nm. Using A375 melanoma cells we tested the contribution of adding GON or GONB nanoparticle suspensions onto cells in the presence of MTS reagent before and after 1 h incubation. Results showed that there is no interference from GOs on OD measurements at 450 nm up to 37 μg/mL for GON or 111 μg/mL in case of GONB (**Supplementary Figure 3**). Therefore, we sought to test the cytotoxic potential of GOs when added in suspension to normal skin cells or melanoma using concentrations up to 37 μg/mL. The viability data as function of nanomaterial concentrations are presented in **Figure 5**. Results showed no significant viability decrease at concentrations up to 37 μg/mL for both GON and GONB on all melanoma cell lines tested in this study, representative for primary, vertical growth phase, and metastatic cancer, as well as for normal skin cells (**Figure 5**). In order to confirm the results, we next performed a live/dead double staining of HDF and

SKmel28 cells. Immunofluorescence microscopy results have shown that GONB are not inducing any toxic reaction in HDF at concentrations up to 111 μg/mL while simple GON evidenced cytotoxicity signs at 12 μg/mL (**Figure 6**, HDF). Analyses of melanoma cells showed ∼ 100% viable cells in all tested conditions (**Figure 6**, SK28). In order to confirm assay specificity, we evaluated both calcein and EthD-1 optimized concentrations on untreated cells or cells treated for 10 min with ethanol. As shown in **Supplementary Figure 4**, dermal fibroblast cells (**Supplementary Figures 4A,B**) and melanocytes (**Supplementary Figures 4C,D**) grown in standard conditions (a and c) are fully viable, while all those fixed in ethanol (b and d) exhibit red-emitting nuclei.

By correlating the live/dead staining (**Figure 6**) and MTS assays (**Figure 5**), we were able to identify safe concentration windows for both nanomaterials.

Testing the Cytotoxic Potential of Nanomaterial MAPLE Thin Films

Prior to laser deposition experiments, we tested the viability of HDF cells when grown onto GON and GONB drop-casts obtained from solutions at two different concentrations: 16 and 48 μg/mL, respectively. Cell viability was preserved in all tested conditions (**Supplementary Figure 5**); plain glass substrate was used as positive control whereas ethanol treatment was used as negative.

Thin coatings were obtained by MAPLE technique starting from GON and GONB cryogenic targets (see coating surface morphologies and topographies in **Figures 3**, **4**). Similar to testing of nanomaterials in colloidal suspension, and as drop-cast, calcein/EthD-1 double staining was performed after 72 h culture, followed by immunofluorescence microscopy analyses to assess GON (**Figure 7A**) and GONB (**Figure 7B**) cytotoxic potential when presented to cells as deposited thin coatings. **Figure 7C** shows the obtaining of the merged images by overlapping the captured fields of view generated on each fluorescence channel, upon fixation and Hoechst nuclei labeling. After scanning the entire samples, no dead cells were detected for all MAPLE samples, with respect to whole spectrum of cell lines used in this study (representative fields of view in **Figure 7**). This complements the MTS assay results obtained on nanomaterial solutions (**Figure 5**). The images revealed biocompatibility for both GON and GONB thin films on normal primary melanocytes and dermal fibroblasts, as well as human melanoma cells grown for 72 h onto MAPLE graphene coatings.

Investigation of Functionalized GONB MAPLE Thin Films Embedding Inhibitors

Benefiting from the fact that GONB thin films do not induce cytotoxic effects *per se*, we have addressed the possibility to fabricate functional thin films incorporating inhibitors for targeting specific signaling pathways/processes associated with malignant transformation. First, we have chosen a BRAF inhibitor, Dabrafenib (DAB), a drug already approved by the FDA in 2013 for the treatment of advanced metastatic melanoma bearing the mutated BRAF gene ($BRAF^{V600E}$) found in ∼70% of melanoma tumors (Davies et al., 2002). It has the advantage of a low IC_{50} index, which makes it effective at nM concentrations. Thin coatings containing DAB in the GONB matrix were assembled on glass substrates by MAPLE. The resulting nano-layers (thickness <50 nm) were tested against SKmel28 cell line, which exhibits the mutant version of the BRAF gene, that constitutively activate the MAPK signaling pathway downstream of this kinase. As a direct effect, a continuous phosphorylation of ERK protein is observed (Wan et al., 2004). The clear proof of DAB activity is quantified in BRAF inhibition and corresponds to a decreased phosphorylated ERK (pERK) expression. In order to evaluate inhibitor potency upon embedding in the MAPLE deposited graphene layers, we performed immunofluorescence microscopy using specific antibodies against pERK in combination with phalloidin that allows visualization of the entire cell based on the actin cytoskeleton footprint (**Figure 8**). Indeed, one could easily notice that the pERK protein expressed in $BRAF^{V600E}$ SKmel28 cells grown on GONB coated glass (**Figure 8A**), is not found in cells grown up to 72 h on DAB containing GONB thin films (**Figure 8B**). As control conditions for these findings, SKmel28 melanoma cells were grown on standard cover slips in the absence (**Figure 8C**) or presence of 0.5 nM DAB (**Figure 8D**), a situation resulting in a similar total suppression of pERK expression. SKmel23 cell line that contains the unmodified version of BRAF gene and which consequently express low steady-state levels of pERK protein were used as negative technical controls for pERK staining specificity (**Figure 8E**).

Second, we have tested the functionality of a histone deacetylase (HDAC) inhibitor, Trichostatin A (TSA), an epigenetic modulator that is currently tested in clinical trials for relapsed or refractory hematologic malignancies. Recently, HDAC inhibitors were shown to dramatically enhance the efficacy of BRAF/MEK inhibitors in sensitive and insensitive RAS pathway–driven melanomas (Maertens et al., 2019). A direct effect of HDACi treatment is the accumulation of acetylated histones in the nucleus, the substrates of histone deacetylases. Acetylated histones are known as epigenetic marks of active genes (Roh et al., 2005). Use of HDACi is expected to recover tumor suppressor genes activity that was lost during the cancer transformation process (Li and Seto, 2016). To validate TSA inhibitor activity upon embedding in the GONB matrix and laser deposited coatings, we performed immunofluorescence microscopy to assess accumulation of acetyl histone H3 in the nucleus of melanoma cells (**Figure 9**). Our results show that culture of SKmel23 melanoma cells for 72 h on TSA containing GONB films induces increase in nuclear signal corresponding to anti-acetyl histone labeling (**Figure 9**).

With a view to demonstrate the high potential for development as drug combinations screening platform, our next aim was to validate the MAPLE grown GON-BSA coatings with compositional gradient of inhibitors by exposing the melanoma cells to its content and explore the potential dose-dependent effect. For this purpose, we used the already described immunofluorescence approaches to assess the dose-dependent response of cells to different concentrations of

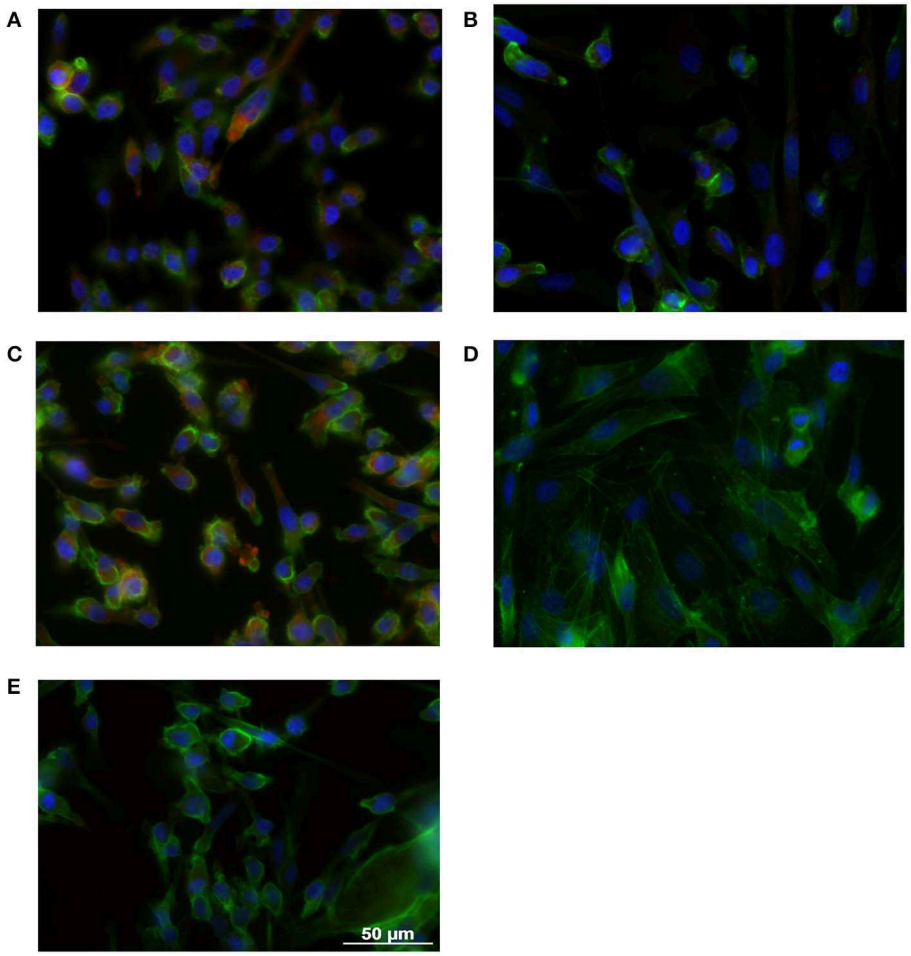

FIGURE 8 | Immunofluorescence microscopy images obtained on SK28 human melanoma cell line grown on GONB MAPLE thin films without **(A)** or with **(B)** DAB BRAF inhibitor. SK28 malignant cells grown in standard conditions in the absence **(C)**, or in the presence **(D)** of 0.5 nM DAB were used as controls of DAB activity. The comparison with SK23 melanoma cells that express wild type BRAF is presented in **(E)**. Cells were stained with anti-phospho-ERK antibodies (red) and Phalloidin (green) for exhibiting MAPK pathway activation and the cellular cytoskeleton consisting of actin filaments, respectively. Nuclei were stained with Hoechst (blue). Scale bar = 50 µm.

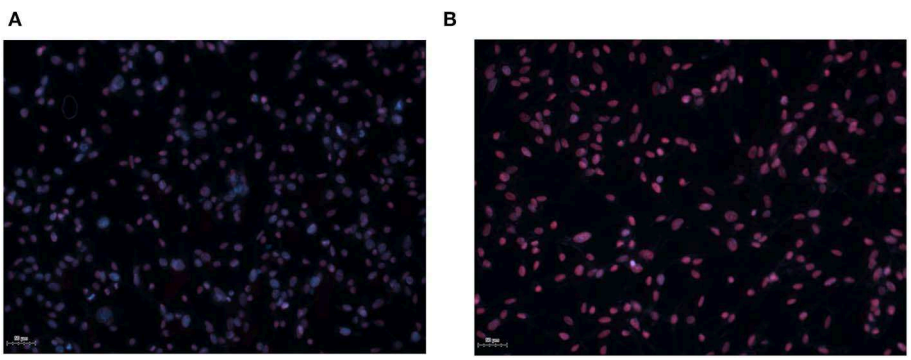

FIGURE 9 | Immunofluorescence microscopy images obtained on SK23 human melanoma cell line grown on GONB MAPLE thin films without **(A)** or with **(B)** TSA HDAC inhibitor. Cells were stained with anti-acetyl histone H3 antibodies (red) and Hoechst (blue) for nuclear labeling. Scale bar = 50 µm.

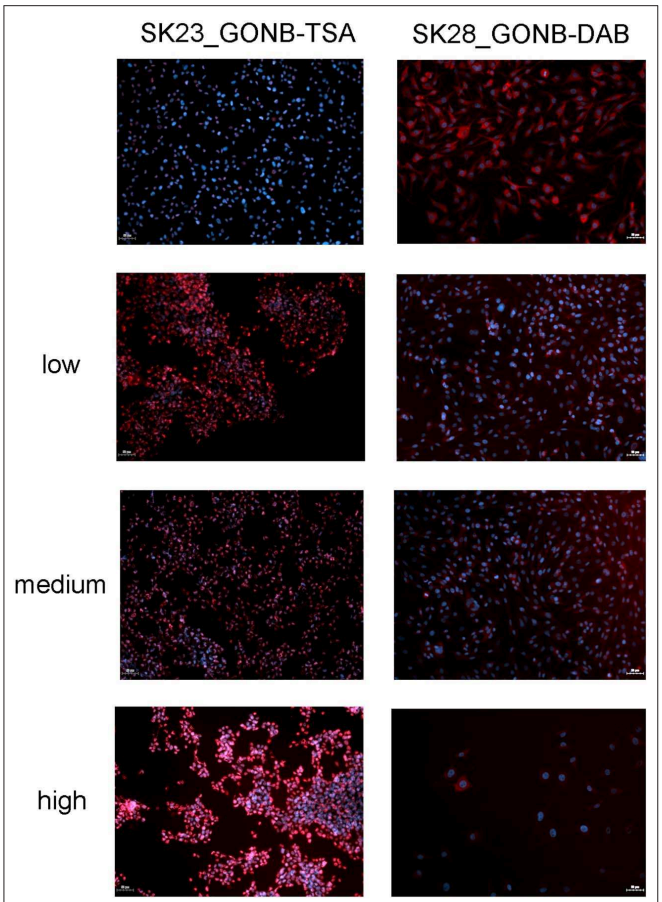

FIGURE 10 | GONB-DAB and GONB-TSA gradients (from low to high) functionality was tested by immunofluorescence microscopy as in **Figures 8**, **9**, respectively, in comparison with GONB only substrates. Expressions of pERK and acetylated histone H3, respectively are labeled in red while nuclei are labeled in blue (Hoechst). Scale bar = 50 μm.

graphene-inhibitor complexes. Increasing concentrations of GONB-TSA induced an increase in fluorescence signal intensity and proportion of SKmel23 cells expressing acetyl histone H3 in the nucleus (**Figure 10**, left panel). Also, increasing concentrations of GONB-DAB induced a stepwise decrease in pERK signal of SKmel28 cells (**Figure 10**, right panel) as compared to cells treated with GONB alone (**Figure 10**, right panel, top image). Simultaneously, we observed a decrease in cell density on graphene coatings carrying a higher concentration of inhibitors, which motivates us to conduct more in-depth studies in the future in order to determine the conditions ensuring specific targeting of cancer cells.

Our results have demonstrated functionality of DAB and TSA inhibitors after laser immobilization in GONB matrix and subsequent assembly as thin coating, against specific molecular targets in melanoma cells. All these results are proving the high potential of functionalized GON nanoscale thin coatings to uptake different signaling pathway inhibitors without losing their activity.

DISCUSSION

In this study, we demonstrate the congruent and controlled transfer by MAPLE of functional assembling systems of GON containing BSA and anti-cancer drugs, on solid substrates. BSA is a neutral protein with a high molecular weight of about 66.5 kDa, having various biochemical applications. It was used with this study for GON functionalization to minimize potential graphene cytotoxicity and as a drug-carrier. Accordingly, one would expect that laser-induced damage of BSA, would result in inhibitors damage and/or loss of functionality. Noteworthy, during the laser mediated process, the drug molecules preserved their inhibitory activities when included in the GONB matrices. Dabrafenib is an inhibitor that proved beneficial activity in clinical trials of phase 1 and 2 in patients with $BRAF^{V600E}$-mutated metastatic melanoma (Huang et al., 2013). Its chemical formula: $C_{23}H_{20}F_3N_5O_2S_2$, reveals a complex stoichiometry and the presence of several volatile elements that could be irreversibly damaged by laser irradiation, and thus, the severe alteration of inhibitor properties. TSA has the chemical formula $C_{17}H_{22}N_2O_3$, exhibiting a complex molecular structure, being an HDAC epigenetic inhibitor used in phase 1 of clinical trials. We demonstrated that GONB-DAB and GONB-TSA composite coatings are effective against melanoma cells during *in vitro* assays. Our choice of compounds for this proof-of-concept study was based on the high therapeutic potential of BRAF and HDAC inhibitors. BRAF inhibitors are targeting the most prevalent melanoma-driving mutation, $BRAF^{V600E}$ (Davies et al., 2002) and several molecules in this category are FDA approved (NIH U. S. National Library of Medicine, 2019). HDAC inhibitors are a promising class of compounds that showed low side effects while constituting an alternative treatment for hematological as well as solid malignancies (Johnstone, 2002; Kelly and Marks, 2005). Two HDAC inhibitors (Vorinostat and FK228) are already FDA approved for the treatment of cutaneous T-cell lymphoma.

MAPLE method preserved drug inhibitor activity of DAB and TSA, as proven by the specific effects on their intracellular molecular targets. Decrease of ERK phosphorylation with increasing gradient concentration of DAB was obtained. Also, nuclear accumulation of acetylated histones in melanoma cells exposed to GONB-TSA was recorded.

Future Combinatorial MAPLE (C-MAPLE) produced thin film bio-platforms (Oner et al., 2016; Axente and Sima, 2020), incorporating other drugs or active substances could be efficient for testing drug combinations co-targeting a specific cancer cell population. Indeed, once safe concentration windows on nanomaterials cytotoxicity are identified, further functionalization offers the possibility to create smart materials, exhibiting improved properties for melanoma therapeutic screening. The main mechanism associated with BRAF inhibitors resistance is the reactivation of the MAPK pathway (Alcala and Flaherty, 2012; Manzano et al., 2016). It is critically important to understand the mechanisms of resistance to targeted therapy and find the means to overcome this situation to maximize patient's survival. In 2017, FDA approved DAB administration in combination with Trametinib, another MAPK inhibitor, for the treatment of a subtype of patients with

non-small cell lung cancer bearing the $BRAF^{V600E}$ mutation. These premises extend the possibility to use combinations including DAB also in other cancers (Ji et al., 2012). HDAC inhibitors were shown to sensitize melanoma cells to BRAF/MEK inhibitors (Maertens et al., 2019). These examples of therapeutic combinations could be further extended using efficient miniaturized platforms able to support the high throughput micro-screening of compounds on biopsies or circulating tumor cells (Tolcher et al., 2018).

Our current research efforts are dedicated to laser-based fabrication of thin coatings with multiple drug combinations for testing their synergy and anti-tumor efficacy.

CONCLUSIONS

BSA and anti-cancer drug functionalized GON nanomaterials were successfully immobilized on solid substrate platforms by MAPLE technique and tested with melanoma cells. GON and GONB treatment determined no significant cell viability decrease in normal and melanoma cells up to concentrations of 37 μg/mL in water solutions. When exposed to MAPLE deposited films, cells showed optimal viability on films obtained from targets containing up to 12 μg/mL for GON and up to 111 μg/mL for GONB when testing on human melanoma and normal fibroblast cells. These safe concentration windows were considered for starting solutions in laser experiments for deposition of inhibitors-containing GONB thin coatings. Hybrid GONB thin coatings incorporating DAB and TSA inhibitors, respectively, were further assembled on solid substrates by MAPLE. It was demonstrated that they preserve drug activity against cells bearing $BRAF^{V600E}$ activating mutation. TSA embedded GONB thin coatings were shown to maintain histone deacetylase inhibitor activity proved by evident accumulation of acetylated histones in treated cancer cells. Thus, the successful laser immobilization of anticancer drugs within GON-BSA matrix was demonstrated by their efficient activities for BRAF and HDAC inhibition. This type of functional bio-platforms present high potential as miniaturized high-throughput platforms for drug screening, and for testing cancer cell response to different drugs and drug doses in precision medicine applications.

DATA AVAILABILITY STATEMENT

The raw data supporting the conclusions of this article will be made available by the authors, without undue reservation, to any qualified researcher.

AUTHOR CONTRIBUTIONS

EA and LS coordinated the project, organized the experiments and tasks, supervised all the experiments, analyzed data, wrote, edited, and reviewed the manuscript. IN and VG performed MAPLE experiments and physical-chemical investigations. LS and GC designed and realized *in vitro* assays and analyzed the data. SO performed AFM and contributed to the realization of *in vitro* assays. GC performed inhibitors release assay. CM performed mass spectrometry analyses. FS supervised MAPLE experiments and physical-chemical characterizations and reviewed the manuscript.

FUNDING

This study received funding from the national projects TE186/2015, 131PED/2017, TE7/2018, and Nucleus LAPLAS VI.

ACKNOWLEDGMENTS

Dr. Claudiu Hapenciuc is acknowledged for AFM training support. UEFISCDI is acknowledged for the kind support of TE186/2015, 131PED/2017, TE7/2018, and Nucleus LAPLACE VI projects.

SUPPLEMENTARY MATERIAL

The Supplementary Material for this article can be found online at: https://www.frontiersin.org/articles/10.3389/fchem.2020.00184/full#supplementary-material

REFERENCES

Alcala, A. M., and Flaherty, K. T. (2012). BRAF inhibitors for the treatment of metastatic melanoma: clinical trials and mechanisms of resistance. *Clin. Cancer Res.* 18, 33–39. doi: 10.1158/1078-0432.CCR-11-0997

Alfazema, L. N., Richards, D. S., Gelebart, S., Mitchell, J. C., and Snowden, M. J. (2005). Rapid, accurate and precise quantitative drug analysis: comparing liquid chromatography tandem mass spectrometry and chip-based nanoelectrospray ionisation mass spectrometry. *Eur. J. Mass Spectrom.*11, 393–402. doi: 10.1255/ejms.772

Axente, E., Ristoscu, C., Bigi, A., Sima, F., and Mihailescu, I. N. (2018). "Combinatorial laser synthesis of biomaterial thin films: selection and processing for medical applications," in *Advances in the Application of Lasers in Materials Science. Springer Series in Materials Science*, Vol. 274, ed P. Ossi (Cham: Springer).

Bhunia, S. K., and Jana, N. R. (2011). Peptide-functionalized colloidal graphene via interdigited bilayer coating and fluorescence turn-on detection of enzyme. *ACS. Appl. Mater. Interfaces* 3, 3335–3341. doi: 10.1021/am2004416

Chang, Y., Yang, S. T., Liu, J. H., Dong, E., Wang, Y., Cao, A., et al. (2011). *In vitro* toxicity evaluation of graphene oxide on A549 cells. *Toxicol. Lett.* 200, 201–210. doi: 10.1016/j.toxlet.2010.11.016

Davies, H., Bignell, G. R., Cox, C., Stephens, P., Edkins, S., Clegg, S., et al. (2002). Mutations of the BRAF gene in human cancer. *Nature* 417, 949–954. doi: 10.1038/nature00766

Dreyer, D. R., Park, S., Bielawski, C. W., and Ruoff, R. S. (2010). The chemistry of graphene oxide. *Chem. Soc. Rev.* 39, 228–240. doi: 10.1039/B917103G

Dusinska, M., Boland, S., Saunders, M., Juillerat-Jeanneret, L., Tran, L., Pojana, G., et al. (2015). Towards an alternative testing strategy for nanomaterials used in nanomedicine: lessons from NanoTEST. *Nanotoxicology* 9(Suppl. 1), 118–132. doi: 10.3109/17435390.2014.991431

Ferrari, A. C., Bonaccorso, F., Fal'ko, V., Novoselov, K. S., Roche, S., Boggild, P., et al. (2015). Science and technology roadmap for graphene, related two-dimensional crystals, and hybrid systems. *Nanoscale* 7, 4598–4810. doi: 10.1039/C4NR01600A

Guadagnini, R., Halamoda, B., Kenzaoui, Walker, L., Pojana, G., Magdolenova, Z., et al. (2015). Toxicity screenings of nanomaterials: challenges due to interference with assay processes and components of classic *in vitro* tests. *Nanotoxicology* 9(Suppl. 1), 13–24. doi: 10.3109/17435390.2013.829590

Hong, G., Diao, S., Antaris, A. L., and Dai, H. (2015). Carbon nanomaterials for biological imaging and nanomedicinal therapy. *Chem. Rev.* 115, 10816–10906. doi: 10.1021/acs.chemrev.5b00008

Hu, W. B., Peng, C., Lv, M., Li, X. M., Zhang, Y. J., Chen, N., et al. (2011). Protein corona-mediated mitigation of cytotoxicity of graphene oxide. *ACS Nano* 5, 3693–3700. doi: 10.1021/nn200021j

Huang, T., Karsy, M., Zhuge, J., Zhong, M., and Liu, D. (2013). B-Raf and the inhibitors: from bench to bedside. *J. Hematol. Oncol.* 6:30. doi: 10.1186/1756-8722-6-30

Ji, Z., Flaherty, K. T., and Tsao, H. (2012). Targeting the RAS pathway in melanoma. *Trends Mol. Med.* 18, 27–35. doi: 10.1016/j.molmed.2011.08.001

Johnstone, R. W. (2002). Histone-deacetylase inhibitors: novel drugs for the treatment of cancer. *Nat. Rev. Drug Discov.* 1, 287–299. doi: 10.1038/nrd772

Kelly, W. K., and Marks, P. A. (2005). Drug insight: histone deacetylase inhibitors–development of the new targeted anticancer agent suberoylanilide hydroxamic acid. *Nat. Clin. Pract. Oncol.* 2, 150–157. doi: 10.1038/ncponc0106

Konios, D., Stylianakis, M. M., Stratakis, E., and Kymakis, E. (2014). Dispersion behaviour of graphene oxide and reduced graphene oxide. *J. Colloid Interface Sci.* 430, 108–112. doi: 10.1016/j.jcis.2014.05.033

Kuzum, D., Takano, H., Shim, E., Reed, J. C., Juul, H., Richardson, A. G., et al. (2014). Transparent and flexible low noise graphene electrodes for simultaneous electrophysiology and neuroimaging. *Nat. Commun.* 5:5259. doi: 10.1038/ncomms6259

Li, X. M., Tao, L., Chen, Z. F., Fang, H., Li, X. S., Wang, X. R., et al. (2017). Graphene and related two-dimensional materials: structure-property relationships for electronics and optoelectronics. *Appl. Phys. Rev.* 4:021306. doi: 10.1063/1.4983646

Li, Y., and Seto, E. (2016). HDACs and HDAC inhibitors in cancer development and therapy. *Cold Spring Harb. Perspect. Med.* 6:a026831. doi: 10.1101/cshperspect.a026831

Liao, K. H., Lin, Y. S., Macosko, C. W., and Haynes, C. L. (2011). Cytotoxicity of graphene oxide and graphene in human erythrocytes and skin fibroblasts. *ACS Appl. Mater. Interfaces* 3, 2607–2615. doi: 10.1021/am200428v

Loh, K. P., Bao, Q., Eda, G., and Chhowalla, M. (2010). Graphene oxide as a chemically tunable platform for optical applications. *Nat. Chem.* 2, 1015–1024. doi: 10.1038/nchem.907

Maertens, O., Kuzmickas, R., Manchester, H. E., Emerson, C. E., Gavin, A. G., Guild, C. J., et al. (2019). MAPK pathway suppression unmasks latent DNA repair defects and confers a chemical synthetic vulnerability in BRAF-, NRAS-, and NF1-mutant melanomas. *Cancer Discov.* 9, 526–545. doi: 10.1158/2159-8290.CD-18-0879

Manzano, J. L., Layos, L., Buges, C., de Los Llanos Gil, M., Vila, L., Martinez-Balibrea, E., et al. (2016). Resistant mechanisms to BRAF inhibitors in melanoma. *Ann. Transl. Med.* 4:237. doi: 10.21037/atm.2016.06.07

Mu, Q., Su, G., Li, L., Gilbertson, B. O., Yu, L. H., Zhang, Q., et al. (2012). Size-dependent cell uptake of protein-coated graphene oxide nanosheets. *ACS Appl. Mater. Interfaces* 4, 2259–2266. doi: 10.1021/am300253c

Negut, I., Grumezescu, V., Sima, L. E., and Axente, E. (2018). "Recent advances of graphene family nanomaterials for nanomedicine," in Fullerens Graphenes Nanotubes. A Pharmaceutical Approach, 413–455. doi: 10.1016/B978-0-12-813691-1.00011-7

Nel, A., Xia, T., Meng, H., Wang, X., Lin, S., Ji, Z., et al. (2013). Nanomaterial toxicity testing in the 21st century: use of a predictive toxicological approach and high-throughput screening. *Acc. Chem. Res.* 46, 607–621. doi: 10.1021/ar300022h

NIH U. S. National Library of Medicine. (2019). *Tafinlar Approval History*. Retrieved from : www.clinicaltrials.gov.; https://www.drugs.com/history/tafinlar.html (accessed October 10, 2019).

Oliveira, S. F., Bisker, G., Bakh, N. A., Gibbs, S. L., Landry, M. P., and Strano, M. S. (2015). Protein functionalized carbon nanomaterials for biomedical applications. *Carbon* 95, 767–779. doi: 10.1016/j.carbon.2015.08.076

Oner, E. T., Hernandez, L., and Combie, J. (2016). Review of Levan polysaccharide: from a century of past experiences to future prospects. *Biotechnol. Adv.* 34, 827–844. doi: 10.1016/j.biotechadv.2016.05.002

Pauthe, E., Pelta, J., Patel, S., Lairez, D., and Goubard, F. (2002). Temperature-induced beta-aggregation of fibronectin in aqueous solution. *Biochim. Biophys. Acta* 1597, 12–21. doi: 10.1016/S0167-4838(02)00271-6

Roh, T. Y., Cuddapah, S., and Zhao, K. (2005). Active chromatin domains are defined by acetylation islands revealed by genome-wide mapping. *Genes Dev.* 19, 542–552. doi: 10.1101/gad.1272505

Sima, F., Axente, E., Ristoscu, C., Gallet, O., Anselme, K., and Mihailescu, I. (2016). "Bioresponsive surfaces and interfaces fabricated by innovative laser approaches," in *Advanced Materials Interfaces*, eds A. Tiwari, H. K. Patra, and X. Wang, 427–462. doi: 10.1002/9781119242604.ch12

Axente, E., and Sima, F. (2020). Biomimetic nanostructures with compositional gradient grown by combinatorial matrix-assisted pulsed laser evaporation for tissue engineering. *Curr. Med. Chem.* 27, 1–16. doi: 10.2174/0929867326666190916145455

Sima, F., Davidson, P., Pauthe, E., Gallet, O., Anselme, K., and Mihailescu, I. N. (2011a). Thin films of vitronectin transferred by MAPLE. *Appl. Phys. A Mater.* 105, 611–617. doi: 10.1007/s00339-011-6601-z

Sima, F., Davidson, P., Pauthe, E., Sima, L. E., Gallet, O., Mihailescu, I. N., et al. (2011b). Fibronectin layers by matrix-assisted pulsed laser evaporation from saline buffer-based cryogenic targets. *Acta Biomater.* 7, 3780–3788. doi: 10.1016/j.actbio.2011.06.016

Sima, F., Davidson, P. M., Dentzer, J., Gadiou, R., Pauthe, E., Gallet, O., et al. (2015). Inorganic-organic thin implant coatings deposited by lasers. *ACS Appl. Mater. Interfaces* 7, 911–920. doi: 10.1021/am507153n

Sima, F., Mutlu, E. C., Eroglu, M. S., Sima, L. E., Serban, N., Ristoscu, C., et al. (2011c). Levan nanostructured thin films by MAPLE assembling. *Biomacromolecules* 12, 2251–2256. doi: 10.1021/bm200340b

Tolcher, A. W., Peng, W., and Calvo, E. (2018). Rational approaches for combination therapy strategies targeting the MAP kinase pathway in solid tumors. *Mol. Cancer Ther.* 17, 3–16. doi: 10.1158/1535-7163.MCT-17-0349

Wan, P. T., Garnett, M. J., Roe, S. M., Lee, S., Niculescu-Duvaz, D., Good, V. M., et al. (2004). Mechanism of activation of the RAF-ERK signaling pathway by oncogenic mutations of B-RAF. *Cell* 116, 855–867. doi: 10.1016/S0092-8674(04)00215-6

Xu, H. L., Yao, N. N., Xu, H. R., Wang, T. S., Li, G. Y., and Li, Z. Q. (2013). Characterization of the interaction between eupatorin and bovine serum albumin by spectroscopic and molecular modeling methods. *Int. J. Mol. Sci.* 14, 14185–14203. doi: 10.3390/ijms140714185

Zhang, L., Laycock, J. D., and Miller, K. J. (2004). Quantitative small molecule bioanalysis using chip-based NanoESI-MS/MS. *J. Assoc. Lab. Autom.* 9, 109–116. doi: 10.1016/j.jala.2004.04.014

Zhang, S. A., Yang, K., Feng, L. Z., and Liu, Z. (2011). *In vitro* and *in vivo* behaviors of dextran functionalized graphene. *Carbon* 49, 4040–4049. doi: 10.1016/j.carbon.2011.05.056

Zhang, Y., Ali, S. F., Dervishi, E., Xu, Y., Li, Z., Casciano, D., et al. (2010). Cytotoxicity effects of graphene and single-wall carbon nanotubes in neural phaeochromocytoma-derived PC12 cells. *ACS Nano* 4, 3181–3186. doi: 10.1021/nn1007176

Conflict of Interest: The authors declare that the research was conducted in the absence of any commercial or financial relationships that could be construed as a potential conflict of interest.

frontiers in Chemistry

REVIEW
published: 21 April 2020
doi: 10.3389/fchem.2020.00297

MXenes and Their Applications in Wearable Sensors

Ming Xin, Jiean Li, Zhong Ma, Lijia Pan and Yi Shi**

Collaborative Innovation Center of Advanced Microstructures, School of Electronic Science and Engineering, Nanjing University, Nanjing, China

MXenes, a kind of two-dimensional material of early transition metal carbides and carbonitrides, have emerged as a unique class of layered-structured metallic materials with attractive features, as good conductivity comparable to metals, enhanced ionic conductivity, hydrophilic property derived from their hydroxyl or oxygen-terminated surfaces, and mechanical flexibility. With tunable etching methods, the morphology of MXenes can be effectively controlled to form nanoparticles, single layer, or multi-layer nanosheets, which exhibit large specific surface areas and is favorable for enhancing the sensing performance of MXenes based sensors. Moreover, MXenes are available to form composites with other materials facilely. With structure design, MXenes or its composite show enhanced mechanical flexibility and stretchability, which enabled its wide application in the fields of wearable sensors, energy storage, and electromagnetic shielding. In this review, recent progress in MXenes is summarized, focusing on its application in wearable sensors including pressure/strain sensing, biochemical sensing, temperature, and gas sensing. Furthermore, the main challenges and future research are also discussed.

Keywords: MXenes, strain sensor, pressure sensor, biosensor, gas sensor

OPEN ACCESS

Edited by:
Dattatray Late,
National Chemical Laboratory (CSIR), India

Reviewed by:
Shweta Jagtap,
Savitribai Phule Pune University, India
Khaled Mohammad Saoud,
Virginia Commonwealth University School of the Arts, Qatar

****Correspondence:***
Yi Shi
yshi@nju.edu.cn
Lijia Pan
ljpan@nju.edu.cn

Specialty section:
This article was submitted to Nanoscience, a section of the journal Frontiers in Chemistry

Received: *14 January 2020*
Accepted: *25 March 2020*
Published: *21 April 2020*

Citation:
Xin M, Li J, Ma Z, Pan L and Shi Y (2020) MXenes and Their Applications in Wearable Sensors. Front. Chem. 8:297. doi: 10.3389/fchem.2020.00297

INTRODUCTION

Wearable devices possessing excellent mechanical compliance and unprecedented sensitivity are attracting vast interest as the next-generation interactive platform for health monitoring, motion detection, robotics, and prosthetics (Khan et al., 2016; Heikenfeld et al., 2018; Bandodkar et al., 2019; Li N. et al., 2019; Yang J. C. et al., 2019). Flexible electronics are in need of surface-mounted wearable devices to fit the complex structure of objects with reliable electrical characteristics under cyclic strain conditions during daily movements (Ray et al., 2019), which is beyond the capability of conventional silicon-based rigid electronics. To this end, researchers have proposed strategies from external circuit structural design, e.g., serpentine mesh metal traces (Xu et al., 2014), to the internal microstructure of device design, e.g., mechanical sensing of pyramid microstructure (Mannsfeld et al., 2010). Although these techniques showed their feasibility in different applications, various challenges still exist in (1) the trade-off between mechanical flexibility and electrical performances (i.e., most materials achieve greater flexibility with its degradation in carrier mobility). (2) The lack of a scalable fabrication process. (3) The presence of local structural surface defects of nanomaterials like carbon nanotubes. Therefore, new materials are anticipated to be discovered for the further development of wearable applications.

In 2011, the birth of MXenes introduced a new family into the two-dimensional (2D) materials and was further proved to be promising in the wearable sensory applications due to its controllable preparation method and fascinating properties. In essence, MXenes are a group of 2D early

transition metal carbides, nitride, or carbonitrides prepared by selectively etching of the group IIIA or IVA element from the three-dimensional (3D) MAX phases. The 3D MAX phases are indicated due to the composition: $M_{n+1}AX_n$ layers (n equals to 1, 2, or 3), in which "M" stands for early transition metal (including Ti, Nb, Cr, Mo, etc.) and "X" is carbon and/or nitrogen that is connected with layers of A atoms, named from the main group element (group IIIA or IVA) (Ma and Sasaki, 2010; Naguib et al., 2011, 2013; Khazaei et al., 2013). As a new star of 2D materials, MXenes combine the metallic conductivity of transition metal carbides/carbonitrides with the hydrophilic nature of their terminated surfaces which is uncommon. Their preparation process makes the surface of MXenes rich in functional groups, and their unique accordion-like appearance endows MXenes with attractive electronic, optical, and magnetic properties, which can draw inspiration in energy storage (Lukatskaya et al., 2013; Ghidiu et al., 2014; Anasori et al., 2017), electromagnetic shielding (Shahzad et al., 2016), and sensing (Chen et al., 2015). As shown in **Figure 1**, with the inspiration of MXenes's fascinating electrical and biological characteristics, researchers began to combine MXenes with wearable devices to obtain sensors with different capabilities.

Herein, we especially focus on MXenes's characteristics as flexible electronics and provide insights into the relevant study. Beginning with summarizing MXenes's synthesis, modifications, and properties, this article reviews several potential applications in wearable sensors of force perception, biomedical analysis, and gas sensors. We also provide discussion about current challenges and outlook into future development.

SYNTHESIS AND ELECTRONIC PROPERTIES

MXenes are prepared by selective etching of the A element layers from the 3D MAX phases which is a large group of the ternary carbides and nitrides. The preparation and modification of MXenes are of great concern, especially in the field of sensors. The synthesis can effectively control the morphology and surface termination of MXenes, which have a great effect on sensory functions. For example, electrical properties are changed under mechanical force with the help of micro/nano morphology; multi-layer morphology is helpful to carry enzymes for biosensors and allow fast diffusion of targeted molecules. The preparation methods of MXenes are various [e.g., bottom–up synthesis methods (Shahzad et al., 2016), synthesize MXenes from non-MAX-phase precursors (Meshkian et al., 2015), etc.] and MXenes possess multifrequency properties (e.g., optical, and magnetic properties), in this section, from the point of view of sensors, we focus on the wet etching (etching with hydrofluoric acid) and electrical properties of MXenes.

Synthesis

Thanks to the relatively weaker strengths of the M-A bonds than M-X bonds, it is possible to remove the more chemical-active "A" atoms without destroying $M_{n+1}X_n$ layered structures. Naguib and colleagues first used aqueous hydrofluoric acid (HF) to replace Al atoms by surface terminations, including hydroxyl (-OH), oxygen terminated surfaces (-O), or fluorine terminated (-F), from Ti_3AlC_2 and separated graphene-like single sheet $M_{n+1}X_n$ layers which labeled MXenes. They provided a typical process to prepare MXenes: the precursors were firstly treated with etching solution (HF or acid-fluorides), the specific concentration mixture is centrifuged or filtered until the solid-liquid separation, washed with deionized water until the pH value of the supernatant solution is between 4 and 6 and were subsequently treated with shearing forces or sonication to obtain a single-layer stack (Naguib et al., 2014; Alhabeb et al., 2017). With this process (**Figure 2A**), the morphology of MXenes can be controlled by adjusting the concentration of etching solution, etching time, ultrasonic time (Malaki et al., 2016), and experimental temperature (Naguib et al., 2012; Persson et al., 2018). According to the principle, more than 20 different compositions of single-layer MXenes or multi-layer stacks (**Figures 2B,D**) have been experimentally obtained by this process. Although recently, different synthesis strategies (Rasid et al., 2017) have been developed including chemical vapor deposition (CVD) (Gogotsi, 2015; Xu et al., 2015; Wang et al., 2017), template method (Jia et al., 2017; Xiao et al., 2017) and plasma-enhanced pulsed laser deposition (PEPLD) (Zhang et al., 2012), wet selective etching is still the main method of MXenes-based sensor fabrication.

The etching is a dynamic control process, and each kind of MXenes needs different etching time to achieve complete conversion. In general, MXenes with larger n in $M_{n+1}C_nT_x$ need stronger etching and longer etching time. For example, under the same etching conditions, the etching time required for $Mo_2Ti_2AlC_3$ ($n = 3$) is twice that of its $n = 2$ counterpart (i.e., Mo_2TiAlC_2) (Anasori et al., 2015). Each new kind of MXenes can be made under different etching conditions, resulting in different quality (defect concentration and surface termination). At present, since HF is still the mainstream etching solution, the characteristics of corrosiveness to the organism, dangerous treatment, and recovery hinder the batch synthesis and application of MXenes. Several synthesis strategies have been explored to avoid or minimize the utilization of HF. The most widely used is the mixture of hydrochloric acid (HCl) and fluoride salt, which forms HF in *situ* (Ghidiu et al., 2014). Other fluoride salts have also been used successfully (NaF, KF, and NH_4F) (Liu et al., 2017a,b), along with different HCl concentration and lithium fluoride (LIF)/HCl molar ratio (Alhabeb et al., 2017). The fluorine-free MXenes can be obtained by hydrothermal treatment of Ti_3AlC_2 powder in the alkali solution (Li et al., 2018). The electrochemical etching of Ti_2AlC in diluted HCl can yield MXenes without F terminations (Sun et al., 2017). These synthesis strategies pave the way for the preparation of biocompatible wearable sensors.

The appearance of MXenes etched by the wet method is the accordion-like shape. Single-layer or few-layer MXenes can be obtained by ultrasonic treatment, which possess a high aspect ratio. Another method is liquid exfoliation by the intercalation of molecules to obtain colloids with high yield (Mashtalir et al.,

FIGURE 1 | An overview of the applications of MXenes in the wearable devices field. Reproduced from Cai et al. (2018) with permission from American Chemical Society; reproduced from Liu et al. (2018) with permission from WILEY-VCH Verlag GmbH & Co; reproduced from Li X.-P. et al. (2019) with permission from Elsevier Inc; reproduced from An et al. (2018); reproduced from Wang et al. (2019); reproduced from Li M. et al. (2019) with permission from Elsevier B.V; reproduced from Kim et al. (2018) with permission from American Chemical Society; reproduced from Lee et al. (2017) with permission from American Chemical Society.

2013; Ghidiu et al., 2016). The introduction of appropriate molecules can cause the expansion of the interlayer space, and weaken the interaction between layers, which can split the multilayer into a single sheet. Both methods utilized depend on the etching method and MXenes composition (Verger, 2019). In all cases, the single MXenes layer is less than 1 nm thick (3,5,7 atomic layers) (**Figure 2C**), with up to tens of microns in the lateral dimension of microns (Huang et al., 2018).

Electronic Properties

The electronic properties of MXenes are the most unique properties compared to other 2D materials, such as graphene.

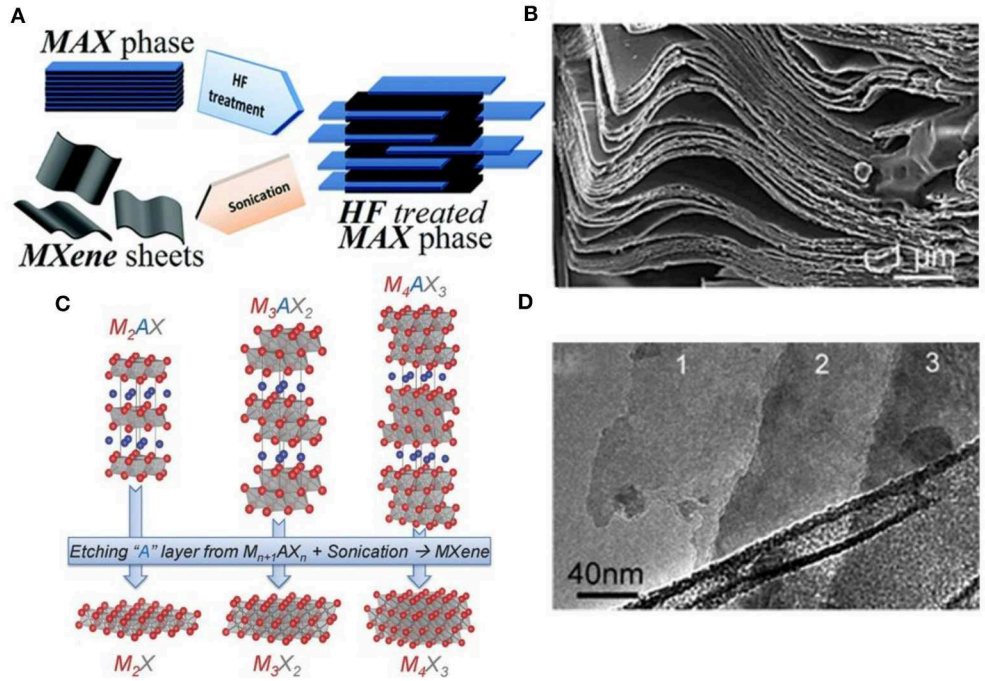

FIGURE 2 | (A) Schematic for the exfoliation process of MAX phases and formation of MXenes; **(B)** The image of the multi-layer of MXenes; **(C)** Structure of MAX phases and the corresponding MXenes; reproduced from Naguib et al. (2013) with permission from WILEY-VCH Verlag GmbH & Co. **(D)** The image of the single-layer of MXenes. **(A,B,D)** are reproduced from Naguib et al. (2012) with permission from American Chemical Society.

Recent research demonstrated that the metal layers (M-layer) are the main factor to affect the electronic properties of MXenes (metallic conductivity of Ti_3 C $_2$ compared with Mo_2 TiC $_2$) (Lipatov et al., 2016). It is confirmed that a delicate balance between temperature and the activity of the etchant needs to be maintained and the electronic behavior from metallic to semiconductor-like can be regulated by changing the two outer transition M-layer of a 2D carbide (Anasori et al., 2016). The electroconductibility can also be influenced by the fabrication methods, because of the surface termination and different extent of defects. The more defects exist, the low electroconductibility MXenes possess, which is due to the destruction of the ordered structure for free movement of electrons. Defects can be controlled by doping different atoms. Through the exchange of ions with different electric densities, the defects of charge imbalance will be produced (Feng et al., 2017). Because most of the etching solution is fluoride, the surface of MXenes usually contains -OH, -O, and -F functional groups. With the surface termination changed (e.g., small molecule adsorption), the electrical conductivity of MXenes has changed accordingly (Zha et al., 2015).

As the early transition metal carbides and carbonitrides, MXenes not only have the conductivity comparable to copper but also have the properties of carbon or nitride. Energy band structure and electronic density of state (DOS) of MXenes have been studied extensively by density functional theory (DFT). The bare MXenes single-layer is predicted to be a metal layer with high electron density close to the Fermi level (Tang et al., 2012; Khazaei et al., 2013). With the sensitive electrical properties, MXenes can be used to detect strain through the crack mechanism, When the MXenes-based sensor is cracked by strain, its conductivity/resistivity will change with the increase of crack. MXenes can be applied in biosensors to detect small molecule adsorption and sensitive detection of several gases. With different composition and concentration, molecules adhere to the MXenes surface termination, the conductivity will change accordingly (Yu et al., 2015). Different molecules have selective adsorption by MXenes materials with different compositions, and their conductivity changes obviously.

Appropriate surface modification/functionalization can enhance its sensing performance and biomedical properties. Through physical absorption or electrostatic attraction, molecules, or atoms with different structures can be selectively adsorbed on the surface of MXenes, which will affect their own electrical properties to achieve the purpose of sense. For instance, the biocompatible polymers, such as soybean phospholipid, are more suitable for surface modification of MXenes because of their large surface area and biodegradability (Dai et al., 2017a,b). MXenes usually display a negative charge because their surface terminals are rich in -OH, -O, and –F functional groups (Khazaei et al., 2013; Shein and Ivanovskii, 2013; Berdiyorov, 2015). The molecules with a positive charge are adsorbed on the surface of MXenes by electrostatic force, enabling the composite with enhanced sensing capabilities (Li S. et al., 2019) or drug transport (Liu G. et al., 2017).

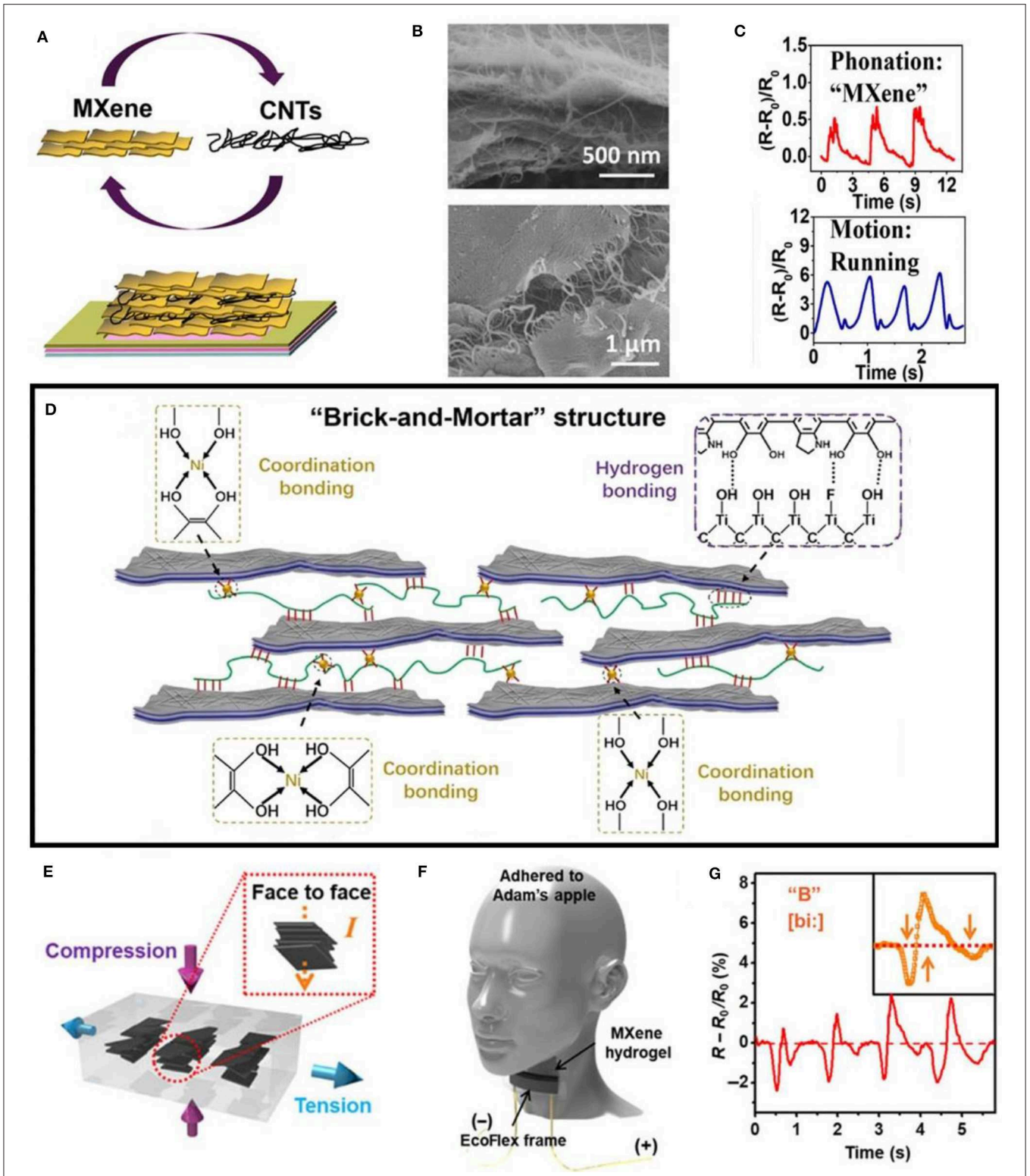

FIGURE 3 | MXenes for strain sensor. **(A)** Fabrication process of a sandwich-like $Ti_3C_2T_x$ MXene/CNT layer; **(B)** SEM images of sandwich-like $Ti_3C_2T_x$ MXene/CNT layers. **(C)** Relative resistance responses of the sensor in phonation and motion; **(A–C)** are reproduced from Cai et al. (2018) with permission from American Chemical Society. **(D)** Schematic illustration of the $Ti_3C_2T_x$-AgNW-PDA/Ni^{2+} sensor based on the "brick-and-mortar" architecture; reproduced from Shi et al. (2019) with permission from American Chemical Society. **(E)** Schematic illustration of the mechanism of the electromechanical responses of M-hydrogel; **(F)** Schematic for vocal sensing and **(G)** Resistance change in response to similarly sounding letters "B." **(E–G)** are reproduced from Zhang et al. (2018).

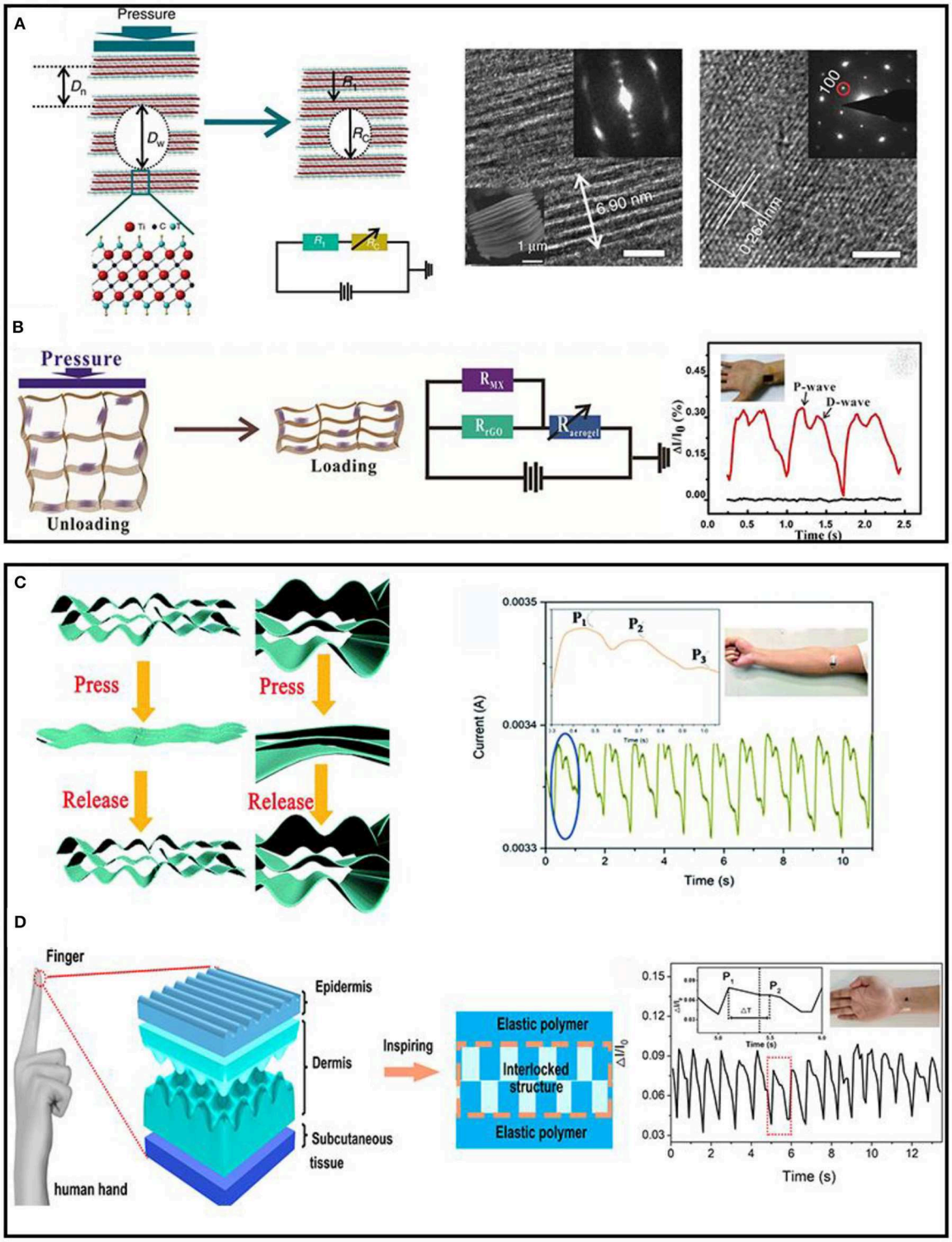

FIGURE 4 | MXenes for pressure sensor. **(A)** Working micromechanism and SEM image of MXenes-material for piezoresistive sensor; reproduced from Ma et al. (2017). **(B)** Schematic illustration and application of MX/rGO aerogel sensor; reproduced from Ma Y. et al. (2018) with permission from American Chemical Society. **(C)** Schematic elasticity mechanisms and application of C-MX/CNC; reproduced from Zhuo et al. (2019) with permission from The Royal Society of Chemistry. **(D)** Schematic of interlocking structure of simulated human skin and the application of pulse measurement; reproduced from Wang et al. (2019) with permission from American Chemical Society.

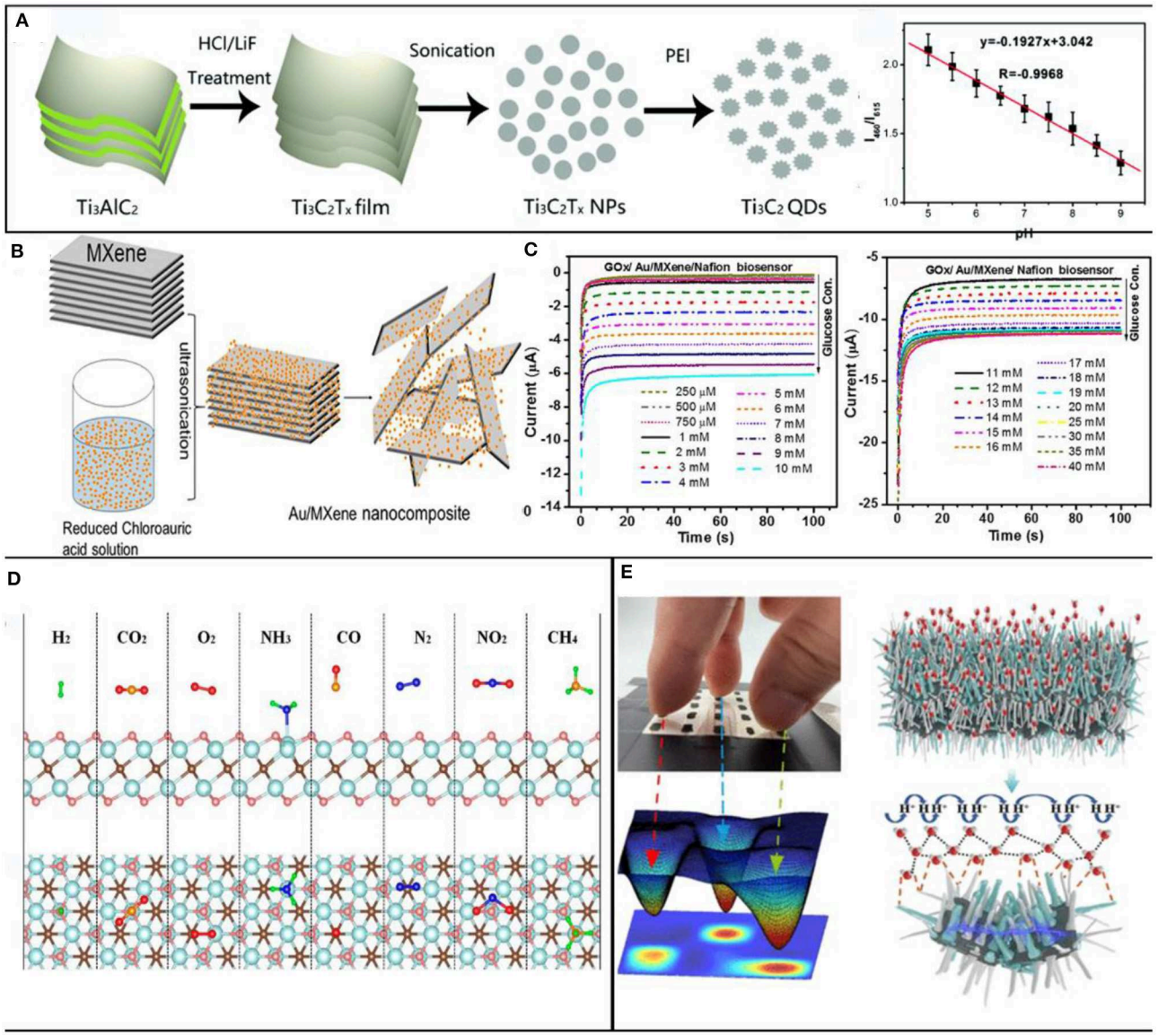

FIGURE 5 | MXenes for biosensor. **(A)** Schematic illustrations for preparing the Ti_3C_2 QDs by using a liquid exfoliation and solvothermal treatment approach; reproduced from Chen et al. (2018) with permission from The Royal Society of Chemistry. **(B)** Schematic showing the synthesis process of Au/MXene nanocomposites; **(C)** GOx/Au/MXene/Nafion/GCE at a constant voltage of−0.402 V; reproduced from Rakhi et al. (2016). **(D)** Application of MXenes for detection of NH_3. **(D)** is reproduced from Yu et al. (2015) with permission from American Chemical Society. **(E)** Schematic of the adsorption process of water molecules at the Ti_3C_2/TiO_2 composite film. Reproduced from Li N. et al. (2019) with permission from American Chemical Society.

PHYSICAL SENSOR

MXenes prepared by chemical liquid etching usually have various functional groups on their surface with strong hydrophilicity and ease in chemical modification. Meanwhile, Mxenes have many excellent properties, such as electronic properties and bending strength comparable to graphene, and the oxidation resistance and electron irradiation resistance superior to graphene (Enyashin and Ivanovskii, 2012; Khazaei et al., 2013; Anasori et al., 2015). MXenes materials can be utilized in the stress sensor to detect tiny shape variables due to their excellent electronic properties. The structure of the accordion-like shape can be used in a super-*sensitive* piezoresistive sensor. MXenes materials can be easily mixed with other materials to improve sensor performance. Therefore, MXenes have gradually attracted more attention in the field of physical sensors.

Strain Sensor

The flexible strain sensor transforms the tensile strain of the device into the resistance signal output (Ma et al., 2019). When the external force is applied to the sensor, the internal conductive materials or networks will crack due to external forces, which

cause the electrical characteristics to be changed accordingly. The conductive network is usually made up of 2D sheets that are closely stacked. Interaction forces such as Vander Waals forces may exist between adjacent sheets. Therefore, under the action of external stress, the sheets cannot achieve effective sliding, but can only disperse the stress by producing large cracks. The crack dimension is proportional to the stress when the external force is strong enough, the conductive path will be blocked and greatly limits the improvement of sensing range and stability.

To reduce the interaction between 2D materials and construct a new conductive network, it is a common method to add the second phase or the nth phase materials of different dimensions into 2D materials. For instance, Cai et al. (2018) utilized $Ti_3C_2T_x$ MXenes flakes combined with hydrophilic single-walled carbon nanotubes (SWNTS) to fabricate sandwich-like sensing layers through a layer-by-layer (LbL) spray coating technique. The layers of $Ti_3C_2T_x$ are in an orderly stacking state, and CNTs with high aspect ratio are disorderly distributed among the layers like fluff. The layers are woven together to form a complete conductive network (**Figures 3A–C**). The sensitivity (GF = (Δ R/R0)/ε) of the flexible strain sensor can reach 64.6 in the range of 0–30% strain and 772.60 in the range of 40–70%. By adding fluffy CNTs, the $Ti_3C_2T_x$ MXenes flakes can be connected in a wide range of strain, which makes the sensor has a wide sensing range. Shi et al. drew inspiration from bionics, they combined silver nanowire (AgNW) with $Ti_3C_2T_x$ and introduced dopamine (DPA) and nickel ions (Ni^{2+}) to construct a nacre-mimetic strain sensor (Shi et al., 2019). $Ti_3C_2T_x$ sheets and AgNW as "bricks" endow the whole composite system with high conductivity and mechanical brittleness, while PDA/Ni^{2+} as "mortal" connects "bricks" through various interface interactions (**Figure 3D**). The GF of this flexible strain sensor is 256.1, 433.3, 1160.8, 2209.1, and 8767.4 in the strain range of 0–15, 15–35, 35–60, 60–77, and 77–83%, respectively. The maximum sensing range is more than 50% and the sensitivity is higher than 200 in the whole range, which exceeds most of the reported flexible strain sensors. Thus, one-dimensional materials like a bridge, connect the MXenes sheets, which endows the device with high sensitivity and a wide strain sensing range.

Since pure Mxenes, like other 2D materials, in general, are not stretchable, adding polymer into MXenes can enhance its mechanical robustness as well as its sensing range (Ling et al., 2014). An et al. utilized $Ti_3C_2T_x$ nanosheets, derived from the parent $Ti_3C_2T_x$ MAX phase through MXenes and poly (diallyldimethylammonium chloride) (PDAC) to form composite films as LbL assembly (An et al., 2018). The conductivity of the film can reach 2,000 S/m, and it can be evenly loaded on various substrates like silicon, polydimethylsiloxane (PDMS), polyethylene terephthalate (PET), indium tin oxide (ITO), and glass. The strain sensor based on MXenes/PDAC composite membrane on PDMS can be stretched to 40%, while the bending sensor on PET can be bent 35%.

In addition to being integrated with other phase materials, it is also an effective method to build new microstructures by adjusting the morphology of MXenes. Yang Y. et al. (2019) utilized the common chemical liquid phase etching method to prepare $Ti_3C_2T_x$ materials. By adjusting the etchant [HF and tetramethylammonium hydroxide (TMAOH)], etching time (6, 18, and 24 h), and ultrasonic time (20 min, 1∼4 h), the morphology of $Ti_3C_2T_x$ was effectively controlled, and the mixed network structure of $Ti_3C_2T_x$ nanoparticles and nanosheets with different proportions was prepared to maximize the synergistic effect. The GF of the sensor is up to 178.4, 505.1, and 1176.7 in the strain range of 0–5, 5–35, and 35–53%, respectively and its maximum sensing range is 53%, which is suitable for all activities of the whole body.

In addition to the above materials used as flexible substrates, hydrogels are often applied in strain sensors because of their excellent stretchability and self-repair ability. In general, conductive materials enter the hydrogel to form conductive hydrogels. Zhang et al. (2018) utilized $Ti_3C_2T_x$ and polyvinyl alcohol (PVA) hydrogel to form conductive MXenes-based hydrogels (M-hydrogel). Because of the cross-linking between the surface end groups of $Ti_3C_2T_x$ and PVA hydrogels (**Figures 3E–G**), the hydrogel has a tensile strength of 3,400% and has a good self-repairing ability. The GF of the sensor in the range of 0–0.5 and 0.5–3.0% is 60–80 and 21, respectively. Different from the crack propagation mechanism, the sensor mainly changes the contact resistance between the $Ti_3C_2T_x$ lamellae caused by the deformation of the hydrogel in response to the external force, to change the mechanical to the electrical signal. Liao et al. combined the prepared $Ti_3C_2T_x$ sheets with hydrogels composed of polyacrylamide and polyvinyl alcohol to obtain MXenes nanocomposite hydrogel (Liao et al., 2019). Then, the composite hydrogel was immersed in the ethylene glycol solution to remove some water molecules. The MXene nanocomposite organohydrogel (MNOH) for strain sensing with high-sensitivity (GF = 44.85), antifreeze, and self-healing was developed.

Pressure Sensor

The multi-layer MXenes with accordion-like shape and single-layer MXenes have been used for flexible piezoresistive sensors. When the pressure acts on the device, the pressure signal is converted into resistance signal output through the deformation of the material.

In a multi-layer MXenes-based piezoresistive sensor, after the A-layer is removed by etching the MAX phase block, the accordion-shaped MXenes block is obtained. Each block is composed of several MXenes monolithic layers. Ma et al. (2017) fabricated a flexible piezoelectric sensor by coating the ethanol dispersed droplets of multilayer $Ti_3C_2T_x$ on the polyimide (PI) integrated electrode. They first used the basic characteristics of greatly changed interlayer distances of MXenes under an external pressure for a real application (**Figure 4A**). The GF of the sensor is 180.1–94.8 and 94.8–45.9 in the range of 0.19–0.82 and 0.82–2.13%, respectively. Moreover, it can be used to explore the full-range human activities (e.g., eye blinking, cheek bulging, and throat swallowing). Because MXenes itself is very fragile and hard to sustain large pressure, MXenes need to be combined with materials with high mechanical strength as the skeleton to support the repeated stress and rebound of the sensor. There are mainly two kinds of MXenes-based flexible piezoresistive sensors, aerogel sensors, and MXenes/elastic matrix sensors.

Aerogels have the characteristics of high porosity, ultralight, and superelasticity, making them excellent choices for fabricating flexible piezoresistive sensors. MXenes lamellae are usually unable to form aerogels independently because of their brittleness. Other high toughness and high elastic materials are needed to improve the mechanical strength of MXenes based aerogels. For instance, Ma Y. et al. (2018) composite graphene oxide with $Ti_3C_2T_x$ to prepare MXene/reduced graphene oxide (MX/rGO) hybrid structures. As is shown in **Figure 4B**, the rGO layer with a larger surface area provides a high mechanical strength skeleton for aerogels, while a better conductive $Ti_3C_2T_x$ enhances the resistance effect of the pressure sensor. The synergistic interaction between the two materials endows the sensor with excellent sensing performance. Similarly, Liu et al. (2018) mixed $Ti_3C_2T_x$ dispersions with poly (amic acid) (PAA) and obtained MXenes/polyimide aerogels after freeze-drying and calcination (MXenes/PI aerogel). The sensor possesses high elasticity and low density, which can sustain compression, bending, and torsion deformation. Zhuo et al. (2019) utilized cellulose nanocrystals (CNCs) as a nano-support to connect MXenes nanosheets into a lamellar carbon aerogel with not only super mechanical performances but also ultrahigh linear sensitivity (**Figure 4C**). Chen et al. (2019) used bacterial cellulose fiber as a nanobinder to connect MXenes (Ti_3C_2) nanosheets into continuous and wave-shaped lamellae to fabricated a kind of compressible and elastic carbon aerogels. Therefore, it is an effective way to prepare high-performance wearable MXenes-based piezoresistive sensors by compounding MXenes with mechanical strength materials and in *situ* growing into aerogels with high elasticity and high conductivity. Wang et al. (2019) developed a skin-inspired Ti_3C_2/natural microcapsule composite film with the interlocked structure that improved the mechanical deformability of the sensing layer. Mimicking the structure and function of human skin (**Figure 4D**), the sensor can amplify the weak pressure signal and possess excellent stability.

In addition, MXenes are directly loaded on the formed high elastic substrate, and the high conductivity of MXenes and the high mechanical properties of the elastic substrate are also used to meet the requirements of the resistance effect and geometric characteristics of the flexible piezoresistive sensor. Yue et al. (2018) prepared MXene-sponge by dip-coating process and made a piezoresistive sensor by combining it with insulated polyvinyl alcohol (PVA) nanowire. The MXene-sponge piezoresistive sensor has ultrahigh sensitivity. The GF in the pressure range of 0–5.37 and 5.37–18.56 kPa is 147 and 442, respectively. Li X.-P. et al. (2019) used the same method to load MXenes lamellae onto the skeleton of a polyurethane (PU) sponge treated with chitosan. Because chitosan is positively charged and the MXenes lamellae surface is negatively charged, MXenes lamellae can be evenly and tightly adsorbed on the sponge. Guo et al. (2019) impregnated the MXene sheet on porous fabric and constructed a sandwich structure with two layers of degradable polylactic acid (PLA) sheet to assemble a transient pressure sensor. In addition, the sensor can be completely degraded after soaking in sodium hydroxide for more than 14 days.

CHEMICAL SENSOR

Besides excellent electronic properties, MXenes are essentially hydrophilic due to their surface functional groups, which endows MXenes great prospect in the field of the wearable sensor. MXenes can selectively adsorb biomolecules (e.g., glucose, dopamine) and gas molecules (e.g., NH_3, NH_4) through morphology control and surface modification, thus changing their electrical properties. Meanwhile, the major elements of MXenes (the M-layer elements) are some of the early transition metals, such as Ta, Ti, and Nb, which are relatively inert to biological organisms, which endows MXenes compounds with excellent biocompatibility. *In vivo* experiments carried out by Lin et al. (2017) showed that MXenes could be degraded and eliminated from the body of mice.

Biosensor

Recently, MXenes had been proven to be a potential intracellular pH sensor. Chen et al. (2018) fabricated a pH-sensitive Ti_3C_2 quantum dots (QDS), and they developed a ratiometric photoluminescence probe to monitor intracellular pH, which can be applied as a promising platform for developing wearable practical fluorescent nanosensors (**Figure 5A**). Besides monitoring intracellular pH, MXenes has also been designed for the detection of other small molecules, such as glucose and phenol. RAKhi reported an Au/MXenes composite biosensor platform for the detection of sensitive enzymatic glucose (Rakhi et al., 2016). The biosensor utilizes the unique electrocatalytic performance and synergistic effect between Au nanoparticles and MXenes nanosheets. Glucose oxidase (GOx) enzyme was immobilized on Nafion gold/MXenes nanocomposite and placed on the glassy carbon electrode to prepare current glucose biosensor (**Figures 5B,C**). The device exhibited excellent electrocatalytic activity toward a low detection limit of 5.9 μM and a wide linear range of detection of glucose from 0 to 18 mM. Li M. et al. (2019) fabricated a 3D porous MXenes-based composite for non-enzymatic glucose sensor. The 3D porous structure of Nickel-Cobalt layered double hydroxide (Nico-LDH) has a high specific surface area and many ion diffusion channels. They exported MXenes/Nico-LDH nanocomposite with a wide linearity range (0.002–4.096 mM) and a low limit of detection (0.53 μM). Novel MXenes-based nanocomposite can detect dopamine (DA), Zheng et al. (2018) synthesized a novel nanomaterial (MXenes/DNA/Pd/Pt) and applied for the development of sensitive DA sensors. Mxenes nanoparticles are used as the conductive matrix of Pd/Pt nanoparticles. DNA is adsorbed on the surface of MXenes by hydrophobic aromatic group, which induces the *in-situ* growth of PdNPs and Pd/Pt nanoparticles. The sensor exhibited excellent linearity in the DA concentration range of 0.2–1,000 μM and high selectivity against ascorbic acid, uric acid, and glucose. More interestingly, H_2O_2 can effectively oxidize the surface functional groups of MXenes, thus significantly increasing the oxygen density of the MXenes surface and promoting the charge transfer process. Wang et al. (2015) developed a new type of accordion-like TiO_2-Ti_3C_2 nanocomposites, and they immobilized hemoglobin (Hb) on this system to fabricate a mediator-free biosensor. The TiO_2

nanoparticles are loaded on the Ti_3C_2 layers substrate to form a sensing platform, which is suitable for enzyme immobilization (Liu et al., 2015).

Besides small molecules, the interaction between metal ions and MXenes produces a similar doping effect. Zhu et al. (2017) studied the electrochemical response of MXenes for the detection of the coexistence of Cd^{2+}, Pb^{2+}, Cu^{2+}, and Hg^{2+}, and proposed a new platform for sensitive detection of heavy metal ions. The detection platform with a detection limit of 0.098, 0.041, 0.032, and 0.130 mM for Cd (II), Pb (II), Cu (II), and Hg (II), respectively. In addition to detect heavy metal ions, MXenes nanosheets also possess the ability to remove heavy metals (e.g., Cu, Li, Na, K atoms) (Guo et al., 2015; Shahzad et al., 2017).

Gas Sensor

In the field of wearable electronics, especially in the field of e-skin, in addition to the sensing demand for force and biological information, it is desirable to be able to transfer environmental factors significantly and gas sensing is a significant challenge for the next generation of wearable sensors (Ma Z. et al., 2018). The unique surface structure of MXenes is very suitable for adsorbing various gas molecules, thus affecting its overall conductivity.

The adsorption/desorption process results in the change of surface electric state of MXenes, and gas absorption can occur at the active defects on the surface of MXenes, or it can be the result of interaction with surface functional groups (Ghosh, 2014). With functional groups, gas adsorption caused by electrostatic force results in relatively small resistance changes due to the weak intermolecular force. Gas absorption may also be due to the substitution of surface functional groups by gas molecules, which leads to the carrier transfer between adsorbent and adsorbate gas, and significant changes in the resistance of materials (Geistlinger, 1993). Yu et al. (2015) have theoretically predicted the potential of MXenes-based composite in gas sensing (H_2, O_2, CO_2, CH_4, NH_3, et al.) by first-principles simulation. They found that the Ti_2C monolayer with oxygen terminations was more selective for NH_3 than other gas molecules (**Figure 5D**). Xiao et al. (2016) considered the interaction between NH_3 and O-terminated semiconducting MXenes (M_2CO_2, M=Sc, Ti, Zr, and Hf) with different charge states utilized first-principles simulations. Due to the NH_3 can be adsorbed on M_2CO_2 with charge transfer, the potential of MXenes-based semiconductor as the NH_3 sensor or capturer is revealed. Lee et al. (2017) utilized TiC_2T_x integrated on flexible polyimide platforms by solution casting method. The sensor performance great in NH_3 detection and the great potential of MXenes as a gas sensor is predicted theoretically. Lee et al. (2020) utilized a scalable wet-spinning process to prepare a $Ti_3C_2T_x$/graphene hybrid fibers that possess excellent mechanical and high electrical conductivity. The optimized bandgap, synergistic effect, and the increased oxygen content in MXenes end atom of $Ti_3C_2T_x$/graphene hybrid fiber significantly improve the NH_3 sensing response. Kim et al. (2018) demonstrated $Ti_3C_2T_x$ MXenes film as metallic channels for volatile organic compounds (VOCs) gas sensors with a high signal-to-noise ratio. Lee et al. (2019) dropped the V_2CT_x solution on the flexible polyimide substrate to form a gas sensor with high sensitivity toward nonpolar gas. Yuan et al. (2018) fabricated high-performance and flexible VOC sensors. The sensor based on the 3D MXenes framework, which was prepared through electrospinning aqueous solution of the positively charged polymer. The sensor exhibited high sensitivity, good flexibility, and wide sensing range. Zhao et al. (2019) utilized polyaniline (PANI) decorated on $Ti_3C_2T_x$ nanosheet surface via in *situ* polymerization at low temperature for a PANI/$Ti_3C_2T_x$ composite. The synergistic properties of composites and highly active $Ti_3C_2T_x$ endow the sensing material both high ethanol sensitivity (41.1%, 200 ppm) and rapid response/recovery time (0.4/0.5 s) at room temperature. Interestingly, MXenes not only possess excellent performance in gas sensing but also in temperature sensing. Chen et al. (2015) synthesized 2D vanadiumcarbide (V_2C) phase by referring to the previous preparation process (Naguib et al., 2013), then graft poly(2-(dimethylamino) ethyl methacrylate) (PDMAEMA) brushes on V_2C materials through self-initiated photographing and photopolymerization (SIPGP). Carbon dioxide and temperature can be used as stimulants to adjust the dispersion state, transmissivity and conduction activity of the system to realize the double correspondence between them.

Sensitivity to water molecules in the atmosphere is also an important factor for the MXenes-based sensor. Since the surface of MXenes is hydrophilic and the interaction between layers is relatively weak, water molecules can be inserted spontaneously under the environmental humidity, which has great potential as the humidity sensor. It has been proven that the resistivity of Ti_3C_2 film increases linearly by 15–80% with the increase of the relative humidity (RH) (Römer et al., 2017). Metal ion intercalation has a great influence on MXenes structure and internal surface hydrodynamics (Ghidiu et al., 2016; Osti et al., 2016). Muckley et al. (2017) demonstrated that the electrical and weight responses of K^+ and Mg^{2+} intercalated Ti_3C_2 films to water vapor were between 20 and 80% RH. They further studied the gravimetric response of the intercalated MXenes to water, and found that the gravimetric response to water is 10 times faster than its electrical response. This is explained the expansion/contraction of the channel between MXenes sheets induced by water molecules results in the capture of water molecules as charge consuming dopants (Muckley et al., 2017). Yang Z. et al. (2019) alkaline-treated the $Ti_3C_2T_x$ synthesized from Ti_3AlC_2 by sodium hydroxide solution. The insertion of alkali metal ions and the increase of the ratio of oxygen to fluorine on the surface can effectively improve the humidity and gas sensitivity at room temperature. An et al. (2019) utilized LbL assembly to prepare the MXene/polyelectrolyte multilayer films that possess ultrafast recovery and response times. When the humidity is changed, water molecules are inserted into the MXene/polyelectrolyte multilayers, resulting in the increase of thickness and the distance between the sheets, thus changing the tunneling resistance between MXenes layers. Li N. et al. (2019) utilized alkali oxidation method to grow in *situ* TiO_2 nanowires on Ti_3C_2 to fabricate the urchin-like Ti_3C_2/TiO_2 composite. The staggered dendritic nanowire structure has excellent adsorption performance at low RH, which is conducive to the formation of a continuous water layer (**Figure 5E**). Liu et al. (2019) developed a vacuum-assisted LbL assembly using AgNW with MXenes sheets to fabricate a highly conductive leaf-like composite on the silk substrate. The Mxenes layer protects AgNW from

oxidation and endows textiles with high sensitivity to humidity, which has tremendous potential in intelligent garments and sensor applications.

SUMMARY AND FUTURE PROSPECTS

MXenes materials gradually occupy a place in the field of wearable sensors because of its excellent conductivity, mechanical properties, hydrophilicity, and ease to control the morphology. In recent years, various kinds of sensors based on accordion-like MXenes materials have revealed that the conductive sensitive material structure, sensing mechanism, and sensor performance analysis have made good progress. By fully considering the advantages of MXenes materials and the target requirements of devices, a new sensing system is formed by combining MXenes materials with other suitable materials, which can maximize the synergistic effect between MXenes and other phase materials, and thus obtain a high-performance sensor with high sensitivity and wide response range.

However, in order to realize the application requirements of MXenes-based sensors in wearable devices, medical detection, and electronic skin, there are still many problems to be solved. The preparation process of MXenes usually requires the use of fluorine-containing reagents, which are toxic to the biological environment. Meanwhile, the widely applied HF etching solution is harmful to organic organisms, and the trace residue will lead to an irreversible effect on the human body. It also has high requirements for the safety and wastes liquid treatment in the mass production process. Therefore, how to realize the fluorine-free preparation is the key to make MXenes practical. For the MXenes-based sensor, it is unable to realize linear induction in a large strain range, which affects the programmed setting of the sensor in practical application. Therefore, it is necessary to further design the microstructure of MXenes and its composite materials to improve the linearity of the sensor. And for MXenes-based biosensor, although several studies have shown that MXenes currently used in biomedical applications are generally biocompatible, some of them can even be biodegraded *in vivo*. But the long-term biosafety of MXenes has not been systematically evaluated. And we still need to fully understand the surface chemistry of MXenes. Understand which functional groups exist on their surface and explore the various properties of functional groups. In addition, the etching of a elements

other than Al needs to be explored to cover all possible ternary carbides and nitrides. Meanwhile, MXenes-based transparent electronic conductors also need to explore. Therefore, it is urgent to explore ways to improve this demand of MXenes for further exploration.

AUTHOR CONTRIBUTIONS

MX wrote the manuscript. JL and ZM modified the manuscript. LP and YS supervised the manuscript.

FUNDING

The authors would like to acknowledge the financial support of the National Natural Science Foundation of China under Grants 61825403, 61674078, 61229401, 41401257, and 11574136, the National Key Research and Development Program of China under Grants 2017YFA0206302 and 2018YFA0209100, and the PAPD program.

REFERENCES

Alhabeb, M., Maleski, K., Anasori, B., Lelyukh, P., Clark, L., Sin, S., et al. (2017). Guidelines for synthesis and processing of two-dimensional titanium carbide ($Ti_3C_2T_x$ MXene). *Chem. Mater.* 29, 7633–7644. doi: 10.1021/acs.chemmater.7b02847

An, H., Habib, T., Shah, S., Gao, H., Patel, A., Echols, I., et al. (2019). Water sorption in MXene/polyelectrolyte multilayers for ultrafast humidity sensing. *ACS Appl. Nano Mater.* 2, 948–955. doi: 10.1021/acsanm.8b02265

An, H., Habib, T., Shah, S., Gao, H., Radovic, M., Green, M. J., et al. (2018). Surface-agnostic highly stretchable and bendable conductive MXene multilayers. *Sci. Adv.* 4:eaaq0118. doi: 10.1126/sciadv.aaq0118

Anasori, B., Lukatskaya, M. R., and Gogotsi, Y. (2017). 2D metal carbides and nitrides (MXenes) for energy storage. *Nat. Rev. Mater.* 2:16098. doi: 10.1038/natrevmats.2016.98

Anasori, B., Shi, C., Moon, E. J., Xie, Y., Voigt, C. A., Kent, P. R. C., et al. (2016). Control of electronic properties of 2D carbides (MXenes) by manipulating their transition metal layers. *Nanoscale Horiz.* 1, 227–234. doi: 10.1039/C5NH00125K

Anasori, B., Xie, Y., Beidaghi, M., Lu, J., Hosler, B. C., Hultman, L., et al. (2015). Two-dimensional, ordered, double transition metals carbides (MXenes). *ACS Nano* 9, 9507–9516. doi: 10.1021/acsnano.5b03591

Bandodkar, A. J., Jeang, W. J., Ghaffari, R., and Rogers, J. A. (2019). Wearable sensors for biochemical sweat analysis. *Annu. Rev. Anal. Chem.* 12, 1–22. doi: 10.1146/annurev-anchem-061318-114910

Berdiyorov, G. R. (2015). Effect of surface functionalization on the electronic transport properties of Ti_3C_2 MXene. *EPL* 111:67002. doi: 10.1209/0295-5075/111/67002

Cai, Y., Shen, J., Ge, G., Zhang, Y., Jin, W., Huang, W., et al. (2018). Stretchable $Ti_3C_2T_x$ MXene/carbon nanotube composite based strain sensor with ultrahigh sensitivity and tunable sensing range. *ACS Nano* 12, 56–62. doi: 10.1021/acsnano.7b06251

Chen, J., Chen, K., Tong, D., Huang, Y., Zhang, J., Xue, J., et al. (2015). CO_2 and temperature dual responsive "'Smart'" MXene phases. *Chem. Commun.* 51, 314–317. doi: 10.1039/C4CC07220K

Chen, X., Sun, X., Xu, W., Pan, G., Zhou, D., Zhu, J., et al. (2018). Ratiometric photoluminescence sensing based on Ti_3C_2 MXene quantum dots for the intracellular pH sensor. *Nanoscale* 10, 1111–1118. doi: 10.1039/x0xx00000x

Chen, Z., Hu, Y., Zhuo, H., Liu, L., Jing, S., Zhong, L., et al. (2019). Compressible, elastic, and pressure-sensitive carbon aerogels derived from 2D titanium carbide nanosheets and bacterial cellulose for wearable sensors. *Chem. Mater.* 31, 3301–3312. doi: 10.1021/acs.chemmater.9b00259

Dai, C., Chen, Y., Jing, X., Xiang, L., Yang, D., Lin, H., et al. (2017a). Two-dimensional tantalum carbide (MXenes) composite nanosheets for multiple imaging-guided photothermal tumor ablation. *ACS Nano* 11, 12696–12712. doi: 10.1021/acsnano.7b07241

Dai, C., Lin, H., Xu, G., Liu, Z., Wu, R., and Chen, Y. (2017b). Biocompatible 2D titanium carbide (MXenes) composite nanosheets for pH-responsive MRI-guided tumor hyperthermia. *Chem. Mater.* 29, 8637–8652. doi: 10.1021/acs.chemmater.7b02441

Enyashin, A. N., and Ivanovskii, A. L. (2012). Atomic structure, comparative stability and electronic properties of hydroxylated Ti_2C and Ti_3C_2

nanotubes. *Comput. Theor. Chem.* 989, 27–32. doi: 10.1016/j.comptc.2012.02.034

Feng, L., Zha, X.-H., Luo, K., Huang, Q., He, J., Liu, Y., et al. (2017). Structures and mechanical and electronic properties of the Ti_2CO_2 MXene incorporated with neighboring elements (Sc, V, B and N). *J. Electr. Mater.* 46, 2460–2466. doi: 10.1007/s11664-017-5311-5

Geistlinger, H. (1993). Electron theory of thin-film gas sensors. *Sensors Actuat. B Chem.* 17, 47–60. doi: 10.1016/0925-4005(93)85183-B

Ghidiu, M., Halim, J., Kota, S., Bish, D., Gogotsi, Y., and Barsoum, M. W. (2016). Ion-exchange and cation solvation reactions in Ti_3C_2 MXene. *Chem. Mater.* 28, 3507–3514. doi: 10.1021/acs.chemmater.6b01275

Ghidiu, M., Lukatskaya, M. R., Zhao, M.-Q., Gogotsi, Y., and Barsoum, M. W. (2014). Conductive two-dimensional titanium carbide 'clay' with high volumetric capacitance. *Nature* 516, 78–81. doi: 10.1038/nature13970

Ghosh, R. (2014). Highly sensitive large-area multi-layered graphene-based flexible ammonia sensor. *Sensors Actuat. B Chem.* 205, 67–73. doi: 10.1016/j.snb.2014.08.044

Gogotsi, Y. (2015). Transition metal carbides go 2D. *Nat. Mater.* 14, 1079–1080. doi: 10.1038/nmat4386

Guo, J., Peng, Q., Fu, H., Zou, G., and Zhang, Q. (2015). Heavy-metal adsorption behavior of two-dimensional alkalization-intercalated MXene by first-principles calculations. *J. Phys. Chem. C* 119, 20923–20930. doi: 10.1021/acs.jpcc.5b05426

Guo, Y., Zhong, M., Fang, Z., Wan, P., and Yu, G. (2019). A wearable transient pressure sensor made with MXene nanosheets for sensitive broad-range human–machine interfacing. *Nano Lett.* 19, 1143–1150. doi: 10.1021/acs.nanolett.8b04514

Heikenfeld, J., Jajack, A., Rogers, J., Gutruf, P., Tian, L., Pan, T., et al. (2018). Wearable sensors: modalities, challenges, and prospects. *Lab Chip* 18, 217–248. doi: 10.1039/C7LC00914C

Huang, K., Li, Z., Lin, J., Han, G., and Huang, P. (2018). Two-dimensional transition metal carbides and nitrides (MXenes) for biomedical applications. *Chem. Soc. Rev.* 47, 5109–5124. doi: 10.1039/C7CS00838D

Jia, J., Xiong, T., Zhao, L., Wang, F., Liu, H., Hu, R., et al. (2017). Ultrathin N-doped Mo2C nanosheets with exposed active sites as efficient electrocatalyst for hydrogen evolution reactions. *ACS Nano* 11, 12509–12518. doi: 10.1021/acsnano.7b06607

Khan, Y., Ostfeld, A. E., Lochner, C. M., Pierre, A., and Arias, A. C. (2016). Monitoring of vital signs with flexible and wearable medical devices. *Adv. Mater. Weinheim.* 28, 4373–4395. doi: 10.1002/adma.201504366

Khazaei, M., Arai, M., Sasaki, T., Chung, C.-Y., Venkataramanan, N. S., Estili, M., et al. (2013). Novel electronic and magnetic properties of two-dimensional transition metal carbides and nitrides. *Adv. Funct. Mater.* 23, 2185–2192. doi: 10.1002/adfm.201202502

Kim, S. J., Koh, H.-J., Ren, C. E., Kwon, O., Maleski, K., Cho, S.-Y., et al. (2018). Metallic Ti3C2Tx MXene gas sensors with ultrahigh signal-to-noise ratio. *ACS Nano* 12, 986–993. doi: 10.1021/acsnano.7b07460

Lee, E., VahidMohammadi, A., Prorok, B. C., Yoon, Y. S., Beidaghi, M., and Kim, D.-J. (2017). Room temperature gas sensing of two-dimensional titanium carbide (MXene). *ACS Appl. Mater. Interfaces* 9, 37184–37190. doi: 10.1021/acsami.7b11055

Lee, E., VahidMohammadi, A., Yoon, Y. S., Beidaghi, M., and Kim, D.-J. (2019). Two-dimensional vanadium carbide mxene for gas sensors with ultrahigh sensitivity toward nonpolar gases. *ACS Sens.* 4, 1603–1611. doi: 10.1021/acssensors.9b00303

Lee, S. H., Eom, W., Shin, H., Ambade, R. B., Bang, J. H., Kim, H. W., et al. (2020). Room-temperature, highly durable Ti3C2Tx MXene graphene hybrid fibers for NH3 gas sensing. *ACS Appl. Mater. Interfaces* 12, 10434–10442. doi: 10.1021/acsami.9b21765

Li, M., Fang, L., Zhou, H., Wu, F., Lu, Y., Luo, H., et al. (2019). Three-dimensional porous MXene/NiCo-LDH composite for high performance non-enzymatic glucose sensor. *Appl. Surf. Sci.* 495:143554. doi: 10.1016/j.apsusc.2019.143554

Li, N., Jiang, Y., Zhou, C., Xiao, Y., Meng, B., Wang, Z., et al. (2019). High-performance humidity sensor based on urchin-like composite of Ti_3C_2 MXene-derived TiO_2 nanowires. *ACS Appl. Mater. Interfaces* 11, 38116–38125.doi: 10.1021/acsami.9b12168

Li, S., Ma, Z., Cao, Z., Pan, L., and Shi, Y. (2019). Advanced wearable microfluidic sensors for healthcare monitoring. *Small* 16:1903822. doi: 10.1002/smll.201903822

Li, T., Yao, L., Liu, Q., Gu, J., Luo, R., Li, J., et al. (2018). Fluorine-free synthesis of high-purity $Ti_3C_2T_x$ (T=OH, O) via alkali treatment. *Angew. Chem. Int. Ed.* 57, 6115–6119. doi: 10.1002/anie.201800887

Li, X.-P., Li, Y., Li, X., Song, D., Min, P., Hu, C., et al. (2019). Highly sensitive, reliable and flexible piezoresistive pressure sensors featuring polyurethane sponge coated with MXene sheets. *J. Coll. Interface Sci.* 542, 54–62. doi: 10.1016/j.jcis.2019.01.123

Liao, H., Guo, X., Wan, P., and Yu, G. (2019). Conductive MXene nanocomposite organohydrogel for flexible, healable, low-temperature tolerant strain sensors. *Adv. Funct. Mater.* 29:1904507. doi: 10.1002/adfm.201904507

Lin, H., Gao, S., Dai, C., Chen, Y., and Shi, J. (2017). A two-dimensional biodegradable niobium carbide (MXene) for photothermal tumor eradication in NIR-I and NIR-II biowindows. *J. Am. Chem. Soc.* 139, 16235–16247. doi: 10.1021/jacs.7b07818

Ling, Z., Ren, C. E., Zhao, M.-Q., Yang, J., Giammarco, J. M., Qiu, J., et al. (2014). Flexible and conductive MXene films and nanocomposites with high capacitance. *Proc. Natl. Acad. Sci. U.S.A.* 111, 16676–16681. doi: 10.1073/pnas.1414215111

Lipatov, A., Alhabeb, M., Lukatskaya, M. R., Boson, A., Gogotsi, Y., and Sinitskii, A. (2016). Effect of synthesis on quality, electronic properties and environmental stability of individual monolayer Ti_3C_2 MXene flakes. *Adv. Electron. Mater.* 2:1600255. doi: 10.1002/aelm.201600255

Liu, F., Zhou, A., Chen, J., Jia, J., Zhou, W., Wang, L., et al. (2017a). Preparation of Ti_3C_2 and Ti_2C MXenes by fluoride salts etching and methane adsorptive properties. *Appl. Surf. Sci.* 416, 781–789. doi: 10.1016/j.apsusc.2017.04.239

Liu, F., Zhou, J., Wang, S., Wang, B., Shen, C., Wang, L., et al. (2017b). Preparation of high-purity V2C MXene and electrochemical properties as Li-Ion batteries. *J. Electrochem. Soc.* 164, A709–A713. doi: 10.1149/2.0641704jes

Liu, G., Zou, J., Tang, Q., Yang, X., Zhang, Y., Zhang, Q., et al. (2017). Surface modified Ti3C2 MXene nanosheets for tumor targeting photothermalphotodynamicchemo synergistic therapy. *ACS Appl. Mater. Interfaces* 9, 40077–40086. doi: 10.1021/acsami.713421

Liu, H., Duan, C., Yang, C., Shen, W., Wang, F., and Zhu, Z. (2015). A novel nitrite biosensor based on the direct electrochemistry of hemoglobin immobilized on MXene-Ti_3C_2. *Sens. Actuat. B Chem.* 218, 60–66. doi: 10.1016/j.snb.2015.04.090

Liu, J., Zhang, H.-B., Xie, X., Yang, R., Liu, Z., Liu, Y., et al. (2018). Multifunctional, superelastic, and lightweight MXene/polyimide aerogels. *Small* 14:1802479. doi: 10.1002/smll.201802479

Liu, L., Chen, W., Zhang, H., Wang, Q., Guan, F., and Yu, Z. (2019). Flexible and multifunctional silk textiles with biomimetic leaf-like MXene/silver nanowire nanostructures for electromagnetic interference shielding, humidity monitoring, and self-derived hydrophobicity. *Adv. Funct. Mater.* 29:1905197. doi: 10.1002/adfm.201905197

Lukatskaya, M. R., Mashtalir, O., Ren, C. E., Dall'Agnese, Y., Rozier, P., Taberna, P. L., et al. (2013). Cation intercalation and high volumetric capacitance of two-dimensional titanium carbide. *Science* 341, 1502–1505. doi: 10.1126/science.1241488

Ma, R., and Sasaki, T. (2010). Nanosheets of oxides and hydroxides: ultimate 2D charge-bearing functional crystallites. *Adv. Mater. Weinheim.* 22, 5082–5104. doi: 10.1002/adma.201001722

Ma, Y., Liu, N., Li, L., Hu, X., Zou, Z., Wang, J., et al. (2017). A highly flexible and sensitive piezoresistive sensor based on MXene with greatly changed interlayer distances. *Nat. Commun.* 8:1207. doi: 10.1038/s41467-017-01136-9

Ma, Y., Yue, Y., Zhang, H., Cheng, F., Zhao, W., Rao, J., et al. (2018). 3D synergistical MXene/reduced graphene oxide aerogel for a piezoresistive sensor. *ACS Nano* 12, 3209–3216. doi: 10.1021/acsnano.7b06909

Ma, Z., Chen, P., Cheng, W., Yan, K., Pan, L., Shi, Y., et al. (2018). Highly sensitive, printable nanostructured conductive polymer wireless sensor for food spoilage detection. *Nano Lett.* 18, 4570–4575. doi: 10.1021/acs.nanolett.8b01825

Ma, Z., Li, S., Wang, H., Cheng, W., Li, Y., Pan, L., et al. (2019). Advanced electronic skin devices for healthcare applications. *J. Mater. Chem. B* 7, 173–197. doi: 10.1039/C8TB02862A

Malaki, M., Maleki, A., and Varma, R. S. (2016). MXenes and ultrasonication. *J. Mater. Chem. A* 4, 51–58. doi: 10.1039/C9TA01850F

Mannsfeld, S. C. B., Tee, B. C.-K., Stoltenberg, R. M., Chen, C. V. H.-H., Barman, S., Muir, B. V. O., et al. (2010). Highly sensitive flexible pressure sensors with microstructured rubber dielectric layers. *Nat. Mater.* 9, 859–864. doi: 10.1038/nmat2834

Mashtalir, O., Naguib, M., Mochalin, V. N., Dall'Agnese, Y., Heon, M., Barsoum, M. W., et al. (2013). Intercalation and delamination of layered carbides and carbonitrides. *Nat. Commun.* 4:1716. doi: 10.1038/ncomms2664

Meshkian, R., Näslund, L.-Å., Halim, J., Lu, J., Barsoum, M. W., and Rosen, J. (2015). Synthesis of two-dimensional molybdenum carbide, Mo 2 C, from the gallium based atomic laminate Mo2 Ga 2 C. *Scr. Mater.* 108, 147–150. doi: 10.1016/j.scriptamat.2015.07.003

Muckley, E. S., Naguib, M., Wang, H.-W., Vlcek, L., Osti, N. C., Sacci, R. L., et al. (2017). Multimodality of structural, electrical, and gravimetric responses of intercalated MXenes to water. *ACS Nano* 11, 11118–11126. doi: 10.1021/acsnano.7b05264

Naguib, M., Halim, J., Lu, J., Cook, K. M., Hultman, L., Gogotsi, Y., et al. (2013). New two-dimensional niobium and vanadium carbides as promising materials for Li-Ion batteries. *J. Am. Chem. Soc.* 135, 15966–15969. doi: 10.1021/ja405735d

Naguib, M., Kurtoglu, M., Presser, V., Lu, J., Niu, J., Heon, M., et al. (2011). Two-dimensional nanocrystals produced by exfoliation of Ti_3AlC_2. *Adv. Mater. Weinheim.* 23, 4248–4253. doi: 10.1002/adma.201102306

Naguib, M., Mashtalir, O., Carle, J., Presser, V., Lu, J., Hultman, L., et al. (2012). Two-dimensional transition metal carbides. *ACS Nano* 6, 1322–1331. doi: 10.1021/nn204153h

Naguib, M., Mochalin, V. N., Barsoum, M. W., and Gogotsi, Y. (2014). 25th anniversary article: MXenes: a new family of two-dimensional materials. *Adv. Mater. Weinheim.* 26, 992–1005. doi: 10.1002/adma.201304138

Osti, N. C., Naguib, M., Ostadhossein, A., Xie, Y., Kent, P. R. C., Dyatkin, B., et al. (2016). Effect of metal ion intercalation on the structure of MXene and water dynamics on its internal surfaces. *ACS Appl. Mater. Interfaces* 8, 8859–8863. doi: 10.1021/acsami.6b01490

Persson, I., el Ghazaly, A., Tao, Q., Halim, J., Kota, S., Darakchieva, V., et al. (2018). Tailoring structure, composition, and energy storage properties of MXenes from selective etching of in-plane, chemically ordered MAX phases. *Small* 14:1703676. doi: 10.1002/smll.201703676

Rakhi, R. B., Nayak, P., Xia, C., and Alshareef, H. N. (2016). Novel amperometric glucose biosensor based on MXene nanocomposite. *Sci. Rep.* 6:36422. doi: 10.1038/srep36422

Rasid, Z. A. M., Omar, M. F., Nazeri, M. F. M., Aziz, M. A. A., and Szota, M. (2017). Low cost synthesis method of two-dimensional titanium carbide MXene. *IOP Conf. Ser: Mater. Sci. Eng.* 209:012001. doi: 10.1088/1757-899X/209/1/012001

Ray, T., Choi, J., Reeder, J., Lee, S. P., Aranyosi, A. J., Ghaffari, R., et al. (2019). Soft, skin-interfaced wearable systems for sports science and analytics. *Curr. Opin. Biomed. Eng.* 9, 47–56. doi: 10.1016/j.cobme.2019.01.003

Römer, F. M., Wiedwald, U., Strusch, T., Halim, J., Mayerberger, E., Barsoum, M. W., et al. (2017). Controlling the conductivity of Ti3C2 MXenes by inductively coupled oxygen and hydrogen plasma treatment and humidity. *RSC Adv.* 7, 13097–13103. doi: 10.1039/C6RA27505B

Shahzad, A., Rasool, K., Miran, W., Nawaz, M., Jang, J., Mahmoud, K. A., et al. (2017). Two-dimensional $Ti_3C_2T_x$ MXene nanosheets for efficient copper removal from water. *ACS Sust. Chem. Eng.* 5, 11481–11488. doi: 10.1021/acssuschemeng.7b02695

Shahzad, F., Alhabeb, M., Hatter, C. B., Anasori, B., Man Hong, S., Koo, C. M., et al. (2016). Electromagnetic interference shielding with 2D transition metal carbides (MXenes). *Science* 353, 1137–1140. doi: 10.1126/science.aag2421

Shein, I. R., and Ivanovskii, A. L. (2013). Graphene-like nanocarbides and nanonitrides of d metals (MXenes): synthesis, properties and simulation. *Micro Nano Lett.* 8, 59–62. doi: 10.1049/mnl.2012.0797

Shi, X., Wang, H., Xie, X., Xue, Q., Zhang, J., Kang, S., et al. (2019). Bioinspired ultrasensitive and stretchable MXene-based strain sensor via nacre-mimetic microscale "brick-and-mortar" architecture. *ACS Nano* 13, 649–659. doi: 10.1021/acsnano.8b07805

Sun, W., Shah, S. A., Chen, Y., Tan, Z., Gao, H., Habib, T., et al. (2017). Electrochemical etching of Ti_2AlC to Ti_2CTx (MXene) in lowconcentration hydrochloric acid solution. *J. Mater. Chem. A* 5, 21663–21668. doi: 10.1039/C5TA06869J

Tang, Q., Zhou, Z., and Shen, P. (2012). Are MXenes promising anode materials for li ion batteries? computational studies on electronic properties and li storage capability of Ti_3C_2 and $Ti_3C_2X_2$ (X = F, OH) monolayer. *J. Am. Chem. Soc.* 134, 16909–16916. doi: 10.1021/ja308463r

Verger, L. (2019). Overview of the synthesis of MXenes and other ultrathin 2D transition metal carbides and nitrides. *Mater. Sci.* 23, 149–163. doi: 10.1016/j.cossms.2019.02.001

Wang, F., Yang, C., Duan, M., Tang, Y., and Zhu, J. (2015). TiO_2 nanoparticle modified organ-like Ti_3C_2 MXene nanocomposite encapsulating hemoglobin for a mediator-free biosensor with excellent performances. *Biosens. Bioelectron.* 74, 1022–1028. doi: 10.1016/j.bios.2015.08.004

Wang, K., Lou, Z., Wang, L., Zhao, L., Zhao, S., Wang, D., et al. (2019). Bioinspired interlocked structure-induced high deformability for two-dimensional titanium carbide (MXene)/natural microcapsule-based flexible pressure sensors. *ACS Nano* 13, 9139–9147. doi: 10.1021/acsnano.9b03454

Wang, Z., Kochat, V., Pandey, P., Kashyap, S., Chattopadhyay, S., Samanta, A., et al. (2017). Metal immiscibility route to synthesis of ultrathin carbides, borides, and nitrides. *Adv. Mater. Weinheim* 29:1700364. doi: 10.1002/adma.201700364

Xiao, B., Li, Y., Yu, X., and Cheng, J. (2016). MXenes: reusable materials for NH3 sensor or capturer by controlling the charge injection. *Sens. Actuat. B Chem.* 235, 103–109. doi: 10.1016/j.snb.2016.05.062

Xiao, X., Yu, H., Jin, H., Wu, M., Fang, Y., Sun, J., et al. (2017). Salt-templated synthesis of 2D metallic MoN and other nitrides. *ACS Nano* 11, 2180–2186. doi: 10.1021/acsnano.6b08534

Xu, C., Wang, L., Liu, Z., Chen, L., Guo, J., Kang, N., et al. (2015). Large-area high-quality 2D ultrathin Mo_2C superconducting crystals. *Nature Mater.* 14, 1135–1141. doi: 10.1038/nmat4374

Xu, S., Zhang, Y., Jia, L., Mathewson, K. E., Jang, K.-I., Kim, J., et al. (2014). Soft microfluidic assemblies of sensors, circuits, and radios for the skin. *Science* 344, 70–74. doi: 10.1126/science.1250169

Yang, J. C., Mun, J., Kwon, S. Y., Park, S., Bao, Z., and Park, S. (2019). Electronic skin: recent progress and future prospects for skin-attachable devices for health monitoring, robotics, and prosthetics. *Adv. Mater. Weinheim* 31:1904765. doi: 10.1002/adma.201904765

Yang, Y., Shi, L., Cao, Z., Wang, R., and Sun, J. (2019). Strain sensors with a high sensitivity and a wide sensing range based on a $Ti_3C_2T_x$ (MXene) nanoparticle–nanosheet hybrid network. *Adv. Funct. Mater.* 29:1807882. doi: 10.1002/adfm.201807882

Yang, Z., Liu, A., Wang, C., Liu, F., He, J., Li, S., et al. (2019). Improvement of gas and humidity sensing properties of organ-like MXene by alkaline treatment. *ACS Sensors.* 4, 1261–1269. doi: 10.1021/acssensors.9b00127

Yu, X., Li, Y., Cheng, J., Liu, Z., Li, Q., Li, W., et al. (2015). Monolayer Ti2CO2: a promising candidate for NH_3 sensor or capturer with high sensitivity and selectivity. *ACS Appl. Mater. Interfaces* 7, 13707–13713. doi: 10.1021/acsami.5b03737

Yuan, W., Yang, K., Peng, H., Li, F., and Yin, F. (2018). A flexible VOCs sensor based on a 3D Mxene framework with a high sensing performance. *J. Mater. Chem. A* 6, 18116–18124. doi: 10.1039/C8TA06928J

Yue, Y., Liu, N., Liu, W., Li, M., Ma, Y., Luo, C., et al. (2018). 3D hybrid porous Mxene-sponge network and its application in piezoresistive sensor. *Nano Energy* 50, 79–87. doi: 10.1016/j.nanoen.2018.05.020

Zha, X.-H., Luo, K., Li, Q., Huang, Q., He, J., Wen, X., et al. (2015). Role of the surface effect on the structural, electronic and mechanical properties of the carbide MXenes. *EPL* 111: 26007. doi: 10.1209/0295-5075/111/26007

Zhang, Y.-Z., Lee, K. H., Anjum, D. H., Sougrat, R., Jiang, Q., Kim, H., et al. (2018). MXenes stretch hydrogel sensor performance to new limits. *Sci. Adv.* 4:eaat0098. doi: 10.1126/sciadv.aat0098

Zhang, Z., Zhang, F., Wang, H., Chan, C. H., Lu, W., and Dai, J. (2012). Substrate orientation-induced epitaxial growth of face centered

cubic Mo_2C superconductive thin film. *J. Mater. Chem. C* 4, 53–61. doi: 10.1039/C5TC02426A

Zhao, L., Wang, K., Wei, W., Wang, L., and Han, W. (2019). High-performance flexible sensing devices based on polyaniline/MXene nanocomposites. *InfoMat*. 1, 407–416. doi: 10.1002/inf2.12032

Zheng, J., Wang, B., Ding, A., Weng, B., and Chen, J. (2018). Synthesis of MXene/DNA/Pd/Pt nanocomposite for sensitive detection of dopamine. *J. Electroanalyt. Chem.* 816, 189–194. doi: 10.1016/j.jelechem.2018.03.056

Zhu, X., Liu, B., Hou, H., Huang, Z., Zeinu, K. M., Huang, L., et al. (2017). Alkaline intercalation of Ti_3C_2 MXene for simultaneous electrochemical detection of Cd(II), Pb(II), Cu(II) and Hg(II). *Electrochimica Acta* 248, 46–57. doi: 10.1016/j.electacta.2017.07.084

Zhuo, H., Hu, Y., Chen, Z., Peng, X., Liu, L., Luo, Q., et al. (2019). A carbon aerogel with super mechanical and sensing performances for wearable piezoresistive sensors. *J. Mater. Chem. A* 7, 8092–8100. doi: 10.1039/C9TA00596J

Conflict of Interest: The authors declare that the research was conducted in the absence of any commercial or financial relationships that could be construed as a potential conflict of interest.

frontiers in Chemistry

ORIGINAL RESEARCH
published: 21 April 2020
doi: 10.3389/fchem.2020.00238

A Fluorescence Resonance Energy Transfer Probe Based on DNA-Modified Upconversion and Gold Nanoparticles for Detection of Lead Ions

Yue Wang[1], *Menghua Lv*[1], *Zehan Chen*[1], *Zilong Deng*[1], *Ningtao Liu*[2]*, *Jianwei Fan*[1,3]* and *Weixian Zhang*[1,3]

[1] State Key Laboratory of Pollution Control and Resources Reuse, College of Environment Science and Engineering, Tongji University, Shanghai, China, [2] Department of Neurosurgery, Shanghai Tongji Hospital Affiliated to Tongji University, Shanghai, China, [3] Shanghai Institute of Pollution Control and Ecological Security, Shanghai, China

OPEN ACCESS

Edited by:
Xiaomin Li,
Fudan University, China

Reviewed by:
Peiyuan Wang,
Fujian Institute of Research on the Structure of Matter (CAS), China
Liang Chen,
Fudan University, China

***Correspondence:**
Ningtao Liu
ningt_liu@163.com
Jianwei Fan
fanjianwei@tongji.edu.cn

Specialty section:
This article was submitted to Nanoscience, a section of the journal Frontiers in Chemistry

Received: 06 January 2020
Accepted: 12 March 2020
Published: 21 April 2020

Citation:
Wang Y, Lv M, Chen Z, Deng Z, Liu N, Fan J and Zhang W (2020) A Fluorescence Resonance Energy Transfer Probe Based on DNA-Modified Upconversion and Gold Nanoparticles for Detection of Lead Ions. Front. Chem. 8:238. doi: 10.3389/fchem.2020.00238

We report a new sensor for the specific detection of lead ions (Pb^{2+}) in contaminated water based on fluorescence resonance energy transfer (FRET) between upconversion nanoparticles (UCNPs) as donors and gold nanoparticles (Au NPs) as receptors. The UCNPs modified with Pb^{2+} aptamers could bind to Au NPs, which were functionalized with complementary DNA through hybridization. The green fluorescence of UCNPs was quenched to a maximum rate of 80% due to the close proximity between the energy donor and the acceptor. In the presence of Pb^{2+}, the FRET process was broken because Pb^{2+} induced the formation of G-quadruplexes from aptamers, resulting in unwound DNA duplexes and separated acceptors from donors. The fluorescence of UCNPs was restored, and the relative intensity had a significant linear correlation with Pb^{2+} concentration from 0 to 50 nM. The sensor had a detection limit as low as 4.1 nM in a buffer solution. More importantly, the sensor exhibited specific detection of Pb^{2+} in complex metal ions, demonstrating high selectivity in practical application. The developed FRET prober may open up a new insight into the specific detection of environmental pollution.

Keywords: upconversion nanoparticles, gold nanoparticles, fluorescence resonance energy transfer, DNA, lead ions

INTRODUCTION

Lead ion (Pb^{2+}), one of the most serious metallic toxicants, can damage cardiovascular, reproductive, neurological, and developmental systems of the human body at low concentrations in the blood (Yoosaf et al., 2007; Zhou et al., 2011; Kim et al., 2012; Li et al., 2013). Although traditional methods including inductively coupled plasma mass spectrometry (Xia et al., 2008; Gao et al., 2009), atomic absorption spectroscopy (Bravo-Sanchez et al., 2001), and high-performance liquid chromatography (Yang et al., 2003) are highly sensitive and accurate, complicated pretreatment, and implementation limit their applicability for on-site rapid detection. Therefore, it is of important significance to develop analytical strategies with facile and straightforward features.

The detection assay composed of fluorescence and DNA molecules has attracted more and more attention mainly due to sensitive fluorescence signal, stable DNA molecules, and highly specific binding ability between specific sequences and target detectors (e.g., protein, ions, virus, and nucleic acid aptamers) (Hamaguchi et al., 2001; Pavlov et al., 2004; Xiao et al., 2005; Chang et al., 2010; Saha et al., 2012). Zhou and co-workers labeled 6-carboxyfluorescein on G-rich DNA strands and monitored the reduction of fluorescence for Pb^{2+} detection (Zhan et al., 2013). Shi and co-workers developed a new strategy based on DNA-templated silver nanoclusters with elevated fluorescence for L-histidine detection (Zheng et al., 2015). However, reported substances or quenchers in the actual environment might weaken the fluorescence and lead to false-positive results. Therefore, the "turn-off–on" detection system based on fluorescence resonance energy transfer (FRET) is introduced to avoid external interferences.

Upconversion nanoparticles (UCNPs) have rapidly emerged owing to their unique luminescent properties (Wang et al., 2005; Mader et al., 2010; Haase and Schaefer, 2011; Chen et al., 2014). Compared to traditional fluorescent markers, the UCNPs presented low auto-fluorescence, narrow emission width, no flicker, and strong light stability, leading to a wide application in biological and environmental monitoring and sensing (Chen and Zhao, 2012; Chen et al., 2013, 2014; Dacosta et al., 2014). Therefore, upconversion luminescence, as sensing signal under excitation of the near-infrared ray (NIR) light, effectively diminished the background noise in a complicated detection system (Wu et al., 2014). Meanwhile, gold nanoparticles (Au NPs) are superior fluorescence quenching agents due to the large extinction coefficient and a wide absorption band in the UV–visible region (Peng et al., 2011; Lin et al., 2013; Liu et al., 2013). The FRET systems were established based on upconversion nanoparticles and gold nanoparticles for the detection of avidin and Cr^{3+} (Wang et al., 2005; Liu et al., 2013).

In this paper, $NaYF_4$: Yb, Er @$NaYF_4$ UCNPs as energy donors and Au NPs as energy receptors are employed as FRET system for the sensitive detection of Pb^{2+}. The donors and receptors are paired by two complementary DNA strands with good quenching ability for UCNPs. Single-stranded DNA for modifying UCNPs is rich in G base, which can fold to G-quadruplex structure in the presence of Pb^{2+}. DNA duplex is then disrupted and the FRET system between UCNPs and Au NPs is cleaved, resulting in the restoration of fluorescence. The concentration of Pb^{2+} can be detected by monitoring the fluorescence recovery.

MATERIALS AND METHODS

Materials

Anhydrous yttrium trichloride (YCl_3, 99.99%), anhydrous ytterbium trichloride ($YbCl_3$, 99.9%), anhydrous erbium chloride ($ErCl_3$, 99.99%), 1-octadecene (ODE, 90%), oleic acid (OA, 90%), sodium hydroxide (NaOH, 96%), and ammonium fluoride (NH_4F, 96%) were purchased from Sigma-Aldrich. Trihydroxy methyl aminomethane (Tris), HCl, NaCl, KCl, $CaCl_2$, $MgCl_2$, $CuCl_2$, $ZnCl_2$, and $FeCl_3$ were obtained from Sinopharm. All chemicals were used directly without any further purification. Deionized water was purified by a Milli-Q system (Millipore, Bedford, MA, USA). The lead standard solution (1,000 mg/L) was purchased from Aladdin Industrial Inc. All nucleic acid molecules were prepared by Bioengineering Co., Ltd. (Shanghai). The sequences were as follows:

DNA1: 5′ >AAGGGT GGGT GGGT<3′

DNA2: 5′ >AAAAA AAAAA AAAAA AAAAA TTTTT CACCC TCCC AC <3′

Synthesis of $NaYF_4$: Yb, Er

The $NaYF_4$: 18% Yb, 2% Er UCNPs were prepared according to the previous report (Li and Zhang, 2008). Typically, YCl_3 (0.80 mmol), $YbCl_3$ (0.18 mmol), $ErCl_3$ (0.02 mmol), OA (6.0 ml), and ODE (15 ml) were mixed and heated to 140°C under vacuum for 1 h before cooling down to room temperature. Thereafter, NH_4F (4.0 mmol) and NaOH (2.5 mmol) in methanol (10 ml) was added to the resulting solution and stirred for 30 min. The mixture was then transferred to a vacuum oven at 70°C for 30 min and heated at 300°C under argon flow for 1 h. $NaYF_4$: 18% Yb, 2% Er cores were obtained as final product. As-prepared nanoparticles were washed with ethanol for several times and dispersed in 10 ml of cyclohexane.

Synthesis of $NaYF_4$: Yb, Er @$NaYF_4$ UCNPs

To prepare $NaYF_4$: Yb, Er @$NaYF_4$ UCNPs, YCl_3 (0.25 mmol), OA (6.0 ml), and ODE (15 ml) were mixed and transferred to a vacuum oven at 140°C for 1 h. The solution was added with $NaYF_4$: Yb, Er initial core solution (5 ml) after cooling down to room temperature and heated at 70°C in a vacuum oven for 30 min to remove cyclohexane. Subsequently, the obtained mixture was further maintained at 280°C under argon atmosphere for 1 h. The $NaYF_4$: Yb, Er @$NaYF_4$ UCNPs were washed before dispersing in cyclohexane.

Surface Modification of $NaYF_4$: Yb, Er @$NaYF_4$ UCNPs

Ligand-free UCNPs were synthesized ahead of DNA modification following the method reported by Bogdan et al. (2011). The oleic acid-capped UCNPs in cyclohexane were centrifuged by adding ethanol as precipitant. Then, 100 mg of UCNPs was mixed with 10 ml water, and the pH of the solution was adjusted to 4 with 0.1 M hydrochloric acid solution. The solution was extracted three times with diethyl ether after stirring for 2 h, and the nanoparticles obtained were transferred to the aqueous layer and precipitated with acetone. Afterward, the oleic acid-ligand layer was removed and the ligand-free UCNPs were dispersed in water (5 ml).

DNA1 (200 nmol) was added to the solution of ligand-free UCNPs (20 μmol Ln^{3+}). Following stirring overnight at room temperature, the mixture was centrifuged to remove excessive DNA1. The resulting DNA1-modified UCNPs were dispersed in Tris-HCl buffer solution (20 mM, 1 mM $MgCl_2$, 2 mM KCl, and 100 mM NaCl, pH 7.4) and stored at 4°C.

Preparation of DNA2-Modified Au NPs

Au NPs were prepared based on the previously reported method (Chen et al., 2012; Pei et al., 2012). The boiling $HAuCl_4$ ($HAuCl_4 \cdot 4H_2O$, 99.99%) solution was added with trisodium citrate solution (1%) with 20 min of stirring and then cooled down to room temperature to obtain Au NPs.

DNA2 was added to citrate-stabilized Au NPs with a stoichiometric ratio of 1:50, and a tiny amount of sodium citrate-hydrochloric acid buffer solution (500 mM, pH 3.0) was then rapidly added to the said mixture to make a final concentration of 10 mM. The solution was centrifuged for several times to remove excessive DNA2. DNA2-modified Au NPs were yielded and dispersed in Tris-HCl buffer solution (20 mM, pH 7.4).

Detection of Pb^{2+}

The concentration of DNA1-modified UCNPs was immobilized, and DNA2-modified AuNPs with varied concentrations were added to the system. The mixture was incubated for 90 min at 37°C. The optimal concentration of AuNPs-DNA2 was determined by the fluorescence quenching efficiency of UCNPs-DNA1.

The Pb^{2+} standard solution with different concentrations was added to a mixed solution including UCNPs-DNA1 and AuNPs-DNA2, which had been incubated for 90 min. The said solution was further incubated for 30 min to measure its fluorescence spectra.

Characterization

Transmission electron microscopy (TEM) images were taken with a JEM-2100F microscope (200 kV, with a Gatan imaging system). The upconversion fluorescence spectra were performed on a Hitachi F4500 fluorescence spectrometer (xenon lamp excitation source with a 980-nm laser). The UV–vis absorption spectra were characterized by a Lambda 750S UV/Vis/NIR spectrometer.

RESULTS AND DISCUSSION

Principle of UCNPs-AuNPs FRET Sensor for the Detection of Pb^{2+}

The sensor for Pb^{2+} detection was based on FRET from modified UCNPs to Au NPs by an aptamer matching its complement (**Figure 1**). Firstly, UCNPs were treated with hydrochloric acid to remove the hydrophobic surface ligands and modified with the aptamers (DNA1). Au NPs were functionalized with the complementary DNA (DNA2). Secondly, the FRET system was established with UCNPs as donors and Au NPS as receptors. The distance between UCNPs and Au NPs was shortened to <10 nm because of complementary DNA hybridization, leading to quenched fluorescence of UCNPs. Thirdly, the aptamers preferred to bind with metal ions and turned into intermolecular G-quadruplexes in the presence of Pb^{2+}. Therefore, the DNA duplexes were unwound and upconversion fluorescence was restored to determine the concentration of Pb^{2+}.

Characterization of DNA-Modified Nanoparticles

The $NaYF_4$: 18% Yb, 2% Er with a diameter of 45 nm was fabricated by the solvent–thermal method in **Figure 2A** (Li et al., 2014) and further coated with the $NaYF_4$ passivation shell for the formation of $NaYF_4$: 18% Yb, 2% Er @$NaYF_4$ core/shell-structured UCNPs with a diameter of about 50 nm (**Figure 2B**). The OA ligands capped on UCNPs were treated

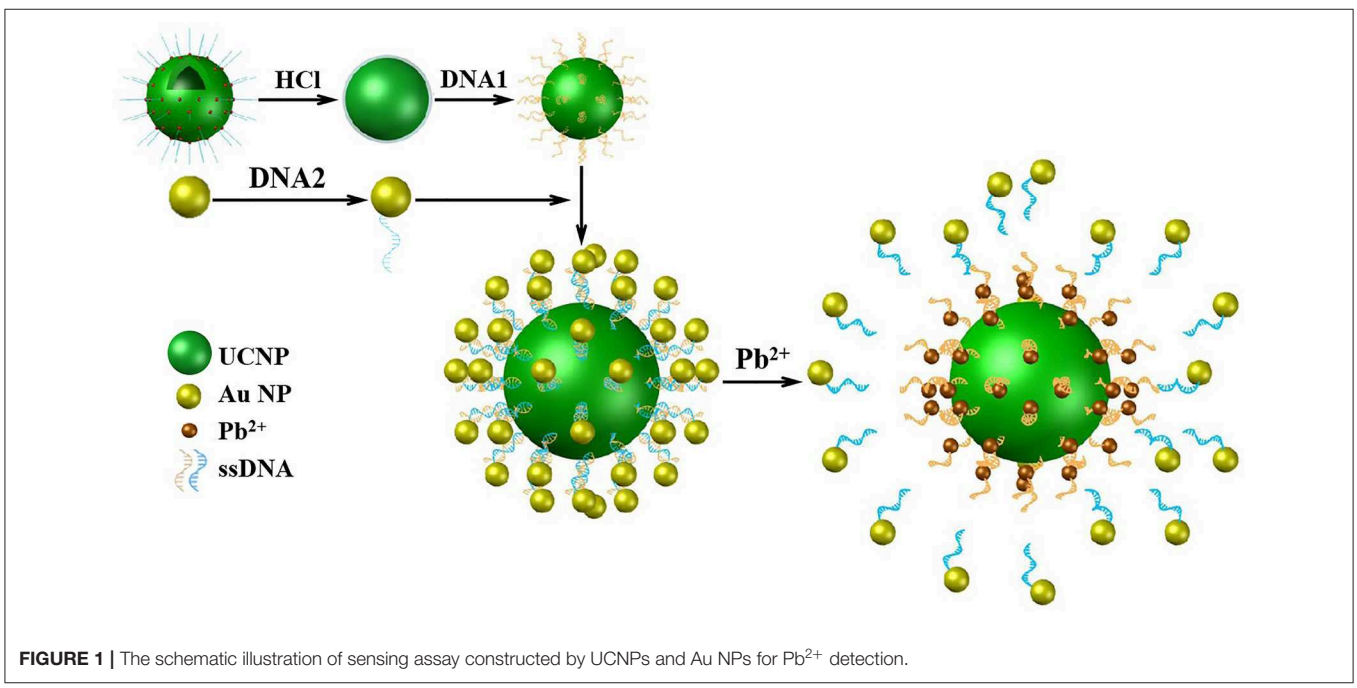

FIGURE 1 | The schematic illustration of sensing assay constructed by UCNPs and Au NPs for Pb^{2+} detection.

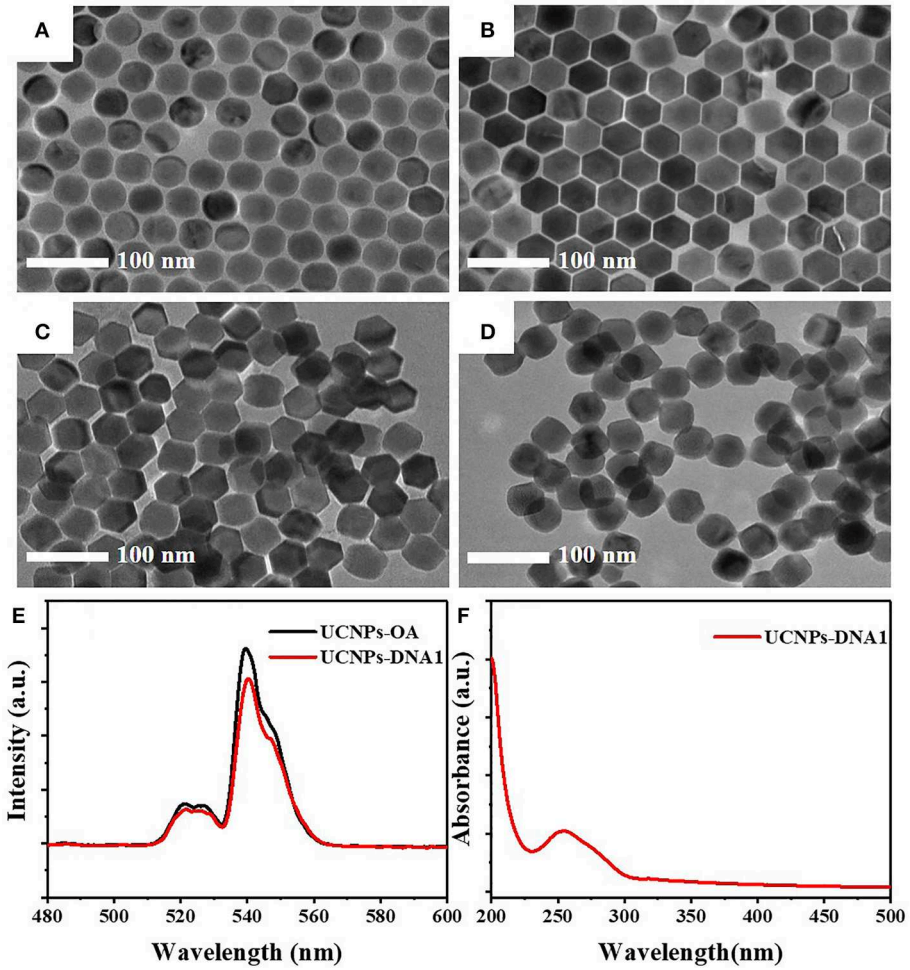

FIGURE 2 | TEM images of **(A)** $NaYF_4$: 18% Yb and 2% Er, **(B)** $NaYF_4$: 18% Yb and 2% Er @$NaYF_4$, **(C)** ligand-free UCNPs, and **(D)** DNA1-modified UCNPs (UCNPs-DNA1). **(E)** The upconversion fluorescence spectra of UCNPs with OA surface ligand (UCNPs-OA) and DNA aptamers (UCNPs-DNA1) under excitation of 980 nm. **(F)** The UV–vis absorption spectra of UCNPs-DNA1.

with hydrochloric acid to form the water-soluble ligand-free UCNPs (**Figure 2C**). The TEM image shows that the obtained water-soluble ligand-free UCNPs remained uniform and monodispersed. Upon DNA1 modification, the UCNPs retained good dispersion with negligible morphological and size alteration (**Figure 2D**). The fluorescence of UCNPs was slightly quenched by water after being modified with DNA1 (**Figure 2E**). A strong absorption peak at 260 nm from the DNA was clearly observed in the spectrum of the DNA1-modified UCNPs, confirming that the UCNPs were successfully modified with DNA-1 (**Figure 2F**).

Au NPs with a diameter of 10 nm (**Figure 3A**) were modified with DNA2 molecules, which were partially complementary with DNA1. The DNA2-modified Au NPs remained of good dispersion (**Figure 3B**). The significant DNA absorption peak was observed at 260 nm, while the maximum absorption peak of Au NPs at 520 nm presented no significant variation (**Figure 3C**). A spectral overlap was illustrated in the range of 510–570 nm between UCNPs and Au NPs (**Figure 3D**).

Optimization of FRET System

The fluorescence intensity of UCNPs gradually decreases along with the elevation of DNA2-modified Au NPs (**Figure 4A**). The concentration of UCNPs was fixed at 6.56 mg/L accompanied by adjusting the concentration of Au NPs. The quenching efficiency of upconversion fluorescence climbed up to 80% at a concentration of 99.75 nM and remained stable at higher concentrations (**Figure 4B**). Therefore, the optimal concentration of the DNA2-modified Au NPs is 99.75 nM. In **Figure 4C**, the UCNPs are surrounded by Au NPs, indicating the construction of the FRET system between UCNPs and Au NPs. Moreover, the fluorescence quenching efficiency reached a plateau (80%) after 90 min of incubation (**Figure 4D**). Therefore, 90 min of incubation is adopted to achieve a stable fluorescence signal.

Detection of Pb^{2+}

The optimal concentrations of UCNPs (6.56 mg/L) and Au NPs (99.75 nM) were chosen for the detection system. After

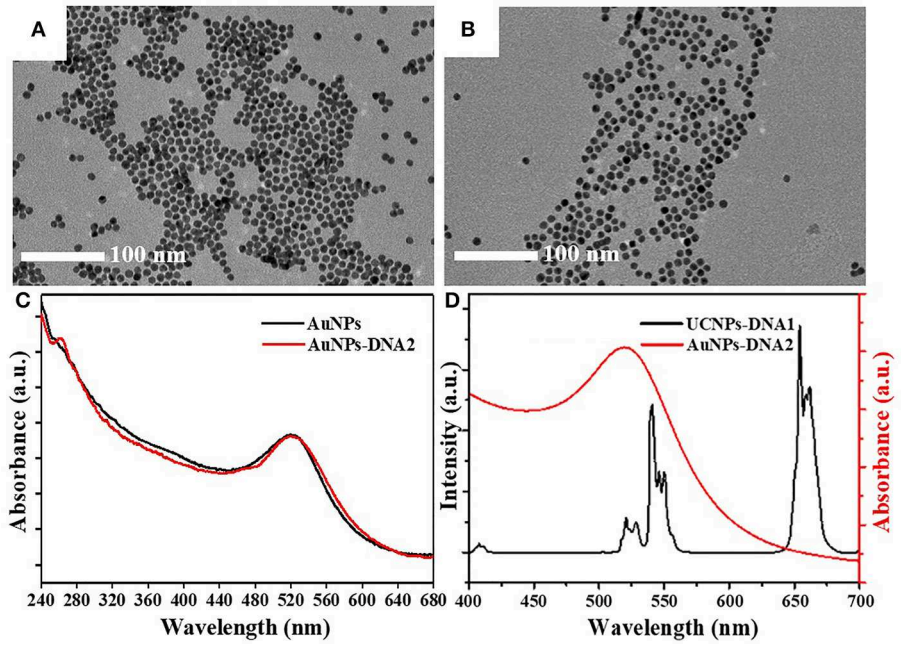

FIGURE 3 | TEM images of **(A)** Au NPs and **(B)** DNA2-modified Au NPs (Au NPs-DNA2). **(C)** The UV–vis absorption spectra of Au NPs and Au NPs-DNA2. **(D)** The upconversion fluorescence spectra of UCNPs-DNA1 and the UV–vis absorption spectra of Au NPs-DNA2.

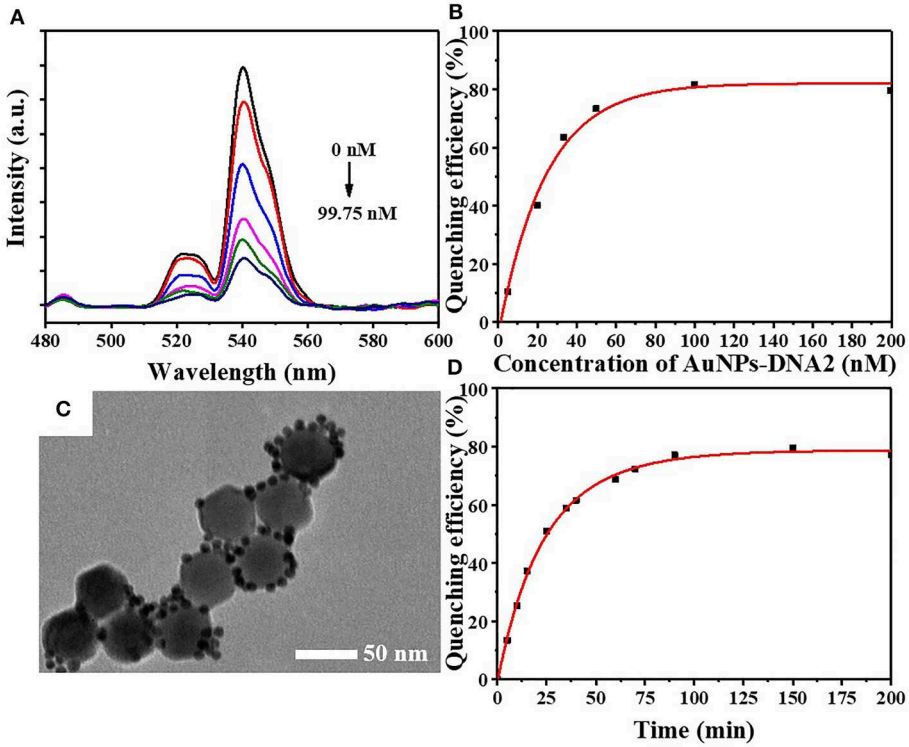

FIGURE 4 | (A) The upconversion fluorescence spectra and **(B)** quenching efficiency of UCNPs-DNA1 after incubation at various concentrations of AuNPs-DNA2 in FRET system. **(C)** TEM image of FRET array fabricated from UCNPs-DNA1 and AuNPs-DNA2. **(D)** The fluorescence quenching efficiency with increasing incubation time.

adding the lead standard solution to the system, the DNA aptamers on the surface of the UCNPs were induced to form G-quadruplexes by Pb^{2+}, leading to the double-stranded DNA unwinding. Subsequently, the energy transfer system between the UCNP energy donors and Au NP receptors was broken, and the upconversion fluorescence was regained (**Figures 5A,B**). The fluorescence is restored gradually along with the elevation of concentration (**Figure 5C**). Linear correlation was demonstrated between the recovery of fluorescence and the concentration of Pb^{2+} in the range of 0 and 50 nM (**Figure 5D**). Determined to be 3σ, the detection limit of the sensor is 4.1 nM. According to the *Guidelines for Drinking-water Quality* in 2017, the Pb^{2+} concentration was recommended to be no more than 10 ppb or 48 nM (World Health Organization, 2017). Therefore, this study elucidated a great potential of the developed FRET-based assay for *in situ* detection of Pb^{2+} in practice. The effect of Pb^{2+} on upconversion fluorescence was demonstrated by adding different concentrations of heavy metal ions. There is no significant effect

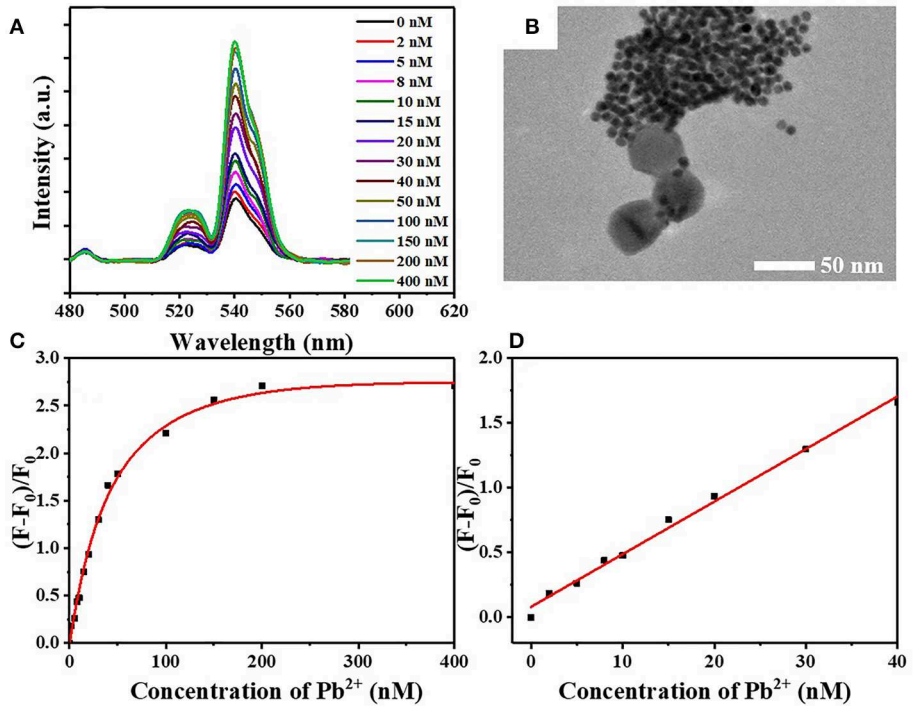

FIGURE 5 | (A) The restoration of fluorescence after incubation at different concentrations of Pb^{2+} in FRET system. **(B)** TEM image of FRET array fabricated from UCNPs-DNA1 and AuNPs-DNA2 after Pb^{2+} incorporation. **(C)** The relationship between relative fluorescence intensity $(F–F_0)/F_0$ and Pb^{2+} concentration. **(D)** Linear correlation between relative fluorescence intensity $(F–F_0)/F_0$ and Pb^{2+} concentration in the range of 0–50 nM.

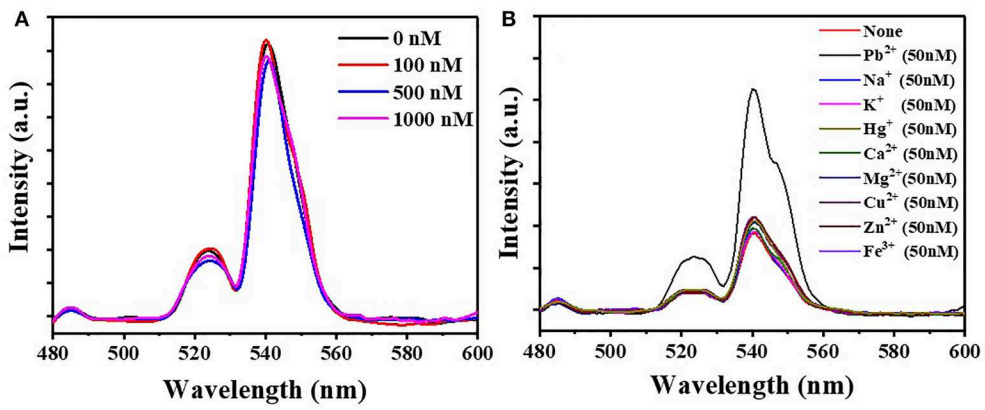

FIGURE 6 | (A) The fluorescence intensity of FRET array after incubation at different concentrations of Pb^{2+}. **(B)** The fluorescence intensity of detection sensor after the incorporation of Pb^{2+}, K^+, Na^+, Ca^{2+}, Mg^{2+}, Hg^{2+}, Cu^{2+}, Zn^{2+}, and Fe^{3+}.

on upconversion fluorescence, even if the Pb^{2+} concentration was increased up to 1,000 nM (**Figure 6A**).

Validation of Selectivity

The selectivity of the sensor for the detection of Pb^{2+} was also tested with different metal ions (**Figure 6B**, **Figure S1**). Pb^{2+} ions led to a dramatic fluorescence recovery (177.9%), while metal ions including K^{+}, Na^{+}, Ca^{2+}, Mg^{2+}, Hg^{2+}, Cu^{2+}, Zn^{2+}, and Fe^{3+} presented little restoration in the fluorescence spectrum. The result demonstrated the high selectivity of the FRET system for Pb^{2+} detection.

CONCLUSIONS

In summary, a highly sensitive Pb^{2+} detection sensor was constructed based on FRET between UCNPs as donors and Au NPs as receptors. The hydrophobic surface ligands of $NaYF_4$: 18% Yb, 2% Er @$NaYF_4$ were removed by hydrochloric acid, resulting in enhanced water-dispersible UCNPs which were further modified with DNA1. Au NPs prepared and modified with DNA2, which was partially complementary with DNA1. The FRET assay was fabricated by hybridizing two complementary DNA strands; thus, the green fluorescence of UCNPs was quenched. The specific Pb^{2+} detection was due to the formation of G-quadruplexes derived from the preferred binding between aptamers of UCNPs and Pb^{2+}, leading to unwound DNA for the recovery of fluorescence. There was a distinct linear correlation between the relative fluorescence intensity and the concentration of Pb^{2+} from 0 to 50 nM. The developed sensor also presented superior sensitivity (4.1 nM) and selectivity, indicating a promising perspective for Pb^{2+} detection.

DATA AVAILABILITY STATEMENT

All datasets generated for this study are included in the article/**Supplementary Material**.

AUTHOR CONTRIBUTIONS

YW: formal analysis, investigation. ML: validation. ZC: software. ZD: data analysis, overall planning, and revision of the manuscript. NL: methodology. JF: conceptualization and methodology. WZ: supervision. All authors wrote and reviewed the manuscript.

FUNDING

This work was supported by the National Natural Science Foundation of China (51878472), and the State Key Laboratory of Pollution Control and Resource Reuse Foundation (No. PCRRK 18001).

SUPPLEMENTARY MATERIAL

The Supplementary Material for this article can be found online at: https://www.frontiersin.org/articles/10.3389/fchem.2020.00238/full#supplementary-material

REFERENCES

Bogdan, N., Vetrone, F., Ozin, G. A., and Capobianco, J. A. (2011). Synthesis of ligand-free colloidally stable water dispersible brightly luminescent lanthanide-doped upconverting nanoparticles. *Nano Lett.* 11, 835–840. doi: 10.1021/nl1041929

Bravo-Sanchez, L. R., De La Riva, B. S., Costa-Fernandez, J. M., Pereiro, R., and Sanz-Medel, A. (2001). Determination of lead and mercury in sea water by preconcentration in a flow injection system followed by atomic absorption spectrometry detection. *Talanta* 55, 1071–1078. doi: 10.1016/S0039-9140(01)00523-9

Chang, H., Tang, L., Wang, Y., Jiang, J., and Li, J. (2010). Graphene fluorescence resonance energy transfer aptasensor for the thrombin detection. *Anal. Chem.* 82, 2341–2346. doi: 10.1021/ac9025384

Chen, G., Qju, H., Prasad, P. N., and Chen, X. (2014). Upconversion nanoparticles: design, nanochemistry, and applications in theranostics. *Chem. Rev.* 114, 5161–5214. doi: 10.1021/cr400425h

Chen, G., Song, F., Xiong, X., and Peng, X. (2013). Fluorescent nanosensors based on Fluorescence Resonance Energy Transfer (FRET). *Industr. Eng. Chem. Res.* 52, 11228–11245. doi: 10.1021/ie303485n

Chen, J., and Zhao, J. X. (2012). Upconversion nanomaterials: synthesis, mechanism, and applications in sensing. *Sensors* 12, 2414–2435. doi: 10.3390/s120302414

Chen, Z., Ren, X., Meng, X., Zhang, Y., Chen, D., and Tang, F. (2012). Novel fluorescence method for detection of alpha-L-fucosidase based on CdTe quantum dots. *Anal. Chem.* 84, 4077–4082. doi: 10.1021/ac300166n

Dacosta, M. V., Doughan, S., Han, Y., and Krull, U. J. (2014). Lanthanide upconversion nanoparticles and applications in bioassays and bioimaging: a review. *Anal. Chim. Acta* 832, 1–33. doi: 10.1016/j.aca.2014.04.030

Gao, R., Hu, Z., Chang, X., He, Q., Zhang, L., Tu, Z., et al. (2009). Chemically modified activated carbon with 1-acylthiosemicarbazide for selective solid-phase extraction and preconcentration of trace Cu(II), Hg(II) and Pb(II) from water samples. *J. Hazard. Mater.* 172, 324–329. doi: 10.1016/j.jhazmat.2009.07.014

Haase, M., and Schaefer, H. (2011). Upconverting nanoparticles. *Angew. Chem. Int. Edn.* 50, 5808–5829. doi: 10.1002/anie.201005159

Hamaguchi, N., Ellington, A., and Stanton, M. (2001). Aptamer beacons for the direct detection of proteins. *Anal. Biochem.* 294, 126–131. doi: 10.1006/abio.2001.5169

Kim, H. N., Ren, W. X., Kim, J. S., and Yoon, J. (2012). Fluorescent and colorimetric sensors for detection of lead, cadmium, and mercury ions. *Chem. Soc. Rev.* 41, 3210–3244. doi: 10.1039/c1cs15245a

Li, X., Wang, R., Zhang, F., and Zhao, D. (2014). Engineering homogeneous doping in single nanoparticle to enhance upconversion efficiency. *Nano Lett.* 14, 3634–3639. doi: 10.1021/nl501366x

Li, X., Xu, B., Lu, H., Wang, Z., Zhang, J., Zhang, Y., et al. (2013). Label-free fluorescence turn-on detection of Pb2+ based on AIE-active quaternary ammonium salt of 9,10-distyrylanthracene. *Anal. Methods* 5, 438–441. doi: 10.1039/c2ay26202a

Li, Z., and Zhang, Y. (2008). An efficient and user-friendly method for the synthesis of hexagonal-phase NaYF(4):Yb, Er/Tm nanocrystals with controllable shape and upconversion fluorescence. *Nanotechnology* 19, 345606–345606. doi: 10.1088/0957-4484/19/34/345606

Lin, F., Yin, B., Li, C., Deng, J., Fan, X., Yi, Y., et al. (2013). Fluorescence resonance energy transfer aptasensor for platelet-derived growth factor detection based on upconversion nanoparticles in 30% blood serum. *Anal. Methods* 5, 699–704. doi: 10.1039/C2AY25519G

Liu, B., Tan, H., and Chen, Y. (2013). Upconversion nanoparticle-based fluorescence resonance energy transfer assay for Cr(III) ions in urine. *Anal. Chim. Acta* 761, 178–185. doi: 10.1016/j.aca.2012.11.035

Mader, H. S., Kele, P., Saleh, S. M., and Wolfbeis, O. S. (2010). Upconverting luminescent nanoparticles for use in bioconjugation and bioimaging. *Curr. Opin. Chem. Biol.* 14, 582–596. doi: 10.1016/j.cbpa.2010.08.014

Pavlov, V., Xiao, Y., Shlyahovsky, B., and Willner, I. (2004). Aptamer-functionalized Au nanoparticles for the amplified optical detection of thrombin. *J. Am. Chem. Soc.* 126, 11768–11769. doi: 10.1021/ja046970u

Pei, H., Li, F., Wan, Y., Wei, M., Liu, H., Su, Y., et al. (2012). Designed diblock oligonucleotide for the synthesis of spatially isolated and highly hybridizable functionalization of DNA-gold nanoparticle nanoconjugates. *J. Am. Chem. Soc.* 134, 11876–11879. doi: 10.1021/ja304118z

Peng, J., Wang, Y., Wang, J., Zhou, X., and Liu, Z. (2011). A new biosensor for glucose determination in serum based on up-converting fluorescence resonance energy transfer. *Biosens. Bioelectr.* 28, 414–420. doi: 10.1016/j.bios.2011.07.057

Saha, K., Agasti, S. S., Kim, C., Li, X., and Rotello, V. M. (2012). Gold nanoparticles in chemical and biological sensing. *Chem. Rev.* 112, 2739–2779. doi: 10.1021/cr2001178

Wang, L. Y., Yan, R. X., Hao, Z. Y., Wang, L., Zeng, J. H., Bao, J., et al. (2005). Fluorescence resonant energy transfer biosensor based on upconversion-luminescent nanoparticles. *Angew. Chem. Int. Edn.* 44, 6054–6057. doi: 10.1002/ange.200501907

World Health Organization (2017). *Guidelines for Drinking-Water Quality: Fourth Edition, Incorporating The First Addendum*. World Health Organization.

Wu, S., Duan, N., Shi, Z., Fang, C., and Wang, Z. (2014). Dual fluorescence resonance energy transfer assay between tunable upconversion nanoparticles and controlled gold nanoparticles for the simultaneous detection of Pb^{2+} and Hg^{2+}. *Talanta* 128, 327–336. doi: 10.1016/j.talanta.2014.04.056

Xia, L., Li, X., Wu, Y., Hu, B., and Chen, R. (2008). Ionic liquids based single drop microextraction combined with electrothermal vaporization inductively coupled plasma mass spectrometry for determination of Co, Hg and Pb in biological and environmental samples. *Spectrochim. Acta B* 63, 1290–1296. doi: 10.1016/j.sab.2008.09.018

Xiao, Y., Lubin, A. A., Heeger, A. J., and Plaxco, K. W. (2005). Label-free electronic detection of thrombin in blood serum by using an aptamer-based sensor. *Angew. Chem. Int. Edn.* 44, 5456–5459. doi: 10.1002/ange.200500989

Yang, G., Zhang, C. M., Hu, Q. F., and Yin, J. Y. (2003). Simultaneous determination of four heavy metal ions in tobacco and tobacco additive by online enrichment followed by RP-HPLC and microwave digestion. *J. Chromatogr. Sci.* 41, 195–199. doi: 10.1093/chromsci/41.4.195

Yoosaf, K., Ipe, B. I., Suresh, C. H., and Thomas, K. G. (2007). In situ synthesis of metal nanoparticles and selective naked-eye detection of lead ions from aqueous media. *J. Phys. Chem. C* 111, 12839–12847. doi: 10.1021/jp073923q

Zhan, S., Wu, Y., Liu, L., Xing, H., He, L., Zhan, X., et al. (2013). A simple fluorescent assay for lead(II) detection based on lead(II)-stabilized G-quadruplex formation. *Rsc Adv.* 3, 16962–16966. doi: 10.1039/C3RA42621A

Zheng, X., Yao, T., Zhu, Y., and Shi, S. (2015). Cu^{2+} modulated silver nanoclusters as an on-off-on fluorescence probe for the selective detection of L-histidine. *Biosens. Bioelectr.* 66, 103–108. doi: 10.1016/j.bios.2014.11.013

Zhou, R., Li, B., Wu, N., Gao, G., You, J., and Lan, J. (2011). Cyclen-functionalized perylenebisimides as sensitive and selective fluorescent sensors for Pb2+ in aqueous solution. *Chem. Commun.* 47, 6668–6670. doi: 10.1039/c1cc11200g

Conflict of Interest: The authors declare that the research was conducted in the absence of any commercial or financial relationships that could be construed as a potential conflict of interest.

frontiers in Chemistry

MINI REVIEW
published: 09 June 2020
doi: 10.3389/fchem.2020.00478

Recent Progress in Surface-Enhanced Raman Scattering for the Detection of Chemical Contaminants in Water

Gustavo Bodelón[1,2]* *and Isabel Pastoriza-Santos*[1,2]*

[1] CINBIO, University of Vigo, Vigo, Spain, [2] Galicia Sur Health Research Institute (IIS Galicia Sur) SERGAS-UVIGO, Vigo, Spain

OPEN ACCESS

Edited by:
Zoe Pikramenou,
University of Birmingham,
United Kingdom

Reviewed by:
Ruoxue Yan,
University of California, Riverside,
United States
Jia Hong Pan,
North China Electric Power
University, China
Pola Goldberg Oppenheimer,
University of Birmingham,
United Kingdom

***Correspondence:**
Gustavo Bodelón
gbodelon@uvigo.es
Isabel Pastoriza-Santos
pastoriza@uvigo.es

Specialty section:
This article was submitted to
Nanoscience,
a section of the journal
Frontiers in Chemistry

Received: 09 December 2019
Accepted: 08 May 2020
Published: 09 June 2020

Citation:
Bodelón G and Pastoriza-Santos I
(2020) Recent Progress in
Surface-Enhanced Raman Scattering
for the Detection of Chemical
Contaminants in Water.
Front. Chem. 8:478.
doi: 10.3389/fchem.2020.00478

Water is a matter of vital importance for all developed countries due to the strong impact on human health and aquatic, wetlands and terrestrial environments. Therefore, the monitoring of water quality is of tremendous importance. The enormous advantages that Surface-enhanced Raman scattering (SERS) spectroscopy offers, such as fingerprint recognition, multiplex capabilities, high sensitivity, and selectivity or non-destructive testing, make this analytical tool very attractive for this purpose. This minireview aims to provide a summary of current approaches for the implementation of SERS sensors in monitoring organic and inorganic pollutants in water. In addition, we briefly highlight current challenges and provide an outlook for the application of SERS in environmental monitoring.

Keywords: plasmonic nanostructures, SERS, sensing, chemical contaminants, water

INTRODUCTION

In recent years, water quality has become a critical concern of most developed countries due to the strong impact on human health and aquatic, wetlands, and terrestrial environments. The growth of human populations, the expansion of industrial and agricultural activities and climate change have been identified as the main threats to cause declining water quality. Therefore, actions for detection, identification, and quantification of pollutants and toxins in water are urgently required. Recently, different agencies such as the European Environment Agency (EEA) or Environmental Protection Agency (EPA, USA) have established legal obligations to protect and restore the quality of water. For instance, the Water Framework Directive (WFD) is the most substantial and ambitious piece of legislation dealing with the protection, monitoring, and management of water quality (European Commission, Introduction to the New EU Water Framework Directive, 2016). For WFD backed up by REACH regulation, which defines the chemical status by environmental quality standards of 41 priority substances.

Scientific findings show that major water pollutants are complex mixtures of chemicals of different categories (biocides, pharmaceuticals and industrial chemicals, pesticides, etc.). Analytical determination of these pollutants is typically carried out by sampling, extraction, and separation of the chemical compounds from the aqueous matrix by high-performance liquid chromatography or gas chromatography, coupled to selective detection methods such as modern mass spectrometry techniques. Generally speaking, these methods have high sensitivity, good specificity, and outstanding precision. However, all of them require complex equipment and laborious operations,

which may lead to inaccurate results because the water samples may undergo chemical and physical transformations. Also, there is an urgent requirement for sensitive detection methods which are simpler and portable for on-site analysis. Thus, the development of improved systems for environmental analysis has attracted a high interest in industry and the research community. Among them, surface-enhanced Raman scattering (SERS) has been extensively applied in various types of ultrasensitive chemical detection in a wide variety of fields (Langer et al., 2019). In SERS, the excitation of localized surface plasmon resonances supported by metal nanostructured leads to a massive intensification of the Raman scattering from molecules adsorbed or located in close proximity to the metallic surface (Schlücker, 2014). This effect has resulted in an ultrasensitive plasmon-enhanced spectroscopic technique, which retains the intrinsic structural specificity, as well as the experimental flexibility of Raman spectroscopy. Owing to continuous advances in nanofabrication techniques facilitating the engineering of rationally design plasmonic nanomaterials (Mosier-Boss, 2017; Hamon and Liz-Marzan, 2018; Langer et al., 2019), SERS is progressively expanding into the realm of viable detection of environmental pollutants, as it has been recently reviewed elsewhere (Jiang et al., 2018; Shi et al., 2018; Tang et al., 2018; Choi et al., 2019; Song et al., 2019).

This minireview intends to provide an overview of current approaches undertaken for the implementation of SERS sensors in monitoring organic and inorganic pollutants in water (**Supplementary Table 1**). Moreover, we aim to reveal the importance and potential of SERS technology for the ultradetection of pollutants in aqueous samples. Finally, a brief challenges and outlook section has been included. Nevertheless, it is out of the scope of this minireview the description of the theory behind SERS or the discussion of the different categories of SERS substrates or methodologies.

SERS DETECTION OF ORGANIC POLLUTANTS

Organic pollutants include many herbicides and insecticides from the agriculture sector, other molecules manufactured for use in various industries [phthalates, polychlorinated byphenyls (PCBs)], by-products of natural or artificial processes [such us, polycyclic aromatic hydrocarbons (PAH), dioxin, etc.], among others.

Direct SERS analysis in natural and contaminated waters is often impaired by the non-specific co-adsorption onto metallic nanostructures of other species in the matrix solution. This can significantly increase the complexity of the vibrational assignment or even completely prevent the interaction with the target analyte, thereby decreasing the sensitivity of the detection assay. In order to circumvent these issues, Marino-Lopez et al. (2019) developed a SERS substrate based on a microporous silica capsule with gold nanoparticles (NPs) in the interior (see **Figure 1A**). The microporous structure acts as molecular sieving avoiding large biomolecules and cells from reaching the plasmonic component while imparting colloidal stability. The applicability for environmental analysis was demonstrated using river water spiked with dichlorodiphenyltrichloroethane (DDT), a pesticide classified as a persistent organic pollutant and a probable human carcinogen. A limit of detection (LOD) of 1.77 μg/L was reached with this sensing platform. Wang et al. (2019) fabricated a ternary film-packaged bimetallic Au/Ag chip as a robust SERS sensor for the quantification of thiabendazole fungicide in drinking water. Interestingly, the plasmonic substrate was protected with polymer films as a proof-of-concept for developing more stable and wearable sensors for on-site monitoring. Detection of the pesticide thiram was achieved employing polydopamine spheres coated with a gold shell bearing gaps and voids (hotspots) (Chen et al., 2018). The nanowaxberry substrate (see **Figure 1B**) achieved a LOD of 2.4 μg/L in spiked environmental water (river water). As the concentration of chemical pollutants in environmental waters is typically in the ng/L to μg/L range (Neale et al., 2018), a pre-concentration step is often required prior to analysis. In this context, plasmonic substrates assembled on filter membranes offer new possibilities for preconcentration and simultaneous detection. Thus, composites of silver NPs and a liquid crystal (LC) polymer supported on polyamide filters has been recently fabricated by Fateixa et al. (2018b) for the extraction and detection of thiram spiked in river samples at 240.4 ng/L. The same group developed a filtering SERS sensor based on polyamide-based composites loaded with plasmonic nanoparticles by filtration (Fateixa et al., 2018a). This SERS-active flexible membrane trapped and concentrated chemical and water pollutants demonstrating detection of crystal violet dye spiked in estuary water samples up to 4.1 pg/L. This work is based on the filter SERS assay originally developed by Yu and White (2012) who reported the field-based application of such sensor for the quantitative detection of ppb concentrations of melamine, a food contaminant, as well as malathion, a widely used organophosphate pesticide, in water. The performance of this SERS assay was up to two orders of magnitude better than the conventional approach of drying a silver colloid onto a surface. In contrast to other solid supports, the three-dimensional structure of paper-based substrates allows both high specific surface and plasmon coupling, further enhancing the SERS signal. The different methods used to fabricate paper and cellulose-based SERS sensors have been recently reviewed elsewhere (Ogundare and van Zyl, 2019; Restaino and White, 2019).

The feasibility for the detection of antibiotics in environmental aquatic samples has been addressed in recent studies (Han et al., 2014; Hidi et al., 2016; Hong et al., 2017; Patze et al., 2017; Fang et al., 2019). Han et al. (2014) used SERS-active Ag nanorod arrays fabricated by oblique angle deposition to detect metronidazole and ronidazole in spiked samples from tap water, lake water, and swamp water. Despite both molecules could be readily detected at μg/mL concentrations regardless of the sample complexity, the LOD in terms of bulk concentrations does not meet mainstream analytical techniques such as liquid chromatography-mass spectrometry (LC-MS), with LODs as low as sub-mg/L. In another study, Ag arrays embedded in a microfluidic system were employed for the SERS detection of the antibiotic sulfamethoxazole down to 0.56 μg/L in spiked aquatic samples (Patze et al., 2017). The combination of a microfluidic setup with a top-down SERS substrate contributed

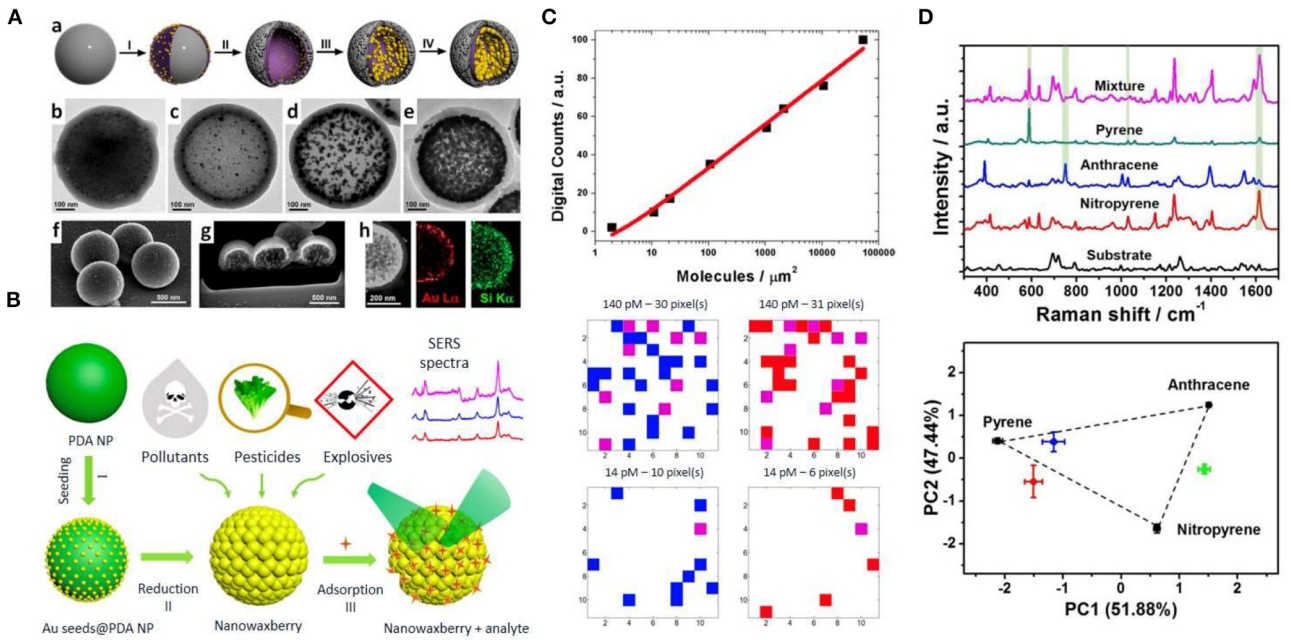

FIGURE 1 | Strategies for SERS detection of organic pollutants. **(A)** Microporous plasmonic capsules. (a) Schematic illustration of the capsules fabrication. (b–e) TEM characterization of the Au NPs growth within the capsules. (f–h) SEM characterization and elemental analysis (h) of the microporous plasmonic capsules. Reproduced from Marino-Lopez et al. (2019) with permission from John Wiley & Sons (Copyright 2019). **(B)** Schematic illustration of the synthesis of nanowaxberry (I-II), and analyte adsorption and SERS detection (III). Reproduced from Chen et al. (2018) with permission from American Chemical Society (Copyright 2018). **(C)** Digital calibration curve generated at ultralow concentration of enrofloxacin (upper panel) and SERS digital mappings obtained from mixtures of two isotopologues of ciprofloxacin. Reproduced from de Albuquerque et al. (2018) with permission from American Chemical Society (Copyright 2018). **(D)** SERS-based multiplex detection of PAHs using pillar[5]arene-based supramolecular plasmonic thin films: Characteristic SERS spectra of pyrene, anthracene, nitropyrene as well as of a mixture of the three PAHs (upper panel) and principal component analysis (PCA) score plot of the first three PCs modeled by the SERS spectra pyrene, anthracene, and nitropyrene (black dots) and their binary mixtures. Reproduced from Montes-Garcia et al. (2017) with permission from American Chemical Society (Copyright 2017).

to robust measurement conditions. Interestingly, the multiplex detection and quantification of the antibiotic enrofloxacin and its metabolite ciprofloxacin to mg/L-level in bi-analyte mixtures was demonstrated through the use of Ag nanogratings fabricated using laser interference lithography (Hong et al., 2017).

A big issue in pollutant analysis is the quantification at ultralow concentrations. Although single-molecule SERS (SM-SERS) is a potential tool for ultrasensitive detection, the strong signal fluctuations at ultralow concentration regimes often limit its expectations as a quantitative analytical technique. Recently, de Albuquerque et al. (2018) developed a procedure based on SM-SERS statistics for ultralow concentration quantification without the need for preconcentration. Thus, signals generated by SM-SERS events are "digitized" (i.e., digital SERS; Dos Santos et al., 2019) and the number of pixels within a given mapping area that provides a SM-SERS response (SERS digital count) could be correlated with the solution concentration (see **Figure 1C**). Finally, the total digital counts recorded for each concentration by SERS mapping were used to generate a calibration curve that enabled to detect enrofloxacin and ciprofloxacin with a low limit of quantification (LOQ) of 1.0 and 0.9 ng/L, respectively. Recently, an aptamer-based conformation cooperated enzyme-assisted SERS technology has been developed for sensitive and high selective detection of antibiotics in trace amounts (Fang et al., 2019). It is based on the enzymatic conversion of the antibiotic to a nucleic acid probe containing a Raman active molecule that is detectable by SERS with high sensitivity. It was demonstrated for chloramphenicol achieving a LOD of 4.8 pg/L in aqueous solution. Another interesting issue is the development of analytical recyclable tools for sensitive detection of environmental contaminants. A proof-of-principle study for recyclable SERS platforms for detection and degradation of the antibiotic tetracycline hydrochloride and the Rhodamine 6G dye was recently developed by Qu et al. (2019). Interestingly, the substrate (graphitic carbon on Ag nanorod arrays) shows self-cleaning abilities under visible light irradiation and could be further reused.

The detection efficiency of pollutants in environmental aquatic samples can be significantly improved employing non-wetting phenomena to concentrate analyte molecules within SERS-active regions (Lee et al., 2019). For instance, a superhydrophobic platform was used to concentrate Rhodamine 6G along with plasmonic nanoparticles within an evaporating liquid droplet, thus enabling to detect this environmentally hazardous dye down to 35.9 fg/L (Yang et al., 2016). With the aim of developing an effective approach for separating oil/water mixture, detecting, and degrading pollutants simultaneously, Xu et al. (2019) reported a superhydrophobic Au/AgCl-coated copper mesh which can separate and solely detect methylene blue (MB) molecules in Sudan III/MB oil/water mixture. After

separation, MB can be further photodegraded by the Au/AgCl-coated copper mesh, suggesting its potential application for wastewater treatment.

Owing to their tunable porous structure and excellent adsorption capacity, metal organic-frameworks (MOFs) have been explored as potential adsorbents for aqueous-phase sorptive removal of emerging environmental contaminants (Dhaka et al., 2019). MOFs have been combined with plasmonic nanostructures to create novel detection systems for the selective molecule diffusion at nanoparticle surfaces (Zheng et al., 2016). By tuning the pore size of plasmonic MOFs it is possible to effectively generate sieving effects, thereby reducing potential interferences arising from the biological matrices during SERS measurements. Recently, Au NPs embedded within MIL-101 demonstrated good sensing capabilities for the quantitative analysis of p-phenylenediamine in environmental water achieving a LOD of 0.10 ng/mL (Hu et al., 2014). Similarly, plasmonic MOF nanocomposites consisting of MOF-199, Uio-66, and Uio-67 with encapsulated gold NPs have been applied for the detection of acetamiprid pesticide with 4.4, 2.0, and 4.4 μg/L LODs, respectively (Cao et al., 2017). Interestingly, MOFs can also act as the host to capture targets through their unique porous structures. This ability was used to detect elusive target analytes lacking metal-affinity groups in water (Choi et al., 2019). In this framework, core-shell HKUST-1@AgNP composites demonstrated good sensing capabilities for polycyclic aromatic hydrocarbons (PAHs) in environmental samples, while preserving the cyclability and selectivity required for reliable quantitative analysis (Li et al., 2019). Remarkably, the performance of this plasmonic composite was compared with that of gas chromatography-mass spectrometry (GC-MS) showing similar detection capabilities, suggesting its potential for on-site detection of these pollutants. Focused on PAHs, host-guest approaches based on the use of pillar[5]arenes have been developed for their quantitative, label-free and multiplex SERS detection (Montes-Garcia et al., 2014, 2017). The AP[5]A exhibits excellent properties for pollutant adsorption from water, trapping non-polar molecules through hydrophobic and π-π interactions (Lan et al., 2017). Recyclable AP[5]A-based supramolecular plasmonic thin films enable the reliable quantification of pyrene, nitropyrene, and anthracene in water, as well as the simultaneous detection of the PAHs in a mixture employing chemometrics (see **Figure 1D**; Montes-Garcia et al., 2017) In a different approach, a substrate made of arrays of gold nanorods functionalized with diazonium salt quantified benzo[a]pyrene, fluoranthene, and naphthalene in water-methanol samples. PAHs were detected via SERS using Au NPs coated with polydopamine (PDA) (Du and Jing, 2019). Interestingly, PDA acted as a reactive scaffold for locking PAHs [phenanthrene, pyrene, benzo[b]fluoranthene, benzo[a]pyrene, and benzo[g,h,i]perylene] into the hotspots for SERS sensing, thereby reaching LOD ranging from 10 to 90 μg/L depending on the PAH (Tijunelyte et al., 2017). This study also showed the identification of the three analytes in the mixture. Recently, a molecularly imprinted polymer (MIP) thin film was combined with Au NP assemblies for SERS recognition of PAHs, such as pyrene or fluoranthene, in the sub μg/L regime (Castro-Grijalba et al., 2020). The role of MIP was to trap the PAH close to the Au surface. The detection of pyrene in creek water and seawater was demonstrated.

In another study, Tu et al. (2019) developed a SERS-based aptasensor for trace analysis of diethylhexylphthalate (DEHP) in tap water, bottled water, and a carbonated beverage employing magnetic particles functionalized with a DEHP aptamer The reported approach showed a detection range from 0.003 to 71 μg/L and a LOD of 3.1 ng/L. In this context, the use of magnetic nanoparticles for SERS detection of environmental pollutants has been recently reviewed (Pinheiro et al., 2018; Song et al., 2019).

SERS DETECTION OF INORGANIC POLLUTANTS

Toxic anions (e.g., nitrite, nitrate, perchlorate ions) and heavy metal (arsenic, mercury, lead, chromium, cadmium, and copper) cations are major environmental contaminants. With the aim to quantify trace amounts of such possible contaminants, environmental monitoring has generated a need for innovative and improved approaches with ever-increasing sensitivity and selectivity for the detection of these hazardous chemical species. In general, oxyanions, especially those with moderate Raman cross-sections (e.g., perchlorate) can be detected by their vibrational signatures. In contrast, direct SERS detection of monatomic metal ions is more challenged due to their small scattering cross-section (Tang et al., 2018).

Sensitive detection of perchlorate anions by SERS relies on the surface functionalization of the plasmonic material with positively charged reagents such as cystamine, 2-dimethyl-aminoethanethiol, or poly(ethyleneimine) (Hao and Meng, 2017; Jubb et al., 2017). Stewart et al. (2015) reported a colloidal detection approach for nitrate and perchlorate, as target analytes, based on formation of hotspots through NaCl induced aggregation of quaternary ammonium-terminated thiocholine stabilized silver colloids. In a recent study, SERS substrates based on gold ellipse dimers functionalized with 2-(dimethylamino)ethane-thiol were used to detect and quantify ClO_4^- contamination at the μg/L level within groundwaters, thereby demonstrating the applicability of this approach for field measurements (Jubb et al., 2017).

Arsenic species, including arsenate (As^{5+}) and arsenite (As^{3+}), which usually exist in the environment as AsO_4^{3-} or AsO_3^{3-}, respectively, can be directly detected by SERS based on the characteristic vibration of As–O stretch mode (Hao et al., 2015). However, since the Raman cross-sections of these inorganic oxyanions are not large and their affinity to metallic surfaces is remarkably low, most reported strategies for the detection of heavy metal cations or oxyanions usually follow indirect approaches. For instance, the surface of SERS substrates can be functionalized with a positively charged layer to enhance the affinity of the metal cation toward the plasmonic surface. In a different approach, the detection takes advantage of the affinity between the metal cation and a Raman active component of the plasmonic substrate. In this context, Wang et al. (2013) fabricated core-shell Ag@polyaniline nanocomposites as active

SERS nanoprobes for the detection of Hg^{2+} ions with a detection limit of 0.2 ng/L. The analysis of the intensity changes of the SERS signal from polyaniline at 1,560 cm^{-1} was shown to be strongly dependent on the concentrations of Hg^{2+}. Carbon nanotubes over a porous anodic alumina membrane were used for the trace detection of Hg^{2+}, Cd^{2+}, and Pb^{2+} (Shaban and Galaly, 2016). Du et al. (2013) fabricated a sensing system consisting of core-shell Au@Ag NPs and an organic ligand 4,4′-Dipyridyl (Dpy) for Hg^{2+} sensing. This molecule induced the aggregation of the NPs, generating strong Raman hotspots and SERS readouts. As Hg^{2+} shows a high affinity toward Dpy, it can inhibit the aggregation of Au@Ag NPs, thus quenching the SERS signal from Dpy. This colloidal-based approach demonstrated high sensitivity, detecting Hg^{2+} residues at the pg/L level, and specificity toward mercury, as it was not responsive to other metal ions tested. Kandjani reported a SERS-active thin film of ZnO/Ag nanoarrays for Hg^{2+} detection. In this study, the change in intensity of the characteristic Raman peak of Rhodamine B at 1,358 cm^{-1} was used for detection and quantification of the Hg^{2+} ions in solution. Additionally, the photocatalytic activity of the nanoarrays allowed the removal of mercury, and reusability of the substrate over many cycles (see **Figure 2A**; Esmaielzadeh Kandjani et al., 2015). This sensing device showed a limit of detection in the sub ppb range, and high selectivity toward Hg^{2+}. In another study, a crown ether derivative (TCE) was self-assembled onto the surface of a nanostructured gold substrate for Hg^{2+} sensing (Sarfo et al., 2017). The coordination of Hg^{2+} to the oxygen atoms of TCE could be monitored by SERS, thereby enabling the detection of mercury in tap water at toxic concentration of 3.35 μg/L using a handheld Raman spectrometer (see **Figure 2B**).

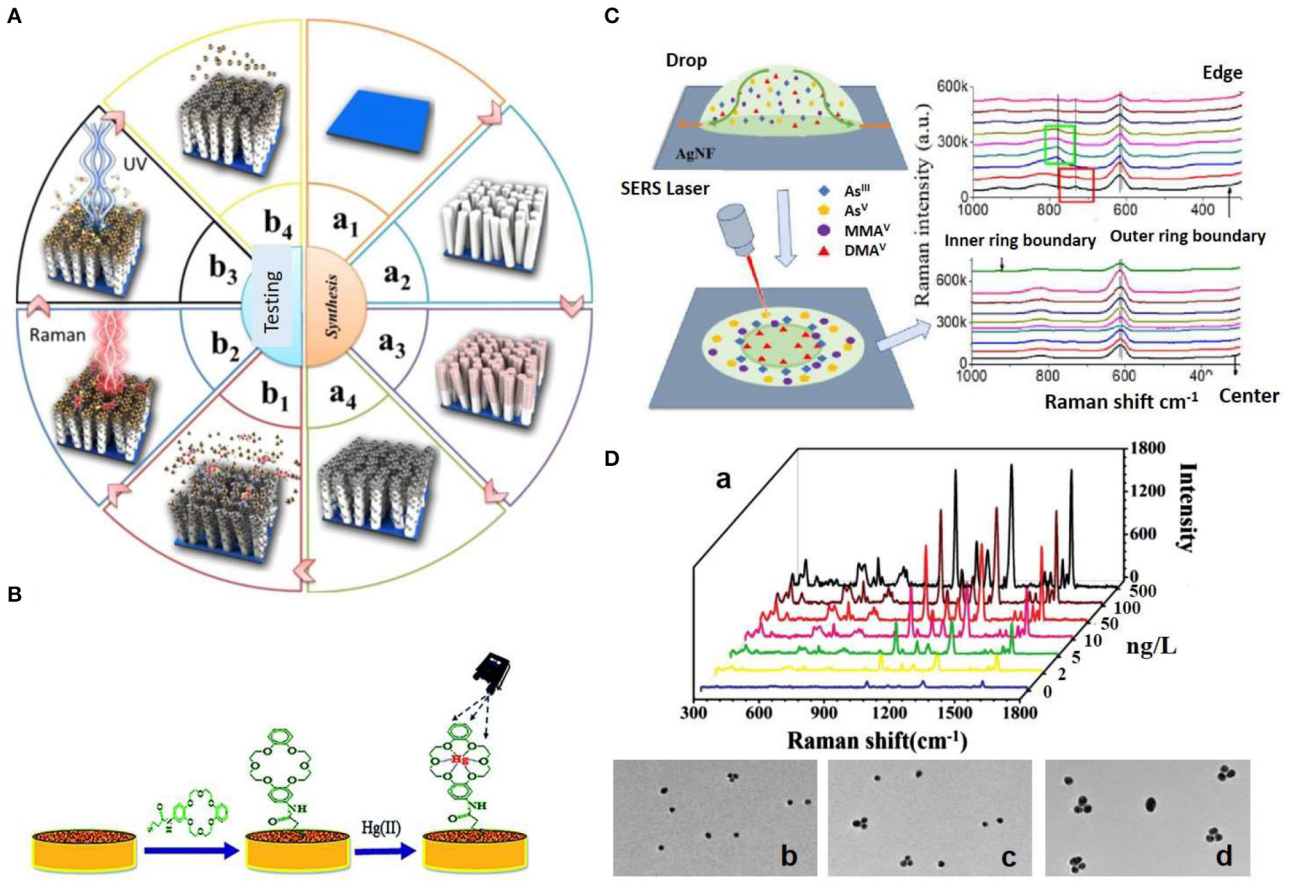

FIGURE 2 | Strategies for SERS detection of inorganic pollutants. **(A)** Schematic illustration of the fabrication of ZnO/Ag nanoarrays for the Hg^{2+} ions SERS detection. (a) The ZnO/Ag nanoarrays were fabricated by growing ZnO nanoarrays via soft hydrothermal method (a1, a2) and the subsequent deposition of Ag nanoparticles via an electroless plating technique (a3, a4). (b) Adsorption of Hg^{2+} ions and subsequent adsorption of Rhodamine B (RB) on the on ZnO/Ag nanoarrays (b1), Hg^{2+} ions detection via SERS monitoring of RB (b2), photocatalytic degradation of RB (b3), and Hg^{2+} removal via heat treatment (b4). Reproduced from Esmaielzadeh Kandjani et al. (2015) with permission from American Chemical Society (Copyright 2015). **(B)** Schematic representation of the modification of nanostructured Au substrate with a crown ether derivative for capturing Hg^{2+}. Reproduced from Sarfo et al. (2017) with permission from The Royal Society of Chemistry. **(C)** SERS method for arsenic speciation by using the separation potential of the coffee ring effect on negatively charged Ag nanofilms. Reproduced from Yang et al. (2019) with permission from American Chemical Society (Copyright 2019). **(D)** Triple Raman label-encoded Au NPs trimer for heavy metal ion detection. (a) SERS spectra under the same concentration of Hg^{2+} and Ag^{+} ranging from 0 to 500 ng/L. (b–d) TEM images of Au NP trimers assembled by the addition of equal concentration of Hg^{2+} and Ag^{+} at different concentrations: 5 (b), 50 (c), and 100 (d) ng/L. Reproduced from Li et al. (2015) with permission from John Wiley & Sons (Copyright 2015).

Accurate analysis of toxic metals and metalloids such as arsenic requires to maintain the integrity of the often labile chemical species, which is often impaired during sample preparation, separation, or detection. In this framework, Yang et al. reported a novel SERS method for arsenic speciation by combining the separation potential of the coffee ring effect on negatively charged silver nanofilms (AgNFs) for the detection of four common arsenic species, AsO_4^{3-}, AsO_3^{3-}, monomethylarsonic acid (MMA^V), and dimethylarsinic acid (DMA^V) (see **Figure 2C**; Yang et al., 2019). The combined interactions of arsenic species with the AgNFs, solvent, and sodium dodecyl sulfate surfactant, made possible arsenic speciation and SERS detection at 0.1 μg/L, demonstrating the potential of this approach for rapid separation and qualitatively SERS analysis. Toward quantitative analysis of Hg^{2+} speciation into methylmercury (CH_3Hg^+), Guerrini et al. (2014) fabricated a sensing platform consisting 4-mercaptopyridine (MPY) functionalized Au NPs anchored onto polystyrene microbeads. The co-ordination of Hg^{2+} and CH_3Hg^+ to the nitrogen atom of the MPY ring yields characteristic changes in the vibrational SERS spectrum of MPY that can be qualitatively and quantitatively correlated with the presence of the two different mercury species. Thus, in aqueous samples a limit of detection of 1.5 and 0.1 μg/L was achieved for CH_3Hg^+ and Hg^{2+}, respectively, when a concentration of beads in solution of 0.8 mg/mL was used.

Simultaneous detection and quantification of different inorganic pollutants is an important asset. Li et al., demonstrated a stable and reliable SERS method for multiplex detection of Hg^{2+} and Ag^+ using triple Raman-encoded Au NP trimers with LODs of 3.4 and 0.92 ng/L, respectively (see **Figure 2D**; Li et al., 2015) Thus, the presence of Hg^{2+} and/or Ag^+ induced the assembly of the Au NPs into trimers producing enhancements of the Raman reporters encoding the NPs. Recently, Cd^{2+} ions were detected by using Au NPs functionalized with dopamine quinone (DQ) (Du and Jing, 2019). The strong binding affinity of DQ toward Cd^{2+} facilitates the entrapment of the ions close to the Au surface, allowing its qualitative determination with a detection limit of 1.1 μg/L. Finally, SERS has also applied for the detection of fluorosurfactants in aqueous solution and in spiked groundwater (Fang et al., 2016).

CHALLENGES AND OUTLOOK

In this minireview we have summarized recent approaches for SERS detection of organic and inorganic chemical pollutants in aqueous media. As shown herein, a wide variety of strategies for detecting analytes have been adopted to potentially overcome the limitations in SERS sensing. SERS can enhance the sensitivity and selectivity of chemical detection, reducing the analytical time, sample consumption, as well as facilitating miniaturization and on-site analysis with portable Raman devices. All these rapid advances offer a bright future for SERS. Nevertheless, although great progress has been made, many challenges still remain for a realistic implementation of SERS in environmental analysis where analytes of diverse nature are to be detected: (i) optical and chemical properties of SERS platforms should be further optimized; (ii) the reproducibility in the synthesis of the SERS substrates in different batches and from different labs is still an issue; (iii) the lack of standardized protocols does not facilitate the comparison of electromagnetic enhancement factors between different laboratories; (iv) most of these new sensing tools are validated only in the lab with model analytes characterized by high Raman cross-section and not actual pollutants; (v) despite the delicate design and finely tuning of SERS substrates their performance in real samples is usually not as good as expected, mainly due to an insufficient consideration of environmental factors that can influence the measurements; (vi) it is also desirable to develop sensing approaches with reusability and recyclability capabilities to make them more cost-effective. Finally, many factors influence the SERS signal such as the strength of the local electromagnetic field, the nature of the analyte, its concentration, the chemical affinity to the nanoparticle surface, as well as the stability of the analyte-nanoparticle among others. Whereas, the interplay between these factors opens up a wide range of possibilities, the rational design of the plasmonic substrate for a specific application is often mandatory, thereby limiting the generalization of its use.

The broad interest in SERS together with the improved control over substrate fabrication, as well as the development of new related-instrumentation has resulted in the continuous development of advanced plasmonic platforms (e.g., chemosensors, chiral-selective systems, SHINERS, intragap core–shell particles), as well as emerging surface-enhanced signal amplification techniques (e.g., TERS, SEIRA, EC-SERS, SESORRS, etc.; Langer et al., 2019). These advancements offer immensely attractive approaches to potentially overcome the limitations in SERS sensing, which will eventually aid to bring this powerful technology out of the laboratory into real world applications. Thus, despite current challenges we envision that this spectroscopic technique will soon become a widespread analytical tool for routine monitoring of environmental waters and wastewater treatment plants in the near future.

AUTHOR CONTRIBUTIONS

GB and IP-S have contributed equally to the writing process of this minireview.

FUNDING

This work was supported by the Ministerio de Economía y Competitividad (MINECO, Spain, grant: MAT2016-77809-R) and Xunta de Galicia/FEDER (grant: GRC ED431C 2016-048).

ACKNOWLEDGMENTS

GB acknowledges CINBIO for his Científico Emerxente Fellowship.

SUPPLEMENTARY MATERIAL

The Supplementary Material for this article can be found online at: https://www.frontiersin.org/articles/10.3389/fchem.2020.00478/full#supplementary-material

REFERENCES

Cao, X., Hong, S., Jiang, Z., She, Y., Wang, S., Zhang, C., et al. (2017). SERS-active metal-organic frameworks with embedded gold nanoparticles. *Analyst* 142, 2640–2647. doi: 10.1039/C7AN00534B

Castro-Grijalba, A., Montes-García, V., Cordero-Ferradás, M. J., Coronado, E. A., Perez-Juste, J. and Pastoriza-Santos, I. (2020). SERS-based molecularly imprinted plasmonic sensor for highly sensitive PAH detection. *ACS Sens. 5,* 693–702. doi: 10.1021/acssensors.9b01882

Chen, D., Zhu, X., Huang, J., Wang, G., Zhao, Y., Chen, F., et al. (2018). Polydopamine@gold nanowaxberry enabling improved SERS sensing of pesticides, pollutants, and explosives in complex samples. *Analy. Chem.* 90, 9048–9054. doi: 10.1021/acs.analchem.8b01348

Choi, J., Kim, J. H., Oh, J. W., and Nam, J. M. (2019). Surface-enhanced Raman scattering-based detection of hazardous chemicals in various phases and matrices with plasmonic nanostructures. *Nanoscale* 11, 20379–20391. doi: 10.1039/C9NR07439B

de Albuquerque, C. D. L., Sobral-Filho, R. G., Poppi, R. J., and Brolo, A. G. (2018). Digital protocol for chemical analysis at ultralow concentrations by surface-enhanced Raman scattering. *Anal. Chem.* 90, 1248–1254. doi: 10.1021/acs.analchem.7b03968

Dhaka, S., Kumar, R., Deep, A., Kurade, M. B., Ji, S. W., Jeon, B. N. (2019). Metal-organic frameworks (MOFs) for the removal of emerging contaminants from aquatic environments. *Coord. Chem. Rev.* 380, 330–352. doi: 10.1016/j.ccr.2018.10.003

Dos Santos, D. P., Temperini, M. L. A., and Brolo, A. G. (2019). Intensity fluctuations in single-molecule surface-enhanced Raman scattering. *Acc. Chem. Res.* 52, 456–464. doi: 10.1021/acs.accounts.8b00563

Du, J., and Jing, C. (2019). One-step fabrication of dopamine-inspired Au for SERS sensing of Cd(2+) and polycyclic aromatic hydrocarbons. *Anal. Chim. Acta* 1062, 131–139. doi: 10.1016/j.aca.2019.02.033

Du, Y., Liu, R., Liu, B., Wang, S., Han, M. Y., and Zhang, Z. (2013). Surface-enhanced Raman scattering chip for femtomolar detection of mercuric ion (II) by ligand exchange. *Anal. Chem.* 85, 3160–3165. doi: 10.1021/ac303358w

Esmaielzadeh Kandjani, A., Sabri, Y. M., Mohammad-Taheri, M., Bansal, V., and Bhargava, S. K. (2015). Detect, remove and reuse: a new paradigm in sensing and removal of Hg (II) from wastewater via SERS-active ZnO/Ag nanoarrays. *Environ. Sci. Technol.* 49, 1578–1584. doi: 10.1021/es503527e

Fang, C., Megharaj, M., and Naidu, R. (2016). Surface-enhanced Raman scattering (SERS) detection of fluorosurfactants in firefighting foams. *Rsc Adv.* 6, 11140–11145. doi: 10.1039/C5RA26114G

Fang, Q., Li, Y., Miao, X., Zhang, Y., Yan, J., Yu, T., et al. (2019). Sensitive detection of antibiotics using aptamer conformation cooperated enzyme-assisted SERS technology. *Analyst* 144, 3649–3658. doi: 10.1039/C9AN00190E

Fateixa, S., Nogueira, H. I. S., and Trindade, T. (2018a). Surface-enhanced Raman Scattering Spectral imaging for the attomolar range detection of crystal violet in contaminated water. *Acs Omega* 3, 4331–4341. doi: 10.1021/acsomega.7b01983

Fateixa, S., Raposo, M., Nogueira, H. I. S., and Trindade, T. (2018b). A general strategy to prepare SERS active filter membranes for extraction and detection of pesticides in water. *Talanta* 182, 558–566. doi: 10.1016/j.talanta.2018.02.014

Guerrini, L., Rodriguez-Loureiro, I., Correa-Duarte, M. A., Lee, Y. H., Ling, X. Y., García de Abajo, F. J., et al. (2014). Chemical speciation of heavy metals by surface-enhanced Raman scattering spectroscopy: identification and quantification of inorganic- and methyl-mercury in water. *Nanoscale* 6, 8368–8375. doi: 10.1039/C4NR01464B

Hamon, C., and Liz-Marzan, L. M. (2018). Colloidal design of plasmonic sensors based on surface enhanced Raman scattering. *J. Colloid. Interface Sci.* 512, 834–843. doi: 10.1016/j.jcis.2017.10.117

Han, C., Chen, J., Wu, X., Huang, Y. W., and Zhao, Y. (2014). Detection of metronidazole and ronidazole from environmental Samples by surface enhanced Raman spectroscopy. *Talanta* 128, 293–298. doi: 10.1016/j.talanta.2014.04.083

Hao, J., Han, M. J., Han, S., Meng, X., Su, T. L., Wang, Q. K. (2015). SERS detection of arsenic in water: a review. *J. Environ. Sci.* 36, 152–162. doi: 10.1016/j.jes.2015.05.013

Hao, J. M., and Meng, X. G. (2017). Recent advances in SERS detection of perchlorate. *Front. Chem. Sci. Eng.* 11, 448–464. doi: 10.1007/s11705-017-1611-9

Hidi, I. J., Heidler, J., Weber, K., Cialla-May, D., and Popp, J. (2016). Ciprofloxacin: pH-dependent SERS signal and its detection in spiked river water using LoC-SERS. *Analy. Bioanaly. Chem.* 408, 8393–8401. doi: 10.1007/s00216-016-9957-2

Hong, K. Y., de Albuquerque, C. D. L., Poppi, R. J., and Brolo, A. G. (2017). Determination of aqueous antibiotic solutions using SERS nanogratings. *Anal. Chim. Acta* 982, 148–155. doi: 10.1016/j.aca.2017.05.025

Hu, Y., Liao, J., Wang, D., and Li, G. (2014). Fabrication of gold nanoparticle-embedded metal-organic framework for highly sensitive surface-enhanced Raman scattering detection. *Anal. Chem.* 86, 3955–3963. doi: 10.1021/ac5002355

Jiang, Y., Sun, D. W., Pu, H., and Wei, Q. (2018). Surface enhanced Raman spectroscopy (SERS): a novel reliable technique for rapid detection of common harmful chemical residues. *Trends Food Sci. Tech.* 75, 10–22. doi: 10.1016/j.tifs.2018.02.020

Jubb, A. M., Hatzinger, P. B., and Gu, B. (2017). Trace-level perchlorate analysis of impacted groundwater by elevated gold ellipse dimer nanoantenna surface-enhanced Raman scattering. *J. Raman Spectr.* 48, 518–524. doi: 10.1002/jrs.5070

Lan, S., Zhan, S., Ding, J., Ma, J., Ma, D. (2017). Pillar[n]arene-based porous polymers for rapid pollutant removal from water. *J. Mater. Chem. A* 5, 2514–2518. doi: 10.1039/C6TA09266G

Langer, J., Jimenez de Aberasturi, D., Aizpurua, J., Alvarez-Puebla, R. A., Auguie, B., Baumberg J. J., et al. (2019). Present and future of surface-enhanced Raman scattering. *ACS Nano*. 14, 28–117. doi: 10.1021/acsnano.9b04224

Lee, H. K., Lee, Y. H., Koh, C. S. L., Phan-Quang, G. C., Han, X., Lay, C. L., et al. (2019). Designing surface-enhanced Raman scattering (SERS) platforms beyond hotspot engineering: emerging opportunities in analyte manipulations and hybrid materials. *Chem. Soc. Rev.* 48, 731–756. doi: 10.1039/C7CS00786H

Li, D., Cao, X. K., Zhang, Q. M., Ren, X., Jiang, L., Li, D., et al. (2019). Facile in situ synthesis of core-shell MOF@Ag nanoparticle composites on screen-printed electrodes for ultrasensitive SERS detection of polycyclic aromatic hydrocarbons. *J. Mater. Chem. A* 7, 14108–14117. doi: 10.1039/C9TA03690C

Li, S., Xu, L., Ma, W., Kuang, H., Wang, L., and Xu, C. (2015). Triple raman label-encoded gold nanoparticle trimers for simultaneous heavy metal ion detection. *Small* 11, 3435–3439. doi: 10.1002/smll.201403356

Marino-Lopez, A., Sousa-Castillo, A., Blanco-Formoso, M., Furini, L. N., Rodriguez-Lorenzo, L., Pazos-Perez, N., et al. (2019). Microporous plasmonic capsules as stable molecular sieves for direct SERS quantification of small pollutants in natural waters. *Chemnanomat* 5, 46–50. doi: 10.1002/cnma.201800355

Montes-Garcia, V., Fernandez-Lopez, C., Gomez, B., Perez-Juste, I., Garcia-Rio, L., Liz-Marzan, L., et al. (2014). Pillar[5]arene-mediated synthesis of gold nanoparticles: size control and sensing capabilities. *Chemistry* 20, 8404–8409. doi: 10.1002/chem.201402073

Montes-Garcia, V., Gomez-Gonzalez, B., Martinez-Solis, D., Taboada, J. M., Jimenez-Otero, N., de Uña-Álvarez, J., et al. (2017). Pillar[5]arene-based supramolecular plasmonic thin films for label-free, quantitative and multiplex SERS detection. *ACS Appl. Mater. Interfaces* 9, 26372–26382. doi: 10.1021/acsami.7b08297

Mosier-Boss, P. A. (2017). Review of SERS substrates for chemical sensing. *Nanomaterials* 7:142. doi: 10.3390/nano7060142

Neale, P. A., Brack, W., Aït-Aïssa, S., Busch, W., Hollender, J., Krauss, M., et al. (2018). Solid-phase extraction as sample preparation of water samples for cell-based and other *in vitro* bioassays. *Environ. Sci. Process. Impacts* 20, 493–504. doi: 10.1039/C7EM00555E

Ogundare, S. A., and van Zyl, W. E. (2019). A review of cellulose-based substrates for SERS: fundamentals, design principles, applications. *Cellulose* 26, 6489–6528. doi: 10.1007/s10570-019-02580-0

Patze, S., Huebner, U., Liebold, F., Weber, K., Cialla-May, D., and Popp, J. (2017). SERS as an analytical tool in environmental science: the detection of sulfamethoxazole in the nanomolar range by applying a microfluidic cartridge setup. *Analy. Chim. Acta* 949, 1–7. doi: 10.1016/j.aca.2016.10.009

Pinheiro, P., Daniel-da-Silva, A. L., Nogueira, H. I. S., and Trindade, T. (2018). Functionalized inorganic nanoparticles for magnetic separation and SERS detection of water pollutants. *Eur. J. Inorganic Chem.* 30, 3443–3461. doi: 10.1002/ejic.201800132

Qu, L. L., Geng, Z. Q., Wang, W., Yang, K. C., Wang, W. P., Han, C. Q., et al. (2019). Recyclable three-dimensional Ag nanorod arrays decorated with

O-g-C3N4 for highly sensitive SERS sensing of organic pollutants. *J. Hazard Mater.* 379:120823. doi: 10.1016/j.jhazmat.2019.120823

Restaino, S. M., and White, I. M. (2019). A critical review of flexible and porous SERS sensors for analytical chemistry at the point-of-sample. *Analy. Chim. Acta* 1060, 17–29. doi: 10.1016/j.aca.2018.11.057

Sarfo, D. K., Sivanesan, A., Izake, E. L., and Ayoko, G. A. (2017). Rapid detection of mercury contamination in water by surface enhanced Raman spectroscopy. *Rsc Adv.* 7, 21567–21575. doi: 10.1039/C7RA02209C

Schlücker, S. (2014). Surface-enhanced Raman spectroscopy: concepts and chemical applications. *Angew Chem. Int. Ed. Engl.* 53, 4756–4795. doi: 10.1002/anie.201205748

Shaban, M., and Galaly, A. R. (2016). Highly sensitive and selective *in-situ* SERS detection of Pb(2+), Hg(2+), and Cd(2+) using nanoporous membrane functionalized with CNTs. *Sci. Rep.* 6:25307. doi: 10.1038/srep25307

Shi, R., Liu, X., and Ying, Y. (2018). Facing challenges in real-life application of surface-enhanced raman scattering: design and nanofabrication of surface-enhanced Raman scattering substrates for rapid field test of food contaminants. *J. Agric. Food Chem.* 66, 6525–6543. doi: 10.1021/acs.jafc.7b03075

Song, D., Yang, R., Long, F., and Zhu, A. (2019). Applications of magnetic nanoparticles in surface-enhanced Raman scattering (SERS) detection of environmental pollutants. *J. Environ. Sci.* 80, 14–34. doi: 10.1016/j.jes.2018.07.004

Stewart, A., Murray, S., and Bell, S. E. (2015). Simple preparation of positively charged silver nanoparticles for detection of anions by surface-enhanced Raman spectroscopy. *Analyst* 140, 2988–2994. doi: 10.1039/C4AN02305F

Tang, H., Zhu, C., Meng, G., and Wu, N. (2018). Review–surface-enhanced raman scattering sensors for food safety and environmental monitoring. *J. Electrochem. Soc.* 165, B3098–B3118. doi: 10.1149/2.0161808jes

Tijunelyte, I., Betelu, S., Moreau, J., Ignatiadis, I., Berho, C., Lidgi-Guigui, N., et al. (2017). Diazonium salt-based surface-enhanced Raman spectroscopy nanosensor: detection and quantitation of aromatic hydrocarbons in water samples. *Sensors* 17:E1198. doi: 10.3390/s17061198

Tu, D., Garza, J. T., and Coté, G. L. (2019). A SERS aptasensor for sensitive and selective detection of bis(2-ethylhexyl) phthalate. *RSC Adv.* 9, 2618–2625. doi: 10.1039/C8RA09230C

Wang, K., Sun, D. W., Pu, H., Wei, Q., and Huang, L. (2019). Stable, flexible, and high-performance SERS chip enabled by a ternary film-packaged plasmonic nanoparticle array. *ACS Appl. Mater. Interfaces* 11, 29177–29186. doi: 10.1021/acsami.9b09746

Wang, X. F., Shen, Y., Xie, A., Chen, S. (2013). One-step synthesis of Ag@PANI nanocomposites and their application to detection of mercury. *Mater. Chem. Phys.* 140, 487–492. doi: 10.1016/j.matchemphys.2013.03.058

Xu, C., Lu, W. Y., Li, M. M., Cao, Y., Pang, H., Cheng, G., et al. (2019). Trifunctional copper mesh for integrated oil/water separation, SERS detection, and pollutant degradation. *Adv. Mater. Interface* 6:1900836. doi: 10.1002/admi.201900836

Yang, M., Liamtsau, V., Fan, C., Sylvers, K. L., McGoron, A. J., Liu, G., et al. (2019). Arsenic speciation on silver nanofilms by surface-enhanced raman spectroscopy. *Anal. Chem.* 91, 8280–8288. doi: 10.1021/acs.analchem.9b00999

Yang, S., Dai, X., Stogin, B. B., and Wong, T. S. (2016). Ultrasensitive surface-enhanced Raman scattering detection in common fluids. *Proc. Natl. Acad. Sci. U.S.A.* 113, 268–273. doi: 10.1073/pnas.1518980113

Yu, W. W., and White, I. M. (2012). A simple filter-based approach to surface enhanced Raman spectroscopy for trace chemical detection. *Analyst* 137, 1168–1173. doi: 10.1039/c2an15947c

Zheng, G., de Marchi, S., López-Puente, V., Sentosun, K., Polavarapu, L., Pérez-Juste, I., et al. (2016). Encapsulation of single plasmonic nanoparticles within ZIF-8 and SERS analysis of the MOF flexibility. *Small* 12, 3935–3943. doi: 10.1002/smll.201600947

Conflict of Interest: The authors declare that the research was conducted in the absence of any commercial or financial relationships that could be construed as a potential conflict of interest.

frontiers in Chemistry

ORIGINAL RESEARCH
published: 19 August 2020
doi: 10.3389/fchem.2020.00620

Biosynthesized Silver Nanoparticles by Aqueous Stem Extract of *Entada spiralis* and Screening of Their Biomedical Activity

Wan Khaima Azira Wan Mat Khalir[1], *Kamyar Shameli*[1]*, *Seyed Davoud Jazayeri*[2]*, *Nor Azizi Othman*[1], *Nurfatehah Wahyuny Che Jusoh*[1] *and Norazian Mohd Hassan*[3]

[1] Department of Chemical and Environmental Engineering, Malaysia-Japan International Institute of Technology, Universiti Teknologi Malaysia, Kuala Lumpur, Malaysia, [2] Centre for Virus and Vaccine Research, School of Science and Technology, Sunway University, Subang Jaya, Malaysia, [3] Kulliyyah of Pharmacy, International Islamic University Malaysia, Kuantan, Malaysia

Silver nanoparticles (Ag-NPs) have been established as antibacterial nanoparticles and have been innovatively developed to overcome the occurrence of antibiotic resistance in the environment. In this study, an environmentally friendly and easy method of the biosynthesis of Ag-NPs plants, mediated by aqueous extract stem extract of *Entada spiralis* (*E. spiralis*), was successfully developed. The *E. spiralis*/Ag-NPs samples were characterized using spectroscopy and the microscopic technique of UV-visible (UV-vis), X-ray Diffraction (XRD), Field Emission Transmission Electron Microscope (FETEM), zeta potential, and Fourier Transform Infrared (FTIR) analyses. Surface Plasmon Resonance (SPR) absorption at 400–450 nm in the UV-vis spectra established the formation of *E. spiralis*/Ag-NPs. The crystalline structure of *E. spiralis*/Ag-NPs was displayed in the XRD analysis. The small size, around 18.49 ± 4.23 nm, and spherical shape of Ag-NPs with good distribution was observed in the FETEM image. The best physicochemical parameters on Ag-NPs biosynthesis using *E. spiralis* extract occurred at a moderate temperature (~52.0°C), 0.100 M of silver nitrate, 2.50 g of *E. spiralis* dosage and 600 min of stirring reaction time. The antibacterial activity was tested against *Staphylococcus aureus, Enterococcus faecalis*, *Escherichia coli*, and *Proteus vulgaris* using an antibacterial disk diffusion assay. Based on the results, it is evident that *E. spiralis*/Ag-NPs are susceptible to all the bacteria and has promising potential to be applied in both the industry and medical fields.

Keywords: silver nanoparticles, biosynthesis, *Entada spiralis*, antibacterial assay, physicochemical parameters

OPEN ACCESS

Edited by:
Cristina Satriano, University of Catania, Italy

Reviewed by:
Raghvendra Ashok Bohara, National University of Ireland Galway, Ireland
Alexandru Mihai Grumezescu, Politehnica University of Bucharest, Romania

***Correspondence:**
Kamyar Shameli
kamyarshameli@gmail.com
Seyed Davoud Jazayeri
sjazayeri@sunway.edu.my

Specialty section:
This article was submitted to Nanoscience, a section of the journal Frontiers in Chemistry

Received: *05 February 2020*
Accepted: *12 June 2020*
Published: *19 August 2020*

Citation:
Wan Mat Khalir WKA, Shameli K, Jazayeri SD, Othman NA, Che Jusoh NW and Hassan NM (2020) Biosynthesized Silver Nanoparticles by Aqueous Stem Extract of Entada spiralis and Screening of Their Biomedical Activity. Front. Chem. 8:620. doi: 10.3389/fchem.2020.00620

INTRODUCTION

The related applications based on nanotechnology, are in great demand nowadays due to the unique biological, electrical, and optical biological properties of metal nanoparticles. Properties such as antibacterial, antifungal, anticancer, antioxidant, wound healing ability, coloration, conductivity, UV blocking, photocatalytic, and self-cleaning activity provide the materials with different functions (Wang et al., 2017; Keshvadi et al., 2019). These nanoparticle properties are widely used in biomedical areas, health care, drug-gene delivery, wound healing, cosmetics, textiles, environmental pollutants, electrical appliances, non-linear optical devices, and photo-electro

chemicals. The nanotechnology design process involves controlling, measuring, and producing materials on a nano scale of ∼1–100 nm. The type of nanoparticles currently used for any application by industries are gold (Au), magnetite (Fe_3O_4), Titanium oxide (TnO_2), Zinc oxide (ZnO), and Copper oxide (CuO) (Nava et al., 2016; Reddy, 2017). Among these metal nanoparticles produced today, silver (Ag) is one of the most popular and valued metals—especially in consumer products and in the medical field (Shameli et al., 2012; Khatoon et al., 2017).

Ag-NPs have antibacterial properties and are well-known to be an effective disinfectant against a wide range of microorganisms and can also treat bacterial infections through a longer time of exposure due to its good stability (Li et al., 2016). Almost 650 microorganisms including Gram-positive bacteria and Gram-negative bacteria, fungi, and viruses are shown to have antimicrobial activity against Ag-NPs (Ahmed et al., 2016). This positive result makes Ag-NPs a potential material to be applied in many applications such as in the medical field, packaging material, environmental pollution, textile industries, fabric, coating of biomaterials, tissue engineering, cancer diagnosis and treatments where antibacterial agents are crucially needed (Nassar and Youssef, 2012; Chouhan et al., 2017; Narasaiah et al., 2018). The exact mechanisms by which Ag-NPs kill bacteria remain a challenge for most researchers. However, predictions by some researchers on possible mechanisms, could be due to the contact action, the release of Ag^+ ions and generation of reactive oxygen species (Wu et al., 2018). Most of the listed applications of Ag-NPs deal with human contact. Therefore, it is compulsory to develop an environmentally friendly synthesis method which eliminates or minimizes the use of toxic chemicals that can affect human health and the environment. The bottom-up methods that use biosynthesis mediated from plant extract are considered to be an environmentally friendly method. This method has caught the attention of researchers due to its ease, biodegradability, biocompatibility, natural abundance, good nanoparticle distribution, small sized nanoparticles, stability in colloidal forms, its low cost, mild reaction, and also, its minimal use of hazardous materials during the synthesis process (Mittal et al., 2013).

The morphology, stability, particle size distribution, and surface charge of metal nanoparticles play a very significant role in the controlled synthesis of Ag-NPs using plant extract as a reductant and stabilizing agent (Rajakumar et al., 2017). These can be controlled by varying the physicochemical parameters such as the initial concentration of silver nitrate, stirring time, and plant dosage (Dwivedi and Gopal, 2010; Polte, 2015; Wu et al., 2018). Besides that, the antibacterial activity performance also depends on the size of Ag-NPs and the gram character of the bacteria. Nowadays, the susceptibility of Ag-NPs toward Gram-positive and Gram-negative bacteria continues to be debated in this research area. A study by Ravichandran et al. (2016) reported that the average size of Ag-NPs obtained is 38 nm using an extract concentration of 1.5 mL of 10% *Artocarpus altilis* leaf extract, 1.0 mM of silver nitrate, reaction time of 60 min, pH 7, and a temperature of 70°C. The prepared Ag-NPs showed that *Escherichia coli* and *Pseudomonas aeruginosa* are more susceptible to Ag-NPs than *Staphylococcus aureus*. In another study, Yan-yu et al. (2016) conducted the biosynthesis of Ag-NPs using *Ginkgo biloba* leaf extract, the reduction of Ag^+ ions to Ag^0 was influenced by changing the silver nitrate concentration. A well-dispersed Ag-NP colloid was obtained at a lower silver nitrate concentration (0.02 M) of pH = 8. The average size of Ag-NPs measured using TEM is between 10 and 16 nm. The Ag-NPs prepared have strong antibacterial activity against both *Staphylococcus aureus* and *Escherichia coli* bacteria. The optimum conditions to prepare Ag-NPs using *Tinospora cordifolia* leaf extract studied by Selvam et al. (2017) occurred at 1.25 M of silver nitrate, 15 h of incubation time, 45°C of temperature and pH 4.5. The size of Ag-NPs determined using Scherrer's equation is 30 nm. The Ag-NPs are susceptible to *Klebsiella* and *Staphylococcus* bacteria species, showing a maximum zone of inhibition of 12.3 and 13.0 mm, respectively, at 10 mg/L of Ag-NPs.

In this study, a comparative study of the effect of physicochemical parameters to synthesis the Ag-NPs using aqueous extract stem extract of *E. spiralis* was performed, with the aim to find the superior parameter conditions for the biosynthesis of Ag-NPs with good properties of Ag-NPs. The effects of different physicochemical parameters studied include the initial concentration of silver nitrate, *E. spiralis* dosage, and stirring reaction time. The properties of Ag-NPs produced by aqueous extract stem extract of *E. spiralis* biosynthesis were characterized using UV-visible, XRD, FETEM, SEM, EDX, zeta potential, and FTIR techniques. The antibacterial activity of Ag-NPs performance was studied based on an antibacterial disk diffusion assay, in order to find the potential for both industrial and medical applications. Four bacteria from Gram-positive and Gram-negative bacteria including *Staphylococcus aureus* (ATCC 29523), *Enterococcus faecalis* (ATCC 29212), *Escherichia coli* (ATCC 25922), and *Proteus vulgaris* (ATCC 33420) were selected in this study.

MATERIALS AND METHODS

Materials

The *E. spiralis* stem was collected from the forest in Tasik Chini, Pahang, Malaysia before being chopped and grounded to obtain *E. spiralis* stem powder. The silver nitrate was purchased from Acros organic, USA and was used without any purification. The deionized water from the ELGA Lab-Water/VWS (UK) purification system was used throughout the experiment. Four species of bacteria, including two Gram-positive species *Staphylococcus aureus* (*S. aureus*) (ATCC 25923) and *Enterococcus faecalis* (*E. faecalis*) (ATCC 29212) as well as two Gram-negative species *Escherichia coli* (*E. coli*) (ATCC 25922) and *Proteus vulgaris* (*P. vulgaris*) (ATCC 33420) were bought from Choice Care Sdn. Bhd, Kuala Lumpur, Malaysia. The stock culture was prepared in the Mueller Hinton broth (Difco, Malaysia) and incubated at 37°C overnight. For further usage, the stock culture was kept in the refrigerator at a temperature of 4–8°C.

Preparation of *E. spiralis* Stem Aqueous Extraction

The aqueous extraction of the *E. spiralis* stem powder was done using the hot percolation method. A ratio of 1.5 g: 150 mL between *E. spiralis* dosage and deionized water was used. The mixture was stirred using a magnetic stirrer for 30 min. The temperature was then set at ∼55°C for this extraction process. After stirring, the mixture was filtered and cooled before being used to synthesize Ag-NPs. The aqueous extract stem extract of *E. spiralis* is abbreviated as *E. spiralis* extract hereafter.

Biosynthesis of *E. spiralis*/Ag-NPs

In general, 15 mL of silver nitrate ($AgNO_3$) solution and 150 mL of *E. spiralis* extract was added in an Erlenmeyer flask. The mixture was stirred at 400 rpm using a magnetic stirrer at a temperature of ∼52°C. The aluminum foil was used to cover the flask used during the Ag-NPs biosynthesis process because of the light-sensitivity of Ag-NPs. The reduction of Ag^+ ions to Ag° (Ag-NPs) was observed preliminarily, based on its color when it changed to brown. The *E. spiralis*/Ag-NPs formation was then established using an UV-visible spectroscopy analysis. The effects of physicochemical parameters such as the initial concentration of $AgNO_3$, *E. spiralis* dosage, and stirring reaction time, which have a significant impact on the shape, size, and distribution of *E. spiralis*/Ag-NPs, were studied. All the Ag-NPs biosynthesis experiments were conducted in batch mode and duplicated. In the end, the average results were reported as explained in the details methods below.

Effect of Initial $AgNO_3$ Concentrations

For the effect of initial concentrations of $AgNO_3$, four different concentrations of $AgNO_3$ were chosen (0.005, 0.050, 0.010, and 0.100 M). A mixture of 0.005 M $AgNO_3$ (15 mL) and *E. spiralis* extract (1.5 g: 150 mL) was added in an Erlenmeyer flask and stirred at 400 rpm using a magnetic stirrer at ∼52°C. During the Ag-NPs synthesis process, 10 mL of *E. spiralis*/Ag-NO_3 solution was taken using a pipette after 15, 30, 60, 90, 120, 180, 240, 360, 480, and 600 min. All of the solutions were then put in a vial sample and kept at 4°C for further characterization studies. The aluminum foil was used to cover the flask used during the Ag-NPs biosynthesis process because of the light-sensitivity of Ag-NPs. The reduction of Ag^+ ions to Ag^0 was then analyzed using an UV-visible spectrophotometer (UV-vis 1800, Shimadzu). The color changes of the solution, after the formation of Ag-NPs, were also observed. The same procedure was then repeated for the initial $AgNO_3$ concentration at 0.050, 0.010, and 0.100 M.

Effect of *E. spiralis* Dosage

Regarding the effect of *E. spiralis* dosage, three different *E. spiralis* dosages were studied (0.5, 1.5, and 2.5 g). A volume of 15 mL $AgNO_3$ (best concentration) and 150 mL of *E. spiralis* extract (0.5 g) was added in an Erlenmeyer flask. The mixture was stirred using a magnetic stirrer at 400 rpm and a temperature of ∼52°C. During the Ag-NPs synthesis process, 10 mL of *E. spiralis*/Ag-NO_3 solution was taken, using a pipette, after 15, 30, 60, 90, 120, 180, 240, 360, 480, and 600 min. All of the solutions were then put in a vial sample and kept at 4°C for further characterization studies. The aluminum foil was used to cover the flask used during the Ag-NPs biosynthesis process because of the light-sensitivity of Ag-NPs. The reduction of Ag^+ ions to Ag^0 was then analyzed using an UV-visible spectrophotometer. The color changes of the solution, after producing Ag-NPs, were also observed. The same procedure was then repeated to study the biosynthesis of Ag-NPs at an *E. spiralis* stem powder dosage of 1.5 and 2.5 g.

Effect of Stirring Reaction Time

The study of the effect of reaction time after 600 min was extended to 720, 840, and 1,440 min. A volume of 15 mL $AgNO_3$ (best concentration) and 150 mL of *E. spiralis* extract (best *E. spiralis* dosage) was added in an Erlenmeyer flask. The mixture was stirred using a magnetic stirrer at 400 rpm and a temperature of ∼52°C. During the Ag-NPs synthesis process, 10 mL of *E. spiralis*/Ag-NO3 solution was taken, using a pipette, after 15, 30, 60, 90, 120, 180, 240, 360, 480, 600, 720, 840, and 1,440 min. All of the solutions were then put in a vial sample and kept at 4°C for further characterization studies. The aluminum foil was used to cover the flask used during the Ag-NPs biosynthesis process because of the light-sensitivity of Ag-NPs. The reduction of Ag^+ ions to Ag^0 was then analyzed using an UV-visible spectrophotometer. The color changes of the solution, after producing *E. spiralis*/Ag-NPs, were also observed.

Characterization of *E. spiralis*/Ag-NPs

The synthesis of Ag-NPs was evaluated using an UV-vis spectroscopy analysis. This important characterization can produce crucial information on the shape, size, and distribution of Ag-NPs. The Ag-NPs solution was scanned from 300 to 700 nm with a UV-vis spectrophotometer at a medium rate. The crystalline structures of *E. spiralis*/Ag-NPs were determined using the X-ray diffractometer (XRD) (PANalytical X'pert PRO, Netherland) at 45 kV and a current of 30 mA with Cu-Kα radiation. The XRD pattern was initiated to scan from 10 to 90° at a 2θ angle. Only a selected sample was chosen for the XRD analysis of this study. The XRD sample of *E. spiralis*/Ag-NPs was ready with dried *E. spiralis*/Ag-NPs solution on the glass surface. The size and distribution of *E. spiralis*/Ag-NPs were investigated using the Field Emission Transmission Electron Microscope (FETEM) (JEOL, JEM-2100F, Japan). The stability of *E. spiralis/Ag-NPs* was determined using a zeta size analyzer (SZ-100, Horiba Scientific, Japan). The plausible mechanisms between Ag-NPs and the functional groups present in the *E. spiralis* extract, were predicted using the Fourier Transform Infrared (FTIR) spectrometer (Perkin Elmer, Frontier, USA) using the potassium bromide (KBr) pellet technique. The sample was scanned from the 4,000 to 400 cm^{-1} wavenumber.

Antibacterial Disk Diffusion Assay

The antibacterial disk diffusion assay on antibacterial activity of *E. spiralis*/Ag-NPs was evaluated using the Kirby-Bauer technique (Bauer et al., 1966), which conformed to the recommended standards of the Clinical and Laboratory Standards Institute (CLSI). Two Gram-positive bacteria (*Staphylococcus aureus* ATCC 25922 and *Enterococcus faecalis*

ATCC 29212) and two Gram-negative bacteria (*Escherichia coli* ATCC 25923 and *Proteus vulgaris* ATCC 33420) were used in this study. Gentamicin (10 μg/mL), plain disk and *E. spiralis* extract were used as positive and negative controls, respectively. The agar plate was prepared by pouring 20 mL of liquid Mueller Hinton agar (MHA) onto disposable sterilized petri dishes. The liquid MHA were allowed to solidify before being stored in the refrigerator at 4°C for further use. The bacteria suspension was prepared by subculturing 100 μL of stock culture bacteria into new Mueller Hinton broth (MHB). The bacteria suspension was incubated overnight at 37°C in the incubator. After incubation, the optical density OD_{600} of the bacterial suspension was adjusted to 0.1 absorbance, using UV spectrophotometer. This OD value corresponds to 1.5×10^6 CFU/mL. The inoculum was then spread evenly over the MHA plate using a sterile cotton bud before applying the *E. spiralis*/Ag-NPs loaded disks. The experiment was carried out in triplicate and the diameter of the inhibition zone was measured after 24 h of incubation at 37°C. The results were recorded as the mean ± standard deviation of the triplicate experiment. All the data of antibacterial analysis were represented as the mean ± standard deviation of triplicate experiments. Sample *t*-test and one-way ANOVA was used to compare the statistical difference between two groups. The statistical data analysis was analyzed using SPSS version 22. A $p < 0.05$ was considered significant.

RESULTS

A preliminary tool was used to confirm the ability of *E. spiralis* extract to biosynthesize Ag-NPs, by observing the appearance of the signatory brown color of the solution. The reduction of Ag^+ ions to Ag^0 after being mixed with *E. spiralis* extract changed the color to dark brown. This color change confirmed the formation of Ag-NPs. In the *E. spiralis* extract, it contains the phytochemical compounds of terpenoid saponin and glycoside (Harun et al., 2015, 2016). Both phytochemical compounds are able to act as a reducing agent due to the presence of carboxyl and hydroxyl groups. According to Joy Prabu and Johnson (2015), these functional groups can reduce Ag^+ ions to Ag^0 by donating electron and hydrogen atoms that are then stabilized by the anionic functional groups in the *E. spiralis* extract. The schematic illustration of the suggested mechanisms of saponin compound presence in *E. spiralis* extract as a reducing and stabilizing agent to synthesize Ag-NPs is shown in **Figure 1**. In **Figure 1**, step (1) shows the hydroxyl groups (-OH) in the saponin compound were

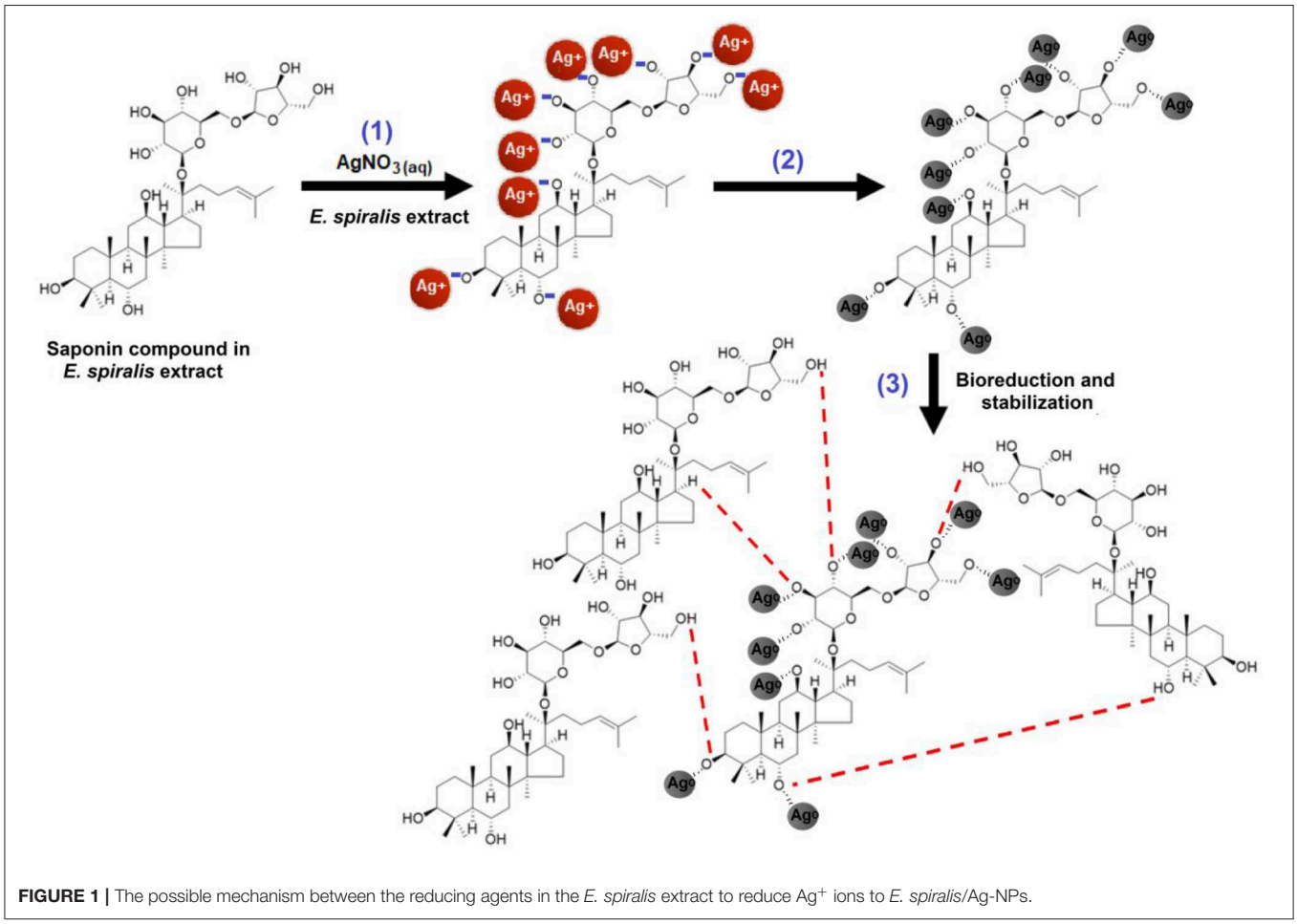

FIGURE 1 | The possible mechanism between the reducing agents in the *E. spiralis* extract to reduce Ag^+ ions to *E. spiralis*/Ag-NPs.

ionized to negatively charge $-O^-$ groups in the aqueous medium, while $AgNO_3$ was dissociated into Ag^+ ions. The negatively charged O^- groups can attract electrostatically with the positively charged Ag^+ ions. Step (2) shows that the reduction of Ag^+ ions to Ag^0 occurred by donating an electron and a hydrogen atom from the hydroxyl groups of the saponin compound which was then stabilized by the negatively charged functional groups in the saponin compound. Step (3) shows that the stabilization process then occurred due to the presence of van der Walls forces between the oxygen and negatively charged functional groups that surround the surface of Ag-NPs. This stabilization process controls the smaller size Ag-NPs in the synthesis process. This process is in agreement with Aramwit et al. (2014), who suggested that the hydroxyl groups are supposed to prevent their aggregation of Ag-NPs.

The solution also changed to a brown color after the reaction of Ag^+ ions with *E. spiralis* extract at different initial concentrations of $AgNO_3$ (0.005–0.100 M), *E. spiralis* dosage (0.5–2.5 g), and stirring reaction times (600–1,440 min) are shown in **Figure 2**. The figures show that the intensity of the brown color formation after the reaction with $AgNO_3$ and *E. spiralis* extract was increased with the increase of the initial concentrations of $AgNO_3$ from 0.005 to 0.100 M $AgNO_3$ (**Figures 2A–D**), respectively. The same color changes observation was seen for the effect of *E. spiralis* stem powder dosage and stirring reaction times. It showed that the intensity of the brown color increased with the increase of the *E. spiralis* stem powder dosage from 0.5 to 2.5 g and the reaction times from 600 to 1,440 min as shown in **Figures 2E–H**, respectively. The different brown colors observed at all parameters is due to the excitation of the surface Plasmon resonance of Ag-NPs at different properties of Ag-NPs. The details of the studies will be reported in the UV-vis spectroscopy analysis. The same dark brown color changes, than the ability of Ag-NPs formation using *Cinnamomum tsoi* aqueous leaf extract, was reported by Maddinedi et al. (2017).

UV-vis Spectroscopy Analysis

The UV-vis spectra can provide valuable information on the shape, size, and distribution of nanoparticles based on Surface Plasmon Resonance (SPR) bands. For instance, the appearance of the Ag peak at a shorter wavelength in the UV-vis spectra reveals the small size of Ag-NPs that were formed, while a longer wavelength indicates bigger Ag-NPs (Mashwani et al., 2016). These SPR bands arise from the interactions between the electron cloud on the Ag-NPs surface and the incoming electromagnetic radiation (Labulo et al., 2016). SPR bands centered between 420 and 430 nm of UV–vis absorption spectra correspond to the peak of Ag. The estimated size of Ag-NPs at these SPR bands range from 10 to 30 nm with a spherical shape (Sowmyya and Lakshmi, 2018).

The plant mediated synthesis of Ag-NPs using *E. spiralis* extract, as a reducing and stabilizing agent, was monitored by applying different initial concentrations of $AgNO_3$, *E. spiralis* stem powder dosage, and stirring reaction times. From these results, the best parameter to synthesize Ag-NPs was chosen for further studies and characterization. The UV-vis spectra of *E. spiralis*/Ag-NPs at different initial concentrations of $AgNO_3$ from 0.005 to 0.100 M and different stirring reaction times are shown in **Figures 2A–D**, respectively. From the results, it was found that the intensity of *E. spiralis*/Ag-NPs increases with increasing initial concentrations of Ag-NPs and reaction times. The initial concentration of $AgNO_3$ should be more than 0.005 M to synthesize Ag-NPs using *E. spiralis* extract. A concentration of Ag^+ ions below 0.005 M, will not be enough to reduce Ag° using *E. spiralis* extract as the reducing and stabilizing agent (Morales-Luckie et al., 2016). At 0.005 M $AgNO_3$, no silver peaks appeared between 400 and 430 nm as shown in **Figure 2A**. The wavelength bands at 600 min of stirring reaction time were shifted to the larger wavelength (red shift) from 418 to 433 nm at 0.010 to 0.100 M $AgNO_3$, respectively, as shown in **Figures 2B–D**. The intensity (absorbance) of *E. spiralis*/Ag-NPs increased from 0.745 to 2.020, respectively. According to Kumar et al. (2018), the larger wavelength of UV-vis indicates that a big sized nanoparticle was formed. The big size of the nanoparticles that was obtained when increasing the initial concentrations of $AgNO_3$ might be due to the number of Ag-NPs being increased and which tend to aggregate each other. The increasing size of *E. spiralis*/Ag-NPs, based on the increase in the initial concentrations of $AgNO_3$, was confirmed using the FETEM analysis. In this study, 0.100 M of $AgNO_3$ at 600 min of reaction time was chosen as the best parameter for further study, considering the highest intensity and more sharpened peaks recorded at this concentration.

The results for the effect of *E. spiralis* dosage from 0.5 to 2.5 g at different stirring reaction times are shown in **Figures 2E,F**. In these figures, the wavelength bands at 600 min were shifted to a short wavelength (blue shift) when increasing the *E. spiralis* dosage from 435 to 433 nm at 0.5 to 2.5 g, respectively. This trend provides information on the smaller size of *E. spiralis*/Ag-NPs that have been formed. The decreased size of *E. spiralis*/Ag-NPs when increasing the *E. spiralis* dosage might be due to the increase of biomolecules (functional groups) that are present in the *E. spiralis* extract, which is able to stabilize the *E. spiralis*/Ag-NPs. The deceasing size of *E. spiralis*/Ag-NPs when increasing the *E. spiralis* dosage was supported by the FETEM analysis. The absorbance intensity of *E. spiralis*/Ag-NPs also increased from 1.005 to 2.703 when increasing the *E. spiralis* dosage. It has been predicted that the number of nanoparticles was increased (Labulo et al., 2016). Therefore, the best *E. spiralis* dosage of 2.5 g at 600 min of reaction time was chosen for further study and characterization.

The subsequent experiment was conducted using a constant value of 0.100 M $AgNO_3$ and 2.5 g of *E. spiralis* stem powder dosage but the reaction times were increased at 720, 840, and 1,440 min. This experiment was conducted to ensure the best reaction time occurred at 600 min and the result is shown in **Figure 2H**. From the result, it shows that at 720 min, the UV-vis spectrum starts to become noise peaks, suggesting that the agglomeration of *E. spiralis*/Ag-NPs start to occur due to the big size of *E. spiralis*/Ag-NPs that has been formed. The wavelengths are moved to the red-shift (larger wavelength) indicating that the size of *E. spiralis*/Ag-NPs was increased when increasing the stirring reaction time. The peak intensity also increased with

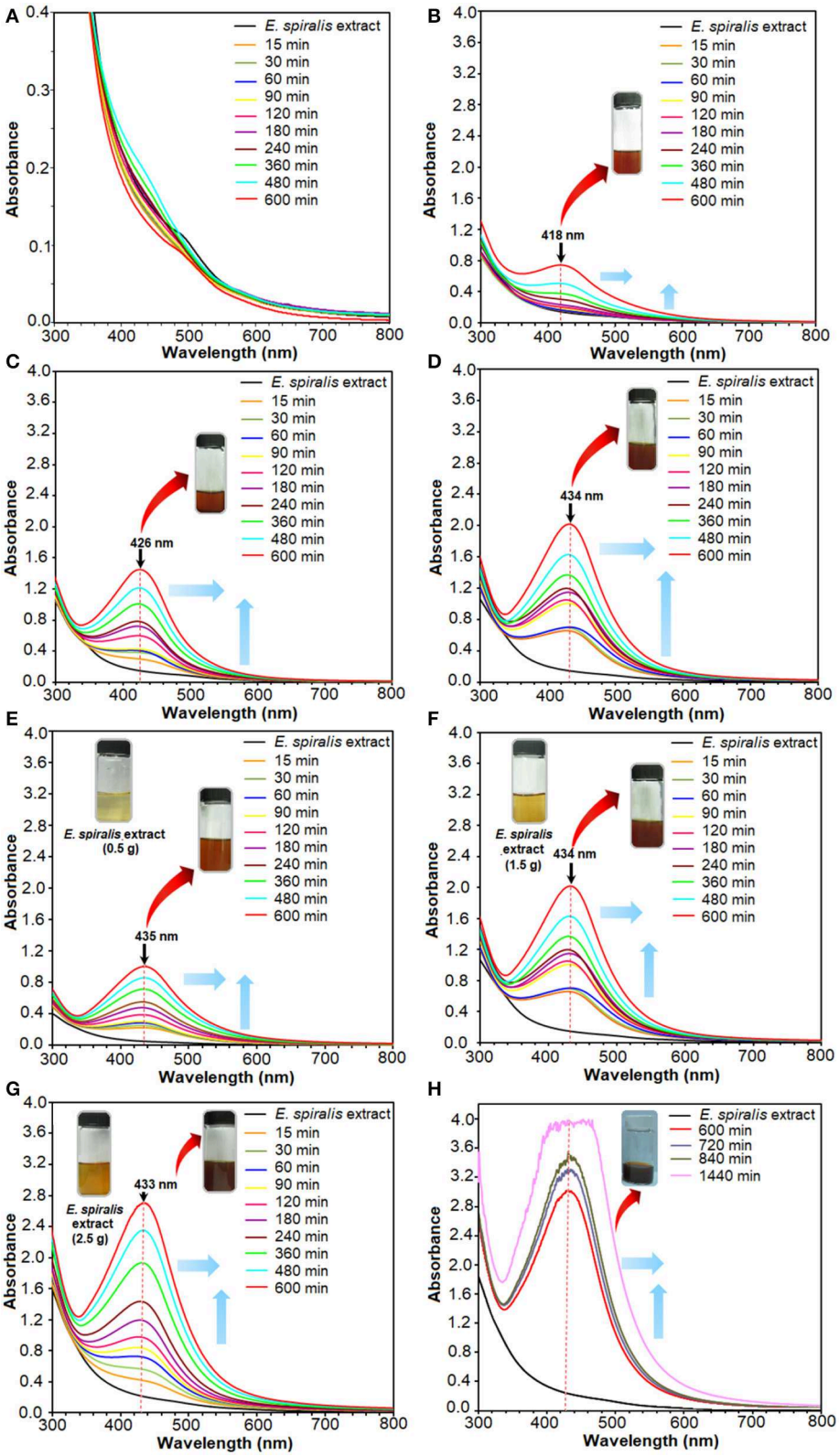

FIGURE 2 | The UV-vis spectra of *E. spiralis*/Ag-NPs after the reaction at different initial concentrations of 0.005, 0.010, 0.050, and 0.100 M $AgNO_3$ **(A–D)**, *E. spiralis* dosage of 0.5, 1.5, and 2.5 g **(E–G)**, and stirring reaction times **(H)**.

reaction time. These indicated an increase in the amount of Ag-NPs and a decrease in the number of Ag^+ ions in the solution (Zhang et al., 2017). Therefore, the reaction time at 600 min was chosen as the reaction time to synthesize *E. spiralis*/Ag-NPs. The bigger size of Ag-NPs might reduce the performance of Ag-NPs for medical application.

XRD Analysis

The crystallinity of Ag-NPs formed after synthesis, using *E. spiralis* extract, can be confirmed based on the XRD pattern. In this study, the sample of *E. spiralis*/Ag-NPs was determined only at the best physicochemical conditions (0.100 M $AgNO_3$; 2.5 g *E. spiralis* stem powder dosage and 600 min of stirring reaction time). The XRD peaks of *E. spiralis* extract show only amorphous peaks at 24.82° with no silver peaks appearing, as shown in **Figure 3A**. In **Figure 3B**, the XRD pattern of *E. spiralis*/Ag-NPs shows the appearance of five diffractions peaks at 38.49°, 44.73°, 64.91°, 77.88°, and 82.07° at 2θ values. This XRD pattern was fitted with the indexed Face Center Cubic (FCC) at (111), (200), (220), and (311) of crystallographic planes of silver peaks (Ref. No. 01-087-0719), thereby confirming the crystalline properties of *E. spiralis*/Ag-NPs in nature. The crystallographic plane of silver data obtained was then further analyzed using SAED pattern and lattice spacing to further confirm the crystalline nature of *E. spiralis*/Ag-NPs.

FETEM Analysis

The FETEM analysis is considered as the most important analysis in nanoparticle characterization studies. This analysis is useful to determine the shape, size, and morphology of Ag-NPs. In general, the *E. spiralis*/Ag-NPs showed mostly a spherical shape with the average particle size ranging from 18.15 ± 9.35 to 19.99 ± 7.44 nm, without significant agglomeration. The size, morphology, and distribution of *E. spiralis*/Ag-NPs at different initial concentrations of $AgNO_3$ are shown in **Figure 3**. For the effect of initial concentrations of $AgNO_3$, the average size of particles increased from 17.56 ± 7.52 to 19.99 ± 7.44 nm when increasing initial concentrations of $AgNO_3$ from 0.010 to 0.100 M as shown in **Figures 4a,b**, respectively. This observation could be due to the increase in the amount of *E. spiralis*/Ag-NPs formed in the solution (Paosen et al., 2017). The increased number of nanoparticles present in the solution can cause agglomeration or cluster nanoparticles, thus increasing the size of nanoparticles. The results obtained are in line with the result of the UV-vis analysis which shows that the UV-vis spectra move to the red-shift, suggesting that the size of Ag-NPs increased when increasing initial concentrations of $AgNO_3$.

For the effect of *E. spiralis* stem powder dosage, the average size of the nanoparticles decreased when increasing *E. spiralis* powder dosage from 1.5 to 2.5 g. The average size of *E spiralis*/Ag-NPs decreased from 19.99 ± 7.44 to 18.89 ± 4.75 nm (figures not shown). These findings proved the important role of *E. spiralis* extract to control the size of Ag-NPs by stabilizing it with the functional groups of *E. spiralis* extract. The increased amount of *E. spiralis* dosage also increases the available functional groups of *E. spiralis* extract and prevents further growth of *E. spiralis*/Ag-NPs. As such, the size of *E. spiralis*/Ag-NPs was decreased. This is because Ag-NPs are easy to agglomerate during the biosynthesis process due to the high tendency of silver nuclei to bond with Ag-NPs and the high surface area of the Ag-NPs (Polte, 2015). The decreasing number of *E. spiralis*/Ag-NPs at a 2.5 g dosage was chosen as the best parameter for further biomedical application, as shown in **Figure 4c**.

For the effect of stirring, reaction times also show that the size of *E. spiralis*/Ag-NPs slightly increased with the increase of reaction time at 60, 180, 360, and 600 min. The average size of *E. spiralis*/Ag-NPs increased slightly from 18.15 ± 9.35, 18.31 ± 6.83, 18.38 ± 5.15, and 18.89 ± 4.75 nm for 60, 180, 360, and 600 min, respectively. These results are in line with the UV-vis analysis, showing that wavelength moves to the red-shift, indicating the increased size of *E. spiralis*/Ag-NPs in the solution.

Overall, FETEM results showed that the average size of *E. spiralis*/Ag-NPs synthesized is <20 nm and is spherical in shape for all physicochemical parameters studied. This finding also supports the UV-vis results mentioned, which show that SPR bands centered between 420 and 430 nm estimated the spherical nanoparticles size range from 10 to 30 nm (Sowmyya and Lakshmi, 2018). According to Zhang et al. (2017), the diameters of the average particles from 5 to 50 nm have been

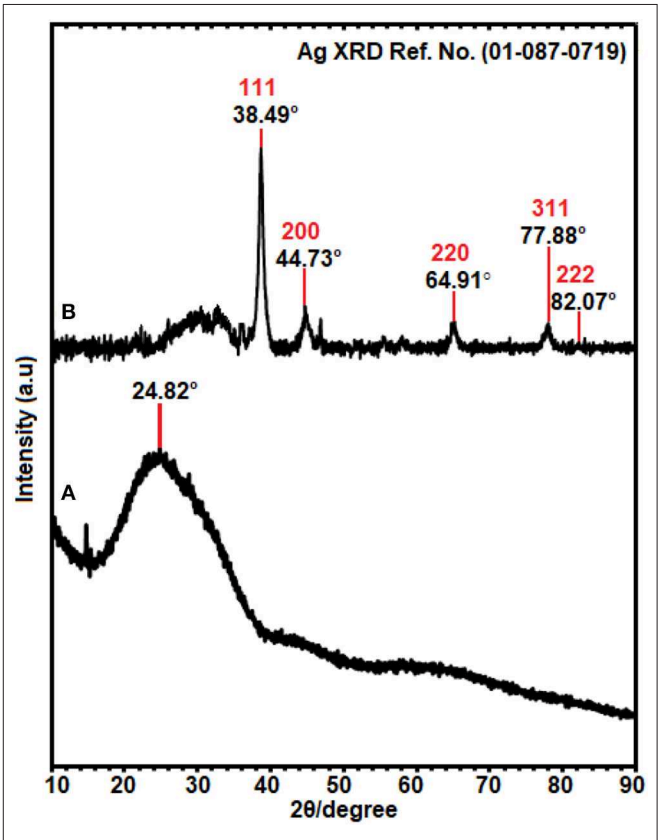

FIGURE 3 | The XRD patterns of **(A)** *E. spiralis* extract (2.5 g) and **(B)** *E. spiralis*/Ag-NPs at the best parameters to synthesize Ag-NPs.

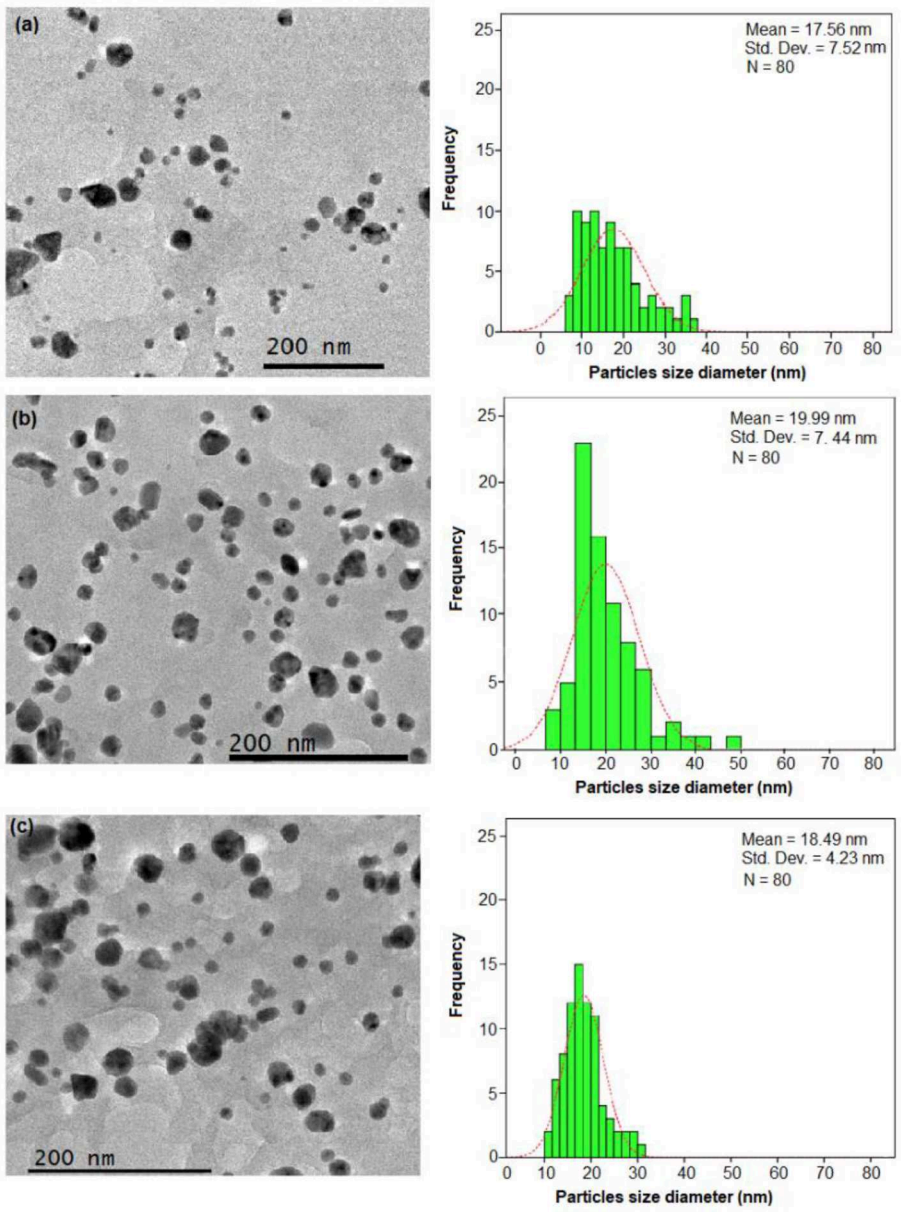

FIGURE 4 | The FETEM images and histogram of the particle size distribution of *E. spiralis*/Ag-NPs at **(a)** 0.010 M of $AgNO_3$ and **(b)** 0.100 M of $AgNO_3$ and **(c)** at its best parameter condition, at 600 min of stirring reaction time.

shown to have strong antibacterial activity. The positive aspects of the antibacterial properties of *E. spiralis*/Ag-NPs was discussed in detail in the antibacterial activity section. From the FETEM results, it shows that Ag-NPs were successfully synthesized using *E. spiralis* extract.

Figure 5 shows the results of the selective area electron diffraction (SAED) pattern at the best parameters. The rings around the SAED pattern are in line with the XRD pattern as shown in **Figure 5a**. The pattern corresponding to the cubic Ag-NPs planes of (111), (200), (220), (311), and (222), qualified the polycrystalline nature of *E. spiralis*/Ag-NPs. In **Figure 5b**, the FETEM image of an individual Ag-NPs with a lattice spacing of ∼0.22 and 0.12 nm correspond to the d spacing of the (111) and (311) cubic plains of Ag-NPs at 38.49° and 77.88° angles, which are consistent with the XRD peak as shown in **Figure 3B**.

The FETEM analysis is also useful to predict the possible mechanism of *E. spiralis*/Ag-NPs mediated by *E. spiralis* extract, as illustrated in **Figure 6**. The mechanisms are related to bottom-up approaches starting with a chemical reaction by the self-assembly of atoms to new nuclei which grow into nanoparticles (Polte, 2015; Ahmed et al., 2016). The

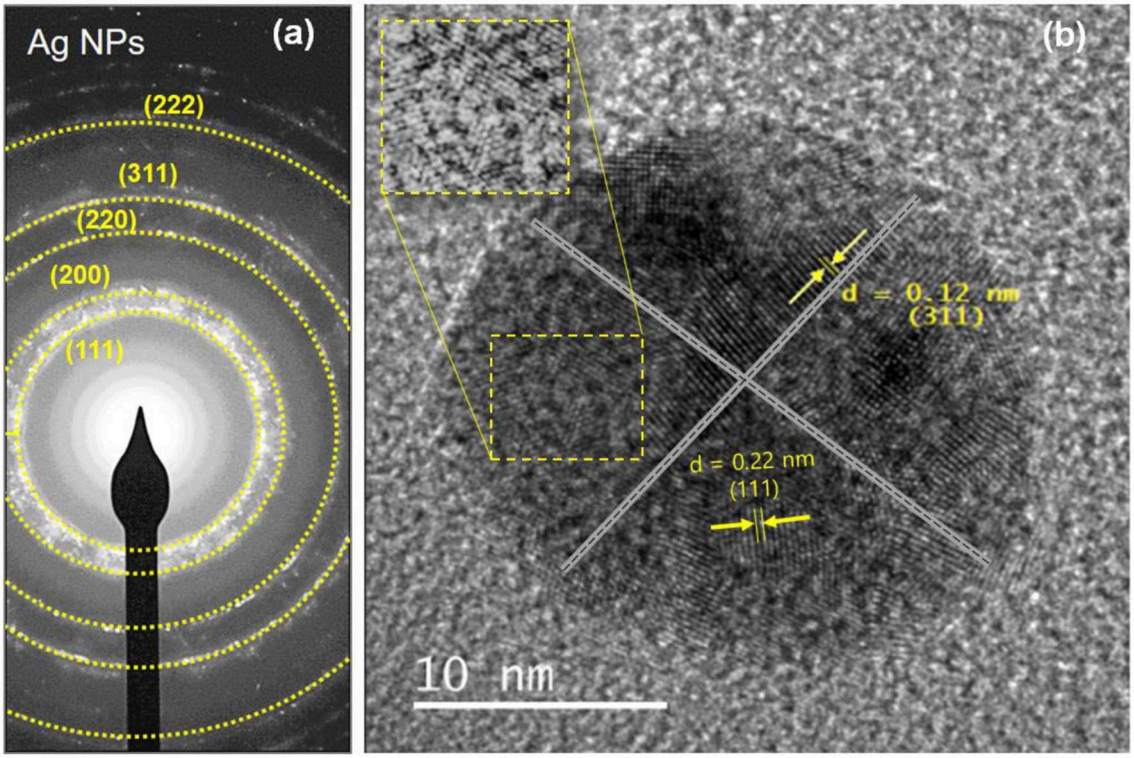

FIGURE 5 | The SAED pattern of **(a)** *E. spiralis*/Ag-NPs and **(b)** the lattice spacing of *E. spiralis*/Ag-NPs.

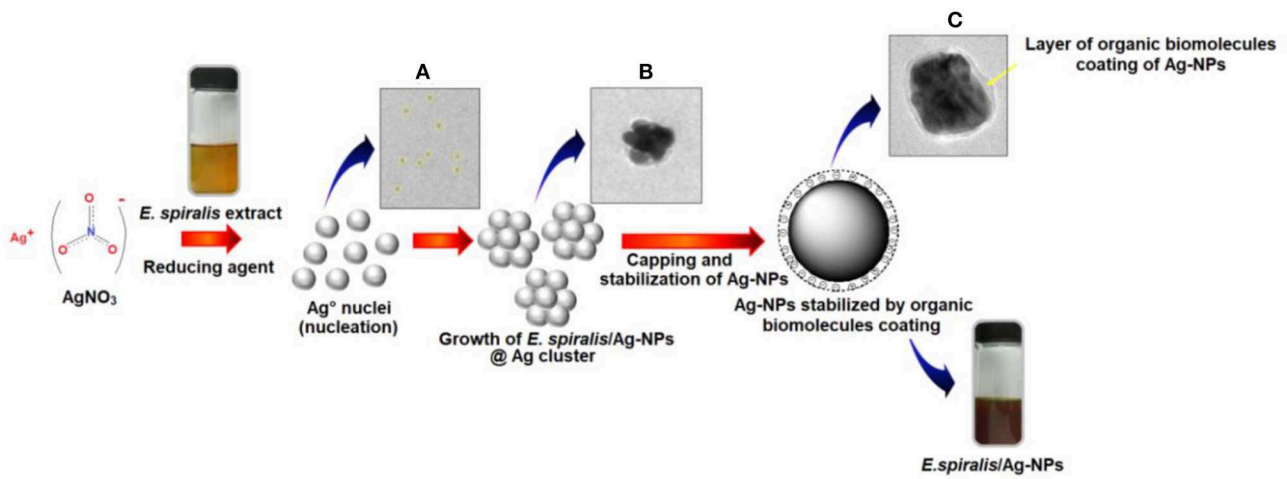

FIGURE 6 | Bottom to top approaches of *E. spiralis*/Ag-NPs formation. **(A)** Formation of Ago nuclei. **(B)** Growth of *E. spiralis*/Ag-NPs. **(C)** Stabilization of Ag-NPs by organic biomolecules of *E. spiralis* extract.

E. spiralis/Ag-NPs are prepared in aqueous solution by the reduction of a dissolved metal precursor of $AgNO_3$, using the reducing agent in the *E. spiralis* extract. The *E. spiralis* extract also acts as a stabilizing agent that controls the Ag-NPs from aggregation or clustering. The stabilizing agent is negatively surface charged and is able to be attached on the positively surface charged Ag-NPs, thus providing the repulsive forces of electrostatic stabilization that can suppress Ag-NPs from aggregation (Banach and Pulit-Prociak, 2017). The negative surface charges of *E. spiralis*/Ag-NPs are confirmed by the zeta potential analysis section. The micrograph image of Ag° nuclei, growth *E. spiralis*/Ag-NPs, and *E. spiralis*/Ag-NPs, stabilized by biomolecules in the *E. spiralis* extract, are shown in **Figures 6A–C**, respectively.

Zeta Potential Analysis

The surface properties and stability of the *E. spiralis* extract and *E. spiralis*/Ag-NPs can be determined using zeta potential analysis. In general, all the samples have shown the negative value of zeta potential. According to Faried et al. (2016), the negative surface value (more than 30 mV) shows the stability of the *E. spiralis*/Ag-NPs colloid. The previous study, reporting on biosynthesized silver nanoparticles using other plant extracts, is summarized in **Table 1**. It was found that the big size and low stability of Ag-NPs have been synthesized. In this study, the value of zeta potential for *E. spiralis* extract at 2.5 g of *E. spiralis* dosage is −80.7 mV, as shown in **Figure 7**. This value shows that the high stability of *E. spiralis* extracts to synthesize Ag-NPs. The negative value of the zeta potential record suggests that the negative surface charge of *E. spiralis* extracts might come from the OH^-, COO^-, CO^- functional groups. The detailed discussion of these functional groups and its possible mechanisms were discussed in detail in the FTIR analysis. The stability of Ag-NPs causes difficulties to agglomerate and increases the performance of Ag-NPs. The zeta potential value of *E. spiralis*/Ag-NPs at different reaction times is decreased with increased reaction time. The zeta potential value at 60, 180, 360, and 600 min, using 2.5 g *E. spiralis* dosage, are; 72.8, −74.4, −78.0, and −83.4 mV, respectively. The high negative zeta potential value might be due to the coordination of anionic stabilizing agents in *E. spiralis* extract with the Ag-NPs. A negatively charged Ag-NPs surface prevented the nanoparticles from aggregation and stabilized Ag-NPs by the electrostatic repulsions among the negative charges (Paosen et al., 2017).

FTIR Spectroscopy Analysis

The shifting in wavenumber or changes in peak intensity explains the types of functional groups involved in the binding mechanisms. The FTIR spectrum for *E. spiralis* extract at 2.5 g of *E. spiralis* dosage showed the absorption bands at 3,399, 2,932, 1,614, 1,522, 1,445, 1,381, 1,258, 1,072, and 530 cm^{-1}, as shown in **Figure 8A**. According to Pavia et al. (2009), the peaks ranging from 3,200 to 3,600 cm^{-1} are related to the O-H (hydroxyl) and -NH_2 (amine) stretching vibrations in the *E. spiralis* extract. The peak at 2,932 cm^{-1} can be assigned to C-H stretching. The peak at 1,614 cm^{-1} represents N-H bending from the glycoside compound in *E. spiralis* extract. The peak at 1,522 cm^{-1} corresponds to the aromatic ring of the terpenoid saponin structure. The carboxylate group can be confirmed by the 1,445 cm^{-1}. The peak at 1,381 cm^{-1} corresponds to the C-H bending of aldehyde groups from the glucose structure in *E. spiralis* extract. The peak at 1,258 cm^{-1} corresponds to the C-C(=O)-O stretching of ester (Silverstein et al., 1991). The peak at 1,072 cm^{-1} corresponds to C-O stretching. The peak at 530 cm^{-1} is related to the bonding of oxygen from the hydroxyl groups.

However, for the *E. spiralis*/Ag-NPs synthesized at best parameters, the FTIR spectrum showed some shifting of the peaks; peak intensity decreased/increased, and disappeared, as observed in **Figure 8B**. The peak shifted, suggesting that the responsible functional groups were involved in the binding mechanism on the Ag-NPs. After the synthesis process, the peaks at 3,399, 2,932, 1,522, and 530 cm^{-1} shifted to 3,402, 2,925, 1,516, and 521 cm^{-1} corresponding to O-H and –NH_2 stretching, C=O, C-H stretching, the aromatic ring of the terpenoid structure, and Ag-O, respectively (Shameli et al., 2012; Banach and Pulit-Prociak, 2017). The appearance of a new peak at 1,829 cm^{-1} represented carboxylate and C=C in the aromatic groups from the terpenoid saponin structure. This peak confirmed that the glucose structure attached at terpenoid saponin as an aldehyde oxidize to gluconic acid. The new peak at 823 cm^{-1} also increased, suggesting that C-H groups might also be bonded with the Ag-NPs. The disappearance of some peaks at 1,445 and 1,258 cm^{-1} has been observed in the *E. spiralis*/Ag-NPs FTIR

TABLE 1 | Summary of the synthesis of Ag-NPs using other plant extracts.

Plant	Size and shape of Ag-NPs	Zeta potential value (mV)	References
Soymida febrifuga (stem bark)	10–30 nm; spherical	−34.7	Sowmyya and Lakshmi, 2018
Sapindus mukorossi and *Acacia concinna* (leaves)	30 nm; spherical	−50 to 55	Sur et al., 2018
Enicostemma axillare (leaves)	18 nm; spherical	−24.6	Raj et al., 2018
Allium ampeloprasum (leaves)	2–43 nm; quasi spherical, spherical, ellipsoidal, hexagonal and irregular	−15.1	Khoshnamvand et al., 2019
Calliandra haematocephala (leaves)	70 nm; spherical	−17.2	Raja et al., 2017

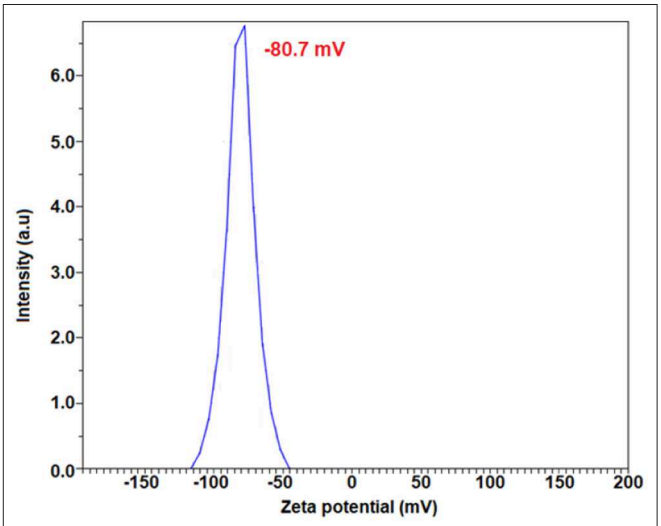

FIGURE 7 | The zeta potential result of *E. spiralis* extract at 2.5 g *E. spiralis* stem powder dosage.

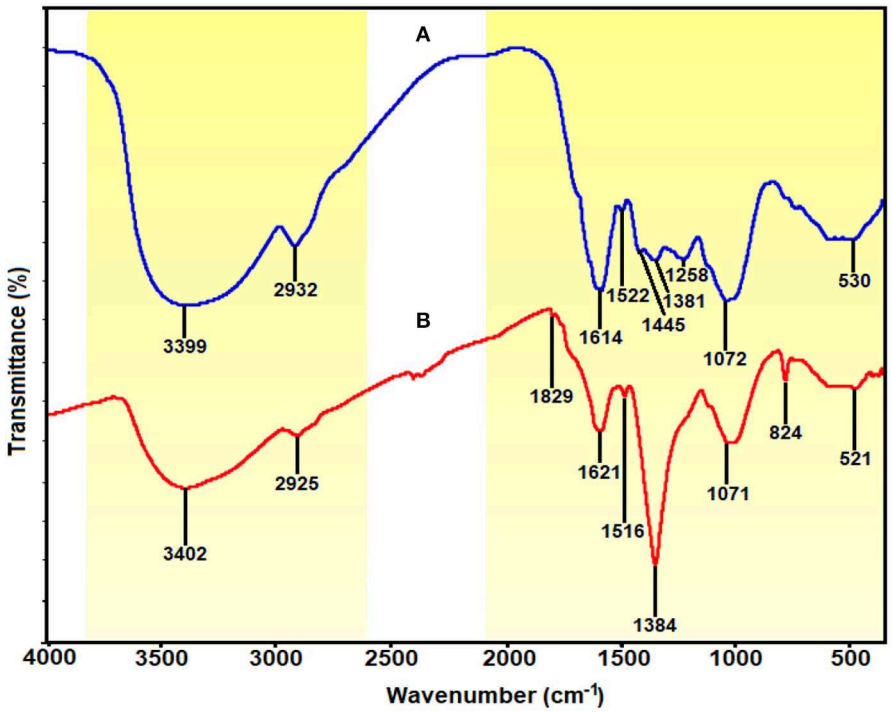

FIGURE 8 | FTIR spectra of **(A)** *E. spiralis* extract at 2.5 g of *E. spiralis* dosage and **(B)** *E. spiralis*/Ag-NPs at best parameters of the biosynthesis process.

spectrum. These peaks suggested that the binding mechanisms of Ag-NPs with *E. spiralis* extract occurred at carboxylate groups and C-C(=O)-O stretching of the ester. The peak intensity at 1,621 cm^{-1} decreased, suggesting the involvement of N-H bending from the glycoside. However, the peak intensity at 1,384 cm^{-1} increased, proposing the C-H bending of aldehyde groups from the glucose structure in *E. spiralis* extract. All the peak changes support the impact of functional groups of *E. spiralis* extract as reducing and stabilizing agents to synthesize Ag-NPs.

Antibacterial Activity of *E. spiralis*/Ag-NPs

The antibacterial activity of *E. spiralis/Ag-NPs* was evaluated based on the diameter of the growth inhibition zone at different parameters and bacteria species, and the results are shown in **Table 2**. The order of the highest antibacterial activity is *S. aureus* > *P. vulgaris* > *E. coli* > *E. faecalis* species, respectively as observed in **Figure 9A**. There are significant differences in the diameter of the growth inhibition zone between the bacteria species based on the *post-hoc* multiple comparisons Tukey HSD test ($p < 0.05$). The significant difference in the diameter of the growth inhibition zone was observed between *S. aureus* and *E. faecalis, E. coli,* and *P. vulgaris.* However, the bacteria of *E. faecalis, E. coli,* and *P. vulgaris* did not significantly increase the diameter of the growth inhibition zone ($p > 0.05$). The weak antibacterial activity of *E. spiralis*/Ag-NPs, at best parameters, toward Gram-negative bacteria might be due to the material like capsule that has been covered on the bacteria cell wall and also the negatively charged outer lipid membrane (lipopolysaccharide) cover (Patil et al., 2018). The negative charge of both Gram-negative bacteria and *E. spiralis*/Ag-NPs caused the electrostatic repulsion between them, and as such hinders the attachment and penetration into the cells (Ahmad et al., 2017). The negative charge of *E. spiralis*/Ag-NPs is evident from the zeta potential value. Further analysis was conducted on the significant

TABLE 2 | The diameter of the growth inhibition zone at different parameters against different types of bacteria species.

Bacteria species	Mean diameter of growth inhibition zone (mm)			
	E. coli	*P. vulgaris*	*E. faecalis*	*S. aureus*
Amount of *E. spiralis*/Ag-NPs (μL)				
10	7.40 ± 0.16	7.57 ± 0.16	7.33 ± 0.14	8.84 ± 0.29
20	7.34 ± 0.13	8.09 ± 0.11	7.94 ± 0.16	9.60 ± 0.36
30	7.69 ± 0.15	8.28 ± 0.10	7.84 ± 0.18	10.06 ± 0.35
40	7.97 ± 0.17	8.34 ± 0.11	8.41 ± 0.17	10.47 ± 0.37
Stirring reaction time (min)				
600	8.19 ± 0.13	8.38 ± 0.25	8.75 ± 0.25	11.38 ± 0.38
360	8.00 ± 0.27	8.00 ± 0.16	7.88 ± 0.30	10.31 ± 0.28
180	7.75 ± 0.16	7.78 ± 0.16	8.13 ± 0.30	11.00 ± 0.27
60	7.88 ± 0.23	7.81 ± 0.13	7.75 ± 0.16	10.50 ± 0.33
Control				
Gentamicin (+ve)	21.00 ± 0.00	24.00 ± 0.00	16.50 ± 0.50	22.00 ± 0.00
E. spiralis extract (–ve)	*NA	*NA	*NA	*NA
Plain disk (–ve)	*NA	*NA	*NA	*NA

*NA means not available; * is mean ± SE of three experiment.*

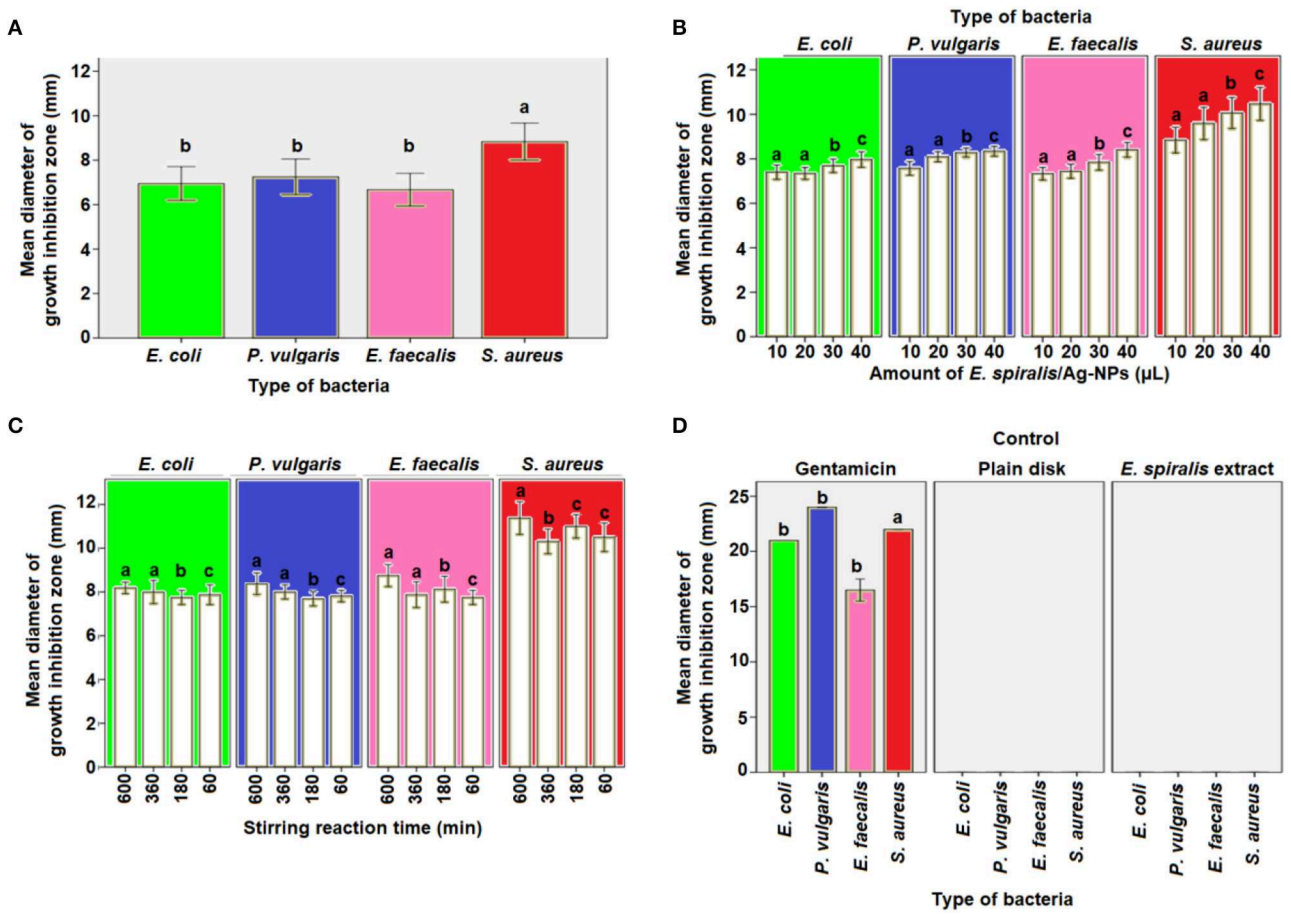

FIGURE 9 | The mean diameter of inhibition zones by *E. spiralis*/Ag-NPs at **(A)** different type of bacteria, **(B)** different amount of *E. spiralis*/Ag-NPs against different type of bacteria, **(C)** different stirring reaction time against different type of bacteria, **(D)** positive and negative control of antibacterial agent. Data with the same letter are not significantly different ($P > 0.05$).

differences in antibacterial activity between Gram-positive and Gram-negative bacteria species. Surprisingly, the differences between these bacteria are not significant ($p > 0.05$). This result proved that the *E. spiralis*/Ag-NPs has the antibacterial activity for both types of Gram-positive and Gram-negative bacteria.

To investigate if the amount of *E. spiralis*/Ag-NPs has any effects on the antibacterial activity, different amounts of *E. spiralis*/Ag-NPs (µL), ranging from 10 to 40 µL, were used. The diameter of the growth inhibition zone was slightly increased when increasing the amount of *E. spiralis*/Ag-NPs from 10 to 40 µL, as shown in **Table 2**. This phenomenon can be explained because more Ag-NPs accumulated on the bacteria surface, entering the cell from inside, damaging the nuclei, and causing bacterial death (Deshmukh et al., 2019). There is a significant difference in the diameter of the growth inhibition zone between the amount of *E. spiralis*/Ag-NPs used ($p < 0.05$). The multiple comparison *post-hoc* test value shows no significant difference in the diameter of the growth inhibition zone between 10 and 20 µL ($p > 0.05$), however, there was a significant difference in the diameter of the growth inhibition zone between 30 and 40 µL ($p < 0.05$), as shown in **Figure 9B**. This explained dose-dependent antibacterial activity by *E. spiralis*/Ag-NPs.

The diameter of the growth inhibition zone at synthesized *E. spiralis*/Ag-NPs at different stirring reaction times, ranging from 60 to 600 min, is shown in **Table 2**. From the table, the diameter of the growth inhibition zone slightly increases when increasing the stirring reaction time. Most of the literature mentions that the antimicrobial activities are better in smaller nanoparticles (Alsammarraie et al., 2018), however, the average size of *E. spiralis*/Ag-NPs was slightly increased when increasing the stirring reaction time, as reported in the FETEM analysis. This phenomenon can be explained by the smaller-sized distribution of *E. spiralis*/Ag-NPs, with an increase in stirring reaction time, as observed in the FETEM analysis (Usman et al., 2013). Therefore, besides smaller sized nanoparticles, good distribution of nanoparticles should also be considered as another factor of positive antibacterial activities. However,

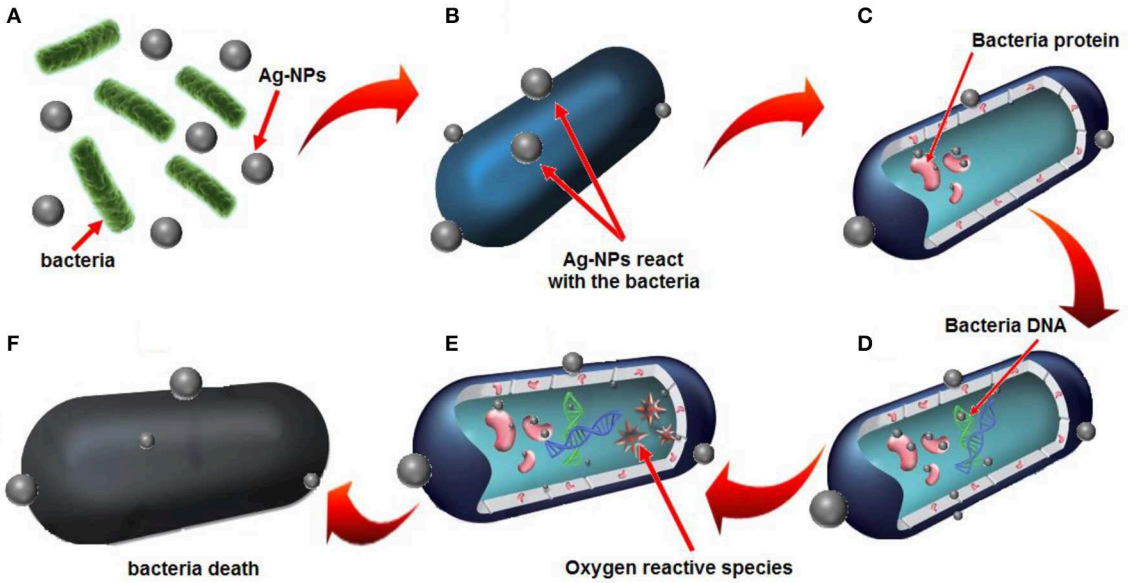

FIGURE 10 | Plausible mechanisms of antibacterial activity by *E. spiralis*/Ag-NPs is based on **(A)** electrostatic attraction of bacteria with *E. spiralis*/Ag-NPs, **(B)** the release of Ag^+ ions, **(C)** electrostatic attraction between Ag^+ ions and bacteria protein, **(D)** the interference with bacterial DNA replication, **(E)** resulting in oxygen reactive species, **(F)** bacteria death.

there is no significant difference, when increasing the stirring reaction time, on the diameter of the growth inhibition zone ($p > 0.05$), as shown in **Figure 9C**. The positive control of the gentamicin antibiotic standard shows the significant differences ($p < 0.05$) between the negative control of *E. spiralis* extract and the plain disk (**Figure 9D**). The negative control of *E. spiralis* extract demonstrates that the antibacterial activity is due to Ag-NPs. According to Pollini et al. (2009), with reference to standard antibacterial test "SNV 195920-1992," a the microbial zone of inhibition of more than 1.0 mm in diameter, can be considered to have potential with good antimicrobial activity. Thus, the *E. spiralis*/Ag-NPs can be considered as a good antibacterial agent for the application in biomedical and wastewater treatment.

The plausible mechanism of antibacterial activity of *E. spiralis*/Ag-NPs can be explained based on the electrostatic attraction between the negatively charged microorganism cell membrane and the Ag^+ ion. Therefore, the Ag^+ ion can interact with thiol groups of enzymes, destroys the DNA replication ability, followed by bacterial cell death (Li et al., 2016). The plausible mechanism of antibacterial activity by *E. spiralis*/Ag-NPs is depicted in **Figure 10**. According to Sabry et al. (2018), the possible mechanisms could be replaced by the contact action of Ag-NPs with the bacterial surface which will combine with the bacterial protein in the cell wall (**Figures 10A–C**). This can interfere with the DNA replication and also promote the generation of reactive oxygen species which will then cause bacterial cell death, as shown in **Figure 10D**.

CONCLUSION

The developed method of the biosynthesis of Ag-NPs mediated by *E. spiralis* extract using an eco-friendly method, good distribution, and high percentage yield, was in fact successful. The effect of physicochemical parameters such as initial concentrations of $AgNO_3$, *E. spiralis* dosage, and stirring reaction time has a significant effect on the properties of *E. spiralis*/Ag-NPs and the antimicrobial activity. The smaller size of *E. spiralis*/Ag-NPs was obtained at highest *E. spiralis* dosage, but the larger size of *E. spiralis*/Ag-NPs was obtained at the highest initial concentration of $AgNO_3$. The formation of *E. spiralis*/Ag-NPs was confirmed by UV-vis spectra in the SPR bands ranging from 418 to 434 nm. The XRD analysis showed the crystalline structure of *E. spiralis*/Ag-NPs silver of FCC at (111), (200), (220), and (311). The FETEM analysis showed the spherical shape of *E. spiralis*/Ag-NPs with a good distribution of nanoparticles and the average size ranged from 18.15 ± 9.35 to 19.99 ± 7.44 nm. The SAED pattern was confirmed, with the XRD results showing that the lattice spacing of ∼0.12 nm corresponds to the d spacing of the (311) cubic plain of Ag-NPs at an angle of 77.88°. The reducing and stabilizing agents might come from O-H and $-NH_2$ stretching, C=O, C-H stretching, the aromatic ring of the terpenoid structure and Ag-O, hydroxyl groups (oxygen), carboxylate groups, and C-C(=O)-O stretching of the ester groups of *E. spiralis* extract, as revealed by FTIR analysis. The prepared Ag-NPs mediated by *E. spiralis* extract also exhibited excellent antimicrobial activity toward pathogenic bacteria namely *S. aureus, E. faecalis, E. coli,* and *P. vulgaris*. Thus,

E. spiralis/Ag-NPs have potential as a promising nanomaterial for biomedical applications such as in wound healing and the coating of biomaterials.

DATA AVAILABILITY STATEMENT

All datasets generated for this study are included in the article/supplementary material.

AUTHOR CONTRIBUTIONS

WW: synthesis, experimental works, and writing original draft. KS: supervision, review, and editing. NC: dye catalytic analysis or interpretation of data, review, and editing. NO: sample characterization. NH: antibacterial analysis or interpretation of data, review, and editing. All authors contributed to the article and approved the submitted version.

ACKNOWLEDGMENTS

The authors would like to express sincere gratitude to the Universiti Teknologi Malaysia for financial support under research University grants (Grants Nos. #4B422, #15H73, #20H33, and #20H55). All authors are thankful to Malaysia-Japan International Institute of Technology (MJIIT) of UTM for providing excellent research environment to complete this work.

REFERENCES

Ahmad, A., Wei, Y., Syed, F., Tahir, K., Rehman, A. U., Khan, A., et al. (2017). The effects of bacteria-nanoparticles interface on the antibacterial activity of green synthesized silver nanoparticles. *Microb. Pathog.* 102, 133–142. doi: 10.1016/j.micpath.2016.11.030

Ahmed, S., Ahmad, M., Swami, B. L., and Ikram, S. (2016). A review on plants extract mediated synthesis of silver nanoparticles for antimicrobial applications: a green expertise. *J. Adv. Res.* 7, 17–28. doi: 10.1016/j.jare.2015.02.007

Alsammarraie, F. K., Wang, W., Zhou, P., Mustapha, A., and Lin, M. (2018). Green synthesis of silver nanoparticles using turmeric extracts and investigation of their antibacterial activities. *Colloids Surfaces B Biointerfaces* 171, 398–405. doi: 10.1016/j.colsurfb.2018.07.059

Aramwit, P., Bang, N., Ratanavaraporn, J., and Ekgasit, S. (2014). Green synthesis of silk sericin-capped silver nanoparticles and their potent anti-bacterial activity. *Nanoscale Res. Lett.* 9, 1–7. doi: 10.1186/1556-276X-9-79

Banach, M., and Pulit-Prociak, J. (2017). Proecological method for the preparation of metal nanoparticles. *J. Clean. Prod.* 141, 1030–1039. doi: 10.1016/j.jclepro.2016.09.180

Bauer, A. W., Kirby, W. M., Sherris, J. C., and Turck, M. (1966). Antibiotic susceptibility testing by a standardized single disk method. *Am. J. Clin. Pathol.* 45, 493–496. doi: 10.1093/ajcp/45.4_ts.493

Chouhan, N., Ameta, R., and Meena, R. K. (2017). Biogenic silver nanoparticles from *Trachyspermum ammi* (Ajwain) seeds extract for catalytic reduction of p-nitrophenol to p-aminophenol in excess of NaBH4. *J. Mol. Liq.* 230, 74–84. doi: 10.1016/j.molliq.2017.01.003

Deshmukh, S. P., Patil, S. M., Mullani, S. B., and Delekar, S. D. (2019). Silver nanoparticles as an effective disinfectant: a review. *Mater. Sci. Eng. C.* 97, 954–965. doi: 10.1016/j.msec.2018.12.102

Dwivedi, A. D., and Gopal, K. (2010). Biosynthesis of silver and gold nanoparticles using *Chenopodium album* leaf extract. *Colloids Surfaces A Physicochem. Eng. Asp.* 369, 27–33. doi: 10.1016/j.colsurfa.2010.07.020

Faried, M., Shameli, K., Miyake, M., Hajalilou, A., Kalantari, K., Zakaria, Z., et al. (2016). Synthesis of silver nanoparticles via green method using ultrasound irradiation in seaweed *Kappaphycus alvarezii* media. *Res. Chem. Intermed.* 42, 7991–8004. doi: 10.1007/s11164-016-2574-z

Harun, A., Mat So'ad, S. Z., and Hassan, N. M. (2016). Two isolated crystalline solids from the stem of *Entada spiralis* Ridl. (akar sintok). *Malaysian J. Anal. Sci.* 20, 238–246. doi: 10.17576/mjas-2016-2002-04

Harun, A., Mat So'ad, S. Z., and Mohd Hassan, N. (2015). Bioassay guided isolation of an antidermatophytic active constituent from the stem bark of *Entada spiralis* Ridl. *Malaysian J. Anal. Sci.* 19, 752–759.

Joy Prabu, H., and Johnson, I. (2015). Plant-mediated biosynthesis and characterization of silver nanoparticles by leaf extracts of *Tragia involucrata*, *Cymbopogon citronella*, *Solanum verbascifolium* and *Tylophora ovata*. *Karbala Int. J. Mod. Sci.* 1, 237–246. doi: 10.1016/j.kijoms.2015.12.003

Keshvadi, M., Karimi, F., and Valizadeh, S. (2019). Comparative study of antibacterial inhibitory effect of silver nanoparticles and garlic oil nanoemulsion with their combination. *Biointerface Res. Appl. Chem.* 9, 4560–4566. doi: 10.33263/BRIAC96.560566

Khatoon, N., Mazumder, J. A., and Sardar, M. (2017). Biotechnological applications of green synthesized silver nanoparticles. *J. Nanosci. Curr. Res.* 2, 1–8. doi: 10.4172/2572-0813.1000107

Khoshnamvand, M., Huo, C., and Liu, J. (2019). Silver nanoparticles synthesized using *Allium ampeloprasum* L. leaf extract: characterization and performance in catalytic reduction of 4-nitrophenol and antioxidant activity. *J. Mol. Struct.* 1175, 90–96. doi: 10.1016/j.molstruc.2018.07.089

Kumar, S. S. D., Houreld, N. N., Kroukamp, E. M., and Abrahamse, H. (2018). Cellular imaging and bactericidal mechanism of green-synthesized silver nanoparticles against human pathogenic bacteria. *J. Photochem. Photobiol. B Biol.* 178, 259–269. doi: 10.1016/j.jphotobiol.2017.11.001

Labulo, A. H., Adesuji, E. T., Dedeke, O. A., Bodede, O. S., Oseghale, C. O., Moodley, R., et al. (2016). A dual-purpose silver nanoparticles biosynthesized using aqueous leaf extract of *Detarium microcarpum*: an under-utilized species. *Talanta* 160, 735–744. doi: 10.1016/j.talanta.2016.07.066

Li, H., Gao, Y., Li, C., Ma, G., Shang, Y., and Sun, Y. (2016). A comparative study of the antibacterial mechanisms of silver ion and silver nanoparticles by Fourier transform infrared spectroscopy. *Vib. Spectrosc.* 85, 112–121. doi: 10.1016/j.vibspec.2016.04.007

Maddinedi, S. B., Mandal, B. K., and Maddili, S. K. S. (2017). Biofabrication of size controllable silver nanoparticles – a green approach. *J. Photochem. Photobiol. B Biol.* 167, 236–241. doi: 10.1016/j.jphotobiol.2017.01.003

Mashwani, Z. R., Khan, M. A., Khan, T., and Nadhman, A. (2016). Applications of plant terpenoids in the synthesis of colloidal silver nanoparticles. *Adv. Colloid Interface Sci.* 234, 132–141. doi: 10.1016/j.cis.2016.04.008

Mittal, A. K., Chisti, Y., and Banarjee, U. C. (2013). Synthesis of metallic nanoparticles using plant extracts. *Biotechnol. Adv.* 31, 346–356. doi: 10.1016/j.biotechadv.2013.01.003

Morales-Luckie, R. A., Lopezfuentes-Ruiz, A. A., Olea-Mejía, O. F., Liliana, A. F., Sanchez-Mendieta, V., Brostow, W., et al. (2016). Synthesis of silver nanoparticles using aqueous extracts of Heterotheca inuloides as reducing agent and natural fibers as templates: *Agave lechuguilla* and silk. *Mater. Sci. Eng. C.* 69, 429–436. doi: 10.1016/j.msec.2016.06.066

Narasaiah, B. P., Mandal, B. K., and Chakravarthula, S. N. (2018). Mitigation of textile industries generated pollution by agro-waste cotton peels mediated synthesized silver nanoparticles. *Res. Appl. Chem.* 8, 3602–3610.

Nassar, M. A., and Youssef, A. M. (2012). Mechanical and antibacterial properties of recycled carton paper coated by PS/Ag nanocomposites for packaging. *Carbohydr. Polym.* 89, 269–274. doi: 10.1016/j.carbpol.2012.03.007

Nava, O. J., Luque, P., Gomez-Gutierrez, C. M., Vilchis-Nestor, A., Castro-Beltran, A., Mota-Gonzalez, C. M., et al. (2016). Influence of *Camellia sinensis* extract on Zinc Oxide nanoparticle green synthesis. *J. Mol. Struct.* 1134, 121–125. doi: 10.1016/j.molstruc.2016.12.069

Paosen, S., Saising, J., Wira Septama, A., and Piyawan Voravuthikunchai, S. (2017). Green synthesis of silver nanoparticles using plants from Myrtaceae family and characterization of their antibacterial activity. *Mater. Lett.* 209, 201–206. doi: 10.1016/j.matlet.2017.07.102

Patil, M. P., Singh, R. D., Koli, P. B., Patil, K. T., Jagdale, B. S., Tipare, A. R., et al. (2018). Antibacterial potential of silver nanoparticles synthesized using *Madhuca longifolia* flower extract as a green resource. *Microb. Pathog*. 121, 184–189. doi: 10.1016/j.micpath.2018.05.040

Pavia, D. L., Lampman, G. M., Kriz, G. S., and Vyvyan, J. R. (2009). *Introduction to Spectroscopy, 4th Edn*. Washington: Brooks/Cole Cengage Learning.

Pollini, M., Russo, M., Licciulli, A., Sannino, A., and Maffezzoli, A. (2009). Characterization of antibacterial silver coated yarns. *J. Mater. Sci. Mater. Med*. 20, 2361–2366. doi: 10.1007/s10856-009-3796-z

Polte, J. (2015). Fundamental growth principles of colloidal metal nanoparticles - a new perspective. *CrystEngComm* 17, 6809–6830. doi: 10.1039/C5CE01014D

Raj, S., Chand Mali, S., and Trivedi, R. (2018). Green synthesis and characterization of silver nanoparticles using *Enicostemma axillare* (Lam.) leaf extract. *Biochem. Biophys. Res. Commun*. 503, 2814–2819. doi: 10.1016/j.bbrc.2018.08.045

Raja, S., Ramesh, V., and Thivaharan, V. (2017). Green biosynthesis of silver nanoparticles using *Calliandra haematocephala* leaf extract, their antibacterial activity and hydrogen peroxide sensing capability. *Arab. J. Chem*. 10, 253–261. doi: 10.1016/j.arabjc.2015.06.023

Rajakumar, G., Gomathi, T., Thiruvengadam, M., Devi Rajeswari, V., Kalpana, V. N., and Chung, I. M. (2017). Evaluation of anti-cholinesterase, antibacterial and cytotoxic activities of green synthesized silver nanoparticles using from *Millettia pinnata* flower extract. *Microb. Pathog*. 103, 123–128. doi: 10.1016/j.micpath.2016.12.019

Ravichandran, V., Vasanthi, S., Shalini, S., Ali Shah, S. A., and Harish, R. (2016). Green synthesis of silver nanoparticles using *Atrocarpus altilis* leaf extract and the study of their antimicrobial and antioxidant activity. *Mater. Lett*. 180, 264–267. doi: 10.1016/j.matlet.2016.05.172

Reddy, K. R. (2017). Green synthesis, morphological and optical studies of CuO nanoparticles. *J. Mol. Struct*. 1150, 553–557. doi: 10.1016/j.molstruc.2017.09.005

Sabry, N., Tolba, S., Kh, F., Abdel-Gawad, F., Bassem, S., Hossam, F., et al. (2018). Interaction between nano silver and bacteria: modeling approach. *Biointerface Res. Appl. Chem*. 8, 3570–3574.

Selvam, K., Sudhakar, C., Govarthanan, M., Thiyagarajan, P., Sengottaiyan, A., Senthilkumar, B., et al. (2017). Eco-friendly biosynthesis and characterization of silver nanoparticles using *Tinospora cordifolia* (Thunb.) Miers and evaluate its antibacterial, antioxidant potential. *J. Radiat. Res. Appl. Sci*. 10, 6–12. doi: 10.1016/j.jrras.2016.02.005

Shameli, K., Bin Ahmad, M., Jazayeri, S. D., Sedaghat, S., Shabanzadeh, P., Jahangirian, H., et al. (2012). Synthesis and characterization of polyethylene glycol mediated silver nanoparticles by the green method. *Int. J. Mol. Sci*. 13, 6639–6650. doi: 10.3390/ijms13066639

Silverstein, R. M., and Bassler, G. C., Morril, T. C. (1991). *Spectrometric Identification of Organic Compounds, 5th Edn*. New York, NY: John Wiley and Sons.

Sowmyya, T., and Lakshmi, G. V. (2018). Spectroscopic investigation on catalytic and bactericidal properties of biogenic silver nanoparticles synthesized using *Soymida febrifuga* aqueous stem bark extract. *J. Environ. Chem. Eng*. 6, 3590–3601. doi: 10.1016/j.jece.2017.01.045

Sur, U. K., Ankamwar, B., Karmakar, S., Halder, A., and Das, P. (2018). Green synthesis of Silver nanoparticles using the plant extract of Shikakai and Reetha. *Mater. Today Proc*. 5, 2321–2329. doi: 10.1016/j.matpr.2017.09.236

Usman, M. S., Zowalaty, M. E. E., Shameli, K., Zainuddin, N., Salama, M., and Ibrahim, N. A. (2013). Synthesis, characterization, and antimicrobial properties of copper nanoparticles. *Int. J. Nanomedicine* 8, 4467–4479. doi: 10.2147/IJN.S50837

Wang, C. X., Ren, Y., Lv, J. C., Zhou, Q. Q., Ma, Z. P., Qi, Z. M., et al. (2017). *In situ* synthesis of silver nanoparticles on the cotton fabrics modified by plasma induced vapor phase graft polymerization of acrylic acid for durable multifunction. *Appl. Surf. Sci*. 396, 1840–1848. doi: 10.1016/j.apsusc.2016.11.173

Wu, Y., Yang, Y., Zhang, Z., Wang, Z., Zhao, Y., and Sun, L. (2018). A facile method to prepare size-tunable silver nanoparticles and its antibacterial mechanism. *Adv. Powder Technol*. 29, 407–415. doi: 10.1016/j.apt.2017.11.028

Yan-yu, R., Hui, Y., Tao, W., and Chuang, W. (2016). Green synthesis and antimicrobial activity of monodisperse silver nanoparticles synthesized using *Ginkgo biloba* leaf extract. *Phys. Lett. Sect. A Gen. At. Solid State Phys*. 380, 3773–3777. doi: 10.1016/j.physleta.2016.09.029

Zhang, M., Lin, H., Wang, Y., Yang, G., Zhao, H., and Sun, D. (2017). Fabrication and durable antibacterial properties of 3D porous wet electrospun RCSC/PCL nanofibrous scaffold with silver nanoparticles. *Appl. Surf. Sci*. 414, 52–62. doi: 10.1016/j.apsusc.2017.04.052

Conflict of Interest: The authors declare that the research was conducted in the absence of any commercial or financial relationships that could be construed as a potential conflict of interest.

frontiers in Chemistry

REVIEW
published: 20 August 2020
doi: 10.3389/fchem.2020.00718

The Most Recent Advances in the Application of Nano-Structures/Nano-Materials for Single-Cell Sampling

Xiaolong Xu[1], *Jianbo Jia*[1]* *and Mingquan Guo*[1,2]*

[1] School of Biotechnology and Health Science, Wuyi University, Jiangmen, China, [2] CAS Key Laboratory of Plant Germplasm Enhancement and Specialty Agriculture, Chinese Academy of Sciences, Wuhan, China

The research in endogenous biomolecules from a single cell has grown rapidly in recent years since it is critical for dissecting and scrutinizing the complexity of heterogeneous tissues, especially under pathological conditions, and it is also of key importance to understand the biological processes and cellular responses to various perturbations without the limitation of population averaging. Although conventional techniques, such as micromanipulation or cell sorting methods, are already used along with subsequent molecular examinations, it remains a big challenge to develop new approaches to manipulate and directly extract small quantities of cytosol from single living cells. In this sense, nanostructure or nanomaterial may play a critical role in overcoming these challenges in cellular manipulation and extraction of very small quantities of cells, and provide a powerful alternative to conventional techniques. Since the nanostructures or nanomaterial could build channels between intracellular and extracellular components across cell membrane, through which cytosol could be pumped out and transferred to downstream analyses. In this review, we will first brief the traditional methods for single cell analyses, and then shift our focus to some most promising methods for single-cell sampling with nanostructures, such as glass nanopipette, nanostraw, carbon nanotube probes and other nanomaterial. In this context, particular attentions will be paid to their principles, preparations, operations, superiorities and drawbacks, and meanwhile the great potential of nano-materials for single-cell sampling will also be highlighted and prospected.

Keywords: single-cell sampling, nanostructure, nanopipette, nanostraw, carbon nanotube probes

OPEN ACCESS

Edited by:
Zhiyuan Xiong,
The University of Melbourne, Australia

Reviewed by:
Xiaopeng Han,
Tianjin University, China
Guillermo Javier Copello,
Consejo Nacional de Investigaciones Científicas y Técnicas (CONICET), Argentina

***Correspondence:**
Jianbo Jia
jbjia@wyu.edu.cn
Mingquan Guo
guomq@wbgcas.cn

Specialty section:
This article was submitted to Nanoscience, a section of the journal Frontiers in Chemistry

Received: *24 April 2020*
Accepted: *13 July 2020*
Published: *20 August 2020*

Citation:
Xu X, Jia J and Guo M (2020) The Most Recent Advances in the Application of Nano-Structures/Nano-Materials for Single-Cell Sampling. Front. Chem. 8:718. doi: 10.3389/fchem.2020.00718

INTRODUCTION

The presence of heterogeneity in cell populations calls for inspection down to single-cell level in nearly all fields of biology and medicine. The unique features of individual cells, even originally with the same genetic information, and from the same multicellular organisms, include but not limited to their structure, composition, and functionality (Guillaume-Gentil et al., 2016). It has been reported an unexpected level of somatic genomic variations in both normal and diseased tissues (Gupta and Sachs, 2017). Taking acute myeloid leukemia (AML) for example, it is a heterogeneous disease both at phenotypic and genotypic levels, and this heterogeneity extends to leukemia stem

cells (Gupta and Sachs, 2017). Differential gene expression leads to the diversity of cell phenotypes resulting in individual cells with highly specialized functions. On the other hand, the randomness of intracellular processes, together with changes in the environment around, further gives rise to different cellular functions, even in the homogenous cell populations. Thus, molecular analysis at a single cell level is essential for the evaluation and inspection of the complexity of heterogeneous tissue, the description of pathological conditions, the study of biological processes, and the cellular response to disturbances, without masking cellular heterogeneity (Guillaume-Gentil et al., 2016). To this end, it is crucial to explore where and when biomolecules exert their functions in regulating the activity of cells. In order to know what is going on in the life cycle of a cell, it is fundamental to elucidate the molecular composition at a given site in real time. These efforts will of key importance not only to understand cell activity and its controlled differentiation, but also to realize the potentially targeted therapy of living cells.

It is well known that the spatial resolution of conventional optical microscopy can reach about 200–300 nm due to the Abbe diffraction limit, which is unable to visualize most of the biomolecule individually in a single living cell. To improve the spatial resolution, the supper resolution optical microscopies have been actively developed, such as stimulated emission microscopy (STED), photoactivated localization microscopy (PALM), and stochastic optical reconstruction microscopy (STORM). Their spatial resolution could achieve down to several ten nanometers, and fluorescence labeling is also necessary. In most cases, the fluorescence image is taken from fluorescent labeling reagent itself instead of the target molecules. Besides, fluorescence labeling may affect the behaviors of cells. To overcome the above limitations, transmission electron microscopy (TEM) and scanning electron microscopy (SEM) have been developed with superior spatial resolution, which can visualize single molecules, but cannot be carried out directly on living cells. Although powerful, these methods are hampered by cell lysis in advance to extract the intracellular contents, which can provide only a single instant snapshot without historical or future information about the cell cycle. Thus, how to conduct accurate sampling from a single cell becomes the key for single cell analysis.

Successful techniques for sampling from a single cell, in other words, extracting small quantities from one or multiple sites into a single cell for long-term tracking of interested activity, must be able to manipulate picoliter-scale volumes with high cell viability, and to accurately reflect the cell's multiple biological components but without influencing the ongoing development of the cell (Higgins and Stevens, 2017). In this sense, nanostructure or nanomaterial may play a critical role in overcoming these challenges, since the nanostructures or nanomaterial could build channels between intracellular and extracellular components across cell membrane, through which cytosol could be pumped out and transferred to downstream analyses. Some recent reviews discussed these questions from different angles. Traditional single cell analysis calls for sampling inside single cell, like RNA or DNA (Sharma et al., 2018). So far, electroporation is still one of the first choices to transport biomolecules across the membrane into or out of the cell (Napotnik and Miklavcic, 2018). Kim and Lee have reported on the delivery of nanoparticles as intracellular carriers by electroporation (Kim and Lee, 2017). Tay and Melosh have tried the tubular nanostructures for cargo delivery into cells (Tay and Melosh, 2019). More recently, nanopipette has shown great potential in DNA detection *in vitro*, it also demonstrates the ability to sample from nucleoplasm or cytoplasm (Wang et al., 2019). Meanwhile, applications of AFM and FluidFM technologies in molecular and cellular biology have also been reviewed recently, especially in the aspects, such as cellular morphology, cellular mechanics, and manipulation of a single cell (Amarouch et al., 2018; Li et al., 2019). In this review, we focus on some most promising methods for single-cell sampling with nanostructures, such as glass nanopipette, nanostraw, carbon nanotube probes and other nanomaterial. In this context, particular attentions will be paid to their principles, preparations, operations, superiorities and drawbacks, and meanwhile the great potential of nano-materials for single-cell sampling will also be highlighted and prospected.

SINGLE-CELL SAMPLING WITH NANOSTRUCTURES

Nanostraw for Single-Cell Sampling

Nanostraws, a random arrangement of hollow cylinders, were made from a variety of materials, such as alumina (VanDersarl et al., 2012; Cao et al., 2017, 2018; He et al., 2018), silica (Peer et al., 2012), silicon nitride (Huang et al., 2019). Typically, the alumina nanostraws were fabricated using track-etched polycarbonate membranes as the template, which are commercially available with different pore sizes and pore densities. Onto the template, an alumina coating was a uniform coating with atomic layer deposition (ALD), and typically 10–30 nm thick. The deposited alumina forms the nanostraw bodies with the nanopore interiors defining the nanostraw wall thickness. After removing the alumina on the top surface and part of the exposed polymer with reactive ion etching (RIE), the nanostraws were obtained, and then they could be put on top of a microfluidic channel, with cell loaded on the other side. In this way, a number of nanostraws covered by cells would penetrate through cell membranes steadily over extended periods. Thus, molecules in extracellular environment, such as ions or plasmids could diffuse from the microchannel into cytosol. In addition, the dimensions of a nanostraw, such as straw wall thickness, and nanostraw height could be independently tuned through adjustments to the track-etched membrane properties (straw outer diameter and density), as shown in **Figure 1A** (reprinted from VanDersarl et al., 2012). Amazingly, the highly uniform nanostraw has been reported with <5% variations for wall thickness, height, and inner diameters as measured by scanning electron microscope images. The authors found that the dimension was important for this method. Nanostraws with diameter of 100 nm could penetrate cell membranes, while larger ones (250 and 500 nm) couldn't. Also, the cell membrane penetration is a stochastic process with roughly <10% efficiency per nanostraw. Thus, it is very

difficult to achieve an ideal straw density, since there must be a compromise between two competing effects. On the one hand, the lower straw concentrations may lead to lower total molecular flux through the membrane; on the other side, very high nanostraw densities could result in less frequent cell penetration, because there exists a bed-of-nails effect when cells resting on the top of the dense nanostraw forest, which is shown in **Figure 1B** (reprinted from VanDersarl et al., 2012).

As mentioned above, the connection between nanostraws and cytoplasm remains open after the penetration over extended periods. Although, such stable fluidic interfaces can facilitate temporal control of their delivery, it is also at risk of leakage of proteins and ions through these channels. Melosh's group developed an electroporation system with similar nanostraw array of large diameter (250 nm), which could not penetrate cell membrane itself. Thus, the fluidic interfaces are temporarily established once the voltage applied, followed by self-healing after removal of the voltage (Xie et al., 2013), as shown in **Figures 1C,D** (reprinted from Cao et al., 2017, 2018, respectively). Biomolecule delivery could be achieved by diffusion via the nanostraws and improved by electrophoresis during pulsing. This system could not only offer excellent spatial, temporal, and dose control for the biomolecule delivery, but also provide high-yield co-transfection and sequential transfection efficiency (Xie et al., 2013). In principle, substance exchange goes both directions once the fluidic interfaces established. From another point of view, the leakage of cytosolic contents could also be regarded as sampling (Cao et al., 2017; He et al., 2018). Melosh's group reported the nanostraws were used as time-resolved, longitudinal extraction method for intracellular proteins and mRNA. In a typical extraction process using this so-called nanostraw extraction system, approximately 5–10% of both big molecules, like proteins and mRNA, and small molecules could diffuse from cell passively, through the nanostraws, and into the extraction solution in microfluidic channels, which is on the other side of the nanostraws. In this way, repeat extractions from the same cell or cell population were demonstrated, and conventional methods, such as fluorescence, enzymatic assays (ELISA), and quantitative real-time PCR, could be used to analyze the extracted contents (Cao et al., 2017). The spatial resolution of the nanostraw extraction system was realized by microfluidic channel design, yet subcellular resolution was not available since the sample spots, and nanostraws-cell interfaces were at a stochastic distribution. It has been estimated that underneath a typically $10\,\mu m \times 10\,\mu m$ adherent cell could be tens to hundreds of nanostraws with only a small portion of them communicating with cytosol stochastically (VanDersarl et al., 2012; Cao et al., 2017). Meanwhile, direct sample extraction from cargo delivery to cell nucleus are still challenged.

In a recent report, the gold coated nanostraws were reported for on-demand intercellular delivery of single particles into a single cell, and they were shaped on a Si_3N_4 substrate which was embedded in a polydimethylsiloxane (PDMS) chamber. The gold coated nanostraws acted simultaneously as nanoelectrodes for electroporation and fluidic interface for delivery of nanoparticles, and also as plasmonic antennas for the enhancement of Raman signals. When illuminated with laser, the gold coated nanostraws were capable of confinement and enhancement of electromagnetic fields, and able to discern the SERS signals from a single nanoparticle upon flowing through the nanostraws. By this means, the delivery of single nanoparticle into a selected cell was accurately counted by SERS (Huang et al., 2019).

Nanoneedle for Single-Cell Sampling

Atomic force microscopy (AFM), a very powerful tool for surface image, and it can be used to scan the sample by a pyramidal tip on a flexible cantilever spring. While the tip is scanning over the sample surface, the interaction forces between the tip and the sample surface distort the cantilever. The distortion is monitored with a laser beam, and could be deduced into topographic image vs. relative position of the tip (Amarouch et al., 2018). Cargo, such as plasmid DNA or dyes, could be deliver into cell by loading them onto normal (Cuerrier et al., 2007) or sharpened AFM tips before its penetration through cell membrane (Obataya et al., 2005; Silberberg et al., 2013). This sharpened tip has more advantages, not only can it access the cytosol, but also penetrate through the nuclear membrane without chromosomal DNA damage or apoptosis, once it is effectively inserted through the plasma membrane of a living cell (Ryu et al., 2013). Moreover, sharpened AFM tips modified with specific antibodies could be used to assess the unbinding forces during evacuation of the tip from the cell. Thus, specific mechanical interactions between the antibody-functionalized tip and the intracellular components could be measured and used for cell screen (Silberberg et al., 2013, 2014; Li et al., 2017, 2019).

AFM has also been used for imaging cell surfaces, estimating cell membrane properties, such as elasticity and viscosity. When decorated with plasmid DNA encoding for the fluorescent protein EGFP, the AFM tip could penetrate through the cell membrane and delivery the plasmid DNA into cell (Cuerrier et al., 2007). Ultrathin probes, such as modified AFM tips, could be developed as tools for single cell biopsy at nanoscale resolution in conjugation with AFM (Han et al., 2005). In this system, the nanoneedles were fabricated from AFM tips using focused ion beam (FIB) etching, with a diameter of 200 nm and a length of 6–8 μm. A molecular force probe was used for the manipulation and force measurement of the nanoneedle (Obataya et al., 2005). When inserting the nanoneedle into the cell, the preloaded plasmid DNA could be detached from the needle surface in about 5 min. This technique has advantages regarding accurate force feedback, which is helpful to judge the critical timing of the cell membrane puncture. Due to the small size and the high aspect ratio, the nanoneedle is a potent tool for the single cell inspection. For example, when antibody-immobilized nanoneedle was inserted into living cells, specific intracellular cytoskeletal proteins could be probed. While the inserting nanoneedle being retracted, the mechanical force to release the binding complexes between the antibody and target proteins could be measured, and in this way the intermediate filament protein, neurofilament and nestin in mouse embryonic carcinoma P19 cells or rat primary hippocampal cells were successfully detected (Mieda et al., 2012; Silberberg et al., 2013). In these cases, the penetration into the nucleus affect neither the

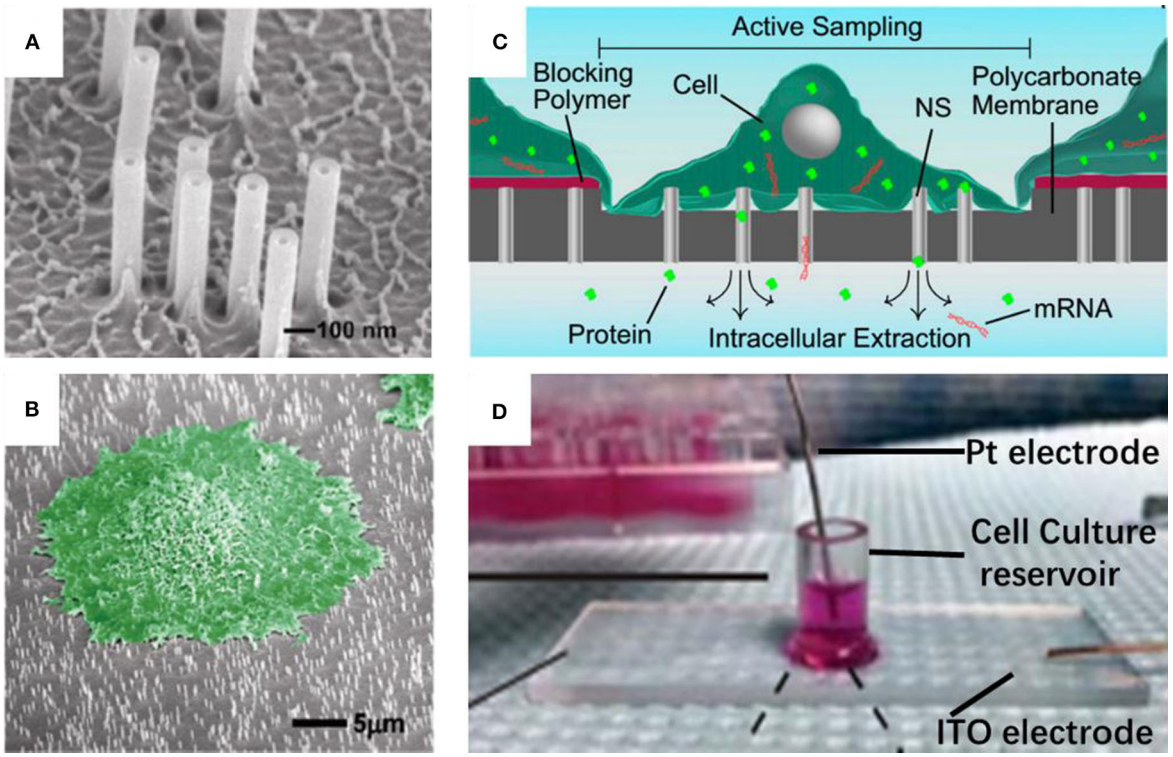

FIGURE 1 | Scanning electron micrograph for nanostraw membrane **(A)** and critical point dried cell cultured on nanostraw membrane (**B**, false colored green); schematic **(C)** and device pictures **(D)** for nanostraw electroporation system.

doubling time of the cells nor double-stranded DNA (Ryu et al., 2013).

By a similar strategy, antibody-functionalized nanoneedle array was fabricated to target individual cells, and separate them from a mixed population of cells on a substrate (Kawamura et al., 2017). The nanoneedle array comprised of 10,000 nanoneedles was fabricated using top-down MEMS (Micro-Electro-Mechanical System) technique with each nanoneedle $<$200 nm diameter and more than 20 μm long. As a proof-of-concept demonstration, nanoneedles were modified with antibody. When this nanoneedle array was inserting into and retracting from the substrate adhesion cells mixture, target cells would be lifted out from the cell mixture due to the specific interactions between the nanoneedle and specific intracellular proteins inside the target cells. Although separation efficiency should be improved before practical applications, this approach is compatible with intact living cells. In the cell separation process, it does not need to transform the cells for fluorescent visualization of target protein expression as required by conventional methods, thus it does not need to remove fluorescently labeled antibodies either, since the antibodies are already covalently attached to the nanoneedle for the intracellular marker proteins. In this way, Yang and co-workers developed a method for the evaluation of enzyme activity using a live cell sandwich method with live cells between two silicon nanoneedle arrays. The substrate nanoneedle array was used to immobilized the cells, and the second nanoneedle array was covalently modified with enzymatic substrates. When the arrays were penetrated into cell membrane, these substrates interact with cytoplasmic enzymes, and the changes were monitored by conventional methods, such as fluorescence microscopy and mass spectrometry (Na et al., 2013).

Fluidic force microscopy (FluidFM), is another powerful tools for the single cell sampling, which combines a conventional AFM with microchannel cantilevers connected to a pressure controlled fluidic circuit, and able to manipulate liquid locally (Guillaume-Gentil et al., 2014; Amarouch et al., 2018). Quantitative extraction of samples from single cells with subcellular spatiotemporal control was demonstrated using FluidFM, and meanwhile, the soluble molecules withdrawn from the cytoplasm or nucleus could be analyzed by transferring the extract sample fluid to TEM, enzyme activity assays, and qPCR (Guillaume-Gentil et al., 2014; Amarouch et al., 2018). The activities of the extract samples were monitored with microscopy, and the volumes were calculated from the size of occupied microchannels with typical volumes ranging from 0.1 to 7.0 in a single cell, as shown in **Figure 2** (reprinted from Guillaume-Gentil et al., 2016).

The aperture of the FluidFM probe is in the range of several tens to a few hundred nanometers. After shrinking the pore size down to a few nanometers provides extra function, the nanopore has been widely used for the single molecule detection and ion current recording. This was done by construction of a nanopore with diameter as small as 5 $\pm$ 1 nm onto the flattened apex of FluidFM probe, so called force-controlled scanning nanopore

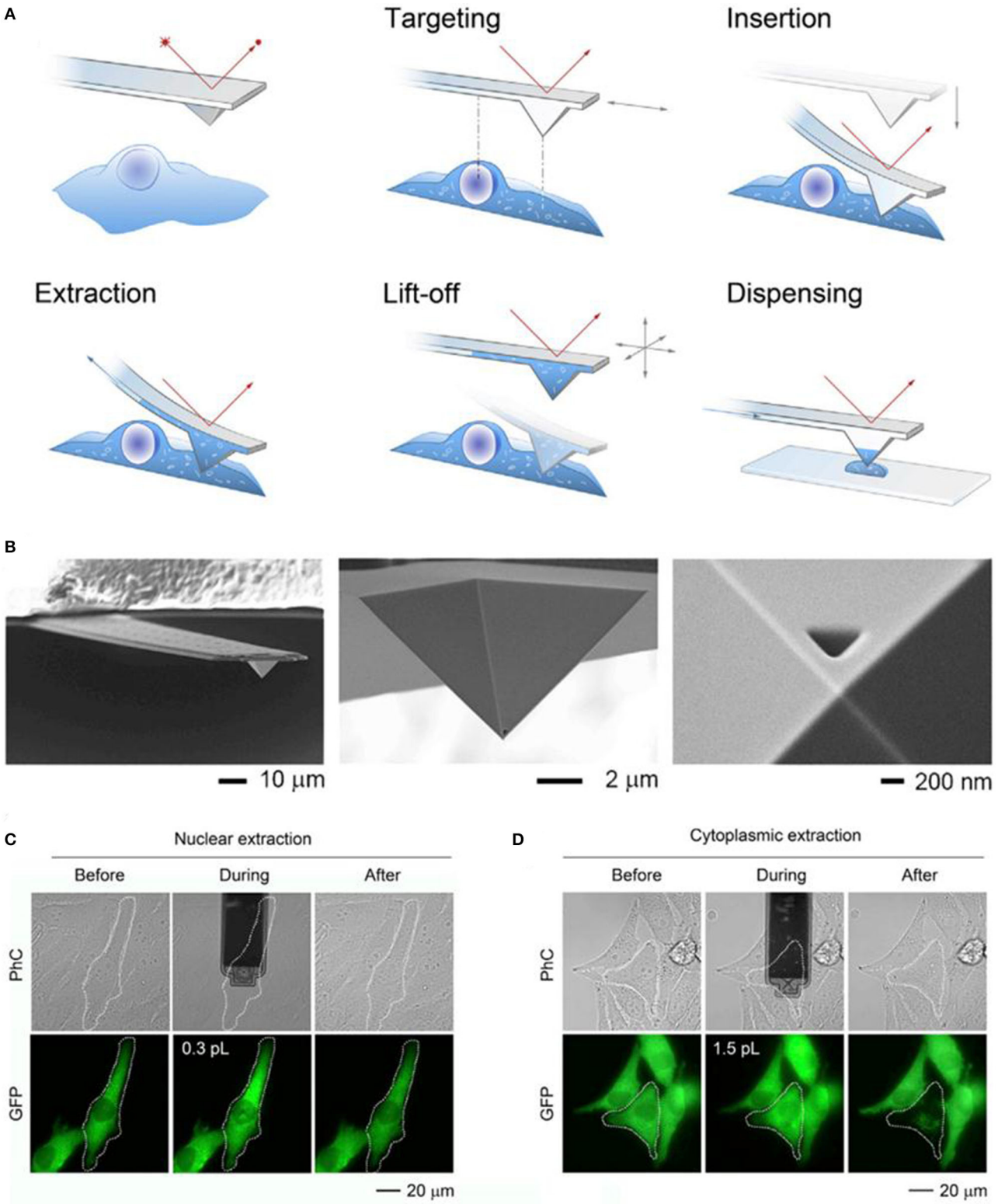

FIGURE 2 | Schematic of the FluidFM based extraction procedure **(A)** and SEM image of a FluidFM probe **(B)**; phase-contrast (PhC) and fluorescent images with GFP of representative extracts from the nucleus **(C)** and cytoplasm **(D)** of the target cells.

microscope. By this means, an integration of solid-state nanopore and AFM was accomplished, and it can be used to stochastically sense the secreted molecules, and the activity of ion channels in arbitrary locations both inside and outside a cell (Aramesh et al., 2019). Besides surface imaging, the detection and delivery of biomolecules on-demand, the introduced system also facilitates flexibility and controllable mechanical engagement with the target samples. In this sense, the translocation of biomolecules and ions through the nanopore can be observed in living cells and in real time, although some of the translocation signals could not be assigned to specific events, since the pristine nanopore detected signals are non-specific without further modification of the nanopore or construction of detectable specific interactions between target molecules and tags.

Nanopipette for Single-Cell Sampling

Nanopipettes, with a conical shape and submicron to nanoscale size of the pore opening at the tip, are suitable for delivery of biomolecules to and/or from a single living cell, or as a probe for the cells. Nanopipettes are usually made from glass capillary by heating to soften the middle part, and then pulling it apart into twin nanopipettes. The most prevalent equipment is laser-based micropipette puller (P-2000, Sutter Instrument). Typically, a glass capillary loaded into the puller bar is laser-soften to a certain degree before hard pull, and the capillary is then separated into twin glass nanopipettes. This machine has five parameters to control the heat, pull, and timing in order to adjust the shape of the as-prepared nanopipettes: HEAT, the output power of the laser, and consequently the amount of energy supplied to the glass capillary; FILAMENT, the scanning pattern of the laser beam that is used to supply HEAT to the glass capillary; VELOCITY, the velocity at which the puller bar must be moving before the hard pull is executed; DELAY, the timing of the start of the hard pull relative to the deactivation of the laser; and PULL, the force of the hard pull. Although there are slight differences between instruments, nanopipettes with diameters of 10–300 nm can be successfully prepared by synergistically adjusting these five parameters. In terms of material selection, borosilicate glass or quartz are usually used to prepare nanopipettes, since quartz is capable of producing stronger and smaller tips, and borosilicate glass is easier to control and cheaper.

Structurally, the cavity of the nanopipettes could act as passage, through which many biological molecules, such as DNA and proteins, could be pressure or electrophoresis driven in and out of single cell cytosol. Conventional methods of cell injection employ micropipettes with tip diameters of 0.5–5 μm that is incompatible to puncture most cells. While nanopipette has a typical tip size <200 nm, there are several advantages, such as little disruption to the cell membrane structure and function, and ease to control the amount of interested substances. As for the driving force of the substance in and out of the cell, concentration gradient, potential difference, electroosmotic flow, electrophoresis and electrowetting are potential options in principle. Pressure, for most of the cases, is out of service for such small orifice, since the pressure applied to drive the substance is beyond the mechanical strength of the glass tip, result in the nanopipette to crush.

Mirkin's group had demonstrated that it was possible to control fluid motion electrochemically using nanopipette, as shown in **Figure 3A** (reprinted from Laforge et al., 2007). They filled the nanopipette with 1, 2-dichloroethane (DCE) and dipped it into aqueous solution, with one reference electrode inside the nanopipette and the other one in the aqueous solution. The potential difference between the two liquid phases could be controlled by applied voltage between these two electrodes, and then, the voltage may change the surface tension through the liquid/liquid interface, and in turn induce the corresponding force to evoke the liquid flow into/out of the nanopipette. When the negative potential is applied to the inner (organic) solution, the shape of the meniscus will change at the interface of the two liquids, and then cause water to enter the pipette. On the contrary, when a sufficiently positive potential is applied to the inner reference electrode, it will induce the expulsion of water (Laforge et al., 2007). With this tool, so called electrochemical atto-syringe, some dyes can be delivered, while they cannot cross a mammalian cell membrane, into a single cell. Volumes that can be manipulated may depend strongly on the orifice radius, and the duration and amplitude of the potential applied. The amount of liquid manipulated could be estimated by calculating the volume of the filled part of the nanopipette, or the corresponding current-voltage curves. At this stage, injection position distinction between cytoplasm and nucleus had not been reported. Extraction cytosol fluid from multiple locations in the same cell could be realized for mapping the various mRNA species to specific subcellular location (Toth et al., 2018).

A multiwalled carbon nanotube, with length of about 50–60 μm and 50 to more than 200 nm outer diameter, was fixed at the tip of micropipette as carbon-nanotube-based endoscope for interrogating the single cell (Singhal et al., 2011). In this case, the intracellular environments even organelles can be probed by the endoscope, and achieve a spatial resolution of about 100 nm without disrupting the cell. When magnetic nanoparticles are used to fill the nanotube, nanoparticles and atto-liter volumes of fluids can be remotely transferred to and from precise locations through the endoscope.

Scanning ion conductance microscopy (SICM), another scanning probe, has gained increasing attention, and can be used to image surfaces of living cells with a high spatial and temporal resolution. An electrolyte filled nanopipette could be used as the probe of SICM (Bulbul et al., 2018). When voltage bias applied, ions flow through the nanopipette orifice. As the nanopipette is scanning over a surface, the magnitude of the ion current may change which reflects the topography of the sample. In this sense, nanopipette could be used as a navigation probe close to target cell and fluidic interface for delivery or extraction of molecules interested into or from target cell. Pourmand's group achieved this by continuous sampling of intercellular contents from single cell (Actis et al., 2014). Subcellular resolution of sample was realized for the isolation of small subpopulations of mitochondria from single living cells. In this way, mutant mitochondrial genomes in those samples could be quantified with high throughput sequencing technology.

One of these reference electrodes could be integrated by sputter coating a thin layer of Ir/Pt outside the nanopipette

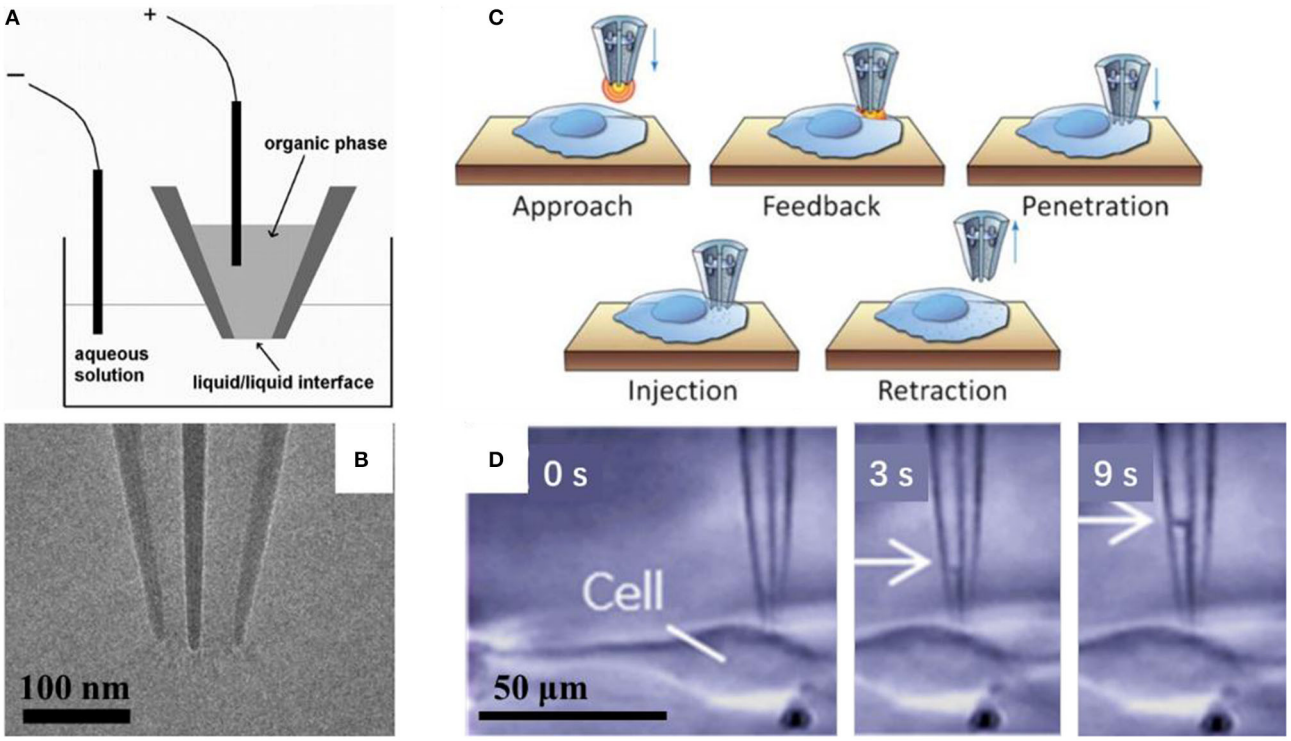

FIGURE 3 | Scheme of the electrochemical attosyringe **(A)**; TEM image **(B)** and illustration of cell surface detection, penetration and injection **(C)**, and sequential micrographs acquired during cytosol collection **(D)** using a double-barrel nanopipette.

(Shekaramiz et al., 2016, 2018). In this case, the whole system has a compact size with no influence on its performances. Shekaramiz and co-workers used this system to transfect single cells. The nanopipette had a tip opening about 140 nm, filled with 1, 2-dichloroethane (DCE), and inserted an Ag/AgCl electrode inside. When the Ag/AgCl electrode was applied to positive bias on the outer Ir/Pt coating layer, small volumes from a single cell could be injected or aspirated depending on the magnitude of voltages applied. In this case, a positive bias larger than 0.5 V results in aspiration, while <0.5 V results in injection. The femtoliter volume of liquid manipulated was calibrated with respect to applied voltages. Typically, an estimated 1,800 molecules of 3.5 kb pmaxGFP plasmid were injected into cells, and could cause cells to express green fluorescent protein (GFP) in 48 h after the injection. The transfection efficiency was evaluated to be close to 100%. With similar system, intracellular proteins could be detected. The cytoplasm could be extracted and deposited onto a coverslip. The quantification was realized by comparing the fluorescent intensity of sample vs. pure protein solutions (Shekaramiz et al., 2018).

Pourmand's group demonstrated that the double-barrel nanopipette based single cell injection, as shown in **Figure 3C** (reprinted from Seger et al., 2012). The double-barrel nanopipettes, as shown in **Figure 3B** (reprinted from Nadappuram et al., 2019), are fabricated with almost the same process with common single barrel nanopipettes, except for a glass capillary tube with a partition in the middle, in other words, with a θ shape cross section. Therefore, the requirement for an external reference electrode is not necessary by using the double-barrel nanopipette for injection. In this case, two reference electrodes insert into each barrel. The distance between the tip and cell surface could be detected by employing one barrel as part of a SICM. When close enough to the cell, the nanopipette can be precisely put in the cell cytoplasm, and then the target material can be transported by biasing one barrel against the other. With an extra barrel, the authors achieved the selective delivery of two distinct fluorescent dyes, even at varying ratios into the same single cell without cross-talk, and each single barrel was loaded with a different dye. While the voltage applied is rather high, in the range of 10–20 V, which may result in the voltage applied across the two orifices, where the resistance is very high, and thus the potential drop is significant there. In turn, it requires the entire injection process <1 min per cell on average, and up to 10 cells can be injected in <5 min (Seger et al., 2012). With similar configuration, evaluating localization of mRNA in a single cell is reported. Also, both aqueous and organic electrolyte solutions could be filled into two barrels in a nanopipette, which were used for SICM and as an electrochemical syringe, respectively. Topography with subcellular resolution, as well as the sample position, was recorded with SICM. Then, the sample was transferred to qPCR analysis to assess cellular status. They demonstrated that mRNA expression depends on cellular position, as shown in **Figure 3D** (reprinted from Nashimoto et al., 2016). With this double

barrel nanopipette, dielectrophoretic trapping of DNA and protein was reported (Nadappuram et al., 2019). This so-called nanotweezer system is comprised of two coplanar semi-elliptical nanopipettes with a dimension of the major and minor axes about 30 nm, which are separated by a 10–20 nm thick partition inherited from the θ shape capillary. With this nanotweezer, manipulation and extraction of DNA and RNA in a single living cell were demonstrated. The authors also envisioned the possible integration of this nanotweezer with SCIM for spatial and temporal quantification of gene expression within a single cell.

Another interesting approach reported, which was named as fluid cell knife (Fluid CK), can be used as a knife to precisely cut off or heal a portion of a single cell in the original adherent culture state. The Fluid CK contains an array of four orthogonal micropipettes. In a typical process, cell lysate was released from one micropipette and drained out from two adjacent ones, forming a local laminar flow. By positioning the laminar flow close enough to a specific area of a target cell, the area covered by the lysate can be precisely "cut off" (Mao et al., 2019). In addition, local operations on target portions of a living single cell could be achieved in its adherent culture state for various types of cells, and also for temporal wound repair.

One of the most prevalent and important applications of nanopipette is single molecule detection. Among them, the most prevalent way was the resistive-pulse sensing (Wang et al., 2013). Like the nanopipette based microinjection system, the prototype device of resistive-pulse sensing is composed of two chambers via the nanopipette. Once a voltage is applied across the nanopore, ions and charged targets or analytes will be induced through the nanosized aperture, and the ion current can be monitored or recorded in this process. When the targets or analytes partially occupying the nanopipette orifice was transferred through a nanopipette, they would usually cause a conductance change and a current change pulse (Wang et al., 2013). Thus, identification of the target molecule or deduction of the interactions of the target molecules could be realized with the nanopipette based on the current-time curve to reflect the frequency, amplitude, and duration of the current pluses. In principle, there is a one-to-one correspondence between the translocation event and the current pulse. In other words, if the current pulse can be resolved in real time and turn the applied potential off at arbitrary time, the number of translocation molecule could be controlled. With this technique coming true, one can expect that a precise number of substances could be injected into or extracted from a single cell at single molecular accuracy (Bulbul et al., 2018; Nadappuram et al., 2019; Wang et al., 2019).

Microfluidic Chip for Single-Cell Sampling

Besides methods mentioned above, some other techniques have also been used for interchanges of molecules between extracellular and intercellular environment. The adherent cells could be operated by nanopipette, however, for suspended cell, microfluidic chip is a good choice. With excellent design and processing capability, the channels in microfluidic chip allow suspended cells to be flowed, immobilized and electroporated. A multiple channel design allows parallel single cell electroporation (Khine et al., 2005). Lee, Choi and coworkers reported a nano-injection system for the delivery of biomolecules into single suspended cells (Yun et al., 2019). The system contained a hybrid (PDMS/glass) microfluidic chip, with microfluidic channel on PDMS and nanoinjection tip on solid glass. In a typical electroporation process, suspended cell was pressure driven in the microfluid channel before reaching and tightly stuck in the trapping zone, where the cell was electroporated by electric field applied through the nanoinjection tip. After electroporation, the processed and original cells were pressure driven into different channels to separated harvesting chambers. A semiquantitative dose control was accomplished by electric flied modulation of the electrokinetic pumping. In addition, the cell viability of this system is >95%, with a gene expression efficiency of up to 51%.

CONCLUSION AND PERSPECTIVES

In recent years, great progress has been made in the field of single cell sampling and some impressive cases have been reported. Some of the technological advances are representative and demonstrated to play powerful roles in biological and medical research. Despite their own advantages and great progress made, none of these approaches above can solve all those problems alone. Firstly, nanostaw sampling is high-throughput, and can be used to study multiple cells simultaneously, while encounter difficulties when it is used for the inspection on specific single cell, or sampling from specific sites of cells, and key factors include the diameter and density of the nanostraws in terms of the penetration validity and cell viability. Although optimality has been given in some cases, the universality has yet to be achieved on a much broader scale. Secondly, the nanopipette, AFM and FluidFM are suitable for targeting specific single cells at the cost of throughput at the same time, and the position distinctions between cytoplasm and nucleus could be easily realized with the aid of microscope. The nanopipette has little cell damage since the outer diameter of the nanopipette could be directly laser pulled down to <10 nm, while AFM or FluidFM tips at this size is on the premise of sophisticated nano-processing technology. In practice, the preparation of laser pulled nanopipette is easy and low cost. The diameter fluctuates within a certain range, and may be problematic for small diameters (<10 nm) at the cost of yield. Cell surface morphology could be mapped by AFM, FluidFM and nanopipette based SICM, yet the force feedback between the tip and the sample is an unique virtue of AFM and FluidFM. With this advantage, additional information about biomolecular interactions can be obtained at the same time of sampling.

With the rapid development of nanotechnology, one could expect the emergence of more nanomaterials and more advanced processing nano-technologies, and their applications for single cell investigation. Dimensions down to a few nanometer or even smaller, such nanomaterial would be compatible with most biomolecules on the same order of magnitude. More sophisticated functionalization with these materials would facilitate to screen the biomolecules or identify their interactions more specifically from their complex environment. The instruments developed

from new principles, from upgrades of specificity of present techniques, or from the collaboration of present instruments or techniques, would provide more possibility of inspection on the biomolecules and their interactions from a more accurate temporal-spatial resolution *in-situ* and on-time.

AUTHOR CONTRIBUTIONS

MG and JJ conceived, designed, and supervised the manuscript. XX collected the literatures, analyzed the data, and wrote the manuscript. All authors reviewed and approved the final manuscript.

ACKNOWLEDGMENTS

We are grateful for financial support from the National Natural Science Foundation of China (Nos. 21305136, 21675147, and 21974097), Special Research Project of Wuyi University for COVID-19 Epidemic Prevention and Control (2020FKZX03), and Science and Technology Bureau of Jiangmen (2019030102360012639).

REFERENCES

Actis, P., Maalouf, M. M., Kim, H. J., Lohith, A., Vilozny, B., Seger, R. A., et al. (2014). Compartmental genomics in living cells revealed by single-cell nanobiopsy. *ACS Nano* 8, 546–553. doi: 10.1021/nn405097u

Amarouch, M. Y., El Hilaly, J., and Mazouzi, D. (2018). AFM and FluidFM technologies: recent applications in molecular and cellular biology. *Scanning* 2018:7801274. doi: 10.1155/2018/7801274

Aramesh, M., Forro, C., Dorwling-Carter, L., Luechtefeld, I., Schlotter, T., Ihle, S. J., et al. (2019). Localized detection of ions and biomolecules with a force-controlled scanning nanopore microscope. *Nat. Nanotechnol.* 14, 791–798. doi: 10.1038/s41565-019-0493-z

Bulbul, G., Chaves, G., Olivier, J., Ozel, R. E., and Pourmand, N. (2018). Nanopipettes as monitoring probes for the single living cell: state of the art and future directions in molecular biology. *Cells* 7:55. doi: 10.3390/cells7060055

Cao, Y., Chen, H., Qiu, R., Hanna, M., Ma, E., Hjort, M., et al. (2018). Universal intracellular biomolecule delivery with precise dosage control. *Sci. Adv.* 4:eaat8131. doi: 10.1126/sciadv.aat8131

Cao, Y., Hjort, M., Chen, H., Birey, F., Leal-Ortiz, S. A., Han, C. M., et al. (2017). Nondestructive nanostraw intracellular sampling for longitudinal cell monitoring. *Proc. Natl. Acad. Sci. U.S.A.* 114, E1866–E1874. doi: 10.1073/pnas.1615375114

Cuerrier, C. M., Lebel, R., and Grandbois, M. (2007). Single cell transfection using plasmid decorated AFM probes. *Biochem. Biophys. Res. Commun.* 355, 632–636. doi: 10.1016/j.bbrc.2007.01.190

Guillaume-Gentil, O., Grindberg, R. V., Kooger, R., Dorwling-Carter, L., Martinez, V., Ossola, D., et al. (2016). Tunable single-cell extraction for molecular analyses. *Cell* 166, 506–516. doi: 10.1016/j.cell.2016.06.025

Guillaume-Gentil, O., Potthoff, E., Ossola, D., Franz, C. M., Zambelli, T., and Vorholt, J. A. (2014). Force-controlled manipulation of single cells: from AFM to FluidFM. *Trends Biotechnol.* 32, 381–388. doi: 10.1016/j.tibtech.2014.04.008

Gupta, S. D., and Sachs, Z. (2017). Novel single-cell technologies in acute myeloid leukemia research. *Transl. Res.* 189, 123–135. doi: 10.1016/j.trsl.2017.07.007

Han, S., Nakamura, C., Obataya, I., Nakamura, N., and Miyake, J. (2005). Gene expression using an ultrathin needle enabling accurate displacement and low invasiveness. *Biochem. Biophys. Res. Commun.* 332, 633–639. doi: 10.1016/j.bbrc.2005.04.059

He, G., Yang, C., Hang, T., Liu, D., Chen, H.-J., Zhang, A.-H., et al. (2018). Hollow nanoneedle-electroporation system to extract intracellular protein repetitively and nondestructively. *ACS Sens.* 3, 1675–1682. doi: 10.1021/acssensors.8b00367

Higgins, S. G., and Stevens, M. M. (2017). Extracting the contents of living cells. *Science* 356, 379–380. doi: 10.1126/science.aan0228

Huang, J.-A., Caprettini, V., Zhao, Y., Melle, G., Maccaferri, N., Deleye, L., et al. (2019). On-demand intracellular delivery of single particles in single cells by 3D hollow nanoelectrodes. *Nano Lett.* 19, 722–731. doi: 10.1021/acs.nanolett.8b03764

Kawamura, R., Miyazaki, M., Shimizu, K., Matsumoto, Y., Silberberg, Y. R., Sathuluri, R. R., et al. (2017). A new cell separation method based on antibody-immobilized nanoneedle arrays for the detection of intracellular markers. *Nano Lett.* 17, 7117–7124. doi: 10.1021/acs.nanolett.7b03918

Khine, M., Lau, A., Ionescu-Zanetti, C., Seo, J., and Lee, L. P. (2005). A single cell electroporation chip. *Lab. Chip.* 5, 38–43. doi: 10.1039/b408352k

Kim, K., and Lee, W. G. (2017). Electroporation for nanomedicine: a review. *J. Mater. Chem. B* 5, 2726–2738. doi: 10.1039/C7TB00038C

Laforge, F. O., Carpino, J., Rotenberg, S. A., and Mirkin, M. V. (2007). Electrochemical attosyringe. *Proc. Natl. Acad. Sci. U.S.A.* 104, 11895–11900. doi: 10.1073/pnas.0705102104

Li, M., Dang, D., Xi, N., Wang, Y., and Liu, L. (2017). Nanoscale imaging and force probing of biomolecular systems using atomic force microscopy: from single molecules to living cells. *Nanoscale* 9, 17643–17666. doi: 10.1039/C7NR07023C

Li, M., Xi, N., Wang, Y., and Liu, L. (2019). Advances in atomic force microscopy for single-cell analysis. *Nano Res.* 12, 703–718. doi: 10.1007/s12274-018-2260-0

Mao, S., Zhang, Q., Liu, W., Huang, Q., Khan, M., Zhang, W., et al. (2019). Chemical operations on a living single cell by open microfluidics for wound repair studies and organelle transport analysis. *Chem. Sci.* 10, 2081–2087. doi: 10.1039/C8SC05104F

Mieda, S., Amemiya, Y., Kihara, T., Okada, T., Sato, T., Fukazawa, K., et al. (2012). Mechanical force-based probing of intracellular proteins from living cells using antibody-immobilized nanoneedles. *Biosens. Bioelectron.* 31, 323–329. doi: 10.1016/j.bios.2011.10.039

Na, Y.-R., Kim, S. Y., Gaublomme, J. T., Shalek, A. K., Jorgolli, M., Park, H., et al. (2013). Probing enzymatic activity inside living cells using a nanowire–cell "sandwich" assay. *Nano Lett.* 13, 153–158. doi: 10.1021/nl3037068

Nadappuram, B. P., Cadinu, P., Barik, A., Ainscough, A., Devine, M. J., Kang, M., et al. (2019). Nanoscale tweezers for single-cell biopsies. *Nat. Nanotechnol.* 14, 80–88. doi: 10.1038/s41565-018-0315-8

Napotnik, T. B., and Miklavcic, D. (2018). *In vitro* electroporation detection methods - an overview. *Bioelectrochemistry* 120, 166–182. doi: 10.1016/j.bioelechem.2017.12.005

Nashimoto, Y., Takahashi, Y., Zhou, Y. S., Ito, H., Ida, H., Ino, K., et al. (2016). Evaluation of mRNA localization using double barrel scanning ion conductance microscopy. *ACS Nano* 10, 6915–6922. doi: 10.1021/acsnano.6b02753

Obataya, I., Nakamura, C., Han, S., Nakamura, N., and Miyake, J. (2005). Nanoscale operation of a living cell using an atomic force microscope with a nanoneedle. *Nano Lett.* 5, 27–30. doi: 10.1021/nl0485399

Peer, E., Artzy-Schnirman, A., Gepstein, L., and Sivan, U. (2012). Hollow nanoneedle array and its utilization for repeated administration of biomolecules to the same cells. *ACS Nano* 6, 4940–4946. doi: 10.1021/nn300443h

Ryu, S., Kawamura, R., Naka, R., Silberberg, Y. R., Nakamura, N., and Nakamura, C. (2013). Nanoneedle Insertion into the Cell Nucleus does not induce double-strand breaks in chromosomal DNA. *J. Biosci. Bioeng.* 116, 391–396. doi: 10.1016/j.jbiosc.2013.03.022

Seger, R. A., Actis, P., Penfold, C., Maalouf, M., Vilozny, B., and Pourmand, N. (2012). Voltage controlled nano-injection system for single-cell surgery. *Nanoscale* 4, 5843–5846. doi: 10.1039/c2nr31700a

Sharma, S., Gioia, L., Abe, B., Holt, M., Costanzo, A., Kain, L., et al. (2018). Using single cell analysis for translational studies in immune mediated diseases: opportunities and challenges. *Mol. Immunol.* 103, 191–199. doi: 10.1016/j.molimm.2018.09.020

Shekaramiz, E., Doshi, R., and Wickramasinghe, H. K. (2018). Protein fishing from single live cells. *J. Nanobiotechnol.* 16:67. doi: 10.1186/s12951-018-0395-5

Shekaramiz, E., Varadarajalu, G., Day, P. J., and Wickramasinghe, H. K. (2016). Integrated electrowetting nanoinjector for single cell transfection. *Sci. Rep.* 6:29051. doi: 10.1038/srep29051

Silberberg, Y. R., Kawamura, R., Ryu, S., Fukazawa, K., Ishihara, K., and Nakamura, C. (2014). Detection of microtubules *in vivo* using antibody-immobilized nanoneedles. *J. Biosci. Bioeng.* 117, 107–112. doi: 10.1016/j.jbiosc.2013.06.019

Silberberg, Y. R., Mieda, S., Amemiya, Y., Sato, T., Kihara, T., Nakamura, N., et al. (2013). Evaluation of the actin cytoskeleton state using an antibody-functionalized nanoneedle and an AFM. *Biosens. Bioelectron.* 40, 3–9. doi: 10.1016/j.bios.2012.06.044

Singhal, R., Orynbayeva, Z., Kalyana Sundaram, R. V., Niu, J. J., Bhattacharyya, S., Vitol, E. A., et al. (2011). Multifunctional carbon-nanotube cellular endoscopes. *Nat. Nanotechnol.* 6, 57–64. doi: 10.1038/nnano.2010.241

Tay, A., and Melosh, N. (2019). Nanostructured materials for intracellular cargo delivery. *Acc. Chem. Res.* 52, 2462–2471. doi: 10.1021/acs.accounts.9b00272

Toth, E. N., Lohith, A., Mondal, M., Guo, J., Fukamizu, A., and Pourmand, N. (2018). Single-cell nanobiopsy reveals compartmentalization of mRNAs within neuronal cells. *J. Biol. Chem.* 293, 4940–4951. doi: 10.1074/jbc.M117.800763

VanDersarl, J. J., Xu, A. M., and Melosh, N. A. (2012). Nanostraws for direct fluidic intracellular access. *Nano Lett.* 12, 3881–3886. doi: 10.1021/nl204051v

Wang, Y. X., Kececi, K., Mirkin, M. V., Mani, V., Sardesai, N., and Rusling, J. F. (2013). Resistive-pulse measurements with nanopipettes: detection of Au nanoparticles and nanoparticle-bound anti-peanut IgY. *Chem. Sci.* 4, 655–663. doi: 10.1039/C2SC21502K

Wang, Z., Liu, Y., Yu, L., Li, Y., Qian, G., and Chang, S. (2019). Nanopipettes: a potential tool for DNA detection. *Analyst* 144, 5037–5047. doi: 10.1039/C9AN00633H

Xie, X., Xu, A. M., Leal-Ortiz, S., Cao, Y., Garner, C. C., and Melosh, N. A. (2013). Nanostraw-electroporation system for highly efficient intracellular delivery and transfection. *ACS Nano* 7, 4351–4358. doi: 10.1021/nn400874a

Yun, C.-K., Hwang, J. W., Kwak, T. J., Chang, W.-J., Ha, S., Han, K., et al. (2019). Nanoinjection system for precise direct delivery of biomolecules into single cells. *Lab. Chip.* 19, 580–588. doi: 10.1039/C8LC00709H

Conflict of Interest: The authors declare that the research was conducted in the absence of any commercial or financial relationships that could be construed as a potential conflict of interest.

frontiers in Chemistry

ORIGINAL RESEARCH
published: 29 September 2020
doi: 10.3389/fchem.2020.580022

Efficient White Electrochemiluminescent Emission From Carbon Quantum Dot Films

Jonathan Ralph Adsetts[1], *Ruizhong Zhang*[1,2], *Liuqing Yang*[1], *Kenneth Chu*[1], *Jonathan Michael Wong*[1], *David A. Love*[3] *and Zhifeng Ding*[1]*

[1] Department of Chemistry, The University of Western Ontario, London, ON, Canada, [2] Tianjin Key Laboratory of Molecular Photoelectronic Sciences, Department of Chemistry, Tianjin University, Tianjin, China, [3] Rosstech Signal Inc., Orillia, ON, Canada

Carbon quantum dots (CQDs) were manufactured from citric acid and urea in a gram-scale synthesis with a controlled size range between 1. 5 and 23.8 nm. The size control was realized by varying volume of the precursor solution in a hydrothermal synthesis method. The prepared CQDs were investigated using electrochemiluminescence (ECL) spectroscopy at interfaces of their electrode films and electrolyte solution containing coreactants rather than conventional optoelectronic tests, providing an in-depth analysis of light-emission mechanisms of the so-called half-cells. ECL from the CQD films with TPrA and $K_2S_2O_8$ as coreactants provided information on the stability of the CQD radicals in the films. It was discovered that $CQD^{\bullet-}$ has a powerful electron donating nature to sulfate radical to generate ECL at a relative efficiency of 96% to the $Ru(bpy)_3Cl_2/K_2S_2O_8$ coreactant system, indicating a strong performance in light emitting applications. The smaller the CQD particle sizes, the higher the ECL efficiency of the film interface, most likely due to the increased presence of surface states per mass of CQDs. Spooling ECL spectroscopy of the system revealed a potential-dependent light emission starting from a deep red color to blue-shifted intensity maximum, cool bright white emission with a correlated color temperature of 3,200 K. This color temperature is appropriate for most indoor lighting applications. The above ECL results provide information on the performance of CQD light emitters in films, permitting preliminary screening for light emitting candidates in optoelectronic applications. This screening has revealed CQD films as a powerful and cost-effective light emitting layer toward lighting devices for indoor applications.

Keywords: carbon quantum dots, electrochemiluminescence (ECL), light emitting electrochemical cell (LEC or LEEC), lighting, half cells

OPEN ACCESS

Edited by:
Yanmin Long,
Jianghan University, China

Reviewed by:
Yuwu Chi,
Fuzhou University, China
Guobao Xu,
Chinese Academy of Sciences, China

***Correspondence:**
Zhifeng Ding
zfding@uwo.ca

Specialty section:
This article was submitted to Nanoscience, a section of the journal Frontiers in Chemistry

Received: *04 July 2020*
Accepted: *18 August 2020*
Published: *29 September 2020*

Citation:
Adsetts JR, Zhang R, Yang L, Chu K, Wong JM, Love DA and Ding Z (2020) Efficient White Electrochemiluminescent Emission From Carbon Quantum Dot Films. Front. Chem. 8:580022. doi: 10.3389/fchem.2020.580022

INTRODUCTION

Light emitting diodes (LEDs) have been at the forefront of lighting technology recently due to their decreased energy consumption over compact fluorescent and incandescent lighting technologies. LEDs are conventionally created by depositing many subsequent layers on a substrate in an inert atmosphere (Zhang et al., 2013; Gao, 2018; Kusamoto and Nishihara, 2018; Yang et al., 2019). Reducing the number of layers and removing the need for an inert atmosphere can drastically

reduce manufacturing costs and operating voltages. To this end, light emitting electrochemical cells (LECs or LEECs) have gained interest. LECs conventionally comprise of two electrodes sandwiching a light-emitting layer that is responsible for both charge transport and light emission (Fresta and Costa, 2017). The light-emitting layer typically consists of a polymer and a salt with an incorporated light emitter which organizes itself into a p-i-n junction when an external bias is applied (Gao, 2018). The polymer electrolyte reduces bulk and contact resistance over LEDs, allowing for air-stable and thicker electrodes. The reduced potentials and simpler device structure allow for cost-effective manufacturing of energy efficient lighting sources.

Developing LEC technology as a consumer product requires research efforts into analyzing the light emitting layer for its polymer consistency, ion rearrangement efficiency, and electron and hole transportation for radiative recombination. Preeminently, a light emitter with poor electron and hole accepting properties will not efficiently radiatively recombine in an LEC, thus not producing substantial light. To understand the solid-state electron and hole transport mechanisms in light emitters, we propose using electrochemiluminescence (ECL) spectroscopy. ECL spectroscopy effectively allows electron and hole transport mechanisms to be studied independently in a light emitting material, as well as the efficiency and characteristics of the resulting radiative recombination for both electron and hole mechanisms. Studying these processes separately allows for a more fundamental understanding of the overall process of light emission from LECs, which allows the light emission to be improved upon.

An attractive light emitting material for use in LECs is carbon quantum dots (CQDs) due to efficient visible light emissions with tunable band gaps (Yuan et al., 2018; Qin et al., 2019; Chen et al., 2020a). First discovered in 2004 (Xu et al., 2004), CQDs are small sp^2 and sp^3 containing carbon particles that have been defined as having sizes below 20 nm, low toxicity, strong chemical stability and a resistance to photobleaching (Gan et al., 2016; Hu et al., 2019; Chen et al., 2020b). This study will use ECL spectroscopy to evaluate CQD's electron and hole transport mechanisms and the efficiency of radiative recombination for applications in optoelectronic. Further, light emission characteristics are reported and the suitability for indoor lighting applications will be assessed.

MATERIALS AND METHODS

Chemicals and Materials

Citric acid ($C_6H_8O_7$, 99%), urea (OCN_2H_4, 99%), potassium persulfate ($K_2S_2O_8$, 99.99%), sodium phosphate monobasic dehydrate ($NaH_2PO_4{\cdot}2\ H_2O$, ≥99%), and tris(2,2'-bipyridyl)-dichlororuthenium(II) hexahydrate [$Ru(bpy)_3Cl_2{\cdot}6\ H_2O$, 97%] were purchased from Sigma-Aldrich (Mississauga, ON). Sodium phosphate (Na_2HPO_4, anhydrous, ≥99%) was obtained from Caledon Laboratory Chemicals (Georgetown, ON). Potassium chloride (KCl, 99%) was purchased from Alfa Aesar (Ward Hill, MA). Carboxymethylchitosan [$(C_{10}H_{19}NO_6)_n$, 99%] was obtained from Santa Cruz Biotechnology, Inc., (Dallas, TX). Ultrapurewater (18.2 MΩ cm, Milli-Q, Millipore) was used to prepare solutions. All chemical reagents were used as received and stored at room temperature with exception of carboxymethylchitosan stored at 4°C.

CQD Synthesis Procedure

The following synthesis procedure was for CQD20, but all syntheses follow the same general format. 1.0 g citric acid and 2.0 g of urea were combined in 20 mL of Milli-Q water and sonicated for 10 min inside a 100 mL Teflon-lined autoclave were acquired from Shanghai Yuhua Instruments Equipment Co. Ltd, China. The steel autoclave used supports pressures up to 3 MPa. A VWR oven was set to warm up to and hold 160°C for 6 h, then cool down. After returning to room temperature, the autoclaves were removed from the oven and the solution was transferred directly into dialysis bags (Shanghai Yuanye Bio-Technology Co. Ltd, China) with a molecular weight cut-off (MWCO) of 1,000 Da. The solution was left to dialyze for at least 8 h, with the water being changed at least 6 times. The solutions were transferred to 50 mL Falcon tubes (VWR Canada), where a Kimwipe was attached to the top with an elastic band. This Falcon tube containing solution was frozen in liquid nitrogen and placed in a Labconco Lyophilizer at −84°C for at 48 h. The obtained product was light and fluffy and ranged from dark green to brown in color. These CQDs were stored in a refrigerator, sealed with Parafilm, and wrapped in tinfoil to prevent any degradation until use.

CQD Characterization

High resolution transmission electron microscopy (HRTEM) images were obtained using a FEI Tecnai G2 F20 microscope. CQD powders were pressed in a sample holder of a FTIR spectrometer (VERTEX 70 FTIR) and measured. Background and blank measurements were taken before spectra acquisition to better identify peaks. UV-visible measurements were taken from 900 to 200 nm using a Varian Cary 50 Spectrophotometer (Varian Inc., North Carolina) where background and blank measurements were taken before for more accurate results. Photoluminescence (PL) measurements were taken with a Fluorolog spectrophotometer (QM-7/2005, Photon Technology International, London. ON) with excitation and emission slit widths of 0.25 and 0.1 mm respectively. All UV-Visible and PL measurements were done in a 10 mm quartz cuvette. The PL quantum yield (QY) was calculated using the following equation:

$$\Phi_{\mathrm{PL}} = \frac{I_x}{I_{st}} \frac{A_{st}}{A_x} \left(\frac{\eta_x}{\eta_{st}}\right)^2 x\ 100\ \%$$

where I is the integrated PL emission intensity of an emission spectra excited at 350 nm, A is the absorbance value measured at 350 nm from the UV-Vis spectra, η is the refractive index of the solvent, x and st refer to the CQDs and the PL standard quinine sulfate in 0.1 M HCl (Eaton, 1988). 350 nm was used for quinine sulfate and the max excitation wavelength for each CQD was used for QY experiments, respectively.

Electrochemical and ECL Experiments

A custom photoelectrochemical cell, with a flat Pyrex window at the bottom to allow the detection of light generated at the

working electrode, was used for all electrochemical and ECL tests. A three-electrode electrochemical system, where a glassy carbon electrode (GCE, 3 mm diameter) was used as the working electrode, a platinum wire was used as the counter electrode and a custom Ag/AgCl electrode calibrated to an industrial standard Ag/AgCl electrode before operation. All solutions used were 0.1 M phosphate buffer solution (PBS) (pH = 7.5) with 0.1 M KCl as the supporting electrolyte. Dissolved oxygen in the system had a quenching effect for CQD ECL systems seen previously (Zhang et al., 2017), so all solutions were purged for 15 min with argon gas before use. For ECL film studies, 3 mg of GQDs were dispersed in 3 mL of Milli-Q water and were sonicated for 10 min before use. Ten Microliter of this solution was dropcasted onto the surface of the GCE and dried at room temperature. To prevent the GQDs dispersing in solution, a thin layer of Chitosan (0.2 mg mL^{-1} in Milli-Q water, 5 μL) was dropcasted on top of the GQD layer.

The voltammetric ECL curves were obtained using an electrochemical workstation (CHI 610A, CH Instruments, Austin TX) coupled with a photomultiplier tube (PMT, R928, Hamamatsu, Japan) held at −750 V with a high-voltage power supply. The ECL generated at the working electrode was collected by the PMT under the Pyrex window at the bottom of the electrochemical cell. The photocurrent from the PMT was transferred into a voltage signal by a picoammeter (Keithley 6487, Cleveland, OH). This signal, along with the potential and current signals from the electrochemical workstation were simultaneously sent through a data acquisition board (DAQ 6036E, National Instruments, Austin TX) to the computer where the entire data was recorded by a homemade LabVIEW (National Instruments) program. Spooling ECL spectra were acquired by placing the electrochemical cell into a holder on a spectrograph (Cornerstone 260 M, Newport, Irvine, CA) with a CCD camera (Andor 420BV, Andor Technology, UK) cooled to −55°C. The exposure time and the number of kinetic series were optimized to produce the clearest ECL spectra. A carefully measured lens system which collimated light produced from the entire electrode surface (∼7 mm^2 circle) onto the spectrometer/CCD camera set, permitting sensitive detection of light emitted from CQD films on the electrode surface while ignoring any other potential light sources. During all experiments, lights in the experimentation room were turned off to reduce the background interference from ambient light. Blackout curtains were also positioned at the entryways to the lab and surrounding the electrochemical cell setup to prevent possible interference. Wavelength calibration was conducted using a mercury-argon source (HG-1, Ocean Optics, Largo, FL). The relative efficiency of the ECL emission was calculated by finding the charge input and the photocurrent output for this specific experimental setup and comparing these values to the gold standard ECL emitter systems, $Ru(bpy)_3^{2+}$ for annihilation systems and $Ru(bpy)_3^{2+}/S_2O_8^{2-}$ for CQD/ $S_2O_8^{2-}$ systems by the following equation:

$$\Phi_{ECL} = \frac{\left(\frac{\int ECL\ dt}{\int Current\ dt}\right)_x}{\left(\frac{\int ECL\ dt}{\int Current\ dt}\right)_{st}} x\ 100\ \%$$

where *st* and *x* refer to the standard $Ru(bpy)_3^{2+}/S_2O_8^{2-}$ and the $CQD/S_2O_8^{2-}$ systems, respectively, for example.

RESULTS AND DISCUSSION

Carbon Quantum Dot Synthesis

Citric acid was used as the carbon precursor for a hydrothermal synthesis owing to the efficient carbonization as reported by Dong et al. (2012). Urea was added as a nitrogen-dopant (N-doped) following our previous studies that report photoluminescence (PL) and ECL enhancements of nitrogen- and sulfur-doped graphene quantum dots (Zhang et al., 2017). Typical hydrothermal procedures were used as following: 50.0 g/L of citric acid and 100.0 g/L of urea in varying volumes of ultrapure water in a 100 mL Teflon-lined autoclave and heated at 160°C for 6 h. The volumes of the starting precursor solution were 10 mL (CQD10), 20 mL (CQD20), 30 mL (CQD30), and 40 mL (CQD40), respectively, as seen in **Scheme 1**. Yields of synthesis were measured by comparing the weight of starting precursors to the weight of the final CQD product and were found to be between 27 and 35%. An important factor for light emitting materials is the bulk low-cost synthesis of the product (Jing et al., 2019). This synthesis procedure created gram-scale CQDs with constant oven settings and constant starting solutions providing ideal conditions for scaling up synthesis of CQDs with tunable light emitting properties. A simple and gram-scaled synthesis is always required for optimization and testing of the CQDs' PL, ECL, and EL emission properties for future device testing. The cost and simplicity of CQDs described above make them an attractive light emitting material for future LEC devices over single molecules (such as highly luminescent carbozolyl derivatives Li et al., 2019), copolymers [e.g., commercially available PPV copolymer PDY-132 Gambino et al., 2013) and ionic transition metal complexes (such as Ru, Ir, and Cd derivatives Costa et al., 2012) typically used for LECs and optoelectronics. Using 100 mL volume autoclaves allows gram scale syntheses of CQDs instead of smaller laboratory amounts.

Characterization

HRTEM of CQDs

High-resolution transmission electron microscopy (HRTEM) images of CQD10 (**Figure 1A**), CQD20 (**Figure 1B**), CQD30 (**Figure 1C**), and CQD40 (**Figure 1D**) were measured (ca. 120 individual CQDs per synthesis method) and statistical distributions were calculated and fitted to the size distributions. These CQDs displayed average sizes of 1.5 ± 0.3, 2.9 ± 1.2, 7.6 ± 3.1, and 23.8 ± 15.2 nm, respectively. The HRTEM results have revealed a gradual increase in the particle size with augmented volume of the starting solution for the hydrothermal synthesis. The increased carbon precursor appears to increase both the size distribution and particle size, **Figures 1A–D**. Reaction temperature, time, and concentration were all kept constant in this study yielding unique CQDs. The above results revealed a relationship between volume of CQD precursors (i.e., precursor availability) and size of CQDs produced, leading to a simple way to control the size of particles during hydrothermal syntheses.

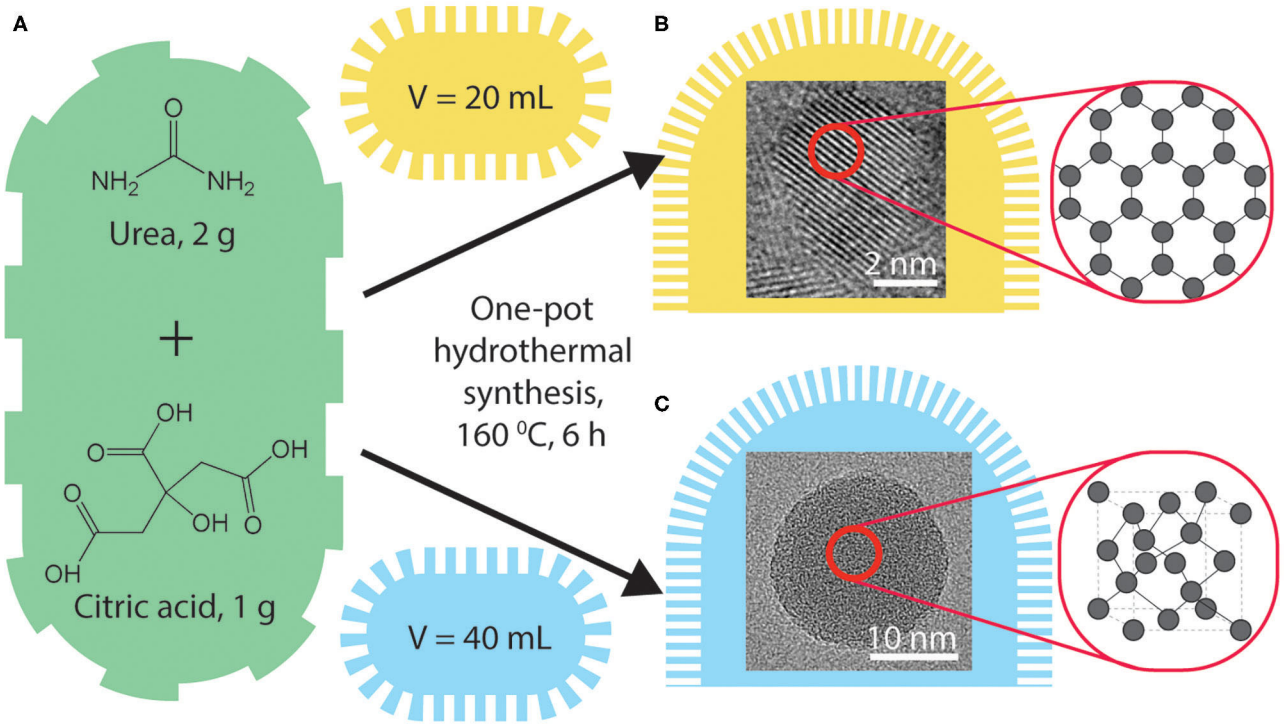

SCHEME 1 | A schematic representation of CQD synthesis from precursors **(A)**. HRTEM images of the created CQDs with carbon arrangements identified, synthesized with autoclave volumes of 10, 20 mL **(B)** and 30, 40 mL **(C)**.

While using different volumes of the same starting solution, higher volumes created larger CQDs. This may be due to increased autoclave pressure increasing energy available during synthesis or availability of reagents available for CQD synthesis. This finding would be significant, because varying CQD sizes has been shown to change physical and electronic properties (Liu et al., 2019; Wang et al., 2019). This control is highly attractive for light emitting materials of future LEC devices.

The HRTEM insets of each panel in **Figure 1** are higher-resolution images of individual CQDs. The insets of **Figures 1A,B** how 0.23 nm graphene lattice spacing corresponding to a (1,120) graphene lattice plane (Cong et al., 2013). We observed this graphitic nature in CQD10 and CQD20, while the larger CQD30 and CQD40 do not. This could be due to increased availability of carbon precursor favoring a disordered carbon sp^3 structure, or a heterogeneous mixture of different carbon bonding states. The differences in the carbon bonding of the CQDs has been shown to affect the emission of CQDs (Liu et al., 2019; Wang et al., 2019). Increased graphene nature can cause greater electron delocalization and stabilize the CQDs. The differences in core states observed by HRTEM should provide changes in the emissions of these CQDs, allowing for a platform to optimize the CQDs for electrogenerated chemiluminescence (ECL) for use in optoelectronics. Also, for optoelectronic devices, consistency and packing of CQD films are of the upmost importance since film quality and properties often rely on particle sizes and how they interact (Winkler et al., 2006). For this reason, the size and crystallinity of CQDs are paramount and should greatly affect the optoelectronic performance of the films.

FTIR of CQDs

Absorptions between 3,000 and 3,300 cm^{-1} correspond to O-H and N-H vibrations as demonstrated in **Figure 2**. The broadness of these peaks indicates that the O-H and N-H are involved in extensive hydrogen bonding between the CQDs. Prolonged freeze-drying at temperatures below 200 K ensure all water was sublimated out from these CQDs, leaving these broad peak identities to be exclusively from hydrogen bonding between CQDs. A broad band at 2,800 cm^{-1} shows C-H stretching characteristic of carbon structures. The bands at 1,700 and 1,600 cm^{-1} were attributed to the vibrational absorption bands of −COOH and C=C, respectively. All FTIR peak assignments agree well with those previously reported studies for CQDs prepared differently (Vinci et al., 2015; Zhang et al., 2017; Dager et al., 2019). No obvious functional group differences between CQDs are demonstrated in **Figure 2,** which suggests synthesis mechanism is similar, if not the same, between all samples. Although contentious, studies demonstrate evidence for PL and ECL emissions from CQDs originating from surface defects, which are loosely defined as functional groups, oxygen-related disorder-induced localized states and surface defects in carbon structures (Gan et al., 2016; Kroupa et al., 2017). Smaller CQDs have more functional groups per mass compared

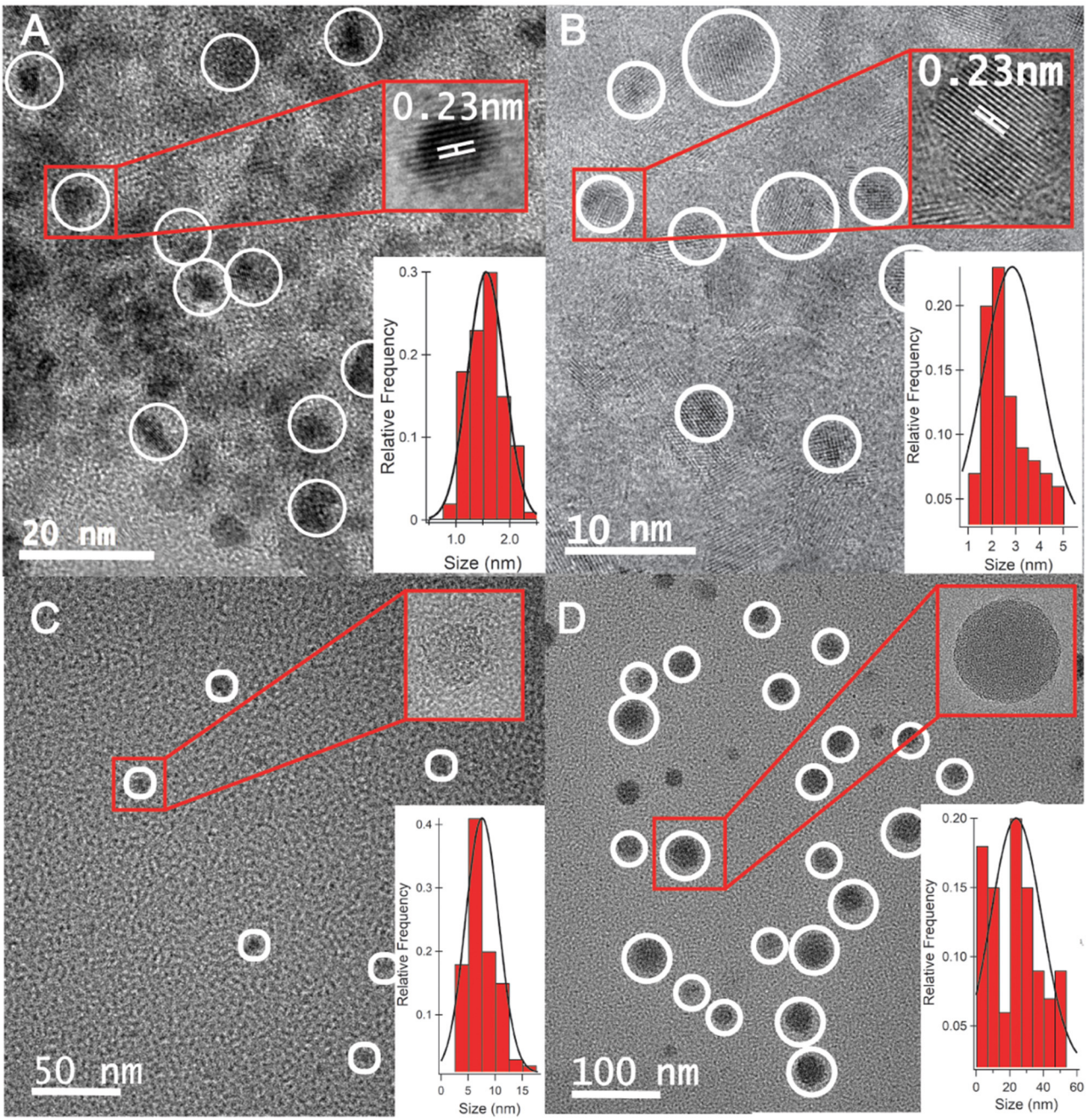

FIGURE 1 | HRTEM analysis of **(A)** CQD10, **(B)** CQD20, **(C)** CQD30, and **(D)** CQD40, each containing a high-resolution image of a single CQD and a histogram of particle sizes fitted with a Gaussian distribution.

to larger CQD particles due to the increased surface area per mass. The variation in functional group density might lead to differences in the PL, ECL, and EL emissions of CQD films.

Tauc Plot

Figure 3A displays a Tauc plot generated from the UV-Vis spectrum of a CQD10 water dispersion at a concentration of 5 g/L. The Tauc plot displays $(ah\nu)^{1/r}$ vs. $h\nu$, where a, h, and ν are absorption coefficients and r is the power factor used as a fit for the set of data. The best fit found from **Figure 3A** is $r = ½$ indicating a direct band gap transformations for the CQD dispersion, aligning well with previously found results on CQDs prepared with hydrothermal methods (Liu et al., 2015; Yang et al., 2015; He et al., 2018). This direct band gap will favor radiative recombination benefitting electrochemiluminescence

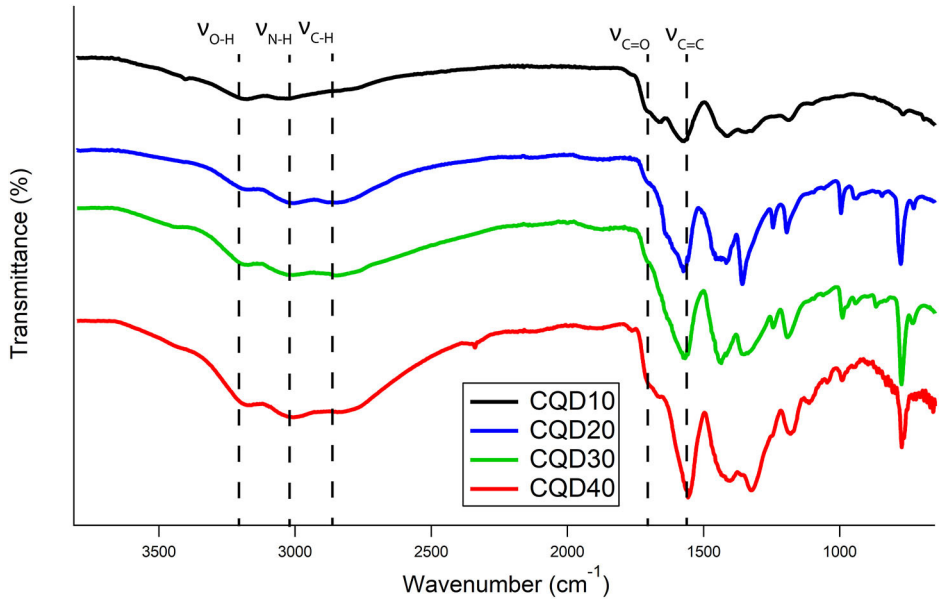

FIGURE 2 | FTIR spectra of CQD10 (black), CQD20 (blue), CQD30 (green), and CQD40 (red).

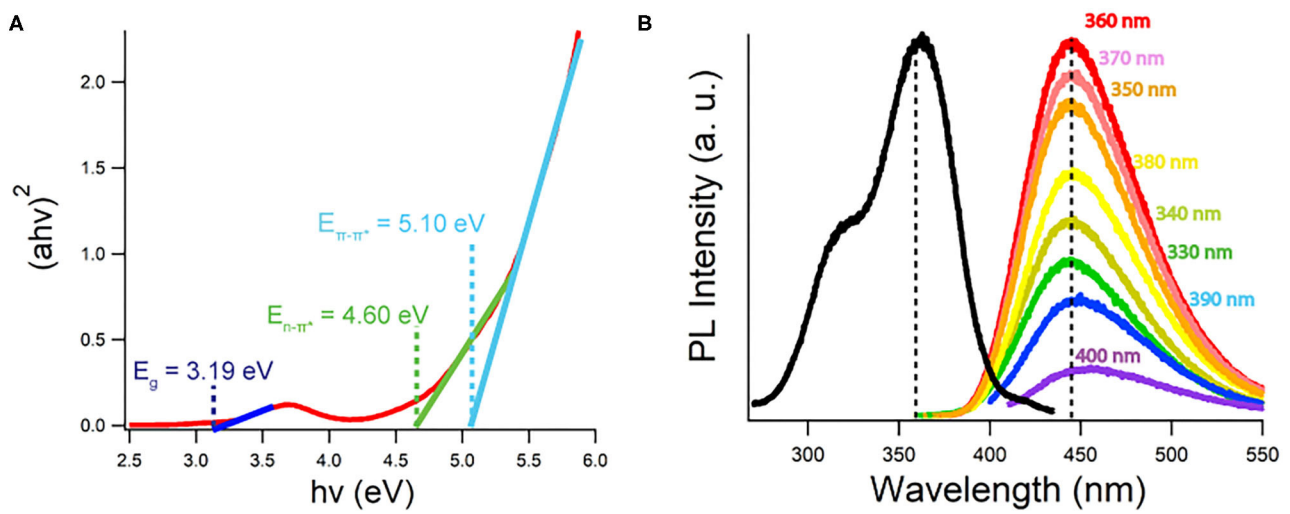

FIGURE 3 | (A) Tauc plot generated from 5 g/L CQD10 UV-Vis absorption data created with a direct band gap ($r = ½$). **(B)** Photoluminescence spectra of 5 g/L of CQD10 in water dispersion at excitation wavelengths listed. Black scan measures 440 nm PL intensity vs. excitation wavelengths.

quantum yield and electroluminescent device efficiencies, as well as achieving strong PL efficiencies. Linear extrapolations to the x-intercept from the low energy side of peaks in the Tauc plots yields specific absorption energies. Tauc plots were constructed for all CQDs, where information gained is summarized in **Table 1**. The lowest energy absorption in the visible range is due to the band gap of the CQDs. No large deviations from the optical band gap are observed indicating that the state responsible for emission, is shared among all CQDs, despite carbon core state differences. An intrinsic semiconductor E_g is illustrated at 3.19 eV corresponding to a blue wavelength absorption. The second peak, common in every Tauc plot generated around 4.60 eV, corresponds to non-bonding electrons in oxygen and nitrogen dopant atoms in the carbon sp^2 or sp^3 matrix (He et al., 2018). A significant 0.3 eV shift is noticed comparing the $E_{n-\pi^*}$ between CQD10 and the other CQDs in this study. CQD20, CQD30 and CQD40's $E_{n-\pi^*}$ is more pronounced indicating a larger number of dopants in the carbon sp^2 or sp^3 matrix (**Supplementary Figure 1**). As noticed above, the IR spectra showed no significant variations in functional groups between

TABLE 1 | Electronic information on all CQDs samples.

Sample name	E_g(eV)	$E_{n-\pi^*}$ (eV)	$E_{\pi-\pi^*}$ (eV)	Emission λ_{PL} (nm)	Φ (% vs. Quinine sulfate)
CQD10	3.18	4.60	5.10	440	18
CQD20	3.26	4.93	5.60	435	34
CQD30	3.25	4.90	5.63	435	18
CQD40	3.16	4.90	5.60	435	24

the synthesized CQDs, thus, following this, the difference in absorptions between the CQDs could be from nitrogen and oxygen dopants in the carbon matrix. The small average size of the CQD10 could prevent the development of more complex types of non-bonding electron containing nitrogen moieties (i.e., pyridinic, and pyrrolic moieties). The subtle differences between syntheses parameters may yield more complex nitrogen doping, leading to different absorptions between some CQDs. This absorption difference may be attributed to a higher presence of non-bonding electron moieties found in larger carbon matrices. The third absorption, which was common to all CQDs, was the $E_{\pi-\pi^*}$ transition attributed to the sp^2 electrons in the carbon matrix (Kroupa et al., 2017).

Excitation Wavelength Dependence of Photoluminescence

By tracking the maximum emission wavelength at 440 nm while varying the excitation wavelength, the black trace in **Figure 3B** is attained for a 5 g/L CQDs dispersion in Milli-Q water. There appears to be two excitation peaks where the maximum PL emission was achieved by using a 360 nm excitation wavelength. Excitations from 330 to 400 nm and their resulting emissions color-coded are shown in **Figure 3B**, where excitation wavelengths outside this range were omitted due to negligible light emission. The same emission maximum wavelength was achieved from all excitation wavelengths tested within a reasonable error. This excitation wavelength independence suggests that one emission pathway is responsible for almost all band gap emissions from the CQDs. Despite the size distribution of the CQDs, no large differences were noticed in the PL emission, suggesting a common emission state. Liu et al. has demonstrated that short wavelength emissions originate from core states and long wavelength emissions emit from surface states (Liu et al., 2019). Gan et al. has also summarized recent findings, describing a common hypothesis that CQDs have an emission resulting from 1 to 5 nm sp^2 carbon centers in all CQD sizes (Gan et al., 2016). Despite large size differences, common emission states existed between all CQDs providing evidence for small sp^2 light emitting sites dominating PL emissions in these CQDs. It is plausible that the emissions seen in **Figure 3B** do not resemble surface state emissions or are dominated solely by one surface state emission due to their excitation wavelength independent emissions.

The peak emission wavelength is seen at 440 nm for CQD10 in **Figure 3B**. Other maximum wavelengths obtained from PL are summarized in **Table 1** for all CQDs in this study. The maximum emission wavelengths from all CQDs are similar with small variation centered around 440 nm. Using the International Commission on Illumination (CIE) standards for relating color to light through red, green and blue (RGB) contributions, the PL emission from all CQDs corresponds to a deep blue emission with CIE coordinates of (0.15, 0.09). This shows that large size differences of the CQDs has little effect on the PL wavelength emitted.

PL quantum yields (Φ_{PL}) of all CQDs were determined relative to a quinine sulfate standard ($C_{40}H_{50}N_4O_8S$), chosen for its similar emission wavelength to CQDs at 450 nm. The most efficient emission is from CQD20 with a relative quantum yield Φ_{PL} of 34 %. There was no obvious trend in the emission efficiency of the four prepared CQDs. This shows that large size differences of the CQDs have little effect on the PL efficiency. The intensity of the emission and direct band gap nature of the CQDs, show favorable properties for efficient emission in optoelectronic devices.

Electrochemistry and Electrochemiluminescence of Carbon Quantum Dots

Electrochemistry of CQD Dispersions

The electrochemistry of dispersed CQD10 in solution was explored in a supporting electrolyte solution of 0.1 M phosphate buffer solution (PBS) at a pH of 7.5 containing 0.1 M KCl by cyclic voltammetry (CV) and differential pulse voltammetry (DPV) as shown in **Figures 4A,B**, respectively, with a glassy carbon electrode (GCE) as the working electrode. All potentials are referred to vs. Ag/AgCl. In **Figure 4A**, a small irreversible peak at −1.7 V and a small slightly more reversible peak can be seen at 1.3 V. To better illustrate these peaks, DPV is shown in **Figure 4B** where background current is suppressed more than in CV. Comparing the red and black traces, representing a solution with and without dispersed CQD10s, respectively, the redox reaction features of the CQDs are well-displayed in **Figure 4B**. The cathodic scan shows two irreversible reductions at formal potentials −1.4 V and −1.7 V. All redox reactions, which may be hidden in the charging current seen in the CV in **Figure 4A**, are very evident in the DPV in **Figure 4B**. The anodic scan illustrates a slightly more reversible oxidation at a formal potential of 1.3 V. Finding these CQD redox reactions allows for the testing of ECL emission.

The electrochemical gap (EE_g) between the first reduction peak and the first oxidation peak for CQD10 is found to be 2.65 V. In fact, EE_g was determined from converting the peak difference in volts to electron volts (eV) using an elementary charge of 1 for an electron. DPV was performed on all CQDs in this study and the corresponding EE_g data is summarized in **Table 2**. The larger CQDs (CQD30 and CQD40) had larger EE_g's likely due to the difference in carbon core. The larger and unordered carbon nature may increase the energy needed for redox reactions in solution due to significant electron transfer barriers between differently ordered states.

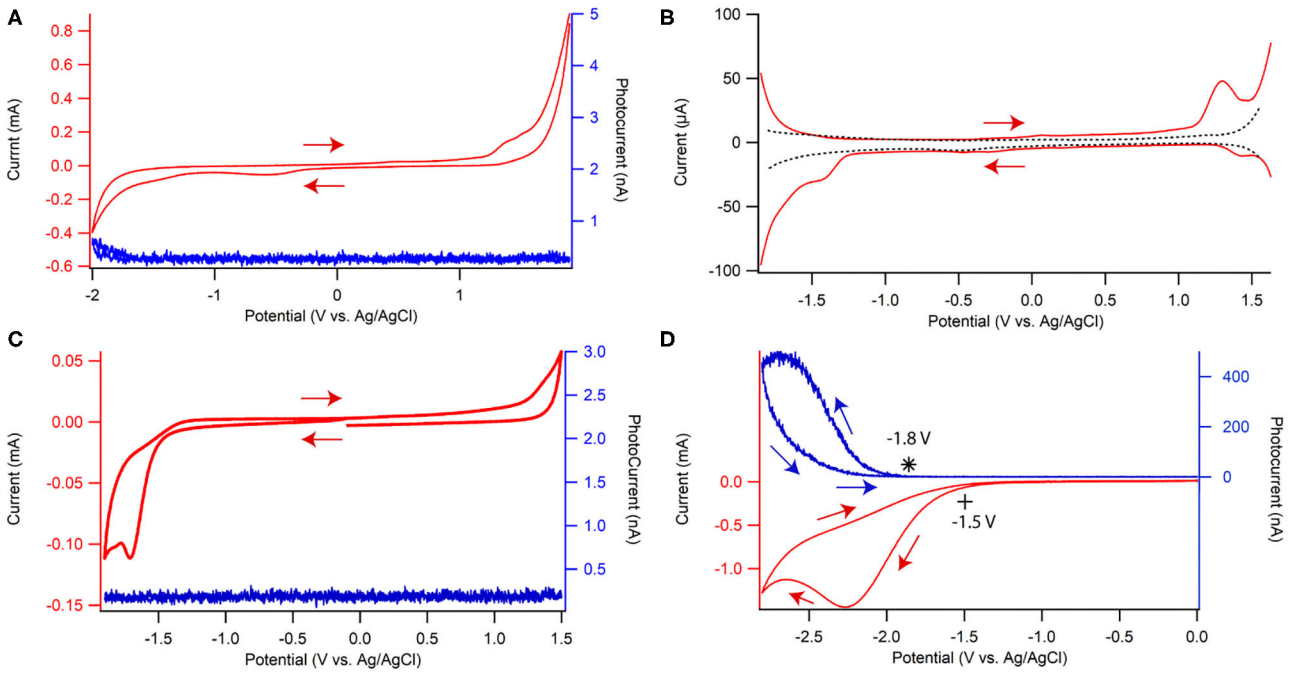

FIGURE 4 | (A) Cyclic voltammogram ECL-voltage curve and **(B)** differential pulse voltammograms of 0.1 g/L CQD10 in 0.1 M phosphate buffer solution at pH of 7.5 with 0.1 M KCl as the supporting electrolyte. Cyclic voltammograms (red) and ECL-voltage curves (blue) of a CQD-modified glassy carbon electrode in the same solution without **(C)** and with **(D)** 100 mM $K_2S_2O_8$, where * denotes the onset of photocurrent during the ECL-Voltage curve. ECL intensity is represented by the photocurrent measured with a photomultiplier tube biased at −750 V.

TABLE 2 | Electrochemical information from differential pulse voltammetry of all CQDs in solution and electrochemiluminescence testing of CQD films in the presence of potassium persulfate.

Sample name	Electrochemical gap (EE_g) (eV)	Maximum emission λ_{ECL} (nm)	Φ_{ECL} (% vs. $Ru(bpy)_3^{2+}$ with 50 mM $K_2S_2O_8$)
CQD10	2.65	680	96
CQD20	2.71	670	23
CQD30	3.01	750	2
CQD40	2.90	750	3

To understand the electrochemical behavior of a CQD film, GCEs were modified by casting 10 μg of CQDs, followed by 1 μg of chitosan to prevent CQDs dispersing in electrolyte solution. Chitosan was used to allow the CQD film to interact with solution species, and for its stability in neutral solution pH (pH > 6.5) (Suginta et al., 2013; Wu et al., 2014; Xiong et al., 2014; Yan et al., 2016; Eksin et al., 2017; Gonzalez et al., 2018; Sun et al., 2018; Tashkhourian et al., 2018; Pan et al., 2019; Sisolakova et al., 2019; Yang et al., 2019). CV scans show a strong reduction centered at −1.7 V and a slight oxidation peak at 1.3 V in **Figure 4C**. The reduction and oxidation peaks match those in the CQD dispersion with larger values probably due to the overall film resistivity increase from chitosan at the solid/electrolyte interface. In polymer films, and more specifically chitosan films, the width of the electrochemical peaks in CVs increases and the current sensitivity toward analytes in the film decreases (Sisolakova et al., 2019). The position of the reduction and oxidation peaks shifts to higher energies relative to analyte in dispersion, owing to the hydrophobic regions of the polymer matrix interacting with the solution and complexing with analytes (Jayaprakash et al., 2017). Despite these matrix effects when using chitosan, analytical responses typically improve for analyte detection and electrochemical stability improves for films, all relative to solution. The above redox peak positions would guide us to perform and understand ECL experiments.

ECL in Annihilation Pathway

The light produced during the CV tests involving both the CQDs dispersion and its film are shown by the voltammetric ECL curves in blue in **Figures 4A,C**. This light typically comes from the relaxation of CQD*, which is produced *via* the reaction between $CQD^{\bullet+}$ and $CQD^{\bullet-}$ at the working electrode surface. Negligible ECL as photocurrent was seen in both CQD dispersion (**Figure 4A**) and film cases (**Figure 4C**) possibly indicating poor electron transfers between CQD radical cations and anions in the film and solution or the poor stability of one or both these electrogenerated intermediates.

Two Half Light-Emitting Electrochemical Cells

To test if the CQD film ECL could be enhanced, coreactants were added. Potassium persulfate ($K_2S_2O_8$) was added to produce sulfate radical anions that can interact with $CQD^{\bullet-}$ for ECL

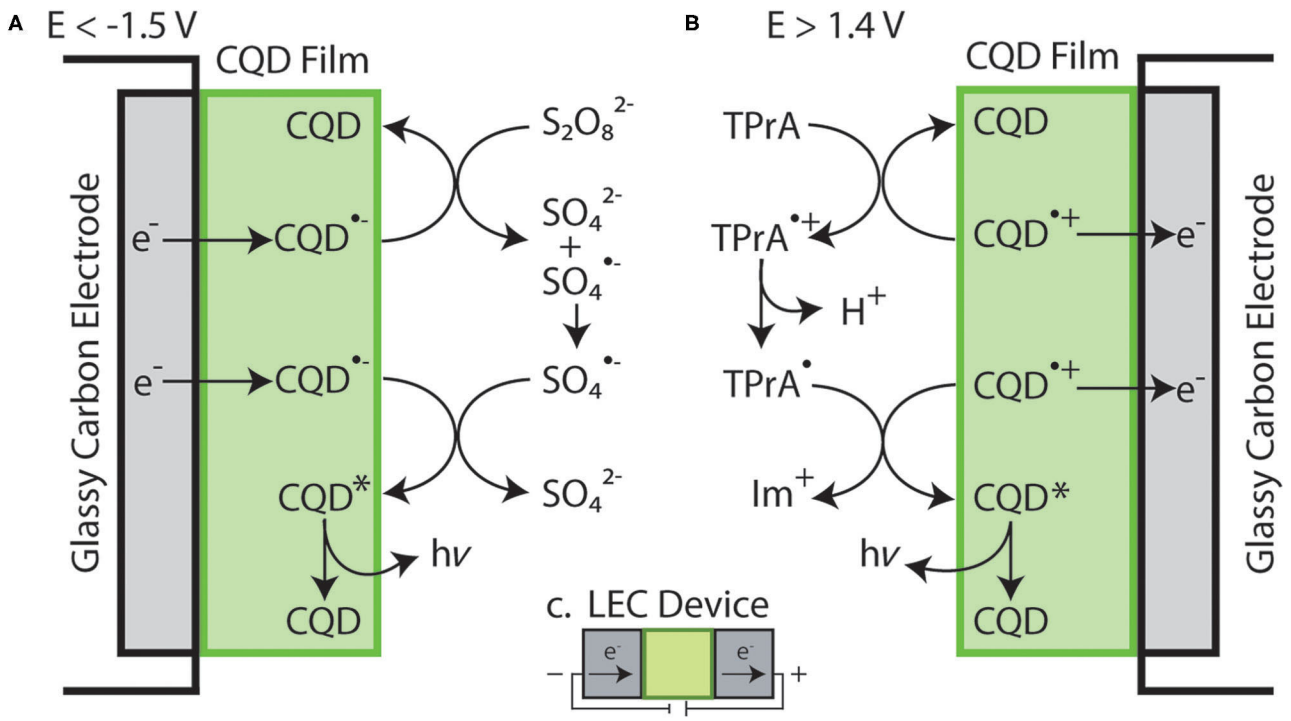

SCHEME 2 | Simplified illustration of reactions occurring at the surface of a CQD film coated on a glassy carbon electrode containing: **(A)** $S_2O_8^{2-}$ at a potential below −1.5 V vs. Ag/AgCl and **(B)** TPrA at a potential above 1.4 V vs. Ag/AgCl. **(C)** Illustration of the electron flow within a theoretical, fully constructed LEC device.

generation (**Figure 4D**) while tripropylamine (TPrA) was used to electrogenerate TPrA radicals which can interact with $CQD^{\bullet+}$ for ECL production (Hesari and Ding, 2016). These two coreactants are easily transferred into radicals at close redox potentials to CQDs, producing both highly oxidizing (sulfate radical anion) or reducing (TPrA radical) intermediates in the vicinity of the working electrode for further reactions for light emission. Here, the two coreactants are newly utilized to form two half light-emitting electrochemical cells for testing CQD films as potential lighting layers.

ECL of CQD Film/$S_2O_8^{2-}$ Interface as the First Half Light-Emitting Electrochemical Cell

$K_2S_2O_8$ is added to solution to test the stability and electron donating nature of $CQD^{\bullet-}$ in film that is formed at −1.70 V, **Figure 4D**. When biasing potentials more negative than −1.50 V, $S_2O_8^{2-}$ is electrochemically reduced, then $S_2O_8^{2-}$ loses SO_4^{2-} to become $SO_4^{\bullet-}$ (**Figure 4D**). $SO_4^{\bullet-}$ may react with a $CQD^{\bullet-}$ upon generation at −1.70 V to create CQD* that may release energy in the form of light (**Scheme 2A**). Significant photocurrent as ECL intensity was seen starting at −1.8 V, due to the formation of CQD* as illustrated by the blue trace in **Figure 4D**. The maximum ECL intensity reaches 530 nA at −2.7 V due to a buildup of both $CQD^{\bullet-}$ and $SO_4^{\bullet-}$ reacting to produce CQD*. When the potential was scanned in the reverse direction, the ECL intensity continues to decrease due to the depletion of $SO_4^{\bullet-}$ at the CQD film/solution interface. A blank sample containing only the coreactant and solvent showed negligible amounts of light at the same potentials (**Supplementary Figure 2**) allowing the light emission to be attributed to the $CQD^{\bullet-}$ reaction with $SO_4^{\bullet-}$ to produce CQD*, then giving off light.

Further, the relative efficiency of the ECL emission from the half-cell was determined by finding the charge input and the ECL output for the specific experimental setup and comparing these values to a common commercial ECL emitter system, $Ru(bpy)_3^{2+}/S_2O_8^{2-}$. ECL efficiency tests on this half-cell were performed from solutions with varying concentrations of $K_2S_2O_8$ yielding an optimized ECL efficiency at a concentration of 50 mM. Other three CQDs were also used to make film electrodes as above and their half-cells were tested as displayed in **Supplementary Figure 3**. ECL efficiencies were calculated for all CQDs at many $S_2O_8^{2-}$ concentrations but only the optimized 50 mM concentration results were summarized in **Table 2**. The smallest CQDs (CQD10) showed the best efficiency and the highest maximum ECL emission. The highest efficiency from CQD10 is roughly the same as the commercially available ECL emitter $Ru(bpy)_3^{2+}$ (96%) (Wallace and Bard, 1979). This half light-emitting electrochemical cell confirms the suitability as the cathodic lighting layer.

For each CQD film electrode, the film thickness is consistent, thus in the smaller CQD10 sample more particles exist on the electrode surface and certainly more functional groups that may produce surface state emissions. Further, only the smaller CQDs (CQD10 and CQD20) showed non-negligible ECL emissions (**Supplementary Figure 3**), providing further evidence for a

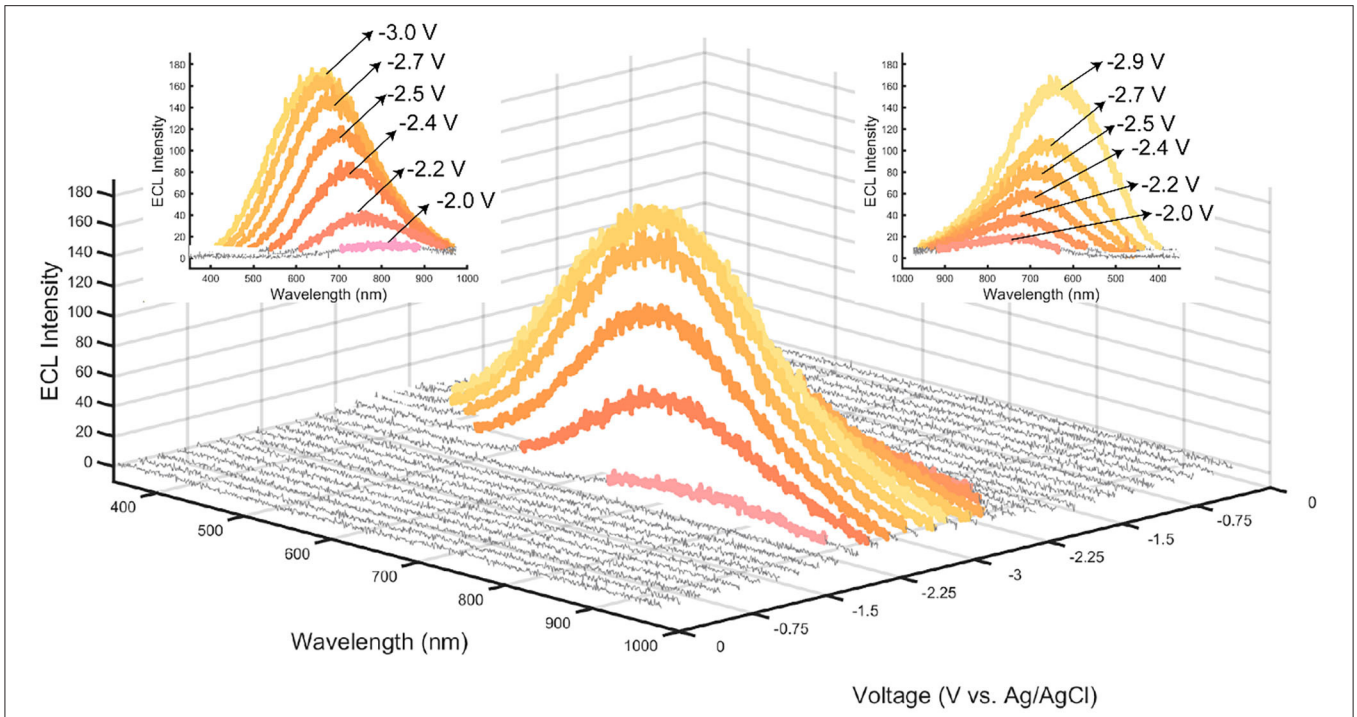

FIGURE 5 | ECL spooling spectra from a film of CQD10 with 50 mM $K_2S_2O_8$ taken with an exposure time of 2 s, a scan rate of 12.5 mV/s, yielding 120 spectra over a 240 s cyclic voltammogram. Color of individual spectra correspond to the RGB coordinates found by converting spectra using CIE coordinates. Spectra that show negligible light are displayed as gray. Insets show the wavelength of light emitted from a. the forward scanning starting at −2.0 V vs. Ag/AgCl and b. the reverse scan starting at −3.0 V vs. Ag/AgCl.

surface state ECL emission. CQD10 should be considered for optoelectronics based on its high ECL emitting efficiency.

ECL of CQD Film/TPrA System as the Second Half Light-Emitting Electrochemical Cell

Supplementary Figure 4 shows the addition of 50 mM TPrA coreactant to a CQD-modified electrode system during a potentiodynamic scan. The onset of oxidation for the TPrA is roughly at 0.7 V, generating $TPrA^+$, then $TPrA^\bullet$ through deprotonation. This $TPrA^\bullet$ can react with the electrogenerated $CQD^{\bullet+}$ created at 1.4 V, to produce an iminium and an excited state CQD*, that can further relax to produce light, **Scheme 2B**. Despite the highly oxidizing nature of $TPrA^\bullet$, negligible photocurrent was observed, indicating $CQD^{\bullet+}$ might not stable enough to react in accepting an electron from $TPrA^\bullet$. Furthermore, the electrochemical potentials to generate $TPrA^\bullet$ and $CQD^{\bullet+}$ are discrete greatly, which is unfavorable for the CQD* generation, probably due to the instability of both radicals. This half-cell suggests that $CQD^{\bullet+}$ stability and reactivity improvement is required for optoelectronic applications.

Comparison of Half-LECs to Full LECs

A simplified illustration of the CQD/$S_2O_8^{2-}$ and the CQD/TPrA systems are included in **Schemes 2A,B**, respectively. These individual systems can be thought of as LEC half-cells, where the cathode is **Scheme 2A** and the anode is **Scheme 2B**. This similarity between the electrochemical setups and a functioning LEC device are seen in **Scheme 2C**. The setup in **Scheme 2** has CQDs in a film in contact with an electrolyte solution and an electrode. LEC devices are similar, where light emitters are dispersed in a film with electrolyte but are between two electrodes instead of in contact with a solution and an electrode. In fact, ECL provides details about the stability of both ions that are electrogenerated, as well as relative light emission efficiencies, by allowing the testing of multiple coreactants with different reductive and oxidative strengths.

Spooling ECL Spectroscopy of the Film/Persulfate Half-Cell

A potential scanning cycle from 0 to −3.0 V was performed on the CQD film shown in **Figure 5**, where individual spectra were taken during this potential scan every 2 s (Hesari and Ding, 2016; Shu et al., 2017; Guo et al., 2018). Capturing spectrum during the scan (otherwise known as spooling spectroscopy), enables tracking the evolution/devolution of light emission processes during CV scans. Noticeable light is produced at −2.0 V indicating that at this potential, the electrogenerated $SO_4^{\bullet-}$ and $CQD^{\bullet-}$ react to create CQD*, emitting light. The PMT that was used to obtain the ECL-voltage curves is generally more sensitive than a CCD camera and was able to detect light emitted from CQD* at an earlier potential than the CCD camera as illustrated in **Figure 4D**. Throughout the cathodic potential scan, the wavelength of ECL light slowly blue shifts from a center of 770 nm at −2.0 V, to 650 nm at −3.0 V. This wavelength

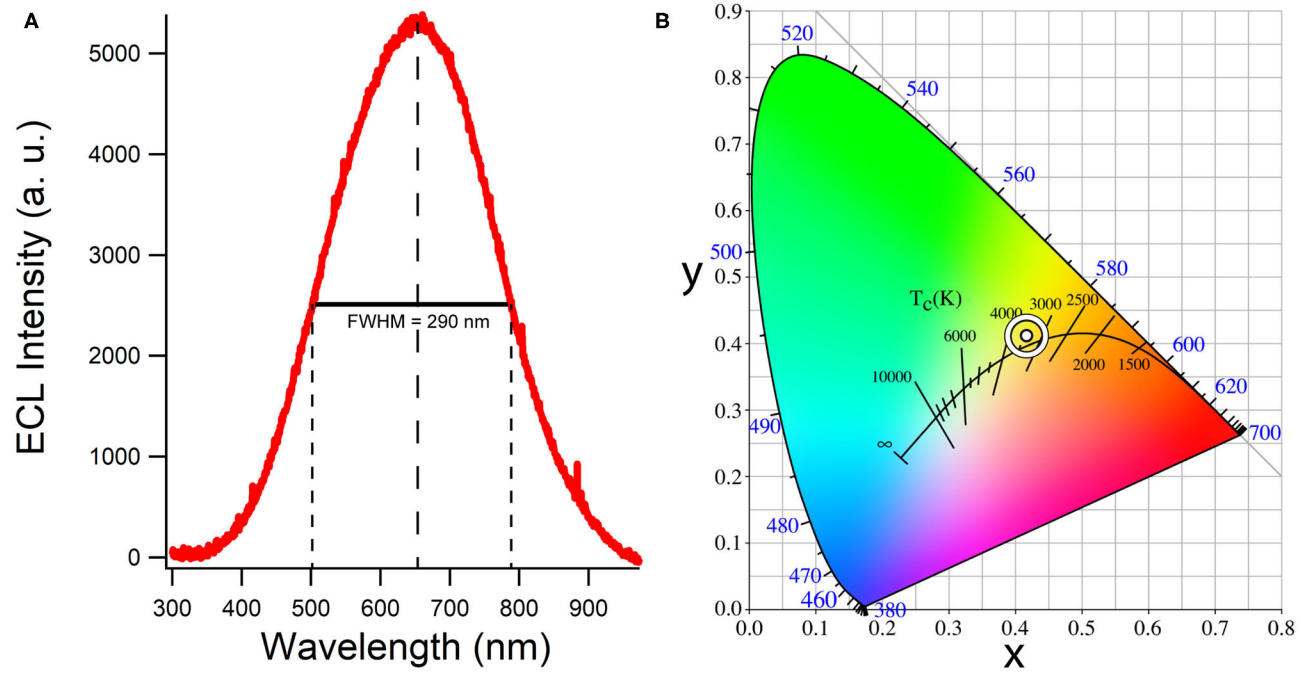

FIGURE 6 | (A) A background-subtracted accumulation of all light emitted during the same cyclic voltammogram of the system described in **Figure 5**. Full-width half maximum is displayed as well as the main emission wavelength. **(B)** The corresponding CIE color space co-ordinates and correlated color temperature.

variation may be due to the coexistence of different oxygen (−OH, −COOH, and −C=O) and nitrogen ($-NH_2$, −NRH, and $-CONH_2$) functional groups on the CQDs. These functional groups on the surface of the CQDs can contribute to many different surface states, all potentially acting as emissive traps at different potentials, thus changing the wavelength of emission (Bard et al., 2005; Gan et al., 2016; Liu et al., 2019). An increase in the overpotential or driving energy to the CQD films, allows accessing these different energy surface states and may lead to a shorter wavelength or higher energy ECL emission.

The color of each spectrum in **Figure 5** illustrates its emission color based on RGB coordinates calculated by a custom MATLAB code produced by our group that uses conventions adopted from the CIE xy chromaticity diagram. By tuning the potential applied to the film, a specific color of light can be achieved between −2.0 and −3.0 V. A wavelength variation is seen during the scan with a slow blue-shift from an emission centered at 790 nm for −2.2 V, to an emission centered at 660 nm for −3.0 V. This wavelength dependency on voltage yields a simple way to achieve multiple colors from one light emitter, providing an attractive emission characteristic for optoelectronic applications.

Accumulation ECL Spectra

Figure 6 illustrates an accumulation ECL spectrum during the potential scan shown in **Figure 4** over 30 s. The color emitted by the CQD film according to CIE color coordinates is a white light (0.42, 0.41) with a correlated color temperature (CCT) of 3,200 K estimated from the CIE diagram in **Figure 6**. This CCT value corresponds to a cool, bright and vibrant white and is generally used for most indoor lighting applications. Small CQD films yield relatively strong and efficient white light most likely due to efficient recombination of CQD* generated from $CQD^{\bullet-}$.

CONCLUSION

Herein, a protocol to prepare CQDs with controlled size was created from cost effective and readily available precursors. Smaller sized CQDs showed ordered graphitic nature observable in HRTEM but had roughly the same blue PL emission efficiency as the larger CQDs. This shows the PL emissions arising from all CQD particles in this study are similar. As a CQD film, the smallest CQDs had strong white light emission when reacted with 50 mM of the coreactant $S_2O_8^{2-}$. This emission was as efficient as a typical ECL standard in the same conditions, $Ru(bpy)_3^{2+}$. This ECL emission was centered at 650 nm and gave CIE co-ordinates of (0.42, 0.41) with a CCT of 3,200 K corresponding to a cool bright white light emission. This color of light is ideal for all indoor lighting conditions. The strong efficiency of light conversion, the ease of synthesis and the color temperature of the white light make CQD films a suitable light emitter candidate for LEC applications. Increased surface states per mass of CQDs for small CQDs may capture more holes from $SO_4^{\bullet-}$, allowing a higher ECL efficiency. These ECL tests serve as a simulated LEC half-cells where the stability of each electrogenerated ion can be probed using coreactants and the efficiency of light emission can be simply probed using comparisons to commercial light emitters. Future tests will focus on the implementation of CQDs

in LEC devices with improved stability and electron accepting nature of $CQD^{\bullet+}$.

DATA AVAILABILITY STATEMENT

The raw data supporting the conclusions of this article will be made available by the authors, without undue reservation.

AUTHOR CONTRIBUTIONS

JA, RZ, and ZD organized the manuscript. JA and ZD wrote the manuscript. LY, KC, JW, and DL discussed the results. ZD finalized the manuscript. All authors approved this manuscript.

FUNDING

We are very grateful to the financial support from Natural Sciences and Engineering Research Council Canada (NSERC, DG RGPIN-2013-201697, DG RGPIN-2018-06556, and SPG STPGP-2016-493924), Canada Foundation of Innovation, Ontario Innovation Trust (CFI/OIT, 9040) and Western University. This research is also partially supported by the opening project of the State Key Laboratory of Physical Chemistry of Solid Surfaces (201803) at Xiamen University in China.

ACKNOWLEDGMENTS

A special thank is owed to Prof. Honggang Liao's group at Xiamen University in China for the TEM characterization. The quality service from the Western Electronic Shop, Glass Shop, and ChemBio Store is very much acknowledged. We thank Dr. Ryan Maar and Daniela Cappello in Prof. Joe B. Gilroy's group for their assistance in utilizing their glovebox. We thank Dr. Rebecca Yardley in Prof. Elizabeth Gillies' lab for the assistance in utilizing their freeze-dryer.

SUPPLEMENTARY MATERIAL

The Supplementary Material for this article can be found online at: https://www.frontiersin.org/articles/10.3389/fchem.2020.580022/full#supplementary-material

REFERENCES

Bard, A., Ding, Z., and Myung, N. (2005). Electrochemistry and electrogenerated chemiluminescence of semiconductor nanocrystals in solutions and in films. *Struct. Bonding* 118, 1–57. doi: 10.1007/b137239

Chen, A., Liang, W., Wang, H., Zhuo, Y., Chai, Y., and Yuan, R. (2020a). Anodic electrochemiluminescence of carbon dots promoted by nitrogen doping and application to rapid cancer cell detection. *Anal. Chem.* 92, 1379–1385. doi: 10.1021/acs.analchem.9b04537

Chen, Y., Cao, Y., Ma, C., and Zhu, J.-J. (2020b). Carbon-based dots for electrochemiluminescence sensing. *Mater. Chem. Front.* 4, 369–385. doi: 10.1039/C9QM00572B

Cong, C. X., Li, K., Zhang, X. X., and Yu, T. (2013). Visualization of arrangements of carbon atoms in graphene layers by Raman mapping and atomic-resolution TEM. *Sci. Rep.* 3:1195. doi: 10.1038/srep01195

Costa, R. D., Orti, E., Bolink, H. J., Monti, F., Accorsi, G., and Armaroli, N. (2012). Luminescent ionic transition-metal complexes for light-emitting electrochemical cells. *Angew. Chem. Int. Ed.* 51, 8178–8211. doi: 10.1002/anie.201201471

Dager, A., Uchida, T., Maekawa, T., and Tachibana, M. (2019). Synthesis and characterization of mono-disperse carbon quantum dots from fennel seeds: photoluminescence analysis using machine learning. *Sci. Rep.* 9:14004. doi: 10.1038/s41598-019-50397-5

Dong, Y. Q., Shao, J. W., Chen, C. Q., Li, H., Wang, R. X., Chi, Y. W., et al. (2012). Blue luminescent graphene quantum dots and graphene oxide prepared by tuning the carbonization degree of citric acid. *Carbon* 50, 4738–4743. doi: 10.1016/j.carbon.2012.06.002

Eaton, D. F. (1988). Reference materials for fluorescence measurement. *Pure Appl. Chem.* 60, 1107–1114. doi: 10.1351/pac198860071107

Eksin, E., Zor, E., Erdem, A., and Bingol, H. (2017). Electrochemical monitoring of biointeraction by graphene-based material modified pencil graphite electrode. *Biosens. Bioelectron.* 92, 207–214. doi: 10.1016/j.bios.2017.02.016

Fresta, E., and Costa, R. D. (2017). Beyond traditional light-emitting electrochemical cells – a review of new device designs and emitters. *J. Mater. Chem. C* 5, 5643–5675. doi: 10.1039/C7TC00202E

Gambino, S., Bansal, A. K., and Samuel, I. D. W. (2013). Photophysical and charge-transporting properties of the copolymer SuperYellow. *Org. Electron.* 14, 1980–1987. doi: 10.1016/j.orgel.2013.03.038

Gan, Z. X., Xu, H., and Hao, Y. L. (2016). Mechanism for excitation-dependent photoluminescence from graphene quantum dots and other graphene oxide derivates: consensus, debates and challenges. *Nanoscale* 8, 7794–7807. doi: 10.1039/C6NR00605A

Gao, J. (2018). Polymer light-emitting electrochemical cells - recent advances and future trends. *Curr. Opin. Electrochem.* 7, 87–94. doi: 10.1016/j.coelec.2017.10.027

Gonzalez, C., Garcia-Beltran, O., and Nagles, E. (2018). A new and simple electroanalytical method to detect thiomersal in vaccines on a screen-printed electrode modified with chitosan. *Anal. Methods* 10, 1196–1202. doi: 10.1039/C8AY00161H

Guo, W., Ding, H., and Su, B. (2018). Electrochemiluminescence of metallated porous organic polymers. *J. Electroanal. Chem.* 818, 176–180. doi: 10.1016/j.jelechem.2018.04.037

He, S., Turnbull, M., Ding, Z. F., Nie, Y., and Sun, X. (2018). Band structures of blue luminescent nitrogen-doped graphene quantum dots by synchrotron-based XPS. *Surf. Sci.* 676, 51–55. doi: 10.1016/j.susc.2018.01.013

Hesari, M., and Ding, Z. (2016). Review—electrogenerated chemiluminescence: light years ahead. *J. Electrochem. Soc.* 163, H3116–H3131. doi: 10.1149/2.0161604jes

Hu, C., Li, M., Qiu, J., and Sun, Y. P. (2019). Design and fabrication of carbon dots for energy conversion and storage. *Chem. Soc. Rev.* 48, 2315–2337. doi: 10.1039/C8CS00750K

Jayaprakash, G. K., Swamy, B. E. K., Casillas, N., and Flores-Moreno, R. (2017). Analytical Fukui and cyclic voltammetric studies on ferrocene modified carbon electrodes and effect of Triton X-100 by immobilization method. *Electrochim. Acta* 258, 1025–1034. doi: 10.1016/j.electacta.2017.11.154

Jing, S. S., Zhao, Y. S., Sun, R. C., Zhong, L. X., and Peng, X. W. (2019). Facile and high-yield synthesis of carbon quantum dots from biomass-derived carbons at mild condition. *ACS Sustainable Chem. Eng.* 7, 7833–7843. doi: 10.1021/acssuschemeng.9b00027

Kroupa, D. M., Voros, M., Brawand, N. P., Mcnichols, B. W., Miller, E. M., Gu, J., et al. (2017). Tuning colloidal quantum dot band edge positions through solution-phase surface chemistry modification. *Nat. Commun.* 8:15257. doi: 10.1038/ncomms15257

Kusamoto, T., and Nishihara, H. (2018). Efficiency breakthrough for radical LEDs. *Nature* 563, 480–481. doi: 10.1038/d41586-018-07394-x

Li, X. J., Pan, F., Sun, C. K., Zhang, M., Wang, Z. W., Du, J. Q., et al. (2019). Simplified synthetic routes for low cost and high photovoltaic performance n-type organic semiconductor acceptors. *Nat. Commun.* 10:519. doi: 10.1038/s41467-019-08508-3

Liu, J., Liu, Y., Liu, N. Y., Han, Y. Z., Zhang, X., Huang, H., et al. (2015). Metal-free efficient photocatalyst for stable visible water splitting via a two-electron pathway. *Science* 347, 970–974. doi: 10.1126/science.aaa3145

Liu, M. L., Chen, B. B., Li, C. M., and Huang, C. Z. (2019). Carbon dots: synthesis, formation mechanism, fluorescence origin and sensing applications. *Green Chem.* 21, 449–471. doi: 10.1039/C8GC02736F

Pan, Q. X., Xu, Z. L., Deng, S. E., Zhang, F. L., Li, H., Cheng, Y. Z., et al. (2019). A mechanochemically synthesized porous organic polymer derived CQD/chitosan-graphene composite film electrode for electrochemiluminescence determination of dopamine. *RSC Adv.* 9, 39332–39337. doi: 10.1039/C9RA06912G

Qin, X., Dong, Y., Wang, M., Zhu, Z., Li, M., Yang, D., et al. (2019). *In situ* growing triethanolamine-functionalized metal-organic frameworks on two-dimensional carbon nanosheets for electrochemiluminescent immunoassay. *ACS Sens.* 4, 2351–2357. doi: 10.1021/acssensors.9b00914

Shu, J., Han, Z., Zheng, T., Du, D., Zou, G., and Cui, H. (2017). Potential-Resolved Multicolor Electrochemiluminescence of N-(4-Aminobutyl)-N-ethylisoluminol/tetra(4-carboxyphenyl)porphyrin/TiO2 Nanoluminophores. *Anal. Chem.* 89, 12636–12640. doi: 10.1021/acs.analchem.7b04175

Sisolakova, I., Hovancova, J., Orinakova, R., Orinak, A., Trnkova, L., Garcia, D. R., et al. (2019). Influence of a polymer membrane on the electrochemical determination of insulin in nanomodified screen printed carbon electrodes. *Bioelectrochemistry* 130:107326. doi: 10.1016/j.bioelechem.2019.06.011

Suginta, W., Khunkaewla, P., and Schulte, A. (2013). Electrochemical biosensor applications of polysaccharides chitin and chitosan. *Chem. Rev.* 113, 5458–5479. doi: 10.1021/cr300325r

Sun, C., Zou, Y., Wang, D. Y., Geng, Z. M., Xu, W. M., Liu, F., et al. (2018). Construction of chitosan-zn-based electrochemical biosensing platform for rapid and accurate assay of actin. *Sensors* 18:1865. doi: 10.3390/s18061865

Tashkhourian, J., Nami-Ana, S. F., and Shamsipur, M. (2018). Designing a modified electrode based on graphene quantum dot-chitosan application to electrochemical detection of epinephrine. *J. Mol. Liq.* 266, 548–556. doi: 10.1016/j.molliq.2018.06.093

Vinci, J. C., Ferrer, I. M., Guterry, N. W., Colon, V. M., Destino, J. F., Bright, F. V., et al. (2015). Spectroscopic characteristics of carbon dots (C-Dots) derived from carbon fibers and conversion to sulfur-bridged C-dots nanosheets. *Appl. Spectrosc.* 69, 1082–1090. doi: 10.1366/14-07749

Wallace, W. L., and Bard, A. J. (1979). Electrogenerated chemiluminescence. 35. temperature dependence of the ECL efficiency of Ru(bpy)2+ in acetonitrile and evidence for very high excited state yields from electron transfer reactions. *J. Phys. Chem.* 83, 1350–1357. doi: 10.1021/j100473a022

Wang, X., Feng, Y. Q., Dong, P. P., and Huang, J. F. (2019). A mini review on carbon quantum dots: preparation, properties, and electrocatalytic application. *Front. Chem.* 7:671. doi: 10.3389/fchem.2019.00671

Winkler, K., Plonska, M. E., Recko, K., and Dobrzynski, L. (2006). Remarkable solvent effect on the structure and electrochemical properties of $[M(bipyridyl)_{(3)}](ClO_4)_{(3)}$ (M = Co, Fe and Ru) films. *Electrochim. Acta* 51, 4544–4553. doi: 10.1016/j.electacta.2006.01.004

Wu, Q. X., Lin, D. Q., and Yao, S. J. (2014). Design of chitosan and its water soluble derivatives-based drug carriers with polyelectrolyte complexes. *Marine Drugs* 12, 6236–6253. doi: 10.3390/md12126236

Xiong, Y., Yan, K., Bentley, W. E., Deng, H. B., Du, Y. M., Payne, G. F., et al. (2014). Compartmentalized multilayer hydrogel formation using a stimulus-responsive self-assembling polysaccharide. *ACS Appl. Mater. Interfaces* 6, 2948–2957. doi: 10.1021/am405544r

Xu, X. Y., Ray, R., Gu, Y. L., Ploehn, H. J., Gearheart, L., Raker, K., et al. (2004). Electrophoretic analysis and purification of fluorescent single-walled carbon nanotube fragments. *J. Am. Chem. Soc.* 126, 12736–12737. doi: 10.1021/ja040082h

Yan, K., Xiong, Y., Wu, S., Bentley, W. E., Deng, H. B., Du, Y. M., et al. (2016). Electro-molecular assembly: electrical writing of information into an erasable polysaccharide medium. *ACS Appl. Mater. Interfaces* 8, 19780–19786. doi: 10.1021/acsami.6b07036

Yang, Y., Kong, W., Li, H., Liu, J., Manman, Y., Huang, H., et al. (2015). Fluorescent N-doped carbon dots as *in vitro* and *in vivo* nanothermometer. *ACS Appl. Mater. Interfaces* 7, 27324–27330. doi: 10.1021/acsami.5b08782

Yang, Z. W., Gao, M. Y., Wu, W. J., Yang, X. Y., Sun, X. W., Zhang, J. H., et al. (2019). Recent advances in quantum dot-based light-emitting devices: challenges and possible solutions. *Mater. Today* 24, 69–93. doi: 10.1016/j.mattod.2018.09.002

Yuan, F. L., Yuan, T., Sui, L. Z., Wang, Z. B., Xi, Z. F., Li, Y. C., et al. (2018). Engineering triangular carbon quantum dots with unprecedented narrow bandwidth emission for multicolored LEDs. *Nat. Commun.* 9:2249. doi: 10.1038/s41467-018-04635-5

Zhang, R., Nie, Y., Sun, X., Adsetts, J., and Ding, Z. F. (2017). Electrochemiluminescence of nitrogen- and sulfur-doped graphene quantum dots. *Carbon* 129, 45–53. doi: 10.1016/j.carbon.2017.11.091

Zhang, X. Y., Zhang, Y., Wang, Y., Kalytchuk, S., Kershaw, S. V., Wang, Y. H., et al. (2013). Color-switchable electroluminescence of carbon dot light-emitting diodes. *ACS Nano* 7, 11234–11241. doi: 10.1021/nn405017q

Conflict of Interest: DL was employed by the company Rosstech Signal Inc.

The remaining authors declare that the research was conducted in the absence of any commercial or financial relationships that could be construed as a potential conflict of interest.

Advantages of publishing in Frontiers

OPEN ACCESS
Articles are free to read for greatest visibility and readership

FAST PUBLICATION
Around 90 days from submission to decision

HIGH QUALITY PEER-REVIEW
Rigorous, collaborative, and constructive peer-review

TRANSPARENT PEER-REVIEW
Editors and reviewers acknowledged by name on published articles

Frontiers
Avenue du Tribunal-Fédéral 34
1005 Lausanne | Switzerland

Visit us: www.frontiersin.org
Contact us: frontiersin.org/about/contact

REPRODUCIBILITY OF RESEARCH
Support open data and methods to enhance research reproducibility

DIGITAL PUBLISHING
Articles designed for optimal readership across devices

FOLLOW US
@frontiersin

IMPACT METRICS
Advanced article metrics track visibility across digital media

EXTENSIVE PROMOTION
Marketing and promotion of impactful research

LOOP RESEARCH NETWORK
Our network increases your article's readership